Top-Quark Physics at Hadron Colliders

Von der Fakultät für Mathematik, Informatik und Naturwissenschaften der RWTH Aachen University zur Erlangung des akademischen Grades eines Doktors der Naturwissenschaften genehmigte Dissertation

vorgelegt von

Master of Science
Paul Fiedler

aus Altdöbern

Berichter: Universitätsprofessor Dr. rer. nat. Michał Czakon
Universitätsprofessor Dr. rer. nat. Werner Bernreuther

Tag der mündlichen Prüfung: 17.03.2017

Diese Dissertation ist auf den Internetseiten der Universitätsbibliothek online verfügbar.

Abstract

Top-quark pair production is one of the fundamental processes under investigation at current hadron-collider experiments and plays an important role in various phenomenological applications within the Standard Model as well as in the search for new-physics contributions. Therefore, a lot of effort is put into the further improvement of its theoretical description to cope with the continuing progress in experimental precision, in particular in the light of the current and upcoming runs of the Large Hadron Collider. For a long time, the state-of-the-art theoretical predictions consisted of a fixed-order perturbative evaluation at next-to-leading order (NLO) in the strong coupling possibly refined by an all-order treatment of dominant radiation effects, either through parton showers or soft-gluon resummation. However, for the total inclusive production cross section in the recent years the first calculations at genuine next-to-next-to-leading order (NNLO) accuracy became available, starting with the results for the quark annihilation channel and soon followed by the $\mathcal{O}(\alpha_s^4)$ contributions to the other partonic production modes containing at least one initial-state fermion.

In this thesis, the methods and tools necessary for such an advanced perturbative analysis are presented focusing in particular on the derivation of the two-loop virtual corrections required for a completion of the NNLO gluon-fusion-channel results. In addition, the corresponding findings are used to determine the NNLO hard matching coefficients that are of special phenomenological interest in next-to-next-to-leading logarithmic soft-gluon resummation. To this end, the soft function that appears in the theoretical description of the partonic cross section close to the pair-production threshold has to be evaluated at NNLO accuracy as well. It is conveniently parametrized in terms of a singlet/octet color basis of the final-state heavy-quark system and describes the emission of massless partons from eikonal lines representing the hard scattering process. While the singlet case may actually be inferred from Drell-Yan production, in this thesis the NNLO soft function for color-octet production is derived.

In order to extend the NNLO theoretical description of top-quark pair production also to the differential level, in a subsequent step the methods of the inclusive analysis are assembled into a unified Monte-Carlo framework that, in principle, allows for the calculation of arbitrary top-quark observables. Afterwards, this implementation is used to compute the long-sought-for $\mathcal{O}(\alpha_s^4)$ corrections to the top-quark forward-backward asymmetry at the Tevatron collider, which helps to finally reconcile the persisting discrepancy between theory and data. Moreover, NNLO predictions for the main kinematic distributions studied within the Tevatron top-quark-physics program are presented and analyzed with respect to their parametric dependence on the parton content of the initial-state (anti-)protons and the top-quark mass.

Zusammenfassung

Die Erzeugung von Top-Quark-Paaren in hadronischen Kollisionen gehört zu den grundlegensten Prozessen, die an aktuellen Beschleunigerexperimenten untersucht werden, und spielt eine wichtige Rolle bei einer Vielzahl von phenomenologischen Anwendungen innerhalb des Standardmodells sowie bei der Suche nach neuer Physik. Daher wird ein großer Aufwand zur stetigen Verbesserung von dessen theoretischer Beschreibung betrieben, um mit dem anhaltenden Fortschritt und der erhöhten Präzision bei der experimentellen Bestimmung mithalten zu können, insbesondere in Hinblick auf die derzeitige und die kommenden Betriebsphasen des Large-Hadron-Colliders. Lange Zeit bestand die genaueste Methode zur theoretischen Vorhersage dieses Prozesses in einer störungstheoretischen Behandlung zur ersten Ordnung in der starken Kopplungskonstanten, die mithilfe unterschiedlicher Verfahren zur Aufsummierung dominierender Strahlungskorrekturen zu allen Ordnungen in der Störungsreihe weiter verfeinert werden konnte. Hinsichtlich des totalen Wirkungsquerschnittes für die Top-Paarerzeugung entwickelte sich jedoch die Situation in den letzten Jahren dahingehend, dass die ersten vollständigen Berechnungen zur zweiten Ordnung in der störungstheoretischen Beschreibung verfügbar wurden, angefangen mit den Ergebnissen für die Erzeugung durch Quark-Annihilation und bald darauf auch für die übrigen Produktionskanäle, die mindestens ein Fermion im Anfangszustand enthalten.

In der vorliegenden Dissertation werden die wichtigsten Konzepte und Methoden vorgestellt, die für so eine fortschrittliche störungstheoretische Behandlung notwendig sind, wobei der Fokus vor allem auf der Herleitung der virtuellen Zwei-Schleifen-Korrekturen liegt, die zur Vervollständigung der theoretischen Vorhersagen im Gluon-Fusions-Kanal zur zweiten Störungsordnung erforderlich sind. Zudem werden die dadurch gewonnenen Erkenntnisse dazu genutzt, um ebenso die harten Matching-Koeffizienten, die von besonderem phenomenologischem Interesse bei der Aufsummierung von großen logarithmischen Korrekturen durch niederenergetische Gluon-Strahlung sind, zur zweiten Störungsordnung zu bestimmen. Zu diesem Zweck muss jedoch auch die sogenannte softe Funktion, die bei der theoretischen Beschreibung des Wirkungsquerschnittes nahe der Paarerzeugungsschwelle auftritt, zur zweiten Ordnung in der Störungsreihe ausgewertet werden. Diese Funktion beschreibt die Emission masseloser Teilchen auf der Basis von eikonalen Strömen, die den zugrundeliegenden harten Streuprozess nachbilden, wobei es am vorteilhaftesten ist den massiven Quark-Endzustand in einer Singlett/Oktett Farbbasis darzustellen. Für den Singlett-Fall kann man dabei auf die vorhandenen Ergebnisse im Drell-Yan-Prozess zurückgreifen, wohingegen die Berechnung für die Oktett-Produktion im Rahmen dieser Dissertation erfolgt.

Um auch bei der Vorhersage von differentiellen Wirkungsquerschnitten für die Top-Paarerzeugung von den Vorteilen durch die verbesserte störungstheoretische Behandlung zu profitieren, werden im darauffolgenden Schritt die verschiedenen Methoden und numerischen Verfahren, die bei der Analyse des totalen Wirkungsquerschnittes zum Einsatz gekommen sind, in ein einheitliches Software-Paket integriert, welches überwiegend auf Monte-Carlo-Methoden basiert.

Anschließend wird diese neuartige Implementierung dazu verwendet, um die fehlenden $\mathcal{O}(\alpha_s^4)$-Korrekturen zur Top-Quark-"forward-backward"-Asymmetrie am Tevatron-Beschleuniger zu berechnen, was dazu beiträgt, dass die theoretischen Vorhersagen endgültig in Einklang mit den vorhandenen experimentellen Daten gebracht werden können. Außerdem werden die Ergebnisse zur zweiten Störungsordnung für die primären kinematischen Verteilungen, die innerhalb des Top-Quark-Forschungsprogramms am Tevatron untersucht worden sind, präsentiert und hinsichtlich ihrer parametrischen Abhängigkeit in Bezug auf den Partongehalt der (Anti-)Protonen im Anfangszustand und die Top-Quark-Masse analysiert.

List of publications

This thesis is based on the author's research conducted at the Institute for Theoretical Particle Physics and Cosmology of the RWTH Aachen university. Parts of this work have already been published in the following series of papers:

Articles

M. Czakon, P. Fiedler and A. Mitov, *Total Top-Quark Pair-Production Cross Section at Hadron Colliders Through $O(\alpha_s^4)$*, *Phys. Rev. Lett.* **110** (2013) 252004, [1303.6254]

M. Czakon and P. Fiedler, *The soft function for color octet production at threshold*, *Nucl. Phys.* **B879** (2014) 236–255, [1311.2541]

P. Baernreuther, M. Czakon and P. Fiedler, *Virtual amplitudes and threshold behaviour of hadronic top-quark pair-production cross sections*, *JHEP* **02** (2014) 078, [1312.6279]

M. Czakon, P. Fiedler and A. Mitov, *Resolving the Tevatron Top Quark Forward-Backward Asymmetry Puzzle: Fully Differential Next-to-Next-to-Leading-Order Calculation*, *Phys. Rev. Lett.* **115** (2015) 052001, [1411.3007]

M. Czakon, P. Fiedler, D. Heymes and A. Mitov, *NNLO QCD predictions for fully-differential top-quark pair production at the Tevatron*, *JHEP* **05** (2016) 034, [1601.05375]

Proceedings

M. Czakon, P. Fiedler, A. Mitov and J. Rojo, *Further exploration of top pair hadroproduction at NNLO*, in *Proceedings, 27th Rencontres de Physique de La Vallee d'Aoste: La Thuile, Aosta, Italy, February 23-March 1, 2013*, 2013. 1305.3892

P. Fiedler, *Top pair cross section at NNLO*, in *Proceedings, 49th Rencontres de Moriond on QCD and High Energy Interactions: La Thuile, Italy, March 22-29, 2014*, pp. 161–164, 2014

Continuing some of the research activities started in the course of his master's program, during his PhD period the author of this thesis also made contributions to the following publications:

M. Misiak et al., *Updated NNLO QCD predictions for the weak radiative B-meson decays*, *Phys. Rev. Lett.* **114** (2015) 221801, [1503.01789]

M. Czakon, P. Fiedler, T. Huber, M. Misiak, T. Schutzmeier and M. Steinhauser, *The $(Q_7, Q_{1,2})$ contribution to $\overline{B} \to X_s\gamma$ at $\mathcal{O}\left(\alpha_s^2\right)$*, *JHEP* **04** (2015) 168, [1503.01791]

Contents

Abstract i

Zusammenfassung iii

List of publications v

1 Prologue: The top quark in the Standard Model and beyond 1
- 1.1 A short history of the top quark . . . 1
- 1.2 Top-quark properties . . . 3
  - 1.2.1 The top-quark mass . . . 3
  - 1.2.2 The total decay width Γ_t . . . 24
  - 1.2.3 Spin . . . 26
  - 1.2.4 Charge, color and weak isospin . . . 27
- 1.3 Top-quark phenomenology . . . 28
  - 1.3.1 Total inclusive top-quark pair production . . . 28
  - 1.3.2 Single top-quark production . . . 42
  - 1.3.3 Top-quark asymmetries . . . 58
  - 1.3.4 Differential distributions . . . 70

2 Theoretical foundation of hadronic $t\bar{t}$ production 85
- 2.1 Factorization theorem . . . 85
- 2.2 The partonic fluxes . . . 88
- 2.3 The partonic cross sections . . . 100
  - 2.3.1 The leading order partonic cross sections . . . 105
  - 2.3.2 The next-to-leading order partonic cross sections . . . 112

3 The total cross section of top-quark pair production at NNLO 135
- 3.1 Threshold effects at NNLO and beyond . . . 137
  - 3.1.1 Threshold expansion . . . 148
  - 3.1.2 Soft-gluon resummation . . . 172
- 3.2 Double-real radiation . . . 179
  - 3.2.1 Antenna subtraction . . . 181
  - 3.2.2 CoLoRFulNNLO (Completely Local subtRactions for Fully differential Predictions at NNLO) . . . 182
  - 3.2.3 Resummation-based approaches . . . 183
  - 3.2.4 STRIPPER . . . 185
- 3.3 Real-Virtual contributions . . . 197
- 3.4 Double-virtual corrections . . . 202
  - 3.4.1 The one-loop-squared contributions . . . 202
  - 3.4.2 The two-loop virtual contributions . . . 204

3.5 Results for the partonic and hadronic cross sections . . . 225
3.5.1 The qg- and $q\tilde{q}$-channels . . . 226
3.5.2 The quark annihilation channel . . . 232
3.5.3 The gluon fusion channel . . . 238
3.5.4 Theory error and comparison to experimental data . . . 245

4 Differential NNLO $t\bar{t}$ production at the Tevatron **257**
4.1 Forward-backward asymmetry . . . 264
4.1.1 Rapidity dependence . . . 268
4.1.2 Invariant-mass dependence . . . 272
4.1.3 Pair-transverse-momentum dependence . . . 277
4.1.4 Angular dependence and Legendre moments . . . 281
4.2 Differential top-quark distributions . . . 286
4.2.1 Top-quark rapidity . . . 287
4.2.2 Invariant mass of the $t\bar{t}$ pair . . . 290
4.2.3 Transverse momentum of the top quark . . . 293

5 Epilogue: Conclusions and perspectives **297**

Appendix **301**
A. UV renormalization . . . 301
B. IR renormalization . . . 304
C. Color dependence of threshold and resummation results . . . 307
D. Differential cross section predictions for the Tevatron . . . 315
E. Software . . . 323

Bibliography **325**

Acknowledgements **373**

Chapter 1

Prologue: The top quark in the Standard Model and beyond

1.1 A short history of the top quark

The top quark first entered the scene of elementary particle physics in 1973 when Kobayashi and Maskawa postulated a third generation of quarks [1] in order to explain the observed CP-violation in neutral Kaon decays [2]. Following the naming convention of the known quark generations, Harari suggested to call the components of this new isospin doublet "top" and "bottom" quark [3]. The first experimental evidence for this new model was provided by the discovery of the tau lepton[1] in 1975 [4] and, soon afterwards, by the detection of bottom-quark bound states at Fermilab in 1977 [5]. At that time an experimental proof of the top quark was anticipated within the near future but the isospin partner of the bottom quark remained hidden. A new hint towards its existence was supplied by electroweak (EW) precision measurements performed at the Large Electron-Positron Collider (LEP). Due to the strong dependence of radiative corrections for electroweak observables on the mass of the top quark, it was possible to derive stringent bounds for this parameter of the yet hypothetical particle[2], which is considered as one of the great successes of the SM. Finally, in 1995, the CDF and DØ collaborations succeeded in directly detecting top-quark pairs (and later also singly produced tops) in the predicted mass range at the Tevatron proton-antiproton collider at Fermilab [7–10] and thus completed the strongly-interacting sector as we know it today.

Due to its unique properties, the discovery of the top quark opened up a rich, new field of research in elementary particle physics. With a (pole) mass of $m_t = 173.34\,\text{GeV}$ [11] it is almost as heavy as a gold atom, a complicated composite object, and yet, to length scales accessible through experiment $\gtrsim 10^{-19}\,\text{m}$, it behaves as a point-like particle. Moreover, its mass is close to the scale of electroweak symmetry breaking rendering top-quark physics an excellent means of probing the SM Higgs mechanism as well as the open questions related to it, e. g. the hierarchy problem or the stability of the SM vacuum. Possible non-standard interactions or couplings to new particles generated by extensions of the SM addressing these unresolved issues, e. g. Supersymmetry (SUSY), extra dimensions, composite Higgs models, etc., could, therefore, first reveal themselves in top-quark data.

Another peculiar feature of the top quark is its very short lifetime $\tau_t \approx 10^{-25}\,\text{s}$, which lies an order of magnitude below the hadronization time $\tau_{Had} \approx 10^{-24}\,\text{s}$. This affords the opportunity to study the properties of a "bare" quark that decays before it can form quarkonium

[1] The renormalizability of the SM is assured by the cancellation of anomalies, which requires the same generation structure in the leptonic and the quark sector.

[2] For an overview on the development of the top-mass bounds see Ref. [6] and references therein.

	Tevatron (Fermilab)	LHC (CERN)
Experiments	CDF , DØ	CMS , ATLAS
Operating period	$1987 - 2011$	$2009-$present
Center-of-mass energy	$1.8\,\text{TeV}$ $1.96\,\text{TeV}$	$7\,\text{TeV}$ $8\,\text{TeV}$ } (Run 1) $13\,\text{TeV}$ (Run 2) $14\,\text{TeV}$ (future)
Integrated luminosity	$\sim 0.1\,\text{fb}^{-1}$ @ $1.8\,\text{TeV}$ $\sim 10\,\text{fb}^{-1}$ @ $1.96\,\text{TeV}$	$\sim 6\,\text{fb}^{-1}$ @ $7\,\text{TeV}$ $\sim 23\,\text{fb}^{-1}$ @ $8\,\text{TeV}$ $\sim 26\,\text{fb}^{-1}$ @ $13\,\text{TeV}$
$t\bar{t}$-pairs produced per experiment	$\sim 7 \times 10^4$	$\sim 3 \times 10^7$
Dominant production channel	$q + \overline{q} \to t + \bar{t}$ $(\sim 85\%)$	$g + g \to t + \bar{t}$ $(\sim 80 - 90\%)$
Single top quarks produced per experiment	$\sim 3 \times 10^4$	$\sim 1 \times 10^7$
Dominant production channel	$u + b \to d + t$	$u + b \to d + t$

Table 1.1: *Key parameters of the Tevatron collider and the LHC relevant for top-quark physics.*

bound states or hadrons and hence can be successfully treated within perturbation theory. As a consequence, it allows for a direct examination of observables related to spin, charge or polarization as well as their correlations, which are inaccessible for lighter quarks due to non-perturbative confinement effects. Furthermore, since the production and decay mechanism for top quarks at hadron colliders is governed by different types of interactions, its short lifetime offers the opportunity to closely study the structure and strength of both QCD (top-quark pair production) and EW (single top-quark production and top-quark decay) vertices providing an additional handle in the search for new-physics phenomena.

A drawback of investigating the properties of such a short-lived particle is its experimental detection as it cannot be measured directly but only through its decay products. Because of its large mass, the top quark almost exclusively decays into on-shell W bosons and bottom quarks $t \to W^+ + b$ [3], where the W bosons decay further, either leptonically $W^+ \to l^+ + \nu_l$ ($l = e, \mu, \tau$) or hadronically $W^+ \to q_u + \overline{q}_d$ ($q_u = u, c$ and $\overline{q}_d = \overline{d}, \overline{s}, \overline{b}$). Therefore, in order to draw meaningful conclusions from experimental data, a theoretical description of such a particle requires the consideration of the complete interplay between production mechanism

[3] Other decay modes are also possible but highly suppressed in the SM either through the Cabibbo-Kobayashi-Maskawa (CKM) matrix, e. g. $t \to W^+ + s$, or due to loop suppression, e. g. $t \to \gamma + c$.

and decay process. Fortunately, the decay width $\Gamma_t = 1.34\,\text{GeV}$ [12, 13] of the top quark is very narrow allowing for a factorization approach which separates these effects and simplifies the calculation of theoretical predictions considerably. In fact, it turns out that this approximation is valid for most applications and only fails for some exclusive observables, which indeed require an exact treatment.

Although being discovered at the Tevatron, a detailed examination of the top quark was limited at this collider by the low statistics in the collected data sample mainly due to the low center-of-mass energy. This changed with the start of operation of the Large Hadron Collider (LHC) at CERN in the end of 2009, which can be considered a top factory producing millions of top quarks in high-energy proton-proton collisions (for some characteristic quantities of the two colliders see Tab. 1.1). So far, it collected a total of $\sim 28\,\text{fb}^{-1}$ of data in Run 1 at 7 TeV and 8 TeV collision energy as well as $\sim 26\,\text{fb}^{-1}$ in Run 2 at 13 TeV allowing for the study of top-quark physics at high precision and enabling the measurement of new top-related quantities inaccessible at the Tevatron. Yet, within the next decade the LHC will be upgraded even further to operate at an energy of 14 TeV by 2020 with the high-luminosity phase scheduled for 2026 reaching up to 7 times its nominal luminosity. This will boost the experimental statistics to a new level and hopefully (at the latest) lead to the first evidence of beyond-the-SM (BSM) physics in top-quark data. Note, however, that due to the composite nature of the particles participating in hadronic collisions the achievable precision for the determination of certain top-related quantities, e. g. the mass or the decay width, is limited (which does not necessarily mean the corresponding measurements are inaccurate). Future lepton colliders, either designed as linear colliders (e. g. ILC) or as circular colliders (e. g. TLEP), could resolve these potential issues and push the experimental limits even further by allowing for a detailed scan of the production threshold [14, 15]. But also concepts for future higher-energy hadron colliders are currently under discussion as they would give us the opportunity to study yet new aspects of this particle, e. g. its parton density inside the proton [16]. Therefore, the top quark remains a key ingredient to our current understanding of nature and can be considered a possible gateway to new physics in current and future experiments.

1.2 Top-quark properties

1.2.1 The top-quark mass

The mass of the top quark m_t is a fundamental parameter of the SM that cannot be derived from first principles and thus has to be determined experimentally. Due to its sizable numerical value it has, unlike the mass of any other quark, a considerable impact on numerous theoretical predictions and therefore its precise measurement serves as an important test of our well-established theoretical framework. Moreover, it can be regarded as a key indicator for new-physics effects since its value may help us to discriminate between a variety of different extensions of the SM.

An important example of its outstanding role within the SM and beyond is the influence of the top-quark mass on radiative corrections in EW theory. These corrections represent an integral part of the higher-order quantum effects entering most EW precision observables

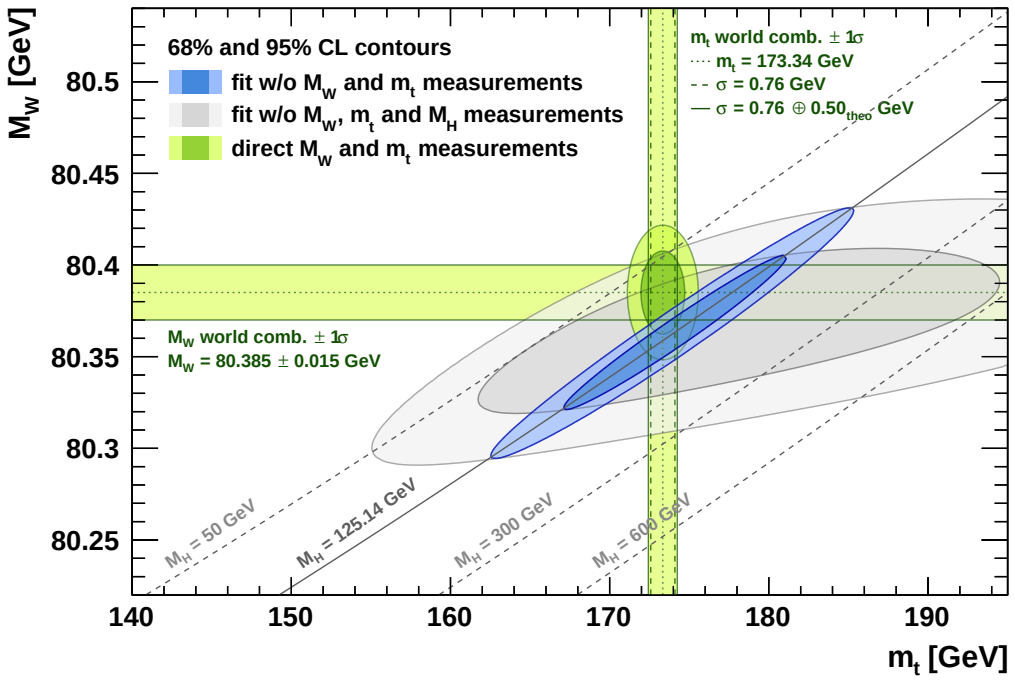

Figure 1.1: *Contours of a global EW fit at 68% and 95% confidence level (C.L.) derived from a scan of the M_W-m_t parameter space with (blue) and without (gray) Higgs mass measurements included. For comparison also the results of the direct experimental determination of the W-boson and top-quark masses are shown [17].*

and are affected by m_t through the universal parameter $\Delta\rho$ that describes the loop-induced contributions to

$$\rho = \frac{1}{1-\Delta\rho} \overset{\text{(LO)}}{=} \frac{M_W^2}{M_Z^2 \cos^2\theta_W}\,, \tag{1.1}$$

which is a measure for the relative interaction strength of the EW neutral and charged currents. As indicated, it can, at leading order (LO), be expressed in terms of the gauge-boson masses M_Z and M_W as well as θ_W, the Weinberg angle that governs the mixing of the weak and electromagnetic couplings. The corrections to ρ can be conveniently parametrized as

$$\Delta\rho = \frac{\Pi_Z(0)}{M_Z^2} - \frac{\Pi_W(0)}{M_W^2} = \frac{G_F m_t^2}{8\sqrt{2}\pi^2}(3 + \delta_{QCD} + \delta_{EW} + \delta_{Mix}) \tag{1.2}$$

where $\Pi_Z(0)$ and $\Pi_W(0)$ denote the transverse part of the EW gauge-boson vacuum polarizations at zero momentum transfer and G_F is the Fermi coupling constant[4]. The leading behavior of $\Delta\rho$ was first calculated in Ref. [18] and the higher-order corrections, parametrized as δ_{QCD}, δ_{EW} and δ_{Mix} and containing yet higher powers of m_t, are presently available to four loops in QCD [19–22] and to three loops for the EW and the mixed QCD/EW contributions [23,24]. The strong dependence on the mass in form of a power series is a feature exclusive to the top quark whereas the impact of all other particles in the SM is considerably weaker.

[4] The mass of the bottom quark is assumed to vanish on the right-hand side of Eq. (1.2).

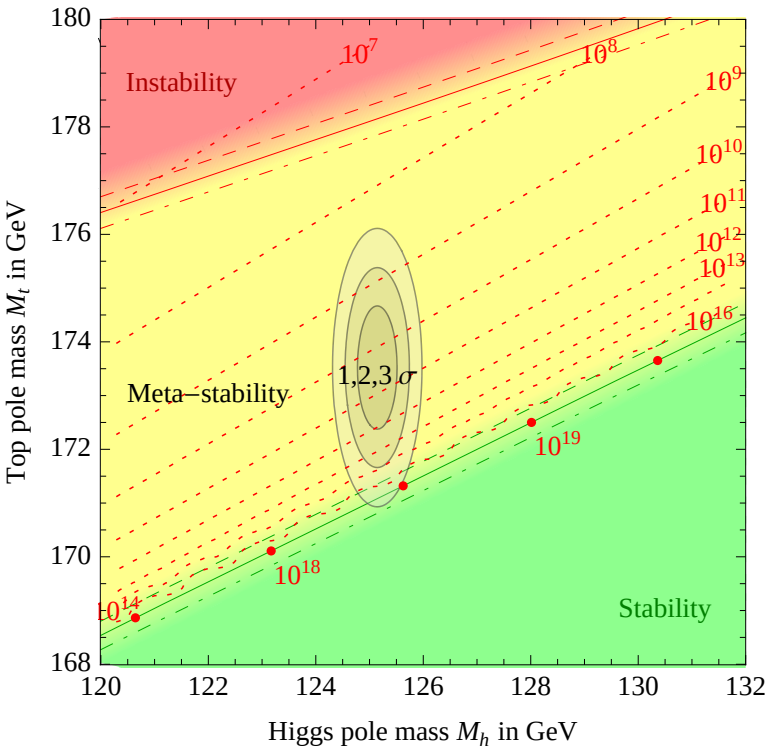

Figure 1.2: *Stability of the SM vacuum as a function of the masses of the Higgs boson and the top quark [30].*

For the mass of the Higgs boson M_H, for instance, the leading behavior is only logarithmic rendering EW precision data less sensitive to its actual value. That is the reason why the mass of the top quark could be reliably predicted prior to its discovery[5] while for the mass of the Higgs only an upper bound could be derived [6]. Since $\Delta\rho$ is an integral part of the radiative corrections to many EW observables, its sensitivity to m_t directly translates to the theoretical prediction of these quantities, e. g. the mass of the W boson [26] or the leptonic effective weak mixing angle $\sin^2\theta^{lept}_{eff}$ [27][6]. This allows for an important consistency check of the SM by comparing the predictions deduced from EW precision measurements as well as from Tevatron and LHC data to a direct experimental determination of these quantities as, for example, illustrated in Fig. 1.1 [17]. Furthermore, the significance of the top-quark mass extends even beyond the SM since these EW observables can be employed in the indirect search for new-physics scenarios, e. g. the Minimal Supersymmetric Standard Model (MSSM) [29]. This, however, requires the precise knowledge of m_t as it serves as an essential input in these searches and represents one of the main sources of uncertainty in the effort to further constrain the parameter space of these models.

[5] EW precision data is, in fact, so sensitive to the top-quark mass that, in the near future, it will allow for an indirect determination of this parameter with a projected precision of below 1 GeV [25].

[6] Apart from the dependence on $\Delta\rho$, EW observables may also be affected by non-universal corrections proportional to m_t^2 as can, for instance, be seen for the effective weak mixing angle for bottom quarks $\sin^2\theta^{b\bar{b}}_{eff}$ [28].

A different aspect that emphasizes the importance of an accurate determination of the mass of the top quark is its role in the analysis of stability of the SM vacuum. It can be traced back to the fact that the Yukawa couplings, which enter the evolution equation of the scalar quartic coupling in the SM Higgs sector, are proportional to the respective fermion masses. In consequence, the top quark, being the heaviest SM particle, has a crucial impact on the number and position of possible ground states of the SM effective potential and thus decides about "the fate of the Standard Model" [30–35] as shown in Fig. 1.2. Indeed, even though it is stable at tree level, the effective potential receives significant modifications through higher-order quantum effects, which allow for the emergence of an additional, lower-energetic vacuum state at large values of the scalar field strength driven by the running quartic coupling becoming negative[7]. In case of two vacua, the tunneling probability between these states [36–38] compared to the lifetime of the universe decides whether the SM is meta-stable or unstable. However, since our universe seems to reside at the boundary between meta-stability and stability, a more accurate determination of m_t is required in order to draw any further conclusions.

As the mass of the top quark is a parameter of the SM Lagrangian (as well as most of its extensions), it is subject to renormalization and thus a convention-dependent quantity. In principle, any renormalization condition is valid to determine its exact definition but in practical applications some of them turn out to be more convenient as they lead to a more reliable theoretical description for the problem at hand. Due to its use in the calculation of a wide range of different observables and phenomena, a variety of schemes for the top-quark mass has been proposed throughout the years. Each of them is tailored to meet certain requirements, relevant for the respective quantity under investigation, and the most common definitions can be summarized as follows:

1. *The pole mass*

   The most natural concept is the pole or on-shell mass, in the following denoted m_t, as it closely corresponds to the position of the peak in the invariant-mass spectrum of the top-quark decay products. It can, however, only be defined in perturbation theory as the real part of the complex-valued pole of the top-quark propagator at $\sqrt{p^2} = m_t - \frac{i\Gamma_t}{2}$ while the full (non-perturbative) propagator has no pole due to confinement. Its current world average value, a combination of measurements by the CDF, DØ, ATLAS and CMS experiments, reads $173.34 \pm 0.76\,\text{GeV}$ [11] where the error[8], which is dominated by systematics, is expected to decrease even further in the near future [39].

   There, however, exists an intrinsic limit to the accessible experimental precision that is related to so-called infrared renormalons, certain divergence patterns in the perturbative expansion of quantum field theories. In consequence, the theoretical definition of the pole mass suffers from an ambiguity of order $\sim \Lambda_{QCD}$, i. e. the scale that governs

[7] The analysis of the stability of the SM vacuum usually assumes the absence of new physics up to the Planck scale.

[8] Note that the quoted top-mass error does not include the uncertainty $\sim 1\,\text{GeV}$ related to the translation of the mass parameter used in the numerical tools for the experimental mass reconstruction to the pole mass scheme. This aspect will be discussed in greater detail below.

the separation of the perturbative and non-perturbative regime in QCD. Since this ambiguity translates to any observable expressed in terms of m_t, it will eventually spoil the experimental determination of the pole mass to higher accuracy. Note, however, that recently the ultimate renormalon-induced uncertainty on m_t has been pinned down to lie only around 70 MeV [40] suggesting that it can, in fact, be safely neglected in current top-mass measurements.

In general, the occurrence of infrared renormalons in perturbative calculations signals the necessity to also include non-perturbative effects in the theoretical analysis[9]. This may be achieved by considering vacuum expectation values of higher-dimensional local operators, which usually cures the ambiguous behavior for the respective observable under consideration. In case of the pole mass, however, this prescription fails due to the absence of an operator with the appropriate quantum numbers, a situation that even persists when the top quark is treated as an unstable particle with finite width [42]. This is quite surprising for one might naively expect that its very short lifetime shields the top quark from non-perturbative QCD effects since it decays before forming bound states. Still, despite its ambiguous behavior the pole mass remains a valid parameter in a wide range of phenomenological applications and only for certain high-precision observables its use could lead to complications in the theoretical description. For these quantities the use of so-called short-distance masses, e. g. the $\overline{\text{MS}}$ mass, is more adequate since they are free of such renormalon contributions.

2. *The $\overline{\text{MS}}$ mass*

The mass in the modified-minimal-subtraction ($\overline{\text{MS}}$) scheme $\overline{m}_t(\mu)$ is defined by subtracting only the divergent contributions (multiplied by a universal normalization constant irrelevant to any physical process) in the renormalization procedure of the underlying dimensionally regularized theory. As a result, it acquires an explicit dependence on the renormalization scale μ. Usually, only pure QCD effects are included in this definition as the corresponding EW corrections are strongly affected by the treatment of so-called tadpole contributions [43]. The scale μ is typically chosen to be of the order of the characteristic energy scale Q of the process under consideration allowing for the resummation of potentially large logarithms of the form $\ln Q/\mu$ that might otherwise spoil the convergence of the perturbative expansion. This, however, implies that there exists some sort of scaling relation that connects the $\overline{\text{MS}}$ mass measured at a certain reference scale μ_0 to any other value of μ in order to guarantee the applicability of this scheme to different processes and experiments and thus maintain the predictive power of the theory. Fortunately, the required scaling behavior can be inferred from pure perturbative considerations yielding

$$\mu^2 \frac{d}{d\mu^2} \overline{m}_t(\mu) = \overline{m}_t(\mu) \gamma_m(\alpha_s) \, . \tag{1.3}$$

This renormalization group equation (RGE) reflects the scale-invariance of the bare, i. e. unrenormalized, mass parameter of the Lagrangian where the mass anomalous

[9] For an excellent review on renormalon physics see Ref. [41].

dimension γ_m is currently known to five-loop accuracy in QCD [44]. By construction, the $\overline{\text{MS}}$ mass is insensitive to physics at larger distance scales and thus, as mentioned above, its experimental determination is unaffected by infrared renormalons. For the top quark it is usually evaluated iteratively at $\mu = \overline{m}_t(\mu)$ where its numerical value can be derived from the known relation to the pole mass. It is available fully analytically to three loops in QCD [45] and has recently been extended to four loops with the help of sophisticated numerical methods [46]

$$\begin{aligned} m_t &= \overline{m}_t(\overline{m}_t)\left(1 + \frac{4}{3}\frac{\overline{\alpha}_s}{\pi} + 8.2364\left(\frac{\overline{\alpha}_s}{\pi}\right)^2 + 73.6375\left(\frac{\overline{\alpha}_s}{\pi}\right)^3\right. \\ &+ \left. 827 \pm 24\left(\frac{\overline{\alpha}_s}{\pi}\right)^4 + \mathcal{O}(\overline{\alpha}_s^5, \Lambda_{QCD})\right) . \end{aligned} \tag{1.4}$$

The running coupling is in this context defined as $\overline{\alpha}_s = \alpha_s(\overline{m}_t)$ while $\mathcal{O}(\Lambda_{QCD})$ indicates the aforementioned renormalon ambiguity likewise present in this expression. The quoted uncertainty on the four-loop coefficient is due to the finite precision of the numerical integration routines employed in the evaluation of the large set of complicated master integrals that form the basis of the $\mathcal{O}(\overline{\alpha}_s^4)$ corrections. Inserting the current world average of the pole mass in Eq. (1.4), the $\overline{\text{MS}}$ mass reads $\overline{m}_t(\overline{m}_t) = 163.6\,\text{GeV}$. Lately, also a direct measurement of $\overline{m}_t$ from the total inclusive cross section of top-quark pair production was performed, which yields a similar result (for details see *Determination from total cross section measurements* below). Note that the difference between the pole and the $\overline{\text{MS}}$ mass of about 10 GeV is quite large and consequently for any LO observable it is necessary to provide a careful explanation for why higher-order contributions are supposedly small in the employed mass scheme, especially when the corresponding quantity is used for top-mass determinations.

3. *Threshold masses*

While the pole mass and the $\overline{\text{MS}}$ mass are common textbook material and provide a valid description for most quantities related to top-quark physics, there are certain observables where their use may lead to a poor convergence in the perturbative treatment. This is quite unsatisfactory since it precludes the derivation of reliable theoretical predictions and, consequently, makes the extraction of any parameters from a comparison with experimental data impossible. In such cases a non-standard mass definition is needed. A good example of such a scenario is the production of top-quark pairs at threshold, e. g. in electron-positron collisions. It is of particular importance since it is expected that a cross section scan at a future lepton collider will yield the most accurate top-mass determination possible. This certainly requires a well-understood theoretical framework for the calculation of this quantity, which is highly non-trivial owing to the presence of sizable non-relativistic contributions. In fact, it turns out that large Coulomb enhancements completely rule out the use of standard QCD perturbation theory such that one has to resort to the effective theory of potential non-relativistic QCD (pNRQCD) to

resum these effects. This may be accomplished by determining a Green function G_C from a Schrödinger-type equation of the form

$$\left(-\frac{\nabla^2}{m_t} + V(r) - E\right) G_C(\vec{r}, 0, E) = \delta^{(3)}(\vec{r}) \tag{1.5}$$

where $V(r)$ is the static QCD potential and the non-relativistic energy is defined as $E = \sqrt{s} - 2m_t$. The total static energy of the $t\bar{t}$ system $E_{stat}(r) = V(r) + 2m_t$, entering Eq. (1.5), is a well-defined physical quantity and therefore free of renormalon ambiguities (despite using the pole mass m_t). Still the NNLO predictions [47–49] derived within this formalism failed to provide satisfactory results as the estimated uncertainty of 0.5 GeV for the top-mass determination was much larger than originally expected. This problem could, however, be resolved by introducing so-called threshold masses, the most prominent examples in top-quark physics being the potential-subtracted (PS) mass [50,51] and the 1S mass [52,53]. Their use leads to a dramatic improvement of the perturbative description and will ultimately allow for measurements with an uncertainty below 100 MeV [54,55].

The main reason for the badly behaved series expansion of the total cross section is the strong infrared sensitivity of the coordinate-space potential

$$V(r) = \int \frac{d^3q}{(2\pi)^3} e^{i\vec{q}\cdot\vec{r}} \tilde{V}(q)\,, \tag{1.6}$$

which may be traced back to contributions from the low momentum region in the Fourier transform. While these contributions cancel in Eq. (1.5) with the leading long-distance behavior of the pole mass, they still spoil the perturbative convergence in the calculation of physical observables. However, by shifting these infrared effects it is possible to redefine both the potential and the mass in such a manner that they exhibit significantly improved convergence properties. In the PS scheme this is achieved by introducing a factorization scale μ_F and excluding the ill-behaved region $|\vec{q}| > \mu_f$ from the Fourier integration,

$$V(r, \mu_F) = V(r) + 2\delta m(\mu_F)\,, \tag{1.7}$$

where

$$\delta m(\mu_F) = -\frac{1}{2} \int\limits_{|\vec{q}|<\mu_F} \frac{d^3q}{(2\pi)^3} \tilde{V}(q)\,. \tag{1.8}$$

Absorbing these contributions into the mass term yields the PS mass,

$$m_t^{PS}(\mu_F) = m_t - \delta m(\mu_F)\,, \tag{1.9}$$

which is free of infrared renormalon ambiguities and can therefore be related to other (more common) short-distance masses, for instance the $\overline{\text{MS}}$ mass, through a well-behaved perturbative expansion. Due to the subtraction prescription, the mass acquires an explicit scale dependence, which cancels in physical observables with the scaling behavior of the subtracted potential. Still, the choice for μ_F is not completely arbitrary as it should respect the perturbative range of the strong coupling α_s ($\mu_F > \Lambda_{QCD}$) as

well as the fact that the potential should only be affected by scales below the physical scale of the process under consideration ($\mu_F < m\alpha_s$). An appropriate value, commonly used in top-quark physics, is $\mu_F = 20\,\text{GeV}$.

The 1S scheme is a somewhat different approach that leads to a similar cancellation of infrared (IR) effects between the mass and the potential but is based on the so-called upsilon expansion, which differs from the usual perturbative expansion in terms of α_s. In this scheme the mass is defined as half the mass of the (for top quarks fictitious) quarkonium $1\,^3S_1$ bound state,

$$\begin{aligned}\frac{m_t^{1S}}{m_t} &= 1 - \frac{2\alpha_s^2(\mu)}{9}\left[\epsilon + \epsilon^2\frac{\alpha_s(\mu)}{\pi}\left(\beta_0\,(L+1) + \frac{a_1}{2}\right)\right. \\ &+ \epsilon^3\left(\frac{\alpha_s(\mu)}{\pi}\right)^2\left(\beta_0^2\left(\frac{3}{4}L^2 + L + \frac{\zeta_3}{2} + \frac{\pi^2}{24} + \frac{1}{4}\right) + \beta_0\frac{a_1}{2}\left(\frac{3}{2}L + 1\right)\right. \\ &+ \left.\left.\frac{\beta_1}{4}\,(L+1) + \frac{a_1^2}{16} + \frac{a_2}{8} + \frac{107\pi^2}{27}\right) + \mathcal{O}(\alpha_s^3)\right]\end{aligned} \tag{1.10}$$

where β_0 and β_1 are the first two coefficients of the QCD β-function and

$$L \equiv \ln\left(\frac{3\mu}{4\alpha_s(\mu)m_t}\right) . \tag{1.11}$$

The constants a_1 and a_2 depend on the static potential at two-loop and three-loop level respectively and for QCD with 5 massless flavors read $a_1 = \frac{43}{9}$ and $a_2 = 352.805$ [56–59]. In the large β_0 limit that governs the leading IR behavior the 1S mass contains terms of order $\alpha_s^{n+2}\beta_0^n$ whereas a perturbative series in general is of the form $\alpha_s^{n+1}\beta_0^n$. Therefore, one would naively expect that expressing a quantity in terms of the 1S mass would lead to a renormalon ambiguity similar as for the pole mass. This mismatch will, however, be cured for large n due to the exponentiation of the logarithmic terms $exp(L) = \frac{3\mu}{4\alpha_s(\mu)m_t}$ allowing for a complete cancellation of renormalon contributions. In order to describe this effect in a theoretically consistent manner to all orders, one introduces an auxiliary parameter $\epsilon = 1$ that is of the order $\alpha_s^{n+1}\epsilon^n$ in Eq. (1.11) and $\alpha_s^n\epsilon^n$ in the series expansion of any other quantity. When expressing an observable through m_t^{1S}, the perturbative expansion is then performed in ϵ rather than α_s. This approach came to be known as the upsilon expansion[10] and has been successfully applied to threshold calculations in top-quark physics and beyond. Using Eq. (1.11) the 1S mass can be reliably related to other short-distance masses but due to the upsilon expansion the resulting relation will contain higher powers of the strong coupling than usually present for other mass schemes.

4. *The MSR mass*

A common feature of short-distance masses is their dependence on an intrinsic infrared scale R whose actual value is a characteristic property of the scheme under consideration. For the masses discussed so far, for instance, this scale reads $R^{\overline{MS}} = \overline{m}_t(\mu)$, $R^{PS} = \mu_F$ and $R^{1S} = \frac{4\alpha_s(\mu)m_t}{3}$. When converting between two such schemes with a strong

[10] The name reflects the fact that this formalism was originally introduced in bottom-quark physics.

hierarchy between the respective scales, the resulting series expansion will contain large logarithms of the scale ratio that might spoil the convergence and thus the desired numerical precision of the resulting mass term. In that case it is possible to resum the logarithmic contributions by interpreting R as a free parameter and constructing a renormalization-group-type equation

$$R\frac{d}{dR}m(R) = -\frac{d}{d\ln R}\delta m(R) \equiv -R\gamma_R\,, \tag{1.12}$$

that can be used for interpolating between different values of the IR scale in a given mass scheme[11]. The anomalous dimension γ_R is defined through the relation of the considered short-distance mass to the pole mass

$$m_t = m(\mu, R) + \delta m(\mu, R) \tag{1.13}$$

with

$$\delta m(\mu, R) = R\sum_{n=1}^{\infty}\sum_{k=0}^{n} a_{nk}\left(\frac{\alpha_s(\mu)}{4\pi}\right)^n \ln^k\left(\frac{\mu}{R}\right)\,. \tag{1.14}$$

Thus, the RGE Eq. (1.12) simply follows from the scale-invariance of the pole mass (after setting $\mu = R$ to avoid large logarithms in δm). This approach defines a new class of mass schemes with running IR scale, the most notable representative being the MSR mass [60], which is defined in terms of a $\overline{\text{MS}}$-like relation to m_t, however, with an arbitrary IR scale in δm,

$$m_t^{MSR}(R) = m_t - R\sum_{n=1}^{\infty} a_{n0}^{\overline{MS}}\left(\frac{\alpha_s(R)}{4\pi}\right)^n\,. \tag{1.15}$$

It can hence be viewed as a smooth interpolation between the $\overline{\text{MS}}$ mass ($R = \overline{m}_t(\overline{m}_t)$) and the pole mass ($R = 0$). Although the well-behaved series expansions of the PS mass and the 1S mass with respect to the $\overline{\text{MS}}$ mass indicate that resumming logarithms is not necessary in these cases, this new concept might play an important role for mass schemes with lower internal scales $R \sim 1\,\text{GeV}$, the typical cutoff parameter in Monte-Carlo (MC) programs used for experimental top-mass determinations at hadron colliders. While an accurate description relating such a MC mass parameter to a renormalized field-theory mass is yet unavailable (see discussion below), the MSR mass can serve as a simplified model to study the perturbative matching uncertainties when converting such a low-scale mass to the $\overline{\text{MS}}$ scheme [61].

The measurement of any of these masses to high precision is a great challenge, both experimentally and theoretically, and led to the development of various dedicated analysis techniques for a reliable extraction from Tevatron and LHC data. As the main production mechanism for top quarks at these colliders is pair production, the experimental signatures in top-quark measurements are usually characterized by the decay products of the W bosons as

[11] In case of a possible renormalization scale dependence $m(\mu, R)$, the mass used in the RGE is defined as $m(R) = m(\mu = R, R)$.

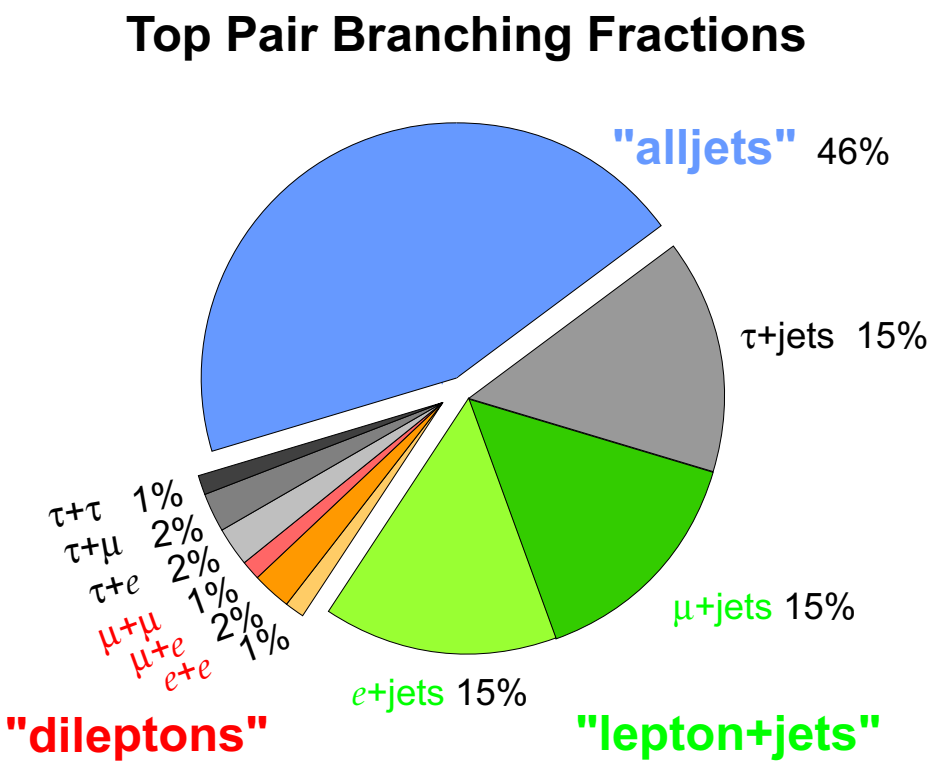

Figure 1.3: *Decay channels in top-quark pair production [64]*

"dilepton channel", "ℓ+jets channel" and "all-jets channel" (see Fig. 1.3). Note that the τ-lepton is generally excluded from this classification as it will, in contrast to the muon, usually decay within the detector and thus lead to a different decay pattern. Each of these topologies involves a different detection efficiency and a unique physical background, which requires an individual treatment of these final-state configurations in the corresponding top-mass determinations. In this context, the two most widely used analysis techniques are the so-called "template method" and "matrix element method" (MEM), which are based on a comparison of MC simulations, combining theory input and detector design, to experimental data and currently yield the most accurate results. These approaches, commonly referred to as "standard methods", are complemented by a number of different analyses that allow for a stringent test of the underlying models that form the basis of the established techniques while resolving some of their conceptual drawbacks. The main features of these top-mass determinations may be summarized as follows[12]:

1. *Standard methods*

   The key idea of the template method is to use MC event generators[13] to model the signal and background processes as well as their detector response for various values of the top-quark mass. The resulting "templates" are then fitted to the observed distribu-

[12] For a detailed review on top-mass measurements see Refs. [62, 63] and references therein.
[13] For a concise overview and description of the most common MC tools used in the simulation of particle physics processes see Ref. [65]

tions, usually with the maximum likelihood method, to determine the mass value that provides the best agreement with data. This, however, requires the use of an observable that is both highly sensitive to the top mass and has only a negligible dependence on any additional nuisance parameters in order to minimize the overall uncertainty of the respective measurement. In practice, this is achieved by generating higher-dimensional templates depending on several variables that are fitted simultaneously. A typical example is the so-called *in situ* fit of the event-by-event based top-mass estimate from a kinematic reconstruction of the decay products (via χ^2 minimization) and the jet energy scale (JES), a scaling factor that corrects the reconstructed jet energy to the particle level (only stable final-state objects). The JES usually represents the dominant source of systematic uncertainty in these measurements (at least in the ℓ+jets and all-jets channel) and therefore a synchronous evaluation of this conversion factor allows for a serious increase of the experimental precision. While this type of analysis is perfectly suited for a treatment of the all-jets and ℓ+jets topologies, the presence of two neutrinos in the dilepton final state calls for a modified approach since it leads to an underconstrained system of kinematic equations insufficient for a complete event reconstruction. The general idea is to restore the full kinematics by introducing (at least) one additional constraint whose impact can be inferred from theoretical considerations or modeled via numerical MC studies. Due to the freedom of choice associated with this method, its actual implementation realized by the experimental collaborations over the years resulted in a number of different algorithms for the extraction of the top-quark mass in the dilepton channel. Yet, as shown in Fig. 1.4, it still remains the topology with the least accurate measurements using standard analysis techniques.

The second of these standard techniques, the matrix element method, was first applied to top-mass determinations by the DØ collaboration and allows for an even more precise description of experimental data since it takes into account the phase space density of the process under investigation. The technique is based on the Bayesian principle with a prior probability to observe a certain detector response for a given mass value that is proportional to the integral of the corresponding matrix element squared multiplied by a phase-space-dependent correction factor. This correction factor is a product of the so-called detector transfer function and an additional function that contains the detector-independent input (parton distribution functions (PDFs), fluxes of colliding particles, etc.). While the former incorporates all contributions related to the transition from the hard scattering process to actual data (parton shower (PS), hadronization, detector simulation, etc.), the latter is needed for a proper normalization of the result. Similar to the template method, these functions also allow for the inclusion of further theoretical or instrumental parameters (e. g. the JES) in the MEM that could otherwise spoil the efficiency of this approach. Due to the complexity of the occurring higher-dimensional integrals, the evaluation of the event probabilities is done numerically via MC methods. As these methods do not always yield results that converge in a satisfactory manner (despite importance sampling, etc.) or the available CPU resources are limited, throughout the years several modifications have been proposed to reduce the computational effort associated with an application of the MEM. With

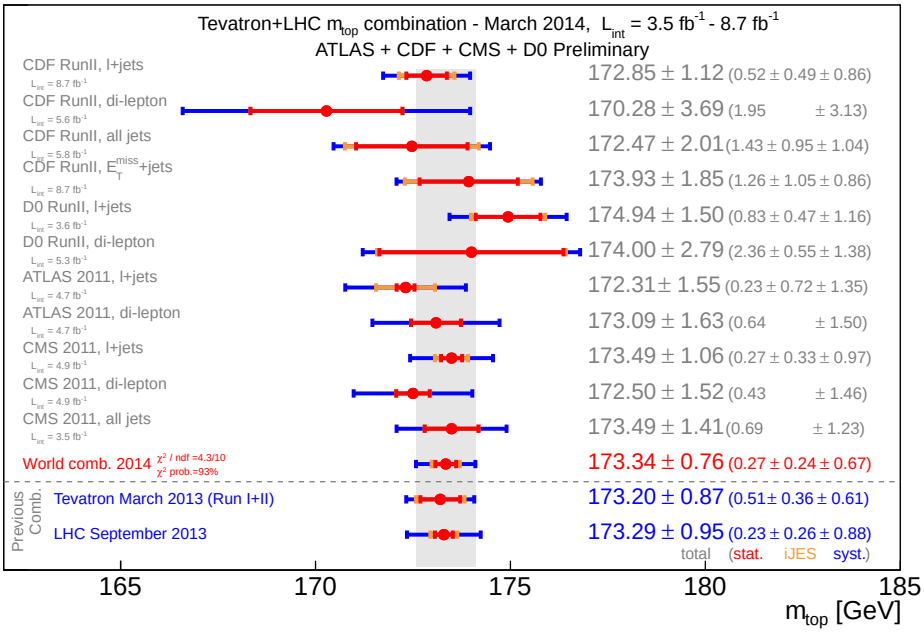

Figure 1.4: *Various top-mass measurements and the resulting world combination as well as separate Tevatron and LHC combinations [11]. The Tevatron combination contains data not included in the world average.*

these improvements, ranging from a simple change of the integration variables to imposing additional constraints that lower the dimensionality of the occurring integrals, the mass of the top quark may then be extracted by finding the maximum of a combined likelihood function constructed as the product of the individual event probabilities of the complete data sample.

There exists a third strategy that is frequently used in top-mass measurements. This so-called "ideogram" method can be considered a mixed approach since it contains aspects of both of the previously discussed techniques. In fact, the most precise single measurement of the top-quark mass currently available (but not included in the world average in Fig. 1.4) is based on this kind of analysis applied to ℓ+jets data collected by the CMS experiment yielding [66]

$$m_t^{exp} = 172.35 \pm 0.51\,\text{GeV}\,. \tag{1.16}$$

Analogous to the MEM, it uses the Bayesian principle to construct a likelihood function for the complete data sample but in this case the calculation of the prior probability is greatly simplified by assuming it to be proportional to MC-generated template distributions and the mass resolution. Therefore, it is usually not regarded as a standalone analysis technique but rather as a modification of the template method.

The result of applying these standard methods is nicely summarized in Fig. 1.4, where one can see the values of the top-quark mass measured by the different collaborations for different channels as well as the combined world average derived by using the best

linear unbiased estimate (BLUE) method. Evidently, the ℓ+jets topology yields the most accurate results for all experiments due to its combination of an enhanced signal-to-background ratio and high statistics. One can also see the impact of the increased production cross section at the LHC, which leads to a much lower statistical error despite a smaller integrated luminosity. In general, these measurements exhibit an impressive degree of understanding of the underlying theoretical and experimental uncertainties and render the top-quark mass a high precision quantity. Moreover, recent studies [67] show that the mass determination from these techniques is expected to further improve in the current and upcoming LHC runs reducing the overall error to the level of a few hundred MeV (see Fig. 1.5), a precision supposedly inaccessible with any other approach.

Yet, the standard methods suffer from an inherent drawback related to the use of parton showers that needs to be carefully investigated in order to be able to profit from the outstanding experimental performance. Since parton shower algorithms are designed to resum leading logarithmic contributions, they are not able to distinguish between different quantum-field-theoretical mass schemes. Thus, any of the definitions discussed previously would be a valid choice for the measured mass parameter, e. g. the pole mass as suggested by the fact that the analyses are based on kinematic reconstructions[14]. However, to ensure a well-behaved perturbative convergence, the chosen mass scheme should minimize the effect of missing higher-order contributions for the particular observables employed in the measurement process. From general considerations one can infer that such a scheme, commonly denoted as MC mass scheme, contains an inherent IR scale $R^{MC} \sim 1\,\text{GeV}$ implying that, following Eq. (1.13), its relation to the pole mass is given as

$$m_t = m_t^{MC}\left(R^{MC}\right) + R^{MC}\left[\alpha_s\left(R^{MC}\right) c_1 + \ldots\right] \tag{1.17}$$

where both the unknown coefficient c_1 and $\alpha_s\left(R^{MC}\right)$ are of order one [68]. In consequence, there exists an inherent uncertainty of approximately 1 GeV in the translation of the top-quark mass determined from standard methods to the pole mass or any short-distance mass defined at low scales. A significant improvement towards a well-defined mass measurement would be a full (i. e. including off-shell effects) NLO description of top-quark production and decay consistently matched to parton shower but such a merged approach is not available yet as it suffers from conceptual problems that have not been completely resolved [69–71]. This is the reason why it is appealing to develop alternative analysis techniques, which are based on a theoretically more rigorous mass definition, in spite of their presumably lower level of precision[15].

[14] The pole mass is, in fact, a common choice in the standard analyses despite the well-known renormalon ambiguity.

[15] Some analyses that utilize more exotic observables, e. g. the transverse decay length of the B-hadrons L_{xy} [72–74], or that account for singly produced tops [75, 76] are also not considered as "standard" despite their use of a similar MC machinery. They therefore suffer from the same discrepancy between measurement and a proper field theory definition, however, without reaching the high precision of the standard methods. Still, they serve as an independent cross-check and help to gain a deeper understanding of the underlying systematics.

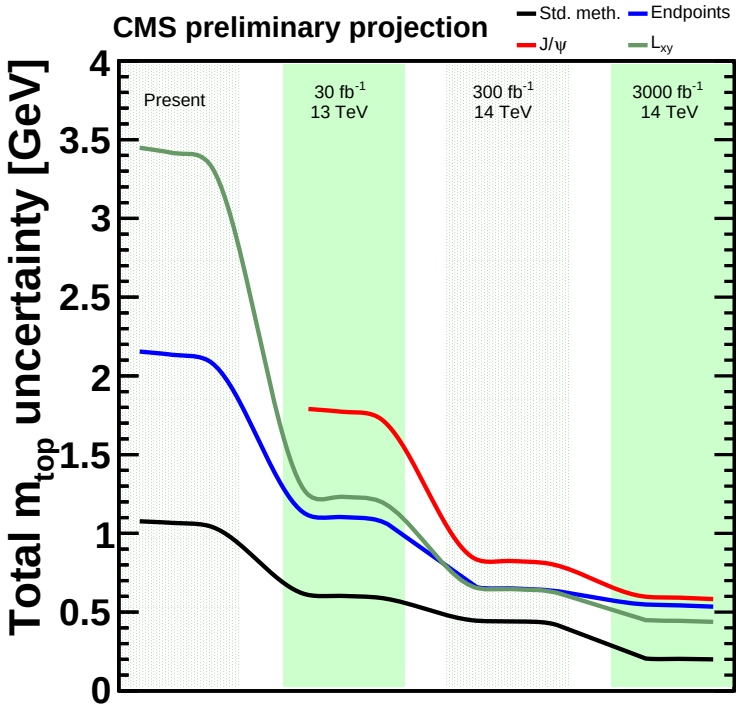

Figure 1.5: *Expected development of the total uncertainty on top-mass measurements for different analysis techniques [67].*

2. *Determination from total cross section measurements*

   The recent completion of the calculation of the full NNLO QCD corrections [77–80] renders the total inclusive production cross section for top-quark pairs $\sigma_{t\bar{t}}^{\mathrm{tot}}$ an excellent means of determining the top mass in a well-defined mass scheme with sufficiently high precision. Indeed, due to its strong sensitivity to this input parameter, which can be parametrized as

$$\frac{\Delta\sigma_{t\bar{t}}^{\mathrm{tot}}}{\sigma_{t\bar{t}}^{\mathrm{tot}}} \approx -5\,\frac{\Delta m_t}{m_t}\,, \tag{1.18}$$

   this quantity has already been employed in previous studies [81, 82] but only the improved theoretical description combined with the latest experimental progress allows for an extraction of the top-quark mass that is competitive [34, 63, 83–86]. The general strategy of this indirect measurement is to construct a likelihood function, usually in form of a convolution of Gaussian distributions, to model the behavior of the theoretical and experimental cross sections. Subsequently, this function is maximized simultaneously with respect to $\sigma_{t\bar{t}}^{\mathrm{tot}}$ and the input mass parameter, which may be interpreted as a determination of the intersection between the two cross section curves in terms of the top-quark mass (see Fig. 1.6).

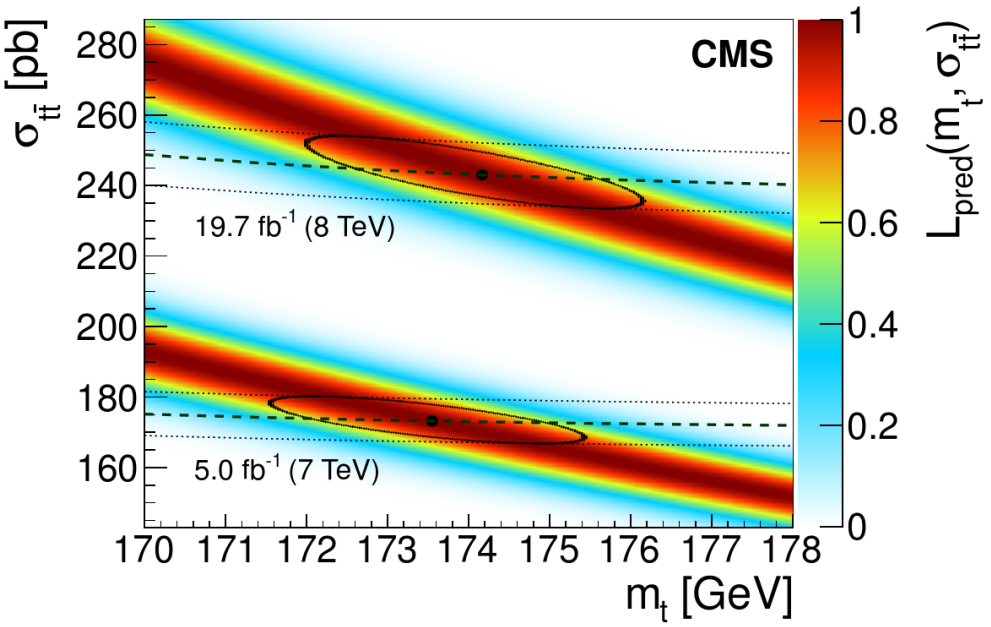

Figure 1.6: *The NNLO+NNLL theory predictions for $\sigma_{t\bar{t}}^{tot}$ at different collider energies as a function of the pole mass obtained with* Top++ *using the* NNPDF3.0 *[90] PDF set. The theoretical uncertainties are properly accounted for in the corresponding likelihood function $L_{pred}(m_t, \sigma_{t\bar{t}})$. The experimental top-mass dependence determined by the* Cms *collaboration is given by the dashed lines where the respective 1σ-uncertainties are indicated by the dotted lines. The extracted values for m_t are represented by the black dots together with the corresponding 1σ-uncertainty contours. Plot taken from Ref. [86]*

The corresponding theory predictions can be obtained from publicly available programs such as Top++ [87], Topixs [88] or Hathor [89] that incorporate the full NNLO contributions and allow for the manipulation of various input parameters that affect the overall theoretical uncertainty, e. g. renormalization and factorization scales, PDF sets and the strong coupling constant. In addition to the fixed-order result, Top++ and Topixs also take into account next-to-next-to-leading logarithmic (NNLL) resummation effects from soft gluons and combined soft and potential gluons respectively. While the central value of the total cross section is only mildly affected by these resummation contributions, leading to an increase of $\sim$2-3%, they significantly reduce the scale dependence of the corresponding theory predictions and are thus included in most top-mass analyses.

The experimental cross section is, in principle, insensitive to any specific value of the top mass. In practice, however, this is not the case as its measurement relies on an extrapolation of the cross section observed in a fiducial volume of the detector to the full reaction phase space, which due to the use of MC simulations introduces an explicit mass parameter. Yet, the dependence on this input MC mass can be reliably quantified by the experiments and its impact is properly accounted for in the corresponding likelihood fits.

So far, the CMS collaboration was able to present the most precise determination of the top-quark mass from the total cross section [86] yielding

$$m_t = 173.8^{+1.7}_{-1.8}\,\text{GeV} \,. \tag{1.19}$$

This analysis is based on μe dilepton data collected at 7 TeV and 8 TeV collision energy where the respective theoretical and experimental top-mass dependence is depicted in Fig. 1.6. A key improvement with regard to earlier studies[16] is the almost vanishing sensitivity to the MC mass which may be parametrized as

$$\begin{aligned} \sigma_{t\bar{t}}^{\text{exp.}}(7\,\text{TeV}, m_t^{\text{MC}}) &= \exp\left[-0.1718\,(m_t^{\text{MC}}/\,\text{GeV} - 178.5)\right] + 170.9\,\text{pb} \\ \sigma_{t\bar{t}}^{\text{exp.}}(8\,\text{TeV}, m_t^{\text{MC}}) &= \exp\left[-0.1603\,(m_t^{\text{MC}}/\,\text{GeV} - 185.4)\right] + 237.0\,\text{pb} \,. \end{aligned} \tag{1.20}$$

Note, however, that one still has to take into account the scheme-related difference between the MC mass and the pole mass, which has been achieved by assuming an additional uncertainty of $\pm 1\,\text{GeV}$ on the respective values of m_t^{MC} entering these cross section formulae. It turns out that for the determination of m_t the corresponding contribution to the total uncertainty is almost negligible suggesting that the benefit from a potential future reduction of the mass ambiguity (or a possibly mass-independent measurement of the total cross section) will only be moderate. An interesting scenario in this context is the analysis proposed in Ref. [67] that assumes an experimental MC mass dependence with a positive slope. This would evidently lead to a further, significant improvement of the overall precision but it remains to be seen whether such an approach is feasible in practice. A different option would be a reduction of the theoretical error. This, however, represents a serious challenge and seems to be unachievable within the near future since the current description of the total cross section has reached a point where a higher precision is only accessible by simultaneously reducing the impact from various sources of uncertainty (see section 3.5.4). Thus, taking into account the expected reduction of experimental uncertainties on the measured cross section, the current precision of about 1% for the top-quark mass seems to lie already close to the realistic lower uncertainty limit attainable with this method.

Although most of these analyses are performed in the pole mass scheme, the measurement of the total inclusive cross section also offers the unique opportunity for a direct extraction of the $\overline{\text{MS}}$ mass [34, 84]. To this end, the fixed-order NNLO result for $\sigma_{t\bar{t}}^{\text{tot}}$ is re-expressed in terms of $\overline{m}_t$ with help of Eq. (1.4). While the $\overline{\text{MS}}$ scheme exhibits a superior perturbative convergence, illustrated by a reduced scale dependence, and is free of renormalon ambiguities, it suffers from a few conceptual drawbacks that require a careful investigation and have to be included in the error estimate of the determined mass parameter. First of all, the scheme-related difference between the MC mass and

[16] Note, however, that the previous analysis by ATLAS [85] already displayed a nearly negligible m_t^{MC}-dependence.

the $\overline{\text{MS}}$ mass is much larger than in the pole mass case which might lead to numerically non-negligible effects in the extraction procedure. This issue could, however, be resolved in future analyses by using cross section measurements with a strongly reduced sensitivity to the input mass parameter as explained above. Another point concerns the proper handling of resummation effects whose derivation is based on the presence of a physical production threshold explicitly utilizing the on-shell condition of the top quark. In spite of the possibility to transform the resummed cross section to the $\overline{\text{MS}}$ scheme, it is not clear how to interpret the resulting expression and whether there is any benefit from such a conversion.

A further important aspect is the role of EW corrections in the theoretical cross section predictions used for a determination of the $\overline{\text{MS}}$ mass. While these effects have been shown to be small in the on-shell scheme [91], their size in the $\overline{\text{MS}}$ scheme crucially depends on the respective treatment of tadpole contributions. Indeed, the relation between m_t and $\overline{m}_t$ derived in Ref. [92] suggests that these contributions may lead to sizable corrections that cannot be neglected in a high-precision observable such as the total cross section. It is, however, possible to exclude this particular class of diagrams, which simply corresponds to a redefinition of the employed mass scheme. This is a very appealing strategy as it reduces the numerical influence of EW effects to the same level as for the pole mass scheme. The prize one has to pay is that the redefined $\overline{\text{MS}}$ mass becomes a gauge-dependent quantity. In principle, this does not pose a problem, since $\overline{m}_t$ is not a physical observable, but it is nonetheless a strange property for a mass parameter. Thus, one may conclude that a proper interpretation of the $\overline{\text{MS}}$ mass determined directly from measurement will always depend on the employed treatment of EW corrections.

Another extraction technique based on the use of the total cross section, which is not applicable at the Tevatron or the LHC but will play an important role at future e^+e^- colliders, is the threshold scan. First studies for the ILC and CLIC [54, 55] estimated the attainable precision of such a measurement to lie in a range of $\leq 100\,\text{MeV}$. In these analyses the top-quark mass is determined from a template fit to the cross section in the threshold region measured as a function of the center-of-mass energy. Since the corresponding templates are generated from the full NNLO cross section prediction (NNNLO [93] once it is available in an automated fashion), the extracted mass parameter corresponds to a well-defined threshold mass that suffers neither from renormalons nor from the MC-induced discrepancies usually connected to the template method. It can therefore also be safely related to other mass schemes by means of a perturbative expansion. However, as these colliders are still at the planning stage, it will take at least another decade before these analyses can be applied to actual data and thus it remains to be seen whether the estimated size of the uncertainty, in particular from systematic effects, is realistic.

3. *Determination from kinematic endpoints*

   The determination of the top-quark mass from the endpoints of kinematic distributions is based on the concept of transverse masses originally introduced in measurements of

the W-boson mass as

$$M_T^2 \equiv m_A^2 + m_B^2 + 2\left(E_T^A E_T^B - \vec{p}_T^{\,A} \cdot \vec{p}_T^{\,B}\right) \tag{1.21}$$

where $E_T = \sqrt{m^2 + \vec{p}_T^{\,2}}$ and $\vec{p}_T = \vec{p} - \vec{p}_z$ (z-axis in beam direction) are the transverse energy and transverse momentum of the respective decay products A and B. Due to the fact that the maximum value of the transverse mass is equal to the mass of the decaying particle, the endpoint of the M_T distribution offers a direct handle for an experimental determination of this quantity. Later, this approach was developed further to allow for the measurement of several unknown masses in systems with two unobservable, identical particles produced in separate decay chains [94]. Although aiming at the use in model-independent searches for BSM physics, this strategy is also well applicable to top-quark decays in the dilepton channel as this topology displays an experimental signature similar to many new-physics scenarios due to the presence of two neutrinos in the final state. The key idea is to construct an observable that incorporates the masses of the parent particles, produced in the hard scattering process, as well as of the undetectable decay products and which accounts for the fact that for the latter only the total missing momentum $\vec{\not{p}}_T$ can be observed experimentally. This is achieved by splitting $\vec{\not{p}}_T = \vec{p}_T^{\,a} + \vec{p}_T^{\,b}$ in all possible ways and, for each of these partitions, determining the maximum value of the resulting transverse masses M_T^a and M_T^b of the parent particles, i. e. the top and the anti-top in case of dileptonic top decays. The unknown masses in the decay process are then directly related to the endpoint of the distribution of a modified transverse mass M_{T2} defined as

$$M_{T2} \equiv \min_{\vec{p}_T^{\,a} + \vec{p}_T^{\,b} = \vec{\not{p}}_T} \left\{ \max\left(M_T^a, M_T^b\right) \right\} , \tag{1.22}$$

which is experimentally well accessible and, moreover, allows for a mass determination with only a limited use of MC tools. In principle, this procedure requires the exact knowledge of the mass of the undetected particles (which is usually unknown a priori) in order to be able to calculate the transverse energy. Fortunately, the dependence of the endpoint on an arbitrary value of this mass $\tilde{m}$, commonly denoted as test mass, is known analytically and can thus be eliminated from the final result. Choosing a value for $\tilde{m}$ different from the true mass, however, introduces an additional dependence on the transverse momentum $P_T = |\vec{P}_T|$ of the underlying two-parent system that affects the position of the endpoint of the M_{T2} spectrum. To resolve this discrepancy, all transverse momenta used in Eq. (1.22) are projected to a direction perpendicular to $\vec{P}_T$, which corresponds to a new definition of the transverse mass, denoted $M_{T2\perp}$ [95, 96], that is invariant under $\vec{P}_T$ boosts and therefore yields a spectrum with a uniquely defined endpoint.

The first measurement of the top-quark mass employing this novel approach was presented by the CMS collaboration [97] providing a value for the pole mass of

$$m_t = 173.9 \pm 0.9\,(\text{stat.})^{+1.7}_{-2.1}\,(\text{syst.})\ \text{GeV} . \tag{1.23}$$

This analysis is based on a maximum likelihood fit to the invariant mass of the b-jet and the lepton, m_{lb}, originating from the same top-quark decay and to a $M_{T2\perp}$-type

variable, μ_{bb}, which treats the W bosons as undetectable particles. The endpoints of these distributions are related to the masses of the top quark, the W boson and the b-jet via

$$\mu_{bb}^{\max} = \frac{m_t}{2}\left(1 - \frac{M_W^2}{m_t^2}\right) + \sqrt{\frac{m_t^2}{4}\left(1 - \frac{M_W^2}{m_t^2}\right)^2 + \tilde{M}_W^2} \tag{1.24}$$

and

$$m_{lb}^{\max} = \sqrt{m_b^2 + (E_W + p_b)(E_b + p_b)} \tag{1.25}$$

where $\tilde{M}_W$ is the test mass used in the construction of the transverse energy and E_W, E_b and p_b are the energies and momenta of the decay products in the top-quark rest frame. While these expressions in principle allow for a simultaneous fit of both m_t and M_W, the mass of the W boson is constrained to its world average value $M_W = 80.358\,\text{GeV}$ [65] in order to determine the best estimate for the top mass. The mass of the b-jet is evaluated on an event-to-event basis with a typical size of $m_b \sim 10\,\text{GeV}$ and due to the JES is the dominant source of systematic uncertainty in this approach. Still, the overall precision of the extracted mass is high, even surpassing some of the earlier standard measurements in the dilepton channel without suffering from the aforementioned discrepancy between MC mass and pole mass definitions. However, as an *in situ* fit of the JES is not possible with the endpoint method, the proper modeling of the b-jet system will remain a limiting factor in future analyses [67].

4. *Determination from kinematic distributions*

   Over the years a variety of methods based on different observables has been developed to exploit the kinematic properties of the top quark and its decay products for a precise mass determination [98–102]. These studies are by no means restricted to the endpoint region of the respective distributions but include various characteristic features that are accessible to experimental investigation. However, only the latest improvements in the understanding of systematic uncertainties as well as the increase in statistics allow to confront these analyses with actual data. Two of the most promising candidates in this context are the J/ψ method and the m_{lb} method.

   Originally proposed in Ref. [103], the J/ψ method uses the experimentally very clean process $pp \to t\bar{t} \to b(\to J/\psi \to l^+l^-)W^+(\to l^+\nu)\bar{b}(\to l^- + X)W^-(\to jj)$ to extract m_t from the invariant-mass distribution of the reconstructed J/ψ and the lepton from the W^+ decay. As a measurement of this quantity involves purely leptonic degrees of freedom, it is virtually unaffected by JES uncertainties, which allows for a very precise experimental determination provided that a sufficiently large data sample is available. This, however, is a highly non-trivial task since the strongly suppressed cross section for this process requires an integrated luminosity of at least $100\,\text{fb}^{-1}$ in order to reach the desired level of precision for the extracted top mass [103]. Alternatively, it is possible to reduce the amount of required data to $\sim 20\,\text{fb}^{-1}$ by imposing a less strict condition on the $\bar{b}$-quark decay at the price of dealing with an increased combinatorial

background [104]. A first measurement based on such a modified approach using 8 TeV $t\bar{t}$ and single-top data yields a top mass of $173.5 \pm 3.0(\text{stat.}) \pm 0.9(\text{syst.})$ GeV [105], which will certainly further improve in the near future once the 13 TeV data sample is included as well.

A different strategy to simplify the theoretical description of this complex final-state configuration is to replace the J/ψ by a B-meson since the $B \to J/\psi$ decay has been intensively studied at B-factories[17] and is well under theoretical control. The corresponding predictions for the m_{Bl} distribution have been derived using standard parton-shower-based MC methods [106, 107] as well as in a dedicated NLO calculation [108]. In the latter analysis the transition of the b-jet into a B-meson is modeled through a NLO fragmentation function taking into account the full production and decay dynamics of the $pp \to t\bar{t} \to b(\to B)W^+\,\bar{b}\,W^-$ process in the ℓ+jets channel. Both of these approaches yield a linear relation between the mass of the top quark and the mean value of the invariant mass $\langle m_{Bl} \rangle$, which can be used to determine m_t with a projected accuracy of about 1.5 GeV with the prospect of a possible future reduction to below 1 GeV [67]. The current LHC run will for the first time provide enough statistics to apply this method to actual data and prove whether such an error estimate is realistic.

A similar type of analysis has also been suggested for the invariant mass of a lepton and a b-jet in dileptonic top decays [98]. In this case, it is possible to construct an estimator for m_t from the mass of the W boson and the average values of m_{lb} and θ_{lb},

$$M_{\text{est}}^2 = M_W^2 + \frac{2\left\langle m_{lb}^2 \right\rangle}{1 - \langle \cos\theta_{lb} \rangle} \tag{1.26}$$

where the latter variable denotes the opening angle between the lepton and the b-jet in the W rest frame. At LO this estimator corresponds exactly to the top mass but due to experimental complications such as kinematic cuts, particle misidentification or mismatching, etc. as well as higher-order QCD corrections to the top-quark decay including additional radiation, this equivalence is diluted in practice. These effects can, however, be quantified and their impact has been explicitly determined through a perturbative calculation at NLO accuracy [108], which similarly to the J/ψ method leads to a linear relation between M_{est} and m_t that can be employed for a measurement of the top-quark mass with an expected precision in the range of ~ 1 GeV.

While this method has not yet been applied to data, the CMS collaboration was recently able to obtain a high-precision estimate for the top mass of $m_t = 171.4^{+1.0}_{-1.1}$ GeV by using a different strategy based on the shape of the m_{lb} distribution [109]. Analogous to the template method, in this approach the mass is determined by constructing a fitting function of m_{lb} in terms m_t and performing a χ^2 analysis to find the best estimator for this quantity. In this case, however, the prediction for the differential cross section σ_{pred} is converted to the detector level via so-called forward folding. The main idea behind this technique is to absorb all effects that contribute to the transition between

[17] Collider experiments such as BABAR or BELLE that have been specifically designed to produce a large number of B-mesons and study their properties are often called "B-factories".

a partonic observable and the reconstructed events into a response matrix that can be obtained from MC simulations and is defined as

$$M_{ij}^{\text{resp}} = \frac{N_{ij}}{\sum_{k=0}^{n} N_{ik}} \,. \tag{1.27}$$

Here, N_{ij} corresponds to the number of events generated in bin i and reconstructed in bin j and $k = 0$ contains events that escaped experimental detection. For an integrated luminosity $\mathcal{L}$ the number of predicted events used in the χ^2 fit is then given by

$$\vec{N}_{\text{pred}} = \mathcal{L}\, M_{ij}^{\text{resp}}\, \vec{\sigma}_{\text{pred}} \,. \tag{1.28}$$

In the study performed by CMS the theory predictions at LO and NLO accuracy were computed with MCFM [110, 111] while the modeling of M_{ij}^{resp} was done with MADGRAPH+PYTHIA [112, 113]. The uncertainties related to the determination of the response matrix turn out to be the dominant contribution to the overall error of the extracted top mass whereas the theory input has virtually no impact on the precision of this analysis. Thus, a further improvement of this method will strongly rely on the progress in describing the transition from fixed-order perturbation theory to complex hadronic final states as observed in the detector although it already yields results with an impressive degree of precision.

5. *Determination from the differential cross section for $t\bar{t}+j$ production*

   Apart from studying the production of top-quark pairs, it is also possible to determine the top mass from a more complex final-state configuration containing an additional hard jet $pp \to t\bar{t}j + X$. While the inclusive cross section for this process exhibits a behavior similar to Eq. (1.18), a novel approach based on the normalized differential cross section

$$\mathcal{R}\,(\rho_s, m_t) = \frac{1}{\sigma_{t\bar{t}j}} \frac{d\sigma_{t\bar{t}j}}{d\rho_s} \quad \text{with} \quad \rho_s = \frac{170\,\text{GeV}}{\sqrt{s_{t\bar{t}j}}} \tag{1.29}$$

   is up to five times more sensitive to m_t rendering it an excellent instrument for high-precision mass measurements [114]. The theoretical description of this quantity is well under control with predictions available at NLO accuracy [115–117] and even allowing for a matching with parton showers [118,119]. Moreover, the normalization of $\mathcal{R}$ is expected to lead to a further reduction of the overall theoretical uncertainty due to cancellations between numerator and denominator. Consequently, the combined error induced by scale variation and PDF uncertainties is estimated to lie below 1 GeV. The attainable precision of this method therefore crucially depends on the experimental bounds on the measured differential cross sections, which should however also profit from an enhanced precision due to correlation effects. A first example of such an analysis has been presented by ATLAS [120] where a proper reconstruction of $\mathcal{R}$ was achieved by applying a kinematic fit to ℓ+jets data to identify the relevant $t\bar{t}+j$ system. Subsequently, the extracted distribution has been unfolded to the parton level where it has been checked that the dependence on the MC mass used in this procedure is negligible. The top mass

has then been determined from a least square fit of the NLO+PS prediction to the thus measured cross section, discarding the less sensitive range $\rho_s < 0.25$, yielding

$$m_t = 173.7 \pm 1.5\,(\text{stat.}) \pm 1.4\,(\text{syst.})^{+1.0}_{-0.5}\,(\text{theo.})\,\text{GeV}\ . \tag{1.30}$$

This result still suffers from rather large statistical uncertainties due to the use of a limited data set of $4.6\,\text{fb}^{-1}$, which will certainly change once the full data sample from the various LHC runs is included. Indeed, in a similar analysis performed by CMS based on $19.7\,\text{fb}^{-1}$ of 8 TeV dilepton data [121] the statistical error has already decreased to 1.1 GeV rendering the systematic error the dominant source of uncertainty. In the future this method might be further improved by fitting to a more restricted domain of $\mathcal{R}$ that is less affected by scale and PDF uncertainties allowing for an additional reduction of the uncertainty related to the employed theory predictions. The systematic uncertainties, on the other hand, depend strongly on the actual decay channel utilized for the experimental analysis and thus any progress relies on a general improvement in the understanding of the underlying measurement process. Taking this into account, a total uncertainty of 1 GeV or lower seems to be well within reach.

A quantity closely related to m_t is the mass difference of top quark and anti-top quark $\Delta m_t \equiv m_t - m_{\bar{t}}$. Its determination allows for an important test of the CPT-symmetry, a fundamental symmetry which follows directly from the formulation of the SM as a Lorentz-invariant, local field theory and implies the exact equality of the masses of particles and anti-particles. Yet, so far all measurements both at the Tevatron [122,123] and the LHC [124–126] are in full agreement with the SM expectation $\Delta m_t = 0$. These analyses rely on the same standard methods used in m_t measurements but in this case the total uncertainty is dominated by statistical rather than systematic effects as can be seen, for instance, for the most accurate result $\Delta m_t = -272 \pm 196\,(\text{stat.}) \pm 122\,(\text{sys.})\,\text{MeV}$ provided by the CMS collaboration [126]. With the recent restart of the LHC it will be interesting to see to what extent this uncertainty can be further reduced and whether there are new-physics contributions hiding behind this mass difference.

1.2.2 The total decay width Γ_t

The total decay width of a particle is not a fundamental parameter of a quantum field theory but can be derived in terms of masses and couplings and thus allows for a detailed examination of the internal structure of the underlying theory provided that all required input parameters are known. Any deviation of the predicted width from the value observed in experiment might hint at either the existence of unidentified particles or a new vertex structure that has not been considered yet. In practice, such a comparison requires a reliable theoretical description of the decay process, usually within perturbation theory, and a preferably model-independent method for its precise measurement, which, as we will see in the following, applies only to a limited extent to the top quark.

As the decay of elementary particles in the SM is mediated by weak interactions, the lowest order top-quark decay is given as $t \to W^+ q$, where $q = b, s, d$ respectively. Since the kinematic properties of these processes are identical, their relative decay rate is completely governed by

the Cabibbo-Kobayashi-Maskawa (CKM) mechanism leading to a strong suppression of decay channels that involve transitions between different quark generations[18]. This is also true for exotic decay modes involving flavor-changing-neutral-currents (FCNC), e. g. $t \to q\,g$ or $t \to q\,Z$, which can only occur at loop level and thus experience an additional suppression that renders them virtually inaccessible for any kind of physical investigation. They are, however, still interesting since various BSM scenarios predict strong enhancements for these processes, which could be detectable in future experiments.

Due to the limited experimental precision of current Γ_t determinations, its theoretical description within the SM is sufficiently well approximated by the partial decay width of the $t \to W^+\,b$ channel. Assuming the intermediate W^+ to be on-shell and neglecting the mass of the bottom quark, the LO prediction for this process reads

$$\Gamma_t^{LO} \equiv \Gamma_t^{LO}(t \to W^+\,b) = \frac{G_F}{8\pi\sqrt{2}} m_t^3 |V_{tb}|^2 \left[1 - 3\left(\frac{M_W^2}{m_t^2}\right)^2 + 2\left(\frac{M_W^2}{m_t^2}\right)^3\right] = 1.50\,\text{GeV} \quad (1.31)$$

where $|V_{tb}|$ is the CKM matrix element for the top-to-bottom transition, G_F is the Fermi constant and the current world average for $m_t = 173.34\,\text{GeV}$ and $M_W = 80.358\,\text{GeV}$ has been used for the numerical evaluation. The effect of considering off-shell W bosons and a non-zero bottom mass is small [131] and turns out to almost completely cancel with the NLO electroweak corrections [132,133]. For this reason, these contributions can be safely neglected and the total width is conveniently expressed in terms of pure QCD corrections

$$\Gamma_t(m_t = 173.34\,\text{GeV}) = \Gamma_t^{LO}\left[1 - 2.51\frac{\alpha_s(m_t)}{\pi} - 17.6\left(\frac{\alpha_s(m_t)}{\pi}\right)^2\right] = 1.34\,\text{GeV}\,. \quad (1.32)$$

The NLO coefficient has already been computed in the late 1980s and is known entirely analytically [134] while the NNLO contributions were first derived as an expansion in various kinematic limits [135–137] and only a few years ago became fully available in the course of the calculation of the $\mathcal{O}(\alpha_s^2)$ corrections to the differential decay rate for the process $t \to b\,l^+\,\nu$ [12,13]. The numerical difference of the full result with respect to the expansions is, however, negligible and hence either of them is suited to accurately predict the SM value of Γ_t.

While the theoretical description of the top decay width is well understood, its measurement is a challenging task that pushes the limits of our current experimental capabilities. Direct determination methods based on template fits suffer from the low sensitivity of kinematic variables to Γ_t and thus require a careful treatment of systematic effects in order to ensure a reliable extraction from data. As a result, the first-ever measurement of the top width was only able to provide an upper bound of $\Gamma_t < 13.1\,\text{GeV}$ [138] and only lately the CDF collaboration came up with a two-sided limit of $1.10\,\text{GeV} < \Gamma_t < 4.05\,\text{GeV}$ at 68% C.L. [139] that, however, by no means matches the available theoretical precision. The limitations of these measurements led to the development of an alternative analysis technique, which is based on additional SM assumptions and thus not as model-independent as the direct determination

[18] Apart from analyses based on the unitarity of the CKM matrix there is also direct experimental evidence for the dominant behavior of $\Gamma(t \to W^+\,b)$ from measurements of $R_{\mathcal{B}} \equiv \frac{\mathcal{B}(t\to W^+b)}{\sum_{q=b,s,d}\mathcal{B}(t\to W^+q)} = \frac{|V_{tb}|^2}{|V_{tb}|^2+|V_{ts}|^2+|V_{td}|^2}$, where the right-hand side is the SM prediction for this ratio [127–130].

methods [140]. It assumes equal $t \to W^+ b$ couplings in top-quark production and decay as well as unitarity of the CKM matrix to derive a relation for the decay width in terms of the t-channel single top-quark production cross section $\sigma_{t-ch.}$, the decay rate $\Gamma(t \to W^+ b)$ and the branching ratio $\mathcal{B}(t \to W^+ b)$,

$$\Gamma_t = \frac{\sigma^{\text{exp.}}_{\text{t-ch.}} \Gamma^{\text{theo.}}(t \to W^+ b)}{\mathcal{B}^{\text{exp.}}(t \to W^+ b) \sigma^{\text{theo.}}_{\text{t-ch.}}} \tag{1.33}$$

where *exp.* and *theo.* denote measured and predicted quantities respectively. This indirect determination method has been employed by DØ and CMS yielding $\Gamma_t^{\text{D0}} = 2.00^{+0.47}_{-0.43}\,\text{GeV}$ [141] and $\Gamma_t^{\text{CMS}} = 1.36 \pm 0.02\,(\text{stat.})^{+0.14}_{-0.11}\,(\text{sys.})\,\text{GeV}$ [130], which is in good agreement with the theoretical SM expectation although the still sizable uncertainty prevents any further conclusions with regard to possible BSM contributions. While the precision of both direct and indirect measurements will certainly increase with the higher statistics of the current and upcoming LHC runs and the associated improvement in the understanding of systematic effects, the most accurate determination of Γ_t will be provided by a future e^+e^- collider. Similar to the top mass it can be inferred from a threshold scan with a projected precision well below 100 MeV [55], which will finally allow for a detailed comparison between theory and data to reveal any type of potentially new physics that might hide in the top-quark sector.

1.2.3 Spin

All fields in the SM Lagrangian are constructed from objects (spinors, vectors, etc.) that transform under a certain finite-dimensional representation of the Lorentz-group, which is connected to the spin of the corresponding particle. Hence, virtually any observable calculable within perturbation theory contains implicit information on the spin of the individual particles involved. Due to the tremendous success of the SM in describing large amounts of data collected at various collider experiments, it is therefore well established that the top quark is a spin 1/2 fermion without an explicit verification through a specifically designed measurement. Since the top quark cannot be observed directly but only through its decay products, one might argue that, although the conservation of total angular momentum requires the top to be a fermion, it would still allow for an exotic spin value of 3/2. This scenario is, however, ruled out by the almost vanishing decay fraction $F_+ = \mathcal{B}(t \to W^+(\lambda_+)\, b)$ for producing W bosons with positive helicity, which has been measured at the Tevatron [142] as well as the LHC [143–145] and is in good agreement with the SM expectation [146]. Moreover, a higher spin would lead to a strongly enhanced pair production cross section [147], which is observed at neither of the existing collider experiments. While there are several other measurements in support of the top quark being a SM fermion, one should mention two observables that are more intuitively related to its spin than the previous examples, namely the top polarization and the $t\bar{t}$ spin correlation (for a detailed discussion of the latter see section 1.3.3). Although primarily aiming at the search for contributions from anomalous couplings, the experimental determination of these quantities serves as an excellent test of the spin 1/2 hypothesis. As all measurements so far proved to be consistent with the SM predictions, any lingering doubts about the actual value of the spin of the top quark should be removed once and for all.

1.2.4 Charge, color and weak isospin

While the electric charge of the lighter quarks has been determined by studying EW production processes at various e^+e^- colliders, the charge of the top quark Q_t is measured by analyzing the charge of its decay products, the W boson and the b-jet. In the SM the top is the weak isospin partner of the bottom quark requiring its charge to assume a value of $Q_t = \frac{3}{2}$ (in units of the elementary charge) in order to ensure the exact cancellation of anomalies and maintain the renormalizability of the theory. However, since top quarks are predominantly produced in pairs, the charge assignment of the $t\bar{t} \to W^+W^-b\bar{b}$ decay chain is not unique and would a priori allow for an exotic top quark with charge $Q_t = -\frac{4}{3}$. Indeed, such a scenario was discussed in the first years after the top discovery to explain deviations of certain EW observables from the SM expectation [148, 149] but it has meanwhile been excluded through direct measurements at the Tevatron [150, 151] and the LHC [152, 153].

These analyses employ ℓ+jets data to reconstruct Q_t from the charges of the lepton and the b-jet originating from the same top-quark decay. Due to the fact that the associated neutrino is neutral the measured lepton charge corresponds directly to the charge of the W boson. The determination of the bottom charge, on the other hand, poses a greater experimental challenge but has been achieved by either exploiting the sensitivity of soft muons inside the b-jet to the flavor of the original quark or by using the so-called jet charge defined as

$$Q_{\mathrm{b-jet}} = \frac{\sum_i Q_i |\vec{j} \cdot \vec{p}_i|^K}{\sum_i |\vec{j} \cdot \vec{p}_i|^K} \,. \tag{1.34}$$

Here, $\vec{j}$ denotes the direction of b-jet axis while Q_i and $\vec{p}_i$ are the charge and the momentum of the i-th track within the jet cluster. The parameter K ensures an optimal separation of b- and $\bar{b}$-jet charges and is usually determined from a simulated data sample prior to the actual analysis. In order to be able to discriminate between the SM and the exotic Q_t model, one constructs a test statistic from the measured charges that clearly separates both scenarios. Although the actual form of this variable differs among the various experimental groups, the result of these hypothesis tests is clearly in favor of the SM. The ATLAS collaboration, for instance, measured a top charge of $Q_t = 0.64 \pm 0.02\,(\mathrm{stat.}) \pm 0.08\,(\mathrm{sys.})$ and was able to set the currently strongest exclusion limit on the $Q_t = -\frac{4}{3}$ model of 8 standard deviations [153].

As the presence of a conserved charge is a consequence of gauge symmetry, it can also be determined by studying the cross section of associated gauge-boson production. In case of the electric top charge the relevant cross section $\sigma_{t\bar{t}\gamma}$, which despite its strong suppression has been measured at both Tevatron [154] and the LHC [155–157], is in agreement with the SM prediction. A more refined determination of Q_t from $\sigma_{t\bar{t}\gamma}$ is complicated by the fact that not only the top quark but also its decay products as well as the initial-state quarks can radiate photons. Although it is possible to remove these unwanted emissions from data by applying additional experimental cuts, such an analysis has not been performed yet as already the measurement of $\sigma_{t\bar{t}\gamma}$ represents a serious challenge due to limited statistics and large

background contributions. This might, however, change with the current and future LHC runs, which will provide significantly more data and thus allow for a more detailed examination of the top-photon interaction.

The remaining gauge groups of the SM, $SU(3)$ and $SU(2)$, also lead to conserved quantities, namely color and weak isospin, which manifest themselves in the vertex structure of the top-gauge boson couplings. As QCD is the dominant theory at hadron colliders, virtually any observable at the Tevatron and the LHC is affected by the correct assignment of color charge despite the impossibility to observe it directly due to confinement. In this sense, all top measurements can be viewed as an indirect determination of this quantum number, which so far have yielded no evidence that stands in contradiction to the top quark forming a fundamental $SU(3)$ triplet as predicted by the SM.

The weak isospin T_3 can be measured in a similar manner as the electric charge from the cross section of associated Z boson production $\sigma_{t\bar{t}Z}$, which proves to be even more challenging as this process is further suppressed compared to $\sigma_{t\bar{t}\gamma}$. Nevertheless, it has recently been observed at the LHC [158–161] either separately or in combination with associated W boson production. Although the measured cross section is in agreement with the SM prediction, the sizable experimental uncertainties prevent any precise quantitative conclusions on the isospin itself. Moreover, since the $Zt\bar{t}$-vertex involves both left-handed $T_3^L = \frac{1}{2}$ and right-handed $T_3^R = 0$ top quarks, an unambiguous determination of the isospin requires an additional observable sensitive to the top-Z-boson coupling. Prior to the discovery of the top, such a measurement has been performed for bottom quarks using EW data from various collider experiments [162], which successfully confirmed the SM isospin content of the b quark and strongly suggested the existence of a $T_3^L = \frac{1}{2}$ top quark. A direct determination of the top isospin based on a similar approach is, however, still missing despite the fact that there have been first attempts to investigate the tZ-coupling in more detail [160]. Such a measurement might, however, become accessible with the increasing statistics of Run 2 of the LHC at 13 TeV that will allow for a more detailed study of EW effects in the QCD-dominated data samples.

1.3 Top-quark phenomenology

Due to its unique properties the top quark offers a wide range of phenomenological applications aiming at both, an in-depth examination and verification of the SM as well as uncovering any type of new-physics effects that might be hiding in Tevatron or LHC data. The following section will give a concise overview on the most interesting and extensively studied observables related to top physics summarizing their current theoretical and experimental status and assessing their future development, in particular in the light of the recent start of Run 2 of the LHC.

1.3.1 Total inclusive top-quark pair production

As top quarks are predominantly produced in pairs in hadronic collisions, one of the most natural observables to study is the total inclusive $t\bar{t}$ production cross section $\sigma_{t\bar{t}}^{\mathrm{tot}}$, which, along with m_t, was the first top-related quantity that was measured when this new type

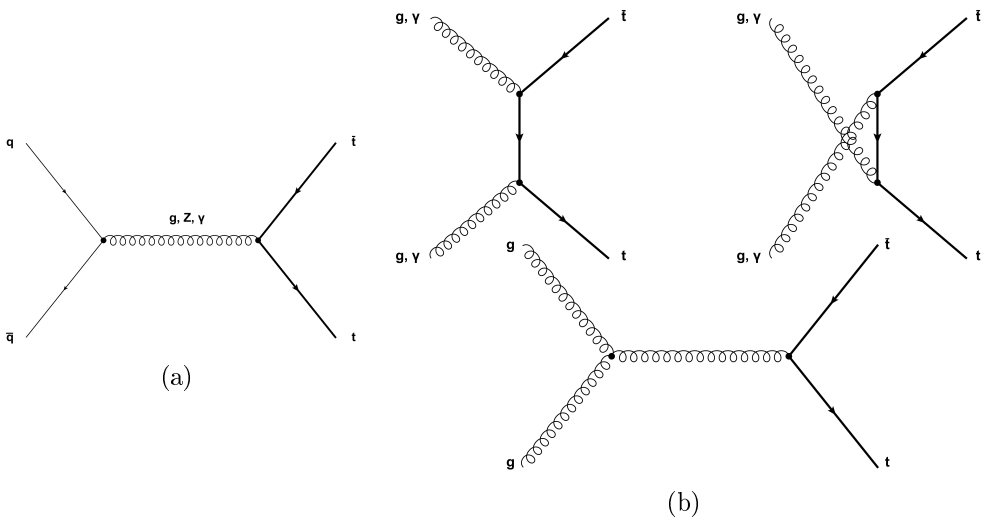

Figure 1.7: *QCD diagrams contributing to the LO partonic cross section for $t\bar{t}$ production in the quark annihilation (a) and gluon fusion channel (b). The EW and mixed QCD-EW diagrams can be obtained from these topologies by replacing a gluon with a photon or a Z boson as indicated above[19]. As their impact on inclusive observables like $\sigma_{t\bar{t}}^{\mathbf{tot}}$ is small compared to the pure QCD contributions, they are commonly omitted from LO calculations and treated as a correction.*

of quark was originally discovered at the Tevatron in 1995 [7, 8]. Meanwhile, it has been thoroughly investigated at both Tevatron [163–172] and the LHC [85, 86, 130, 173–197] at various center-of-mass energies with the latest determinations reaching a remarkable level of precision of 5% and below [85, 86, 163, 182, 197]. The experimental techniques have, in fact, become so refined that they allow for applications of $\sigma_{t\bar{t}}^{\mathbf{tot}}$ that go beyond a simple comparison of theory and data, e. g. a compatible extraction of SM quantities such as m_t [34,63,83–86] and α_s [83] or even searches for certain non-SM scenarios in top-quark events [85, 198–207]. Such dedicated analyses, however, require a well-understood theoretical framework that provides reliable predictions in terms of various input parameters and that is constantly improved in order to be able to cope with the progress in experimental precision.

This is fortunately the case for inclusive $t\bar{t}$ production where the total cross section can be well described perturbatively by utilizing the QCD factorization theorem. It separates the short-distance contributions into a so-called partonic cross section $\hat{\sigma}_{ij\to t\bar{t}+X}$ and the long-distance contributions into the PDFs $f_i^A(x, \mu_F)$, which can be interpreted as the probability of finding a parton i inside a hadron A carrying a certain longitudinal momentum fraction x at a factorization scale μ_F:

$$\begin{aligned}\sigma_{t\bar{t}}^{\mathbf{tot}}(s, m_t) &= \sum_{ij} \int_0^1 \int_0^1 dx_1 dx_2 \, f_i^A(x_1, \mu_F) f_j^B(x_2, \mu_F) \, \hat{\sigma}_{ij\to t\bar{t}+X}\left(m_t^2, \hat{s}, \mu_R, \mu_F, \alpha_s(\mu_R)\right) \\ &+ \mathcal{O}(\Lambda_{QCD})\end{aligned} \tag{1.35}$$

Here, s and $\hat{s} = x_1 x_2 s$ denote the square of the hadronic and partonic center-of-mass energy, μ_R and μ_F are the renormalization and factorization scale and the sum runs over all partons contained inside the hadrons A and B (proton and anti-proton for the Tevatron and protons for the LHC), i. e. 5 massless quark flavors and gluons (and, in principle, also photons). While the PDFs cannot be derived from first principles and have to be determined through an explicit measurement[20], the partonic cross section can be computed as a perturbative expansion in the couplings involved in the process using the standard Feynman rule formalism. The leading QCD diagrams for $t\bar{t}$ production are depicted in Fig. 1.7 and include two different production modes, denoted as gluon fusion and quark annihilation channels, whose relative contribution to $\sigma_{t\bar{t}}^{\mathbf{tot}}$ depends on the hadronic center-of-mass energy as well as on the nature of the colliding particles. At the Tevatron quark annihilation is the main production mechanism due to the presence of valance quarks and anti-quarks in the initial state whereas at the LHC the cross section is dominated by the gluon fusion channel. Higher perturbative orders (in QCD) open up additional production modes, e. g. the quark-gluon channel or initial states consisting of two differing (anti-)quark flavors, but these processes only contribute at the sub-percent level to the total cross section.

A major step towards a more solid theoretical description of $\sigma_{t\bar{t}}^{\mathbf{tot}}$ was accomplished in the late 80's with the calculation of the NLO QCD corrections [211, 212], which had a sizable impact on the resulting theory predictions and helped to significantly reduce the theoretical error due to missing higher-order effects conventionally estimated via scale variation. These findings were, however, obtained using purely numerical methods and it took another 20 years to derive the fully analytical expressions of the $\mathcal{O}(\alpha_s^3)$ terms revealing the true complexity of their kinematic dependencies [213].

Meanwhile, new techniques for the all-order resummation of logarithmic enhancements due to soft-gluon emissions, originally developed for Drell-Yan production, had been further improved to be also applicable to heavy-quark production [214–217]. These soft contributions behave as $\alpha_s^n \ln^m \beta$ ($\beta = \sqrt{1 - \frac{4m_t^2}{\hat{s}}}$ is the top-quark velocity in the $t\bar{t}$ rest frame and $0 \leq m \leq 2n$) and thus strongly affect the partonic cross sections in the threshold region $\beta \to 0$ accounting for a fair portion of the higher-order corrections to $\sigma_{t\bar{t}}^{\mathbf{tot}}$ at both Tevatron and the LHC. It is, therefore, highly desirable to include these effects in the theoretical description to all orders in perturbation theory as such a treatment will dramatically improve the precision of the resulting cross section predictions. In the original resummation formalism the factorization of soft-gluon radiation from the hard scattering amplitude is performed in Mellin N-space where the partonic cross sections assume a particularly simple form as a product of hard and soft contributions. The logarithmic enhancements present in the so-called soft function can then be resummed using a RG-type equation whose input parameters can be determined perturbatively and are currently known to NNLL accuracy [218–220] (for a detailed discussion

[19] There exist additional contributions to $q\bar{q} \to t\bar{t}$ and $q\bar{q}' \to t\bar{t}$ ($q' \neq q$) where the top pair is produced via t-channel W-boson exchange and thus cannot be deduced from the diagrams displayed above through a simple interchange of gauge bosons due to the differing vertex structure.

[20] Despite their non-perturbative nature, the scaling behavior of the PDFs can be described within perturbation theory via the DGLAP equations [208–210] hence rendering them applicable for processes that involve scales different from their measurement scale.

see section 3.1). This strategy was later also extended to more exclusive top-quark observables where the soft limit may be parametrized in terms of either pair-invariant-mass (PIM) kinematics, $\frac{(p_t+p_{\bar{t}})^2}{\hat{s}} \to 1$, or single-particle-inclusive (1PI) kinematics, defined for an inclusive final state X that contains the anti-top and any additional radiation as $p_X^2 \to m_t^2$ (and vice versa in case of anti-top observables). In contrast to the original resummation approach these modified definitions allow for a systematic treatment of logarithmic enhancements in the entire β-range as the soft emissions are no longer restricted to low-velocity regime. While these differential techniques were primarily aimed at improving the theoretical predictions for top-related distributions, they can be subsequently integrated to yield resummed results for the total cross section as well [221–224].

In the recent years the rapid progress in the field of Soft-Collinear Effective Theory (SCET) led to the development of a novel resummation formalism that works directly in momentum space [81, 225, 226] (also denoted as x-space in literature). Moreover, it allows for the factorization of an additional source of threshold enhancements due to the exchange of so-called potential gluons between the outgoing $t\bar{t}$ pair [81]. In the partonic threshold region the heavy-quark final state forms a non-relativistic two-particle system similar to, for example, positronium (but far more complicated due to the presence of color charges) whose dynamics is governed by various interaction potentials including the well-known Coulomb potential. Despite the fact that its exceptionally short lifetime prevents the top from forming actual bound states, these binding effects still affect the functional behavior of the partonic cross sections close to threshold giving rise to inverse powers of β and, at higher orders, to non-relativistic $\ln\beta$ terms. These enhancements may, however, be resummed as well by perturbatively solving a Schrödinger-type equation currently known to NLO accuracy[21], which complements the pure soft-gluon-based description of top-quark pair production at NNLL accuracy. The perturbative precision of the various resummation techniques was, in fact, so high that in the absence of a genuine NNLO calculation they offered a basic means of approximating the yet missing higher-order contributions by re-expanding the resummation formulae through $\mathcal{O}(\alpha_s^4)$ [227–229] even allowing for the derivation of the threshold-enhanced contributions in a fully analytical fashion [230].

While all approaches to soft-gluon resummation are equivalent in the sense that they yield the same leading behavior, the treatment of subleading contributions is somewhat ambiguous leading to numerically differing predictions for the total cross section at both NLO+NNLL and approximate NNLO. This triggered the development of a variety of publicly available software packages, the most prominent examples being Top++ [87] (N-space), Topixs [88] (x-space, soft+Coulomb) and Hathor [89] (N-space, soft+high-energy), which incorporated the different resummation methods and made them thus easily accessible for a broad spectrum of phenomenological applications. The increasing experimental precision, however, soon caught up with the theoretical progress calling for an evaluation of $\sigma_{t\bar{t}}^{\mathrm{tot}}$ at full NNLO accuracy despite the numerous approximations on the market. This was mainly

[21] The impact of non-relativistic logarithms, generated at NNLO through terms in the non-Coulomb potentials, has been shown to be negligible and they are therefore omitted from the resummation of potential contributions [81].

	Tevatron [pb]	LHC			
		7 TeV [pb]	8 TeV [pb]	13 TeV [pb]	14 TeV [pb]
LO	$6.784^{+3.005\ +0.149}_{-1.908\ -0.127}$	$123.7^{+49.5\ +3.2}_{-32.6\ -3.3}$	$176.2^{+68.2\ +4.2}_{-45.5\ -4.4}$	$583.2^{+199.4\ +11.2}_{-138.2\ -12.8}$	$692.5^{+232.1\ +12.8}_{-161.9\ -14.9}$
NLO	$6.851^{+0.366\ +0.186}_{-0.772\ -0.128}$	$162.0^{+20.0\ +4.3}_{-21.7\ -5.4}$	$231.6^{+28.5\ +5.7}_{-30.4\ -7.2}$	$763.3^{+92.5\ +14.4}_{-92.5\ -17.4}$	$903.8^{+109.2\ +16.4}_{-108.1\ -16.8}$
NNLO	$7.186^{+0.266\ +0.173}_{-0.383\ -0.124}$	$171.1^{+6.8\ +4.7}_{-10.9\ -4.8}$	$244.8^{+9.5\ +6.2}_{-15.2\ -6.4}$	$805.5^{+27.7\ +14.6}_{-44.8\ -15.8}$	$953.3^{+32.5\ +16.4}_{-52.1\ -17.9}$
NLO+NLL	$7.218^{+0.203\ +0.188}_{-0.434\ -0.131}$	$176.2^{+15.7\ +4.6}_{-14.9\ -5.8}$	$250.9^{+22.5\ +6.1}_{-21.5\ -7.6}$	$816.0^{+74.0\ +15.1}_{-72.3\ -18.2}$	$964.4^{+87.6\ +17.2}_{-85.8\ -17.7}$
NLO+NNLL	$7.593^{+0.035\ +0.179}_{-0.311\ -0.128}$	$182.3^{+10.9\ +4.9}_{-13.9\ -5.0}$	$260.0^{+15.6\ +6.4}_{-19.7\ -6.6}$	$847.1^{+51.7\ +15.0}_{-64.5\ -16.4}$	$1001^{+61\ +17}_{-76\ -19}$
NNLO+NNLL	$7.345^{+0.112\ +0.173}_{-0.205\ -0.124}$	$176.4^{+4.8\ +4.8}_{-6.0\ -4.9}$	$251.8^{+6.8\ +6.3}_{-8.7\ -6.5}$	$824.4^{+21.1\ +14.8}_{-29.3\ -16.0}$	$975.0^{+24.8\ +16.5}_{-34.8\ -18.2}$

Table 1.2: *Theoretical predictions for $\sigma_{t\bar{t}}^{\mathrm{tot}}$ at the Tevatron and the LHC including different orders of perturbative QCD corrections and soft-gluon resummation ($m_t = 172.5\,\mathrm{GeV}$, MSTW2008 PDFs at 68% C.L. [231]). The quoted uncertainties are due to the variation of renormalization and factorization scale and the parametric error of the PDFs.*

due to the conceptual problem of determining a reliable theory error estimate owing to the numerical importance of the subleading terms in these resummation procedures. Indeed, while the individual errors on the approximate cross section predictions was fairly small, a conservative error estimate involving a combination of different approaches in order to assess the impact of these subleading contributions resulted in a considerably larger uncertainty estimate that was only somewhat smaller than the NLO error and therefore made a complete NNLO calculation indispensable.

Although there were already results available at NNLO for Drell-Yan, vector-boson, Higgs and diphoton production, extending the computational methods developed for these processes to top-quark pair production was a substantially more challenging task as it, for the first time at such a high level of precision, involved a final-state configuration with massive particles that carry color charge. The calculation was, however, eventually made possible by the invention of a novel subtraction scheme [232,233] (see section 3.2.4) that allowed for an efficient treatment of the contributions from double-real radiation, which proved to be the bottleneck of the $t\bar{t}$ NNLO program. Starting with the evaluation of the quark annihilation channel in spring of 2012 [77], soon all partonic production modes containing at least one initial-state fermion became available at full NNLO accuracy [78, 79] until, finally, in 2013 the NNLO analysis of the total cross section was concluded with the publication of the results for the purely gluon-initiated reactions [80]. The numerical impact of the separate production channels on the total cross section predictions, however, turned out to be very different. While the fermionic contributions ($qg \to t\bar{t} + X$,$q\,(\bar{q}) \to t\bar{t} + X$ and $q\,\bar{q}' \to t\bar{t} + X$, where $(\bar{q})'$ is a (anti-)quark of different flavor than q) only had a moderate effect on the central value of $\sigma_{t\bar{t}}^{\mathrm{tot}}$ compared to the approximate NNLO results, the corrections in the gluon fusion channel were quite sizable amounting to as much as 5% at the LHC. This had not necessarily been expected beforehand implying that a considerable portion of the NNLO contributions originates in the off-threshold regime $\beta \gtrsim 0.2$.

Another important feature of the full calculation, common to all production modes, was the further reduction of the scale dependence to about 5%, even decreasing to as low as 3% when soft-gluon resummation is included (see Tab. 1.2). Moreover, it eliminated the strong sensitivity to subleading terms in the resummation formalisms (which, as mentioned above, was one of the main motivations for going to full NNLO) and allowed for a first numerical estimate of the so-called NNLO hard matching coefficients, constant terms in the resummation formulae that could not be predicted in advance[22]. Additional sources of theoretical uncertainty that enter the predictions for $\sigma_{t\bar{t}}^{\mathbf{tot}}$ are the PDF error and the experimental uncertainties on the strong coupling constant and the top mass. They vary between 1-3% and are thus comparable to the error due to missing higher-order effects creating an intricate situation where a further reduction of the overall uncertainty requires a simultaneous effort on several fronts. Nonetheless, there have been recent attempts to construct approximate next-to-next-to-next-to-leading order (NNNLO) results [235,236] but since these analyses basically rely on the same information as already contained in the NNLO+NNLL predictions, the numerical difference between these approaches is only marginal lying well within the quoted errors of the latter.

A similar situation may be encountered for the EW interaction effects, which, despite the fact that they clearly constitute an additional contribution to the theoretical description of $\sigma_{t\bar{t}}^{\mathbf{tot}}$, only amount to as much as $\sim$0.5% at the Tevatron and $\sim$-1% at the LHC [91]. Taking into account the exchange of massive vector bosons ($W^{\pm}$,Z) and photons as well as of the Higgs boson, these contributions are usually classified as purely EW $\mathcal{O}(\alpha^2)$ or mixed QCD-EW $\mathcal{O}(\alpha_s^2\alpha)$ corrections[23] [91,237–243], where $\alpha = \frac{e^2}{4\pi}$ denotes the electromagnetic coupling constant. All other contributions are suppressed even further, either by an additional factor of α, the smallness of the corresponding CKM mixing angle or an almost vanishing partonic flux (defined as the convolution of the PDFs in the cross section formula Eq. (1.35), see also Eq. (2.1)). Although one might have expected beforehand that the impact of EW corrections would be subdominant with respect to the pure QCD contributions due to the substantially smaller coupling, the presence of large Sudakov logarithms in the high-energy regime $\hat{s} \gg M_{W/Z}^2$ can lead to strong enhancements that spoil this naive picture. This is indeed the case for several differential observables as well as certain asymmetries (see sections 1.3.3 and 1.3.4). The total cross section, however, proves to be virtually insensitive to these Sudakov effects, which is mainly due to the fact that for the currently available collider energies the relevant region of phase space is suppressed by the partonic fluxes. Thus, in practice EW corrections are commonly neglected in phenomenological applications involving $\sigma_{t\bar{t}}^{\mathbf{tot}}$.

So far, we restricted our discussion of $t\bar{t}$ production to the case where the top quarks are considered as stable particles, which is quite contradictory to our previous statement of the top being a highly elusive particle with a mean lifetime of $\tau_t \approx 10^{-25}$ s. Fortunately, it turns out

[22] A more dedicated determination of the hard matching coefficients was performed in Ref. [234] confirming the first numerical analyses in Refs. [77, 80] within the quoted errors. Furthermore, it revealed an additional logarithmic Coulomb enhancement absent in the original approximate NNLO prediction [230], whose numerical impact, however, turned out to be negligible.

[23] An interesting feature of the photonic corrections [237], a subclass of the mixed QCD-EW contributions, is the occurrence of initial-state photons that requires the introduction of a photon PDF as well as the inclusion of EW effects in the DGLAP equations.

that an inclusive observable such as the total cross section is only mildly affected by the details of the decay processes, which typically introduce corrections of the order of $\mathcal{O}\left(\frac{\Gamma_t}{m_t}\right) \sim 1\%$, rendering the on-shell approximation a valuable tool for the theoretical description of these narrow resonances. In general, the treatment of unstable particles at the quantum level requires the resummation of certain self-energy contributions introducing an imaginary part in the particles' propagators that can be identified with the total decay width,

$$\frac{1}{p^2 - m^2} \to \frac{1}{p^2 - m^2 + im\Gamma} \,. \tag{1.36}$$

This is, however, highly non-trivial as the resummation procedure can lead to matrix elements that violate gauge invariance due to the interweaving of different orders of the perturbative expansion. An elegant solution to this problem is given by the so-called complex mass scheme [244–246] where the renormalized mass and the corresponding counterterm vertex become complex parameters such that the imaginary part of both quantities cancels at the level of the bare Lagrangian. This prescription manifestly conserves gauge invariance since a complex mass term does not spoil the validity of the resultant algebraic identities, however, to the price of violating unitarity. But as this violation is formally a higher-order effect that cannot induce any spurious enhancements, it does not cause any problems in practical calculations and in consequence the complex mass scheme has been successfully applied to a variety of processes that involve unstable particles. In fact, it has also been employed in the determination of the complete off-shell effects for top-quark pair production at NLO QCD [247–250] (including finite bottom mass effects [251, 252]), albeit only for the dileptonic decay chain $p\,(\overline{p}) \to t\bar{t} + X \to W^+W^-b\bar{b} + X \to e^+\nu_e\mu^-\overline{\nu}_\mu b\bar{b} + X$ owing to the high computational effort of such a dedicated analysis[24]. It contains contributions from double-, single- and non-resonant diagrams, i. e. from diagrams containing two, one or no potentially on-shell top quark, and, moreover, imposes certain kinematic selection criteria in order to allow for a direct comparison with experimental data. At first glance, this seems to prevent us from quantitatively assessing the impact of off-shell effects on $\sigma_{t\bar{t}}^{\mathbf{tot}}$ with respect to the stable-top approximation since such an analysis would require the incorporation of (differential) top-quark decays into the cross section calculation while still preserving the on-shell nature of the top quarks. This can, however, be achieved by utilizing the so-called narrow-width approximation (NWA) in which one neglects the single- and non-resonant contributions (a strategy commonly referred to as double-pole approximation) and subsequently performs the limit $\frac{\Gamma_t}{m_t} \to 0$ leading to delta functions that force the top quarks to lie on their mass shell,

$$\left|\frac{1}{p_t^2 - m_t^2 + im_t\Gamma_t}\right|^2 = \frac{1}{(p_t^2 - m_t^2)^2 + m_t^2\Gamma_t^2} \xrightarrow{\frac{\Gamma_t}{m_t}\to 0} \frac{\pi\delta(p_t^2 - m_t^2)}{m_t\Gamma_t} \,. \tag{1.37}$$

While the double-pole approximation generally includes both factorizable and nonfactorizable diagrams (see Fig. 1.8), the contributions of the latter vanish in the NWA [253–255] reducing

[24] The case of equal lepton flavors is excluded in these analyses since without imposing additional cuts it would lead to collinear singularities stemming from $\gamma^* \to l^+l^-$ photon splittings. The contribution from these diagrams is supposedly small ($\sim 0.5\%$ at LO for inclusive cut selections) and thus the full dilepton cross section (without τ leptons) can be estimated by multiplying the $e^+\mu^-$ result by a factor of 4.

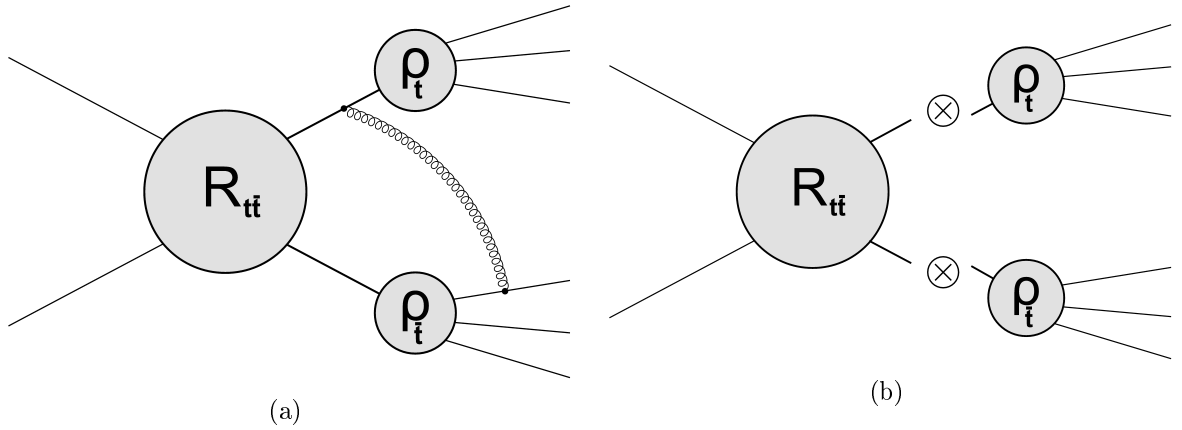

Figure 1.8: *Schematic representation of nonfactorizable (a) and factorizable (b) diagrams contributing to $t\bar{t}$ production in the double-pole approximation.*

the computational effort tremendously owing to the clear separation of production and decay processes. This becomes particularly evident when the cross section is expressed as

$$\sigma^{\mathrm{tot}}_{t\bar{t}\to X+Y} \propto \mathrm{Tr}\left(\mathbf{R}_{t\bar{t}}\,\boldsymbol{\rho}_{t\to X}\,\boldsymbol{\rho}_{\bar{t}\to Y}\right) \tag{1.38}$$

where $\mathbf{R}_{t\bar{t}}$, $\boldsymbol{\rho}_{t\to X}$ and $\boldsymbol{\rho}_{\bar{t}\to Y}$ are density matrices in spin space of the t and $\bar{t}$ quarks encoding the production (up to order $\mathcal{O}(\alpha_s^3)$ [256] and $\mathcal{O}(\alpha_s^2\alpha)$ [91,239]) and decay dynamics (up to order $\mathcal{O}(\alpha_s\alpha^2)$ [256–258]), respectively. This formalism was originally developed for the theoretical description of spin-dependent observables but it can be employed for the total cross section as well. In that case Eq. (1.38) may be simplified even further yielding

$$\sigma^{\mathrm{tot}}_{t\bar{t}\to anything} \propto \sum_X \sum_Y \sigma^{\mathrm{tot}}_{t\bar{t}}\,\mathfrak{B}(t\to X)\,\mathfrak{B}(\bar{t}\to Y) = \sigma^{\mathrm{tot}}_{t\bar{t}} \tag{1.39}$$

where $\mathfrak{B}$ denotes the corresponding top and anti-top branching ratios. This completely factorized form explains why treating top quarks as stable particles works so well. The NWA has, however, also been extended to more realistic scenarios that consider only specific decay channels with arbitrary cuts on the final-state particles [259] and are thus closer to the actual experimental conditions. While these analyses have so far only been performed at NLO in QCD, the latest results for NNLO stable-top pair production [77–80] in combination with the $\mathcal{O}(\alpha_s^2)$ corrections to the fully differential top-quark decays [12, 13], in principle, provide all ingredients necessary for a full NNLO treatment of this process within the NWA framework. Once available, such an evaluation will certainly lead to a further improvement in the theoretical description of hadronic $t\bar{t}$ production, in particular for more exclusive observables related to the top-quark decay products.

But not only the theoretical description of $t\bar{t}$ production has experienced some major progress over the last decade, also the experimental techniques were successively refined to allow for a ever more precise determination of the total cross section at both the Tevatron [163–172] and the LHC [85, 86, 130, 173–197] reaching an accuracy at the low percent-level now. All these

measurements exhibit an excellent agreement with the corresponding theory predictions (see, for instance, Fig. 1.9) and hence serve as a strong validation of the SM in general and QCD in particular. Due to the finite detector geometry and the necessity of kinematic cuts for the selection of top-quark events, such an experimental analysis is, however, inherently restricted to a fiducial region of the reaction phase space. Thus, it always constitutes an indirect determination of $\sigma_{t\bar{t}}^{\mathrm{tot}}$ that relies on additional assumptions for the extrapolation to the full phase space volume. Furthermore, as the experimental signatures of the various decay channels are quite different, they have to be treated individually with methods that are specifically tailored for the respective final-state configuration. The simplest measurement technique in this context is the so-called cut-and-count analysis that relates the total cross section to the number of observed $t\bar{t}$ events N (after applying selection cuts) via

$$\sigma_{t\bar{t}}^{\mathrm{tot}} = \frac{N - N_B}{\mathcal{A}\,\mathcal{L}} \tag{1.40}$$

where N_B denotes the number of background events, $\mathcal{A}$ is the experimental acceptance, an extrapolation factor that incorporates the geometrical acceptance of the detector, the detection efficiency as well as the branching fraction of the decay channel under consideration, and $\mathcal{L}$ is the integrated luminosity. While the latter is a universal property of the respective collider that can be determined by an independent measurement, the background and the acceptance are usually assessed via MC simulations or from control samples in data. Because of its high sensitivity to background modeling effects this method is only suitable for processes with a large signal-to-background ratio (SBR) and therefore yields the most accurate results for the dilepton channel[25]. The SBR in these measurements can be further improved by requiring at least one of the detected jets in a potential top-quark event to be identified as a b-jet (b-tagging). Although such an additional constraint reduces the overall detection efficiency, the associated increase of statistical uncertainties can be neglected in a sufficiently large data sample. This is the reason why at the LHC the accuracy of cross section measurements in the dilepton channel is limited by the luminosity determination rather than statistical or systematic effects[26].

Indeed, some of the most precise experimental results for the total cross section to date are based on a cut-and-count analysis of dilepton ($e\mu$) data with exactly one or two b-tagged jets published by the ATLAS collaboration [85]. This type of measurement has the advantage that it allows for a simultaneous determination of $\sigma_{t\bar{t}}^{\mathrm{tot}}$ and the b-tagging efficiency, thus minimizing the related systematic uncertainties. Moreover, as this analysis has been performed for both 7 TeV and 8 TeV data sets, it offers the unique opportunity to study the cross section ratio $R_{t\bar{t}}^{8/7} \equiv \sigma_{t\bar{t}}^{\mathrm{tot},\,8\,\mathrm{TeV}} / \sigma_{t\bar{t}}^{\mathrm{tot},\,7\,\mathrm{TeV}}$, which is subject to sizable uncertainty cancellations, both on the experimental and the theory side, due to the high correlation between the two center-of-mass energies. New-physics contributions that only have a minor impact on the cross section itself

[25] It has even been employed in case of $e\tau$ and $\mu\tau$ dilepton final states with hadronically decaying τ leptons [181], which as mentioned before are usually excluded from the dilepton analyses.

[26] The CDF collaboration was able to dramatically reduce the luminosity-induced uncertainty (in favor of the much smaller theoretical error on $\sigma_{Z/\gamma^* \to l^+l^-}^{\mathrm{tot}}$) by extracting the total cross section from a measurement of the cross section ratio $\frac{\sigma_{t\bar{t}}^{\mathrm{tot}}}{\sigma_{Z/\gamma^* \to l^+l^-}^{\mathrm{tot}}}$ [165], a technique that might also be applicable at the LHC.

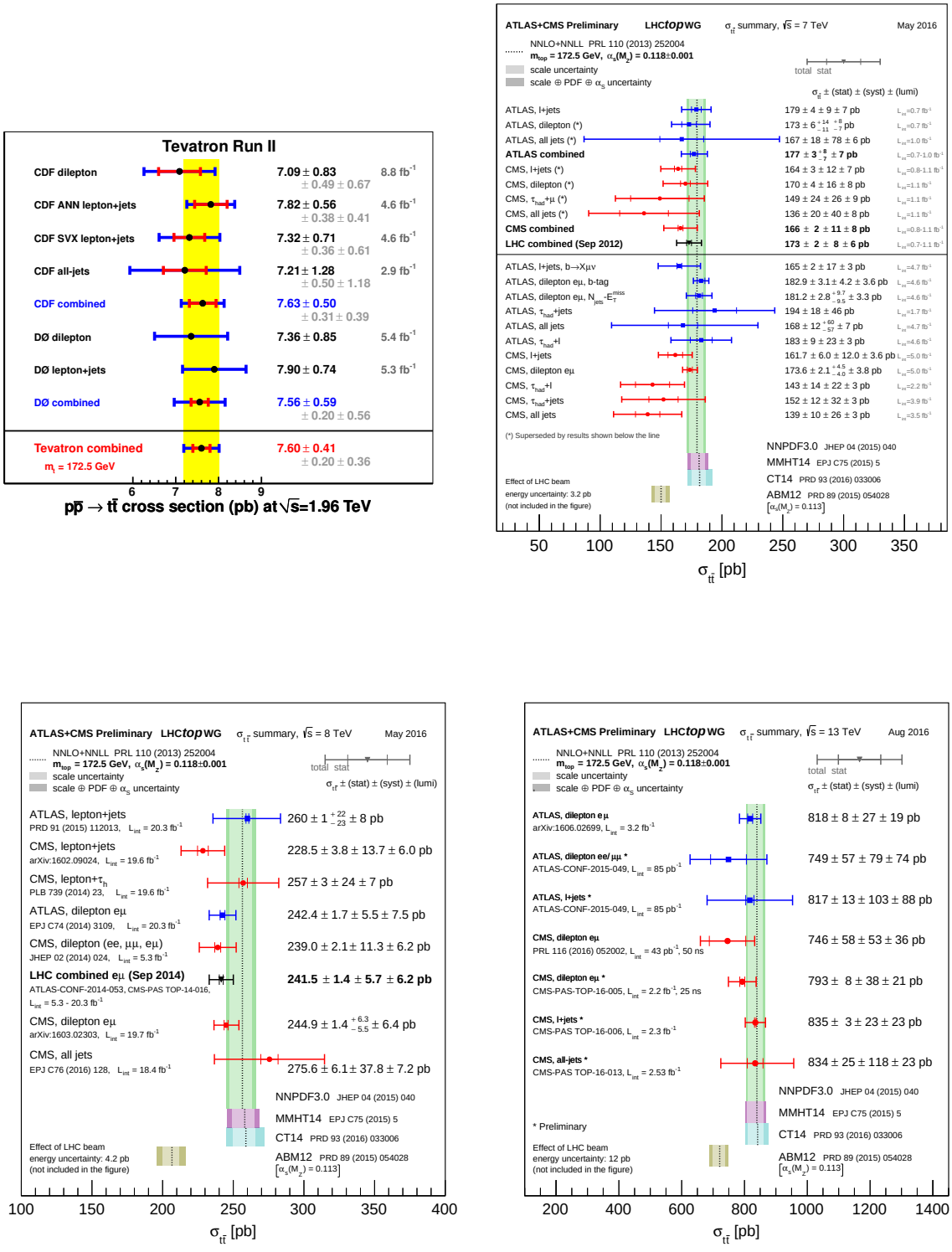

Figure 1.9: *Summary of $t\bar{t}$ total cross section measurements at the Tevatron [163](upper left) as well as at the LHC for 7 TeV (upper right), 8 TeV (lower left) and 13 TeV (lower right) center-of-mass energy [260].*

might therefore manifest themselves more evidently in this quantity. However, so far the experimental value is consistent with the theory prediction at NNLO+NNLL and can therefore be considered as a further validation of the SM (see section 3.5.4). A complementary analysis by the CMS collaboration based on a binned likelihood fit to multi-differential final-state distributions comes to the same conclusion [86, 186]. Nonetheless, the investigation of cross section ratios will certainly remain of interest, particularly with regard to the increased amount of data provided by the current Run 2 of the LHC, since even in the absence of BSM effects these ratios could still be employed for improving PDF and luminosity determinations [261, 262]. A first step in this direction are the latest dilepton results by ATLAS for $\sqrt{s} = 13\,\text{TeV}$ [197] that utilize the same cut-and-count analysis with simultaneous b-tagging employed at lower collision energy ultimately allowing for an evaluation of $R_{t\bar{t}}^{13/7}$ and $R_{t\bar{t}}^{13/8}$. Apart from that, the ATLAS collaboration also provided their first result for the ℓ+jets channel [196] at this energy, which is, however, only based on a limited data set and hence still suffers from significant systematic uncertainties.

The CMS collaboration also published their first cross section measurements based on 13 TeV data and aside from the dilepton and ℓ+jets channels [183, 185, 187] were able to measure $\sigma_{t\bar{t}}^{\text{tot}}$ in the all-jets channel [188] as well. Regardless of the collider energy such an analysis in a purely hadronic final state requires a more sophisticated approach owing to the substantially increased QCD background. This to some extent also applies to the ℓ+jets and τ+jets topologies. The general idea is to exploit the different kinematic properties of the signal and background processes by constructing a discriminant from several experimental observables that allows for a reliable extraction of $\sigma_{t\bar{t}}^{\text{tot}}$ with minimal background effects. The actual implementation of this basic concept was, however, realized quite differently by the experimental collaborations ranging from various types of likelihood analyses to even more advanced techniques involving neural network discriminants or boosted decision trees[27]. Still, these measurements do usually not reach the same level of precision as the cross section results in the dilepton channel mainly due to the sizable systematic uncertainties related to signal and background modeling[28]. Nonetheless, they represent independent determinations of $\sigma_{t\bar{t}}^{\text{tot}}$ and thus serve as an important test of the established theoretical framework.

Furthermore, a discrepancy between the cross section measurements in the various decay channels might hint at additional contributions from BSM particles either in the production or the decay process rendering these measurements a potential tool for the indirect detection of new-physics scenarios. A prime example of such a BSM particle that might affect the $\sigma_{t\bar{t}}^{\text{tot}}$ determinations is a charged Higgs bosons $H^{\pm}$, common to several extensions of the SM with non-minimal Higgs sector, e. g. the Two-Higgs-Doublet Model or the MSSM. If its mass is smaller than the top-quark mass, it will open up a new decay mode via $t \to H^+ b$ lowering the number of observed top-quark events in both the dilepton and ℓ+jets channel irrespective of whether the charged Higgs decays leptophilic ($H^+ \to \tau^+ \overline{\nu}$) or leptophobic ($H^+ \to c\overline{s}$). The main reason for this reduction is the optimization of the experimental selection criteria

[27] Note that, while these methods are essential for final states with hadronic top decays, they can be employed for measurements in the dilepton channel as well.

[28] At the Tevatron, the precision of the measurement in the ℓ+jets channel may indeed surpass that in the dilepton channel because of the higher significance of statistical uncertainties [163].

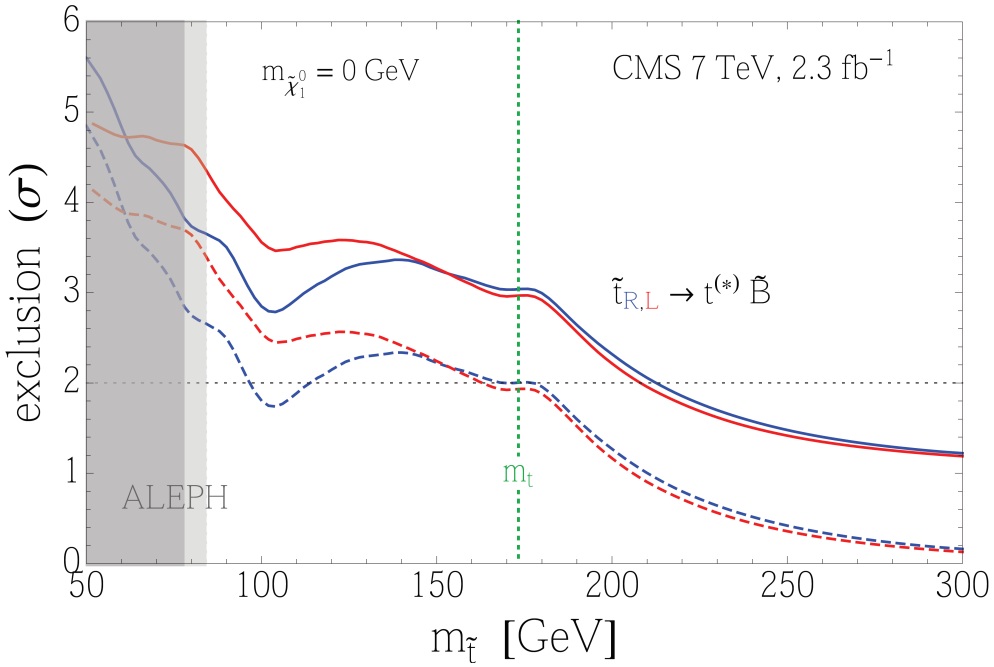

Figure 1.10: *Exclusion limit for a stop decaying into a bino-like LSP for left (red) and right (blue) stop polarization. Solid and dashed lines correspond to observed and expected limits respectively, and the shaded region has already been excluded by the* Aleph *collaboration at LEP [205].*

to SM decays, which allows a fair portion of the BSM events to escape detection. The various experiments at both the Tevatron and the LHC searched for such discrepancy between expected and observed top-quark event yields but found no evidence for charged Higgs production [198, 201–204, 206, 207]. Alternatively, the DØ [199] and Atlas [200] collaborations adopted a different strategy, comparing cross section and event yield ratios rather than absolute numbers, yet unable to find any significant deviations from the SM expectation either. Still, these analyses can be used to set limits on the branching fraction $\mathfrak{B}(t \to H^+ b)$ depending on m_{H^+} and the BSM model under consideration.

Another case where the total cross section may be employed to extract a possible BSM signal is the production of top squarks $\tilde{t}$ (also denoted stops), the supersymmetric partners of the top quarks. In SUSY scenarios that provide the most natural solution to the hierarchy problem[29] these particles are expected to be light, meaning their masses are not far from the electroweak scale $\mathcal{O}(100\,\text{GeV})$. They predominantly decay into tops and the lightest supersymmetric particle (LSP) of the theory under consideration. While most experimental searches in this mass range exploit the kinematic differences between SUSY signal and SM top background, such an analysis becomes increasingly more challenging as the stop mass approaches m_t due to the kinematic similarities of stop and top decays in this limit. Therefore, it has been recently

[29] In the SM the Higgs mass receives large ultraviolet quantum corrections that would require an incredible amount of fine-tuning in order to explain the observed value of $m_H \sim 125\,\text{GeV}$. This unnaturalness is related to the large hierarchy between the electroweak and the Planck scale and thus referred to as "hierarchy problem".

proposed to switch to a different tactic and take advantage of these similarities by treating the stops as a contamination in the SM $t\bar{t}$ measurements [205]

$$\sigma_{t\bar{t}}^{obs} = \sigma_{t\bar{t}}^{\mathbf{tot}}(m_t) + R_\epsilon(m_t, m_{\tilde{t}})\,\sigma_{\tilde{t}\tilde{t}^*}^{\mathbf{tot}}(m_{\tilde{t}}) \tag{1.41}$$

where $\sigma_{t\bar{t}}^{obs}$ denotes the cross section observed in experiment, $\sigma_{t\bar{t}}^{\mathbf{tot}}$ and $\sigma_{\tilde{t}\tilde{t}^*}^{\mathbf{tot}}$ are the theoretical predictions for top and stop pair production respectively, and R_ϵ accounts for possible differences in the acceptance and detection efficiencies of t and $\tilde{t}$. This approach relies crucially on the available experimental and theoretical precision of these quantities and hence has only recently, with the latest measurements at the LHC and even more importantly the full NNLO+NNLL result for $\sigma_{t\bar{t}}^{\mathbf{tot}}$, become a serious alternative to the established methods. A first application using CMS dilepton data already allowed for an exclusion of the critical $m_{\tilde{t}} \sim m_t$ region for a light bino-like LSP scenario [205] (see Fig. 1.10) demonstrating the predictive power of this new technique. A similar analysis was also presented by ATLAS [85] which, based on $e\mu$ dilepton measurements, was able to confirm these findings. Due to these successes it is conceivable that this method may in the near future be extended to other SUSY scenarios as well allowing to further constrain their respective parameter space in order to reduce the vast number of possible SM extensions.

Both examples, the production of a charged Higgs and stop pairs, prove that the total cross section may serve as a powerful tool for BSM searches but it can also be employed for improving the experimental determination of SM parameters, most notably by providing important constraints on the poorly-known large-x gluon PDF [84,88,90,262,264]. As the production of top-quark pairs at the LHC is dominated by the gluon fusion channel, it exhibits a high sensitivity to the distribution of the gluons inside the proton[30], particularly in the region $x \gtrsim 0.1$. A dedicated comparison of ATLAS and CMS cross section measurements with the theory calculations at NNLO+NNLL accuracy thus allows for a sizable reduction of the parametric uncertainty of up to 20% (see Fig. 1.11) in this regime. This greatly benefits the theoretical description of processes that are predominantly initiated by gluons, in fact, not only in the SM but also in BSM physics where a lot of reactions are driven by gluon-gluon interactions. Indeed, the ABM [84], NNPDF [90] and MMHT [264] collaborations have recently started to include $t\bar{t}$ cross section measurements in their global PDF fits, which makes the advanced gluon PDF publicly available for a broad spectrum of phenomenological applications. Using these updated PDF sets, for instance, for the derivation of $\sigma_{t\bar{t}}^{\mathbf{tot}}$ predictions for the current and upcoming LHC runs, the associated PDF uncertainty is already slightly reduced with respect to previous analyses. In this context it is interesting to note that the corresponding central cross section values are in most cases further enhanced quite opposite to what one would expect from the functional behavior in Fig. 1.11. This suggests that the effect of $t\bar{t}$ data on the central PDF predictions is somewhat undermined by other newly added features in the PDF fits, e. g. additional measurements, especially from the first LHC runs, or a different treatment of systematic effects. In order to assess the genuine impact of incorporating $\sigma_{t\bar{t}}^{\mathbf{tot}}$ measurements in PDF determinations, it is therefore more enlightening to work with the

[30] Including top-quark data in PDF analyses evidently also affects the quark PDFs but the overall impact is negligible.

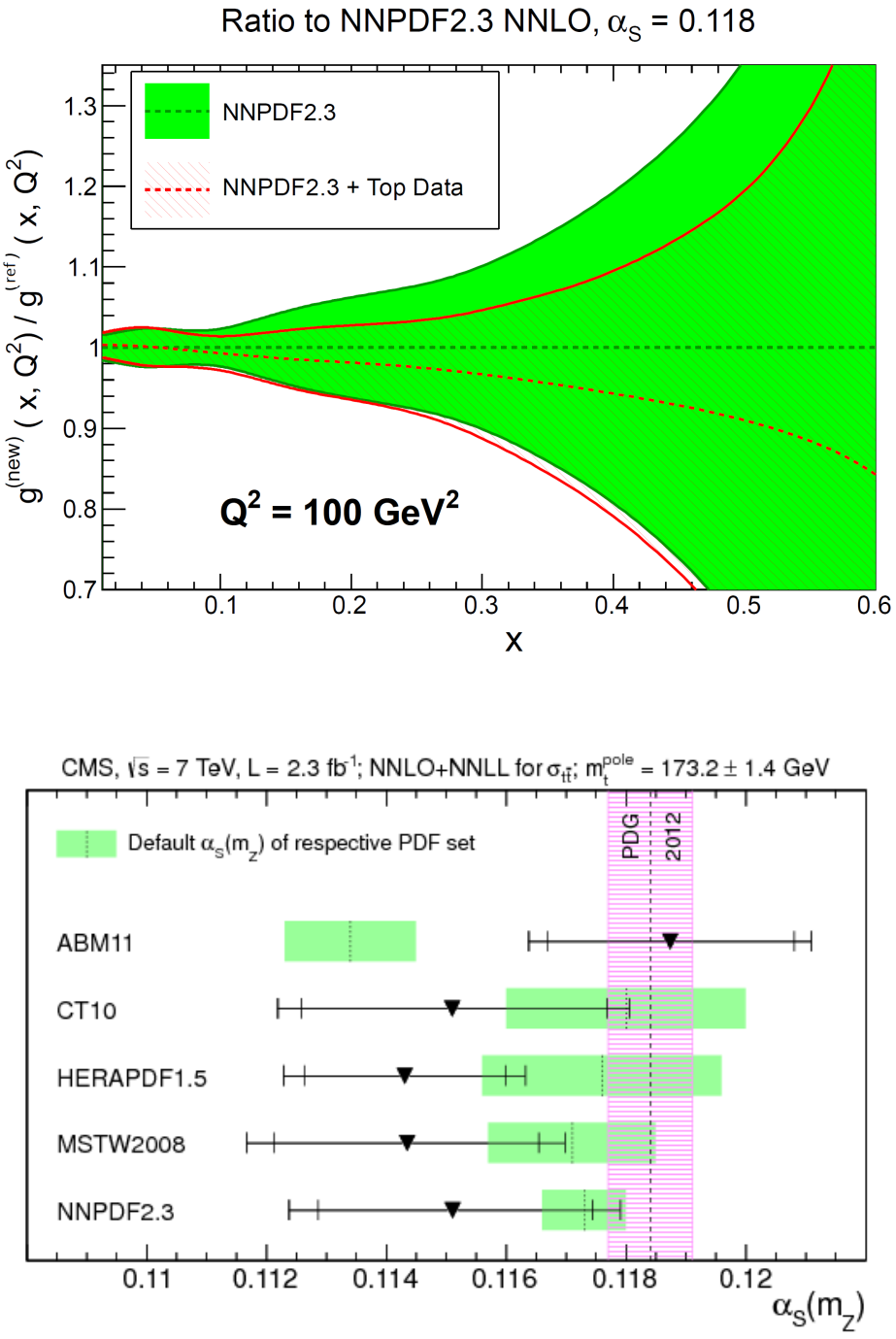

Figure 1.11: *Top: The ratio of the default NNLO gluon PDF obtained from the* NNPDF2.3 *[263] set and the modified distribution after inclusion of Tevatron and LHC top-quark data [262]. Bottom: Values of the strong coupling constant extracted from a comparison of $t\bar{t}$ cross section data with the NNLO+NNLL predictions from different PDF sets [83]. The inner error bars contain the uncertainties on the measured cross section and the LHC beam energy as well as the theoretical uncertainties due to PDF and scale variation while the outer error bars also include the uncertainty on the top mass. The hatched band indicates the current world average.*

open-source QCD fitting framework xFitter (former HERAFitter [265]), which allows for a user-defined implementation of top-quark data in the PDF analysis without introducing further modifications. Moreover, this software package provides a unique means of studying the parton content of the proton in differential top-quark observables as well (see also section 1.3.4) which might become important for the use in future PDF fits.

Apart from this indirect impact on SM measurements via PDF optimization, for some quantities an extraction based on the precise theoretical knowledge of the total cross section actually represents a true alternative to the established measurement techniques. The most prominent example is certainly the measurement of the top-quark mass that was discussed in detail in section 1.2.1. In this measurement the value of the strong coupling constant is fixed to its world average value while m_t is a free parameter fitted to data. By inverting this logic it is also possible to use $\sigma_{t\bar{t}}^{\mathrm{tot}}$ for a determination of α_s by previously specifying the value of the top mass. The result of such an analysis based on dilepton data collected by the Cms collaboration [83] is shown in Fig. 1.11 for various choices of PDF sets. The thus measured values of α_s are in general lower than the world average, which may be attributed to the lower value of the employed experimental cross section result. Indeed, performing the same analysis with the full LHC data set will presumably yield a higher value for α_s [266]. Still, within its errors the measured coupling is compatible with the world average. The total uncertainty of about 2-3% is, however, considerably larger rendering this method inappropriate for a high-precision determination of this quantity. Still, it represents the first measurement of α_s at NNLO accuracy at a hadron collider and therefore provides an important consistency check of the SM.

1.3.2 Single top-quark production

Although at present hadron collider experiments the top quark is preferably produced in pairs via the strong interaction, the SM also allows for the creation of individual tops and anti-tops by means of EW interactions. Measuring these single-top events offers the unique opportunity to directly investigate the strength and structure of the Wtb vertex in a manner complementary to top-quark decays. Contributions from new particles or interactions could, for instance, lead to a noticeable enhancement of the total cross section or affect the shape of differential observables related to single top-quark production. It can thus be considered an excellent probe to new physics. Naively, one would, however, expect this process to be highly suppressed with respect to $t\bar{t}$ production due to the substantially smaller coupling $\frac{\alpha^2}{\alpha_s^2} \sim 0.01$ rendering it inaccessible to an experimental observation with today's measurement techniques. Fortunately, this suppression factor is partially compensated, on the one hand, by the lower production threshold which leads to larger partonic fluxes and, on the other hand, by enhancements in the high energy regime due to t-channel vector-boson exchange. As a result, the cross section is only diminished by a factor of 3-5 compared to top-quark pair production and still lies in the detection range of the Tevatron and LHC experiments (see Tab. 1.3).

Nonetheless, single-top production suffers from a considerably increased background owing to the smaller number of jets and leptons available for the event identification, which made its experimental verification an extremely challenging task. For this reason it took the Cdf

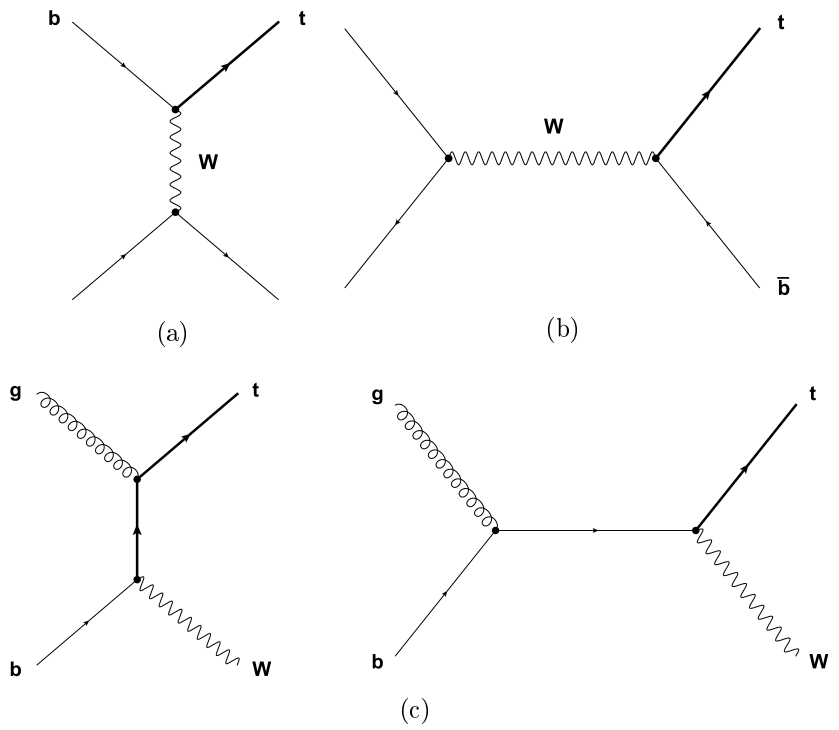

Figure 1.12: *Feynman diagrams contributing to the LO partonic cross section for single top-quark production in the t-channel (a), the s-channel (b) and associated tW production (c).*

and DØ collaborations another 14 years from the discovery of top-quark pairs to rigorously establish the existence of singly produced top quarks in Tevatron data [9,10]. The multivariate analysis methods developed in this context have since then become an indispensable tool in many new-physics searches and, for instance, provided a significant contribution to the discovery of the Higgs boson in 2012 [267]. Meanwhile, single top-quark production has also been observed at the LHC for center-of-mass energies of both 7 TeV and 8 TeV (see Fig. 1.14) and very recently at 13 TeV [268,269] as well. There, in contrast to the Tevatron[31], the initial state is not a CP eigenstate and thus the number of singly produced tops is larger than the number of anti-tops, which can be traced back to the different abundances of up-type and down-type quarks inside the proton. Therefore, it is not only interesting to determine the total number of produced tops and anti-tops, $\sigma^{\mathrm{tot}}_{t+\bar{t}}$, but moreover to measure their individual contributions or, likewise, the corresponding cross section ratio $R_t = \frac{\sigma^{\mathrm{tot}}_{t}}{\sigma^{\mathrm{tot}}_{\bar{t}}}$ [268–271] in order to detect possible deviations from the SM expectation.

Another intriguing feature of this process is the possibility to distinguish between three different production modes (provided that the top is treated as a stable particle) that, according to the amplitude-level behavior of the W boson, are denoted as t-channel, s-channel and associated tW production. The LO diagrams contributing to the respective channels are depicted in Fig. 1.12. From the theoretical point of view such a separation is only allowed

[31] Although the CP symmetry is violated within the SM by the complex phase of the CKM matrix, this effect is negligible for single top-quark production resulting in a virtually identical number of tops and anti-tops.

if the individual contributions do not mix, i. e. the interference terms of the corresponding matrix elements vanish, even in the presence of higher-order corrections. While this condition is evidently fulfilled for the tW-channel due to the additional massive particle in the final state, color conservation guarantees a clear separation of the t- and s-channel contributions up to NLO in QCD[32]. Interference effects from higher QCD orders as well as from EW corrections are, however, possible but expected to be very small, still justifying the treatment as individual production modes. This even holds if one considers more realistic scenarios that include top-quark decays, either in the NWA [273–275] or with the full finite width contributions [276–278]. Experimentally, distinguishing between these two channels is also connected with certain conceptual difficulties and a sharp distinction is actually only given for LO event topologies. Statements that go beyond can only be of a probabilistic nature as the identical final-state configurations at higher orders do not allow for a separation on an event-by-event basis. Still, it is possible to measure both the t- and s-channel cross sections individually by exploiting the differing event kinematics albeit always relying on additional theoretical assumptions.

The same applies to the tW-channel, which indeed does not mix with the other single-top modes but rather with $t\bar{t}$ production thus requiring similar analysis techniques in order to be able to thoroughly disentangle both of these production modes. Due to the large number of top pairs created in hadronic collisions a precise experimental determination of the tW cross section is, however, exceptionally difficult. In fact, this entanglement already exists on the theory side when the LO top-quark decays are included in the perturbative calculations. In that case the NLO QCD corrections to tW production lead to the same gluon-induced reaction $gg \to W^+W^-b\bar{b}$ that can be found already at LO in top-quark pair production. This additional production mechanism actually spoils the perturbative convergence of the tW cross section predictions, which is why these interference effects are addressed more rigorously in the so-called four-flavor scheme (4FS) where the b quark is removed from the PDFs and treated as massive [251, 252].

Despite these conceptional difficulties it is still common practice to regard each of the single top-quark production modes separately, at least when considering fairly inclusive observables. In the following we will briefly discuss the current theoretical and experimental status of the total cross section for each of these channels and address the specific problems and challenges related to them:

1. *t-channel production*

   The production via t-channel vector boson exchange is the primary source of single top quarks at the Tevatron as well as at the LHC and, therefore, the only channel that was observed in both proton-proton and proton-antiproton collisions. The NLO QCD corrections for this process have already been calculated 20 years ago for the total cross section [279–281] and, subsequently, also for fully differential observables [282–284]. Due to large (and presumably accidental) cancellations between different partonic subchannels

[32] This statement only applies to the case of massless b quarks. In case the b quark is considered massive the interference effects are, however, still color suppressed allowing for a separate treatment of both channels in good approximation [272].

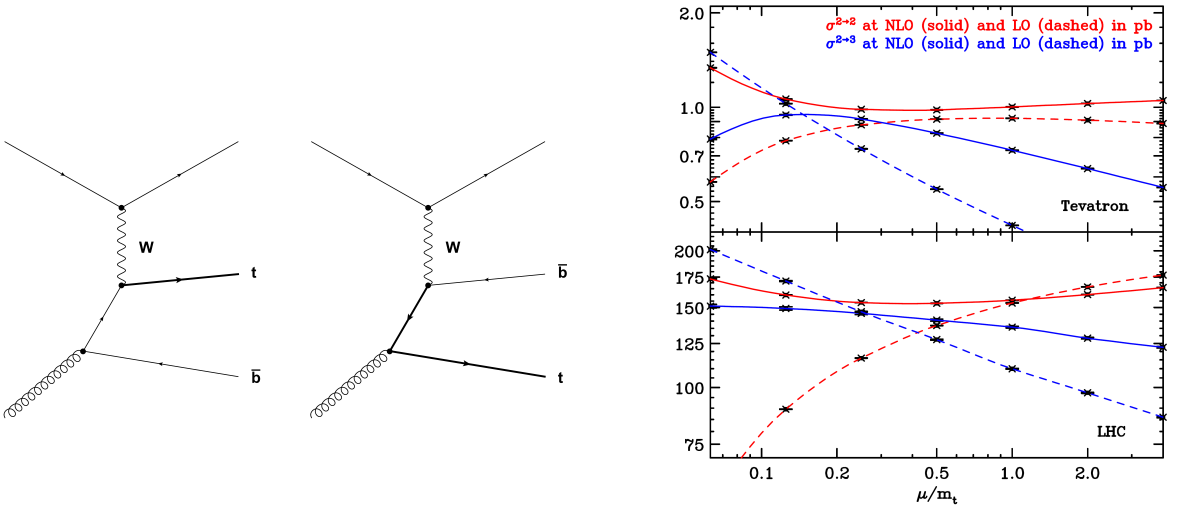

Figure 1.13: *Left: Feynman diagrams contributing to the LO partonic cross section for t-channel single top-quark production in the 4FS. Right: Scale dependence of the LO (dashed) and NLO (solid) cross section predictions at the Tevatron and the LHC (*14 TeV*) in the 4FS (blue) and 5FS (red) [272].*

the cross section predictions are only moderately affected by these corrections increasing the LO results by merely a few percent. This raises the question of whether the perturbative expansion is convergent and yields reliable predictions or if the NLO and NNLO corrections are of the same order of magnitude. It has been partially answered by the recently published approximate NNLO results [285] that include all vertex-type corrections but are still missing contributions from color-suppressed diagrams where the heavy- and light-quark lines are connected by gluons. It turns out that indeed these corrections are of similar size as the $\mathcal{O}(\alpha_s)$ contributions leading to slightly reduced cross section predictions for both top and anti-top quarks.Still, despite its small impact on the central value the approximate NNLO calculation constitutes a considerable improvement over the pure NLO result as the residual scale dependence is decreased to the sub-percent level now indicating a significant stabilization of the perturbative expansion. Other sources of theoretical uncertainty, e. g. PDF errors or top- and bottom-mass effects, have so far not been evaluated at this level of precision but a systematic study of these contributions has been postponed to a future analysis.

All of the aforementioned calculations were performed in the five-flavor scheme (5FS) where the bottom quark is treated as massless and part of the sea-quark content of the (anti-)proton. Similar results, however, also exist for the 4FS up to NLO in QCD [272, 286]. They take into account the full m_b-dependence and allow for a more accurate description of observables that are directly related to the presence of final-state b quarks (also denoted as spectator b quarks). This is due to the fact that in the 4FS the absence of initial-state b quarks in combination with the need for a CKM-allowed top-quark transition results in diagrams that are initiated via gluon splittings (hence the t-channel is often referred to as W-gluon channel in the literature).

	Tevatron	LHC 8 TeV	
	$\sigma_{t,\bar{t}}^{\mathrm{tot}}$ [pb]	$\sigma_{t}^{\mathrm{tot}}$ [pb]	$\sigma_{\bar{t}}^{\mathrm{tot}}$ [pb]
t-channel	$1.01^{+0.03\ +0.03}_{-0.02\ -0.03}$	$55.5^{+1.7\ +0.3}_{-1.1\ -0.3}$	$30.3^{+0.9\ +0.3}_{-0.6\ -0.3}$
t-channel (4FS)	$0.889^{+0.071+0.026}_{-0.104-0.028}$	$52.5^{+2.4\ +0.3}_{-2.8\ -0.3}$	$28.5^{+1.3\ +0.3}_{-1.5\ -0.3}$
s-channel	$0.453^{+0.026+0.015}_{-0.023-0.011}$	$3.36^{+0.09\ +0.07}_{-0.08\ -0.05}$	$1.94^{+0.05\ +0.04}_{-0.05\ -0.03}$
tW-channel	$0.073^{+0.003+0.008}_{-0.002-0.009}$	$9.32^{+0.41\ +0.30}_{-0.45\ -0.37}$	

Table 1.3: *Theoretical predictions for single top-quark production at the Tevatron and the LHC obtained with* MCFM *[110,111]($m_t = 172.5\,\mathrm{GeV}$,* MSTW2008 *PDFs at 68% C.L. [231]). The quoted uncertainties are due to the variation of renormalization and factorization scale and the choice of PDFs.*

Consequently, they contain b quarks in the final state already at the lowest order in perturbation theory, as illustrated in Fig. 1.13. A potential drawback of this scheme is the strong hierarchy of scales involved in the theoretical description, which gives rise to logarithmic enhancements of the form $\alpha_s \ln^2\left(\frac{m_t}{m_b}\right)$ that might spoil the convergence of the perturbative expansion and lead to unreliable predictions for the total cross section. It has, however, been checked that this does not apply to t-channel single top-quark production and that in this particular case both schemes actually yield similar results (see Fig. 1.13 and Tab. 1.3). In fact, the enhanced logarithms are also present in the 5FS although not explicitly but rather hidden in the initial conditions for the evolution of the b quark PDF. By evolving the PDF to the scale of the hard scattering process these terms are partially resummed, which eliminates their potentially dangerous behavior and improves the stability of the perturbation series [287]. A comparison of the latest approximate NNLO predictions with the NLO 4FS results indicates that these resummation effects may not be negligible and should be included to provide more accurate theoretical predictions. Moreover, since the NLO diagrams in the 4FS are a subtopology of the 5FS NNLO diagrams, the latter approach is suited equally well for the adequate modeling of spectator-b-quark effects, which was one of the main motivations for employing the 4FS.

In the context of top-quark pair production we have already encountered a different type of resummation formalism related to soft-gluon radiation. It has been applied to single top-quark production as well but its overall impact on the t-channel cross section is rather small, amounting at most to a few percent shift of the central values without significantly reducing the theory error budget [224,288–290]. The situation is similar for higher-order EW corrections [291,292] that can indeed be sizable in the high-energy tails of certain distributions but only amount to about -1% for the total cross section, which is why they are usually discarded. With regard to the moderate size of the fixed-order QCD corrections it might, however, still be worth considering the inclusion of these contributions in future theoretical predictions.

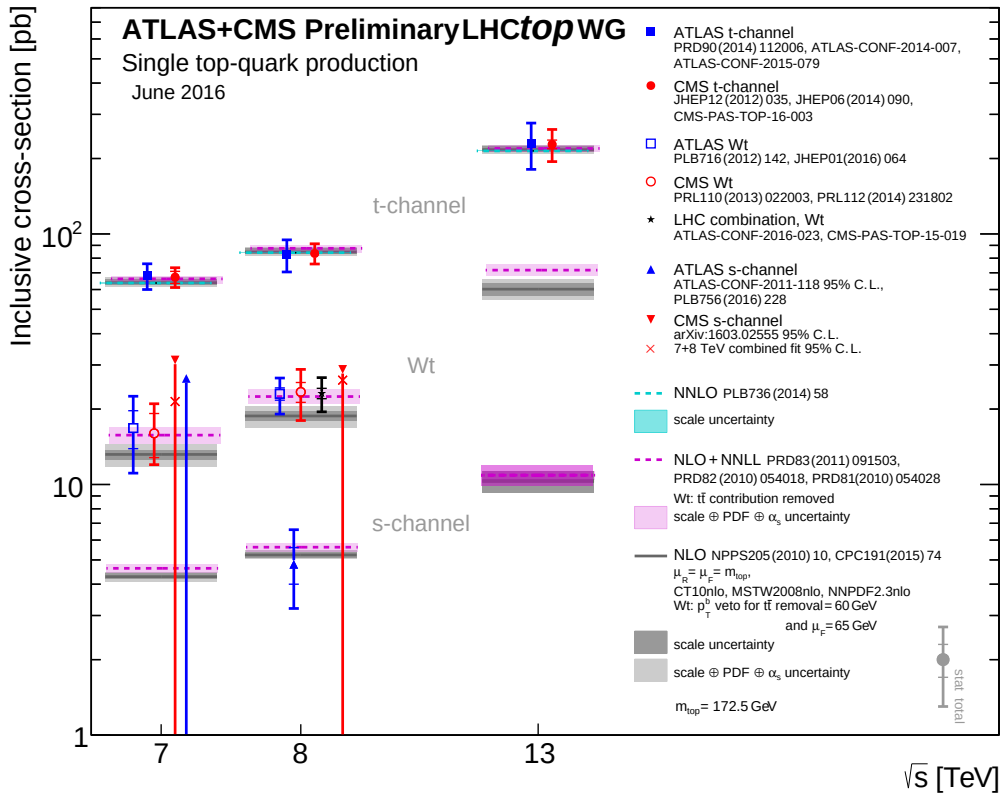

Figure 1.14: *Summary of LHC cross section measurements for the three single top-quark production channels at different center-of-mass energies compared to the SM expectation [260]. For the s-channel both upper limits as well as the first result at a signal significance of 3.2 standard deviations are presented [293].*

This will become even more important when the theory results are used in experimental analyses aiming at a precise extraction of SM parameters from the measured cross sections or in BSM searches that focus on the detection of a small excess of single-top events over the SM expectation. As already mentioned before, such measurements suffer from large background contaminations that require refined analysis techniques to filter out the relevant signal components. They are usually performed in the ℓ+jets channel[33] to reduce the QCD multijet background and exploit the specific kinematic properties of t-channel production, for instance the presence of a light jet in the forward region of the detector or a value of the invariant mass $m_{l\nu b}$ close to the top-quark mass. The remaining background mainly consists of W+jets events and contributions from other top-quark processes, primarily $t\bar{t}$ production but depending on the collider also from the other single-top production modes as can be inferred from the cross section predictions in Tab. 1.3. For this reason the earliest measurements at the Tevatron were actually combined determinations of t- and s-channel production [9, 10, 295].

[33] The CDF collaboration also performed measurements using events without an isolated lepton but with jets and a significant amount of missing transverse energy, which are complementary to the determinations from ℓ+jets event samples [9, 294].

Meanwhile, both the CDF and the DØ collaboration were able to perform separate measurements of the t-channel cross section using the full dataset of up to $9.7\,\text{fb}^{-1}$ of integrated luminosity [294, 296, 297]. Although the individual results from the two experiments differ by about two standard deviations, they are consistent with the SM expectation (see Fig. 1.18). The corresponding experimental uncertainties are dominated by the limited statistics as well as by the difficulties in accurately modeling the signal and background contributions and lie well above 10%, even if the findings from both experiments are combined.

At the LHC the situation is different. First of all, t-channel production is by far the most dominant production mode for single top quarks, which to some extent simplifies the disentanglement of the various channels. In fact, due to the absence of valence anti-quarks associated tW production even supersedes the s-channel as the most prominent single-top background. Moreover, the enhanced cross section values related to the higher center-of-mass energies increase the number of observable single-top events considerably, which reduces the impact of statistical uncertainties in the experimental analyses. Apart from that, the measurement techniques are similar to the methods employed at the Tevatron. After imposing certain topological constraints (one isolated lepton, one b-tagged jet, etc.) and applying kinematic cuts to identify the ℓ+jets event sample, various strategies such as likelihood analyses, neural networks or boosted decision trees are used to discriminate the background contributions and extract the total cross section from data. The most precise of these measurements for 7 TeV and 8 TeV [270, 271, 298–300] have been summarized in Fig. 1.14. So far, all results both by ATLAS and CMS show full agreement with the corresponding theory predictions providing further experimental evidence in favor of the SM. There, however, still remain sizable uncertainties connected to the proper signal and background modeling despite the higher statistics and the improved SBR. Nonetheless, these measurements have reached a new level of precision for single top-quark production with total experimental uncertainties of about 10% and below. Recently, also the first experimental results for t-channel single top-quark production at 13 TeV became available [268, 269]. Similar to the previous determinations at lower collision energies the measured cross sections suffer from rather large experimental errors but are consistent with the SM expectation. It thus remains to be seen whether the current LHC run will ultimately reach a higher level of precision once the systematic effects are under better experimental control.

All of the measurements discussed so far do not differentiate between tops and anti-tops but since the production rates for these particles differ at the LHC[34], it is interesting to not only measure their sum but also their individual contributions. This can be achieved by considering the charge of the isolated leptons in the ℓ+jets events, which is directly related to the charge of the decaying W boson and thus allows for a reliable classification into t or $\bar{t}$ events. By subsequently applying the same analysis techniques

[34] In principle, it would also be interesting to measure the individual rates of top and anti-top production at the Tevatron in order to verify whether they are indeed equal as predicted by the SM. Such a measurement would, however, suffer from even larger statistical uncertainties which is the main reason why it has not been done yet.

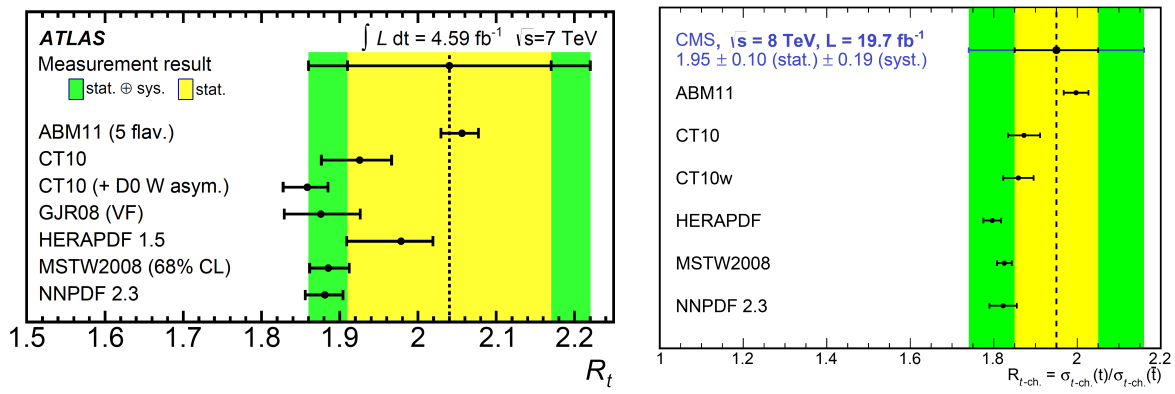

Figure 1.15: *Comparison of the measured cross section ratio R_t at 7 TeV (left) and 8 TeV (right) with the NLO predictions derived from various PDF sets [270, 271].*

as for the determination of $\sigma_{t+\bar{t}}^{\mathrm{tot}}$, both ATLAS and CMS were able to extract σ_t^{tot} as well as $\sigma_{\bar{t}}^{\mathrm{tot}}$ from the 7 TeV [270], 8 TeV [271] and 13 TeV [268, 269] datasets without significantly deteriorating the relative experimental precision. Similar to the sum of both contributions, they also find full agreement with the SM predictions for the individual t and $\bar{t}$ cross sections.

Due to the high correlation between these measurements an effective method to further reduce the overall experimental uncertainty lies in the examination of the cross section ratio R_t offering additional insights on SM as well as BSM physics. While the total rate for the production of tops and anti-tops is suited for constraining the b-quark PDF (once the experimental precision is sufficiently increased), the ratio is sensitive to the u- and d-quark content of the proton providing a valuable means for discriminating between different PDF set predictions as illustrated in Fig. 1.15. Although all PDF sets yield results that are consistent with the measured R_t-values at both center-of-mass energies owing to the still limited experimental precision, the obtained predictions show a certain variation that is larger than their quoted error estimates. In case of a further reduction of the uncertainties on the measured cross section ratio, including t-channel single top-quark data in the future PDF analyses would therefore help resolving the tension between the predictions of the various PDF collaborations. Complementary information could also be provided by the ratio $R_{t+\bar{t}}^{8/7} = \sigma_{t+\bar{t}}^{\mathrm{tot},\,8\,\mathrm{TeV}}/\sigma_{t+\bar{t}}^{\mathrm{tot},\,7\,\mathrm{TeV}}$ [271], which has, however, not been studied in full detail yet.

BSM searches would benefit from a precise determination of R_t as well since new-physics contributions, despite the fact that they may be sizable, could cancel in the combination of σ_t^{tot} and $\sigma_{\bar{t}}^{\mathrm{tot}}$ but not in their ratio [301, 302]. While new particles are in general more likely to reveal themselves in the s-channel due to the possibility of being produced resonantly, the t-channel may be used to investigate new kinds of couplings and interaction vertices that could lead to observable deviations from the SM predictions even in fully inclusive observables like the total production cross section [303]. Two of the most sought-for scenarios in this context involve FCNCs, which are loop-suppressed in the SM and thus generally inaccessible through experiment, and anomalous Wtb

couplings. In order to guarantee an unbiased analysis of the experimental data with respect to these non-SM interactions, they are usually parametrized in terms of a model-independent effective Lagrangian that consists of operators of mass dimension four and five[35] [98,304–306],

$$\begin{aligned}
\mathcal{L}_{eff} &= -\frac{g_{\mathrm{EW}}}{\sqrt{2}}\left[\bar{b}\,\gamma^{\mu}\left(f_V^L P_L + f_V^R P_R\right) t W_{\mu}^{-} - \bar{b}\,\frac{i\sigma^{\mu\nu}\partial_{\nu}W_{\mu}^{-}}{M_{\mathrm{W}}}\left(f_T^L P_L + f_T^R P_R\right) t\right] && \Big\} \; Wtb \\
&- g_s \sum_{q=u,c} \frac{\kappa_q^g}{\Lambda}\,\bar{t}\,\sigma^{\mu\nu} T^a \left(f_q^g + i h_q^g \gamma_5\right) q\, G_{\mu\nu}^a && \Big\} \; gqt \\
&- e \sum_{q=u,c} \frac{\kappa_q^{\gamma}}{\Lambda}\,\bar{t}\,\sigma^{\mu\nu}\left(f_q^{\gamma} + i h_q^{\gamma}\gamma_5\right) q\, A_{\mu\nu} && \Big\} \; \gamma qt \\
&- \frac{g_{\mathrm{EW}}}{2\cos\theta_{\mathrm{W}}} \sum_{q=u,c} \bar{t}\,\gamma^{\mu}\left(v_q^Z - a_q^Z\gamma_5\right) q\, Z_{\mu} + \frac{\kappa_q^Z}{\Lambda}\,\bar{t}\,\sigma^{\mu\nu}\left(f_q^Z + i h_q^Z\gamma_5\right) q\, Z_{\mu\nu} && \Big\} \; Zqt \\
&- \frac{g_{\mathrm{EW}}}{2\sqrt{2}} \sum_{q=u,c} \kappa_q^H\,\bar{t}\left(f_q^H + i h_q^H\gamma_5\right) q\, H && \Big\} \; Hqt \\
&+ \text{h.c.}
\end{aligned} \tag{1.42}$$

where

$$\begin{aligned}
P_{R,L} &= \frac{1 \pm \gamma_5}{2} \\
\sigma^{\mu\nu} &= \frac{i}{2}(\gamma^{\mu}\gamma^{\nu} - \gamma^{\nu}\gamma^{\mu}) \\
G_{\mu\nu}^a &= \partial_{\mu} G\nu^a - \partial_{\nu} G_{\mu}^a \qquad \text{(and similar for the other gauge bosons)} .
\end{aligned} \tag{1.43}$$

Here, g_s and g_{EW} are the strong and EW couplings respectively while the electric charge and the EW mixing angle are denoted as e and $\cos\theta_{\mathrm{W}}$. The scale of new physics Λ, which acts as a suppression factor in some of these interactions, is expected to be of order $\mathcal{O}(1\,\mathrm{TeV})$. Note that because of the distinct experimental signature of additional EW final-state particles it is more promising to look for the Zqt, Hqt and γqt currents directly in exotic $t\bar{t}$ decays [307–314] or in rare associated production processes $p\,(\bar{p}) \to t\,X$ with $X = Z, H, \gamma$ [315, 316] rather than in small deviations of the single top-quark production cross section from the SM expectation.

The strong FCNC and the modified Wtb vertex, however, have the same final-state configuration as t-channel single top-quark production and therefore it is only natural to search for these scenarios by employing $\sigma_{t+\bar{t}}^{\mathrm{tot}}$ or R_t measurements. In practice, this means that the experimental collaborations have to adapt their SM analysis techniques to the different kinematic requirements induced by the anomalous couplings to increase the sensitivity for a possible BSM signal, for instance by reassessing the observables that enter the likelihood fits or by training their neural networks and decision trees under the

[35] In principle, the effective Lagrangian can contain even higher dimensional operators, which are, however, suppressed by additional powers of Λ^{-1}, as well as CP-violating phase factors.

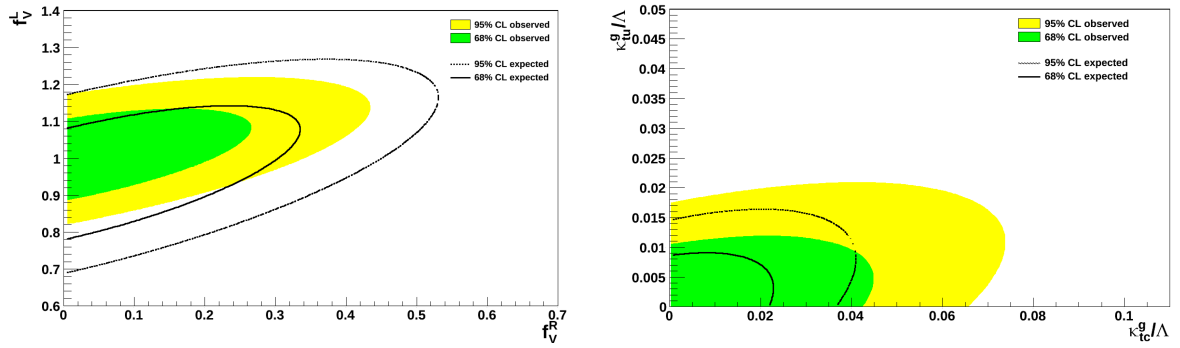

Figure 1.16: *Two-dimensional exclusion limits for anomalous Wtb couplings (left) and strong FCNCs (right) at 68% and 95% C.L. [317].*

novel kinematic conditions. Moreover, they also consider the possibility of anomalous contributions in the decay of the (anti-)top quarks. Nonetheless, there has so far not been found any evidence for either of the two scenarios, neither at the Tevatron [318–321] nor the LHC [317,322–324]. Hence, the experimental results could only be used to set exclusion limits on the different coupling parameters as shown exemplarily in Fig. 1.16 for an analysis performed by CMS at 7 TeV using 5.0 fb^{-}1 of data [317]. An additional strategy in this context involves the search for so-called monotop events [325,326], i. e. events that only contain a single (anti-)top quark and possibly missing transverse energy (MET) but no additional partons. Such an experimental signature could be produced by strong FCNC interactions but in case of additional MET it might also be a sign for the presence of a highly elusive particle, stemming for instance from associated production of a top quark and dark matter. However, in the present absence of a monotop signal the experiments at the Tevatron [320,327] and the LHC [322,323,328,329] are again only able to provide upper bounds on the anomalous couplings or masses of the respective new particles. Still, single top-quark data will continue to be a promising searching ground for BSM physics, especially if the relevant backgrounds can be further reduced by improving the theoretical and experimental methods for SM single top-quark production.

Even without any direct evidence for a modified vertex structure a close examination of the Wtb interaction remains of particular interest as it allows for a stringent test of the SM coupling strength, namely the magnitude of CKM mixing angle V_{tb}. Indeed, it is also possible to determine this quantity from top-quark decays by measuring the ratio [127–130]

$$R_{\mathcal{B}} \equiv \frac{\mathcal{B}(t \to W^+ b)}{\sum\limits_{q=b,s,d} \mathcal{B}(t \to W^+ q)} = \frac{|V_{tb}|^2}{|V_{tb}|^2 + |V_{ts}|^2 + |V_{td}|^2} = |V_{tb}|^2 \tag{1.44}$$

where the last equality is only valid for three quark generations and under the condition that the CKM matrix is unitary. In order to verify these assumptions or detect possible deviations from the SM, it is therefore necessary to measure $|V_{tb}|^2$ directly which can be achieved by comparing the measured single-top cross sections with the respective

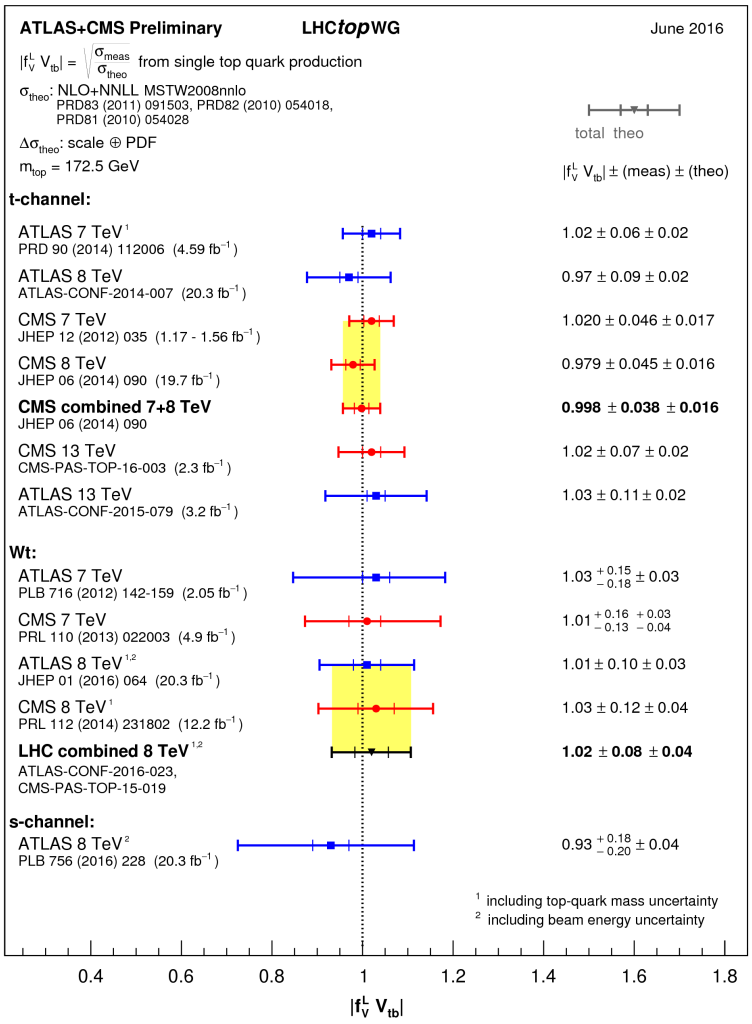

Figure 1.17: *Summary of* ATLAS *and* CMS *determinations of* $|f_V^L\, V_{tb}|$ *in different single top-quark production channels [260].*

theory predictions

$$|f_V^L\, V_{tb}| = \sqrt{\frac{\sigma_{t+\bar{t}}^{\mathbf{tot},\,exp.}}{\sigma_{t+\bar{t}}^{\mathbf{tot},\,theo.}}} = |V_{tb}|\ . \tag{1.45}$$

Here, the left-hand side still takes into account possible anomalous coupling effects while the right-hand side corresponds to a true SM-like interaction. The only requirement that enters this relation is $|V_{tb}| \gg |V_{td}|, |V_{ts}|$. Since all single-top production modes are proportional to $|V_{tb}|^2$, this analysis is not restricted solely to the t-channel [268–271, 298, 299] but can be applied to all channels [293, 330–334] and, in principle, also to individual t or $\bar{t}$ cross sections. A summary of various $|V_{tb}|$ determinations at the LHC is depicted in Fig. 1.17, classified according to the three production modes. At the Tevatron, t- and s-channel results were usually combined yielding $|V_{tb}| = 1.02^{+0.06}_{-0.05}$ for the latest joined analysis by CDF and DØ using the full dataset [297]. The theoretical

calculations that enter these analyses are usually at NLO+NNLL accuracy and, so far, have not been updated to incorporate the recent approximate NNLO result for t-channel production [285]. But since the dominant contribution to the overall error stems from experimental uncertainties, including these new findings will not lead to a significant improvement on the precision of $|V_{tb}|$. All measurements both at the Tevatron and the LHC are consistent with the indirect determinations based on additional SM assumptions. Hence, it is common to convert the measured values of $|V_{tb}|$ into one-sided limits by imposing the unitarity condition $|V_{tb}| \leq 1$ in order to achieve a better comparability of the different approaches. It turns out that under these conditions the measurement of the branching fraction ratio in Eq. (1.44) results in a much stricter limit of $|V_{tb}| > 0.975$ at 95% C.L. [130] due to the smaller experimental uncertainties whereas the best direct determination based on 7 TeV and 8 TeV CMS data only yields $|V_{tb}| > 0.92$ at 95% C.L. [271].

Considering the latest progress both in the theoretical description and the experimental determination of the t-channel production cross section, one may wonder whether these improvements can be employed to measure two of the most fundamental quantities in top-quark physics, namely m_t and Γ_t. As a matter of fact, as already explained in section 1.2.2, the experimental results for $R_{\mathcal{B}}$ and $\sigma^{\mathbf{tot}}_{t+\bar{t}}$ can be used to indirectly measure the total decay width with yet unprecedented precision of about 10%. For the top-quark mass the situation is different. As the sensitivity of the t-channel cross section to the value of m_t is substantially lower than for $t\bar{t}$ production, a similar analysis based on total cross section measurements seems not feasible even with an optimistic estimate of the future reduction of experimental and theoretical uncertainties. In spite of this, single top-quark data is, in general, still relevant for m_t measurements that employ the standard methods known from top-quark pair production. Due to the distinct experimental signature of single-top events these measurements represent a statistically independent determination of the top mass and, moreover, are affected differently by the various sources of systematic uncertainty. Such an analysis has, in fact, already been performed both by the ATLAS [75] and the CMS [76] collaboration, the latter providing the most precise result $m_t = 172.60 \pm 0.77(\text{stat.})^{+0.97}_{-0.93}(\text{syst.})\,\text{GeV}$ which is in good agreement with the current world average. Unfortunately, there will probably be no essential improvement of this determination method when including 13 TeV single-top data as the increase of the dominant $t\bar{t}$-background will be more significant than the actual gain in the signal cross section. Therefore it remains to be seen to what extent this development can be compensated by a re-optimization of the selection criteria.

2. *s-channel production*

The second major source of single (anti-)top quarks at the Tevatron is the production via s-channel W-boson exchange as illustrated in Fig. 1.12 part (b), which profits significantly from the presence of valence anti-quarks in the initial state. At the LHC, on the contrary, the corresponding partonic fluxes are much lower leading to a severe suppression of the s-channel cross section $\sigma^{s}_{t+\bar{t}}$ with respect to the other single-top production modes despite the increased center-of-mass energy. This suppression

is indeed so strong that the s-channel is surpassed by the tW-channel to become the weakest production mechanism at this collider rendering its measurement a serious experimental challenge.

From the theoretical point of view the description of the total rate for s-channel single top-quark production also contains some unresolved issues. The NLO QCD corrections [335] have been known for almost 20 years[36] and turn out to be quite sizable, about 50%, which a priori could not have been inferred from the naive LO scale variation. There exist processes, for instance vector-boson pair production, where such a behavior can be attributed to the emergence of an additional production mode with an enhanced partonic flux. This is, however, not the case here as the contributions from the newly arising qg initial state only amount to at most a few percent [110]. Another striking feature of the NLO result is the relatively small theoretical uncertainty estimated from scale variation and the PDF errors (see Tab. 1.3). While the small PDF uncertainty can be explained by the fact that s-channel production is mainly initiated by light-quark interactions whose distributions are rather well constrained, the modest scale dependence again suggest that the impact of yet missing higher-order contributions is negligible. Lacking a full NNLO calculation for this process, one has to resort to calculations that incorporate effects beyond fixed-order perturbation theory, most notably soft-gluon resummation [224, 288, 289, 341, 342], to verify this assumption. Surprisingly, the corrections to the total cross section from these soft emissions are also sizable, which indicates that the NLO scaling error may be accidentally small and the full NNLO contributions could indeed be large. A possible explanation for the presumably poor perturbative convergence might be an inappropriate choice for the central scales $\mu_F = \mu_R = m_t$ but this aspect has not been thoroughly investigated yet as it would require a complete knowledge of these higher-order corrections.

Because of the quite limited precision of $\sigma^s_{t+\bar{t}}$ measurements a comparison between theory and experiment will, however, be clearly dominated by experimental uncertainties even if the theoretical error was truly underestimated. This is mainly due to the fact that the number of s-channel single-top events corresponds only to about half the number of singly produced top quarks in the t-channel. Moreover, the kinematic features of these events are less characteristic, which makes it more difficult to adequately separate signal from background contributions. For this reason it required the combined effort of the CDF and DØ collaborations to finally establish the existence of this production mode with a significance of over five standard deviations [344] (see Fig. 1.18). In their analyses, performed either in the ℓ+jets (CDF [345] and DØ [296]) or in the MET+jets (CDF [346] only) channel, they again used multivariate discriminants to suppress the large backgrounds that are of similar nature as for the t-channel measurements (QCD multijet, W+jets, other top production modes) allowing for an extraction of the s-channel cross section with an accuracy of about 20%. At the LHC these backgrounds are even more

[36] Meanwhile, the NLO calculations have been extended to the fully differential level [282] including decays [273, 336] and the study of off-shell top-quark effects [277, 337, 338]. The impact of EW corrections was examined in Refs. [339, 340] and found to be small.

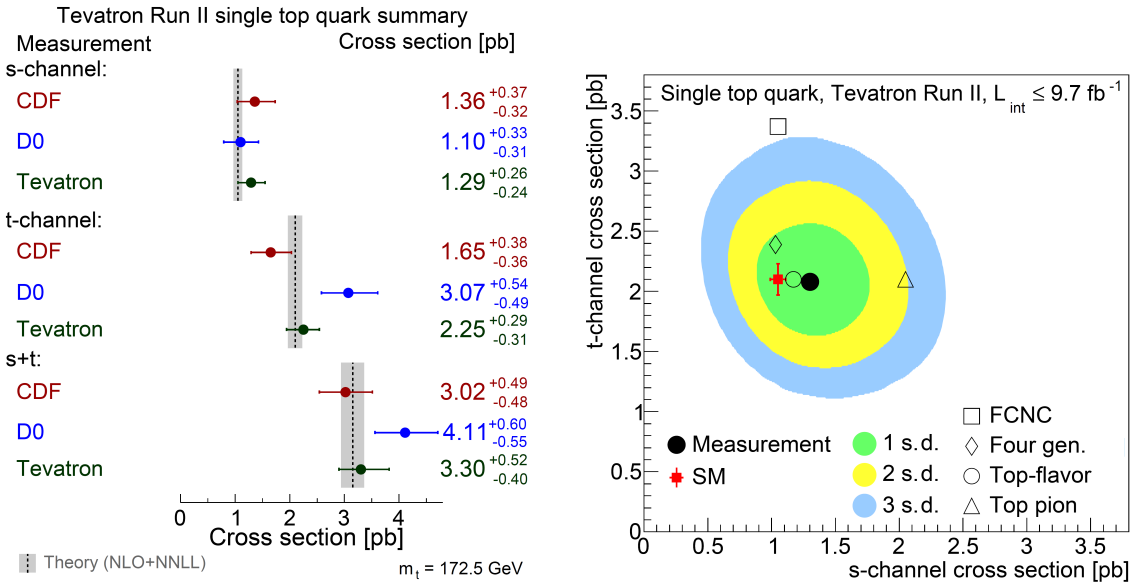

Figure 1.18: *Left: Summary of different s- and t-channel measurements at the Tevatron as well as their combination compared to the theoretical prediction at NLO+NNLL [297]. Right: Two-dimensional contour plot of Tevatron s- and t-channel measurements compared to the SM prediction at NLO+NNLL and several BSM scenarios [297](FCNC with* $\frac{\kappa_{tu}^{g}}{\Lambda} = 0.036$ *[303], four quark generations with* $|V_{ts}| = 0.2$ *[343], top-flavor scenario with new heavy boson of mass* $m_{W'} = 1\,\text{TeV}$ *[303], top-pion model with* $m_{\pi^\pm} = 250\,\text{GeV}$ *[303]).*

dominant as they grow rapidly with increasing center-of-mass energy, which to this day prevents a clear experimental observation of this channel in proton-proton collisions. Both ATLAS [347] and CMS [348] were merely able to provide upper limits on the cross sections at 7 TeV and 8 TeV and only very recently ATLAS presented the first evidence of *s*-channel single top-quark production at the LHC with a significance of 3.2 standard deviations and a measured cross section of $\sigma_t^s = 4.8 \pm 0.8(\text{stat.})^{+1.6}_{-1.3}(\text{syst.})\,\text{pb}$ [293] (see Fig. 1.14). The main sources of systematic uncertainty in all of these measurements are related to the proper modeling of signal and background processes and, since the *s*-channel final state contains at least two *b*-quarks, to the *b*-tagging efficiencies of the individual experiments.

As the measured cross sections are consistent with the SM predictions at NLO+NNLL accuracy, they can, in principle, be combined with the *t*-channel measurements into a two-dimensional analysis to constrain the parameter space of several SM extensions as illustrated for the Tevatron results in Fig. 1.18. Due to the large experimental uncertainties the discriminating power of such an approach is, however, not sufficient to seriously probe these new-physics scenarios and it thus seems more promising to look for these effects directly in the *s*-channel final-state topology, which is particularly sensitive to contributions from new charged heavy bosons [303]. Indeed, there have

been extensive searches for new heavy gauge-bosons W' based on a model-independent effective Lagrangian approach both at the Tevatron [349, 350] and the LHC [351–354]. So far, no significant excess above the SM background could be detected leading to various exclusion limits depending on the underlying vertex structure of the respective BSM models. The DØ collaboration also searched for charged Higgs bosons $H^{\pm}$ in s-channel final-state configurations [355], which is complementary to the analyses based on top-quark decays, but again no deviations from the SM expectation could be observed. It remains to be seen whether the new LHC run at 13 TeV will reveal any new-physics contributions in this particular channel or if it will merely lead to a further extension of the current exclusion bounds.

3. *Associated tW production*

The last of the three production modes for single (anti-)top quarks, the tW-channel, is fundamentally different as it, in contrast to the previous channels, contains two massive particles in the final state. This aspect, in combination with the comparatively small partonic flux, which may be attributed to the presence of initial-state b-quarks, leads to a strong suppression of the total cross section $\sigma_{t+\bar{t}}^{tW}$ (see Tab. 1.3) rendering an experimental observation at the Tevatron impossible. The enhanced center-of-mass energy at the LHC increases the available phase space for this process, which improves the prospects of a successful detection considerably allowing the experimental collaborations to present first evidence for this yet missing production mode at both 7 TeV [330, 331] and 8 TeV [356]. Finally, in the beginning of 2014, CMS was able to provide the first measurement of the tW-channel with a significance of more than five standard deviations [332], thus completing the experimental verification of single top-quark production. Due to the close similarity of the tW-signal (two isolated leptons, MET, one tagged b-jet) to dilepton $t\bar{t}$ production, the analysis strategy again consisted of a multivariate approach based on several kinematic and topological variables that allows for a sufficient discrimination of the large background contributions. The CMS result has meanwhile been confirmed by the ATLAS collaboration providing the most precise individual determination of this production mode to date [333]. Still, there remains a sizable overall experimental uncertainty connected to these measurements resulting in a current precision of merely $\sim 20\%$ [332–334] as can be inferred from Fig. 1.19. Nonetheless, the observed cross sections agree with the theoretical predictions at NLO+NNLL accuracy, which may be interpreted as a further argument in favor of the SM.

However, as already mentioned before, the theoretical description of associated tW production as well contains some conceptual difficulties that are closely related to its similarity to top-quark pair production. While at LO it seems that both processes are well defined and distinguishable, already the calculation of the NLO QCD corrections reveals the inherent problems connected with this naive theoretical picture. As shown in Fig. 1.19, these corrections contain radiative contributions with internal top propagators that can become resonant such that an integration over the full phase space would actually yield infinite results. The solution to this problem is well-known and consists of treating the top quark as an unstable particle, e. g. by introducing an imaginary

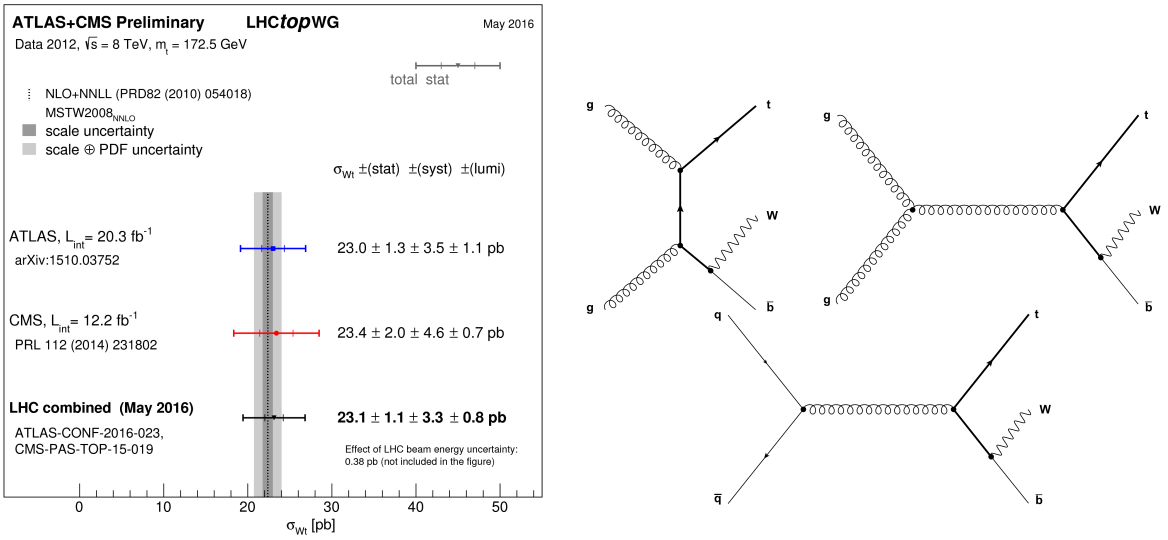

Figure 1.19: *Left: Summary of the individual cross section measurements for associated tW production by* Atlas *and* Cms *as well as their combination compared to the theoretical prediction at NLO+NNLL [334]. Right: Feynman diagrams with resonant top-quark propagators contributing to the NLO radiative corrections for tW production.*

part in the propagators or by using the complex mass scheme [244,245]. This, however, means giving up the concept of tW and $t\bar{t}$ production being separate processes but rather regarding them as overlapping subtopologies of $W^+W^-b\bar{b}$ production, a more realistic final-state configuration that is much closer to what is actually measured by the experiments. Such a calculation is most conveniently performed in the 4FS in order to avoid large NLO corrections induced by the sizable contributions from the newly arising gluon fusion and quark annihilation channels [251,252].

While it is possible to enhance the single resonant components in the combined description by applying appropriate kinematic cuts, the computational effort of such an analysis is high and for practical reasons it would be preferable to maintain the stable-top approximation and still be able to disentangle tW and $t\bar{t}$ production in a meaningful manner. There have been several proposals on how to solve this problem ranging from fairly inclusive approaches, e. g. abandoning all resonant diagrams [357] or introducing suitable subtraction terms to remove the contributions from $t\bar{t}$ production [357–359], to cut-based strategies that exclude certain kinematic regions in the phase space integration, e. g. by imposing restrictions on the invariant mass of the $W^-\bar{b}$ system [360,361] or the transverse momentum of the additional b-quark in the real-emission contributions [362]. Although all of these approaches yield similar predictions, there remains a certain scheme dependence that can be seen as an additional source of theoretical uncertainty and should also be accounted for in the experimental analysis. These fixed-order results can be extended to include also the resummed

contributions from soft-gluon radiation up to NNLL accuracy [224,288,289,363], which has a noticeable impact on the total cross section albeit far less significant than for s-channel production. Apart from QCD corrections also the NLO EW effects [364,365] have been studied but they turn out to be at the low percent-level and are therefore commonly neglected in practical applications.

Since the LO description of associated tW production contains a diagram with s-channel b-quark exchange, it is affected by new fermionic degrees of freedom in various BSM scenarios. Similar to the searches for new heavy bosons, these additional contributions are conveniently parametrized by an effective Lagrangian, which allows for a model-independent analysis of the relevant data samples. Note, however, that it is again more promising to search directly for these new heavy fermions rather than trying to detect a deviation from the SM expectation in tW cross section measurements. So far, no significant excess above the SM background could be observed resulting in stringent exclusion bounds for the mass of these particles well above 1 TeV [366–368]. The current and upcoming LHC runs will show whether these limits will increase or if we may eventually get a first glimpse on some new physics in the single top-quark sector.

1.3.3 Top-quark asymmetries

So far, we have restricted our discussion to fully inclusive top-quark observables since both their theoretical description as well as their experimental determination feature the most advanced analysis techniques on the market allowing for an in-depth test of our current understanding of particle physics. Nevertheless, there also exists a rich spectrum of phenomenological applications for more exclusive quantities as they offer the unique opportunity for a more focused inspection of the SM and its extensions. In this context asymmetries, specifically tailored difference relations constructed from kinematically constrained event yields, are of particular interest since they constitute a perfect compromise of inclusive and differential observable. In contrast to a more universal quantity as, for instance, a total cross section, they usually display an enhanced sensitivity to formally suppressed contributions that would otherwise be inaccessible to a direct examination. Indeed, these quantities are not necessarily Lorentz invariant and can, in general, be only thoroughly defined in certain reference frames which are chosen such that, on the one hand, the IR-safety of the theoretical description is guaranteed and, on the other hand, an experimental observation is still feasible.

In the following we will only focus on asymmetry observables associated with stable top quarks. Note, however, that there also exist studies [369–378] on the asymmetric behavior of the top-decay products, in particular the electrons and muons from the leptonic W-decays. Even though within the SM these asymmetries are basically generated from the original $t\bar{t}$ asymmetries, they in general constitute independent observables that are sensitive to possible new-physics effects which leave the hard scattering unaffected. For a concise overview on the current theoretical and experimental status of these leptonic asymmetries we refer the reader to Ref. [379].

Tevatron

The most intensively studied asymmetry observable in top-quark physics is certainly the forward-backward asymmetry at the Tevatron, which may in general be defined as

$$\mathrm{A_{FB}}(Q) = \frac{\sigma^{+}_{t\bar{t}}(Q) - \sigma^{-}_{t\bar{t}}(Q)}{\sigma^{+}_{t\bar{t}}(Q) + \sigma^{-}_{t\bar{t}}(Q)} = \frac{\sigma^{+}_{t\bar{t}}(Q) - \sigma^{-}_{t\bar{t}}(Q)}{\sigma^{\mathrm{tot}}_{t\bar{t}}} \tag{1.46}$$

where

$$\sigma^{\pm}_{t\bar{t}}(Q) = \int \theta\left(\pm Q\right)\, d\sigma_{t\bar{t}} \tag{1.47}$$

and Q is a kinematic variable that divides the underlying reference frame into two separate hemispheres. The crucial point is that due to the distinct nature of the colliding $p\bar{p}$ pairs it is possible to assign the produced top quarks a specific direction with regard to the beam axis (usually in terms of the proton momentum) such that Q can be used to directly investigate their spatial distribution within the detector. Thus, this quantity is most conveniently defined in the laboratory frame, common choices being $Q = \cos\hat{\vartheta}$ [380–383], with $\hat{\vartheta}$ denoting the angle between the top-quark and proton momenta, or $Q = \Delta y \equiv y_t - y_{\bar{t}}$ [377,384,385] where the rapidity y can be expressed in terms of the energy E and the three-momentum in proton direction (z-axis) of the respective particle as

$$y = \frac{1}{2}\,\ln\frac{E + p_z}{E - p_z}\,. \tag{1.48}$$

The latter definition is particularly suited for an experimental analysis and has been employed in virtually every measurement of $\mathrm{A_{FB}}$ performed by CDF [386–389] and DØ [390–393]. Nevertheless, there also exist alternative approaches that evaluate the asymmetry rather in the $t\bar{t}$ rest frame [377] where the top and anti-top quarks are back-to-back implying $\Delta y' = y'_t - y'_{\bar{t}} = 2\,y'_t$ (hence the name forward-backward asymmetry). Note, however, that all of these definitions are formally equivalent only in the limit of vanishing transverse momentum of the $t\bar{t}$-system, $p_{T,t\bar{t}} \equiv |\vec{p}_{T,t} + \vec{p}_{T,\bar{t}}|$, and one thus has to be careful when comparing results based on different choices of Q. In particular, the CDF and DØ collaborations commonly assume that the contributions from larger values of $p_{T,t\bar{t}}$ to $\mathrm{A_{FB}}$ are negligible such that the difference Δy measured in the laboratory frame due to the invariance with respect to longitudinal boosts corresponds directly to the rest frame rapidity $\Delta y'$. While there is evidence that the numerical discrepancy between these two approaches is indeed small (see section 4.1.4), it has not been thoroughly investigated yet and we therefore in the following treat the respective measurements[37] as asymmetries in Δy rather than $\Delta y'$.

The reason why this particular observable attracted so much attention well beyond the scope of SM top-quark phenomenology was the fact that both CDF and DØ observed a large excess of "forward" $t\bar{t}$-events lying significantly above the SM theory prediction for $\mathrm{A_{FB}}$ [386,387,390]. Since this anomalous behavior persisted even when the amount of collected data increased, it was commonly interpreted as a potential sign of new physics sparking major research activity

[37] There also exist measurements of the so-called laboratory frame asymmetry [387] based on $Q = y_t$ which due to kinematics is smaller than $\mathrm{A_{FB}}(\Delta y)$. However, since it has been discarded in the latest CDF and DØ analyses, we will restrict our discussion to the more extensively studied case $Q = \Delta y$.

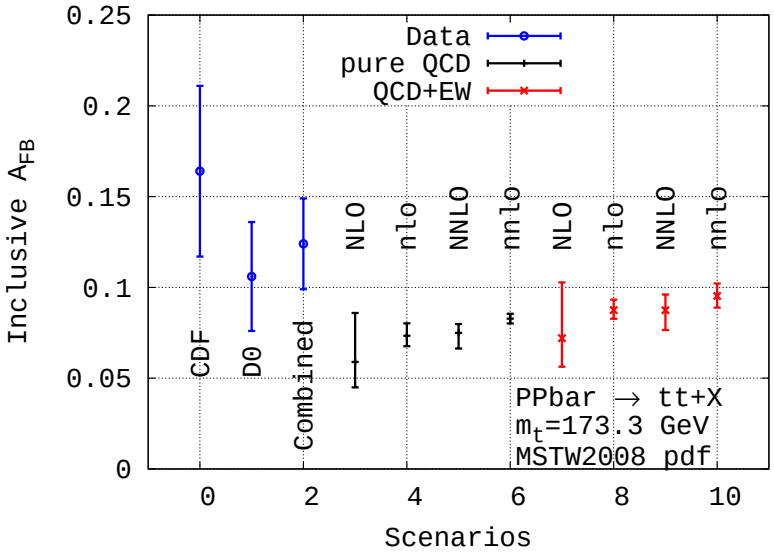

Figure 1.20: *The inclusive asymmetry* $A_{FB}(\Delta y)$ *as predicted in pure QCD (black) and augmented with EW corrections [377](red). Capital letters (NLO, NNLO) correspond to the unexpanded ratio in Eq. (1.49), while small letters (nlo, nnlo) refer to the definition in Eq. (1.50). The* CDF *and* DØ *results are taken from Refs. [388, 392] whereas their (naive) average is adopted from Ref. [379]. The error bands are due to scale variation only.*

both in SM and BSM physics [379, 394, 395]. Meanwhile, the gap between theory and experiment has been considerably reduced to a level where the DØ result is in full agreement with the SM prediction [392, 393] and the discrepancy of the CDF measurement merely amounts to about 1.4σ [388, 389] (see Fig. 1.20). On the one hand, this development can be attributed to the use of more refined measurement techniques as well as the advanced statistics of the full Tevatron data set leading to a tremendous improvement of the overall precision in the A_{FB} determinations. In fact, these experimental innovations even allowed for asymmetry measurements in the previously inaccessible dilepton channel [389, 392, 393], which are in agreement with the ℓ+jets results albeit suffering from larger uncertainties due to the information loss induced by the presence of two undetectable neutrinos.

On the other hand, there has been major progress in the theoretical description of A_{FB}, which is more severely affected by perturbative effects than, for instance, the total cross section. This may be explained by the fact that the contributions to the numerator in Eq. (1.46) are exclusively mediated via quark interactions. In consequence, the forward-backward asymmetry at LO in the strong coupling, where $\sigma_{t\bar{t}}^{\pm}(Q)$ is governed by pure s-channel exchange unable to distinguish between t and $\bar{t}$, completely vanishes. Hence, a non-zero value for A_{FB} is formally a NLO effect rendering it potentially more sensitive to higher-order corrections, an aspect that for a long time hampered a conclusive comparison between SM prediction and experimental observation. Indeed, only when including the recent results for the fixed-order NNLO contributions [385] derived in the course of this thesis (see section 4.1), the discrepancy between

theory and experiment eventually disappears[38] as shown in Fig. 1.20. Contrary to previous indications from soft-gluon resummation[39] [383, 399–401], especially when augmented with the conclusions drawn in Ref. [117] for a related asymmetry observable in the $t\bar{t}j$ final state, these corrections turn out to be quite sizable amounting to over 10% of the NLO predictions. This suggests that the asymmetric NNLO contributions mostly originate from harder radiation and thus cannot be well approximated within NNLL resummation even when taking into account $t\bar{t}$ pairs with arbitrary kinematics [401].

Another interesting feature in the theoretical description of A_{FB} is the unexpectedly large impact of EW corrections [377,382,384] consisting of pure $\mathcal{O}(\alpha^2)$ terms as well as mixed $\mathcal{O}(\alpha_s^2\alpha)$ contributions. They lead to a further increase of about 15% compared to the NNLO result moving the SM expectation closer to the values observed in experiment. Apart from that, the effect of including all-order Sudakov enhancements has been studied in Ref. [402], which is, however, much smaller, merely amounting to 5% of the NLO prediction. Incorporating both fixed-order QCD and EW corrections in Eq. (1.46) the current theory status may hence be summarized as follows

$$A_{FB} \equiv \frac{N_{EW} + \alpha_s^3 N_3 + \alpha_s^4 N_4 + \mathcal{O}(\alpha_s^5)}{\alpha_s^2 D_2 + \alpha_s^3 D_3 + \alpha_s^4 D_4 + \mathcal{O}(\alpha_s^5)} \tag{1.49}$$

$$= \alpha_s \frac{N_3}{D_2} + \frac{N_{EW}}{\alpha_s^2 D_2} + \alpha_s^2 \left(\frac{N_4}{D_2} - \frac{N_3 D_3}{D_2^2} \right) - \frac{N_{EW} D_3}{\alpha_s D_2^2} + \mathcal{O}(\alpha_s^3) \tag{1.50}$$

where the expansion of the asymmetry ratio in powers of α_s has been applied after convolution with the PDFs, which is not entirely consistent with the condition that Eq. (1.49) and Eq. (1.50) should be equivalent through NNLO but still compatible with the existing literature. In that sense, the difference between the two approaches can be interpreted as a measure for the sensitivity of A_{FB} to even higher-order terms in the perturbative expansion that are currently missing in our analysis. The individual results for the numerators and denominators as well as the corresponding asymmetry predictions are given in Tab. 1.4. Note that we have ignored the (insignificant) EW contributions to $\sigma_{t\bar{t}}^{\mathrm{tot}}$, i. e. the denominator of A_{FB}, and also, for the power counting in Eq. (1.50), discarded the inherent α_s-dependence of N_{EW} in order to allow for a combined treatment of the various EW effects.

[38] There exists an alternative approach based on NLO QCD corrections with an unconventional scale setting [396–398] that was able to reproduce the large excess in A_{FB} observed by the experiments. Its applicability, in particular to exclusive $t\bar{t}$ production, is, however, not yet fully established and needs to be further substantiated through data.

[39] Indeed, the predictions in Refs. [399, 400] are somewhat higher than for the remaining soft-gluon analyses, presumably due to a difference in the subleading behavior. While this leads to a better agreement with the experimental findings, it also suggests that these terms are not under good theoretical control calling for a full NNLO treatment.

[40] The numbers for the expanded asymmetry Eq. (1.50) at NNLO and NNLO+EW have been derived from pure NNLO PDFs whereas in Ref. [385] the corresponding predictions involve both NLO and NNLO fluxes. The numerical difference between these two approaches of about 1% is, however, negligible.

	Numerator [pb]	Denominator [pb]	A_{FB}[%] (Eq. (1.49))	A_{FB}[%] (Eq. (1.50))
LO+NLO	$0.394^{+0.211}_{-0.127}$	$6.682^{+0.356}_{-0.753}$	$5.89^{+2.70}_{-1.40}$	$7.34^{+0.79}_{-0.64}$
NNLO	$0.148^{+0.035}_{-0.142}$	$0.554^{+0.322}_{-0.130}$	–	–
EW	$0.088^{+0.030}_{-0.020}$	–	–	–
LO+NLO+EW	$0.482^{+0.241}_{-0.148}$	$6.682^{+0.356}_{-0.753}$	$7.21^{+3.07}_{-1.57}$	$8.98^{+0.61}_{-0.50}$
LO+NLO+NNLO	$0.525^{+0.055}_{-0.085}$	$7.009^{+0.259}_{-0.374}$	$7.50^{+0.50}_{-0.86}$	$8.36^{+0.21}_{-0.27}$
LO+NLO+NNLO+EW	$0.613^{+0.085}_{-0.105}$	$7.009^{+0.259}_{-0.374}$	$8.75^{+0.86}_{-1.09}$	$9.64^{+0.61}_{-0.61}$
CDF [388, 389]	–	–	$16.4^{+4.7}_{-4.7}$	
	–	–	$16.0^{+4.5}_{-4.5}$	
DØ [392, 393]	–	–	$10.6^{+3.0}_{-3.0}$	
	–	–	$11.8^{+2.8}_{-2.8}$	

Table 1.4: *Comparison of the latest experimental results for A_{FB} with various SM theory predictions derived at different orders in perturbative QCD in combination with EW effects[40]. The latter contributions have been adopted from Ref. [377] where we have checked that the impact of using of a different PDF set and top-quark mass is negligible (for details see section 4.1). The quoted uncertainties are due to scale variation only ($\mu_F \neq \mu_R$ for pure QCD, $\mu_F = \mu_R$ for EW and QCD+EW).*

It turns out that, regardless of the perturbative precision, the expanded ratio yields the most pronounced predictions for A_{FB} albeit the difference with respect to Eq. (1.49) steadily decreases with the inclusion of higher-order corrections. Interestingly, the numerical impact of these corrections depends crucially on the employed definition for A_{FB} such that one can observe no clear hierarchy between EW and NNLO QCD contributions. For the ratio-type asymmetry the latter corrections induce the largest shift with respect to the NLO prediction whereas for the expanded expression in Eq. (1.50) EW effects are numerically most important. The reason for this peculiar behavior is, in fact, twofold. On the one hand, it may be attributed to the different values of α_s used in the derivation of the asymmetry at different orders in QCD. On the other hand, it is related to truncation effects, which somewhat mitigate the impact of the NNLO QCD contributions on the expanded A_{FB}. Nevertheless, the various predictions are generally consistent within their respective uncertainties, which are completely dominated by the error due to scale variation while the other sources of theoretical uncertainty as, for instance, the PDF error are, due to cancellation effects, further suppressed. Similar to the central values, the error size also critically depends on the underlying definition used for A_{FB} with the ratio in Eq. (1.49) being more sensitive to the actual choice of μ_F and μ_R than the expanded expression in Eq. (1.50). Note, however, that with the inclusion of EW and NNLO QCD effects both approaches become increasingly more stable with regard to missing higher-order contributions such that the corresponding predictions now provide a very reliable estimate of the SM asymmetric behavior. They are, in particular, much more precise than the experimental determination of A_{FB}, as can be inferred also

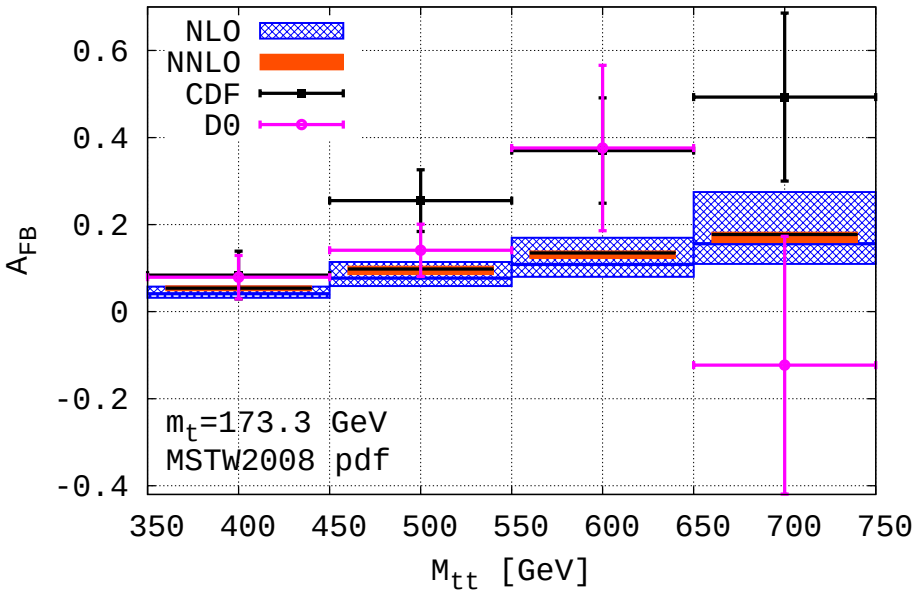

Figure 1.21: The differential $m_{t\bar{t}}$-asymmetry in pure QCD at NLO (blue) and NNLO (orange) compared to CDF [388] and DØ [392] data. The uncertainty bands only include the perturbative error due to scale variation. For improved readability some bins are plotted slightly narrower. The highest bin contains overflow events and the lowest bin includes all events down to the partonic production threshold at $2m_t$.

from Tab. 1.4, a situation that due to the final shutdown of the Tevatron will henceforth not further improve[41] preventing a more detailed analysis of this observable at that collider.

Still, it is possible to draw further conclusions on the asymmetric behavior of the top quark from the available Tevatron data by considering so-called differential asymmetries. They can be defined analogous to the inclusive $\mathrm{A_{FB}}$ as a ratio of cross-section-type functions, however, with the modification that the integration in Eq. (1.47) is restricted to a certain value of an additional variable Q'. In practice, this may be achieved by introducing a binning function $\theta_{\mathrm{bin}}(Q')$ that assumes the values zero or unity such that the kinematics of the $t\bar{t}$ pair are constrained to lie in a prespecified range of Q',

$$\sigma^{\pm}_{t\bar{t},\,\mathrm{bin}}(Q,Q') = \int \theta\left(\pm Q\right)\ \theta_{\mathrm{bin}}(Q')\ d\sigma_{t\bar{t}}\,. \tag{1.51}$$

The resulting asymmetry is then a distribution in Q' given as

$$\mathrm{A_{FB}}(Q,Q') = \frac{\sigma^{+}_{t\bar{t},\,\mathrm{bin}}(Q,Q') - \sigma^{-}_{t\bar{t},\,\mathrm{bin}}(Q,Q')}{\sigma^{+}_{t\bar{t},\,\mathrm{bin}}(Q,Q') + \sigma^{-}_{t\bar{t},\,\mathrm{bin}}(Q,Q')}\,. \tag{1.52}$$

[41] There have been suggestions the experimental access in $\mathrm{A_{FB}}$ could be related to the asymmetric behavior of the subtracted $t\bar{t}$ backgrounds [403] as well as from interactions of the final-state products with the remnants of the colliding (anti-)protons [404]. Reanalyzing the available data with regard to these proposals might therefore still lead to a noticeable shift of the measured asymmetry results.

Note that the denominator no longer corresponds to the total cross section but has been replaced by a differential quantity as well. In consequence, an expanded definition of $A_{FB}(Q, Q')$ similar to Eq. (1.50) might not necessarily be feasible as becomes clear when considering the case $Q' = p_{T,t\bar{t}}$ [116,405] where the LO prediction is confined entirely to the first bin. Other common choices that have already been employed in experimental analyses [387–389,391,392] are the absolute rapidity difference $Q' = |\Delta y|$ and $Q' = m_{t\bar{t}} \equiv \sqrt{(p_t + p_{\bar{t}})^2}$, the invariant mass of the $t\bar{t}$ pair. In particular, the asymmetry $A_{FB}(\Delta y, m_{t\bar{t}} > 450\,\text{GeV})$ attracted a lot of attention since it displayed an even larger discrepancy between theory and data [387] than the fully inclusive A_{FB} suggesting that it might, in fact, be the main source of the observed excess in the latter. Meanwhile, it has been measured with finer granularity [388,392] both by CDF and DØ as shown in Fig. 1.21 whereas the theoretical description has likewise improved to NNLO accuracy [385,406]. Similar to the inclusive asymmetry the DØ result is in good agreement with the SM prediction while the CDF measurements tend to be higher, especially in the range $m_{t\bar{t}} > 450\,\text{GeV}$ where the difference with respect to NNLO QCD can be up to about 2σ. The inclusion of soft-gluon resummation [383,401] and EW corrections [377,382,384] might help to further reduce this gap but unfortunately the corresponding results have not been published in the same binning as the experimental analyses thus (currently) hampering a combination of these effects. In particular for the latter it is well-known that in differential observables at high invariant masses Sudakov logarithms may become numerically important. A more profound examination of these contributions to all orders in perturbation theory, however, suggests that for the differential $m_{t\bar{t}}$-asymmetry their impact is still moderate [402].

The shape of the $A_{FB}(\Delta y, m_{t\bar{t}})$ distribution indicates that there might exist a linear relation of the form

$$A_{FB}(\Delta y, m_{t\bar{t}}) = \alpha_M \, m_{t\bar{t}} + \beta_M \tag{1.53}$$

that allows for a compact representation of the $m_{t\bar{t}}$-asymmetric behavior in terms of its slope. Such an analysis has recently been performed both by the CDF [388] and the DØ [392] collaborations turning out quite differently,

$$\begin{aligned} \alpha_M^{\text{CDF}} &= 1.55 \pm 0.48 \times 10^{-3}\,\text{GeV}^{-1} \\ \alpha_M^{\text{D}\O} &= 0.39 \pm 0.44 \times 10^{-3}\,\text{GeV}^{-1}\,. \end{aligned} \tag{1.54}$$

Again, only the DØ result is consistent with the SM value $\alpha_M^{\text{NNLO}} = 0.404^{+0.001}_{-0.040} \times 10^{-3}\,\text{GeV}^{-1}$ [406] whereas the CDF determination lies significantly above the NNLO QCD prediction[42]. A similar behavior can also be observed for the differential asymmetry $A_{FB}(\Delta y, |\Delta y|)$ where the corresponding linear dependence can be further simplified by the fact that the intercept vanishes, yielding

$$A_{FB}(\Delta y, |\Delta y|) = \alpha_y \, |\Delta y|\,. \tag{1.55}$$

The respective slopes measured by the two experiments at the Tevatron read [389,392]

$$\begin{aligned} \alpha_y^{\text{CDF}} &= 0.227 \pm 0.057 \\ \alpha_y^{\text{D}\O} &= 0.154 \pm 0.043 \end{aligned} \tag{1.56}$$

[42] A direct comparison of the CDF result with the NNLO theory prediction should be done with caution since the intercept β_M has not been specified in Ref. [388]

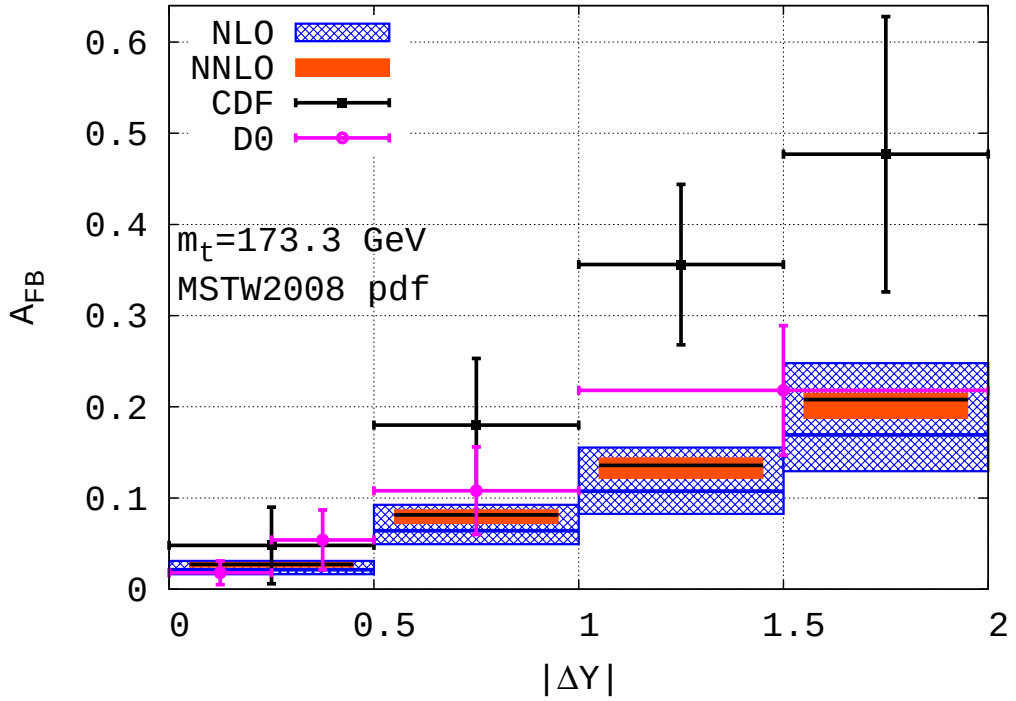

Figure 1.22: The differential $|\Delta y|$-asymmetry in pure QCD at NLO (blue) and NNLO (orange) compared to CDF [388] and DØ [392] data. The uncertainty bands only include the perturbative error due to scale variation. For improved readability some bins are plotted slightly narrower. The highest bin contains overflow events.

where the value provided by CDF is actually based on a combination of ℓ+jets and dilepton data. Interestingly, the latter, $\alpha_y^{\text{CDF}(\ell\ell)} = 0.14 \pm 0.15$, is in full agreement with the NNLO QCD prediction $\alpha_y^{\text{NNLO}} = 0.114^{+0.006}_{-0.012}$ [406], as is the DØ result, and only the inclusion of the ℓ+jets channel leads to a sizable excess above the SM expectation. Note, however, that a closer examination of the $|\Delta y|$-asymmetry on the theory side implies that its functional dependence is presumably not linear (see section 4.1.1 for details) such that one has to be careful when drawing any further conclusions from a comparison of these slopes.

The experimental results for $\text{A}_{\text{FB}}(\Delta y, |\Delta y|)$ itself [388, 392] are shown in Fig. 1.22 and, as may be anticipated from Eq. (1.56), exhibit a steadily increasing discrepancy between theory and data for the CDF measurement (except for the highest $|\Delta y|$-bin) while being in perfect agreement with the NNLO QCD prediction for DØ. Similar to the invariant mass, higher-order QCD effects from soft-gluon resummation [400, 401] as well as EW corrections [377, 384] are, in principle, available but not directly applicable due to the differing format that does not match the experimental specifications presented above. A naive comparison of the NLO QCD result with the findings in Ref. [377], however, suggests that, in particular the latter might have the potential to further reduce the tension between theory and experiment albeit it remains to be seen whether it can be completely resolved.

LHC

At the LHC the parity-invariant pp initial state precludes the construction of a forward-backward asymmetric observable such as A_{FB}, at least within the SM[43]. Still, it is possible to derive a somewhat related quantity by exploiting the fact that, at the parton level, valence quarks on average carry a larger fraction of the proton momentum than the sea anti-quarks. Consequently, a top quark typically possesses a larger (absolute) rapidity than the corresponding top anti-quark such that the expectation value of the variable $\Delta|y| \equiv |y_t| - |y_{\bar{t}}|$ does not vanish. The associated so-called charge asymmetry (sometimes also denoted "forward-central" asymmetry) is then given by

$$A_C(\Delta|y|) = \frac{\sigma^+_{t\bar{t}}(\Delta|y|) - \sigma^-_{t\bar{t}}(\Delta|y|)}{\sigma^+_{t\bar{t}}(\Delta|y|) + \sigma^-_{t\bar{t}}(\Delta|y|)} = \frac{\sigma^+_{t\bar{t}}(\Delta|y|) - \sigma^-_{t\bar{t}}(\Delta|y|)}{\sigma^{\mathbf{tot}}_{t\bar{t}}} \tag{1.57}$$

with $\sigma^{\pm}_{t\bar{t}}(\Delta|y|)$ defined in Eq. (1.47) and $\Delta|y|$ evaluated in the laboratory frame. Since this asymmetry is, similar to A_{FB}, solely mediated by fermionic degrees of freedom, it will be less pronounced than its counterpart at the Tevatron diluted by the overwhelming presence of purely gluon-initiated $t\bar{t}$ events at the LHC. Nevertheless, it has been observed in 7 TeV [374,375,407,408] and 8 TeV [409–413] data both by CMS and ATLAS through a dedicated analysis performed in the ℓ+jets as well as the dilepton channel. A concise summary of these measurements can be found in Fig. 1.23 (the latest results [411,413] for the dilepton channel have not yet been included) displaying a nearly perfect agreement with the SM expectation albeit the quite sizable experimental uncertainties somewhat prevent us from gaining any deeper physical insights from such a comparison.

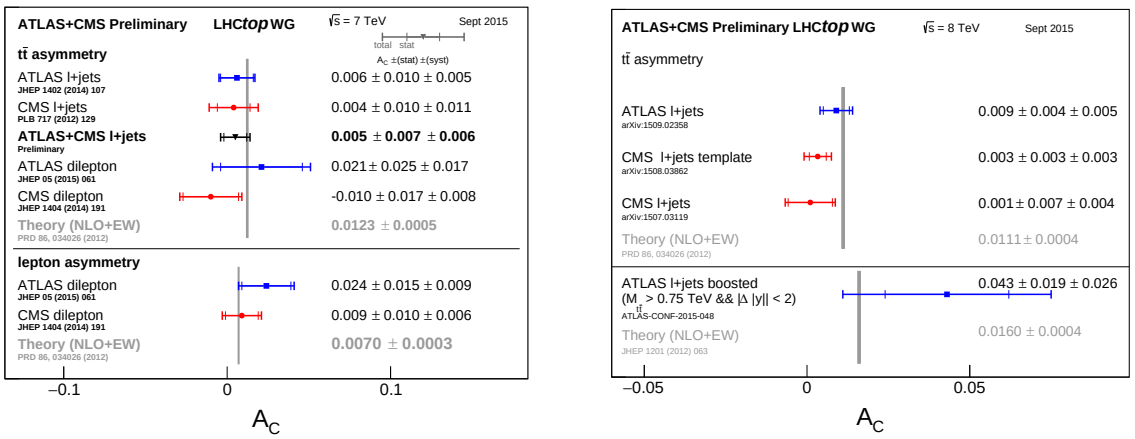

Figure 1.23: *Summary of LHC charge asymmetry measurements at* 7 TeV *(left) and* 8 TeV *(right) center-of-mass energy [260] compared to the respective NLO+EW theory predictions. The* 7 TeV *plot also contains results of lepton-based asymmetry measurements whereas the* 8 TeV *plot includes an additional analysis based on boosted* $t\bar{t}$ *events.*

[43] Strictly speaking, there exists a minor forward-backward asymmetry induced by parity-violating weak interactions, which is, however, severely suppressed by the QCD background such that it could never be observed in experiment.

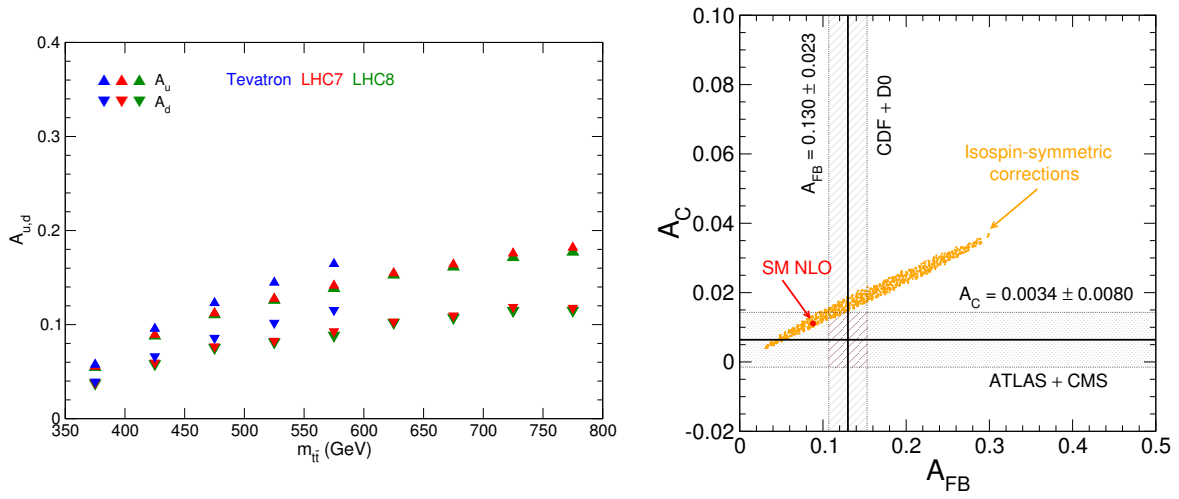

Figure 1.24: *Left: Invariant mass dependence of the intrinsic asymmetries* $A_{u,d}$ *evaluated within the SM for the Tevatron and the LHC. Right: Impact of isospin-symmetric variations of* $A_{u,d}$ *on* A_{FB} *and* A_C *(at 7 TeV) compared to experimental data. Both plots taken from Ref. [379]*

In order to have a better handle on potential new-physics effects, it is thus preferable to consider more differential asymmetry observables by applying additional constraints to the kinematic variables that characterize the heavy-quark system, e. g. $p_{T,t\bar{t}}$, $m_{t\bar{t}}$ or $|y_{t\bar{t}}|$. This has the advantage that the kinematic restrictions may be chosen such that the relative contribution of the quark-annihilation channel is significantly enhanced leading to an increased asymmetry, in particular when employing the latter variable. The transverse momentum and invariant mass, on the other hand, are more sensitive to a modification of the underlying parton kinematics, for instance through radiative corrections or interactions with new heavy particles. However, while these differential asymmetries have been intensively studied both in 7 TeV [407,408] and 8 TeV [409,412,413] data, they so far show no deviation from the SM expectation further constraining the parameter space of possible BSM models.

The theoretical predictions employed in these differential analyses as well as for the inclusive A_C are of NLO accuracy in QCD incorporating additional EW contributions of order $\mathcal{O}(\alpha^2)$ and $\mathcal{O}(\alpha_s^2\alpha)$ that, similar to A_{FB}, are non-negligible [377,382]. Considering the good agreement of theory and data, the inclusion of higher-order QCD corrections seems currently unnecessary, in particular since the corresponding theoretical uncertainty is already at the low percent-level. Still, in the light of the recent NNLO Tevatron analysis it would be interesting to see whether the LHC predictions for A_C are really as robust as suggested by these small errors.

Even though A_{FB} and A_C are, in principle, independent observables, it is nonetheless quite striking that they both behave so differently when it comes to comparing the experimental findings with the SM expectation. Therefore, it has been proposed to rather use collider-independent asymmetry definitions [379,414,415] based on a more parton-like picture where

the asymmetric behavior is generated by interactions of u and d quarks (and their respective anti-quarks) and subsequently washed out by collider-specific dilution effects. Denoting these intrinsic asymmetry observables $\mathrm{A_u}$ and $\mathrm{A_d}$, their relation to $\mathrm{A_{FB}}$ and $\mathrm{A_C}$ can be parametrized as

$$\begin{aligned} \mathrm{A_{FB}} &= \mathrm{A_u}\, F_u + \mathrm{A_d}\, F_d \\ \mathrm{A_C} &= \mathrm{A_u}\, F_u\, D_u + \mathrm{A_d}\, F_d\, D_d \end{aligned} \tag{1.58}$$

where $\mathrm{F_{u,d}}$ can be interpreted as the relative cross section contribution of the $u\bar{u}$- and $d\bar{d}$-channels and $D_{u,d}$ are additional LHC correction factors that account for $q\bar{q}$ events where the initial anti-quark carries a larger momentum fraction than the quark. As shown in Fig. 1.24, the collider-independent behavior is in practice only confined to a rather small range of $m_{t\bar{t}}$, which may, however, be further extended by employing additional kinematic cuts [414, 415], for instance on the transverse $t\bar{t}$ momentum. Nevertheless, measuring these asymmetries at the LHC, which admittedly represents a serious experimental challenge, would put us in the unique position to directly test the anomalous asymmetric behavior observed at the Tevatron. Combining both LHC and Tevatron data for the determination of $\mathrm{A_{u,d}}$, on the other hand, would allow for a further discrimination of possible BSM scenarios as illustrated in Fig. 1.24. There, the SM prediction for $\mathrm{A_{FB}}$ and $\mathrm{A_C}$ has been modified by applying random isospin-symmetric corrections [379] to $\mathrm{A_{u,d}}$ indicating that the resulting variations are not arbitrary but, in fact, highly correlated. In consequence, a potential isospin-symmetric extension of the SM that simultaneously satisfies the experimental results for both $\mathrm{A_{FB}}$ and $\mathrm{A_C}$ could be strongly constrained by such a joined analysis. Still, it remains to be seen whether this approach is really feasible in practice.

Another asymmetry observable that is sensitive to possible BSM physics and has been recently studied at the LHC [416–421] is the double spin asymmetry

$$C_{t\bar{t}}(\vec{a},\vec{b}) = \left\langle 4\left(\vec{a}\cdot\vec{S}_t\right)\left(\vec{b}\cdot\vec{S}_{\bar{t}}\right)\right\rangle = \frac{N(\uparrow\uparrow)+N(\downarrow\downarrow)-N(\uparrow\downarrow)-N(\downarrow\uparrow)}{N(\uparrow\uparrow)+N(\downarrow\downarrow)+N(\uparrow\downarrow)+N(\downarrow\uparrow)}\,, \tag{1.59}$$

which measures the correlation of the top ($\vec{S}_t$) and anti-top ($\vec{S}_{\bar{t}}$) spins with respect to the arbitrary reference axes $\vec{a}$ and $\vec{b}$ (the corresponding spin orientation indicated by up and down arrows). The actual choice of these axes turns out to be crucial in practice since it strongly influences the size of these correlation effects. Commonly employed reference vectors are, for example, the normalized proton momentum $\vec{a} = \vec{b} = \vec{\hat{p}}_p = \vec{p}_p/|\vec{p}_p|$, corresponding to the so-called beam basis, or the directions of top and anti-top, $\vec{a} = \vec{\hat{p}}_t = \vec{p}_t/|\vec{p}_t|$ and $\vec{b} = \vec{\hat{p}}_{\bar{t}} = \vec{p}_{\bar{t}}/|\vec{p}_{\bar{t}}|$, generally denoted as helicity basis. Note that, in order to guarantee the IR-safety of $C_{t\bar{t}}$, these vectors have to be evaluated in the $t\bar{t}$ rest frame while otherwise it is not possible to correctly account for collinear initial-state radiation.

Owing to the different spin structure of the initial parton states, the correlation in these spin bases depends on the partonic production mode, which becomes particularly obvious when evaluating Eq. (1.59) close to threshold where the $t\bar{t}$ pair is produced in an s-wave. For the quark annihilation channel, conservation of angular momentum then implies that the spins of top and anti-top with respect to the beam axis are aligned, such that $C_{t\bar{t}} = 1$,

Measurement	$C_{t\bar{t}}$	$C_{t\bar{t}}^{\mathrm{SM}}$ [422, 423]
CMS 7 TeV $\ell\ell$ [416]	$0.084^{+0.142}_{-0.142}$	$0.310^{+0.006}_{-0.006}$
ATLAS 7 TeV $\ell\ell$ [419]	$0.40^{+0.09}_{-0.08}$	
ATLAS 7 TeV $\ell\ell, \ell$+jets [420]	$0.23^{+0.09}_{-0.09}$ $0.37^{+0.07}_{-0.07}$ (indirect) $0.27^{+0.05}_{-0.05}$ (indirect)	
CMS 8 TeV ℓ+jets [417]	$0.23^{+0.6}_{-0.5}$	$0.318^{+0.005}_{-0.005}$
CMS 8 TeV $\ell\ell$ [418]	$0.278^{+0.084}_{-0.084}$	
ATLAS 8 TeV $\ell\ell$ [421]	$0.38^{+0.04}_{-0.04}$	
DØ $\ell\ell, \ell$+jets [424, 425]	$0.66^{+0.23}_{-0.23}$ $0.89^{+0.22}_{-0.22}$	$0.798^{+0.012}_{-0.015}$

Table 1.5: *Summary of LHC spin correlation measurements in the helicity basis at 7 TeV and 8 TeV center-of-mass energy compared to the respective NLO+EW theory predictions $C_{t\bar{t}}^{\mathrm{SM}}$. For completeness we also provide the result of the Tevatron spin analysis in the off-diagonal basis performed by* DØ.

whereas in the gluon fusion channel they tend to be anti-parallel resulting in a negative correlation $C_{t\bar{t}} = -1$. This is a tremendous advantage since it, in principle, allows us to distinguish between these individual production mechanisms, which are oftentimes affected quite differently by new-physics contributions. Note, however, that $C_{t\bar{t}}$ in general also depends on the partonic center-of-mass energy such that these correlation effects are, in practice, further diluted. An interesting aspect in this context is the fact that for the $q\bar{q}$ initial state it is possible to define a reference vector

$$\vec{d} = \frac{-\vec{\hat{p}}_p + (1-\gamma)\left(\vec{\hat{p}}_p \cdot \vec{\hat{p}}_t\right)\vec{\hat{p}}_t}{\sqrt{1-\left(\vec{\hat{p}}_p \cdot \vec{\hat{p}}_t\right)^2(1-\gamma^2)}}\,, \qquad \gamma = \frac{E_t}{m_t} \tag{1.60}$$

for which t and $\bar{t}$ are always maximally correlated regardless of their respective velocities. Unfortunately, this so-called off-diagonal basis cannot be utilized for the gluon fusion channel, i. e. not with the same energy-independent correlation behavior, such that it is, similar to the beam basis, only suited for measurements at the Tevatron.

While there indeed exists experimental evidence for spin correlations in Tevatron $t\bar{t}$ data [424, 425], this observable is not very well accessible at that collider. At the LHC, on the other hand, these correlation effects, evaluated in the helicity basis, have meanwhile been fully established both at 7 TeV [416, 419, 420] and 8 TeV [417, 418, 421] center-of-mass energy using dilepton and ℓ+jets data. The results are summarized in Tab. 1.5 and, similar to $\mathrm{A_C}$, in full agreement with the corresponding SM predictions at NLO+EW accuracy [422, 423]. They may hence be used to derive exclusion limits for possible BSM scenarios, especially

when augmented with the results for the other asymmetry observables A_{FB} and A_C [379]. It will be interesting to see whether an extension of these analyses to the data collected in the current and future LHC runs can further improve the situation. However, since the relative contribution of the symmetric gluon fusion channel will clearly increase in these measurements, one has to most likely resort to more differential asymmetry observables in order to uncover possible new-physics effects.

1.3.4 Differential distributions

Despite the fact that the behavior of elementary particles, apart from their internal quantum numbers, is usually characterized by inclusive quantities such as the total production cross section, the study of differential observables is indeed even more essential to our current understanding of nature and can be considered the backbone of high-energy particle physics. The reason for this lies in the measurement techniques employed at hadron collider experiments, which due to the finite detector geometry are almost exclusively based on the determination of kinematic distributions or other exclusive quantities that are subject to a direct observation, e. g. counting observables. This, in particular, also applies to inclusive observables or more fundamental theory parameters such as masses, couplings or spins that are only accessible through some sort of comparison at the differential level.

The need to adequately model the relevant physical processes therefore triggered the development of a vast variety of sophisticated methods and tools that allow for the determination of reliable predictions at different levels of the theoretical description: the parton level, the particle level (after decay, parton showering and construction of jets) and the detector level (only observable final-state objects including measurement effects). Especially the use of MC event generators turned out to be essential in this context as they provide a direct interface to these conceptually separable parts of the theory analysis. This is quite important since it enables us to establish a relation between the actual detector response and the perturbative predictions for the fundamental hard scattering process, a procedure commonly denoted as unfolding [426]. Ideally, it leads to detector-independent results that allow, on the one hand, for a combination of measurements from different experiments and, on the other hand, for a comparison with a broader spectrum of theoretical predictions, in particular with calculations at higher orders in QCD, which are the main subject of this thesis. Hence, we may in the following focus only on the case of stable top quarks laying special attention on the latest progress in the theoretical description of differential observables due to completion of the $t\bar{t}$ NNLO QCD program [406, 427–429].

Before that, the state of the art consisted of fixed-order NLO calculations, which can nowadays be performed in a multitude of self-contained MC frameworks such as MCFM [110], POWHEG [430], aMC@NLO [431], SHERPA [432] or HELAC-NLO [433], additionally refined by an all-order treatment of dominant radiation effects, either through parton showers or soft-gluon resummation. The impact of these latter methods on the corresponding theory predictions is, however, quite different. Parton shower algorithms are designed to complement the hard scattering amplitudes, evaluated at LO or NLO accuracy, by a finite number of collinear emissions, which can be interpreted as a resummation of leading-logarithmic contributions

down to a certain cutoff scale. As the splitting probability, governed by the so-called Sudakov form factor, is preserved at each step of the showering process, the total cross section will not be changed through this procedure such that only the relative shape of the resulting theory predictions will differ from the fixed-order analysis. Despite this fairly simple concept, its actual implementation involves a variety of schematic and technical subtleties that may have a non-negligible impact on the final outcome and led to the development of a wide selection of parton showering models. In practice, the corresponding algorithms are usually embedded in general-purpose MC event generators[44], e. g. HERWIG [434, 435], PYTHIA [113, 436] or SHERPA [432], that can be used to derive NLO+PS predictions for all top-related observables currently under investigation at the Tevatron and the LHC.

The results based on soft-gluon resummation, on the other hand, contain genuine higher-order contributions that alter both the overall normalization and the shape of differential distributions. Therefore, they have commonly been employed as an estimate for the, at that point, still missing NNLO corrections determined either at NLO+NNLL accuracy [225, 226] or, by expanding the resummation formula to a finite order in α_s, at approximate NNLO [223, 224, 399, 437–439]. For some observables the latter procedure has recently even been extended to approximate NNNLO [440] although in contrast to the inclusive cross section results [235] the matching is still performed at NLO level. This is, in fact, a crucial point as the absence of the full NNLO corrections in these resummation-based approaches renders the corresponding predictions more sensitive to the treatment of subleading terms, which can lead to sizable numerical differences. It would therefore be desirable to update these analyses by incorporating the latest findings of Refs. [406, 427–429] in the respective resummation formulae, which would eventually lead to a more robust theoretical description of differential top-quark production.

Another source of perturbative corrections that may become important in this context are EW interactions [91, 237–243, 422, 441–443] that are usually neglected at the level of fully inclusive cross sections. For more exclusive quantities, however, these contributions, consisting of both purely EW $\mathcal{O}(\alpha^2)$ and mixed QCD-EW $\mathcal{O}(\alpha_s^2\alpha)$ effects, can be of similar size as the corresponding NNLO QCD corrections. They most notably affect the tails of kinematic distributions where the impact of Sudakov logarithms of the form $\ln^2\left(Q^2/M_{W,Z}^2\right)$ becomes large, the relevant energy scale Q being typically of order $\mathcal{O}(\text{TeV})$. Considering the fact that this is also the region where new-physics contributions are expected to appear, EW corrections should generally be included in any precise comparison of theory and data. Note, however, that a recent analysis of photon-induced contributions [443], especially from the γg initial state, suggests that there exists a potential discrepancy in modeling the photon density inside the proton with predictions from different PDF sets in the highly-boosted top regime differing by as much as the total size of the EW effects. Indeed, such a behavior is not surprising since already the pure QCD results in this regime suffer from sizable PDF uncertainties [428]. In particular with regard to the current LHC run at 13 TeV, which allows us to

[44] For an excellent review and comparison of these event generators see Ref. [68]. Note that a key feature of these tools is that the parton shower algorithms can be also interfaced by external software, in particular the NLO MC frameworks mentioned above.

probe this region of phase space at an unprecedented precision, these aspects of the theoretical description have to be further clarified in order to guarantee the best possible predictions over the full kinematic range.

But not only PDF uncertainties, also the procedure of estimating missing higher-order contributions via scale variation needs to be thoroughly revisited when dealing with differential observables. While the concept of employing the residual scale dependence, evaluated in an interval $[\frac{1}{2}, 2]$ around a central scale μ_0, to quantify the theoretical uncertainty due to the use of perturbation theory is, in fact, well-established across processes and observables[45], the value to be chosen for μ_0 is not as clear as in the case of inclusive quantities. The reason for this is the broader spectrum of characteristic energy and momentum scales associated with a differential treatment reflecting the explicit kinematic range covered by the corresponding observables. The strong hierarchy of these scales implies that, in order to avoid large logarithmic corrections in all corners of phase space, μ_F and μ_R have to become dynamic, i. e. dependent on the underlying kinematics. While this leads to a far more reliable description of the respective differential cross sections, there still exists a certain ambiguity in defining these dynamic scales such that, in practice, different calculations of the same observable may be based on alternative central scale settings. The most common choices in hadronic top-quark production are

$$\begin{aligned}
\mu_0 &\sim m_T = \sqrt{m_t^2 + p_{T,t/\bar{t}}^2} \\
\mu_0 &\sim H_T = \sqrt{m_t^2 + p_{T,t}^2} + \sqrt{m_t^2 + p_{T,\bar{t}}^2} \\
\mu_0 &\sim H_T' = \sqrt{m_t^2 + p_{T,t}^2} + \sqrt{m_t^2 + p_{T,\bar{t}}^2} + \sum_i p_{T,i} \\
\mu_0 &\sim E_T = \sqrt{\sqrt{m_t^2 + p_{T,t}^2}\sqrt{m_t^2 + p_{T,\bar{t}}^2}} \\
\mu_0 &\sim H_{T,\text{int}} = \sqrt{(m_t/2)^2 + p_{T,t}^2} + \sqrt{(m_t/2)^2 + p_{T,\bar{t}}^2} \\
\mu_0 &\sim m_{t\bar{t}}
\end{aligned} \tag{1.61}$$

where the transverse momentum $p_{T,t/\bar{t}}$ depends on whether the considered observable is related to top/anti-top quarks, and the sum in the definition of H_T' runs over all massless final states contributing to the real-emission phase space integration. The corresponding proportionality constants can be fixed by using the *Principle of Fastest Perturbative Convergence* (PFPC), which has been introduced in Ref. [428] and can be applied to both inclusive and differential $t\bar{t}$ cross sections[46]. It exploits the high perturbative precision of these observables to determine the scale μ_0 that minimizes the deviation of the respective K-factors from unity over the entire kinematic range. One thus arrives at the following prescription for the "optimal" dynamic

[45] Recent work on alternative methods of assigning theoretical uncertainties can be found in Refs. [444–446].

[46] Other approaches to scale setting employed in past (and present) cross section analyses include the *Principle of Minimal Sensitivity* [447,448], the *Complete Renormalization Group Improvement* approach [449] and the Brodsky-Lepage-Mackenzie (BLM) scale setting procedure [396] (as well as its further refinement commonly denoted as *Principle of Maximum Conformality* (PMC) [397, 450–454]).

scales to be employed in the theoretical description of differential top-quark pair production [428]:

$$\mu_0 = \begin{cases} \frac{m_T}{2} & \text{for } p_{T,t} \text{ and } p_{T,\bar{t}} \text{ (as well as their average)} \\ \\ \frac{H_T}{4} & \text{for all other distributions} \end{cases} \tag{1.62}$$

Note that this result, in general, also leads to a reduced scale variation, i. e. a smaller theoretical uncertainty, and is moreover independent of the choice of PDFs. Conversely, the use of an alternative set of scales may lead to artificially large higher-order corrections, which becomes particularly important when merging the fixed-order analysis with an all-order treatment of soft-gluon radiation. Since such a combined strategy is already affected by potentially large subleading contributions, an additional, scale-related enhancement of the corresponding theory predictions may result in a significant overestimate of the size of missing higher-order terms in the perturbative expansion. With this in mind, it would hence be interesting to see how the various resummation-based approaches behave under different scale choices in order to assess to what extent they influence the final cross section predictions.

Indeed, a comparison at the fully inclusive level indicates that the numerical impact of soft-gluon resummation may be strongly suppressed when evaluating the NNLO total cross section with the PFPC scale setting procedure [428]. Assuming a similar behavior also for differential top-quark production, the corresponding NNLO distributions represent the most advanced theoretical predictions currently available for this class of observables. In the following we will therefore discuss how well they describe the experimental data collected at the Tevatron and the LHC and review some possible future prospects of employing these quantities in high-precision SM phenomenology as well as in searches for new-physics scenarios.

Tevatron

Due to the limited statistics associated with a lower center-of-mass energy, the examination of the kinematic properties of the produced top quarks at the Tevatron turned out to be quite challenging. In consequence, it took the CDF and DØ collaborations more than a decade to move from an inclusive $t\bar{t}$ analysis to the differential level[47], the first measured distributions being the invariant mass $m_{t\bar{t}}$ of the top pair [457] and the transverse momentum $p_{T,t}$ of the individual top quarks [458]. Meanwhile, these quantities have been studied in greater detail using the full $9.7\,\text{fb}^{-1}$ data set [459] allowing for a dedicated comparison of the experimental findings in the ℓ+jets channel with the respective NNLO QCD predictions [406] as shown in Fig. 1.25.

For the invariant mass the available data has been split into five bins of variable width spanning the range $m_{t\bar{t}} \in [240\,\text{GeV}, 1200\,\text{GeV}]$ albeit the lower physical bound is, of course, located at $\sim 2m_t$. In all of these bins one can observe an excellent agreement between the measured

[47] There, in fact, exist earlier kinematic studies [455,456] performed at 1.8 TeV center-of-mass energy that provided a first glimpse at differential $t\bar{t}$ production. They, however, still suffered from tremendous statistical constraints offering only limited physical insights.

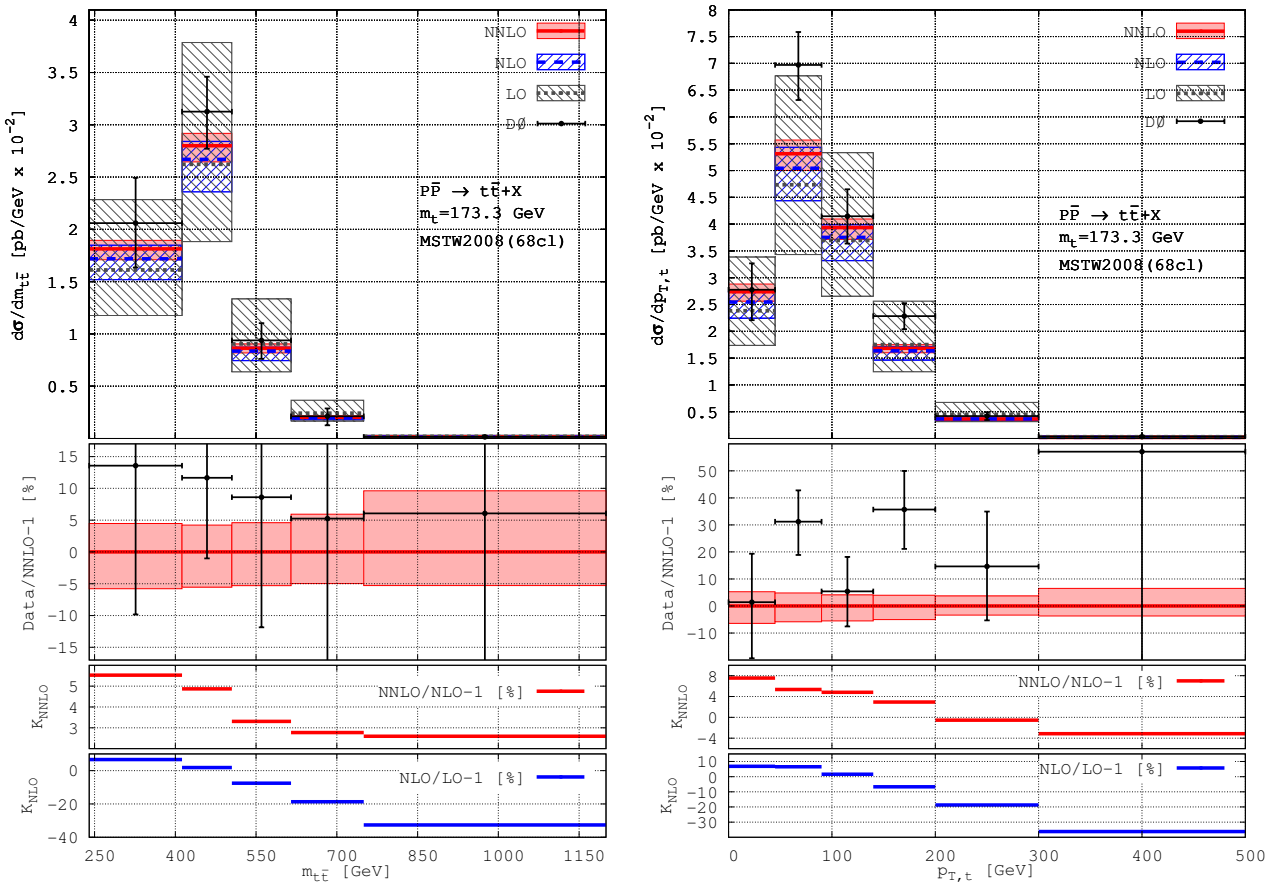

Figure 1.25: *The $m_{t\bar{t}}$ and $p_{T,t}$ distributions evaluated at different orders in perturbative QCD [406] and compared to data collected by the DØ collaboration [459]. The plots also show the ratio of data to NNLO QCD as well as the NNLO/NLO and NLO/LO K-factors K_{NLO} and K_{NNLO}. The error of the theory predictions at NLO and NNLO is obtained from adding scale and PDF uncertainties in quadrature. The experimental error contains both statistical and systematic effects whose relative contribution, however, differs among the various bins.*

results and the corresponding theory predictions with the experimental errors clearly dominating over the theoretical uncertainties from scale variation[48] and the PDFs. The fact that the experimental data lies systematically above the NNLO results however indicates that the resulting total cross section will be somewhat higher than the SM expectation suggesting that an examination of the normalized distribution $1/\sigma_{t\bar{t}}^{\mathrm{tot}}\, d\sigma/dm_{t\bar{t}}$ might be even more instructive. An additional advantage of such an analysis would be a further reduction of theoretical and experimental uncertainties due to correlation effects, which could help reveal possible deviations in the shape of the corresponding distributions. Yet, so far only the theory predictions have been provided in this normalized fashion (see section 4.2.2) and a comparison to actual data is currently still missing.

[48] In the Tevatron NNLO analysis a fixed scale $\mu_0 = m_t$ is used rather than the dynamic scales defined in Eq. (1.62). See the discussion in chapter 4.

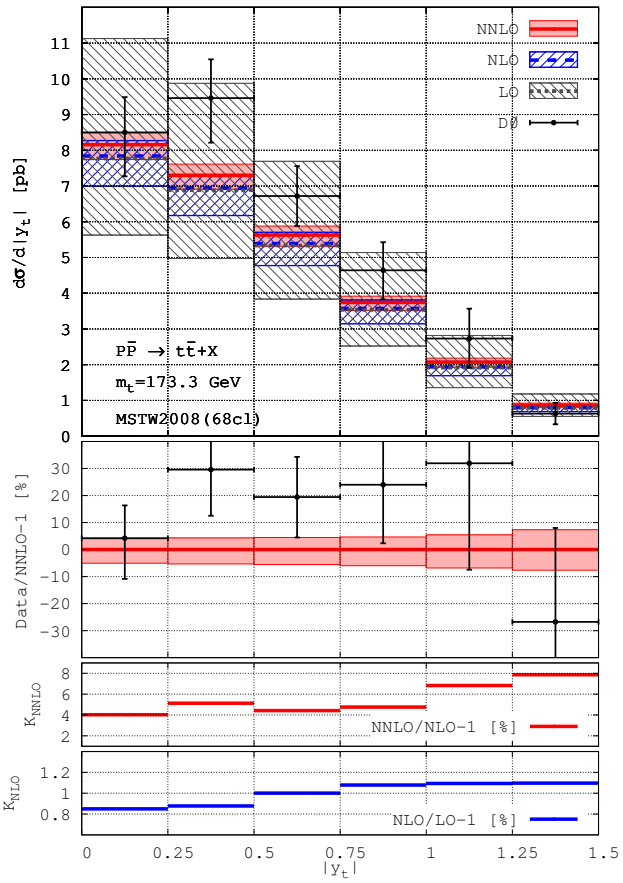

Figure 1.26: *The $|y_t|$ distribution evaluated at different orders in perturbative QCD [406] and compared to data collected by the DØ collaboration [459]. In addition, the ratio of data to NNLO QCD as well as the NNLO/NLO and NLO/LO K-factors K_{NLO} and K_{NNLO} are shown. The error of the theory predictions at NLO and NNLO is obtained from adding scale and PDF uncertainties in quadrature while at LO it consists of the scale uncertainty only. The experimental error contains both statistical and systematic effects whose relative contribution, however, differs among the various bins.*

For the $p_{T,t}$ spectrum the collected $t\bar{t}$ events have been combined into six bins unequally distributed over the interval $p_{T,t} \in [0\,\text{GeV}, 500\,\text{GeV}]$. Note that, in contrast to the invariant mass, the transverse momentum is not invariant under Lorentz transformations forcing us to specify a certain reference frame for the determination of this observable, usually the laboratory frame. Moreover, the contributions from top and anti-top quarks have been averaged since they are formally equal and one can thereby increase the statistical yield of the underlying data sample. Still, the resulting experimental errors are significantly larger than the corresponding theory uncertainties as can be inferred from the comparison shown in Fig. 1.25. Again, the experimental results are consistent with the SM expectation albeit in two of the bins data exceeds theory by about 2σ. A further investigation of the normalized $p_{T,t}$ distribution might help clarify the origin of this deviations but, similar to the $m_{t\bar{t}}$ spectrum, correspondent experimental results are not available yet.

Motivated by its use in the experimental determination of the inclusive and differential forward-backward asymmetry, the DØ collaboration also provided a measurement of the top-quark rapidity [459] defined in Eq. (1.48), however, only in terms of the absolute value $|y_t|$, again allowing for a combination of top and anti-top data. The corresponding result consists of six equal-width bins in the range $|y_t| \in [0, 1.5]$ and is shown in Fig. 1.26 compared to the NNLO theory predictions presented in Ref. [406]. Except for the last bin the measured rapidity data lies constantly above the SM expectation albeit being fully consistent within the respective error estimates, which are once more dominated by the experimental uncertainty. In the second bin the excess with respect to the theoretical result, despite the fact that it is below 2σ, is even so large that it leads to a qualitatively different shape of the experimental distribution. It would therefore be interesting to see whether this deviation becomes further enhanced in the normalized cross section $1/\sigma_{t\bar{t}}^{\text{tot}}\, d\sigma/d|y_t|$ or, conversely, the shape is shifted closer towards the corresponding NNLO predictions (see section 4.2.1). Yet, so far neither DØ nor CDF provided data in the required format to perform such a comparison of normalized distributions leaving still room for improvement in future analyses.

Despite the fact that for all of these exclusive observables the experimental uncertainty is significantly larger than the theory error, it is nevertheless important to assess the overall quality of the predicted cross sections by studying the impact of the newly-derived higher-order corrections on the theoretical precision. To this end, we have in Fig. 1.25 and Fig. 1.26 also plotted the NNLO/NLO and NLO/LO K-factors, K_{NNLO} and K_{NLO}, defined as the bin-wise ratio of the respective LO, NLO and NNLO differential cross sections. They reveal that for the invariant-mass and transverse-momentum spectra higher-order contributions tend to increase the theoretical predictions near the peak of the distributions while in the tails they lead to a further reduction. As the overall size of K_{NNLO} is up to ten times smaller than of K_{NLO}, one can conclude that the inclusion of the NNLO corrections has a considerable stabilizing effect on the shape of the theoretical spectra, which is particularly important with regard to possible phenomenological applications that go beyond a simple comparison to data, e. g. top-mass measurements or PDF determinations. For the rapidity spectrum the situation is quite different with both K-factors increasing almost linearly with $|y_t|$ and, moreover, K_{NNLO} being roughly five times larger than K_{NLO}. This behavior does, however, not signal a breakdown of the perturbative expansion as the NNLO results are still consistently contained within the NLO error band even when being estimated from scale variation only. Hence, it rather stresses the significance of going to full NNLO also in differential top-quark production to guarantee that the corresponding SM predictions are under good theoretical control.

Another interesting aspect is in this context the comparison shown in Fig. 1.27 of the exact NNLO results with the previously used NLO+NNLL resummed [225, 226] and approximate NNLO [223, 399, 437, 438] predictions. The setup of these calculations is quite similar, all based on the MSTW2008 PDF set, with only minor differences in the value employed for the top-quark mass ($m_t = 172.5\,\text{GeV}$ for Ref. [225], $m_t = 173\,\text{GeV}$ for Refs. [223, 399], $m_t = 173.1\,\text{GeV}$ for Ref. [226], $m_t = 173.3\,\text{GeV}$ for Refs. [406, 437, 438]) and the central scale choice ($\mu_F = \mu_R = m_{t\bar{t}}$ for Ref. [225], $\mu_F = \mu_R = 2\,m_t$ for Ref. [226], $\mu_F = \mu_R = m_t$ otherwise), which should be negligible with respect to the conceptual differences in the

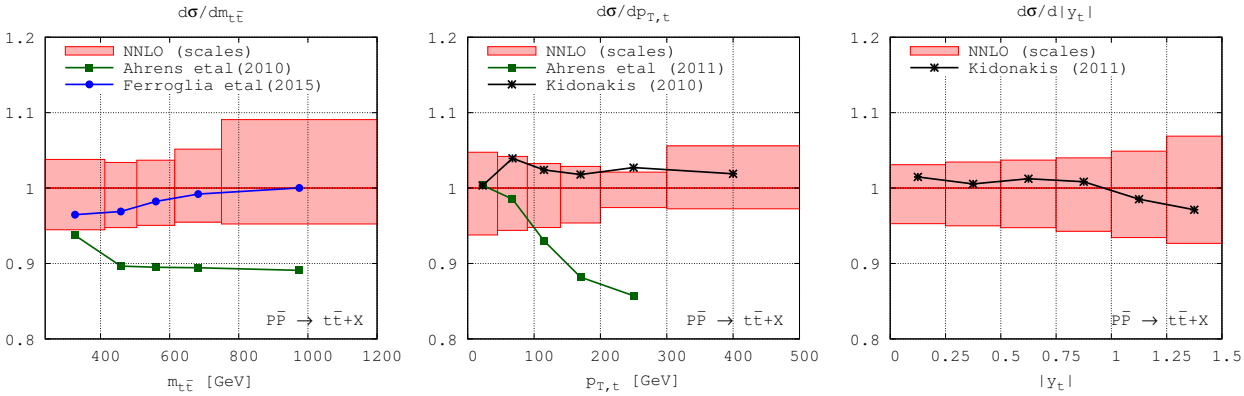

Figure 1.27: *Differential cross section ratios of various approximate NNLO [223, 399, 437, 438]/resummed NLO+NNLL [225, 226] predictions to the exact NNLO QCD results [406] for the main top-quark distributions studied at the Tevatron.*

treatment of the $\mathcal{O}(\alpha_s^4)$ corrections. Indeed, one can see that both the shape and the normalization of the various soft-gluon-based results may differ quite substantially from one another with the resummed predictions lying constantly below the expansion-type cross section approximations. This is a direct indication for the numerical importance of subleading terms in the resummation formalism that cannot be further constrained and thus effectively increase the theoretical uncertainty of these approaches. Nevertheless, the individual results are in good agreement with the exact NNLO evaluation suggesting that soft-gluon resummation is, to some extent, able to reproduce the higher-order behavior of the $m_{t\bar{t}}$, $p_{T,t}$ and $|y_t|$ distributions. In the future, it would, however, be theoretically far more robust to use an updated version of the resummation procedure where, analogous to $\sigma_{t\bar{t}}^{\mathbf{tot}}$, the matching to the fixed-order cross sections is performed at NNLO accuracy presumably reducing the sensitivity to subleading contributions.

Such an NNLO+NNLL analysis would certainly also experience a further reduction of the scale dependence allowing for a more refined examination of the quark PDFs as well as the remaining non-perturbative input parameters m_t and α_s. These aspects will be addressed in more detail in section 4.2 albeit only for the fixed-order NNLO results, which, due to the large experimental uncertainties dominating any practical application at the differential level, makes conceptually no difference. Nevertheless, from the comparison of theory and data in Fig. 1.25 and Fig. 1.26 one can already infer that the precision of such an analysis will be rather limited, at least when working with un-normalized distributions. Still, any measurement based on differential top-quark observables will always represent a valuable consistency check of the SM since it will, in general, be affected by different types of systematics than other, potentially more accurate, analysis techniques. As we will see next, at the LHC the situation is entirely different profiting from the significantly larger number of produced top quarks that allows for a much broader spectrum of phenomenological applications.

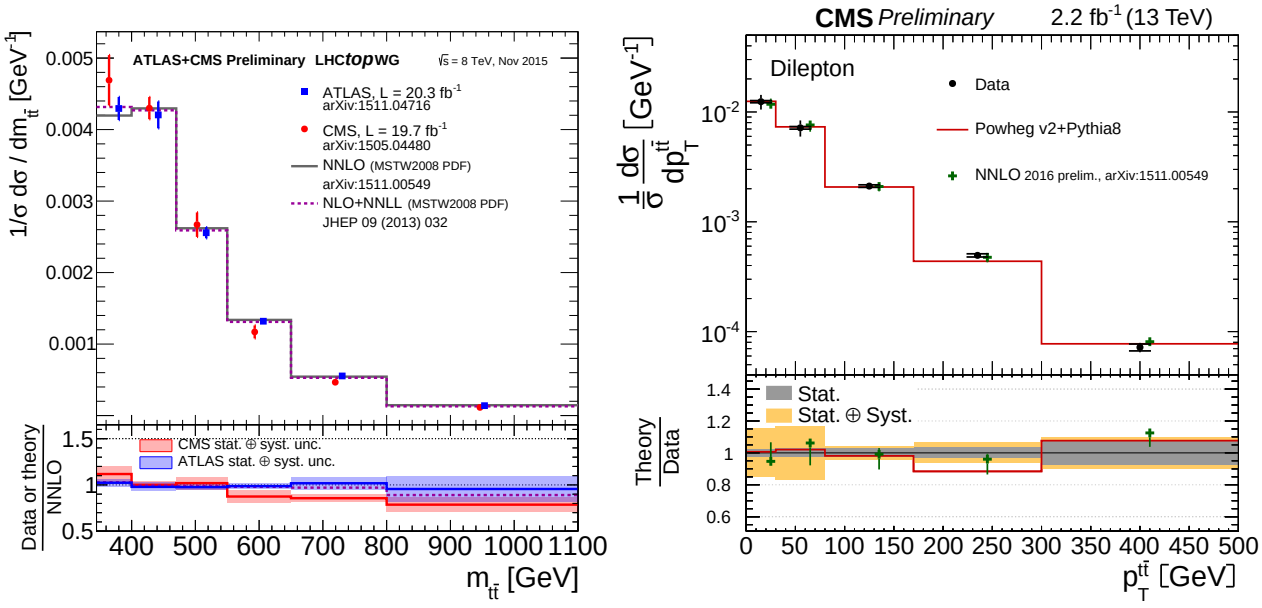

Figure 1.28: *The normalized $m_{t\bar{t}}$ and $p_{T,t\bar{t}}$ distributions extracted from 8 TeV ℓ+jets [260,460,461] and 13 TeV dilepton [462] data respectively and compared to various theory predictions at NLO+PS [430,436], NLO+NNLL [437] and full NNLO [427] accuracy. For the latter measurement the inner (outer) error bars indicate the statistical (combined statistical and systematic) uncertainty whereas otherwise only the combination of statistical and systematic errors are shown.*

LHC

At the LHC, being a veritable top factory with millions of $t\bar{t}$ pairs produced already in the first runs at 7 TeV and 8 TeV center-of-mass energy, statistical limitations are virtually non-existent thus allowing for a far more precise determination of kinematic top-quark distributions, i. e. both with a finer binning and a reduced uncertainty per bin. The amount of available data is, in fact, so high that the differential cross section analysis can now be directed at specific regions of phase space, for instance the highly-boosted top regime $p_{T,t} \gtrsim 300\,\text{GeV}$ [463, 464], or further extended to even more exclusive observables such as two-dimensional distributions [465][49]. Moreover, differential measurements are no longer restricted to $t\bar{t}$ production alone but have also been performed for singly produced top quarks [270, 466, 467], which allows for a closer examination of the interplay between strong and weak interactions.

Apart from the spectra of $m_{t\bar{t}}$, $p_{T,t}$ and y_t, which have already been studied at the Tevatron, the ATLAS and CMS collaborations usually also include the transverse momentum and rapidity of the top-quark pair, $p_{T,t\bar{t}}$ and $y_{t\bar{t}}$, in their analyses since they provide additional insights on the dynamics of the heavy-quark system. Indeed, each of these quantities has meanwhile been measured at different center-of-mass energies and for all main $t\bar{t}$ final-state topologies [183, 184, 188, 460–462, 468–474], even in the dilepton channel where the presence

[49] The differential asymmetry measurements performed at the Tevatron [387–389, 391, 392] are, in principle, also two-dimensional distributions albeit with a much lower granularity.

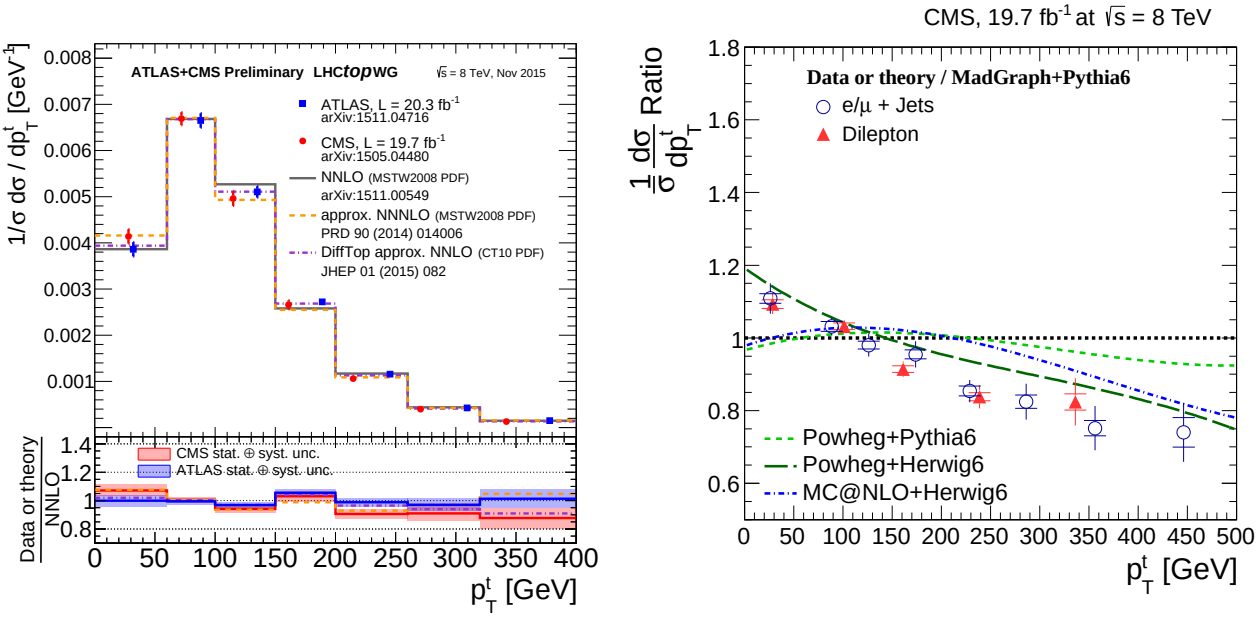

Figure 1.29: *The normalized $p_{T,t}$ distribution extracted from 8 TeV ℓ+jets [260, 460, 461] and dilepton [460] data compared to various theory predictions at approximate [439] and full NNLO [427], approximate NNNLO [235, 440] (left) as well as different (N)LO+PS implementations (right). In the right plot, theory and measurement are presented relative to a prediction obtained from* MadGraph+Pythia6 *[112, 113] where the inner (outer) error bars of the* CMS *data points correspond to the statistical (combined statistical and systematic) uncertainty.*

of two neutrinos leads to further complications in the kinematic reconstruction of the top-quark system (at least for one-parton observables such as $p_{T,t}$ or y_t). Similar to the total cross section, the differential parton-level results should in principle be independent of the specific decay mode such that a possible deviation of measurements in different final-state configurations would be a direct hint to new physics (provided that the unfolding procedure works correctly, see below). So far, however, all experimental findings are in good agreement and, moreover, fully consistent with the corresponding SM predictions at NNLO QCD as can be inferred from Fig. 1.28, Fig. 1.29 and Fig. 1.30.

As mentioned before, this high level of perturbative precision is, in fact, necessary to resolve the ambiguities associated with the incoherent treatment of subleading contributions in the various resummation-based approaches and PS implementations. Especially the latter results were not always able to properly reproduce the shape of the top-quark distributions observed in experiment, the most prominent example being certainly the so-called "$p_{T,t}$-discrepancy". As shown in Fig. 1.29, the different NLO+PS predictions for the transverse momentum spectrum appear to be systematically harder than the actual data, a feature that seems to be independent of the specific final-state topology or collider energy [183, 188, 460, 462, 463, 468–471, 473, 474]. Such a discrepancy is potentially problematic as it suggests that the MC event generators employed in the unfolding procedure are not able to adequately model the kinematic properties of the top-quark system. Since at the LHC top quarks are the dominant background for a broad class of processes, both in the SM

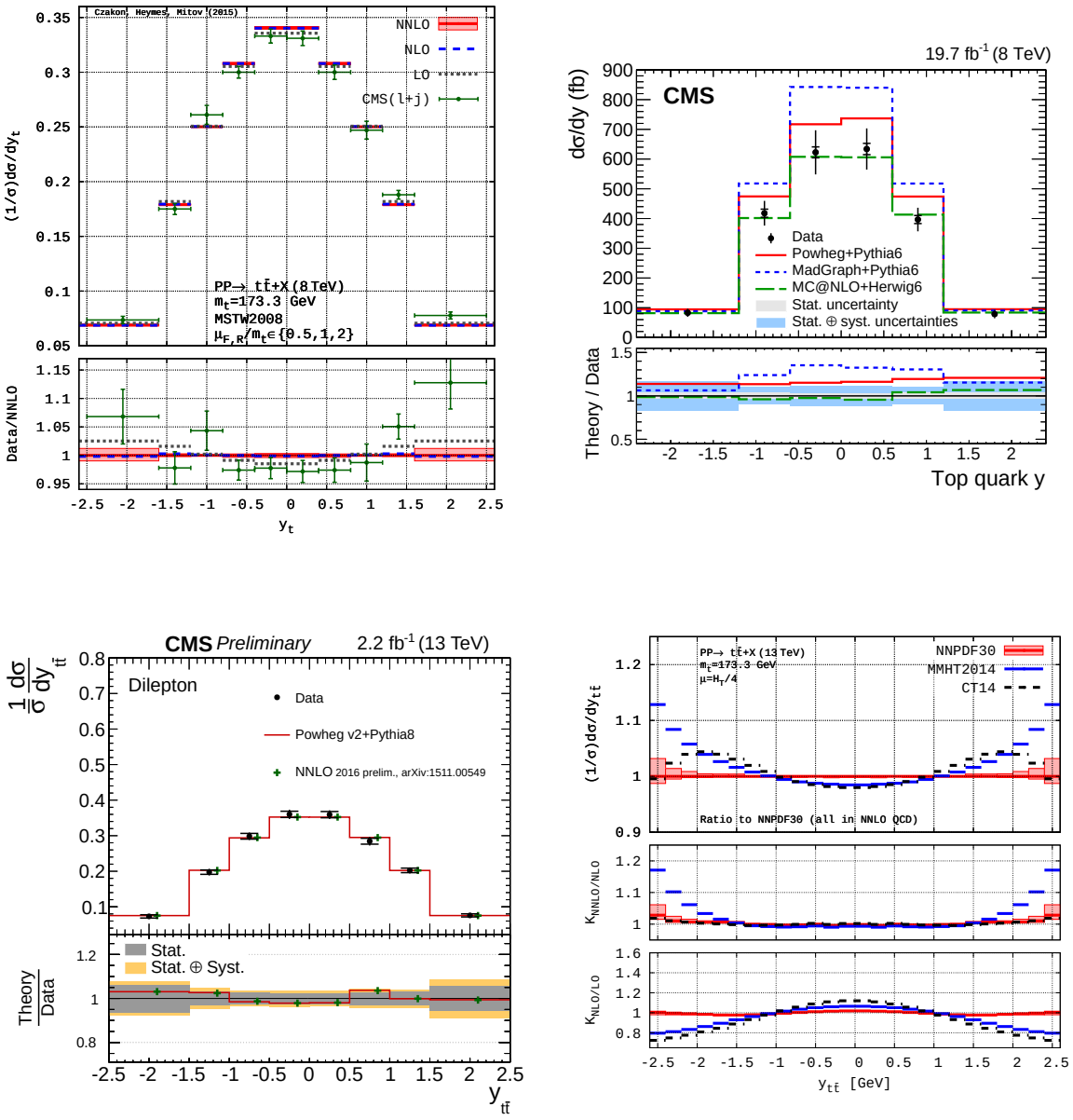

Figure 1.30: *Comparison of the NNLO QCD theory predictions [427] for the (normalized) rapidity distribution of the top quark (upper left) and top-quark pair (lower left) with data collected by the* CMS *experiment at* 8 TeV *(ℓ+jets channel) [460] and* 13 TeV *(dilepton channel) [462] center-of-mass energy respectively. In the former case, an additional measurement performed in the highly-boosted top regime [464] as well as the corresponding (N)LO+PS predictions are presented(upper right). Moreover, for $y_{t\bar{t}}$ the relative impact of using different PDF sets [428] in the determination of the NNLO differential cross section as well as the NNLO/NLO and NLO/LO K-factors is shown (lower right). Theoretical errors in all plots are from scale variation only whereas for the experimental data points the inner (outer) error bars correspond to the statistical (combined statistical and systematic) uncertainty.*

and beyond, an inaccurate description of their experimental signatures could lead to serious impediments in the analysis of ATLAS and CMS data. The inclusion of the NNLO QCD corrections finally closes this alleged gap between the parton-level SM predictions and LHC measurements [427], thus dispelling any concerns regarding the validity of the unfolding procedure. Unfortunately, these higher-order contributions cannot (yet) be directly accessed with PS algorithms, but still they constitute a valuable input for the further improvement of the MC event generators used by the experimental collaborations for a proper modeling of $t\bar{t}$ signals and backgrounds.

This is particularly important for future studies of the highly-boosted top regime where the current NLO+PS description is probably not sufficient to detect a possible BSM contamination in the predicted top-quark spectra as indicated for the rapidity distribution in Fig. 1.30. There, even for the central bins the various MC predictions differ by several tens of percent, which, when taking this spread as an estimate for the theoretical uncertainty, somewhat spoils the discriminating power of this observable in BSM searches. Hence, a further refinement of the theoretical description in this part of phase space is inevitable, either by tuning the PS-based approaches such that they yield predictions with a softer large-$p_{T,t}$ behavior or, preferably, by computing the corresponding NNLO distributions directly. Another possible gateway to the discovery of new-physics effects is the search for distortions in the shape of the invariant-mass spectrum caused by the decay of an unknown particle Φ into a $t\bar{t}$ pair. This so-called bump-hunting strategy [429,475] has the advantage that it is fairly model-independent and, moreover, provides a direct means of determining the mass m_Φ and decay width Γ_Φ of this new particle. In practice, however, the overall success of this approach depends crucially on the available statistics as well as on the chosen binning, especially if Φ is a narrow resonance located in the high-energy tail of the $m_{t\bar{t}}$ distribution. While the former constraint will become irrelevant with the high data volume generated in the current and upcoming LHC runs, the binning will remain a limiting factor even in the high-luminosity phase of the LHC since it is related to systematic effects, e. g. the detector resolution or the efficiency of the unfolding procedure [426].

The key idea is thus to reduce the uncertainty of the SM background as much as possible such that even with a relatively large bin size (compared to Γ_Φ) the detection of a small BSM excess is still feasible. This strategy, of course, profits tremendously from the recent calculation of the invariant-mass spectrum at NNLO accuracy [427,428] whose precision may be further enhanced by working with normalized distributions of the form $1/N\, d\sigma/dm_{t\bar{t}}$ [429]. The corresponding normalization factor N has to be chosen such that, on the one hand, the scale and PDF uncertainties as well as the experimental errors are considerably minimized (via correlation effects) and, on the other hand, the sensitivity to the top-quark mass remains moderate, i. e. the uncertainty on m_t only constitutes a small fraction of the total theory error. This is best demonstrated through the explicit example shown in Fig. 1.31 for the two contrasting cases $N = 1$ and $N = \sigma(600\,\text{GeV} < m_{t\bar{t}} < 700\,\text{GeV})$. It has been adopted from Ref. [429] where the main features of this bump-hunting approach are illustrated with the

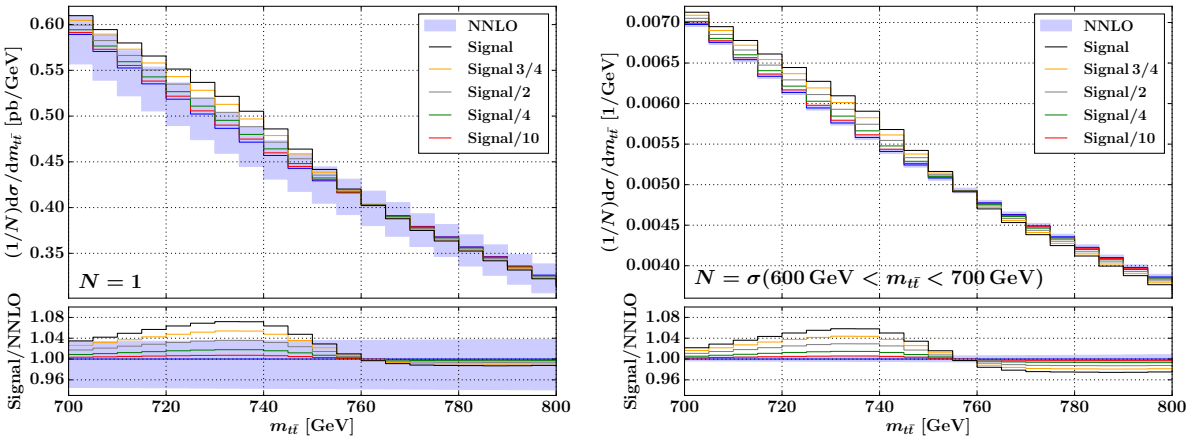

Figure 1.31: *The $m_{t\bar{t}}$ distribution evaluated at NNLO QCD for a LHC center-of-mass energy of* 13 TeV*, including the combined scale and PDF uncertainty (blue band), compared to the NNLO QCD + BSM central predictions for various signal strength of the $\Phi \to t\bar{t}$ decay described in the text [429]. While the left plot shows the un-normalized result $N = 1$, in the right plot the invariant mass spectrum has been modified by a semi-inclusive normalization factor $N = \sigma(600\,\mathrm{GeV} < m_{t\bar{t}} < 700\,\mathrm{GeV})$.*

help of a hypothetical spin zero resonance[50] with $\Gamma_\Phi \sim 40\,\mathrm{GeV}$ and $m_\Phi \sim 750\,\mathrm{GeV}$ emerging in 13 TeV top-quark data. As can be seen, for the un-normalized distribution the BSM signal is still consistent with the background-only hypothesis lying within the 2σ confidence interval of the corresponding NNLO SM prediction. Using as normalization factor the inclusive cross section in a $m_{t\bar{t}}$-range just below the expected signal region, on the other hand, leads to a significantly reduced theory uncertainty, which allows to effectively distinguish between SM background and BSM resonance, even if the latter is further suppressed compared to the default model employed for Φ. In practice, however, the lowest possible bin size accessible in this part of phase space will, due to experimental constraints, presumably be only of order $\sim 50\,\mathrm{GeV}$ [429], i. e. broader than the decay width Γ_Φ, such that the detection efficiency will strongly depend on the position of the bins' edges in the signal region. In order to still guarantee that the BSM signal can be unambiguously identified, it is therefore advisable to use sliding bins in the bump-hunting analysis since a flexible binning will allow for a scan of the relevant invariant-mass window for the highest signal significance.

As this search strategy is entirely universal, it can be easily applied to other kinematic regions providing a valuable tool for the detection of potential BSM resonances hiding in the current and forthcoming LHC data samples. In the future it might be even possible to extend this analysis to other differential $t\bar{t}$ observables as well considering the fact that the main ingredients for a precise theoretical description of the SM background are already available. Since these types of observables are presumably sensitive to a different class of BSM models, such an approach would be complementary to the search in the invariant-mass spectrum. It, however,

[50] This scenario was motivated by the 750 GeV di-gamma excess observed in an early batch of 13 TeV LHC data [476–479]. Meanwhile this anomaly has, however, disappeared suggesting that it was merely a statistical fluctuation [480, 481].

remains to be seen whether the use of normalized distributions for other kinematic quantities leads to a similar degree of signal-to-background separation or if the NNLO bump-hunting strategy will be restricted exclusively to $m_{t\bar{t}}$.

As already mentioned before, a serious drawback in the theoretical description of the high-energy tails of kinematic distributions is the sizable PDF uncertainty. Indeed, this problem might even persist when resorting to a normalized treatment of differential observables, at least in the highly-boosted regime $\gtrsim 1\,\text{TeV}$, which somewhat dilutes the predictive power of the NNLO QCD results in this part of phase space. The increased sensitivity to the parametrization of the proton structure however also implies that top-quark data may be utilized to impose stricter constraints on the functional form of the PDFs. While for the total cross section the benefits of including $t\bar{t}$ cross section measurements in global PDF fits have already been demonstrated in Refs. [84,88,90,262,264] (see also section 1.3.1), the lack of precision in the theoretical description of exclusive top-quark observables so far precluded their use in state-of-the-art PDF analyses. With the recent extension of the NNLO $t\bar{t}$ program to the differential level the situation has changed, and we are now able to incorporate also top-quark distributions in the determination of future PDF sets. The most promising candidates in this context are certainly the normalized rapidity spectra of the individual top quark (usually averaged over t and $\bar{t}$) and of the top-quark pair since they both display an exceptionally small scale dependence and are, moreover, less sensitive to the value of the top-quark mass than, for instance, the normalized $m_{t\bar{t}}$ distribution. As can be inferred from Fig. 1.30, the shape of these observables is significantly affected by the choice of PDFs, the largest discrepancies occurring in the extreme forward/backward region at $|y_{t\bar{t}}| \geq 1.5$. This suggests that not only the uncertainty of the individual PDF sets could be further reduced through an inclusion of differential $t\bar{t}$ cross section measurements in the PDF fits but the theory predictions from different PDF sets would presumably become more homogeneous as well.

An additional improvement could be achieved by extending the PDF analysis also to double differential distributions which may be even more sensitive to the kinematic properties of the initial-state partons. The required data for such an advanced PDF determination has been recently provided by the CMS collaboration [465], which was able to measure the $t\bar{t}$ cross section as a function of various combinations of the kinematic variables $p_{T,t}$, y_t, $m_{t\bar{t}}$ and $y_{t\bar{t}}$ (see Fig. 1.32). Due to the high statistics of the full 8 TeV data sample the precision of these experimental results is, in fact, already compatible with the corresponding theory predictions at NLO QCD [482] allowing for a first estimate of the discriminating power of these observables. It turns out that, similar to the total cross section, the inclusion of two-dimensional $t\bar{t}$ distributions in the PDF fits in particular affects the functional behavior of the gluon PDF in the poorly-constrained large-x regime. Still, the overall gain in precision is quite different for the various combinations of kinematic variables considered in Fig. 1.32 such that, in practice, it would probably be sufficient to focus only on the normalized $m_{t\bar{t}}$-$y_{t\bar{t}}$-spectrum. Note, however, that in order to guarantee the highest possible phenomenological applicability of these results, the corresponding PDF analysis should be extended to NNLO accuracy, which requires the derivation of the respective differential cross sections to order $\mathcal{O}(\alpha_s^4)$. Even though

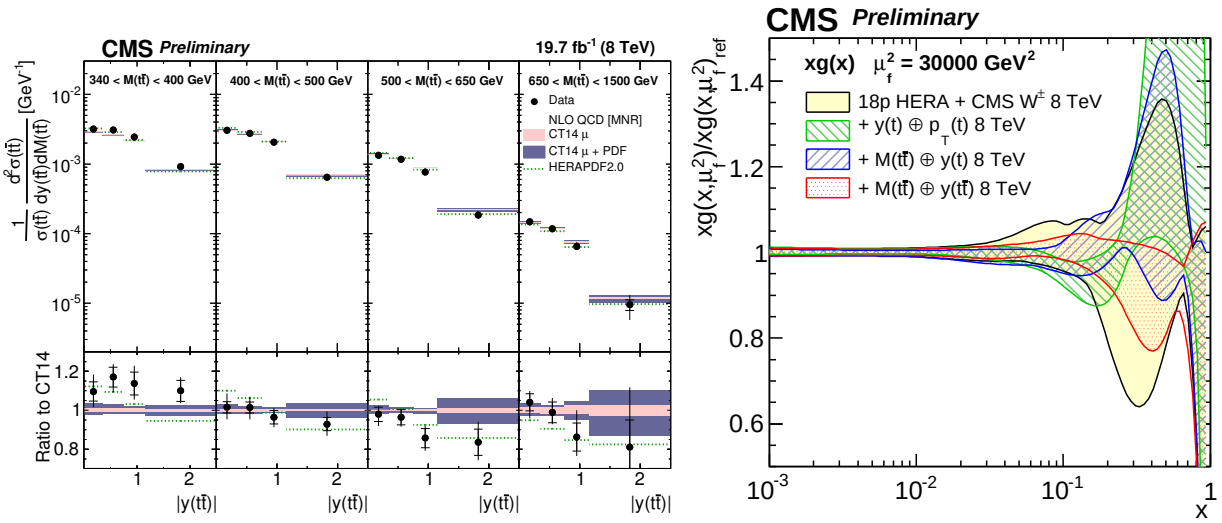

Figure 1.32: *The normalized $t\bar{t}$ differential cross section as a function of $m_{t\bar{t}}$ and $y_{t\bar{t}}$, evaluated at NLO QCD [482] using different PDF sets, compared to dilepton data [465] collected by the* CMS *collaboration at 8 TeV center-of-mass energy (left). The inner error bars correspond to the statistical uncertainty while the outer error bars indicate the combined statistical and systematic uncertainty. In the right plot also the relative impact of including various combinations of double differential $t\bar{t}$ measurements in an 18-parameter PDF fit, based on deep inelastic scattering and W-boson charge asymmetry data, is shown [465]. The total parametric uncertainty of each distribution has been normalized to the default prediction without top-quark data and is indicated by the shaded (or hatched) bands.*

such an advanced calculation is currently still missing for the LHC, its general feasibility has already been established through the NNLO differential treatment of A_{FB} discussed in section 1.3.3 and it thus poses no conceptual difficulty. Taking into account also the expected improvement of experimental uncertainties in the current and upcoming LHC runs, the use of double differential top-quark measurements in future PDF fits will certainly help to pave the way for a new generation of high-precision PDF sets.

Apart from the explicit examples presented above, there exist a series of other possible applications of the differential NNLO QCD predictions that have not yet been fully explored, e. g. their use in m_t or α_s determinations, illustrating the tremendous phenomenological potential of these results. Still, for a more realistic description of exclusive top-quark pair production it will be important to eventually extend the NNLO analysis also to the case of unstable top quarks. Indeed, as the corresponding decay processes are already available to $\mathcal{O}(\alpha_s^2)$ [12, 13], they can be consistently merged with the results from Refs. [427, 428] within the NWA framework discussed in section 1.3.1, a step that can certainly be expected for the near future. Such a treatment will open up a whole new class of high-precision observables and, consequently, allow for an even greater number of phenomenological applications both in the SM and beyond. Maybe the thus enriched LHC top-quark program will finally be able to uncover some of the long-looked-for new-physics effects.

Chapter 2

Theoretical foundation of hadronic $t\bar{t}$ production

2.1 Factorization theorem

Over the last decades, perturbative QCD has proven to be extremely successful in predicting the outcome of high-energy experiments that involve the collision and/or production of hadronic bound states. The basis for this overwhelming success is the possibility to separate the various mass and energy scales, naturally arising in the theoretical description of such a scattering process, into individual parts that can either be calculated from first principles or determined through an explicit measurement. Despite the fact that QCD is only asymptotically free and the inability to quantitatively describe the internal structure of these strongly-coupled bound states with our present understanding of quantum field theory, this splitting allows us to derive meaningful predictions for a broad spectrum of physical processes. Otherwise the discovery of new particles as for instance the top quark or the Higgs boson would be impossible at hadron collider facilities such as the Tevatron or the LHC.

The theoretical framework for the separation of the different scales is provided by the factorization theorem whose form, in general, depends on the process under consideration[1]. In case of hadronic $t\bar{t}$ production the corresponding expression for the total cross section is given by Eq. (1.35). Due to the strong mass hierarchy in the quark sector, $m_t \gg m_q$ with $q = \{u, d, s, c, b\}$, all quarks except the top can be treated as massless, which, in absence of EW corrections, leaves only two physical scales remaining in the theoretical description of this process, namely the top-quark mass and the hadronic center-of-mass energy. For dimensional reasons the partonic cross sections can thus only depend on either one of these quantities and their ratio $\rho_{\mathrm{H}} \equiv \frac{4m_t^2}{s}$ or rather $\rho \equiv \frac{\rho_{\mathrm{H}}}{x_1 x_2}$ when taking into account the convolution with the PDFs. In practice, it is, however, more convenient to rewrite the factorization formula in terms of the top-quark velocity $\beta = \sqrt{1-\rho} = \sqrt{1-\frac{4m_t^2}{\hat{s}}}$ and m_t by introducing the so-called partonic flux for the initial-state partons i and j

$$\Phi_{ij}(\beta, \mu_F) = \frac{2\beta}{1-\beta^2}\, \mathcal{L}_{ij}\left(\frac{1-\beta_{\mathrm{H}}^2}{1-\beta^2}, \mu_F\right) \tag{2.1}$$

[1] For a comprehensive summary of QCD factorization see Ref. [483]

where $\beta_{\mathrm{H}} \equiv \sqrt{1-\frac{4m_t^2}{s}}$ denotes the collider-specific maximum value of β and the partonic luminosity $\mathcal{L}_{ij}(x,\mu_F)$ is defined as

$$\begin{aligned}\mathcal{L}_{ij}(x,\mu_F) \equiv x\left(f_i^A \otimes f_j^B\right)(x,\mu_F) &= x\int_0^1 dy \int_0^1 dz\, \delta(x-yz)\, f_i^A(y,\mu_F)\, f_j^B(z,\mu_F) \\ &= x\int_x^1 \frac{dz}{z}\, f_i^A\left(\frac{x}{z},\mu_F\right) f_j^B(z,\mu_F)\,.\end{aligned} \tag{2.2}$$

The total cross section is then given as

$$\sigma_{t\bar{t}}^{\mathbf{tot}}(s,m_t) = \sum_{ij}\int_0^{\beta_{\mathrm{H}}} d\beta\, \Phi_{ij}(\beta,\mu_F)\, \hat{\sigma}_{ij}\left(\beta, m_t^2, \mu_R, \mu_F, \alpha_s(\mu_R)\right) + \mathcal{O}(\Lambda_{QCD})\,. \tag{2.3}$$

This reparametrization has the advantage that the partonic cross sections are now universal functions independent of the hadronic center-of-mass energy. All information concerning the characteristic features of the respective collider experiments are completely encoded in the partonic fluxes and the upper bound of the β-integration. The known partonic results can thus be employed for various experimental setups by simply recalculating the corresponding flux factors, which in practice is connected with much less computational effort, at least if going to higher orders in perturbation theory.

Apart from the two physical scales the expression for the total cross section also contains two additional scales whose origin is of an entirely different nature. The renormalization scale μ_R is introduced in the context of dimensional regularization in order to preserve the dimensionlessness of the strong coupling constant in $d = 4-2\epsilon$ dimensions and is therefore related to the ultraviolet (UV) behavior of the partonic cross sections. The factorization scale μ_F, on the other hand, governs the separation of short and long distance effects, which is by no means unique in the sense that the factorization procedure allows for a shift of finite contributions between these two different parts. Partons with a transverse momentum below μ_F are treated as an unresolved fraction of the parent hadron and are thus absorbed into the PDFs whereas partons with a larger transverse momentum are considered part of the hard scattering process. As both μ_R and μ_F are related to a particular choice of renormalization or factorization scheme[2], they do not constitute intrinsic parameters of the underlying theory and hence any physical observable must be independent of these artificial scales. In practice, however, a residual scale dependence remains due to the fact that our theoretical description relies on a perturbative expansion in some small parameter that is truncated after a finite number of terms. For the total cross section known to n-th order in the strong coupling, this means that

$$\mu_R^2 \frac{d\sigma_{t\bar{t}}^{\mathbf{tot},(n)}}{d\mu_R^2} = \mathcal{O}\left(\alpha_s^{n+1}(\mu_R)\right) \tag{2.4}$$

[2] Similar to choosing between different renormalization schemes, it is also possible to define different factorization schemes by explicitly adding finite pieces to the unambiguous singular terms. The most commonly used scheme is the $\overline{\mathrm{MS}}$ scheme [484] but for certain applications other schemes have been employed as well, for instance the deep inelastic scattering (DIS) scheme [485].

and similarly for the derivative with respect to μ_F, which indicates that the sensitivity to these scales decreases as we include higher orders in perturbation theory. Provided that an observable is described by a well converging series, which is certainly the case for $\sigma_{t\bar{t}}^{\mathbf{tot}}$ (see section 3.5.4), the residual scale dependence may therefore serve as an estimate of yet uncalculated higher-order contributions. Although both scales can be assigned arbitrary values, they should be chosen of the order of the relevant physical scale(s) Q of the process under consideration in order to avoid large logarithms of the form $\ln(Q/\mu_{R/F})$ that might spoil the perturbative expansion. It has thus become common practice to set $\mu_R = \mu_F = \mu = Q$ for the central theoretical prediction and to evaluate the corresponding uncertainty by varying both scales independently in the range

$$\frac{1}{2} \leq \frac{\mu_F}{\mu_R} \leq 2 \qquad \text{with} \qquad \mu_{R/F} \in \left\{ \frac{Q}{2}\,,\, Q,\, 2Q \right\} . \tag{2.5}$$

In case of the total cross section for $t\bar{t}$ production the most natural scale choice is $\mu_R = \mu_F = m_t$ since m_t is the only remaining physical parameter in Eq. (2.3) with a non-zero mass dimension that does not depend on the actual collider setup. The general scaling behavior $\mu_R \neq \mu_F \neq m_t$ can then be recovered without any additional computational effort from Eq. (2.4) (and similarly for any other observable), which otherwise would be quite cumbersome when going beyond leading order.

Both the partonic fluxes and the partonic cross sections crucially depend on the initial-state parton content and, in order to obtain finite results for the hadronic cross section, it is absolutely essential to consider all partonic channels that may contribute at a given order of the perturbative expansion. This is due to the fact that the different channels mix under collinear renormalization, which is required to remove IR singularities that do not cancel by the Kinoshita-Lee-Nauenberg (KLN) theorem. Nonetheless, it is common to organize theoretical calculations according to the respective initial-state configurations which may even be achieved in a finite manner by rearranging certain contributions connected to the collinearly divergent behavior as demonstrated in section 2.3. Yet, there is no physical meaning in treating the various partonic channels separately as their relative size will depend on the factorization scheme employed in the definition of the PDFs. However, since the vast majority of theoretical calculations is performed in the $\overline{\text{MS}}$ scheme, a separation may still be useful for comparing or combining different predictions.

As previously mentioned, the partonic channels contributing to top-quark pair production are

$$q\bar{q} \;\to\; t\bar{t} + X \tag{2.6}$$

$$gg \;\to\; t\bar{t} + X \tag{2.7}$$

$$(\bar{q})g \;\to\; t\bar{t}(\bar{q}) + X \tag{2.8}$$

$$q\tilde{q} \;\to\; t\bar{t}q\tilde{q} + X \quad \text{with } \tilde{q} = q, q', \bar{q}' \text{ and } q \neq q' \tag{2.9}$$

where X denotes any number of additional light partons. The channels in Eq. (2.6) and Eq. (2.7) start at LO in QCD whereas the reactions in Eq. (2.8)[3] and Eq. (2.9) arise at NLO

[3] In the following we will denote the quark-gluon channel by "qg" always implying both quark and anti-quark contributions.

	Tevatron	LHC			
		7 TeV	8 TeV	13 TeV	14 TeV
$q\bar{q}$	86.3%	16.7%	14.8%	9.8%	9.2%
gg	15.4%	84.8%	86.3%	89.8%	90.2%
$\bar{q}\,g$	−1.7%	−1.6%	−1.1%	0.3%	0.5%

Table 2.1: *The relative contribution of the different partonic production modes to the NNLO+NNLL total cross section at the Tevatron and the LHC ($m_t = 173.3\,\text{GeV}$[4], MSTW2008 PDFs at 68% C.L. [231].*

and NNLO respectively. Including EW corrections will generally lead to initial-state photons as well but these effects are small and thus not considered here. The relative contributions of the production channels in Eq. (2.6)-(2.8) with regard to the total cross section at NNLO+NNLL are presented in Tab. 2.1 (the impact of channel (2.9) is at the sub-permille level and thus numerically irrelevant).

As one may have suspected beforehand, the quark annihilation channel and the gluon fusion channel are the dominant production mechanisms at the Tevatron and the LHC respectively whereas the quark-gluon channel only contributes at the low percent-level. Interestingly enough, its overall impact on the total cross section can even become negative, which again stresses the fact that a distinction between different production channels is somewhat unphysical.

Before we present in detail the methods used to derive these NNLO predictions, we will discuss the general properties of the two main ingredients of such a $\sigma_{t\bar{t}}^{\mathbf{tot}}$ calculation, namely the partonic fluxes and cross sections. Furthermore, for the latter, we will give a concise overview on the LO and NLO results since they represent the theoretical foundation for the description of top-quark pair production in hadronic collisions.

2.2 The partonic fluxes

Since the partonic flux is defined as a convolution of the PDFs, it contains all information on the types of hadrons used as particle beams or targets in the respective collider experiments as well as on how the different partons are distributed inside these hadrons. The higher the available center-of-mass energy, the more precisely the hadronic substructure may be resolved, which in case of a massive final state such as $t\bar{t}$ affects the lowest possible momentum fraction x that may contribute to the hard scattering process, allowing for ever lower-energetic partons to participate in the reaction. As the PDFs describe the long-distance behavior of the scattering process, they cannot be derived perturbatively due to the strong coupling strength of QCD at low energy scales. They have to be extracted from experimental data by studying a number of different observables and systematically comparing the measured values for these quantities with the corresponding theory predictions. This is necessary because the sensitivity

[4] While in the introduction we commonly used a value of $m_t = 172.5\,\text{GeV}$ compatible with the experimental analyses, we will in the following employ a top mass that is closer oriented towards the current world average [11].

of a particular process is usually limited to specific partons in a certain x-range and, in order to obtain a complete picture of the momentum spectra of all partons, complementary measurements have to be taken into account. Since PDFs are a universal property of the respective hadron, these measurements are neither restricted to a certain center-of-mass energy nor by the type of particle that serves as a collision partner in the hadronic reactions, which simplifies their determination considerably and guarantees the predictive power of the factorization theorem. The data sets relevant for constraining the proton PDFs[5], in the following denoted as $f_i(x, \mu_F)$, therefore include results acquired by utilizing diverse experimental setups, ranging from fixed-target experiments over DIS data, collected by the ZEUS and H1 collaborations at HERA, to pp and $p\bar{p}$ measurements performed at the Tevatron and the LHC [65].

Despite their non-perturbative nature, the resulting PDFs may still be classified in terms of perturbative orders in QCD, which can be directly attributed to the fact that their determination relies on the matching of experimental data with results from perturbative calculations. As a consequence, both the shape and the uncertainty of the extracted PDFs crucially depend on the theoretical precision of the observables employed in this matching procedure. Conversely, the number of potential input parameters is limited by the aspired accuracy of the PDF analysis. This means that at a certain point an improvement of the PDF determination may only be accomplished by computing the respective observables to higher orders in perturbation theory regardless of the available experimental precision.

Apart from the matching conditions there exists an additional aspect where perturbative QCD enters the PDF analysis, namely the evolution equations for the PDFs and α_s. The dependence of these quantities on the factorization scale μ_F is governed by the differential equations

$$\begin{aligned} \mu_F^2 \frac{df_i(x, \mu_F)}{d\mu_F^2} &= \left(P_{ij} \otimes f_j\right)(x, \mu_F) \\ \mu_F^2 \frac{d\alpha_s(\mu_F)}{d\mu_F^2} &= \beta\left(\alpha_s(\mu_F)\right) , \end{aligned} \tag{2.10}$$

which follow directly from the scale independence of the bare (i. e. unrenormalized) quantities $f_i^0(x)$ and α_s^0. Provided that the boundary conditions are fixed, they allow for a prediction of the PDFs and α_s at arbitrary values of μ_F. This is important for two reasons. First of all, the processes that enter the matching procedure, in general, contain very different mass and energy scales preventing a direct combination of the various input measurements. Only by exploiting Eq. (2.10) it is possible to evolve all relevant quantities to a common matching scale μ_0, which allows for the incorporation of results from different experiments into a global PDF fit. Secondly, the evolution equations enable us to set μ_F to the natural scale of the process under consideration, which is necessary to avoid potentially large logarithms that might spoil the perturbative convergence as explained previously. Solving Eq. (2.10) can thus be interpreted as an effective method to resum these contributions to all orders in perturbation theory.

[5] Since the anti-proton is related to the proton via charge conjugation, its PDFs can be expressed in terms of the proton PDFs as $f_{\bar{q}}^{\bar{p}}(x, \mu_F) = f_q(x, \mu_F)$.

The functions $P_{ij}(x)$ and $\beta(\alpha_s)$ that appear on the right-hand side of these equations are the Altarelli-Parisi splitting kernels (or simply splitting functions) and the well-known QCD beta function (not to be confused with the top-quark velocity). While the latter determines the effective coupling strength of the strong interaction, the former describe the probability of emitting a (collinear) parton i with momentum fraction x from the parent parton j. They may both be expanded in terms of α_s,

$$\begin{aligned} P_{ij}(x) &= \sum_{n=0} \left(\frac{\alpha_s(\mu_F)}{2\pi}\right)^{n+1} P_{ij}^{(n)}(x) \\ \beta\left(\alpha_s(\mu_F)\right) &= -4\pi \sum_{n=0} \left(\frac{\alpha_s(\mu_F)}{4\pi}\right)^{n+2} \beta_n \,, \end{aligned} \tag{2.11}$$

with coefficient functions β_n and $P_{ij}^{(n)}(x)$ that can be explicitly computed within perturbation theory[6] and are currently known to $\mathcal{O}(\alpha_s^5)$ [486, 487] and $\mathcal{O}(\alpha_s^3)$ [488, 489] respectively. Hence, the μ_F-evolution does not rely on any additional experimental input but is completely determined by the underlying theory.

Depending on the maximum power of α_s used in the matching conditions and the evolution equations, one then distinguishes between LO, NLO and NNLO PDF sets. The impact of going to higher orders in perturbation theory depends on additional factors such as the exact treatment of α_s (see below) but the numerical differences between the different sets generally becomes less pronounced with increasing perturbative precision, i. e. the difference between LO and NLO sets is usually bigger than between NLO and NNLO sets. In practical applications the employed precision is determined by the perturbative order of the hard scattering amplitudes. As the theoretical uncertainty of a physical observable is assessed from its residual scale dependence, which relies on a delicate cancellation between contributions from the PDFs and the hard scattering, it is necessary to use the same level of precision in both parts of the calculation. Otherwise one might introduce spurious correlations that could result in a misleading error estimate. This, consequently, also applies to the partonic fluxes in the NNLO $t\bar{t}$ analysis, which need to be constructed from NNLO PDFs in order to match the precision of the partonic cross sections.

Examples of such NNLO fluxes for the Tevatron and the LHC at 8 TeV are shown in Fig. 2.1. While the absolute size of the various channels depends on the details of the hadronic collisions, i. e. the center-of-mass energy and the type of initial-state hadrons, their shape is quite similar even when comparing results from different colliders. Interestingly, the dominant fluxes at both Tevatron and the LHC belong to the higher-order qg- and $q\tilde{q}$-reactions and not to the quark annihilation and gluon fusion channels as one may have naively expected. There are different reasons for that. At the Tevatron, the quark annihilation channel benefits from the presence of valence quarks and anti-quarks and is thus strongly enhanced with respect to the pure gluonic flux. This, however, also applies to the $q\tilde{q}$-channel, which is additionally favored for mere combinatorial reasons as it simply contains more subchannels

[6] Unless specifically noted otherwise, the definition of the splitting kernels and the beta function assumes n_l (number of light quarks) active quark flavors.

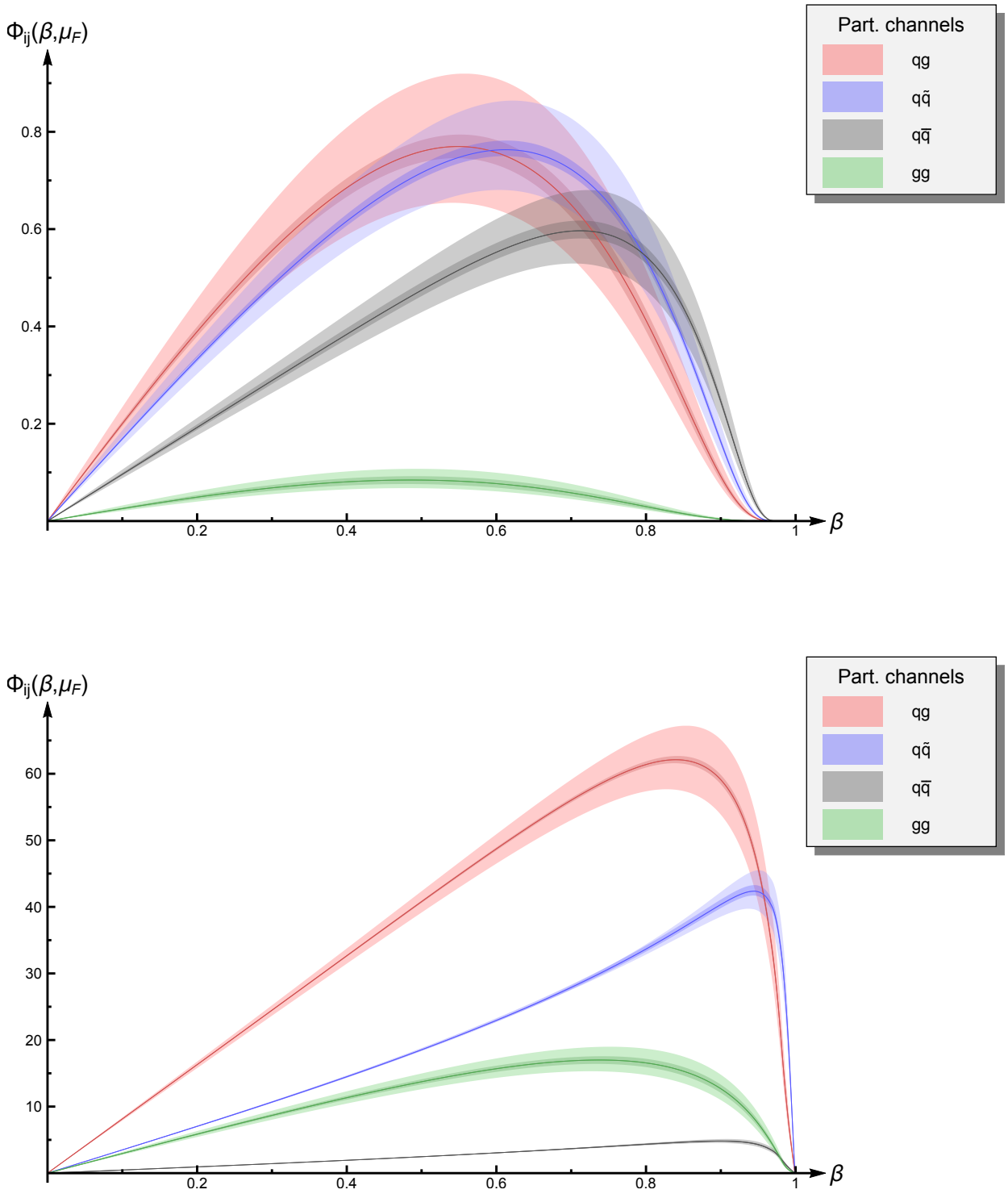

Figure 2.1: *Partonic fluxes generated from the* MSTW2008 *PDF set [231] (68% C.L., $\mu_F = m_t = 173.3\,\text{GeV}$) contributing to the NNLO cross section of top-quark pair production at the Tevatron (top) and the LHC at 8 TeV (bottom). The solid lines represent the central values while the shaded bands indicate the PDF error (dark) and the effect of varying the factorization scale between $m_t/2 \leq \mu_F \leq 2m_t$ (light).*

that may significantly contribute to the total flux. Similarly, the qg-channel, even though it might be smaller when considering specific quark flavors, profits from the greater number of non-vanishing subprocesses, which in sum results in a larger partonic flux. Since the gluon PDF is equal for protons and anti-protons and Φ_{qg} includes the sum over all (anti-)quark flavors, this argument also holds at the LHC. There, the absence of valence anti-quarks leads to a substantial reduction of the $q\bar{q}$-flux whereas the $q\tilde{q}$-channel is further enhanced by the increased qq-fluxes. The quark annihilation channel is even surpassed by the gluon fusion channel, which can be mainly attributed to the higher center-of-mass energy. The PDFs as well as the partonic luminosities generally favor lower values of x or β with the gluonic contributions dominating in the $x \lesssim 0.1$ regime. An increase of the collision energy will therefore lead to an enhancement of gluon-initiated fluxes as illustrated in Fig. 2.2 for the $q\bar{q}$- and gg-fluxes. The higher the available center-of-mass energy, the larger becomes the gap between these two channels. Moreover, the peak position of the flux distributions is gradually shifted towards the high-energy domain $\beta \sim 1$ with increasing collision energy, which is a common feature of all channels and can be explained by the velocity-dependent prefactor in the definition of the partonic flux, Eq. (2.1), that overcompensates the preference of the partonic luminosities for low β-values.

The displayed error bands in Fig. 2.1 and Fig. 2.2 account for the PDF errors as well as for the uncertainty due to different choices of the factorization scale. As the scale dependence can be computed exactly within perturbation theory, the latter is not an uncertainty in the classical sense but it rather illustrates the impact of varying the scale in the range of $m_t/2 \leq \mu_F \leq 2m_t$ needed for the evaluation of the theoretical error on the total cross section. The PDF errors, on the contrary, reflect the lack of knowledge concerning the exact functional form of the PDFs and the limited experimental abilities to constrain them. They are thus sensitive to the statistical and systematic uncertainties of the measurements employed in the matching procedure as well as to the parametrization chosen for the extraction of the PDFs. In general, the functional dependence at the matching scale is given as

$$x\, f_i(x) = x^{a_i}\,(1-x)^{b_i}\, p_i(x) \tag{2.12}$$

with free exponents a_i and b_i that govern the behavior in the low- and high-x regime and functions $p_i(x)$ that contain additional free parameters and allow for a flexible description of the intermediate range. Although motivated by physical considerations, the explicit form of these functions is not uniquely defined admitting a certain degree of freedom in choosing a suitable PDF parametrization. As a result, several PDF analysis groups have formed over the last decade proposing different approaches for $p_i(x)$ with a varying number of free parameters that along with the exponents a_i and b_i need to be determined from a fit to experimental data[7]. The data sets included in this fitting procedure are also not unique but may be chosen freely by the individual collaborations yielding numerically different results for the extracted PDFs even when using an identical functional form. The corresponding parametric uncertainties can be assessed with the help of two different approaches commonly denoted as Hessian [490–492]

[7] There also exist some theoretical constraints on the form of the PDFs expressed through so-called sum rules that reflect certain physical requirements such as momentum conservation or the number of valence quarks.

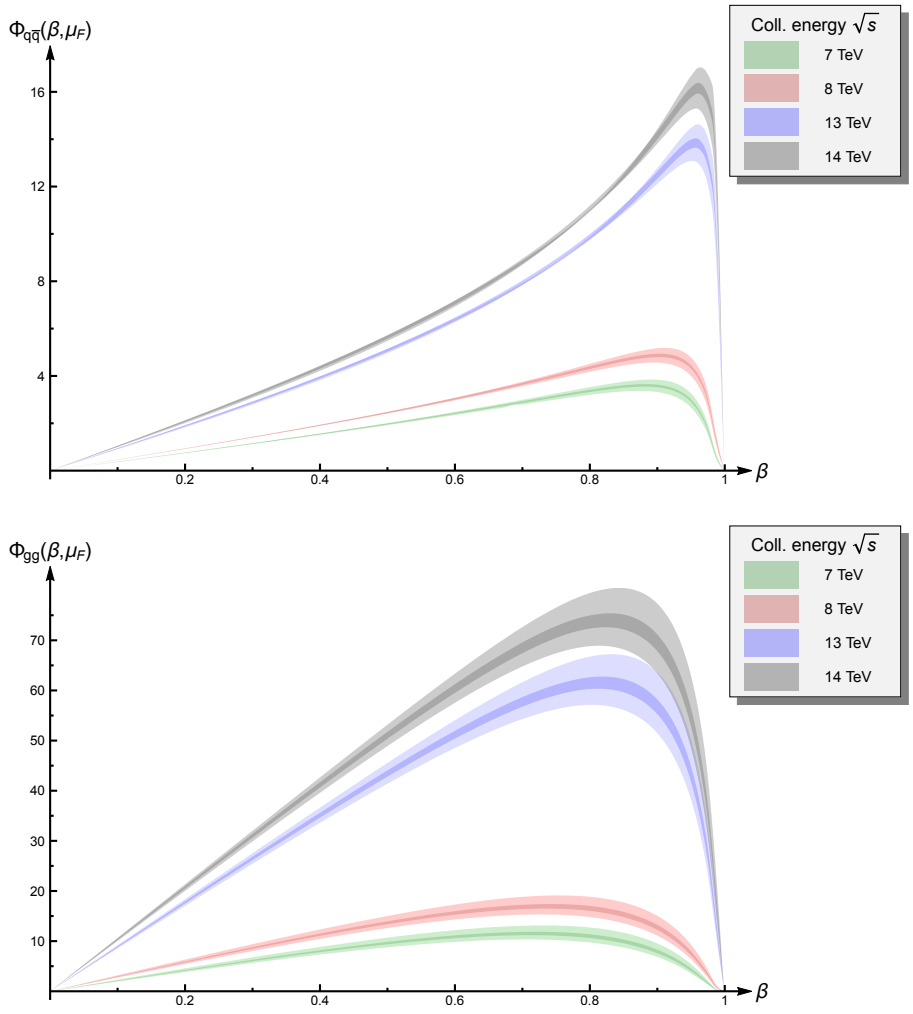

Figure 2.2: *Center-of-mass energy dependence of the $q\bar{q}$ (top) and gg (bottom) fluxes at the LHC* (MSTW2008 *at 68% C.L. [231], $\mu_F = m_t = 173.3\,\text{GeV}$, $n_l = 5$).*

and MC method [493]. They both rely on the construction of a set of additional PDFs $\tilde{f}_i^k(x)$ with $k = \{1, \ldots, N_{\text{PDF}}\}$, called eigenvectors (Hessian) or replicas (MC), that describe the deviation from the central predictions $\bar{f}_i(x)$ within a certain validity range. For the Hessian approach their actual number N_{PDF} is related to the number of free parameters in Eq. (2.12) whereas for the MC method it depends on the specific problem under consideration varying between $\mathcal{O}(100)$ and $\mathcal{O}(1000)$. In the latter case the determination of the PDF uncertainty for a generic observable $X(f_i(x))$ is fairly straightforward amounting simply to a computation of the standard deviation

$$\Delta X = \sqrt{\frac{1}{N_{\text{PDF}} - 1} \sum_{k=1}^{N_{\text{PDF}}} \left(X(\tilde{f}_i^k(x)) - \overline{X} \right)^2} \tag{2.13}$$

with the mean value defined as usual via

$$\overline{X} = \frac{1}{N_{\text{PDF}}} \sum_{k=1}^{N_{\text{PDF}}} X(\tilde{f}_i^k(x)) \,. \tag{2.14}$$

Note that, in general, $\overline{X}$ does not exactly correspond to the central prediction obtained from $\bar{f}_i(x)$ such that the final PDF error may, in fact, be asymmetric

$$\delta_{\text{PDF}}^{\text{MC}} = \overline{X} \pm \Delta X - X(\bar{f}_i(x)) \,. \tag{2.15}$$

In the Hessian approach it is also possible to determine an asymmetric uncertainty. To this end, one has to derive two eigenvectors $\tilde{f}_i^{k,\pm}(x)$ for each of the $k \in \{1, \ldots, N_{\text{par}}\}$ fit parameters that describe the effect of their respective $\pm 1\sigma$-variations on the PDFs (at 68% C.L.). The resulting PDF error for $X(f_i(x))$ then reads [491,492]

$$\delta_{\text{PDF}}^{\text{Hessian}} = \pm \sqrt{\sum_{k=1}^{N_{\text{par}}} \left[\max\left(\pm\left[X(\tilde{f}_i^{k,+}(x)) - X(\bar{f}_i(x))\right], \pm\left[X(\tilde{f}_i^{k,-}(x)) - X(\bar{f}_i(x))\right], 0\right)\right]^2} \,. \tag{2.16}$$

In practice, usually both $\delta_{\text{PDF}}^{\text{MC}}$ and $\delta_{\text{PDF}}^{\text{Hessian}}$ provide a reliable estimate for the underlying parametric PDF uncertainty such that currently both methods are actively used by the various PDF collaborations. Nevertheless, they generally differ numerically, similar to the theoretical predictions obtained from the corresponding central PDF members. In consequence, a thorough analysis of the PDF error should not only take into account the uncertainty of a single PDF set but ideally investigate the impact of using different sets, which may, however, in practice be connected with a considerable computational effort, especially when studying higher orders in perturbation theory.

At NNLO accuracy the most commonly used PDF sets are provided by the MSTW [231,495], HERAPDF [496–498], CT [499,500], ABM [84,501] and NNPDF [90,263] collaborations, which, apart from using different parametrizations and data samples, also differ in the treatment of heavy quarks (charm, bottom and top), the strong coupling constant and the light-quark sea, i. e. in the assumptions made for the behavior of the non-valence quark content of the proton. All of these collaborations have released several updated versions of their original analyses and in the following we will restrict our discussion to the MSTW2008 [231], HERAPDF1.5 [497], CT10 [499], ABM11 [501] and NNPDF3.0 [90] sets. While in the latter case the corresponding parametric uncertainty is evaluated via the MC method, the other analysis groups prefer the use of the Hessian approach albeit for the CT10 set the respective error estimates have to be rescaled by a factor of 1.645 to account for a higher C.L. of 90%. Moreover, in the ABM11 analysis PDF and α_s uncertainties are treated simultaneously resulting in a symmetric error estimate of the form [501]

$$\delta_{\text{PDF}}^{\text{ABM11}} = \pm \sqrt{\sum_{k=1}^{N_{\text{par}}} \left[X(\tilde{f}_i^k(x)) - X(\bar{f}_i(x))\right]^2} \,. \tag{2.17}$$

[8] Including model and parametrization uncertainties in the HERAPDF1.5 error budget leads to a total PDF uncertainty of about 20% [494].

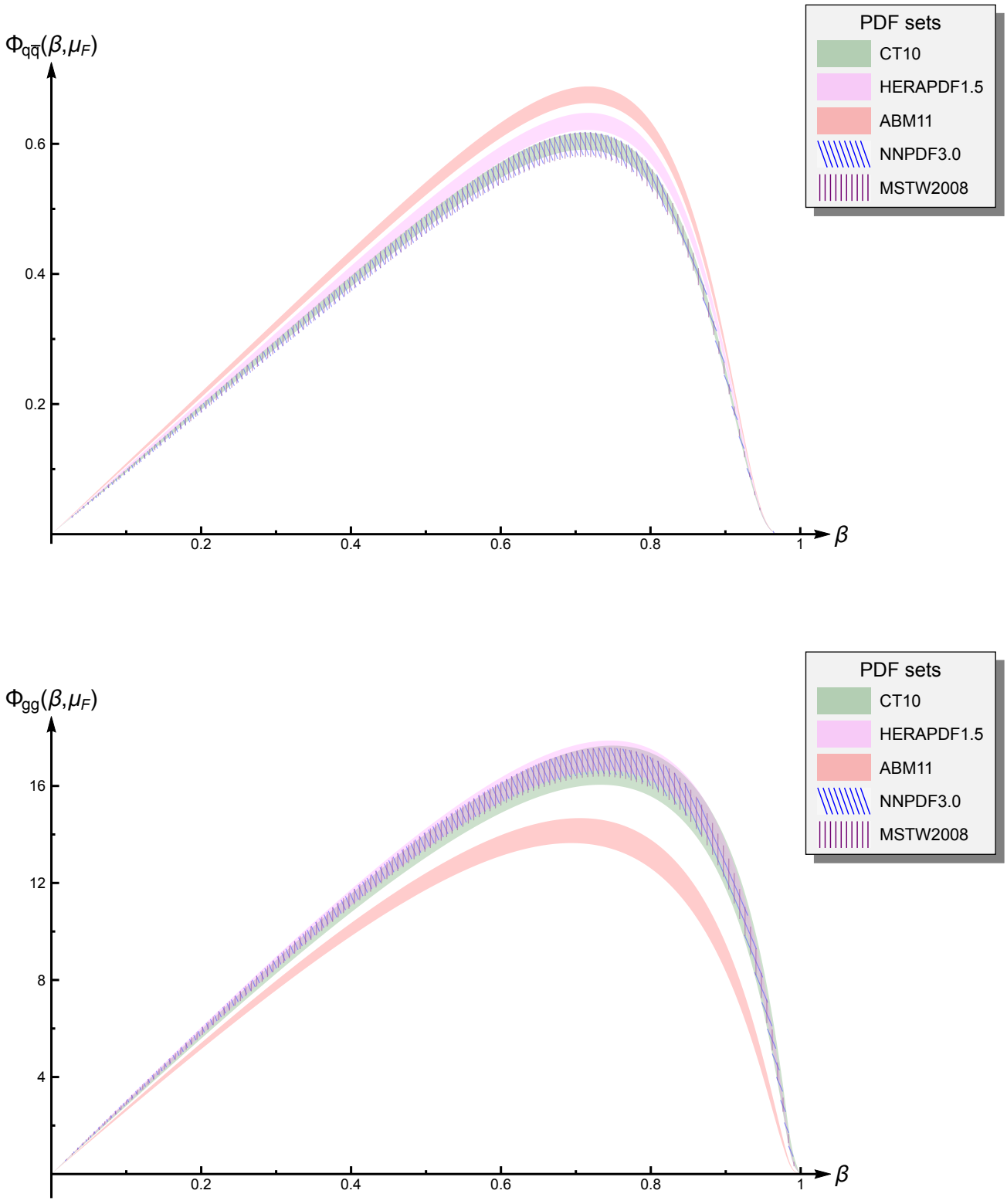

Figure 2.3: *Partonic-flux predictions for the $q\bar{q}$-channel at the Tevatron (top) and the gg-channel at the 8 TeV LHC (bottom) derived from different NNLO PDF sets ($\mu_F = m_t = 173.3\,\text{GeV}$). The displayed uncertainty bands account for the 68% C.L. PDF errors determined according to the prescriptions given by each of the PDF collaborations. Following Ref. [262], the results provided by* HERAPDF1.5 *only contain experimental uncertainties*[8] *while the* CT10 *errors have been rescaled by a factor of 1.645 in order to correct for the higher C.L. of 90%. Moreover, one should note that the* ABM11 *error bands also include the uncertainty on α_s since in the* ABM11 *PDF analysis both sources of uncertainty are treated simultaneously.*

All PDF sets can be conveniently accessed via the LHAPDF interface [502–504], a general-purpose software package that uses the discretised data files provided by the different PDF groups to construct interpolation functions with a standardized input/output format which can be easily handled by the common user. A comparison of these sets is shown in Fig. 2.3 for the fluxes of the numerically most dominant channels (with regard to the total cross section), $q\bar{q}$ at the Tevatron and gg at LHC. Despite their intrinsic differences, the PDFs determined by the various analysis groups yield similar results both for the shape and the overall size of the considered fluxes. The agreement is, in fact, so high that the different predictions overlap within their PDF uncertainty bands. The only exception are the fluxes obtained from the ABM11 set, which indeed display a similar shape but with a different normalization lying either above ($q\bar{q}$) or below (gg) the curves of the other groups.

This behavior can at least partly be attributed to the use of a fixed-flavor-number scheme (FFNS) for the treatment of heavy-quark contributions. In this scheme only the n_l light-quark flavors enter the PDF evolution Eq. (2.10) while the remaining quarks are treated as massive, which means that they are only present as intermediate and final states in the hard scattering amplitudes. The transition between n_l and n_l+1 light flavors can then be achieved by computing certain operator matrix elements that serve as matching conditions for the PDFs in the respective FFN schemes. Such an approach is particularly suitable for processes where the relevant scale(s) Q^2 are of the same order as the heavy-quark mass m_Q. It might, however, become unreliable for scales that are much larger as it fails to resum logarithms of the form $\ln(Q^2/m_Q^2)$, which could lead to large perturbative corrections. This potentially problematic situation may be resolved by introducing a so-called general-mass-variable-flavor-number scheme (GM-VFNS) which allows for a resummation of these logarithmic contributions through the PDF evolution while still reproducing the correct low-energy behavior. The actual implementation of this scheme is by no means unique and was realized very differently by the MSTW, NNPDF, CT and HERAPDF collaborations. The good agreement of the resulting fluxes, however, demonstrates that the extracted PDFs only moderately depend on the technical details of these implementations. A major difference of the GM-VFNS compared to the FFNS is the considerably larger gluon PDF in the $x \gtrsim 0.1$ regime, which results in the aforementioned deviation of the gluon fluxes shown in Fig. 2.3. The discrepancy for the $q\bar{q}$-channel can, however, not be explained by the different scheme choices. A closer examination reveals that it is rather caused by a difference in the general normalization of the experimental data used in the PDF fits, which in particular affects the u- and d-quark distributions [501]. Employing the same normalization factors in the ABM11 analysis as, for instance, in the MSTW2008 fits, leads to a noticeable reduction of these distributions suggesting that the quark-antiquark flux will also decrease and show a better agreement with the results of the other groups.

Another important aspect in this context is the treatment of the strong coupling constant since its numerical value has a direct influence on the matching of theory and experiment. Moreover, it enters the evolution equations of the PDFs and thus affects their shapes and individual normalizations regardless of the boundary conditions. While the running of α_s is uniquely defined through Eq. (2.10), the initial condition for this evolution, $\alpha_s(\mu_0)$, cannot

be predicted directly from theory[9] but needs to be determined by an explicit measurement. This is a crucial point since there is no common consensus on which measurement(s) to include in this determination and therefore the PDF analysis groups have adopted different strategies which in practice lead to different numerical implications. As the experimental data used in the PDF fits is also sensitive to α_s, the most natural approach consists of treating $\alpha_s(\mu_0)$ as an additional free fit parameter and determining its value along with the other unknown constants required for an adequate description of the PDFs (see Eq. (2.12)). Needless to say, the result of such a fitting procedure will depend on the precision of the perturbative calculations employed in the matching process as well as on further technical details, e. g. the chosen PDF parametrization or heavy-flavor scheme. Hence, the value of $\alpha_s(\mu_0)$ may in general be quite different even if its determination is based on the same data set.

Another widely used strategy is to perform the entire analysis with a prespecified value of $\alpha_s(\mu_0)$ regardless of whether the PDFs are extracted at LO, NLO or NNLO accuracy. In that case, the actual value may be chosen arbitrarily under the condition that it is consistent with existing α_s determinations and, therefore, it is usually oriented towards the current world average. In order to guarantee a flexible application of the resulting PDF sets in a broad variety of theoretical calculations, the analysis can be repeated with different values of $\alpha_s(\mu_0)$ that cover a wide range of physical scenarios. Furthermore, such a strategy allows for a reliable assessment of the propagation of the α_s uncertainty to the extracted parton distributions.

As the various PDF groups use different values for the initial scale μ_0, a meaningful comparison is only possible at a common reference scale, which is usually chosen as the mass of the Z boson, $M_Z = 91.1876\,\text{GeV}$ [65], mainly due to historical reasons. The result of such a comparison for the MSTW2008, NNPDF3.0, CT10, ABM11 and HERAPDF1.5 sets is shown in Fig. 2.4 along with the current world average. In this context, the values provided by MSTW2008 and ABM11 are particularly interesting since they have been obtained from a global PDF fit to data, however, yielding very contrasting results. While the value quoted by MSTW2008 is consistent with the world average and thus very similar to the default values chosen in the NNPDF3.0, CT10 and HERAPDF1.5 fits, the ABM11 result is significantly smaller, which can to a large extent be attributed to the FFNS employed in the PDF analysis. Such a behavior could have already been inferred from Fig. 2.3 since the strong coupling is highly correlated with the gluon PDF and, consequently, to some degree also with the resultant flux factors. As the determination of the gluon PDF is governed by DIS data, which is sensitive to the product of both of these quantities rather than to their individual contributions, a smaller value of α_s usually leads to a larger initial gluon PDF in the small- and intermediate-x range. Due to DGLAP evolution and constraints from the momentum sum rule such an increase translates into a reduction in the large-x regime relevant for $t\bar{t}$ production as shown in Fig. 2.5. A decreased gluon flux may therefore indicate a weaker coupling strength of the strong interaction as is the case in the ABM11 analysis.

[9] It is possible to determine α_s indirectly from purely theoretical considerations by employing certain short-distance observables that can be computed by means of lattice QCD. Comparing these results with perturbative calculations allows for a very accurate extraction of the strong coupling constant [65].

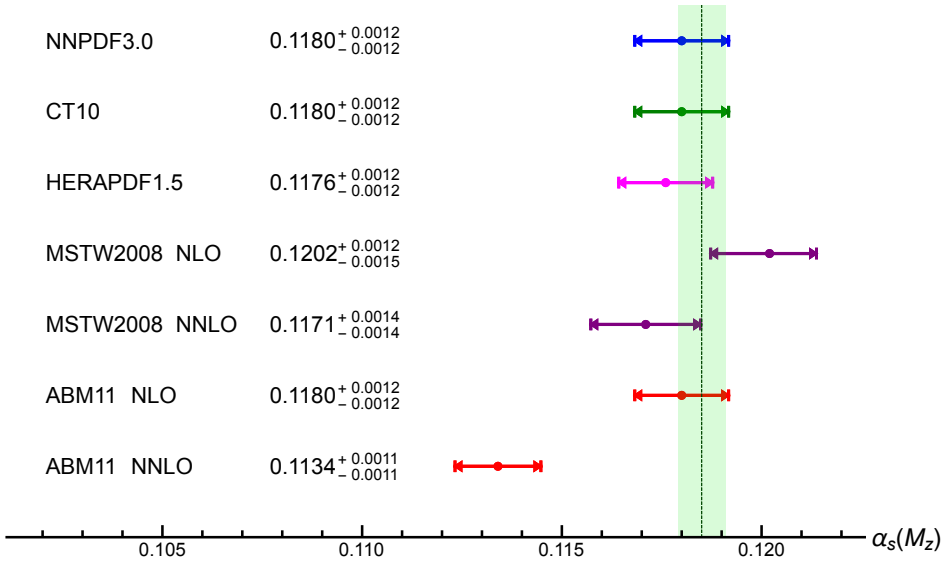

Figure 2.4: *The default α_s-values used by different PDF fitting groups compared to the current world average $\alpha_s(M_Z) = 0.1185 \pm 0.0006$ [65]. Unless noted otherwise, the theoretical precision of the given results corresponds to NNLO accuracy. The quoted errors only account for the uncertainties of the experimental data employed in the fits. The theory uncertainty due to missing higher orders is not considered here. For the predefined α_s-values provided by the* NNPDF, CT *and* HERAPDF *collaborations we follow Refs. [505, 506] and assign an uncertainty of $\sigma_{\alpha_s} = \pm 0.0012$, which is in good agreement with the results from the fits.*

As already mentioned, the actual value of the strong coupling constant does not only depend on the employed heavy-flavor scheme but also on the precision of the perturbative calculations used for the α_s extraction. This becomes particularly evident when looking at the MSTW2008 and ABM11 results that belong to the corresponding NLO sets (see Fig. 2.4). Both values are considerably larger than the respective NNLO couplings, which in the ABM11 case leads to a much better agreement with the current world average and the predefined NNPDF3.0, CT10 and HERAPDF1.5 values (although technically such a comparison is not entirely valid due to the different perturbative orders involved). Still, it remains well below the value provided by the MSTW collaboration. Although being quite sizable, the numerical difference between NLO and NNLO couplings is still compatible with the quoted theoretical uncertainty of $\mathcal{O}(0.004)$ [501,507] indicating a reasonably good perturbative convergence of the α_s determination from PDF fits. Nonetheless, it means that increasing the perturbative precision of the PDF analysis will not only affect the expansion depth of the matching conditions and evolution equations but also the initial value $\alpha_s(\mu_0)$ itself. This is quite contrary to the case where $\alpha_s(\mu_0)$ is fixed in advance regardless of the current expansion order. Still, the various PDF sets yield similar results for the partonic fluxes both at NLO and NNLO (except for the previously discussed deviations of the ABM11 results), which may be interpreted as further indication for the validity of the different approaches employed by the various PDF groups. Moreover, it shows the strong correlation between the chosen α_s prescription and the extracted PDFs, which has direct consequences for other parts of the total cross section calculation as well.

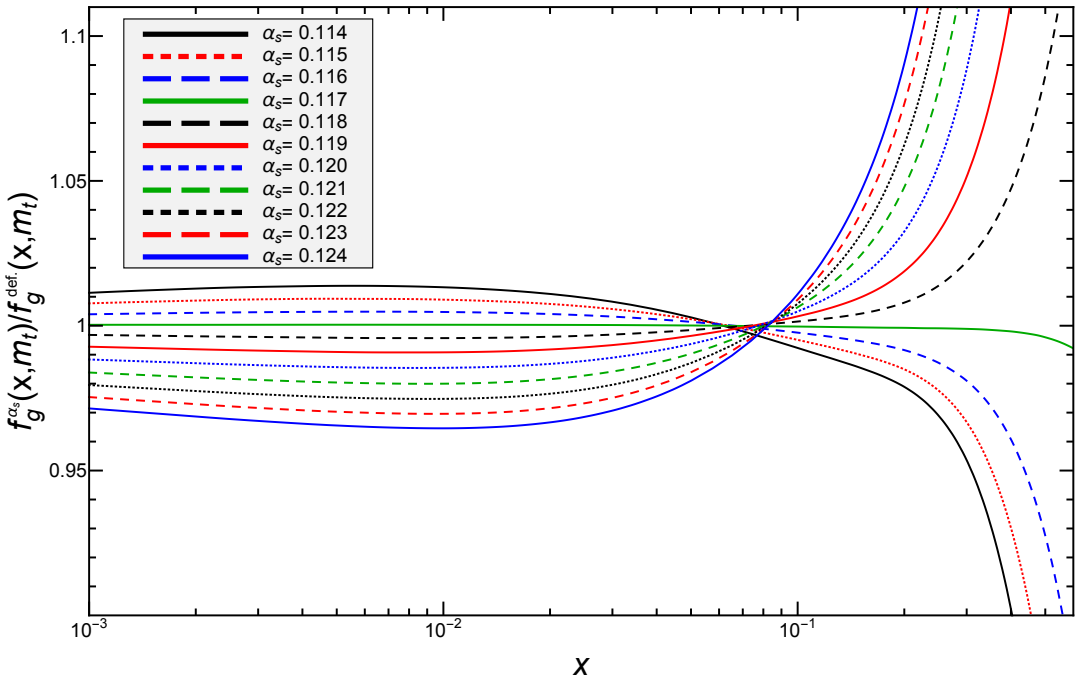

Figure 2.5: *The NNLO gluon PDF ($\mu_F = m_t$) obtained from the* MSTW2008 *PDF set evaluated for different values of $\alpha_s(M_Z)$ and normalized to the default gluon PDF at $\alpha_s(M_Z) = 0.1171$.*

In order to guarantee a consistent theoretical description of $\sigma_{t\bar{t}}^{\text{tot}}$ (and, in fact, any physical observable), it is necessary to use the same value for α_s in all parts of the calculation including the hard scattering process. This means that the value that enters the partonic cross sections cannot be chosen arbitrarily (within the current uncertainty bounds) but is uniquely determined by the respective PDF set. Otherwise one might introduce spurious contributions in the cross section calculation that could lead to false predictions. Consequently, it is possible to use the information contained in Fig. 2.3 and Fig. 2.4 to qualitatively assess the impact of different PDF sets on the NNLO result prior to its actual calculation. As the fluxes and α_s-values of the MSTW2008, NNPDF3.0, CT10 and HERAPDF1.5 sets are very similar, one also expects the corresponding NNLO predictions to lie close together. A more detailed analysis suggests that at the LHC the NNPDF3.0 and HERAPDF1.5 sets will yield the largest cross sections, depending on the respective center-of-mass energy, while at the Tevatron the prediction based on the HERAPDF1.5 set will give the highest value for $\sigma_{t\bar{t}}^{\text{tot}}$. Due to the combination of a reduced gluon flux and a small coupling constant the ABM11 results will lie clearly below the predictions of the other groups although this discrepancy will be less pronounced at the Tevatron where this effect can be partly compensated by the enhanced $q\bar{q}$-flux. It will be interesting to see whether the ABM11 cross sections are still consistent with the results of the other PDF sets and how the different predictions compare to the available experimental data. However, as the answer to these questions requires the explicit calculation of $\sigma_{t\bar{t}}^{\text{tot}}$ to NNLO accuracy, we postpone this discussion to section 3.5.4 where we will analyze in detail the different sources of theoretical uncertainty that enter the $t\bar{t}$ cross section predictions.

2.3 The partonic cross sections

The second main ingredient for the theoretical description of the total cross section are the partonic cross sections. While the partonic fluxes contain all relevant information on the actual experimental setup, the partonic cross sections incorporate all process-dependent contributions to $\sigma_{t\bar{t}}^{\mathbf{tot}}$, which can be computed from first principles without any further input from experiment (except for the value of the top mass and α_s). Since QCD is asymptotically free at high energies, the hard scattering of initial-state partons into a $t\bar{t}$ pair plus additional gluon and light-quark emissions may be described perturbatively by performing an expansion in terms of the strong coupling constant, which is small at the top-mass scale. The partonic cross section can thus be written as

$$\begin{aligned}
\hat{\sigma}_{ij}\left(\beta, m_t, \mu_F, \alpha_s\right) = \frac{\alpha_s^2(\mu_R)}{m_t^2} \underbrace{\sum_{n=0}^{\infty} \sum_{k=0}^{n} \sum_{l=0}^{n-k} \alpha_s^n(\mu_R)\, \hat{\sigma}_{ij}^{n,k,l}(\beta)\, \ln^k\left(\frac{\mu_R^2}{m_t^2}\right) \ln^l\left(\frac{\mu_F^2}{m_t^2}\right)}& \\
\left.\begin{aligned}
&\hat{\sigma}_{ij}^{(0)}(\beta) \equiv \hat{\sigma}_{ij}^{(0,0,0)}(\beta) \\
&\hat{\sigma}_{ij}^{(1,0,0)}(\beta) + \hat{\sigma}_{ij}^{(1,1,0)}(\beta) \ln\left(\frac{\mu_R^2}{m_t^2}\right) + \hat{\sigma}_{ij}^{(1,0,1)}(\beta) \ln\left(\frac{\mu_F^2}{m_t^2}\right) \\
&\hat{\sigma}_{ij}^{(2,0,0)}(\beta) + \hat{\sigma}_{ij}^{(2,1,0)}(\beta) \ln\left(\frac{\mu_R^2}{m_t^2}\right) + \hat{\sigma}_{ij}^{(2,2,0)}(\beta) \ln^2\left(\frac{\mu_R^2}{m_t^2}\right) \\
&+\hat{\sigma}_{ij}^{(2,0,1)}(\beta) \ln\left(\frac{\mu_F^2}{m_t^2}\right) + \hat{\sigma}_{ij}^{(2,0,2)}(\beta) \ln^2\left(\frac{\mu_F^2}{m_t^2}\right) \\
&+\hat{\sigma}_{ij}^{(2,1,1)}(\beta) \ln\left(\frac{\mu_R^2}{m_t^2}\right) \ln\left(\frac{\mu_F^2}{m_t^2}\right)
\end{aligned}\right.
\begin{aligned}
&\Big\} \text{ LO} \\
&\Big\} \text{ NLO} \\
&\Big\} \text{ NNLO}
\end{aligned}
\end{aligned} \tag{2.18}$$

where the m_t-dependent prefactor has been introduced in order to render the coefficients $\hat{\sigma}_{ij}^{(n,k,l)}$ dimensionless functions of a single kinematic variable, which we chose to be the top-quark velocity β. A positive side effect of this trivial mass dependence is the possibility to apply the partonic results derived for $t\bar{t}$ production to other processes as well provided that they are subject to the same QCD-like interaction structure. Examples of such processes are the pair production of bottom quarks or of new heavy particles belonging to a fourth quark generation. Due to the scale invariance of the physical cross section not all of these coefficient functions are independent. In fact, only the coefficients $\hat{\sigma}_{ij}^{(n,0,0)}$ have to be computed explicitly whereas the scale-controlling contributions $k, l > 0$ can be inferred from

$$\begin{aligned}
\mu_R^2 \frac{d\hat{\sigma}_{ij}}{d\mu_R^2} &= 0 \\
\mu_F^2 \frac{d\hat{\sigma}_{ij}}{d\mu_F^2} &= -\left(1-\beta^2\right)\left(P_{ki} \otimes \frac{\hat{\sigma}_{kj}\left(\sqrt{1-\bar{\rho}}\right)}{\tilde{\rho}} + P_{kj} \otimes \frac{\hat{\sigma}_{ik}\left(\sqrt{1-\bar{\rho}}\right)}{\tilde{\rho}}\right).
\end{aligned} \tag{2.19}$$

Note that the conditions for the renormalization and factorization scales are not identical as the former is present exclusively in the partonic cross sections while the latter also determines the behavior of the partonic fluxes (as explained in the previous section), which has to be taken into account in order to guarantee the correct cancellation of the μ_F-dependent contributions in $\sigma_{t\bar{t}}^{\mathbf{tot}}$.

The scale-invariant pieces can be derived via the standard Feynman rule formalism and contain contributions from higher loop orders as well as from additional (massless) partons in the final state. Since their calculation in practice involves different computational methods, these parts are usually treated separately. However, due to the presence of massless particles the intermediate results may then contain IR singularities that will only cancel in the final expressions for the partonic cross sections. Therefore, the calculation of the individual contributions requires the introduction of a suitable regularization procedure that parametrizes the divergent behavior in such a way that it allows for a meaningful evaluation of the arising loop and/or phase space integrals. A widely used method in this context is dimensional regularization (DR) [508], which is based on an analytic continuation in the number of space-time dimensions. It preserves both Lorentz and gauge symmetry and allows for the treatment of divergences in various kinematic limits. Moreover, it is particularly suited for automation, a not inconsiderable aspect when going to higher orders in perturbation theory, a step usually connected with a substantial computational effort due to the large number of Feynman diagrams with increasing complexity involved in such analyses. There exists a variety of different implementations of this basic concept, some of them specifically tailored for a certain set of theories or applications (e. g. dimensional reduction [509], four-dimensional helicity [510, 511]), some designed for a more general use (e. g. 't Hooft-Veltman scheme [508]). For the calculation of $\sigma_{t\bar{t}}^{\mathbf{tot}}$ we employ the so-called conventional dimensional regularization (CDR) scheme [512], which is probably the most straightforward variation of DR as it simply amounts to treating all momenta and spin degrees of freedom as $d = 4 - 2\epsilon$ dimensional quantities regardless of whether they correspond to internal or external particles. The analytic continuation to four dimensions is then achieved by taking the limit $\epsilon \to 0$ which usually results in a Laurent series where the divergent behavior is encoded in the $1/\epsilon^n$ poles.

Apart from IR phenomena, these poles can also be caused by interactions at the other end of the spectrum. Since the momenta flowing in closed quantum loops are not bounded from above by any physical restrictions (conservation laws, symmetries, etc.), they may induce UV singularities in the transition amplitudes that describe the hard scattering process. Due to the fact that these singularities do not depend on the external kinematics, they can be absorbed into the free parameters of the underlying theory, in our case the wave functions, the top-quark mass and the strong coupling constant. This may be accomplished by introducing multiplicative renormalization constants that establish a connection between the bare, i. e. divergent, quantities and the UV-finite ones,

$$\alpha_s^0 = \left(\frac{e^{\gamma_E}\mu_R^2}{4\pi}\right)^{\epsilon} Z_{\alpha_s}^{(n_f)}\, \alpha_s^{(n_f)}(\mu_R) \tag{2.20}$$

$$m_t^0 = Z_m\, m_t \tag{2.21}$$

$$\Psi_p^0 = Z_p\, \Psi_p \tag{2.22}$$

where $p = g, q, Q$ denotes the gluon field and the light- and heavy-quark (t,$\bar{t}$) fields respectively and the additional prefactor in Eq. (2.20) has been introduced to keep the coupling dimensionless and remove unnecessary normalization factors in the loop/phase space integrals. The renormalization constants can be expanded in terms of $\alpha_s^{(n_f)}$ and in CDR their generic form

is given by

$$Z = 1 + \sum_{n=1} \left(\frac{\alpha_s^{(n_f)}}{2\pi} \right)^n Z^{(n)} = 1 + \sum_{n=1} \left(\frac{\alpha_s^{(n_f)}}{2\pi} \right)^n \sum_{m=-n} z^{(n,m)} \, \epsilon^m \, . \tag{2.23}$$

While the pole structure is uniquely defined[10] by the requirement that it cancels the arising UV divergences, the finite part can be chosen freely resulting in a variety of different renormalization schemes. For the calculation of the partonic cross sections we worked in the on-shell scheme for the mass and the wave functions and in the $\overline{\text{MS}}$ scheme for the coupling constant. The respective renormalization constants up to two-loop order can be found in appendix A. The UV-finite $t\bar{t}$ amplitudes are then given by

$$\begin{aligned} |\mathcal{M}^R_{i_1\cdots i_n}\left(\alpha_s^{(n_f)}, m_t, \mu_R, \epsilon\right)\rangle &= \left(\frac{e^{\gamma_E}\mu_R^2}{4\pi}\right)^{-\frac{n}{2}\epsilon} Z_Q \sqrt{Z_{i_1}} \cdots \sqrt{Z_{i_n}} \, |\mathcal{M}^B_{i_1\cdots i_n}\left(\alpha_s^0, m_t^0, \epsilon\right)\rangle \\ &\equiv \sum_{k=0} \left(\alpha_s^{(n_f)}(\mu_R)\right)^{\frac{2k+n}{2}} |\mathcal{M}^{(k)}_{i_1\cdots i_n}\left(m_t, \mu_R, \epsilon\right)\rangle \end{aligned} \tag{2.24}$$

where the different production modes are characterized by their unique composition of massless external particles $i_k \in \{q, \bar{q}, g, q', \bar{q}'\}$ (the first two indices determine the initial state while any additional i_k accounts for radiative corrections). Similar to Eq. (2.20) the ϵ-dependent prefactor guarantees that the dimensionality of the amplitudes is preserved and the results are free of spurious normalization factors. In practice, we are usually interested in a perturbative expansion in terms of the coupling constant which for the bare amplitudes reads

$$\begin{aligned} |\mathcal{M}^B_{i_1\cdots i_n}\left(\alpha_s^0, m_t^0, \epsilon\right)\rangle &= \left(\alpha_s^0\right)^{\frac{n}{2}} \sum_{k=0} \left(\alpha_s^0\right)^k |\widetilde{\mathcal{M}}^{(k)}_{i_1\cdots i_n}\left(m_t^0, \epsilon\right)\rangle \\ &= \sum_{k=0} \left[\left(\frac{e^{\gamma_E}{\mu_R}^2}{4\pi}\right)^{\epsilon} Z_{\alpha_s}^{(n_f)} \, \alpha_s^{(n_f)}(\mu_R)\right]^{\frac{2k+n}{2}} |\widetilde{\mathcal{M}}^{(k)}_{i_1\cdots i_n}\left(Z_m \, m_t, \epsilon\right)\rangle \, . \end{aligned} \tag{2.25}$$

In the second line the bare mass and coupling parameters have been expressed in terms of the UV-finite quantities in order to obtain manifestly physical results. Moreover, it shows that, when working directly with the renormalized mass and coupling constant, the renormalization procedure retains its multiplicative property even at the amplitude level. This is a great advantage in actual calculations as it means that one can apply the standard Feynman rule formalism and remove the emerging UV poles afterwards. The only exception is the mass renormalization, which can, in fact, be attributed to the presence of m_t^0 in the bare top-quark propagator and, hence, only affects diagrams with internal top lines. Fortunately, there exists a simple prescription how to deal with these contributions. The basic idea is to move the

[10] In theories with massless particles the renormalization constants may also contain IR singularities that, when regularized dimensionally, might lead to deviations in the pole structure of different schemes. Furthermore, the poles and hence the renormalization constants can be gauge-dependent. These scheme dependencies will, however, drop out in any physical observable.

renormalization constant Z_m from the denominator to the numerator to restore the multiplicative behavior. This is achieved by employing a so-to-speak inverse Dyson resummation

$$\begin{aligned}
\frac{i}{\not{p} - m_t^0 + i\epsilon} &= \frac{i}{\not{p} - m_t - (Z_m - 1)\, m_t + i\epsilon} \\
&= \frac{i}{\not{p} - m_t + i\epsilon} \sum_{k=0} \left(\frac{(Z_m - 1)\, m_t}{\not{p} - m_t + i\epsilon} \right)^k \\
&= \frac{i}{\not{p} - m_t + i\epsilon} + \left(\frac{\alpha_s^{(n_f)}}{2\pi} \right) \frac{i\, Z_m^{(1)}\, m_t}{\left(\not{p} - m_t + i\epsilon\right)^2} \\
&+ \left(\frac{\alpha_s^{(n_f)}}{2\pi} \right)^2 \left(\frac{i\, Z_m^{(2)}\, m_t}{\left(\not{p} - m_t + i\epsilon\right)^2} + \frac{i \left(Z_m^{(1)}\, m_t \right)^2}{\left(\not{p} - m_t + i\epsilon\right)^3} \right) + \mathcal{O}\left(\left(\frac{\alpha_s^{(n_f)}}{2\pi} \right)^3 \right) .
\end{aligned} \tag{2.26}$$

The expanded result reveals that the mass renormalization at a given order in perturbation theory requires the evaluation of lower-order contributions with additional insertions of the top propagator. This is, however, no conceptual problem and oftentimes does not even cause any further computational effort as the corresponding diagrams may usually be reduced to the original single propagator case, for example via integration-by-parts relations.

As indicated, the entire renormalization procedure traditionally assumes $n_f = n_l + n_h$ active quark flavors in the calculation of higher loop orders where n_l and n_h are the number of light and heavy quarks respectively. While this is perfectly valid at the partonic level, for the hadronic cross section one has to take into account the number of active flavors contributing to the PDF evolution as well. As current collider experiments do not provide enough energy to predominantly produce top quarks at the highly relativistic end of the spectrum, they cannot be treated as massless particles and are thus excluded from the parton content of the (anti-)proton. Consequently, it is only natural to employ a scheme with n_l active flavors in the evolution equations Eq. (2.10), i. e. one refrains from resumming logarithmic top-mass effects, which at the available center-of-mass energies only amount for a small portion of the total cross section. In order to avoid inconsistencies regarding the treatment of α_s, one has to decouple the heavy-quark contributions in the partonic cross sections as well[11], which may be accomplished by means of the relation

$$\alpha_s^{(n_f)} = \zeta_{\alpha_s} \underbrace{\alpha_s^{(n_l)}}_{\equiv \alpha_s} . \tag{2.27}$$

The finite decoupling constant ζ_{α_s} is currently known to four-loop order [513, 514] where the explicit expressions up to $\mathcal{O}(\alpha_s^2)$ can be found in appendix A. The running of α_s is then governed by the beta function defined in Eq. (2.11), consistent with the PDF evolution, leading to the generic expansion shown in Eq. (2.24).

[11] Throughout this thesis the decoupled matrix elements are also denoted by the symbols introduced in Eq. (2.24) and Eq. (2.25). It should be clear from the context which of the two cases is meant.

As mentioned earlier, UV renormalization and the inclusion of additional radiation are not sufficient to yield finite results for the partonic cross sections. The reason for this are singularities caused by collinear emissions in the initial state. In this case the KLN theorem does not apply since the momentum configuration of the initial partons is fixed to a specific value rather than being summed over. In order to eliminate these divergences, one resorts to a similar procedure as for the UV poles, namely one absorbs them into a free parameter of the underlying theory. As the collinear limit corresponds to the long-range, i. e. non-perturbative, domain of QCD and, moreover, the singular behavior is confined exclusively to the initial state, the most natural choice for such a parameter are the PDFs. Analogous to the free parameters of the Lagrangian, they can be regarded as bare, unphysical quantities, $f_i^0(x)$, that are related to the observable distributions, $f_i(x, \mu_F)$, via

$$f_i^0(x) = Z_{ij} \otimes f_j = \int_x^1 \frac{dz}{z}\, Z_{ij}\left(\frac{x}{z}, \mu_F\right)\, f_j(z, \mu_F)\,. \tag{2.28}$$

Note that this relation is the origin of the factorization scale μ_F, which is introduced in a similar manner as μ_R in UV renormalization. Furthermore, it is responsible for the mixing of the various production channels discussed in the beginning of this chapter since all quantities involved represent vectors or matrices in parton space spanned by the different (anti-)quark flavors and the gluon. The collinear-renormalization constants, i. e. the matrix elements Z_{ij} appearing on the right-hand side, are process-independent functions that can be expressed in terms of the Altarelli-Parisi splitting functions in Eq. (2.11). In the $\overline{\text{MS}}$ scheme up to NNLO they read

$$\begin{aligned} Z_{ij}(x, \mu_F) &= \delta_{ij}\,\delta(1-x) + \frac{\alpha_s(\mu_F)}{2\pi}\,\frac{P_{ij}^{(0)}(x)}{\epsilon} \\ &+ \left(\frac{\alpha_s(\mu_F)}{2\pi}\right)^2 \left[\frac{P_{ij}^{(1)}(x)}{2\epsilon} + \frac{1}{2\epsilon^2}\left((P_{ik}^{(0)} \otimes P_{kj}^{(0)})(x) - \frac{\beta_0}{2}\,P_{ij}^{(0)}(x)\right)\right] \\ &+ \mathcal{O}(\alpha_s^3(\mu_F))\,. \end{aligned} \tag{2.29}$$

These relations can be used to construct the collinear counterterms needed to obtain finite expressions for the partonic cross sections of $t\bar{t}$ production. In this context it is sufficient to consider the case $\mu_F = \mu_R = m_t$ as the scale dependence may be restored afterwards using Eq. (2.19) as explained previously. Following the notation of Eq. (2.18), we define the collinearly unrenormalized cross sections as

$$\tilde{\sigma}_{ij}(\rho, m_t, \alpha_s, \epsilon) = \frac{\alpha_s^2}{m_t^2}\left(\tilde{\sigma}_{ij}^{(0)}(\rho, \epsilon) + \alpha_s\,\tilde{\sigma}_{ij}^{(1)}(\rho, \epsilon) + \alpha_s^2\,\tilde{\sigma}_{ij}^{(2)}(\rho, \epsilon) + \mathcal{O}(\alpha_s^3)\right) \tag{2.30}$$

where the functions $\tilde{\sigma}_{ij}^{(n)}$ contain all contributions from higher loop orders and additional radiation as well as from UV renormalization and the remaining collinear poles are indicated by the residual ϵ-dependence. Note, however, that in contrast to Eq. (2.18) these functions are now expressed in terms of ρ rather than β which is more convenient when dealing with convolutions since it is naturally bounded from below by the threshold condition $\rho \geq 4m_t^2/s$

as required by the defining equation 2.3. The finite $\overline{MS}$-subtracted partonic cross sections $\hat{\sigma}_{ij}^{(n,0,0)}$ are then given as

$$\begin{aligned}
\hat{\sigma}_{ij}^{(0)}(\beta) &= \tilde{\sigma}_{ij}^{(0)}(1-\beta^2,\epsilon) \\
\hat{\sigma}_{ij}^{(1,0,0)}(\beta) &= \tilde{\sigma}_{ij}^{(1)}(1-\beta^2,\epsilon) + (1-\beta^2)\left[Z_{ki}^{(1)} \otimes \frac{\tilde{\sigma}_{kj}^{(0)}(\tilde{\rho},\epsilon)}{\tilde{\rho}} + Z_{kj}^{(1)} \otimes \frac{\tilde{\sigma}_{ik}^{(0)}(\tilde{\rho},\epsilon)}{\tilde{\rho}}\right](1-\beta^2,\epsilon) \\
\hat{\sigma}_{ij}^{(2,0,0)}(\beta) &= \tilde{\sigma}_{ij}^{(2)}(1-\beta^2,\epsilon) + (1-\beta^2)\left[Z_{ki}^{(2)} \otimes \frac{\tilde{\sigma}_{kj}^{(0)}(\tilde{\rho},\epsilon)}{\tilde{\rho}} + Z_{kj}^{(2)} \otimes \frac{\tilde{\sigma}_{ik}^{(0)}(\tilde{\rho},\epsilon)}{\tilde{\rho}}\right. \\
&\quad + \left. Z_{ki}^{(1)} \otimes \frac{\tilde{\sigma}_{kj}^{(1)}(\tilde{\rho},\epsilon)}{\tilde{\rho}} + Z_{kj}^{(1)} \otimes \frac{\tilde{\sigma}_{ik}^{(1)}(\tilde{\rho},\epsilon)}{\tilde{\rho}} + Z_{ki}^{(1)} \otimes Z_{lj}^{(1)} \otimes \frac{\tilde{\sigma}_{kl}^{(0)}(\tilde{\rho},\epsilon)}{\tilde{\rho}}\right](1-\beta^2,\epsilon)
\end{aligned} \tag{2.31}$$

where $Z_{ij}^{(1)}$ and $Z_{ij}^{(2)}$ are the NLO and NNLO coefficients of the collinear-renormalization constants in Eq. (2.29). As can be seen from these expressions, the collinear counterterms for a specific perturbative order are completely determined by the lower-order cross section results and thus do not require any additional input although the actual numerical evaluation of the respective convolutions may still pose a serious computational challenge. It is, however, necessary to know the lower-order results to higher powers of ϵ as these subleading terms yield finite contributions when combined with the poles of the collinear-renormalization constants (at least when working in CDR). In practice, these $\mathcal{O}(\epsilon^n)$ terms are not always available in the literature, especially when going beyond leading order. Since this was indeed the case for top-quark pair production, we had to extend the findings of Refs. [211–213] to $\mathcal{O}(\epsilon)$ in order to provide all necessary ingredients for the collinear counterterm at NNLO. A more explicit form of both the NLO and NNLO counterterms organized according to the different production modes will be given below.

Having discussed the general structure of the partonic cross sections, we will now briefly address the known LO and NLO results for $\sigma_{t\bar{t}}^{\mathbf{tot}}$ since they play an important role for the scale-controlling contributions at NNLO as well as in the different renormalization procedures.

2.3.1 The leading order partonic cross sections

At leading order in perturbative QCD the production of a top-quark pair is mediated by the following partonic scattering processes

$$q(p_1) + \bar{q}(p_2) \longrightarrow t(p_3, m_t) + \bar{t}(p_4, m_t) \tag{2.32}$$

$$g(p_1) + g(p_2) \longrightarrow t(p_3, m_t) + \bar{t}(p_4, m_t)\,. \tag{2.33}$$

The relevant diagrams contributing to these reactions are depicted in Fig. 1.7. Since the top quarks are treated as stable particles, their momenta fulfill the on-shell condition $p_3^2 = p_4^2 = m_t^2$ while the initial state is considered to be massless $p_1^2 = p_2^2 = 0$ as required by the factorization theorem. The resulting scattering amplitudes are thus conveniently described by a set of

modified Mandelstam variables[12]

$$s = (p_1 + p_2)^2 \quad t = m_t^2 - (p_1 - p_3)^2 \quad u = m_t^2 - (p_1 - p_4)^2 \tag{2.34}$$

which satisfy an alternative summation relation

$$s = t + u\,. \tag{2.35}$$

However, due to constraints from four-momentum conservation and symmetry arguments the kinematics of a 2-to-2 process can be completely parametrized in terms of only two independent quantities, which we choose to be the top-quark velocity β and the scattering angle θ defined through

$$t = \frac{s}{2}\left(1 - \beta\cos\theta\right)\,. \tag{2.36}$$

This choice is not unique but well-motivated by the fact that it leads to an appropriate description of $t\bar{t}$ production over the full kinematic range, from the threshold region at $\beta \approx 0$ ($\rho \approx 1$) to the high-energy regime at $\beta \approx 1$ ($\rho \approx 0$).

In order to obtain results for the partonic cross sections, one has to take the complex amplitude square, sum over all possible color and spin configurations and integrate the subsequent expression over the two-particle phase space

$$\begin{aligned} dP_2^{(ij)} &= \frac{\rho}{8\,c_i c_j s_i s_j}\left(\frac{e^{\gamma_E}\mu_R^2}{4\pi}\right)^{\epsilon} \underbrace{\frac{d^{d-1}p_3}{(2\pi)^{d-1}2\,E_3}\frac{d^{d-1}p_4}{(2\pi)^{d-1}2\,E_4}\,(2\pi)^d\,\delta^{(d)}\left(p_1 + p_2 - p_3 - p_4\right)}_{d\Phi_2} \\ &\overset{\epsilon=0}{=} \frac{\rho}{8\,c_i c_j s_i s_j}\,\frac{d^3p_3}{(2\pi)^3 2\,E_3}\frac{d^3p_4}{(2\pi)^3 2\,E_4}\,(2\pi)^4\,\delta^{(4)}\left(p_1 + p_2 - p_3 - p_4\right) \end{aligned} \tag{2.37}$$

where $E_i = \sqrt{\vec{p}_i^{\,2} + m_t^2}$ denotes the energy of the respective final-state particles. The prefactor contains the initial-state flux (not to be confused with the partonic flux), expressed through the dimensionless variable ρ to guarantee the proper normalization of the cross section predictions, as well as the average over initial-state spins (s_i = number of possible spin states for parton i) and colors (c_i = number of possible color states for parton i). For quarks and gluons the corresponding d-dimensional averaging factors read

$$\begin{aligned} s_q &= 2 & c_q &= N_c \\ s_g &= 2 - 2\epsilon & c_g &= N_c^2 - 1 \end{aligned} \tag{2.38}$$

where N_c is the dimensionality of the fundamental representation of the underlying SU(N) symmetry group, i. e. $N_c = 3$ for QCD. An interesting feature of the massive two-particle phase space is that the integration over the energy components yields a suppression factor

$$\int dP_2^{(ij),\,\epsilon=0} \propto \rho\beta \int d\cos\theta \tag{2.39}$$

[12] Unless specifically noted otherwise, all kinematic quantities in the following discussion refer to the parton level. We therefore refrain from using the usual "^" symbol to explicitly indicate their partonic nature.

that affects both ends of the β-spectrum. This is particularly important for the ultra-relativistic limit $\beta \to 1$ as it regulates the singular behavior at $\cos\theta = \pm 1$, known from massless 2-to-2 scattering, and therefore allows for the determination of fully inclusive cross section predictions without the need to impose any kinematic cuts. Still, the differential cross sections may be strongly enhanced in these regions as can be seen in Fig. 2.6 for the gluon fusion channel. Since such an enhancement requires the exchange of a particle in the t- or u-channel (see (b) in Fig. 1.7), the LO quark annihilation channel remains unaffected in this kinematic limit.

Integrating these differential results over the scattering angle, one arrives at the final expression for the LO partonic cross sections

$$\hat{\sigma}_{q\bar{q}}^{(0)}(\beta) = \frac{\pi}{6}\frac{T_F C_F}{N_c}\beta\,(1-\beta^2)\,(3-\beta^2) \tag{2.40}$$

$$\begin{aligned}\hat{\sigma}_{gg}^{(0)}(\beta) &= \frac{\pi}{4}\frac{T_F}{N_c^2-1}\beta\,(1-\beta^2)\left(C_F\left[\frac{6-2\beta^4}{\beta}\ln\frac{1+\beta}{1-\beta} - 8 + 4\beta^2\right]\right.\\ &+ \left. C_A\left[\frac{(1-\beta^2)^2}{\beta}\ln\frac{1+\beta}{1-\beta} - 3 + \frac{5}{3}\beta\right]\right)\end{aligned} \tag{2.41}$$

where $C_F = (N_c^2-1)/(2N_c) = \frac{4}{3}$ and $C_A = N_c = 3$ are the Casimir operators of the fundamental and adjoint representation of the SU(3) respectively and $T_F = \frac{1}{2}$ is the corresponding Dynkin index. Both functions are plotted in Fig. 2.7 and display quite different shapes with the $q\bar{q}$ contribution being rather symmetric while the gluonic result is shifted towards higher values of β. This behavior can be attributed to the high-energy enhancements at low/large scattering angle, which is encoded in Eq. (2.41) as

$$\ln\frac{1+\beta}{1-\beta} \propto \ln(1-\beta^2) = \ln\rho \tag{2.42}$$

This logarithmic rise is a common feature of processes that involve t- and/or u-channel exchange and we will encounter it at higher perturbative orders as well where, as we will see, it can be even more pronounced. Interestingly, the overall size of both production modes is very similar whereas naively one would have expected the gluon fusion channel to be more dominant as it contains more diagrams contributing to the scattering amplitude. A closer investigation shows that the reason for this discrepancy lies in the color-averaging factor in Eq. (2.37) that scales the a priori larger gluon fusion result down to the level of the fermionic contributions.

Another important aspect is the threshold behavior of the LO partonic cross sections, in the following denoted as $\hat{\sigma}_{ij}^{(0)}|_{\beta\to 0} \equiv \bar{\sigma}_{ij}^{(0)}$, since it enters the approximate NNLO predictions as well as the resummation formalism (see section 3.1.2). For these applications it is crucial to decompose the color structure of the top-quark pair into irreducible representations of the SU(3) gauge group. This is achieved by utilizing the fact that the tensor-product[13] space spanned by the single-particle color representations corresponds to a direct sum of invariant subspaces, which in case of a quark-antiquark pair amounts to

$$\mathbf{3} \otimes \bar{\mathbf{3}} = \mathbf{1} \oplus \mathbf{8}, \tag{2.43}$$

[13] Tensor products and convolutions are commonly denoted by the same symbol "$\otimes$" but it should be clear from the context which one is meant.

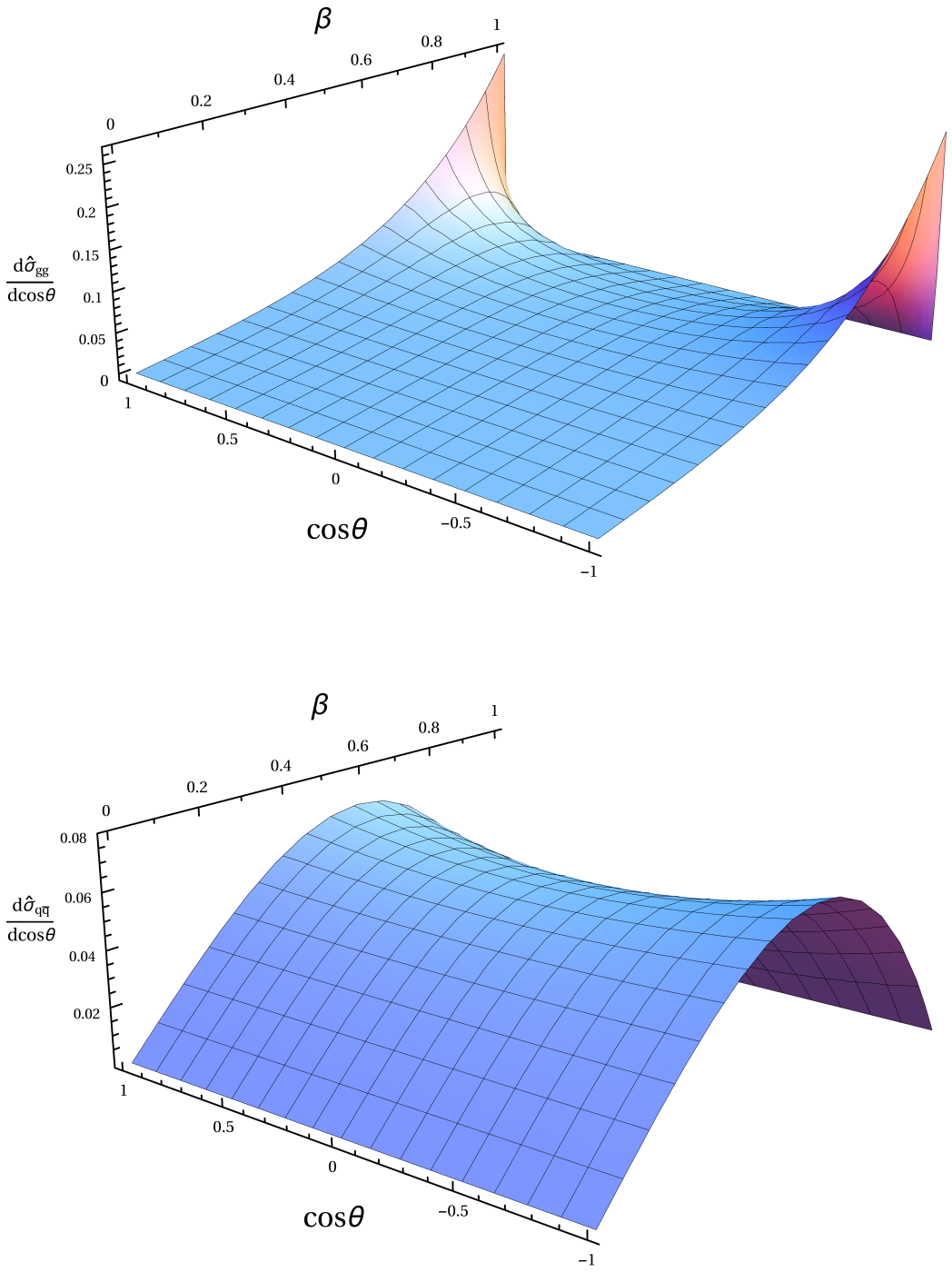

Figure 2.6: *The LO differential cross section* $\frac{d\hat{\sigma}_{ij}}{d\cos\theta}(\beta, \cos\theta)$ *in the gluon fusion (top) and the quark annihilation (bottom) channel. Note that both channels are symmetric in* $\cos\theta$*, which in the gluonic case is due to parity conservation but for the fermionic contributions cannot be explained by symmetry arguments.*

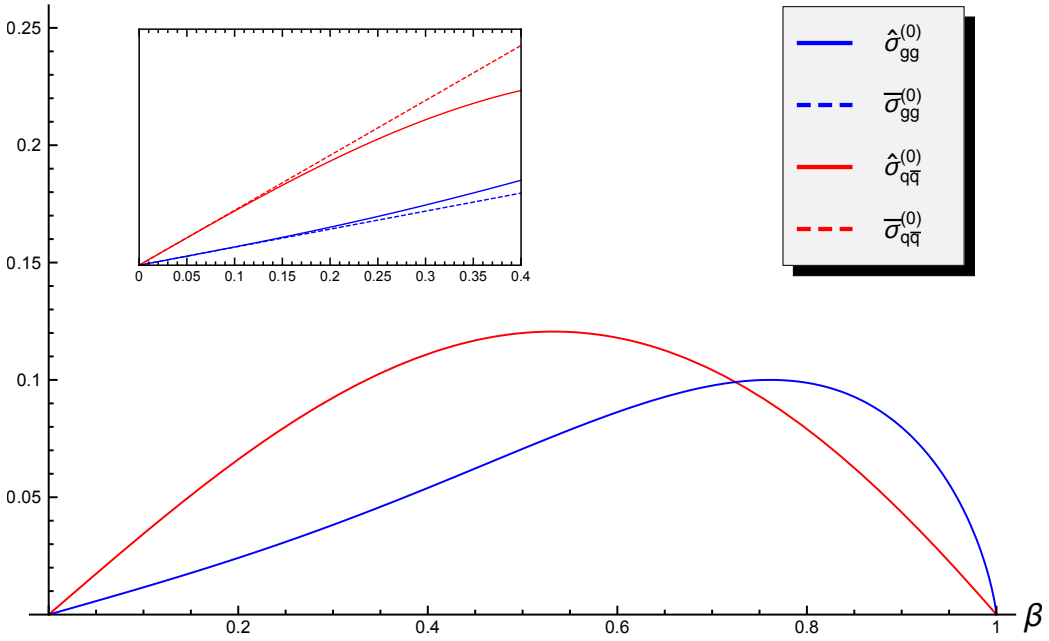

Figure 2.7: *The LO partonic cross sections $\hat{\sigma}^{(0)}_{ij}$ (solid) as well as their respective threshold limits (dashed). For the gluon fusion channel the combined threshold expansion is given as $\bar{\sigma}^{(0)}_{gg} \equiv \bar{\sigma}^{(0)}_{gg,\mathbf{1}} + \bar{\sigma}^{(0)}_{gg,\mathbf{8_S}}$.*

i. e. the final-state system is either in a singlet or octet configuration. The key point is that these configurations are orthogonal, which is a great benefit in practical applications as it dramatically reduces the computational effort. Color conservation implies that the initial state belongs to an equivalent representation, which in case of identical particles may, however, not be sufficient for an unambiguous determination of its color configuration. Indeed, for the gluon fusion channel the decomposition into irreducible representations,

$$\mathbf{8} \otimes \mathbf{8} = \mathbf{1} \oplus \mathbf{8_S} \oplus \mathbf{8_A} \oplus \mathbf{10} \oplus \overline{\mathbf{10}} \oplus \mathbf{27}\,, \tag{2.44}$$

contains two distinct octet configurations that differ in their symmetry properties being either symmetric or antisymmetric under interchange of the gluon color indices. Nevertheless, orthogonality is still preserved due to Bose symmetry and hence there are no mixing effects between these configurations. Analogous to the addition of angular momentum in quantum mechanics the transition to the new color basis $|b^R_\alpha\rangle$ is given by a unitary transformation [515]

$$|b_i\rangle \otimes |b_j\rangle = \sum_R C^R_{ij\alpha}\, |b^R_\alpha\rangle \tag{2.45}$$

where $|b_k\rangle$ are the vectors of the one-particle color basis and the sum runs over all distinct irreducible representations R. The Clebsch-Gordon coefficients $C^R_{ij\alpha}$ can be used to construct projection operators that allow for the decomposition of any color structure (present in $t\bar{t}$ production) into a linear combination of the new basis vectors. For the quark annihilation channel these projectors read

$$P^{\mathbf{3}\otimes\bar{\mathbf{3}}|\mathbf{1}}_{ijkl} = \frac{1}{N_c}\,\delta_{ij}\,\delta_{kl} \qquad P^{\mathbf{3}\otimes\bar{\mathbf{3}}|\mathbf{8}}_{ijkl} = \frac{2}{\sqrt{N_c^2-1}}\,T^a_{ij}\,T^a_{kl}\,, \tag{2.46}$$

while for the gluon fusion channel they are given by

$$P_{abij}^{\mathbf{8}\otimes\mathbf{8}|\mathbf{1}} = \frac{1}{\sqrt{N_c(N_c^2-1)}}\,\delta^{ab}\,\delta_{ij} \qquad P_{abij}^{\mathbf{8}\otimes\mathbf{8}|\mathbf{8_S}} = \sqrt{\frac{2N_c}{(N_c^2-1)(N_c^2-4)}}\,d^{abc}\,T_{ij}^c$$
$$P_{abij}^{\mathbf{8}\otimes\mathbf{8}|\mathbf{8_A}} = \sqrt{\frac{2}{N_c(N_c^2-1)}}\,if^{abc}\,T_{ij}^c \tag{2.47}$$

where T_{ij}^a are the SU(3) generators in the fundamental representation, f^{abc} are the structure constants and the symmetric tensor d^{abc} is defined through the trace $\mathrm{Tr}\,T^aT^bT^c = (d^{abc} + if^{abc})/4$. The normalization has been chosen such that the absolute value squared yields

$$P_{ijkl}^{\mathbf{R}\otimes\mathbf{R}'|\tilde{\mathbf{R}}}\,P_{ijkl}^{\mathbf{R}\otimes\mathbf{R}'|\tilde{\mathbf{R}}\;*} = 1\,. \tag{2.48}$$

Although these projectors are designed to act at the level of matrix elements, their orthogonality guarantees that the decomposition into singlet and octet configurations persists also at the cross section level. As a consequence, there are potentially five different color structures contributing to $t\bar{t}$ production. At LO the quark annihilation channel can, however, only be in a pure octet state since in QCD it is not possible to connect two separate quark lines by a single gluon without inducing a net color exchange. Higher-order corrections lift this restriction and also allow for top pairs in the singlet state. In the gluonic reactions all color configurations are already present at LO albeit displaying a quite different behavior at threshold. Due to the phase space suppression factor Eq. (2.39) both channels, quark annihilation and gluon fusion, vanish in the limit $\beta \to 0$ regardless of the internal color structure. Yet, for the gluonic case, the singlet and symmetric octet contributions,

$$\bar{\sigma}_{gg,\mathbf{1}}^{(0)}(\beta) = \pi\,T_F\,\beta\,\frac{1}{2N_c(N_c^2-1)} \tag{2.49}$$
$$\bar{\sigma}_{gg,\mathbf{8_S}}^{(0)}(\beta) = \pi\,T_F\,\beta\,\frac{1}{4(N_c^2-1)}\left(4\,C_F - C_A - \frac{2}{N_c}\right), \tag{2.50}$$

are strongly enhanced with respect to the antisymmetric octet cross section

$$\bar{\sigma}_{gg,\mathbf{8_A}}^{(0)}(\beta) = \pi\,T_F\,\beta^3\,\frac{C_A}{12(N_c^2-1)}\,. \tag{2.51}$$

This additional suppression in the threshold regime cannot be attributed to any particular symmetry of the system but is rather a coincidental feature of the LO matrix elements. As the $t\bar{t}$ final state at threshold can be effectively treated as a fictitious spin-1 particle, it is tempting to utilize the well-known Landau-Yang theorem that addresses the decay of such a spin-1 state into a pair of identical massless spin-1 particles. It does, however, not apply to gluons since their additional color quantum number renders the original line of argumentation invalid [516,517]. For the quark annihilation channel the threshold expansion reads

$$\bar{\sigma}_{q\bar{q},\mathbf{8}}^{(0)}(\beta) = \pi\,T_F\,\beta\,\frac{C_F}{2N_c}\,. \tag{2.52}$$

As indicated in Fig. 2.7, these approximations fail to adequately describe the functional behavior away from the threshold region and are thus not well suited to serve as an estimate

	Tevatron [pb]	LHC			
		7 TeV [pb]	8 TeV [pb]	13 TeV [pb]	14 TeV [pb]
$q\bar{q}$	$6.069^{+2.559}_{-1.658}$	$29.76^{+8.84}_{-6.32}$	$37.61^{+10.71}_{-7.74}$	$81.67^{+20.58}_{-14.94}$	$91.23^{+22.99}_{-16.69}$
gg	$0.5505^{+0.3727}_{-0.2042}$	$91.02^{+39.47}_{-25.52}$	$134.5^{+56.0}_{-36.7}$	$488.9^{+175.4}_{-120.4}$	$586.4^{+205.6}_{-142.1}$
$\sigma_{t\bar{t}}^{\mathbf{tot},\mathrm{LO}}$	$6.619^{+2.932\ +0.146}_{-1.862\ -0.124}$	$120.8^{+48.3\ +3.1}_{-31.8\ -3.2}$	$172.1^{+66.7\ +4.2}_{-44.4\ -4.3}$	$570.6^{+195.2\ +10.9}_{-135.3\ -12.5}$	$677.6^{+227.2\ +12.5}_{-158.4\ -14.6}$

Table 2.2: *The LO theoretical predictions for $\sigma_{t\bar{t}}^{\mathbf{tot}}$ at the Tevatron and the LHC ($m_t = 173.3\,\mathrm{GeV}$, MSTW2008 PDFs at 68% C.L. [231]). The quoted uncertainties are due to the variation of renormalization and factorization scale and, for the full result, the parametric error of the PDFs.*

of the full cross section results (at this particular order in QCD), especially when taking into account that the partonic fluxes favor larger values of β.

In order to be able to better assess the interplay between the partonic cross sections and fluxes, in Fig. 2.10 we show the product of these two components for the Tevatron as well as for the LHC at 8 TeV. The area beneath these curves then directly corresponds to the contribution of the respective channel to the total cross section (modulo some global prefactor). Since the fluxes at the Tevatron behave opposite to the cross sections, i. e. the gluonic flux is rather symmetric while the $q\bar{q}$-flux is shifted towards the higher-energetic part of the spectrum, both functions peak at a similar value of $\beta \approx 0.65$ although they, of course, differ in their overall normalization. At the LHC both curves tend to even larger values of β as the preference of the fluxes for high-energy production becomes more pronounced with increasing center-of-mass energy. The gluon fusion channel is, however, clearly dominating now. Despite these differences it is apparent that independent of the production mode the bulk of the total cross section can be attributed to velocities in the intermediate range. Nonetheless, this does not mean that approximations based on expansions in certain kinematic limits might not be useful at higher orders in perturbation theory as we will see below.

The corresponding LO predictions for $\sigma_{t\bar{t}}^{\mathbf{tot}}$ at the two different colliders are given in Tab. 2.2 together with the individual contributions of each channel. Despite the fact that the latter are unobservable, they allow us to quantitatively assess the impact of the two production modes on the full result. As expected, the quark annihilation channel, with over 90%, accounts for the major part of the predicted $t\bar{t}$ pairs at the Tevatron whereas at the LHC it is only responsible for 13-25% gradually decreasing with the available center-of-mass energy. The central prediction itself displays a completely opposite behavior increasing as the center-of-mass energy becomes larger which may be traced back to the properties of the partonic fluxes (see Fig. 2.2). The PDF error, on the other hand, always assumes a value of 2-3% regardless of the specific collider setup. Interestingly, for the relative theory error due to scale variation we also observe a decreasing energy dependence. As the LO μ_R-dependence is confined solely to the global prefactor of $\alpha_s^2(\mu_R)$, this behavior can be directly attributed to the interplay of factorization scale and energy dependence in the flux factor. Nonetheless, with a about 20-30% it remains sizable making a calculation of higher-order corrections inevitable.

2.3.2 The next-to-leading order partonic cross sections

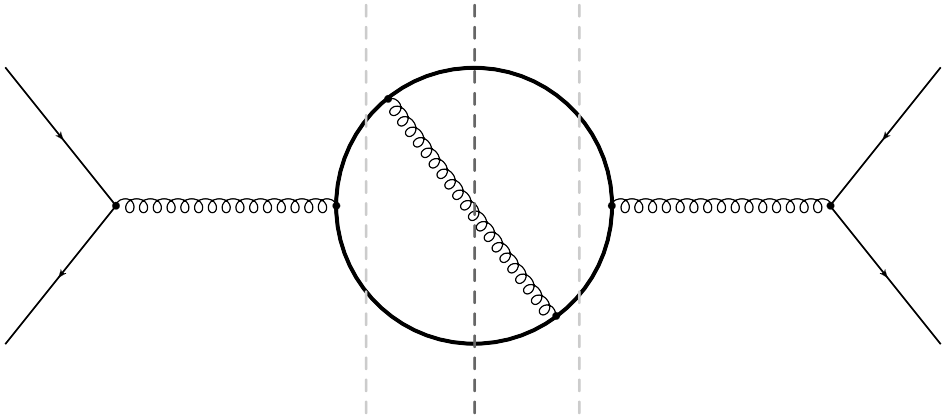

Figure 2.8: *Cut diagram contributing to the NLO partonic cross section in the quark annihilation channel. All particles (as usual top quarks are represented by bold lines) crossing a unitarity cut are constrained to lie on their mass shell thus eliminating parts of the loop integration and resulting in the virtual (light gray) and real (dark gray) corrections described below.*

At NLO in the strong coupling constant the situation becomes more complex since it does not only involve a new partonic production mode, the quark-gluon channel, but also additional radiation and closed quantum loops, which increases the computational effort tremendously. This is the reason why it took another 20 years from the first numerical evaluation of these contributions [211, 212] to the derivation of a fully analytical result [213]. Following the notation of Eq. (2.18), the NLO corrections can be parametrized as

$$\begin{aligned}
\hat{\sigma}_{q\bar{q}}^{\mathrm{NLO}}(\beta) &= \hat{\sigma}_{q\bar{q}}^{(1,0,0)}(\beta) + \frac{\beta_0}{2\pi}\,\hat{\sigma}_{q\bar{q}}^{(0)}(\beta)\,\ln\left(\frac{\mu_R^2}{m_t^2}\right) - \frac{1-\beta^2}{\pi}\left(P_{qq}^{(0)} \otimes \frac{\hat{\sigma}_{q\bar{q}}^{(0)}(\tilde{\rho})}{\tilde{\rho}}\right)\ln\left(\frac{\mu_F^2}{m_t^2}\right) \\
\hat{\sigma}_{gg}^{\mathrm{NLO}}(\beta) &= \hat{\sigma}_{gg}^{(1,0,0)}(\beta) + \frac{\beta_0}{2\pi}\,\hat{\sigma}_{gg}^{(0)}(\beta)\,\ln\left(\frac{\mu_R^2}{m_t^2}\right) - \frac{1-\beta^2}{\pi}\left(P_{gg}^{(0)} \otimes \frac{\hat{\sigma}_{gg}^{(0)}(\tilde{\rho})}{\tilde{\rho}}\right)\ln\left(\frac{\mu_F^2}{m_t^2}\right) \\
\hat{\sigma}_{qg}^{\mathrm{NLO}}(\beta) &= \hat{\sigma}_{qg}^{(1,0,0)}(\beta) - \frac{1-\beta^2}{2\pi}\left(P_{gq}^{(0)} \otimes \frac{\hat{\sigma}_{gg}^{(0)}(\tilde{\rho})}{\tilde{\rho}} + P_{qg}^{(0)} \otimes \frac{\hat{\sigma}_{q\bar{q}}^{(0)}(\tilde{\rho})}{\tilde{\rho}}\right)\ln\left(\frac{\mu_F^2}{m_t^2}\right)
\end{aligned} \tag{2.53}$$

where $\beta_0 = \frac{11}{3}\,C_A - \frac{4}{3}\,T_F\,n_l$ is the leading coefficient of the QCD beta function and the explicit form of the scale-dependent terms has been derived using Eq. (2.19). While the coefficients that govern the μ_R-dependence are directly proportional to the respective LO cross sections, the μ_F-controlling parts involve a convolution with the LO splitting functions as could have been anticipated, given the particular structure of the latter equation. Still, the determination of these contributions comes at comparatively low computational cost and is hence considered trivial by today's standards. Note that the quark-gluon channel is independent of the renormalization scale (except for a global factor of $\alpha_s^3(\mu_R)$) since it only contains radiative corrections that do not require UV renormalization.

The scale-invariant functions $\hat{\sigma}_{ij}^{(1,0,0)}$ are generally divided into three conceptually different pieces that can be computed separately: The virtual corrections, the real corrections and the contributions from collinear factorization. The latter have already been defined in Eq. (2.31) and are closely related to the μ_F-dependent functions $\hat{\sigma}_{ij}^{(1,0,1)}$. The virtual and the real contributions, on the other hand, have to be derived from first principles and thus their actual calculation requires a more detailed discussion, especially as the computational methods employed in the NLO analysis form the basis for the advanced numerical techniques used for the evaluation of the NNLO cross sections.

The virtual corrections

The NLO virtual corrections consist of LO diagrams that are dressed with an additional quantum loop and, therefore, only affect the quark annihilation and the gluon fusion channel. Despite the simple 2-to-2 kinematics their evaluation may become highly non-trivial due to the necessity to take into account all possible configurations of the internal loop momentum consistent with the relativistic conservation laws. In order to deal with the corresponding loop integrals, a variety of sophisticated methods has been developed over the last decades[14], not solely limited to the case of heavy-quark production but allowing for the evaluation of higher-order effects in a broad spectrum of physical applications. While all of these methods have to ultimately give the same answer, the success of a particular approach will in general depend on various factors that are specific to the problem at hand such as the number of loops and external legs or the number of independent kinematic invariants and masses needed to describe a particular process. Moreover, most practical applications nowadays call for computational tools that are suited for automation in order to be able to handle the large number of Feynman diagrams (and, consequently, loop integrals) involved in such a calculation, an aspect one has to keep in mind when choosing a suitable evaluation method. Still, there exists no unique strategy on how to treat specific classes of virtual corrections and the actual choice will eventually be a matter of experience and personal taste.

In the following we will, thus, focus solely on the approach employed in the analytical NLO analysis of top-quark pair production, namely integration-by-parts (IBP) reduction in combination with the use of differential equations, since we will encounter an analogous strategy also at NNLO. The main idea is to employ recurrence relations to reduce the number of loop integrals to a minimal set of independent master integrals that can then be evaluated by exploiting the fact that a differentiation with respect to the kinematic invariants and masses is again proportional to a linear combination of these master integrals. A key feature of this method is that it allows for a high degree of automation and, furthermore, can be used to evaluate the emerging loop integrals either analytically or purely numerically depending on the overall complexity of the problem at hand.

In the computation of NLO $t\bar{t}$ production the first step is to extract the underlying Lorentz structure of the (renormalized) one-loop amplitude $|\mathcal{M}_{ij}^{(1)}\rangle$ with a suitable projection operator since it is more convenient to work with scalar integrals than with tensor-valued expressions.

[14] A comprehensive overview of these tools can be found in the works V.A. Smirnov [518–520], one of the driving forces in the field of evaluating complex Feynman integrals.

The most natural choice for such an operator is the corresponding LO amplitude $|\mathcal{M}_{ij}^{(0)}\rangle$ as the overall contribution of the virtual corrections to the partonic cross section is given by

$$\hat{\sigma}_{ij}^{V}(\beta) = 2 \int dP_2^{(ij)} \, \mathrm{Re}\, \langle \mathcal{M}_{ij}^{(0)} | \mathcal{M}_{ij}^{(1)} \rangle \; . \tag{2.54}$$

Evaluating the occurring color and spinor traces results in a linear combination of scalar one-loop integrals with coefficients constructed from SU(3) color factors, the Mandelstam variables in Eq. (2.34), the top-quark mass and the number of space time dimensions $d = 4 - 2\epsilon$. These integrals may contain irreducible numerators, i. e. scalar products of the loop momentum with the external momenta that cannot be manipulated such that they cancel with the corresponding propagator structures in the denominator. For a generic loop process involving N_k loop integrations and N_p independent external momenta the number of numerators and denominators N_{N+D} is fixed to

$$N_{N+D} = N_p N_k + \frac{N_k(N_k+1)}{2} \, . \tag{2.55}$$

While the employed regularization scheme is generally a matter of choice, it is in this case crucial to work in dimensional regularization as the identity used to derive the recurrence relations is not valid for arbitrary regularization schemes. The basic idea is to exploit translational invariance which for a d-dimensional loop integral depending on the external momenta p_i and masses m_j amounts to

$$\int d^d k \, f\left(k, p_i, m_j^2\right) = \int d^d k \, f\left(k + l, p_i, m_j^2\right) \tag{2.56}$$

where l is an arbitrary d-dimensional Lorentz vector. As both sides are independent of this vector, one obtains

$$0 = \int d^d k \, \frac{\partial}{\partial l_\mu} \, f\left(k + l, p_i, m_j^2\right) \; . \tag{2.57}$$

This relation can be recast in a more convenient form commonly denoted as IBP identity [521, 522]:

$$0 = \int d^d k \, \frac{\partial}{\partial k} \cdot q \, f\left(k, p_i, m_j^2\right) \quad \text{with } q^\mu = k^\mu \text{or} \, p_i^\mu \tag{2.58}$$

It allows us to express any integral of a given topology, i. e. propagator structure, as a linear combination of integrals of the same topology or a corresponding subtopology which is obtained from the original integral definition by removing one or more propagators. The resulting homogeneous system of linear equations is underdetermined (otherwise all integrals would vanish) but may be used to eliminate a large fraction of the initial set of loop integrals in favor of a small basis of irreducible master integrals. This procedure may be best demonstrated through a toy example. Consider the following scalar integral

$$I(a_1, a_2) = \mathcal{N}_\epsilon \int \frac{d^d k}{(2\pi)^d} \, \frac{1}{(k^2 - m^2)^{a_1} \left((k-p)^2\right)^{a_2}} \tag{2.59}$$

with integer powers $a_i \geq 0$ and the on-shell condition $p^2 = m^2$. The d-dimensional loop measure $\mathcal{N}_\epsilon$ drops out in any physical observable and can, thus, be chosen freely (as long as

it tends to unity for $\epsilon \to 0$). Suppose we are interested in all solutions $a_1 + a_1 > 0$ expressed in terms of the simplest integrals of the given topology[15], $I(1,0)$ and $I(1,1)$. Applying the differential operators $\frac{\partial}{\partial k} \cdot k$ and $\frac{\partial}{\partial k} \cdot p$ leads to

$$\begin{aligned} 0 &= (d - 2a_1 - a_2)\, I(a_1, a_2) - 2a_1 m^2\, I(a_1 + 1, a_2) - a_2\, I(a_1 - 1, a_2 + 1) \\ 0 &= (a_2 - a_1)\, I(a_1, a_2) + a_1\, I(a_1 + 1, a_2 - 1) - 2a_1 m^2\, I(a_1 + 1, a_2) - a_2\, I(a_1 - 1, a_2 + 1)\,. \end{aligned} \tag{2.60}$$

Setting $a_2 = 0$ in the first expression directly yields

$$I(a_1, 0) = \frac{d - 2a_1 + 2}{2(a_1 - 1)m^2}\, I(a_1 - 1, 0) \tag{2.61}$$

while for the case $a_2 \neq 0$ further manipulation results in

$$I(a_1, a_2) = \frac{1}{2m^2} \left(\frac{d - 2a_1 - a_2 + 1}{d - a_1 - 2a_2}\, I(a_1, a_2 - 1) - (a_2 - 1)\, I(a_1 - 1, a_2) \right) . \tag{2.62}$$

These recurrence identities can now be used to relate integrals with arbitrary powers a_i to the basic integrals $I(1,0)$ and $I(1,1)$. Moreover, Eq. (2.62) evaluated for $a_1 = a_2 = 1$ reveals that the latter integral is not independent but may be expressed in terms of $I(1,0)$ as

$$I(1,1) = \frac{1}{2m^2} \left(\frac{d-2}{d-3} \right) I(1,0)\,. \tag{2.63}$$

So the entire problem is reduced to the iterative application of the recurrence relations down to a single master integral. For the evaluation of this master integral we have to resort to a different method but still the gain is significant since a complete class of integrals can now be computed at virtually no cost by performing only one explicit integration.

In practice, however, the size of the system of scalar integrals usually becomes so large that a symbolic treatment of the IBP identities, i. e. with general powers of numerators and denominators, is no longer feasible. In order to still be able to exploit the information encoded in Eq. (2.58), S. Laporta developed an algorithm [523] that allows for a reduction to master integrals in a fully numerical fashion. Numerical in this context only refers to the exponents of the numerators and denominators which have to be specified in advance. The rational coefficients constructed from kinematic invariants, masses and the dimensionality parameter d may still be treated symbolically. The basic idea behind this algorithm is to generate a large but finite set of explicit IBP identities and solve the resulting system of linear equations, for instance with the well-known Gaussian elimination procedure, for the most complicated integrals. For a sufficiently large number of identities the remaining group of integrals will eventually stabilize and form a minimal master basis[16]. This implies the existence of an

[15] Note that scaleless integrals such as $I(0, a_2)$ are conventionally set to zero in DR as their contribution to any physical quantity drops out.

[16] There exists no strict mathematical proof that the basis obtained with the Laporta algorithm is minimal in the sense that it is linearly independent but experience shows that compared to the original set of integrals the number of masters is very small. In practice, this number may be reduced even further by taking into account additional symmetries.

ordering mechanism that decides which integral in a particular identity is the most complicated and should be eliminated. As the complexity of a loop integral in general increases with the number of internal propagators as well as with their respective exponents, these quantities represent the most natural ordering parameters. A more distinct differentiation also includes the sum of numerator and denominator powers and the underlying topology. It turns out to be most efficient to apply this ordering not only in the elimination process but already when generating the identities. Processing the integrals on the basis of their complexity starting with the lowest number of denominators will minimize the computational effort and result in a potentially simple master basis. Due to the clear prescriptions this method is very well-suited for automation and there exist several public implementations of this algorithm, e. g. Air [524], Fire [525] or Reduze2 [526], making it available to a wider audience.

Another useful property of the IBP relation in Eq. (2.58) is that it also holds for inclusive phase space integrals, a feature that is particularly handy when dealing with total cross sections or decay widths. It is closely connected to the optical theorem and the concept of Cutkosky cutting rules [527]. The optical theorem states that the imaginary part of a forward-scattering amplitude is equivalent to a phase space integral over the absolute squared matrix element of all possible intermediate configurations

$$2\,\mathrm{Im}\,\mathcal{M}(a \to a) = \sum_f \int d\Phi_f |\mathcal{M}(a \to f)|^2 \tag{2.64}$$

where a and f are arbitrary multiple-particle states. Since this relation includes contributions from different final-state particle multiplicities, it constitutes an elegant method to prove the cancellation of IR divergences in inclusive observables. In practice, a straightforward calculation of the imaginary part can, however, be quite cumbersome which led to the development of the cutting rule formalism. It is based on the fact that the imaginary part of an amplitude described by a kinematic variable s can be expressed in terms of a branch cut discontinuity that usually starts at a certain threshold value $s > s_0$ depending on the specific problem under consideration

$$2i\,\mathrm{Im}\,\mathcal{M}(s + i\epsilon) = i\,\mathrm{Im}\,\mathcal{M}(s + i\epsilon) - i\,\mathrm{Im}\,\mathcal{M}(s - i\epsilon) \equiv \mathrm{Disc}\,\mathcal{M}(s)\,. \tag{2.65}$$

The discontinuity of the amplitude can be computed by replacing the propagators that correspond to a particular n-particle intermediate state through delta functions

$$\frac{1}{p^2 - m^2 + i\epsilon} \to -2\pi i\,\delta\left(p^2 - m^2\right) \tag{2.66}$$

which effectively cuts the associated diagram into two separate pieces turning the loop integration into a phase space integral. An example of such a cut diagram is displayed in Fig. 2.8 for the quark annihilation channel where the two- and three-particle cuts correspond to the NLO virtual and real corrections to the total cross section explicitly demonstrating the cancellation of IR divergences between these contributions. In order to be able to apply the IBP reduction also to inclusive phase space integrals one has to resort to a somewhat reversed cutting prescription. First of all, the phase space integrations are transformed into

d-dimensional loop-like integrations via

$$\int \frac{d^{d-1}p}{(2\pi)^{d-1}\,2E_p} = \int \frac{d^dp}{(2\pi)^d}\,2\pi\delta\left(p^2-m^2\right)\,. \tag{2.67}$$

With the help of the identity

$$\frac{1}{x\pm i\epsilon} = P\frac{1}{x} \mp i\pi\delta(x) \tag{2.68}$$

where P denotes the Cauchy principal value, the arising delta functions may then be expressed in terms of propagators with opposite $i\epsilon$-prescriptions

$$2\pi\,\delta(p^2-m^2) = \frac{i}{p^2-m^2+i\epsilon} - \frac{i}{p^2-m^2-i\epsilon}\,. \tag{2.69}$$

This cut propagator can now be utilized in the usual IBP formalism even allowing for an automated treatment within the Laporta algorithm [528]. The only difference with respect to a normal propagator concerns the cancellation of numerators and denominators. While propagators can usually be removed from the integrand by a corresponding expression in the numerator effectively reducing the original topology to a specific subtopology, the special form of Eq. (2.69) will set the respective integrand to zero when encountering a numerator structure of the type p^2-m^2. This makes sense as it prevents the mixing of integrals with different final-state multiplicities. The master basis of an n-particle cut observable will thus only contain integrals with the same number of cut propagators.

As indicated by the term "master basis", the choice of master integrals is not unique regardless of whether they correspond to standard loop or cut diagrams and with the help of the IBP relations it is always possible to transform to a different set of irreducible integrals. This is quite useful in actual calculations because it allows us to remove so-called spurious poles that may arise when a loop-induced quantity $F(p_i, m_j^2, \epsilon)$ is expressed in terms of master integrals

$$F(p_i, m_j^2, \epsilon) = \sum_k C_k(p_i, m_j^2, \epsilon)\, M_k(p_i, m_j^2, \epsilon)\,. \tag{2.70}$$

Even if $F(p_i, m_j^2, \epsilon)$ is finite (which is not necessarily the case in practice) the rational coefficients $C_k(p_i, m_j^2, \epsilon)$ might still contain $1/\epsilon^n$ poles that will only cancel in the sum over all masters. These poles are not an inherent feature of the considered quantity but of the specific master basis and thus pose no conceptual problem. Nonetheless, they require an evaluation of the corresponding integrals to higher orders in ϵ, a task that can become arbitrarily difficult (or even impossible by current computational standards) for quantities involving complex topologies. It is therefore preferable to avoid these unnecessary complications by changing to a new basis that is free of such spurious poles. Unfortunately, there exists no clear prescription on how to construct such a basis and for complex problems one often has to content oneself with modifying the set of masters such that at least the coefficients of the most complicated integrals are finite.

Once such a basis is found, the next step is to determine the explicit value of the corresponding master integrals usually in the form of a Laurent expansion in the regularization parameter ϵ. To this end, we employ the method of differential equations [529–535] which

profits from a wide selection of well-established solution procedures implemented in various publicly available software packages that allow for an evaluation either in an analytical or purely numerical fashion. It is based on the common observation that for a general Feynman integral it is almost always possible to deduce its asymptotic behavior in a particular kinematic limit whereas the determination of the overall dependence on the masses and external momenta is quite challenging, especially when multiple scales and/or higher loop orders are involved. These are, however, ideal conditions for the use of differential equations which incorporate the complete functional behavior of the integrals once the boundary values are fixed. These boundaries do not even have to lie in the physical spectrum but may correspond to an abstract limit such as an infinite mass or infinite momentum expansion [536], which is a great advantage in actual calculations as these expansion methods allow for an effective separation of scales[17].

The construction of the differential equations again relies heavily on the use of IBP relations, which is the reason why both methods are often employed in combination. The first step is to decide upon a set of differential operators $\mathcal{D}^{(n)}$ that correspond to the independent variables needed to describe the particular process at hand, i. e. the masses and the external momenta. However, since we prefer to deal with scalar quantities, these operators are rather constructed from kinematic invariants than from actual four-momenta. Applying them to the set of master integrals results in linear combinations of integrals with different numerator and denominator powers. Via IBP relations these integrals are then expressed in terms of the original master basis leading to a system of coupled differential equations

$$\mathcal{D}^{(n)}\, M_k(p_i, m_j^2, \epsilon) = \sum_l J_{kl}^{(n)}(p_i, m_j^2, \epsilon)\, M_l(p_i, m_j^2, \epsilon)\,. \tag{2.71}$$

As the IBP reduction respects the topological structure of the integrals and due to the underlying Laporta ordering, the right-hand side of this equation will only contain masters of the same topology or related subtopologies allowing us to bring the square matrix $J_{kl}^{(n)}(p_i, m_j^2, \epsilon)$ into a triangular form. As a consequence, the system of differential equations can be decomposed into smaller subsystems that may be solved iteratively starting from the integral with the lowest number of internal propagators, a strategy that is particularly appealing when aiming at analytical results. Since we are interested in solutions in the form of a Laurent series, it is advantageous to perform the $\epsilon \to 0$ expansion already at the equation level by replacing all quantities in Eq. (2.71) with their respective series representations

$$\begin{aligned} M_k(p_i, m_j^2, \epsilon) &= \sum_{m=p_k^-}^{p_k^+} \epsilon^m\, M_k^{(m)}(p_i, m_j^2) \\ J_{kl}^{(n)}(p_i, m_j^2, \epsilon) &= \sum_{m=p_{kl}^-}^{p_k^+ - p_l^-} \epsilon^m\, j_{kl}^{(n,m)}(p_i, m_j^2)\,. \end{aligned} \tag{2.72}$$

[17] These limits may in certain cases increase the effective number of master integrals due to the necessity to suspend some of the physical constraints, e. g. on-shellness conditions.

The maximum power p_k^+ depends on the requested expansion depth of the problem under consideration whereas the minimum powers are an intrinsic property of the chosen master basis. Despite the fact that the pole structure of the individual integrals is not known prior to their evaluation[18], it is still possible to determine the overall degree of divergence of a given loop order, which acts as a lower bound for p_k^-. In general, a one-loop integral can contain several singularities of different origin, i. e. from different regions of the loop momentum. Higher poles in ϵ will, however, only occur if two or more of these regions overlap. As long as we consider integrals with SM-like propagators[19], this is only the case for soft and collinear divergences, i. e. singularities that appear when the loop momentum vanishes or becomes parallel to a massless external momentum, inducing an overall $1/\epsilon^2$ pole. Since the one-loop integrals serve as building blocks for the higher loop orders, the degree of divergence of a general n-loop integral is at most $2n$ and thus $p_k^- \geq -2n$. In practice, p_k^- can be deduced from the precalculated boundary conditions provided that their kinematic configuration allows for the same singularity structure.

The minimum power p_{kl}^-, on the other hand, is completely specified by the actual system of differential equations and cannot be predicted in advance. It may, in general, assume negative values, which, however, in case of $k = l$ implies that the corresponding integral M_k is not a master. The reason for this is that the lowest order in ϵ of an order-by-order comparison of Eq. (2.71) would contain no differential operator and thus be a regular algebraic equation that uniquely determines the value of $M_k^{(p_k^-)}$. The result can then be used to successively eliminate the differential components in the higher-order equations as well expressing M_k completely in terms of other master integrals (or setting it to zero). So for a true master integral the condition $p_{kk}^- \geq 0$ has to be fulfilled. In case $k \neq l$, Eq. (2.71) may also include purely algebraic relations provided that $p_{kl}^- + p_l^- \leq p_k^-$. The resulting constraints effectively reduce the number of independent variables but are usually ignored in practical applications as their impact on the global computational costs is negligible. They may, however, serve as an additional cross-check.

In order to be able to treat all orders in ϵ simultaneously, the master components $M_k^{(m)}(p_i, m_j^2)$ are grouped into a new vector $\widetilde{M}_k(p_i, m_j^2)$ that satisfies the following differential equation

$$\mathcal{D}^{(n)}\, \widetilde{M}_k(p_i, m_j^2) = \sum_l \tilde{J}_{kl}^{(n)}(p_i, m_j^2)\, \widetilde{M}_l(p_i, m_j^2)\,. \tag{2.73}$$

The square matrix $\tilde{J}_{kl}^{(n)}(p_i, m_j^2)$, which has been constructed from the components $j_{kl}^{(n,m)}(p_i, m_j^2)$, can again be brought into a triangular form through a proper ordering in $\widetilde{M}_k(p_i, m_j^2)$. Hence, it allows for a similar decomposition into subsystems as the original matrix $J_{kl}^{(n)}(p_i, m_j^2, \epsilon)$.

To illustrate how this works in practice, we again consider our toy example, Eq. (2.59), but this time for $p^2 \neq m^2$. In this case we have two master integrals, $I(1,0)$ and $I(1,1)$, that depend on the independent kinematic variables m^2 and p^2. Therefore, we choose the following

[18] It is possible to estimate the highest pole of a Feynman integral using power counting arguments, which may, however, become quite cumbersome for complex topologies.

[19] In effective theories it is possible to have linear propagators of the form $\frac{1}{p\cdot k}$ which can lead to different types of divergences that may overlap with the common UV and IR singularities.

differential operators

$$\mathcal{D}^{(1)} = m^2 \frac{d}{dm^2} \qquad \mathcal{D}^{(2)} = p^2 \frac{d}{dp^2} = \frac{1}{2} p_\mu \frac{d}{dp_\mu} \tag{2.74}$$

that when applied to the master basis yield

$$\begin{aligned} m^2 \frac{d}{dm^2} \begin{pmatrix} I(1,0) \\ I(1,1) \end{pmatrix} &= \begin{pmatrix} 1-\epsilon & 0 \\ \frac{1-\epsilon}{p^2-m^2} & \frac{(2\epsilon-1)m^2}{p^2-m^2} \end{pmatrix} \begin{pmatrix} I(1,0) \\ I(1,1) \end{pmatrix} \\ p^2 \frac{d}{dp^2} \begin{pmatrix} I(1,0) \\ I(1,1) \end{pmatrix} &= \begin{pmatrix} 0 & 0 \\ \frac{\epsilon-1}{p^2-m^2} & \frac{m^2-\epsilon(p^2+m^2)}{p^2-m^2} \end{pmatrix} \begin{pmatrix} I(1,0) \\ I(1,1) \end{pmatrix} \end{aligned} \tag{2.75}$$

Suppose we are interested in a solution up to $\mathcal{O}(\epsilon^0)$. Using power counting arguments it can be shown that $I(1,0)$ and $I(1,1)$ only contain a single UV pole. Consequently, the whole system may be described by the vector

$$\vec{I}(p^2, m^2) = \begin{pmatrix} I^{(-1)}(1,0) \\ I^{(0)}(1,0) \\ I^{(-1)}(1,1) \\ I^{(0)}(1,1) \end{pmatrix} \tag{2.76}$$

that satisfies a new set of differential equations

$$\begin{aligned} m^2 \frac{d}{dm^2} \vec{I}(p^2, m^2) &= \begin{pmatrix} 1 & 0 & 0 & 0 \\ -1 & 1 & 0 & 0 \\ \frac{1}{p^2-m^2} & 0 & \frac{-m^2}{p^2-m^2} & 0 \\ \frac{-1}{p^2-m^2} & \frac{1}{p^2-m^2} & \frac{2m^2}{p^2-m^2} & \frac{-m^2}{p^2-m^2} \end{pmatrix} \vec{I}(p^2, m^2) \\ p^2 \frac{d}{dp^2} \vec{I}(p^2, m^2) &= \begin{pmatrix} 0 & 0 & 0 & 0 \\ 0 & 0 & 0 & 0 \\ \frac{-1}{p^2-m^2} & 0 & \frac{m^2}{p^2-m^2} & 0 \\ \frac{1}{p^2-m^2} & \frac{-1}{p^2-m^2} & -\frac{p^2+m^2}{p^2-m^2} & \frac{m^2}{p^2-m^2} \end{pmatrix} \vec{I}(p^2, m^2) \,. \end{aligned} \tag{2.77}$$

The general solution can be obtained by splitting the system into separate differential equations that are then solved iteratively resulting in

$$\vec{I}(p^2,m^2) = \begin{pmatrix} m^2 & 0 & 0 & 0 \\ -m^2\,\ln m^2 & m^2 & 0 & 0 \\ 1 & 0 & -\left(1-\frac{m^2}{p^2}\right) & 0 \\ \begin{matrix}1-\ln m^2-\\ \left(1-\frac{m^2}{p^2}\right)\ln\left(1-\frac{p^2}{m^2}\right)\end{matrix} & 1 & \begin{matrix}\left(1-\frac{m^2}{p^2}\right)\left(\ln p^2+\right.\\ \left.2\ln\left(\frac{m^2}{p^2}-1\right)\right)\end{matrix} & -\left(1-\frac{m^2}{p^2}\right) \end{pmatrix} \begin{pmatrix} B^{(-1)}(1,0) \\ B^{(0)}(1,0) \\ B^{(-1)}(1,1) \\ B^{(0)}(1,1) \end{pmatrix} . \quad (2.78)$$

When substituting in the boundary vector $\vec{B} = K(\epsilon)\ (1,1,0,0)$, we finally arrive at

$$\begin{aligned} I(1,0) &= K(\epsilon)\,m^2\left(\frac{1}{\epsilon}+1-\ln m^2\right) \\ I(1,1) &= K(\epsilon)\left(\frac{1}{\epsilon}+2-\ln m^2-\left(1-\frac{m^2}{p^2}\right)\ln\left(1-\frac{p^2}{m^2}\right)\right) \end{aligned} \quad (2.79)$$

where the prefactor $K(\epsilon)$ depends on the loop measure $\mathcal{N}_\epsilon$ and does not affect the kinematic dependencies. Note that the result exhibits a rather simple functional behavior, which is a further advantage of working with series representations. While for this example it would be possible to find a solution at general ϵ and expand afterwards, the intermediate result would be a complicated expression containing generalized hypergeometric functions and gamma functions suggesting that such a strategy is not feasible for problems that involve more complex Feynman integrals. Of course, the system size in actual applications is substantially larger with a potentially higher degree of coupling, which might prevent us from finding an exact solution not even in the form of a Laurent series but in such cases it is usually still possible to employ numerical techniques. A treatment at general ϵ, however, inevitably leads to complications when aiming at a numerical evaluation of the differential equations.

This does not apply to the NLO $t\bar{t}$ analysis where the set of differential equations is well-behaved allowing for a purely analytical treatment of the virtual corrections. The key idea is to address both loop and phase space integrations simultaneously such that all master integrals are described by a single variable. In contrast to the LO calculation, which is naturally described in terms of the top-quark velocity, it is in this case more convenient to work with an alternative variable

$$x = \frac{1-\beta}{1+\beta} \quad (2.80)$$

as it leads to a particularly compact form of the final result in terms of harmonic polylogarithms and rational functions in x and $1 \pm x$. The boundary values are obtained either from the known threshold behavior or via Mellin-Barnes techniques [537, 538]. The latter are a useful tool for an effective separation of scales at the integrand level, however, at the cost of introducing additional integrations over some auxiliary parameters. The basic Mellin-Barnes formula reads

$$\frac{1}{(X+Y)^\lambda} = \frac{1}{\Gamma(\lambda)}\,\frac{1}{2\pi i}\int\limits_{-i\infty}^{+i\infty} dz\,\Gamma(z+\lambda)\,\Gamma(-z)\,\frac{Y^z}{X^{\lambda+z}} \quad (2.81)$$

where the integration contour is chosen such that the poles of the gamma functions with argument $+z$ lie left and with argument $-z$ right of it (in the following denoted as left and right poles). Similar to the use of Feynman parameters, the common strategy is to repeatedly apply this relation to the integrand of a given Feynman integral until it is simple enough[20] to perform the loop integration analytically. Take, for instance, our toy example $I(a_1, a_2)$. Using a Mellin-Barnes representation for the massive propagator it can be transformed into a massless integral that can be easily evaluated even for arbitrary powers of the denominators

$$\begin{aligned} I(a_1,a_2) &= \frac{\mathcal{N}_\epsilon}{2\pi i\,\Gamma(a_1)} \int\limits_C dz\,\Gamma(a_1+z)\,\Gamma(-z)\,\left(-m^2\right)^z \int \frac{d^dk}{(2\pi)^d}\,\frac{1}{(k^2)^{a_1+z}}\,\frac{1}{\left((k-p)^2\right)^{a_2}} \\ &= \frac{(-1)^{a_1+a_2}\mathcal{N}_\epsilon\,\pi^{\frac{d}{2}}}{(2\pi)^{d+1}\,(-p^2)^{a_1+a_2-2+\epsilon}}\,\frac{\Gamma(2-\epsilon-a_2)}{\Gamma(a_1)\,\Gamma(a_2)} \\ &\quad \int\limits_C dz\,\frac{\Gamma(a_1+a_2-2+\epsilon+z)\,\Gamma(-z)\,\Gamma(2-\epsilon-a_1-z)}{\Gamma(4-a_1-a_2-2\epsilon-z)}\,\left(-\frac{m^2}{p^2}\right)^z \end{aligned} \tag{2.82}$$

We are now left with the integration over z (with the contour C according to Eq. (2.81)) whose evaluation crucially depends on whether the integral is finite or contains some pole(s) in ϵ. A common feature of the remaining integrals over the auxiliary parameters is that they consist of rational expressions in terms of gamma functions and a possible dependence on the kinematic invariants in form of a power law. If the left and right poles of these gamma functions are well separated, as is for example the case for $a_1 = 2$ and $a_2 = 1$, the corresponding integral is finite and can be computed explicitly by utilizing Cauchy's theorem, i. e. by closing the integration contour and taking residues. This effectively reduces the integration to the evaluation of an infinite sum, which may be brought into a closed form either by hand or with the help of publicly available software for the symbolic manipulation of nested sums such as Summer [539] or Xsummer [540]. Furthermore, the absence of any singularities allows for a safe expansion of the integral in terms of ϵ already at the integrand level, which usually leads to much simpler expressions in the summation of the residues.

This is, however, no longer possible if a left and a right pole coincide in the limit $\epsilon \to 0$ since it would violate the original definition of the integration contour rendering the respective integral divergent. Consider, for instance, the case

$$I(1,1) = \frac{\mathcal{N}_\epsilon\,\pi^{\frac{d}{2}}\,\Gamma(1-\epsilon)}{(2\pi)^{d+1}\,(-p^2)^\epsilon} \int\limits_C dz\,\frac{\Gamma(\epsilon+z)\,\Gamma(-z)\,\Gamma(1-\epsilon-z)}{\Gamma(2-2\epsilon-z)}\,\left(-\frac{m^2}{p^2}\right)^z . \tag{2.83}$$

Apparently, the functions $\Gamma(\epsilon+z)$ and $\Gamma(-z)$ collide for $\epsilon = z = 0$ making it impossible to assign a specific value to this kind of integral. The solution is to work at general ϵ and perform a shift of integration contours such that the left pole at $z = -\epsilon$ becomes a right pole. Mathematically, this amounts to taking the residue at this point

$$\mathrm{Res}_{z=-\epsilon}\,\frac{\Gamma(\epsilon+z)\,\Gamma(-z)\,\Gamma(1-\epsilon-z)}{\Gamma(2-2\epsilon-z)}\,\left(-\frac{m^2}{p^2}\right)^z = \frac{\Gamma(\epsilon)}{\Gamma(2-\epsilon)}\,\left(-\frac{m^2}{p^2}\right)^{-\epsilon} . \tag{2.84}$$

[20] Note that it is no longer possible to discard scaleless integrals when using Mellin-Barnes representations since it would otherwise allow us to set any integral to zero.

The divergent behavior is now completely encoded in the function $\Gamma(\epsilon)$ whose expansion in the limit $\epsilon \to 0$ is well-known. Consequently, the ambiguous situation at $\epsilon = 0$ is resolved for the integration over the new contour C' allowing for an expansion to arbitrary powers of ϵ. The corresponding integral to $\mathcal{O}(\epsilon^0)$ may again be evaluated with the help of Cauchy's theorem yielding

$$\int\limits_{C'} dz \, \frac{\Gamma(\epsilon+z)\,\Gamma(-z)\,\Gamma(1-\epsilon-z)}{\Gamma(2-2\epsilon-z)} \left(-\frac{m^2}{p^2}\right)^z = 2\pi i \underbrace{\sum_{n=0}^{\infty} \frac{1}{(n+1)(n+2)} \left(\frac{p^2}{m^2}\right)^{n+1}}_{1-\left(1-\frac{m^2}{p^2}\right)\ln\left(1-\frac{p^2}{m^2}\right)} . \quad (2.85)$$

Combining these findings results in the expression given in Eq. (2.79). In general, the determination of a suitable integration contour can be become quite tedious, especially when dealing with multiple Mellin-Barnes representations. Fortunately, there exists a very efficient implementation of the algorithm introduced in Ref. [538], the MB package[21] [542], that allows for the shifting of contours and collecting of residues in a fully automated fashion resulting in expressions that can be safely expanded around $\epsilon = 0$ and further processed either analytically or numerically. Another important tool for the simplification of Mellin-Barnes integrals are the two so-called Barnes lemmas

$$\frac{1}{2\pi i} \int\limits_{-i\infty}^{+i\infty} dz \, \Gamma(\lambda_1+z)\,\Gamma(\lambda_2+z)\,\Gamma(\lambda_3-z)\,\Gamma(\lambda_4-z) = \frac{\Gamma(\lambda_1+\lambda_3)\,\Gamma(\lambda_1+\lambda_4)\,\Gamma(\lambda_2+\lambda_3)\,\Gamma(\lambda_2+\lambda_4)}{\Gamma(\lambda_1+\lambda_2+\lambda_3+\lambda_4)}$$

$$\frac{1}{2\pi i} \int\limits_{-i\infty}^{+i\infty} dz \, \frac{\Gamma(\lambda_1+z)\,\Gamma(\lambda_2+z)\,\Gamma(\lambda_3+z)\,\Gamma(\lambda_4-z)\,\Gamma(\lambda_5-z)}{\Gamma(\lambda_6+z)} = \frac{\Gamma(\lambda_1+\lambda_4)\,\Gamma(\lambda_2+\lambda_4)\,\Gamma(\lambda_3+\lambda_4)\,\Gamma(\lambda_1+\lambda_5)\,\Gamma(\lambda_2+\lambda_5)\,\Gamma(\lambda_3+\lambda_5)}{\Gamma(\lambda_1+\lambda_2+\lambda_4+\lambda_5)\,\Gamma(\lambda_1+\lambda_3+\lambda_4+\lambda_5)\,\Gamma(\lambda_2+\lambda_3+\lambda_4+\lambda_5)} \quad (2.86)$$

that, depending on the actual form of the integrand[22], may be employed to eliminate one or more of the auxiliary integrations. An aspect particularly interesting for the determination of boundary conditions for a set of master integrals, is, however, the possibility to perform asymptotic expansions in the kinematic variables, especially when there is a clear hierarchy of scales involved in the considered problem. Since the functional dependence of the integrand on these variables is usually given in form of a power law, as for example in Eq. (2.83), the evaluation of the corresponding integral via Cauchy's theorem will automatically result in a power series expansion provided that the integration contour has been chosen appropriately.

[21] The original package has meanwhile been extended to include a collection of different MB Tools [541] for the efficient treatment of Mellin-Barnes integrals.

[22] Sometimes it might be necessary to perform a linear transformation before being able to apply a Barnes lemma. A routine for the automated determination of such a transformation (if possible) is also included in the MB Tools package.

Due to the intrinsic ordering it is then sufficient to determine a finite number of residues, which leads to significant simplifications when dealing with multi-scale integrals and/or multiple Mellin-Barnes representations as we will see later for the virtual NNLO corrections. At NLO the situation is different since one only has to cope with integrals of a single variable x. Still, the evaluation of these integrals in some asymptotic limit may become quite complex because of the additional phase space integration and Mellin-Barnes techniques provide a valuable tool to address these challenges.

After combining the results of the differential equations with the boundary conditions the explicit values for master integrals can be inserted into the one-loop amplitudes yielding the bare virtual NLO corrections. In order to employ this result in total cross section predictions, it still requires UV renormalization as well as the decoupling of heavy-quark loops. At this level of perturbation theory, the latter contribution is, however, proportional to $\ln(\mu_R^2/m_t^2)$ and thus already accounted for in the scale-controlling functions $\hat{\sigma}_{ij}^{(1,1,0)}$. Due to the multiplicative nature of the renormalization procedure, it can be equally well applied directly at the cross section level. The corresponding counterterms for the quark annihilation and gluon fusion channel read[23]

$$\begin{aligned}
\hat{\sigma}_{q\bar{q}}^{\mathrm{CT}} &= \frac{\hat{\sigma}_{q\bar{q}}^{(0)}}{\pi}\left(Z_{\alpha_s}^{(1)} + Z_Q^{(1)}\right) = \frac{\hat{\sigma}_{q\bar{q}}^{(0)}}{6\pi\epsilon}\left(-9\,C_F - 11\,C_A + 4\,T_F\,n_f - 12\,C_F\,\epsilon\right) \\
\hat{\sigma}_{gg}^{\mathrm{CT}} &= \frac{\hat{\sigma}_{gg}^{(0)}}{\pi}\left(Z_{\alpha_s}^{(1)} + Z_Q^{(1)} + Z_g^{(1)}\right) + \frac{\hat{\sigma}_{gg}^{(0),\,Z_m}}{\pi} Z_m^{(1)} \\
&= \frac{\hat{\sigma}_{gg}^{(0)}}{6\pi\epsilon}\left(-9\,C_F - 11\,C_A + 4\,T_F\,n_l - 12\,C_F\,\epsilon\right) - \frac{\hat{\sigma}_{gg}^{(0),\,Z_m}}{2\pi\epsilon}\left(3\,C_F + 4\,C_F\,\epsilon\right)
\end{aligned} \tag{2.87}$$

where $Z_{\alpha_s}^{(n)} \equiv Z_{\alpha_s}^{(n_f),(n)}$ and the contributions from renormalization of the light-quark wave function vanish at NLO since the relevant diagrams that enter $Z_q^{(1)}$ are completely scaleless. Furthermore, the $q\bar{q}$-channel does not require mass renormalization as the LO diagram does not contain internal top-quark lines. The gluonic counterterm, on the other hand, receives contributions from diagrams with additional propagator insertions, denoted as $\hat{\sigma}_{gg}^{(0),Z_m}$, which are, however, no longer proportional to the regular Born cross section. This is due to the fact that, while the individual diagrams can be reduced to the single propagator case, not all diagrams are affected by mass renormalization leading to a different composition of color structures. Nonetheless, the evaluation itself remains trivial such that the construction of the gg counterterm poses no serious computational problem. Combining both the bare results and the renormalization contributions, we end up with the UV-finite virtual corrections, which, however, still contain IR poles starting at $1/\epsilon^2$. As we will see in section 3.1, it is possible to predict these poles in advance such that, in principle, only the finite parts constitute a genuine NLO effect.

[23] Note that, unlike for the amplitudes and partonic cross sections, the expansion of the UV renormalization constants is, as indicated in Eq. (2.23), given in terms of $\alpha_s^{(n_f)}/2\pi$.

The real corrections

The NLO real corrections consist of LO diagrams with an additional parton in the final state, which may be achieved by either appending a further gluon line or by splitting an existing external gluon into a quark pair. In contrast to the virtual corrections where potential divergences already arise at the amplitude level, the corresponding real-emission matrix elements are finite for generic momentum configurations and only in certain corners of phase space they reveal their singular nature. Since we are dealing with an inclusive quantity, it is thus necessary to introduce a regularization procedure for the phase space integration as well. In CDR the respective n-particle phase space is given as

$$dP_n^{(ij)} = \frac{\rho}{8\, c_i c_j s_i s_j} \left(\frac{e^{\gamma_E}\mu_R^2}{4\pi}\right)^{(n-1)\epsilon} \underbrace{\prod_{m=3}^{n+2} \frac{d^{d-1}p_m}{(2\pi)^{d-1} 2\, E_m} (2\pi)^d\, \delta^{(d)}\left(p_1 + p_2 - \sum_{m=3}^{n+2} p_m\right)}_{d\Phi_n} \,. \tag{2.88}$$

Here, the normalization has been chosen such that the dimensionality of all cross-section-type contributions, i. e. legit combinations of phase space integration and squared matrix element, is preserved. In $t\bar{t}$ production the divergent behavior can be traced back to the case where the momentum of the additional parton either vanishes or becomes parallel to the incoming momenta p_1 and p_2. Hence, it would be sufficient to treat only this momentum in d dimensions but in practice it is usually more convenient to handle all momenta in the same manner. The corresponding contributions to the partonic cross section are then given by

$$\hat{\sigma}_{ij}^R(\beta) = \int dP_3^{(ij)}\, \langle \mathcal{M}_{ijk}^{(0)} | \mathcal{M}_{ijk}^{(0)} \rangle \,, \tag{2.89}$$

which may be directly employed in an analytic evaluation, for instance, by expressing the phase space integration in terms of cut diagrams and applying the same strategy as for the virtual corrections, i. e. IBP reduction and a subsequent computation of the master integrals via differential equations [213]. As anticipated, the quark annihilation and gluon fusion channels contain poles of order $1/\epsilon^2$ whereas the quark-gluon channel is only affected by initial-state collinear divergences yielding merely a single pole. This is due to the fact that the emitted parton is a quark rather than a gluon and hence does not induce any soft singularities in the scattering process. The reason for this is that a potentially softly diverging propagator will always be compensated by the Dirac/spinor structure in the numerator. Therefore, soft divergences can be exclusively associated with the emission of gluons.

Unlike the loop-induced results, the real contributions cannot be brought entirely into a closed form in terms of standard special functions such as harmonic polylogarithms, which stresses the mathematical complexity of this analytical analysis. In general, such an analytical treatment is, however, not feasible, especially when considering more exclusive observables as, for example, differential distributions, and one has to resort to numerical evaluation techniques. Then the question that naturally arises is how to perform a numerical integration in arbitrary d-dimensions or, in other words, how to extract the singular behavior such that the IR poles can be explicitly canceled with the virtual and collinear-factorization contributions. There have been different proposals to solve this issue but the concept that ultimately prevailed was

the use of subtraction methods as they may be applied to arbitrary processes and, moreover, allow for a numerically stable and efficient implementation [543, 544]. The main idea is to regulate the real-emission integrand $d\hat{\sigma}^R_{n+1} = d\Phi_{n+1}\ \langle \mathcal{M}^{(0)}_{n+1} | \mathcal{M}^{(0)}_{n+1} \rangle$ (with $n+1$ external particles) in the singular limits by introducing a suitable subtraction term $d\hat{\sigma}^S_{n+1}$ such that the resulting integral can be evaluated in the physical $d = 4$ dimensions

$$\hat{\sigma}^R_{n+1} = \int \left(d\hat{\sigma}^R_{n+1} - d\hat{\sigma}^S_{n+1} \right)_{\epsilon=0} + \int d\hat{\sigma}^I_n \,. \tag{2.90}$$

The pole structure is then completely encoded in the integrated subtraction term

$$d\hat{\sigma}^I_n = \int_1 d\hat{\sigma}^S_{n+1} \,, \tag{2.91}$$

which is obtained by an integration over the one-particle phase space of the unresolved parton. In order for this approach to work, $d\hat{\sigma}^S_{n+1}$ has to fulfill two conditions. On the one hand, it has to correctly mimic the IR behavior of $d\hat{\sigma}^R_{n+1}$, on the other hand, it has to be simple enough to be at least partially integrated analytically thus allowing for an explicit expansion in terms of ϵ. Interestingly, it are the fundamental properties of QCD itself that provide all necessary ingredients to construct such a subtraction term. As IR divergences are, diagrammatically spoken, solely related to insertions on the external legs, they can be factorized from the squared matrix elements in the singular limits

$$\begin{aligned} &\langle \mathcal{M}^{(0)}_{n+1}(\ldots, p_i, p_j, \ldots) | \mathcal{M}^{(0)}_{n+1}(\ldots, p_i, p_j, \ldots) \rangle \xrightarrow{\text{IR}} \\ &\qquad 4\pi\, {\mu_R}^{2\epsilon}\, \alpha_s\ \langle \mathcal{M}^{(0)}_n(\ldots, p_i + p_j, \ldots) | \boldsymbol{\mathcal{O}}^{\text{IR},(0)}_{a_i a_j} | \mathcal{M}^{(0)}_n(\ldots, p_i + p_j, \ldots) \rangle \,. \end{aligned} \tag{2.92}$$

The IR operator $\boldsymbol{\mathcal{O}}^{\text{IR},(0)}_{a_i a_j}$ acts on the spin and color space of the reduced amplitudes $|\mathcal{M}_n\rangle$ and depends only on the type of IR limit and particles $a_k = q, \bar{q}, g$ involved but not on the details of the underlying hard scattering process. Thus, it enables us to predict the IR behavior of NLO QCD reactions with an arbitrary number of external partons, which is one of the main reason why subtraction methods are so successful. What is more, the particularly convenient form of the IR approximation, proportional to the spin- or color-correlated LO results, also allows for an immediate factorization of the phase space, which simplifies the determination of the integrated subtraction terms considerably. In the limit

$$p_j^\mu \to \lambda\, q^\mu \qquad \text{where} \qquad \lambda \to 0 \tag{2.93}$$

the IR operator is given in terms of the so-called LO eikonal current $\mathbf{J}^{\mu\,(0)}_a(q)$ [545, 546] that governs the emission of soft gluons from both massless and massive external lines

$$\begin{aligned} \boldsymbol{\mathcal{O}}^{\text{Soft},(0)}_{a_i a_j} = \frac{\mathbf{J}^{(0)\,\dagger}_a \cdot \mathbf{J}^{(0)}_a}{\lambda^2} &= \frac{1}{\lambda^2} \left(\sum_{i=1}^n \mathbf{T}^a_i \frac{p_i^\mu}{p_i \cdot q} \right) \left(\sum_{k=1}^n \mathbf{T}^a_k \frac{p_{k\,\mu}}{p_k \cdot q} \right) \\ &= \frac{2}{\lambda^2} \sum_{i=1}^n \frac{1}{p_i \cdot q} \sum_{k=1}^n \mathbf{T}_i \cdot \mathbf{T}_k \frac{p_i \cdot p_k}{(p_i + p_k) \cdot q} \,. \end{aligned} \tag{2.94}$$

The entire dependence on the particle content a_k is contained in the charge operators $\mathbf{T}_i^a$, which act on the color indices of the i-th particle and assume the following form:

$$\begin{aligned}
(\mathbf{T}^a)_{bc} &= -\,i\,f^{abc} && \text{for gluons} \\
(\mathbf{T}^a)_{bc} &= \;\; T^a_{bc} && \text{for outgoing quark/incoming anti-quark} \\
(\mathbf{T}^a)_{bc} &= -\,T^a_{cb} && \text{for incoming quark/outgoing anti-quark}
\end{aligned} \tag{2.95}$$

Due to color conservation, which implies

$$\sum_{i=1}^{n} \mathbf{T}_i^a \; |\mathcal{M}_n\rangle = 0 \,, \tag{2.96}$$

not all combinations of $\mathbf{T}_i \cdot \mathbf{T}_j = \mathbf{T}_i^a \, \mathbf{T}_j^a$ in Eq. (2.94) are independent. In a colored 2-to-2 process such as top-quark pair production all charge projectors can, for instance, be expressed in terms of $\mathbf{T}_1 \cdot \mathbf{T}_2$, $\mathbf{T}_1 \cdot \mathbf{T}_3$ and the Casimir operators $\mathbf{T}_i \cdot \mathbf{T}_i = \mathbf{T}_i^2 = C_i$ ($C_i = C_F$ for quarks and $C_i = C_A$ for gluons).

In the collinear limit, which is conveniently defined by introducing the auxiliary vectors p^μ, $k_\perp^\mu$ and n^μ such that

$$\begin{aligned}
p_i^\mu = z p^\mu + k_\perp^\mu - \frac{k_\perp^2}{z}\,\frac{n^\mu}{2p\cdot n} \qquad & p_j^\mu = (1-z)p^\mu - k_\perp^\mu - \frac{k_\perp^2}{1-z}\,\frac{n^\mu}{2p\cdot n} \\
\text{with} \qquad & p^2 = n^2 = p\cdot k_\perp = n \cdot k_\perp = 0 \\
\Longrightarrow \qquad & 2p_i \cdot p_j = -\frac{k_\perp^2}{z(1-z)} \;\;, \;\; k_\perp \to 0
\end{aligned} \tag{2.97}$$

the IR operator is given as [547]

$$\boldsymbol{\mathcal{O}}^{\text{Col.},(0)}_{a_i a_j} = \frac{\hat{P}^{ss'\,(0)}_{a_i a_j}(z, k_\perp, \epsilon)}{p_i \cdot p_j} \tag{2.98}$$

where $\hat{P}^{ss'\,(0)}_{a_i a_j}(z, k_\perp, \epsilon)$ are the d-dimensional, spin-dependent LO Altarelli-Parisi splitting functions[24] for the generic process

$$a(p) \to a_i \left(zp + k_\perp + \mathcal{O}\left(k_\perp^2\right)\right) + a_j \left((1-z)p - k_\perp + \mathcal{O}\left(k_\perp^2\right)\right) \,. \tag{2.99}$$

[24] The more familiar splitting functions $P_{ij}^{(0)}(x)$, responsible for the leading PDF evolution, can be obtained from these expressions by performing a spin average and adding loop-induced corrections. Note, however, that the naming convention is different and, hence, the indices a_k have to be adjusted accordingly.

They act on the spin indices s, s' (μ, ν in the gluonic case) of the parent parton a and read [210]

$$\hat{P}_{qg}^{ss'}(z,k_\perp,\epsilon) = \delta_{ss'}\,C_F\left(\frac{1+z^2}{1-z}-\epsilon(1-z)\right) \tag{2.100}$$

$$\hat{P}_{gq}^{ss'}(z,k_\perp,\epsilon) = \delta_{ss'}\,C_F\left(\frac{1+(1-z)^2}{z}-\epsilon z\right) \tag{2.101}$$

$$\hat{P}_{qq}^{\mu\nu}(z,k_\perp,\epsilon) = T_F\left(-g^{\mu\nu}+4z(1-z)\frac{k_\perp^\mu k_\perp^\nu}{k_\perp^2}\right) \tag{2.102}$$

$$\hat{P}_{gg}^{\mu\nu}(z,k_\perp,\epsilon) = 2C_A\left(-g^{\mu\nu}\left(\frac{z}{1-z}+\frac{1-z}{z}\right)-2(1-\epsilon)z(1-z)\frac{k_\perp^\mu k_\perp^\nu}{k_\perp^2}\right)\,. \tag{2.103}$$

Note that the above momentum assignment assumes the collinear particles to be in the final state. The case of initial-state radiation relevant for the calculation of the $t\bar{t}$ cross section can, however, be easily recovered by using variable transformations and exploiting crossing symmetries. An interesting feature of the collinear splittings is their dependence on the explicit nature of the participating partons as indicated by the indices $a_{i,j}$. In consequence, the IR limit of a particular matrix element may be described by a stripped amplitude (i. e. with one parton less) belonging to a different partonic production mode. This is, for instance, the case for the quark-gluon channel which does not receive any $\mathcal{O}(\alpha_s^2)$ contributions and therefore in the collinear limit is related to $\hat{\sigma}_{q\bar{q}}^{(0)}$ and $\hat{\sigma}_{gg}^{(0)}$. This is, however, not surprising as it shows a similar behavior under collinear renormalization, which due to the absence of soft singularities is the only remaining source of IR poles available for the construction of a finite partonic cross section.

As the soft and collinear limits commute, both IR operators coincide in the overlapping soft-collinear regime, which is reached when q becomes parallel to p_i in Eq. (2.94) or $z \to 0, 1$ in Eq. (2.98). Consequently, the resulting operator is completely diagonal in spin and color, i. e. directly proportional to the square of the LO matrix elements, free of any correlation effects. As we will see later, this soft-collinear behavior is the origin of the double-logarithmic velocity enhancements present in the NLO partonic cross sections and, in fact, has been used to predict these terms analytically without any further knowledge of the full result. The equality of $\boldsymbol{\mathcal{O}}_{a_i a_j}^{\text{Soft},\,(0)}$ and $\boldsymbol{\mathcal{O}}_{a_i a_j}^{\text{Col.},\,(0)}$ in this limit also leads to practical implications for the construction of subtraction terms since one has to be careful to avoid potential double-counting effects.

While the IR operators can be used to unambiguously define the divergence structure of real-emission amplitudes, a subtraction term may in general also contain finite pieces that govern its behavior away from the singular limits. Similar to the definition of the renormalization constants, each choice of these non-divergent terms will specify a different subtraction scheme, the most famous certainly being Catani-Seymour dipole subtraction [548, 549] and Frixione-Kunszt-Signer (FKS) subtraction [550]. Although the final theory predictions are, of course, independent of a particular scheme choice, the success of the intermediate calculation may rely crucially on the actual form of the subtraction terms in all corners of phase space since they affect the efficiency and stability of resulting subtraction algorithm. In the Catani-Seymour

approach they are given in terms of a phase space convolution

$$d\hat{\sigma}_{n+1}^{S} = \sum_{\{ij,k\}} d\hat{\sigma}_{n}^{LO} \otimes d\mathcal{V}_{ij,k} \tag{2.104}$$

where the universal dipole factors $d\mathcal{V}_{ij,k}$ depend on the momenta and quantum numbers of two "emitter" partons i and j as well as a "spectator" parton k. They allow for a smooth interpolation between the various IR limits and thus regulate all divergences simultaneously. Their actual form depends on whether the participating partons are in the initial or final state and has been determined in Ref. [548] and Ref. [549] for the massless and massive case respectively. The latter is, in principle, only necessary to handle soft singularities but in practice there may also be large contributions from so-called quasi-collinear emissions, i. e. in the limit where the mass of the radiating parton is substantially smaller than the kinematic scale of the hard scattering. These emissions need to be properly regulated since otherwise they might spoil the numerical convergence of the integration routines. In general, the computational costs for the evaluation of a particular observable with a Catani-Seymour-based algorithm scale cubically with the number of external particles. This makes it less attractive for processes with large parton multiplicities. A different but somewhat related subtraction scheme originally developed by Nagy and Soper [551], designed for the use in an improved parton shower formalism, reduces this scaling to a mere quadratic dependence at the price of introducing more complicated subtraction terms, which makes the integration over the phase space of the unresolved parton more challenging. This may, however, be compensated by using semi-numerical methods to extract the explicit pole structure [552] rendering this approach a valuable alternative to the standard Catani-Seymour subtraction.

The FKS scheme, another widely used subtraction method, also scales quadratically with the number of particles but is conceptually inherently different. The main idea is to decompose the phase space integration such that each partition contains at most one soft and/or collinear divergence, which can then be trivially regularized by means of plus distributions[25]. This procedure can be implemented in a numerically highly-efficient manner [553] as it only requires the evaluation of two distinct kinematic configurations per sector and phase space point and is furthermore naturally suited for parallelization. At NNLO we will encounter an extension of this method to the case of double-real radiation.

NLO predictions for the partonic and hadronic cross sections

Combining virtual and real corrections with the contributions from collinear renormalization, we finally arrive at the full NLO partonic cross sections. As the resulting expressions are quite lengthy, we refrain from quoting them here explicitly and refer the reader to Ref. [213]. Their β-dependence for $\mu_R = \mu_F = m_t$ is shown in Fig. 2.9 revealing the full kinematic structure of the $\mathcal{O}(\alpha_s^3)$ contributions, which, as anticipated, is far more complex than for the LO result. For the gluon fusion and quark annihilation channels the bulk of the corrections still comes from intermediate velocities, however with a clear trend towards threshold production. The reason for this are two different types of enhancements. The first are non-relativistic effects of

[25] For a definition, see Eq. (3.139).

the final-state top-quark pair that can be described by effective interaction potentials, most notably the Coulomb potential. At NLO these contributions manifest themselves through inverse powers of β relative to the Born cross section. The second source of threshold enhancements are soft-gluon emissions that lead to logarithms of the velocity up to $\ln^2\beta$. Both contributions factorize for $\beta \to 0$ as we will see in section 3.1.1 and thus their explicit form could actually be derived prior to the knowledge of the fully analytical result. This is important as it allows us to resum these terms to all orders in perturbation theory, which further stabilizes the total cross section predictions. Using the color decomposition introduced in section 2.3.1 the NLO threshold expansion reads

$$
\begin{aligned}
\bar{\sigma}^{\mathrm{NLO}}_{gg,\mathbf{1}}(\beta) &= \frac{\bar{\sigma}^{(0)}_{gg,\mathbf{1}}(\beta)}{\pi}\left[C_F\,\frac{\pi^2}{2\beta} + 8\,C_A\ln^2\beta + C_A(-16+24\ln 2)\ln\beta + C_F\left(-5+\frac{\pi^2}{4}\right)\right.\\
&+ C_A\left(17-\frac{7\pi^2}{12}+16\ln^2 2-24\ln 2\right) + \ln\left(\frac{\mu_R^2}{m_t^2}\right)\left(\frac{11}{6}\,C_A-\frac{2}{3}\,T_F\,n_l\right)\\
&+ \left.\ln\left(\frac{\mu_F^2}{m_t^2}\right)\left(-4\,C_A\ln\beta + C_A\left(\frac{13}{6}-4\ln 2\right)+\frac{2}{3}\,T_F\,n_l\right)+\mathcal{O}(\beta)\right]\\
\bar{\sigma}^{\mathrm{NLO}}_{gg,\mathbf{8_S}}(\beta) &= \frac{\bar{\sigma}^{(0)}_{gg,\mathbf{8_S}}(\beta)}{\pi}\left[\left(C_F-\frac{C_A}{2}\right)\,\frac{\pi^2}{2\beta} + 8\,C_A\ln^2\beta + C_A(-18+24\ln 2)\ln\beta\right.\\
&+ C_A\left(21-\frac{17\pi^2}{24}-26\ln 2+16\ln^2 2\right) + C_F\left(-5+\frac{\pi^2}{4}\right)\\
&+ \ln\left(\frac{\mu_F^2}{m_t^2}\right)\left(-4\,C_A\ln\beta + C_A\left(\frac{13}{6}-4\ln 2\right)+\frac{2}{3}\,T_F\,n_l\right)\\
&+ \left.\ln\left(\frac{\mu_R^2}{m_t^2}\right)\left(\frac{11}{6}\,C_A-\frac{2}{3}\,T_F\,n_l\right)+\mathcal{O}(\beta)\right]\\
\bar{\sigma}^{\mathrm{NLO}}_{q\bar{q},\mathbf{8}}(\beta) &= \frac{\bar{\sigma}^{(0)}_{q\bar{q},\mathbf{8}}(\beta)}{\pi}\left[\left(C_F-\frac{C_A}{2}\right)\,\frac{\pi^2}{2\beta} + 8\,C_F\ln^2\beta + \left(C_F\,(-16+24\ln 2)-2\,C_A\right)\ln\beta\right.\\
&+ C_F\left(8-\frac{\pi^2}{3}-21\ln 2+16\ln^2 2\right) + C_A\left(\frac{77}{9}-\frac{\pi^2}{4}-5\ln 2\right)\\
&+ T_F\,n_l\left(-\frac{10}{9}+\frac{4}{3}\ln 2\right)-\frac{8}{9}+\ln\left(\frac{\mu_R^2}{m_t^2}\right)\left(\frac{11}{6}\,C_A-\frac{2}{3}\,T_F\,n_l\right)\\
&+ \left.\ln\left(\frac{\mu_F^2}{m_t^2}\right)\left(-4\,C_F\ln\beta + C_F\left(\frac{5}{2}-4\ln 2\right)\right)+\mathcal{O}(\beta)\right]\,.
\end{aligned}
\tag{2.105}
$$

The remaining color structures, i. e. the antisymmetric gluon octet and the $q\bar{q}$-singlet, are further suppressed and do not contribute to the leading β behavior. The same also applies to the quark-gluon channel, which contains neither soft nor Coulomb gluons and therefore vanishes at threshold. Note that, while it is possible to predict the singular terms of the β-expansion, the constant coefficients in Eq. (2.105) have to be determined in a different manner. In fact, there existed two contradicting results for these terms, a numerical approximation [211] and a value extracted from studies on quarkonium production [554], and the situation could

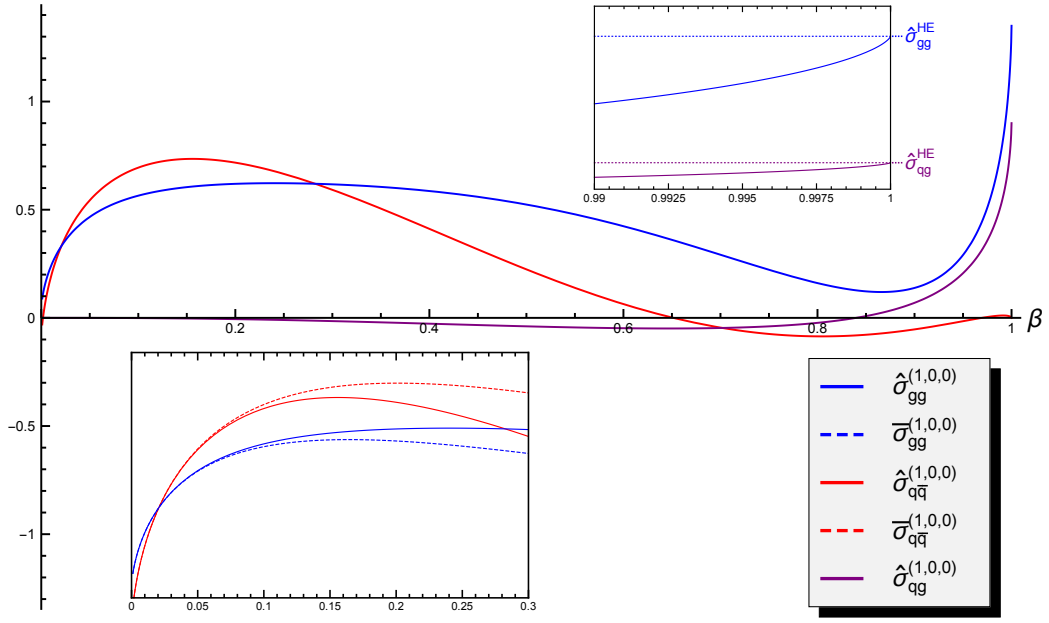

Figure 2.9: *The NLO partonic cross sections* $\hat{\sigma}_{ij}^{(1,0,0)}$ *(solid) as well as their respective threshold (dashed) and high-energy (dotted) limits. The number of light flavors has been set to* $n_l = 5$*. For the gluon fusion channel the combined threshold expansion is given as* $\bar{\sigma}_{gg}^{\mathrm{NLO}} \equiv \bar{\sigma}_{gg,\mathbf{1}}^{\mathrm{NLO}} + \bar{\sigma}_{gg,\mathbf{8_S}}^{\mathrm{NLO}}$*. The result of the quark-gluon channel has been rescaled by a factor of* 3 *for improved visibility.*

only be resolved after the fully analytical NLO analysis became available. This was an important step towards higher-precision cross section predictions since the numerical impact of these coefficients, although being subleading in β, may be significant when considering resummation effects.

Similar to the LO case, the threshold approximation fails to adequately describe the shape of the cross section curves for intermediate and large velocities, especially for the quark annihilation channel. While the β-expansion is positive over the whole physical range, the full result becomes negative at $\beta \approx 0.65$, which leads to cancellation effects when calculating the total cross section. This applies even more to the quark-gluon channel, which is dominated by collinear radiation resulting in negative cross section values over nearly the whole β-range becoming positive only above $\beta \approx 0.85$. Thus, it will crucially depend on the shape of the partonic flux whether the overall effect of this production mode on $\sigma_{t\bar{t}}^{\mathbf{tot}}$ is enhancing or diminishing. The logarithmic rise at the ultra-relativistic end of the spectrum may again be traced back to t-channel gluon exchange, a behavior that can be observed for the gluon fusion channel as well. While the functional dependence in the high-energy limit can only be determined through an explicit evaluation of the partonic cross sections, the endpoint of the t-channel enhancements can actually be predicted from high-energy factorization

and BFKL evolution [555]

$$\begin{aligned} \hat{\sigma}_{qg}^{\mathrm{HE}}(\rho) &= \frac{77}{225} N_c - \frac{41}{108} \frac{1}{N_c^2} \\ \hat{\sigma}_{gg}^{\mathrm{HE}}(\rho) &= \frac{2C_A}{C_F} \hat{\sigma}_{qg}^{\mathrm{HE}}(\rho) \,. \end{aligned} \tag{2.106}$$

As indicated, both channels are not independent but their ratio is related to the color charge of the external line associated with the gluon exchange [211]. The additional factor of 2 is due to the fact that in the purely gluonic case both initial states may contribute. Despite the fact that these high-energy constants are irrelevant for phenomenological applications at current collider experiments, they still serve as an important cross-check of the analytical result at this end of the β-spectrum.

In order to adequately assess the impact of the partonic results on the total cross section, in Fig. 2.10 we again consider the corresponding product of partonic flux and cross section for the Tevatron and the LHC at 8 TeV. At the former collider the quark annihilation channel provides the largest portion of the NLO corrections although it loses some of its dominant behavior compared to the LO result. The reason for this are the negative cross section contributions at the upper end of the spectrum that lead to a partial compensation of the positive corrections in the low and intermediate range. This cancellation effect is even more significant at the LHC where the peak position of the flux factor is shifted further towards $\beta = 1$. The quark-gluon channel suffers from a similar problem albeit with negative and positive contributions interchanged. Therefore, its overall contribution to $\sigma_{t\bar{t}}^{\mathrm{tot}}$ is negative for both of the selected collider setups. It may, however, be anticipated that qg corrections will eventually become positive as the operating energy of the LHC is further increased since the fluxes will then be gradually shifted towards the large β regime. The gluon fusion channel, on the other hand, is positive over the entire physical velocity range with the overall size of the NLO corrections increasing with the available collider energy as well. Its relative contribution to the total cross section is therefore further enhanced with respect to the LO case, irrespective of the particular collider setup, making it by far the most dominant source of top-quark pairs at the LHC and also increasingly more important for the Tevatron.

This becomes particularly obvious when looking at the integrated results in Tab. 2.3. At the Tevatron the NLO gluon fusion results make up almost 50% of the $q\bar{q}$ corrections whereas at LO it was merely about 8%. Nevertheless, the overall effect of going to NLO is rather modest amounting to only a 1% increase of the total cross section. This is not simply because of the cancellation effects at the partonic level but also due to the differences in the LO and NLO flux factors and coupling constant. At the LHC the situation is quite different with NLO corrections that lead to a remarkably constant increase of $\sigma_{t\bar{t}}^{\mathrm{tot}}$ of approximately 30% regardless of the collision energy. As expected, the greatest share can be attributed to gluonic production with the remaining channels becoming less and less important as the energy is increased. Interestingly, though, the quark-gluon channel not only becomes positive but it even surpasses the NLO $q\bar{q}$ corrections at 14 TeV. The reason for this are the t-channel enhancements that ultimately dominate over the negative cross section contributions.

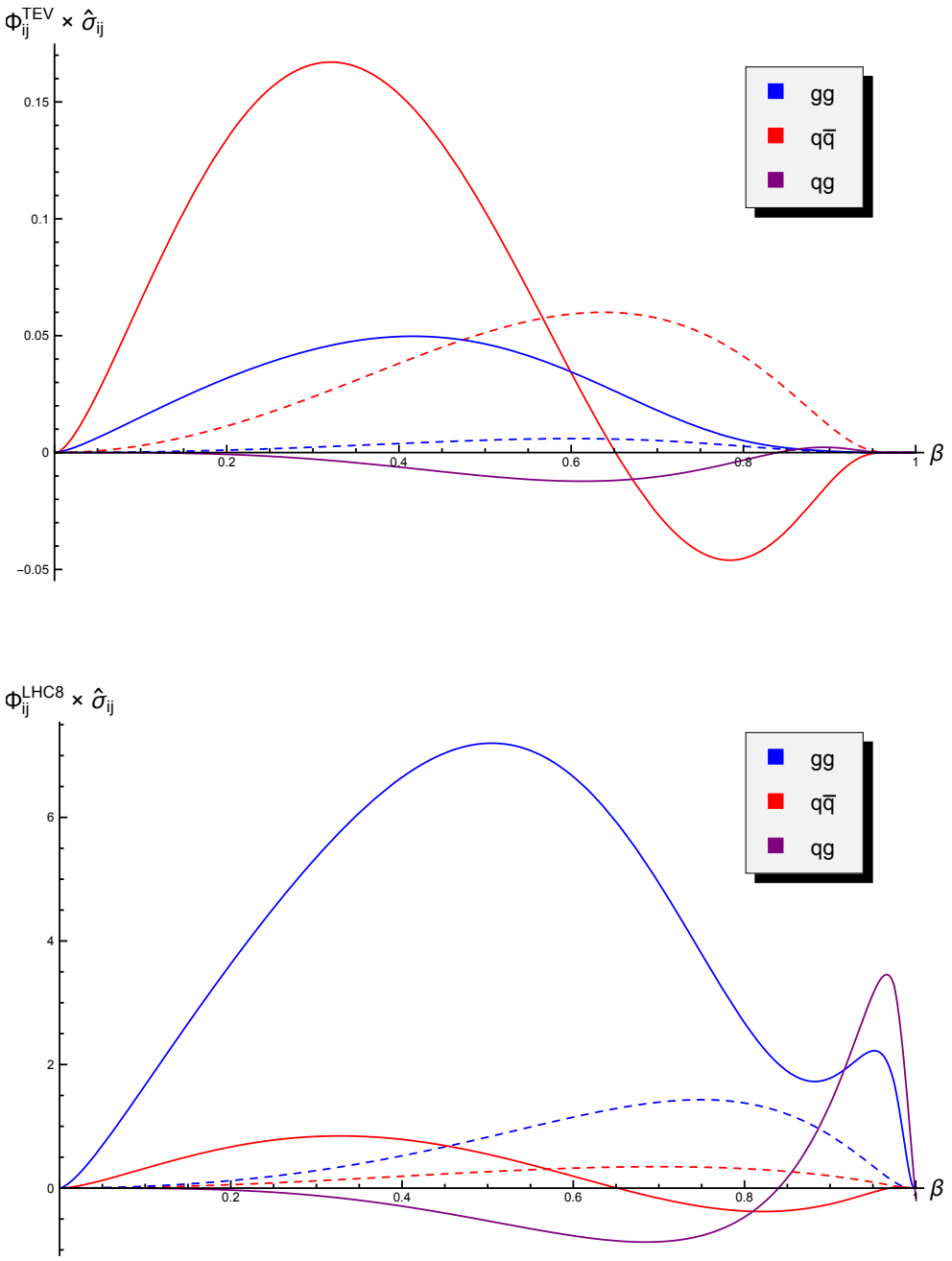

Figure 2.10: *Contribution of the individual production modes to* $\sigma_{t\bar{t}}^{tot}$ *at LO (dashed) and NLO (solid) in QCD for the Tevatron (top) and the LHC (bottom) at* 8 TeV (MSTW2008 *at 68% C.L. [231],* $\mu_R = \mu_F = m_t = 173.3\,\text{GeV}$, $n_l = 5$).

Common to both colliders is the good perturbative convergence, all NLO predictions lie within the error of the LO results, and the dramatic reduction of the scale dependence to a level of 11-13%, which confirms our original assumption that $t\bar{t}$ productions can be very well described perturbatively. The only exception is the positive scale error at the Tevatron, which amounts to only about 5%, an effect that is, however, entirely accidental and has no

	Tevatron [pb]	LHC			
		7 TeV [pb]	8 TeV [pb]	13 TeV [pb]	14 TeV [pb]
$q\bar{q}$	$0.974^{+0.691}_{-1.728}$	$3.596^{+4.004}_{-7.947}$	$4.387^{+5.138}_{-9.972}$	$8.58^{+11.60}_{-20.91}$	$9.46^{+13.01}_{-23.21}$
gg	$0.4176^{+0.0649}_{-0.1795}$	$48.74^{+12.10}_{-25.71}$	$70.26^{+17.45}_{-36.47}$	$235.3^{+56.1}_{-110.4}$	$279.1^{+65.7}_{-128.2}$
qg	$-0.0743^{+0.0876}_{-0.0542}$	$-0.92^{+14.90}_{-9.17}$	$-0.48^{+21.65}_{-13.38}$	$7.01^{+72.98}_{-46.04}$	$9.65^{+86.38}_{-54.69}$
$\sum_{ij}$ NLO	$1.317^{+0.670}_{-1.820}$	$51.42^{+4.95}_{-18.76}$	$74.16^{+6.65}_{-24.79}$	$250.9^{+16.7}_{-58.3}$	$298.2^{+18.8}_{-65.0}$
$\sigma_{t\bar{t}}^{\mathbf{tot},\,\mathrm{NLO}}$	$6.682^{+0.356\ +0.182}_{-0.752\ -0.125}$	$158.1^{+19.5\ +4.2}_{-21.2\ -5.3}$	$226.3^{+27.8\ +5.6}_{-29.7\ -7.0}$	$746.9^{+90.4\ +14.1}_{-90.4\ -17.1}$	$884.5^{+106.8\ +16.1}_{-105.8\ -19.4}$
K_{NLO}	$1.009^{+0.237\ +0.034}_{-0.273\ -0.028}$	$1.309^{+0.231\ +0.036}_{-0.259\ -0.035}$	$1.314^{+0.225\ +0.033}_{-0.250\ -0.032}$	$1.309^{+0.199\ +0.026}_{-0.216\ -0.024}$	$1.305^{+0.195\ +0.026}_{-0.210\ -0.023}$

Table 2.3: *The NLO theoretical predictions for $\sigma_{t\bar{t}}^{\mathbf{tot}}$ at the Tevatron and the LHC ($m_t = 173.3\,\mathrm{GeV}$,* MSTW2008 *PDFs at 68% C.L. [231]). For comparison, we also present the pure NLO corrections, grouped by production mode and in total ($\sum_{ij}$), as well as the NLO K-factor $K_{NLO} = \sigma_{t\bar{t}}^{\mathbf{tot},\,\mathrm{NLO}}/\sigma_{t\bar{t}}^{\mathbf{tot},\,\mathrm{LO}}$. The quoted uncertainties are due to the variation of renormalization and factorization scale and, for the full result as well as the K-factor, the parametric error of PDFs.*

deeper physical meaning. Another striking feature is the scale dependence of the individual NLO corrections to the quark annihilation and the quark-gluon channel which lies significantly above the value for the central scale choice. This means that the contributions of the scale-controlling functions $\hat{\sigma}_{ij}^{(1,k,l)}$ are sizable for these production modes. The PDF error, on the other hand, remains at 2-3% being rather negligible compared to the perturbative error. Therefore, the total uncertainty of the cross section predictions can only be noticeably reduced by going to NNLO accuracy or by at least estimating the dominant NNLO behavior.

Chapter 3

The total cross section of top-quark pair production at NNLO

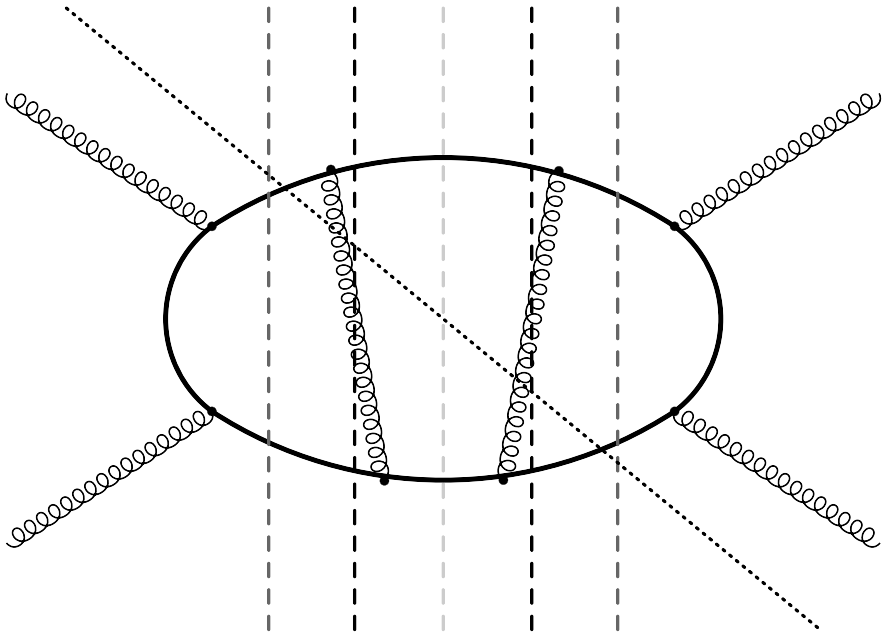

Figure 3.1: *Cut diagram contributing to the NNLO partonic cross section in the gluon fusion channel. The different cuts correspond to the double-real (short dashed), real-virtual (black), two-loop virtual (dark gray) and one-loop-squared (light gray) corrections described below.*

For a long time the NLO corrections (in combination with the all-order resummation of soft-gluon radiation) remained the state of the art for the theoretical description of top-quark pair production with an overall precision that exceeded the measurement capabilities of the available collider experiments. The launch of the LHC, however, made it necessary to reevaluate our treatment of $\sigma_{t\bar{t}}^{\mathbf{tot}}$ calling for theory predictions with an even higher level of precision that could only be reached by going to full NNLO accuracy. This task posed a serious challenge that, as we will see, required both the development of new computational methods and the improvement of existing approaches and it took more than a quarter of a century from the original NLO analysis until it was finally completed. Following the notation

of Eq. (2.18), the NNLO corrections are best parametrized as

$$\begin{aligned}
\hat{\sigma}_{ij}^{\mathrm{NNLO}}(\beta) &= \hat{\sigma}_{ij}^{(2,0,0)}(\beta) + \left(\frac{\beta_1}{8\pi^2}\,\hat{\sigma}_{ij}^{(0)}(\beta) + \frac{3\beta_0}{4\pi}\,\hat{\sigma}_{ij}^{(1,0,0)}(\beta)\right)\ln\left(\frac{\mu_R^2}{m_t^2}\right) \\
&+ \frac{3\beta_0^2}{(4\pi)^2}\,\hat{\sigma}_{ij}^{(0)}(\beta)\ln^2\left(\frac{\mu_R^2}{m_t^2}\right) - \left[\frac{1-\beta^2}{(2\pi)^2}\left(P_{ki}^{(1)}\otimes\frac{\hat{\sigma}_{kj}^{(0)}(\tilde{\rho})}{\tilde{\rho}} + P_{kj}^{(1)}\otimes\frac{\hat{\sigma}_{ik}^{(0)}(\tilde{\rho})}{\tilde{\rho}}\right)\right. \\
&+ \left.\frac{1-\beta^2}{2\pi}\left(P_{ki}^{(0)}\otimes\frac{\hat{\sigma}_{kj}^{(1,0,0)}(\tilde{\rho})}{\tilde{\rho}} + P_{kj}^{(0)}\otimes\frac{\hat{\sigma}_{ik}^{(1,0,0)}(\tilde{\rho})}{\tilde{\rho}}\right)\right]\ln\left(\frac{\mu_F^2}{m_t^2}\right) + \left[\frac{\beta_0\left(1-\beta^2\right)}{(4\pi)^2}\right. \\
&\left(P_{ki}^{(0)}\otimes\frac{\hat{\sigma}_{kj}^{(0)}(\tilde{\rho})}{\tilde{\rho}} + P_{kj}^{(0)}\otimes\frac{\hat{\sigma}_{ik}^{(0)}(\tilde{\rho})}{\tilde{\rho}}\right) + \frac{1-\beta^2}{(2\pi)^2}\left(\frac{1}{2}\,P_{ki}^{(0)}\otimes P_{lk}^{(0)}\otimes\frac{\hat{\sigma}_{lj}^{(0)}(\tilde{\rho})}{\tilde{\rho}}\right. \\
&+ \left.\left.\frac{1}{2}\,P_{kj}^{(0)}\otimes P_{lk}^{(0)}\otimes\frac{\hat{\sigma}_{il}^{(0)}(\tilde{\rho})}{\tilde{\rho}} + P_{ki}^{(0)}\otimes P_{lj}^{(0)}\otimes\frac{\hat{\sigma}_{kl}^{(0)}(\tilde{\rho})}{\tilde{\rho}}\right)\right]\ln^2\left(\frac{\mu_F^2}{m_t^2}\right) \\
&- \frac{3\beta_0\left(1-\beta^2\right)}{8\pi^2}\left(P_{ki}^{(0)}\otimes\frac{\hat{\sigma}_{kj}^{(0)}(\tilde{\rho})}{\tilde{\rho}} + P_{kj}^{(0)}\otimes\frac{\hat{\sigma}_{ik}^{(0)}(\tilde{\rho})}{\tilde{\rho}}\right)\ln\left(\frac{\mu_R^2}{m_t^2}\right)\ln\left(\frac{\mu_F^2}{m_t^2}\right)\,.
\end{aligned} \tag{3.1}$$

The explicit form of the scale-controlling contributions has been derived with the help of Eq. (2.19) and reveals a far more complex structure than in the NLO case. Nonetheless, the computational effort for the determination of the scale dependence is negligible compared to the calculation of the genuine NNLO contributions $\hat{\sigma}_{ij}^{(2,0,0)}$. In general, they can be divided into four conceptually different pieces, which is best demonstrated by means of cut diagrams as for instance shown in Fig. 3.1. The first contribution stems from double-real radiation, i. e. the emission of two extra partons with respect to the Born diagrams. As both of these partons are massless, this leads to further IR divergences in the resulting phase space integrals. The second class, the real-virtual corrections, consists of one-loop amplitudes with an additional massless particle in the final state. Hence, it receives poles from both the loop and the phase space integration and, moreover, requires UV renormalization. The purely virtual contributions are, in contrast to the NLO case, twofold. On the one hand, they consist of LO diagrams that are dressed with two internal quantum loops and, on the other hand, they also contain the square of the one-loop amplitudes that we have already encountered at NLO. However, due to the presence of IR poles the latter now need to be evaluated to higher orders in ϵ when working in CDR. The last part of the NNLO program, the contributions from collinear renormalization, cannot be represented by cut diagrams since they involve convolutions with the Altarelli-Parisi splitting kernels. Similar to the NLO analysis they are closely related to the functions that govern the scale dependence and their determination can thus be considered the least problematic part of the NNLO evaluation.

As the different classes of NNLO corrections require an individual treatment, we will address each of them separately and discuss in detail the strategies that we used to calculate their respective contribution to the total cross section. However, before we turn to the full NNLO analysis it is worth looking at the various approximations that have been developed throughout

the years in an effort to find a reliable estimate for the dominant NNLO behavior. From the physical point of view these approximate results are important because they allow us to gain a deeper insight in the internal structure of perturbative QCD, which eventually leads to an improvement of our theoretical predictions. In practice, they serve as an important cross-check of our findings as they correctly describe the functional dependence of the partonic cross sections in different kinematic limits. Conversely, the full result allows us to reassess the quality of the different approximation methods, which might be useful when going to even higher orders in QCD or when applying them to different processes. As we have already seen at NLO, a large portion of the higher-order corrections in $t\bar{t}$ production comes from threshold enhancements caused by potential-gluon exchange and soft-gluon radiation. In the following we will thus lay our focus on these particular contributions, which, in fact, account for the vast majority of NNLO approximations in the literature.

3.1 Threshold effects at NNLO and beyond

The general idea behind any approximation method is to simplify a given problem by either dividing it into less complex substructures that can be computed separately or by relating it to quantities that are already known from other processes. In order to describe the dominant threshold behavior for $t\bar{t}$ production, we employ a bit of both of these approaches, namely we modify a method originally developed for Drell-Yan production [556,557] that is based on the factorization of soft-radiation effects such that it can also be applied to a massive final state that carries color charge. To this end, consider the definition of the total cross section, however, expressed in a slightly different notation that is more suited for the problem at hand[1]

$$\sigma_{t\bar{t}}^{\mathbf{tot}} = \sum_{ij} \phi_{i/h_1}^0 \otimes \phi_{j/h_2}^0 \otimes \hat{\sigma}_{ij}^0 \tag{3.2}$$

with $\hat{\sigma}_{ij}^0$ denoting the (collinearly) bare partonic cross sections and ϕ_{k/h_x}^0 representing the bare PDF for the parton k inside the hadron h_x. Now suppose we are close to threshold where the total energy of the system is strongly restricted from above. As a consequence the final-state heavy-quark pair is almost at rest, i. e. moving with velocities in the non-relativistic regime, and any additional radiation is bound to be soft. As we have learned in the discussion of the NLO subtraction terms, the partonic matrix elements factorize in this particular limit into the basic hard scattering process and an eikonal current that governs the low-energetic radiation effects. Fortunately, this factorization procedure can be extended to an arbitrary number of soft emissions such that the partonic cross sections can be written as (parton indices suppressed)

$$\hat{\sigma}^0 = \sum_{\alpha\beta} H_{\alpha\beta}^0 \otimes S_{\alpha\beta}^0 \,, \tag{3.3}$$

with a hard function $H_{\alpha\beta}^0$ that contains all information on the underlying 2-to-2 cross sections including higher-loop corrections and a soft function $S_{\alpha\beta}^0$ that incorporates the interaction of

[1] Note that this total cross section definition is only valid in the threshold regime. For arbitrary kinematics one has to resort to the definition given in Eq. (2.3).

the eikonal currents to all orders in perturbation theory. Mathematically these interactions are best described in terms of Wilson line operators defined as

$$\mathbf{\Phi}_\beta^{(\boldsymbol{R})}(x;b,a) = P\exp\left(ig_s^0\int_a^b dt\,\beta\cdot A^c(x+t\,\beta)\,\boldsymbol{T}^{(\boldsymbol{R})\,c}\right) \tag{3.4}$$

corresponding to the path integral of a quasi-classical particle charged under the representation $\boldsymbol{R}$ of the gauge group traveling in a straight line between $x+a\beta$ and $x+b\beta$. As the color operators do in general not commute, one has to apply a proper path-ordering P, which allows for the correct treatment of the color-state evolution of the particle due to gluon emissions. Finally, $g_s^0 = \sqrt{4\pi\alpha_s^0}$ denotes the bare QCD coupling. Since the soft phenomena we are interested in are solely associated with external lines, it will be renormalized with $n_l = 5$ active quark flavors. A key feature of the eikonal current is its rescaling invariance with respect to the hard momentum variable which must, consequently, also hold for the Wilson line restricting the integration bounds to $a, b \in \{-\infty, 0, +\infty\}$. Using the sum representation of the exponential

$$\mathbf{\Phi}_\beta^{(\boldsymbol{R})} = \sum_n\sum_\sigma \frac{\left(ig_s^0\right)^n}{n!}\int\limits_{0\le t_{\sigma(1)}\cdots\le t_{\sigma(n)}}\prod_i dt_i\;\beta\cdot A^{c_{\sigma(n)}}(x+t_{\sigma(n)}\,\beta)\,\boldsymbol{T}^{c_{\sigma(n)}}\cdots\beta\cdot A^{c_{\sigma(1)}}(x+t_{\sigma(1)}\,\beta)\,\boldsymbol{T}^{c_{\sigma(1)}} \tag{3.5}$$

it can then be easily shown via Fourier transformation and with the help of the identity

$$\int\limits_{0\le t_1\cdots\le t_n}\prod_i^n dt_i\;\exp\left(-\sum_j^n t_j\,x_j\right) = \frac{1}{x_n}\,\frac{1}{x_n+x_{n-1}}\cdots\frac{1}{x_n+\cdots+x_1} \tag{3.6}$$

that at each order in perturbation theory the Wilson operator reproduces the correct combination of eikonal currents taking into account all possible permutations $\sigma = \{t_1,\ldots,t_n\}$ of soft-gluon emissions[2].

Due to the non-abelian nature of QCD the factorization into hard and soft contributions is in general not diagonal but involves the sum over the color structures α and β of the underlying hard matrix elements. A schematic representation of this factorization is depicted in Fig. 3.2 in form of a generalized cut diagram. Wilson lines are conventionally denoted by double lines whereas the single lines correspond to the external states participating in the hard scattering. As indicated by the $\otimes$ symbol, the insertion of color structures occurs at the matrix element level, i. e. independently on both sides of the unitarity cut, which nicely illustrates the origin of the color sum in Eq. (3.3). Note that the factorization at the cross section level is, however, not complete, i. e. the resulting expression is a convolution rather than a simple product, a fact that may be attributed to the modified phase space integration. Even though the soft radiation has been separated from the hard scattering process, it still affects the available phase space volume of the massive two-particle final state via

$$(p_1+p_2-K)^2 = \hat{s} - 2\sqrt{\hat{s}}\omega + \left(\omega^2 - \vec{k}^2\right) \approx \hat{s} - 2\sqrt{\hat{s}}\omega \tag{3.7}$$

[2] Due to the infinite integration bounds one has to introduce a regulation factor $\exp(\pm\epsilon t)$ in the exponent of Eq. (3.4), with $\epsilon \to 0^+$ and sign chosen such that the resulting integral is convergent. This factor then reproduces the correct $+i\epsilon$-prescription in the eikonal propagators of the current operators.

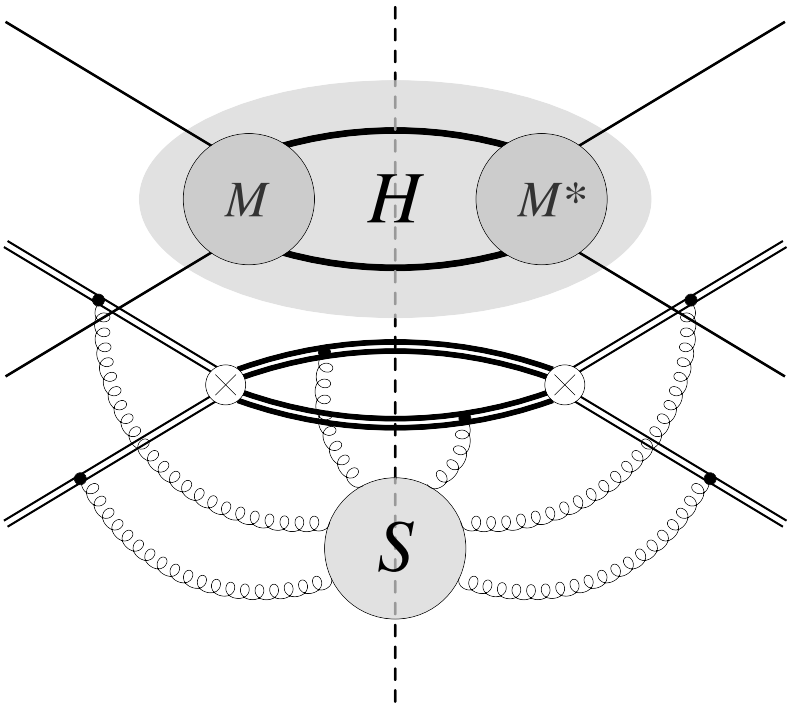

Figure 3.2: *Schematic representation of soft factorization in $t\bar{t}$ production. H and S stand for the hard and soft function, respectively. The double lines denote Wilson lines, whereas the dashed line indicates the unitarity cut. The $\otimes$ symbols corresponds to an insertion of the underlying color structure of the hard matrix element.*

where p_1, p_2 and $K = \left(\omega, \vec{k}\right)$ are the four-momenta of the initial-state partons (in the center-of-mass frame) and the combined soft radiation respectively and the last approximation provides the leading behavior in the limit $\omega \to 0$. In practice, it is more convenient to parametrize the total energy of the soft gluons in terms of the invariant mass of the final state at threshold $Q = 2m_t$ as

$$\omega = \frac{Q}{2}(1 - z) \tag{3.8}$$

such that the phase space volume assumes a particularly simple form

$$\hat{s} - 2\sqrt{\hat{s}}\omega \approx \hat{s}z \; . \tag{3.9}$$

The convolution of the hard and soft function will then be given in terms of the dimensionless variable $z \in [0, 1]$ leading to the familiar integral representations defined in Eq. (2.3). There exists, however, no unique prescription for the actual evaluation of the resulting factorization formula but Eq. (3.3) rather forms the theoretical basis for a variety of different threshold approximations working either in Mellin-moment space or directly in momentum space. In principle, all of these approaches are equivalent but due to the numerical importance of subleading contributions the corresponding cross section predictions turn out to be quite different. In the following we will focus on the approach introduced in Refs. [234, 558] that is essentially oriented towards the original N-space formalism [214–220], however, with a, in our opinion, more simplified notation.

The starting point of this alternative N-space approach is the observation that the hard and soft functions can be diagonalized by choosing an appropriate color basis in terms of the final-state singlet and octet configurations introduced in section 2.3.1. As a consequence, the factorization formula reduces to [515]

$$\hat{\sigma}^0 = \sum_\alpha H_\alpha^0 \otimes S_\alpha^0 \tag{3.10}$$

where the sum now runs over $\alpha \in \{\mathbf{1}, \mathbf{8}\}$ or $\alpha \in \{\mathbf{1}, \mathbf{8_S}, \mathbf{8_A}\}$ for the quark annihilation and gluon fusion channel respectively. So far we have ignored the impact of final-state potential-gluon exchange and tacitly assumed that the inclusion of these non-relativistic effects does not interfere with the factorization properties of the partonic cross sections. Indeed, it can be shown that non-relativistic and soft contributions factorize as well provided that the hard function is decomposed into the aforementioned singlet/octet basis and contains only s-wave effects [559]. Note, however, that the absence of higher partial waves is not a general feature of the total cross section at threshold and it is, in fact, to be expected that beyond NNLL accuracy these terms will become relevant. Nevertheless, they do not lead to any complications in our treatment of the threshold behavior since up to NNLO they may only occur in the velocity-independent contributions that are not enhanced by any soft-radiation effects. The presence of non-relativistic corrections in Eq. (3.10) implies that the matrix elements entering the hard function have to be expanded in terms of β, in contrast to the soft function where the velocity must be explicitly set to zero. In principle, it would be possible to further decompose the hard contributions into a potential function that contains all Coulomb enhancements and a velocity-independent prefactor that incorporates the remaining components of the hard scattering process. This would allow us to resum these potential interaction effects to all orders in perturbation theory [559]. However, since the numerical impact of such a Coulomb resummation on the final cross section predictions is negligible, we refrain from treating these contributions separately.

Apparently, the partonic cross sections defined through Eq. (3.10) still require collinear renormalization to remove the residual initial-state divergences that are, of course, also present in the threshold limit. However, in addition to these known singularities the factorization procedure induces further IR divergences into the hard and soft function that will only cancel in the final expression for the convoluted result. Fortunately, it is possible to predict these additional poles in advance, i. e. their structure is a universal property of the underlying theory, which allows us to define a general IR renormalization prescription that renders both functions separately finite. To this end, it is convenient to introduce the concept of finite remainder functions. Consider the UV renormalized $t\bar{t}$ amplitudes in Eq. (2.24) but this time with the heavy degrees of freedom already decoupled from the running of α_s. It has been shown that the remaining IR poles can then be completely removed by an additional multiplicative renormalization constant $\mathbf{Z}_\mathcal{F}$ [560–562] defining the finite remainder of the amplitudes as

$$|\mathcal{F}_{i_1\cdots i_n}(\alpha_s, m_t, \mu_R)\rangle = \mathbf{Z}_\mathcal{F}^{-1}\left(\{\underline{p}\}, m_t, \mu_R, \epsilon\right) |\mathcal{M}^R_{i_1\cdots i_n}(\alpha_s, m_t, \mu_R, \epsilon)\rangle \ . \tag{3.11}$$

In contrast to its UV counterpart this IR renormalization factor is an operator of the SU(3) gauge group that acts on the color indices of the external partons and, moreover, exhibits

a non-trivial dependence on the momenta $\{\underline{p}\} = \{p_1, \ldots, p_k\}$ and mass parameters involved in the scattering process. Note that Eq. (3.11) is not limited to the threshold region but holds for arbitrary kinematics. In fact, it is not even restricted to $t\bar{t}$ production and has been formulated for general QCD amplitudes. As for all renormalization procedures it is again possible to specify different schemes by adding finite terms to the predefined pole structure. In the $\overline{\text{MS}}$ scheme the actual form of the (generalized) IR constant can be derived from

$$\frac{d}{d\ln\mu}\,\mathbf{Z}_{\mathcal{F}}\left(\{\underline{p}\},\{\underline{m}\},\mu_R,\epsilon\right) \;=\; -\mathbf{Z}_{\mathcal{F}}\left(\{\underline{p}\},\{\underline{m}\},\mu_R,\epsilon\right)\,\mathbf{\Gamma}_{\mathcal{F}}\left(\{\underline{p}\},\{\underline{m}\},\mu_R\right)\;, \tag{3.12}$$

which is governed by the anomalous dimension matrix [562–565]

$$\begin{aligned}
\mathbf{\Gamma}_{\mathcal{F}}\left(\{\underline{p}\},\{\underline{m}\},\mu_R\right) \;=\; & \sum_{(i,j)} \frac{\mathbf{T}_i\cdot\mathbf{T}_j}{2}\,\gamma_{\text{cusp}}(\alpha_s)\,\ln\frac{\mu_R^2}{-s_{ij}} \;+\; \sum_i \gamma^i(\alpha_s) \\
& - \sum_{(I,J)} \frac{\mathbf{T}_I\cdot\boldsymbol{T}_J}{2}\,\gamma_{\text{cusp}}(\beta_{IJ},\alpha_s) \;+\; \sum_I \gamma^I(\alpha_s) \;+\; \sum_{I,j} \mathbf{T}_I\cdot\boldsymbol{T}_j\,\gamma_{\text{cusp}}(\alpha_s)\,\ln\frac{m_I\,\mu_R}{-s_{Ij}} \\
& + \sum_{(I,J,K)} i\,f^{abc}\,\mathbf{T}_I^a\,\mathbf{T}_J^b\,\mathbf{T}_K^c\,F_1(\beta_{IJ},\beta_{JK},\beta_{KI}) \\
& + \sum_{(I,J)}\sum_k i\,f^{abc}\,\mathbf{T}_I^a\,\mathbf{T}_J^b\,\mathbf{T}_k^c\,f_2\left(\beta_{IJ},\ln\frac{-\sigma_{Jk}\,v_J\cdot p_k}{-\sigma_{Ik}\,v_I\cdot p_k}\right) \;+\; \mathcal{O}(\alpha_s^3)
\end{aligned} \tag{3.13}$$

encoding the full singularity structure up to two-loop order. The summation includes all massless (indices i,j,k) and massive (indices I,J,K) partons where $(i,j,...)$ corresponds to unordered tuples of respective indices and $\mathbf{T}_i^a$ are the charge operators defined in Eq. (2.95). The kinematic dependence is given in terms of the Lorentz invariants $s_{ij} = 2\sigma_{ij}\,p_i\cdot p_j + i0^+$ and the cusp angles β_{IJ} defined through

$$\cosh\beta_{IJ} = \frac{-s_{IJ}}{2m_I m_J} = -\sigma_{IJ}\,v_I\cdot v_J - i0^+ \tag{3.14}$$

where $v_I = p_I/m_I$ is the massive parton velocity. The sign factor σ_{ij} appearing in these expressions depends on the direction of the external momenta with $\sigma_{ij} = +1$ for both partons incoming or outgoing and $\sigma_{ij} = -1$ otherwise. Interestingly, for top-quark pair production the anomalous dimension is further simplified due to the fact that the contributions of the triple-color-correlators vanish when being applied to the corresponding Born amplitudes [219,564]. Indeed, it can be shown that this is a general feature for contractions with real matrix elements provided that the latter have been averaged over spin and color [558]. This means that as long as the Lagrangian does not contain any complex masses or couplings, these three-parton-correlations will only start to contribute at three-loop order.

As a consequence, the generic form of the IR renormalization constant for top quarks is given by

$$\mathbf{Z}_{\mathcal{F}}^{t\bar{t}}\left(\alpha_s,\beta,\cos\theta,m_t,\mu_R,\epsilon\right) = 1 + \sum_{n=1}^{2}\alpha_s^n \underbrace{\sum_{m=-2n}^{-1}\mathbf{z}_{\mathcal{F}}^{(n,m)}\left(\beta,\cos\theta,m_t,\mu_R\right)\,\epsilon^m}_{\equiv\mathbf{Z}_{\mathcal{F}}^{t\bar{t},\,(n)}} + \mathcal{O}\left(\alpha_s^3\right)\;, \tag{3.15}$$

i. e. we recover the pole structure naively expected from counting potential soft and collinear singularities. The coefficients $\mathbf{z}_{\mathcal{F}}^{(n,m)}$ depend on the anomalous dimension coefficients for massless ($\gamma_{\text{cusp}}(\alpha_s)$, $\gamma^i(\alpha_s)$) and massive ($\gamma_{\text{cusp}}(\beta_{IJ},\alpha_s)$, $\gamma^I(\alpha_s)$) partons (see appendix B) as well as on the remaining dipole-correlators which, as explained before, can, by means of color conservation, be further reduced to only two independent color operators[3], e. g. $\mathbf{T}_1\cdot\mathbf{T}_2$ and $\mathbf{T}_1\cdot\mathbf{T}_3$. Note, however, that at $\mathcal{O}\left(\alpha_s^2\right)$ there can also occur combinations of the type

$$\mathbf{T}_i\cdot\mathbf{T}_j \;\; \mathbf{T}_i\cdot\mathbf{T}_k\,, \tag{3.16}$$

which do generally not commute (unless both dipole-operators are equal $j=k$) requiring close attention to the correct ordering when deriving the corresponding terms from Eq. (3.12). Yet, since the potentially problematic commutator can be expressed as

$$\mathbf{T}_i^a\,\mathbf{T}_j^a \;\; \mathbf{T}_i^b\,\mathbf{T}_k^b - \mathbf{T}_i^b\,\mathbf{T}_k^b \;\; \mathbf{T}_i^a\,\mathbf{T}_j^a = \mathbf{T}_j^a\,\mathbf{T}_k^b \;\; \Big[\mathbf{T}^a,\mathbf{T}^b\Big]_i = i\,f^{abc}\,\mathbf{T}_i^c\,\mathbf{T}_j^a\,\mathbf{T}_k^b\,, \tag{3.17}$$

its contribution to the two-loop pole structure vanishes when being contracted with the Born amplitudes[4] leaving only the three combinations

$$\begin{aligned}
&\mathbf{T}_1\cdot\mathbf{T}_2 \;\; \mathbf{T}_1\cdot\mathbf{T}_2\\
&\mathbf{T}_1\cdot\mathbf{T}_3 \;\; \mathbf{T}_1\cdot\mathbf{T}_3\\
&\mathbf{T}_1\cdot\mathbf{T}_2 \;\; \mathbf{T}_1\cdot\mathbf{T}_3\,.
\end{aligned} \tag{3.18}$$

So far, we have restricted our discussion of finite remainders to the case of full $t\bar{t}$ matrix elements but this procedure can be naturally extended to color-projected amplitudes as well

$$|\mathcal{M}^R_{\mathbf{R}\otimes\mathbf{R}'|\tilde{\mathbf{R}}}\left(\alpha_s,m_t,\mu_R,\epsilon\right)\rangle = \mathbf{P}^{\mathbf{R}\otimes\mathbf{R}'|\tilde{\mathbf{R}}}\;|\mathcal{M}^R_{i_1i_2}\left(\alpha_s,m_t,\mu_R,\epsilon\right)\rangle \tag{3.19}$$

where we have already assumed that we work in the aforementioned singlet/octet basis with the projection operators $\mathbf{P}^{\mathbf{R}\otimes\mathbf{R}'|\tilde{\mathbf{R}}}$ defined in Eq. (2.46) and Eq. (2.47) respectively. The initial state is now characterized by its distinct color representation $\mathbf{R}\otimes\mathbf{R}'$ while the final-state configuration is denoted by $\tilde{\mathbf{R}}$. As can be anticipated from the generic form of $\mathbf{Z}_{\mathcal{F}}^{t\bar{t}}$, the different color structures mix under IR renormalization when considering arbitrary kinematics and, thus, the resultant finite remainders are linear combinations of these renormalized singlet and octet states. At threshold, however, the series coefficients $\mathbf{Z}_{\mathcal{F}}^{t\bar{t},\,(n)}$ become diagonal such that the finite remainders inherit the color representation of the original matrix elements

$$|\mathcal{F}_{\mathbf{R}\otimes\mathbf{R}'|\tilde{\mathbf{R}}}\left(\alpha_s,\beta,\cos\theta,m_t,\mu_R\right)\rangle \overset{\beta\to 0}{=} \left(Z_{\mathcal{F}}^{\mathbf{R}\otimes\mathbf{R}'|\tilde{\mathbf{R}}}\right)^{-1}\;|\mathcal{M}^R_{\mathbf{R}\otimes\mathbf{R}'|\tilde{\mathbf{R}}}\left(\alpha_s,\beta,\cos\theta,m_t,\mu_R,\epsilon\right)\rangle \tag{3.20}$$

with the color-projected renormalization constant given by

$$Z_{\mathcal{F}}^{\mathbf{R}\otimes\mathbf{R}'|\tilde{\mathbf{R}}} = \lim_{\beta\to 0}\;\mathbf{P}^{\mathbf{R}\otimes\mathbf{R}'|\tilde{\mathbf{R}}\;*}\,\mathbf{Z}_{\mathcal{F}}^{t\bar{t}}\,\mathbf{P}^{\mathbf{R}\otimes\mathbf{R}'|\tilde{\mathbf{R}}}\,. \tag{3.21}$$

[3] For a general process involving n external partons the number of independent combinations $\mathbf{T}_x\cdot\mathbf{T}_y$ is $(n^2-3n)/2$.

[4] As a consequence, $\mathbf{\Gamma}_{\mathcal{F}}$ and $\mathbf{Z}_{\mathcal{F}}$ commute up to $\mathcal{O}\left(\alpha_s^2\right)$ allowing us to reverse the order on the right-hand side of Eq. (3.12) as can be commonly found in the literature.

Knowing this, we are now able to construct the renormalized hard function as

$$\begin{aligned} H_{\mathbf{R}\otimes\mathbf{R}'|\tilde{\mathbf{R}}}\left(\alpha_s,\rho,m_t,\frac{\mu_R}{Q}\right) &= \int dP_2\ \langle\mathcal{F}_{\mathbf{R}\otimes\mathbf{R}'|\tilde{\mathbf{R}}}|\mathcal{F}_{\mathbf{R}\otimes\mathbf{R}'|\tilde{\mathbf{R}}}\rangle\Big|_{\beta^0} \\ &= \left(Z_H^{\mathbf{R}\otimes\mathbf{R}'|\tilde{\mathbf{R}}}\right)^{-1}\int dP_2\ \langle\mathcal{M}^R_{\mathbf{R}\otimes\mathbf{R}'|\tilde{\mathbf{R}}}|\mathcal{M}^R_{\mathbf{R}\otimes\mathbf{R}'|\tilde{\mathbf{R}}}\rangle\Big|_{\beta^0} \\ &= \left(Z_H^{\mathbf{R}\otimes\mathbf{R}'|\tilde{\mathbf{R}}}\right)^{-1} H^0_{\mathbf{R}\otimes\mathbf{R}'|\tilde{\mathbf{R}}}\left(\alpha_s,\rho,m_t,\frac{\mu_R}{Q},\epsilon\right)\,. \end{aligned} \tag{3.22}$$

As indicated, it is most naturally described in terms of ρ rather than the velocity, especially with regard to the convolution integrals. The restriction $|_{\beta^0}$ limits the corresponding matrix elements to the threshold region, which due to the presence of Coulomb effects implies an expansion in terms of β as already noted above resulting in different power-logarithmic enhancement factors. The IR renormalization constant

$$Z_H^{\mathbf{R}\otimes\mathbf{R}'|\tilde{\mathbf{R}}}\left(\alpha_s,\frac{\mu_R}{Q},\epsilon\right) = Z_{\mathcal{F}}^{\mathbf{R}\otimes\mathbf{R}'|\tilde{\mathbf{R}}\,*}\,Z_{\mathcal{F}}^{\mathbf{R}\otimes\mathbf{R}'|\tilde{\mathbf{R}}} = \left|Z_{\mathcal{F}}^{\mathbf{R}\otimes\mathbf{R}'|\tilde{\mathbf{R}}}\right|^2\,, \tag{3.23}$$

on the other hand, is finite for $\beta\to 0$ and, moreover, independent of the scattering angle $\cos\theta$. The latter feature is a direct consequence of the fact that $Z_H^{\mathbf{R}\otimes\mathbf{R}'|\tilde{\mathbf{R}}}$ can also be used to remove all singular terms from the soft function (apart from the initial-state collinear divergences), which, as we will see, does not depend on the particular nature of the final state, i. e. it is the same regardless of whether we are considering the production of a top pair at rest or a single scalar particle. The only relevant input is the underlying color configuration, a property that must then also apply to the corresponding IR renormalization factor of the hard function rendering it insensitive to the kinematic details of the scattering process. Similar to the original IR renormalization constant, it satisfies a differential equation of the form

$$\frac{d}{d\ln\mu}\,Z_H^{\mathbf{R}\otimes\mathbf{R}'|\tilde{\mathbf{R}}}\left(\alpha_s,\frac{\mu_R}{Q},\epsilon\right) = -\Gamma_H^{\mathbf{R}\otimes\mathbf{R}'|\tilde{\mathbf{R}}}\left(\alpha_s,\frac{\mu_R}{Q}\right)\,Z_H^{\mathbf{R}\otimes\mathbf{R}'|\tilde{\mathbf{R}}}\left(\alpha_s,\frac{\mu_R}{Q},\epsilon\right)\,, \tag{3.24}$$

which, however, now contains only (color-)scalar quantities due to color projection. The corresponding anomalous dimension is related to $\mathbf{\Gamma}_{\mathcal{F}}$ via

$$\Gamma_H^{\mathbf{R}\otimes\mathbf{R}'|\tilde{\mathbf{R}}}\left(\alpha_s,\frac{\mu_R}{Q}\right) = \lim_{\beta\to 0}\,2\,\mathrm{Re}\left(\mathbf{P}^{\mathbf{R}\otimes\mathbf{R}'|\tilde{\mathbf{R}}\,*}\,\mathbf{\Gamma}_{\mathcal{F}}\left(\alpha_s,\beta,\cos\theta,\frac{\mu_R}{Q}\right)\,\mathbf{P}^{\mathbf{R}\otimes\mathbf{R}'|\tilde{\mathbf{R}}}\right) \tag{3.25}$$

and can be used to determine $Z_H^{\mathbf{R}\otimes\mathbf{R}'|\tilde{\mathbf{R}}}$ directly without the need to explicitly evaluate Eq. (3.21) or Eq. (3.23). Note that, while the hard anomalous dimension $\Gamma_H^{\mathbf{R}\otimes\mathbf{R}'|\tilde{\mathbf{R}}}$ is also finite and independent of the scattering angle[5], the imaginary part of the general anomalous dimension matrix $\mathbf{\Gamma}_{\mathcal{F}}$ contains Coulomb enhancements of the form $1/\beta$ that enter the resulting renormalization constants $Z_{\mathcal{F}}^{\mathbf{R}\otimes\mathbf{R}'|\tilde{\mathbf{R}}}$ and thus affect the singularity structure of the corresponding matrix elements. The argument concerning the independence from the final-state multiplicity is therefore only valid at the cross section level.

[5] For explicit results, see appendix B.

Before we discuss how $Z_H^{\mathbf{R}\otimes\mathbf{R}'|\tilde{\mathbf{R}}}$ can be employed in the renormalization of the soft components as well, we have to address the overall structure of the respective soft functions and, in particular, their dependence on the final-state color configuration. As already explained, the key element for the description of soft-radiation effects are the Wilson line operators defined in Eq. (3.4). Working in the singlet/octet basis and using the shorthand notation

$$\Phi^{(\boldsymbol{R})}_{\beta,cd}(b,a) = \left(\boldsymbol{\Phi}^{(\boldsymbol{R})}_{\beta}(x=0;b,a)\right)_{cd} \tag{3.26}$$

the bare soft function for $t\bar{t}$ production can be expressed in terms of these operators as

$$\begin{aligned} S^0_{\mathbf{R}\otimes\mathbf{R}'|\tilde{\mathbf{R}}}(\omega) &= \frac{Q}{2}\sum_X \delta(\omega - E_X) \\ &\times \sum_{abcd}\left| P^{\mathbf{R}\otimes\mathbf{R}'|\tilde{\mathbf{R}}}_{a'b'c'd'} \langle X|T\left[\Phi^{(\mathbf{R})}_{n,b'b}(0,-\infty)\Phi^{(\mathbf{R}')}_{\bar{n},a'a}(0,-\infty)\Phi^{(\mathbf{3})}_{v,cc'}(+\infty,0)\Phi^{(\bar{\mathbf{3}})}_{\bar{v},dd'}(+\infty,0)\right]|0\rangle\right|^2 \end{aligned} \tag{3.27}$$

where the summation in the first line includes all possible soft emissions (gluons and at higher orders also light-quark and ghost pairs) with energy E_X and the directions of the incoming light-cone states and outgoing heavy-quark states read $n^\mu = (1, \vec{\mathbf{0}}^{(d-2)}, 1)$, $\bar{n}^\mu = (1, \vec{\mathbf{0}}^{(d-2)}, -1)$ and $v^\mu = \bar{v}^\mu = (1, \vec{\mathbf{0}}^{(d-1)})$ respectively. Due to the equality of the latter the final-state Wilson lines may be combined into a single operator[6]

$$\begin{aligned} \Phi^{(\mathbf{3})}_{v,aa'}(+\infty,0)\, V^{(\tilde{\mathbf{R}})}_{a'b'c}\, \Phi^{(\bar{\mathbf{3}})}_{\bar{v},bb'}(+\infty,0) &= \left(\boldsymbol{\Phi}^{(\mathbf{3})}_{v}(+\infty,0)\, \mathbf{V}^{(\tilde{\mathbf{R}})}_{c}\, \boldsymbol{\Phi}^{(\mathbf{3})\dagger}_{v}(+\infty,0)\right)_{ab} \\ &= \begin{cases} \delta_{ab} & \text{for } \tilde{\mathbf{R}} \in \{\mathbf{1}\} \\ T^{(\mathbf{3}),d}_{ab}\, \Phi^{(\mathbf{8})}_{v,dc}(+\infty,0) & \text{for } \tilde{\mathbf{R}} \in \{\mathbf{8}, \mathbf{8_S}, \mathbf{8_A}\} \end{cases} \end{aligned} \tag{3.28}$$

where the vertex factors

$$V^{(\tilde{\mathbf{R}})}_{abc} = \begin{cases} \delta_{ab} & \text{for } \tilde{\mathbf{R}} \in \{\mathbf{1}\} \\ T^{(\mathbf{3}),c}_{ab} & \text{for } \tilde{\mathbf{R}} \in \{\mathbf{8}, \mathbf{8_S}, \mathbf{8_A}\} \end{cases} \tag{3.29}$$

[6] For a proof see, for instance, Ref. [558]

are part of the projection operators that connect the different Wilson lines in color space. As a result, the soft function assumes an even simpler form

$$\begin{aligned} S^0_{\mathbf{R}\otimes\mathbf{R}'|\mathbf{1}}(\omega) &= \frac{Q}{2}\sum_X \delta(\omega - E_X) \\ &\times \sum_{ab} \left| C^{\mathbf{R}\otimes\mathbf{R}'|\mathbf{1}}_{a'b'} \langle X|T\left[\Phi^{(\mathbf{R})}_{n,b'b}(0,-\infty)\Phi^{(\mathbf{R}')}_{\bar{n},a'a}(0,-\infty)\right]|0\rangle\right|^2 , \\ S^0_{\mathbf{R}\otimes\mathbf{R}'|\mathbf{8_x}}(\omega) &= \frac{Q}{2}\sum_X \delta(\omega - E_X) \\ &\times \sum_{abc} \left| C^{\mathbf{R}\otimes\mathbf{R}'|\mathbf{8_x}}_{a'b'c'} \langle X|T\left[\Phi^{(\mathbf{R})}_{n,b'b}(0,-\infty)\Phi^{(\mathbf{R}')}_{\bar{n},a'a}(0,-\infty)\Phi^{(\mathbf{8})}_{v,cc'}(+\infty,0)\right]|0\rangle\right|^2 , \end{aligned} \tag{3.30}$$

with the reduced projection operators defined as

$$\begin{aligned} C^{\mathbf{3}\otimes\bar{\mathbf{3}}|\mathbf{1}}_{ab} &= \frac{1}{\sqrt{N_c}}\,\delta_{ab} & C^{\mathbf{8}\otimes\mathbf{8}|\mathbf{1}}_{ab} &= \frac{1}{\sqrt{{N_c}^2-1}}\,\delta^{ab} \\ & & C^{\mathbf{3}\otimes\bar{\mathbf{3}}|\mathbf{8}}_{abc} &= \sqrt{\frac{2}{{N_c}^2-1}}\,T^c_{ab} \\ C^{\mathbf{8}\otimes\mathbf{8}|\mathbf{8_S}}_{abc} &= \sqrt{\frac{N_c}{({N_c}^2-1)({N_c}^2-4)}}\,d^{abc} & C^{\mathbf{8}\otimes\mathbf{8}|\mathbf{8_A}}_{abc} &= \frac{1}{\sqrt{N_c({N_c}^2-1)}}\,if^{abc} , \end{aligned} \tag{3.31}$$

which are still orthogonal and fulfill the normalization relation

$$C^{\mathbf{R}\otimes\mathbf{R}'|\tilde{\mathbf{R}}}_{abc}\, C^{\mathbf{R}\otimes\mathbf{R}'|\tilde{\mathbf{R}}\ *}_{abc} = 1\,. \tag{3.32}$$

At threshold the emission of soft particles from a 2-to-2 process can thus be effectively described by the production of a single object that carries the combined color charge of the final-state configuration. In the singlet case this means that radiative corrections are, similar to Drell-Yan production, exclusively confined to the initial state. Conversely, all non-trivial effects of going from a colorless to a strongly-interacting final state are completely contained in the octet contributions.

Due to the presence of additional partons in the final state one could expect that the prediction of the pole structure of $S^0_{\mathbf{R}\otimes\mathbf{R}'|\tilde{\mathbf{R}}}$ is rather complicated. However, since we already know how to remove the singular IR terms from the hard function, the renormalization of the soft

function can be directly inferred from the finiteness of the total cross section

$$\begin{aligned}
\sigma_{t\bar{t}}^{\mathbf{tot}} &= \sum_{\substack{ij\in\\ \{q\bar{q},gg\}}} \phi_{i/h_1}\otimes\phi_{j/h_2}\otimes Z_{\phi_i}\otimes Z_{\phi_i}\otimes\sum_{\tilde{\mathbf{R}}} H^0_{\mathbf{R}\otimes\mathbf{R}'|\tilde{\mathbf{R}}}\otimes S^0_{\mathbf{R}\otimes\mathbf{R}'|\tilde{\mathbf{R}}} \\
&= \sum_{\substack{ij\in\\ \{q\bar{q},gg\}}} \phi_{i/h_1}\otimes\phi_{j/h_2}\otimes\sum_{\tilde{\mathbf{R}}} H_{\mathbf{R}\otimes\mathbf{R}'|\tilde{\mathbf{R}}}\otimes Z_{\phi_i}\otimes Z_{\phi_i}\otimes\left(Z_H^{\mathbf{R}\otimes\mathbf{R}'|\tilde{\mathbf{R}}} S^0_{\mathbf{R}\otimes\mathbf{R}'|\tilde{\mathbf{R}}}\right) \\
&= \sum_{\substack{ij\in\\ \{q\bar{q},gg\}}} \phi_{i/h_1}\otimes\phi_{j/h_2}\otimes\sum_{\tilde{\mathbf{R}}} H_{\mathbf{R}\otimes\mathbf{R}'|\tilde{\mathbf{R}}}\otimes S_{\mathbf{R}\otimes\mathbf{R}'|\tilde{\mathbf{R}}}
\end{aligned} \tag{3.33}$$

where we exploited the well-known fact that the off-diagonal splitting functions entering the collinear-renormalization constants are free of soft enhancements, i. e. their contribution in the limit $z\to 1$ can be neglected, yielding

$$\begin{aligned}
Z_{\phi_i}\equiv Z_{ii}(x,\mu_F) &= \delta(1-x)+\frac{\alpha_s(\mu_F)}{2\pi}\,\frac{P_{ii}^{(0)}(x)}{\epsilon} \\
&+ \left(\frac{\alpha_s(\mu_F)}{2\pi}\right)^2\left[\frac{P_{ii}^{(1)}(x)}{2\epsilon}+\frac{1}{2\epsilon^2}\left((P_{ii}^{(0)}\otimes P_{ii}^{(0)})(x)-\frac{\beta_0}{2}\,P_{ii}^{(0)}(x)\right)\right] \\
&+ \mathcal{O}(\alpha_s^3(\mu_F))\,.
\end{aligned} \tag{3.34}$$

Note that due to the independence of $Z_H^{\mathbf{R}\otimes\mathbf{R}'|\tilde{\mathbf{R}}}$ from the underlying kinematics it is unaffected by the convolutions and can, hence, be directly multiplied to the bare soft function. Still, the number of integrations is quite sizable rendering the evaluation of $\sigma_{t\bar{t}}^{\mathbf{tot}}$ in momentum space rather cumbersome. An elegant solution to this computational drawback is the transformation of the total cross section to Mellin space (also denoted as N-space) via

$$\begin{aligned}
\sigma_{t\bar{t},N}^{\mathbf{tot}} &= \int_0^1 d\rho_{\mathrm{H}}\,{\rho_{\mathrm{H}}}^{N-1}\,\sigma_{t\bar{t}}^{\mathbf{tot}}(\rho_{\mathrm{H}}) \\
&= \int_0^1 d\rho_{\mathrm{H}}\,{\rho_{\mathrm{H}}}^{N-1}\sum_{\substack{ij\in\\ \{q\bar{q},gg\}}}\int_0^1\int_0^1\int_0^1 dx_1\,dx_2\,d\rho\,\phi_{i/h_1}(x_1)\,\phi_{j/h_2}(x_2)\,\delta(\rho_{\mathrm{H}}-x_1x_2\rho) \\
&\times \sum_{\tilde{\mathbf{R}}}\int_0^1\int_0^1 dz\,d\rho'\,S_{\mathbf{R}\otimes\mathbf{R}'|\tilde{\mathbf{R}}}(z)\,H_{\mathbf{R}\otimes\mathbf{R}'|\tilde{\mathbf{R}}}(\rho')\,\delta(\rho-z\rho') \\
&= \sum_{\substack{ij\in\\ \{q\bar{q},gg\}}}\phi_{i/h_1,N}\,\phi_{j/h_2,N}\sum_{\tilde{\mathbf{R}}} S_{\mathbf{R}\otimes\mathbf{R}'|\tilde{\mathbf{R}},N}\,H_{\mathbf{R}\otimes\mathbf{R}'|\tilde{\mathbf{R}},N}
\end{aligned} \tag{3.35}$$

where the N-th Mellin moment of a function $f(z)$ is defined as

$$f_N=\int_0^1 dz\,z^{N-1}\,f(z)\,. \tag{3.36}$$

In consequence, the convolution integrals are replaced by a simple product of N-space functions, which is a significant improvement from the computational point of view provided, of course, that the transformation itself is well-defined and does not introduce any additional complications. Note that this type of factorization is not a unique property of $\sigma_{t\bar{t}}^{\mathbf{tot}}$ but holds for convolution integrals in general

$$\int_0^1 dz\, z^{N-1}\, (f \otimes g)(z) = f_N\, g_N\,. \tag{3.37}$$

As a result, the renormalized soft function in Mellin space is given as

$$S_{\mathbf{R}\otimes\mathbf{R}'|\tilde{\mathbf{R}},\,N} = Z^2_{\phi_i,\,N}\, Z_H^{\mathbf{R}\otimes\mathbf{R}'|\tilde{\mathbf{R}}}\, S^0_{\mathbf{R}\otimes\mathbf{R}'|\tilde{\mathbf{R}},\,N}\,, \tag{3.38}$$

i. e. it can be rendered completely finite by a simple multiplicative constant similar to the hard function. Since we are only interested in the behavior at threshold, we actually do not need to determine the full N-dependence of the corresponding Mellin-space functions but it is sufficient to consider the limit $N \to \infty$, which corresponds to the soft limit $z \to 1$ in momentum space. Thus, the logarithmic enhancements of the form $\ln^n \beta$, entering the partonic cross sections, will directly translate into logarithms in N that can be resummed using renormalization group techniques. For potential-gluon effects, however, the situation is different as they are formally subleading in N, which is also the reason why the resummation of these terms is performed more conveniently in x-space [559]. In order to still be able to include at least the fixed-order Coulomb contributions in the threshold description, one therefore has to take into account the subleading behavior of the hard function as well. This uniquely fixes the value of its Mellin moment to N whereas in the absence of potential effects it could in principle be decreased or incremented with respect to the Mellin moment of the partonic cross section without altering the threshold behavior. This is, of course, only true for a shift $\Delta_N = N - \tilde{N}$ that is small compared to N such that it does not interfere with limiting process $N \to \infty$. For the soft function this restricted N-invariance still holds, i. e.

$$S_{\mathbf{R}\otimes\mathbf{R}'|\tilde{\mathbf{R}},\,N+1} - S_{\mathbf{R}\otimes\mathbf{R}'|\tilde{\mathbf{R}},\,N} = \mathcal{O}\left(\frac{1}{N}\right)\,, \tag{3.39}$$

which is the reason why in the literature there exist alternative formulations of the N-space cross section Eq. (3.35), the most common (translated to our notation) being [216, 220]

$$\sigma_{t\bar{t},\,N}^{\mathbf{tot}} = \sum_{\substack{ij\,\in\\ \{q\bar{q},gg\}}} \phi_{i/h_1,\,N+1}\, \phi_{j/h_2,\,N+1} \sum_{\tilde{\mathbf{R}}} S_{\mathbf{R}\otimes\mathbf{R}'|\tilde{\mathbf{R}},\,N+1}\, H_{\mathbf{R}\otimes\mathbf{R}'|\tilde{\mathbf{R}},\,N}$$

Both definitions are equivalent in the large-N limit and can thus be employed conceptually equally well in the analysis of threshold phenomena.

Regardless of which cross section formula one chooses to work with in practice, they both form the basis for essentially two different NNLO approximation methods, the fixed-order threshold expansion on the one hand and the NNLL soft-gluon resummation on the other. In the following we will summarize the benefits and drawbacks of these methods as well as their

numerical impact on the total cross section predictions. Note that they can both, in principle, be extended beyond NNLO but currently only for the resummation approach all necessary ingredients are known to sufficiently high precision to systematically include higher-order effects. This means that the knowledge of the full NNLO corrections will not only improve the precision of the fixed-order predictions but also of the resummed cross section results providing us with the most accurate description of $t\bar{t}$ production yet.

3.1.1 Threshold expansion

The main idea behind this approach is to estimate the overall size of the fixed-order NNLO contributions through the known velocity enhancements due to soft-gluon radiation and Coulomb exchange. The validity of such an approximation is supported by the clear tendency towards lower values of β observed in the LO and NLO partonic cross section results (see Fig. 2.7 and Fig. 2.9 respectively). Still, one has to keep in mind that the partonic fluxes behave opposite and favor the production of $t\bar{t}$ pairs at high energies, which increases the numerical importance of subleading contributions in the calculation of approximate total cross section predictions that have to be properly taken into account. Nevertheless, the threshold expansion represents a valuable tool for assessing the impact of higher-order effects, especially as the methods developed therein can be applied to the production of potential BSM states as well [559], which due to their supposedly larger masses are more strictly confined to the threshold regime.

As we have already learned, the threshold behavior of the total cross section is most conveniently described in terms of irreducible representations of the SU(3) gauge group. Accordingly, the relevant partonic cross sections in the limit $\beta \to 0$ can be parametrized as

$$\begin{aligned}
\hat{\sigma}_{ij}\left(\beta, m_t, \mu_F, \alpha_s\right) \overset{\beta\to 0}{=}\; & \frac{\alpha_s^2(\mu_R)}{m_t^2} \sum_{\tilde{R}} \bar{\sigma}_{ij,\tilde{\mathbf{R}}}^{(0)}(\beta) \left\{ 1 + \alpha_s(\mu_R) \left[\bar{\sigma}_{ij,\tilde{\mathbf{R}}}^{(1,0,0)}(\beta) + \bar{\sigma}_{ij,\tilde{\mathbf{R}}}^{(1,1,0)}(\beta) \ln\left(\frac{\mu_R^2}{m_t^2}\right) \right.\right. \\
& + \left.\left. \bar{\sigma}_{ij,\tilde{\mathbf{R}}}^{(1,0,1)}(\beta) \ln\left(\frac{\mu_F^2}{m_t^2}\right) \right] + \alpha_s^2(\mu_R) \left[\bar{\sigma}_{ij,\tilde{\mathbf{R}}}^{(2,0,0)}(\beta) + \bar{\sigma}_{ij,\tilde{\mathbf{R}}}^{(2,1,0)}(\beta) \ln\left(\frac{\mu_R^2}{m_t^2}\right) \right.\right. \\
& + \bar{\sigma}_{ij,\tilde{\mathbf{R}}}^{(2,2,0)}(\beta) \ln^2\left(\frac{\mu_R^2}{m_t^2}\right) + \bar{\sigma}_{ij,\tilde{\mathbf{R}}}^{(2,1,1)}(\beta) \ln\left(\frac{\mu_R^2}{m_t^2}\right) \ln\left(\frac{\mu_F^2}{m_t^2}\right) \\
& + \left.\left. \bar{\sigma}_{ij,\tilde{\mathbf{R}}}^{(2,0,1)}(\beta) \ln\left(\frac{\mu_F^2}{m_t^2}\right) + \bar{\sigma}_{ij,\tilde{\mathbf{R}}}^{(2,0,2)}(\beta) \ln^2\left(\frac{\mu_F^2}{m_t^2}\right) \right] + \mathcal{O}\left(\alpha_s^3(\mu_R)\right) \right\} \\
& + \mathcal{O}\left(\beta^2\right)
\end{aligned} \tag{3.40}$$

where the generic velocity dependence of the coefficient functions $\bar{\sigma}_{ij,\tilde{\mathbf{R}}}^{(n\geq 1,k,l)}$ is given by

$$\bar{\sigma}_{ij,\tilde{\mathbf{R}}}^{(n,k,l)} = \sum_{a=0}^{n-k-l} \sum_{b=0}^{2n-2a-k-l} c_{ij,\tilde{\mathbf{R}}}^{(n,k,l;a,b)} \frac{1}{\beta^a} \ln^b \beta + \mathcal{O}(\beta) \ . \tag{3.41}$$

Note that due to $\mathcal{O}\left(\beta^3\right)$-suppression of $\bar{\sigma}_{gg,\mathbf{8_A}}^{(0)}$ the threshold expansion in the antisymmetric octet configuration contains subleading effects that cannot be reliably predicted with the theoretical methods currently available. In order to still ensure a consistent treatment of these velocity enhancements, Eq. (3.40) is defined such that only terms up to $\mathcal{O}(\beta)$ may

contribute to the expansion in accordance with the functional behavior of the remaining final-state configurations. As usual, only the $\bar{\sigma}^{(n,0,0)}_{ij,\tilde{\mathbf{R}}}$-terms are actually independent while the remaining coefficients can be inferred from the known scaling behavior of $\hat{\sigma}_{ij,\tilde{\mathbf{R}}}$. Hence, we will in the following focus on the case $\mu_F = \mu_R = m_t$ and only return to the general scale dependence where it seems fit. In order to determine the unknown coefficients $c^{(n,0,0;a,b)}_{ij,\tilde{\mathbf{R}}}$, we compare the threshold expansion of the partonic cross section to the α_s-expanded version of Eq. (3.33) yielding

$$\bar{\sigma}^{(0)}_{ij,\tilde{\mathbf{R}}} = H^{(0)}_{\mathbf{R}\otimes\mathbf{R}'|\tilde{\mathbf{R}}} \otimes S^{(0)}_{\mathbf{R}\otimes\mathbf{R}'|\tilde{\mathbf{R}}} \tag{3.42}$$

$$\bar{\sigma}^{(1,0,0)}_{ij,\tilde{\mathbf{R}}} = \frac{1}{\pi} \frac{H^{(1)}_{\mathbf{R}\otimes\mathbf{R}'|\tilde{\mathbf{R}}} \otimes S^{(0)}_{\mathbf{R}\otimes\mathbf{R}'|\tilde{\mathbf{R}}} + H^{(0)}_{\mathbf{R}\otimes\mathbf{R}'|\tilde{\mathbf{R}}} \otimes S^{(1)}_{\mathbf{R}\otimes\mathbf{R}'|\tilde{\mathbf{R}}}}{H^{(0)}_{\mathbf{R}\otimes\mathbf{R}'|\tilde{\mathbf{R}}} \otimes S^{(0)}_{\mathbf{R}\otimes\mathbf{R}'|\tilde{\mathbf{R}}}} \tag{3.43}$$

$$\bar{\sigma}^{(2,0,0)}_{ij,\tilde{\mathbf{R}}} = \frac{1}{\pi^2} \frac{H^{(2)}_{\mathbf{R}\otimes\mathbf{R}'|\tilde{\mathbf{R}}} \otimes S^{(0)}_{\mathbf{R}\otimes\mathbf{R}'|\tilde{\mathbf{R}}} + H^{(1)}_{\mathbf{R}\otimes\mathbf{R}'|\tilde{\mathbf{R}}} \otimes S^{(1)}_{\mathbf{R}\otimes\mathbf{R}'|\tilde{\mathbf{R}}} + H^{(0)}_{\mathbf{R}\otimes\mathbf{R}'|\tilde{\mathbf{R}}} \otimes S^{(2)}_{\mathbf{R}\otimes\mathbf{R}'|\tilde{\mathbf{R}}}}{H^{(0)}_{\mathbf{R}\otimes\mathbf{R}'|\tilde{\mathbf{R}}} \otimes S^{(0)}_{\mathbf{R}\otimes\mathbf{R}'|\tilde{\mathbf{R}}}} \tag{3.44}$$

with $H^{(n)}_{\mathbf{R}\otimes\mathbf{R}'|\tilde{\mathbf{R}}}$ and $S^{(n)}_{\mathbf{R}\otimes\mathbf{R}'|\tilde{\mathbf{R}}}$ defined through

$$\begin{aligned} H_{\mathbf{R}\otimes\mathbf{R}'|\tilde{\mathbf{R}}} &= \frac{\alpha_s^2}{m_t^2} \sum_n \left(\frac{\alpha_s}{\pi}\right)^n H^{(n)}_{\mathbf{R}\otimes\mathbf{R}'|\tilde{\mathbf{R}}} \\ S_{\mathbf{R}\otimes\mathbf{R}'|\tilde{\mathbf{R}}} &= \sum_n \left(\frac{\alpha_s}{\pi}\right)^n S^{(n)}_{\mathbf{R}\otimes\mathbf{R}'|\tilde{\mathbf{R}}} \,. \end{aligned} \tag{3.45}$$

The first relation, Eq. (3.42), implies that $S^{(0)}_{\mathbf{R}\otimes\mathbf{R}'|\tilde{\mathbf{R}}} \sim \delta(1-z)$, which is indeed the case when looking at the explicit expressions in Eq. (3.27) where the normalization has already been chosen such that $H^{(0)}_{\mathbf{R}\otimes\mathbf{R}'|\tilde{\mathbf{R}}} = \bar{\sigma}^{(0)}_{ij,\tilde{\mathbf{R}}}$. In consequence, the convolution integral containing the highest α_s-coefficient of the hard function at a given expansion order is eliminated such that its contribution to the threshold approximation can be evaluated directly in momentum space. This is a tremendous advantage in practice since at NNLO this term represents the most complex input parameter in the expansion formula. The remaining convolutions can be readily evaluated in the N-space formalism as they solely contain functions that are completely known analytically. In principle, one would have to transform the resulting expressions back to x-space but in practice it is more convenient to determine the corresponding contributions to $c^{(n,0,0;a,b)}_{ij,\tilde{\mathbf{R}}}$ by converting Eq. (3.41) to N-space and matching the generic coefficients to the Mellin products of the hard and soft function $H^{(0)}_{\mathbf{R}\otimes\mathbf{R}'|\tilde{\mathbf{R}},N} S^{(2)}_{\mathbf{R}\otimes\mathbf{R}'|\tilde{\mathbf{R}},N}$ and $H^{(1)}_{\mathbf{R}\otimes\mathbf{R}'|\tilde{\mathbf{R}},N} S^{(1)}_{\mathbf{R}\otimes\mathbf{R}'|\tilde{\mathbf{R}},N}$. The corresponding hard coefficients at NLO can be inferred from

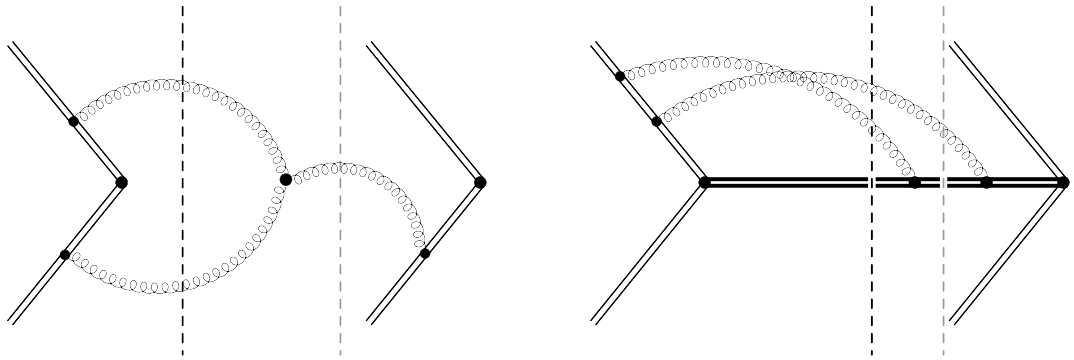

Figure 3.3: *Eikonal cut diagrams contributing to the NNLO soft function for singlet (left) and octet (right) production. The different cuts correspond to purely real (black) and real-virtual (gray) corrections.*

Eq. (2.105) by subtracting the soft-radiation components and read[7]

$$
\begin{aligned}
H^{(1)}_{\mathbf{8}\otimes\mathbf{8}|\mathbf{1}}\left(\rho,\frac{\mu_R^2}{m_t^2}\right) &= \bar{\sigma}^{(0)}_{gg,\mathbf{1}}(\beta)\left[C_F\,\frac{\pi^2}{2\beta}+C_F\left(-5+\frac{\pi^2}{4}\right)+C_A\left(1+\frac{\pi^2}{3}-2\ln^2 2\right)\right.\\
&- \left.\frac{C_A}{2}\ln^2\left(\frac{\mu_R^2}{m_t^2}\right)+2\,C_A\ln 2\,\ln\left(\frac{\mu_R^2}{m_t^2}\right)\right]\\
H^{(1)}_{\mathbf{8}\otimes\mathbf{8}|\mathbf{8_S}}\left(\rho,\frac{\mu_R^2}{m_t^2}\right) &= \bar{\sigma}^{(0)}_{gg,\mathbf{8_S}}(\beta)\left[\left(C_F-\frac{C_A}{2}\right)\frac{\pi^2}{2\beta}+C_A\left(2+\frac{5\pi^2}{24}+\ln 2-2\ln^2 2\right)\right.\\
&+ \left.C_F\left(-5+\frac{\pi^2}{4}\right)-\frac{C_A}{2}\ln^2\left(\frac{\mu_R^2}{m_t^2}\right)+C_A\ln\left(\frac{\mu_R^2}{m_t^2}\right)\left(-\frac{1}{2}+2\ln 2\right)\right]\\
H^{(1)}_{\mathbf{8}\otimes\mathbf{8}|\mathbf{8_A}}\left(\rho,\frac{\mu_R^2}{m_t^2}\right) &= \bar{\sigma}^{(0)}_{gg,\mathbf{8_A}}(\beta)\left(C_F-\frac{C_A}{2}\right)\frac{\pi^2}{2\beta}=\mathcal{O}\left(\beta^2\right)\\
H^{(1)}_{\mathbf{3}\otimes\bar{\mathbf{3}}|\mathbf{8}}\left(\rho,\frac{\mu_R^2}{m_t^2}\right) &= \bar{\sigma}^{(0)}_{q\bar{q},\mathbf{8}}(\beta)\left[\left(C_F-\frac{C_A}{2}\right)\frac{\pi^2}{2\beta}+C_F\left(-8+\frac{7\pi^2}{12}+3\ln 2-2\ln^2 2\right)\right.\\
&+ C_A\left(\frac{50}{9}-\frac{\pi^2}{4}-2\ln 2\right)+T_F\,n_l\left(-\frac{10}{9}+\frac{4}{3}\ln 2\right)-\frac{8}{9}\\
&- \left.\frac{C_F}{2}\ln^2\left(\frac{\mu_R^2}{m_t^2}\right)+\ln\left(\frac{\mu_R^2}{m_t^2}\right)\left(\frac{4}{3}\,C_A+C_F\left(-\frac{3}{2}+2\ln 2\right)-\frac{2}{3}\,T_F\,n_l\right)\right]\,.
\end{aligned}
\tag{3.46}
$$

Note that the terms associated with potential-gluon exchange are independent of the initial state, a feature that will not persist through NNLO due to the emergence of non-Coulombic contributions in the heavy-quark potentials that distinguish between different spin states.

[7] For completeness, we here give the full scale dependence whereas it is understood that the functions entering Eq. (3.42) - (3.44) correspond to the choice $\mu_R = m_t$.

The soft coefficients in Eq. (3.44), on the other hand, correspond to so-called eikonal cross sections, which may be determined from diagrams of the type displayed in Fig. 3.3. These cross sections are based on a fixed-order expansion of the Wilson line operators as explained in the beginning of section 3.1. The resulting products of eikonal currents can then be treated systematically by introducing a set of modified Feynman rules:

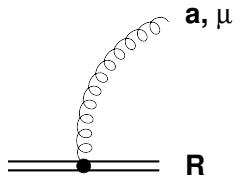

$= i\, g_s^0\, p^\mu\, \boldsymbol{T}^{(\boldsymbol{R})\, a}$

soft-gluon vertex where p is the hard momentum flowing through the eikonal line

$= \dfrac{i}{\mp p \cdot k + i\epsilon}$

Eikonal propagator where k is the sum of all gluon momenta emitted before/after an ingoing/outgoing line (negative/positive sign in denominator)

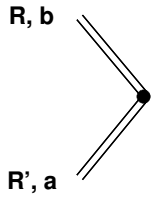

$= C_{ab}^{\mathbf{R}\otimes\mathbf{R}'|\mathbf{1}}$

Singlet interaction with the explicit form of the vertex factor given in Eq. (3.31)

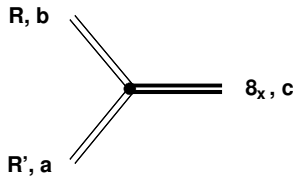

$= C_{abc}^{\mathbf{R}\otimes\mathbf{R}'|\mathbf{8_x}}$

Octet interaction with the explicit form of the vertex factor given in Eq. (3.31)

These prescriptions allow for the construction of eikonal amplitudes that may also contain virtual corrections as indicated by the unitarity cuts in Fig. 3.3. Interestingly, the purely loop-induced contributions vanish in CDR as the rescaling invariance of the eikonal currents with respect to the external momenta implies that the corresponding integrals are completely scaleless. Thus, they will only start to effectively contribute to the soft function at NNLO accuracy. The resulting eikonal amplitudes, real and virtual, are subsequently squared and integrated over the soft-gluon phase space

$$d\mathrm{PS}_n = \frac{Q}{2} \int \prod_{i=1}^{n} \frac{d\Omega_{d-1}^{(i)}}{(2\pi)^{d-1}} \frac{E_i^{d-3}}{2}\, \delta(\omega - \sum_{i=1}^{n} E_i)\ , \tag{3.47}$$

yielding the bare soft function

$$S^0_{\mathbf{R}\otimes\mathbf{R}'|\tilde{\mathbf{R}}}(z) = \delta(1-z) + \frac{1}{1-z} \sum_{n=1} \left(\frac{Z_{\alpha_s}\, \alpha_s}{\pi}\right)^n \left(\frac{\mu}{Q\,(1-z)}\right)^{2n\epsilon} s^{(n)}_{\mathbf{R}\otimes\mathbf{R}'|\tilde{\mathbf{R}}}(\epsilon) \tag{3.48}$$

where the generic form of the perturbative expansion can be deduced from general dimensionality arguments. The singular coefficients $s^{(n)}_{\mathbf{R}\otimes\mathbf{R}'|\tilde{\mathbf{R}}}(\epsilon)$ are independent of the soft kinematics

and can be characterized in terms of the Casimir operators of the color representations involved (i. e. $C_R \in \{C_F, C_A\}$, $C_{\tilde{R}} \in \{0, C_A\}$ and C_A) as well as by the number of light quarks n_l (as usual, accompanied by a factor T_F). Thus, the corresponding Mellin function in the leading N approximation is given by

$$\begin{aligned} S^0_{\mathbf{R}\otimes\mathbf{R}'|\tilde{\mathbf{R}},\,\tilde{N}} &= \int_0^1 dz\, z^{\tilde{N}-1}\, S^0_{\mathbf{R}\otimes\mathbf{R}'|\tilde{\mathbf{R}}}(z) \\ &= 1 + \sum_{n=1} \left(\frac{Z_{\alpha_s}\,\alpha_s}{\pi}\right)^n e^{2n\epsilon(L-\gamma_E)}\,\Gamma(-2n\epsilon)\, s^{(n)}_{\mathbf{R}\otimes\mathbf{R}'|\tilde{\mathbf{R}}}(\epsilon) \,+\, \mathcal{O}\left(\frac{1}{N}\right) \end{aligned} \tag{3.49}$$

where we have used a slightly different Mellin variable $\tilde{N} = Ne^{-\gamma_E}$ to remove the artificial γ_E constants that arise in the expansion of the Gamma function $\Gamma(-2n\epsilon)$ that governs the global soft-divergence structure. Note, however, that in contrast to the $\overline{\text{MS}}$-prescription where all γ_E-dependent normalization factors may be completely absorbed by a proper redefinition of the coupling constant, the functional form of the N-space cross section in terms of a power-logarithmic expansion only allows for a shift of these constants between the hard and soft contributions. Therefore, they have to be adequately accounted for when converting back to x-space, a feature that is naturally implemented in the matching procedure described above.

The Mellin transformation reveals that the bare soft function actually depends on $L = \ln \frac{\mu N}{Q}$ rather than on $\frac{\mu}{Q}$ and N separately, a property that also holds for the renormalized result Eq. (3.38). This is due to the fact that the anomalous dimensions controlling the singularity structure of $Z_H^{\mathbf{R}\otimes\mathbf{R}'|\tilde{\mathbf{R}}}$ and $Z_{\phi_i,\,N}$ display an equivalent functional behavior in the soft-collinear limit, i. e.

$$\begin{aligned} \Gamma_H^{\mathbf{R}\otimes\mathbf{R}'|\tilde{\mathbf{R}}} &\xrightarrow{\text{soft-col.}} -4\,C_R\,\gamma_{\text{cusp}}(\alpha_s)\ln\frac{\mu}{Q} \\ P^{\mathbf{R}}_{\tilde{N}} \equiv \int dz\, z^{\tilde{N}-1}\, P_{ii}(z) &\xrightarrow{\text{soft-col.}} -C_R\,\gamma_{\text{cusp}}(\alpha_s)\ln N\ . \end{aligned} \tag{3.50}$$

In consequence the logarithmic enhancements entering $S_{\mathbf{R}\otimes\mathbf{R}'|\tilde{\mathbf{R}},\,\tilde{N}}$ can be entirely predicted from its known scale dependence

$$\frac{dS_{\mathbf{R}\otimes\mathbf{R}'|\tilde{\mathbf{R}},\,\tilde{N}}}{d\ln\mu}(\alpha_s(\mu^2), L) = -\left(\Gamma_H^{\mathbf{R}\otimes\mathbf{R}'|\tilde{\mathbf{R}}} + 4\,P^{\mathbf{R}}_{\tilde{N}}\right)(\alpha_s(\mu^2), L)\, S_{\mathbf{R}\otimes\mathbf{R}'|\tilde{\mathbf{R}},\,\tilde{N}}(\alpha_s(\mu^2), L) \tag{3.51}$$

where so far we assumed that $\mu_F = \mu_R = \mu$. The general case $\mu_F \neq \mu_R$ may be restored by employing

$$\frac{dS_{\mathbf{R}\otimes\mathbf{R}'|\tilde{\mathbf{R}},\,\tilde{N}}}{d\ln\mu_F^2}(\alpha_s(\mu_R^2), L, L_\mu) = -2\,P^{\mathbf{R}}_{\tilde{N}}(\alpha_s(\mu_R^2), L_\mu)\, S_{\mathbf{R}\otimes\mathbf{R}'|\tilde{\mathbf{R}},\,\tilde{N}}(\alpha_s(\mu_R^2), L, L_\mu) \tag{3.52}$$

with $L = \ln\frac{\mu_R N}{Q}$ and $L_\mu = \ln\frac{\mu_R^2}{\mu_F^2}$, and the boundary condition

$$S_{\mathbf{R}\otimes\mathbf{R}'|\tilde{\mathbf{R}},\,\tilde{N}}(\alpha_s(\mu^2), L, 0) = S_{\mathbf{R}\otimes\mathbf{R}'|\tilde{\mathbf{R}},\,\tilde{N}}(\alpha_s(\mu^2), L)\ . \tag{3.53}$$

The N-dependence of the result will then, however, be no longer given in terms of L alone but there will be isolated logarithms of N that cannot be combined with the L_μ-terms to form a single argument. Note that due to the factorization of hard and soft contributions the entire μ_F-dependence is contained in $S_{\mathbf{R}\otimes\mathbf{R}'|\tilde{\mathbf{R}},N}$ whereas $H_{\mathbf{R}\otimes\mathbf{R}'|\tilde{\mathbf{R}},N}$ remains a function of μ_R only, which simplifies the determination of the general scale dependence of the N-space partonic cross sections considerably.

The non-logarithmic parts of the soft function, which contribute to the constant coefficients of the threshold expansion in Eq. (3.41), on the other hand, cannot be deduced from renormalization group arguments and have to be determined through an explicit calculation. The singlet result may actually be directly inferred from Drell-Yan production [566] (for the gluonic case with the replacement $C_F \to C_A$) while the NLO octet functions have already been evaluated in Refs. [219, 515, 567]. In the course of this work we were able to determine the missing NNLO octet contributions [558] and somewhat extend the previous analyses by providing expressions for the bare soft coefficients $s^{(n)}_{\mathbf{R}\otimes\mathbf{R}'|\tilde{\mathbf{R}}}(\epsilon)$ up to $\mathcal{O}\left(\alpha_s^2\right)$ in a completely analytical form that is, moreover, valid in d dimensions[8], i. e. given in a closed form in terms of ϵ. To this end, we considered the diagrams depicted in Fig. 3.4 that were subsequently translated into eikonal cross sections of different complexity, the most complicated case being the interference of categories (A) and (B). In order to efficiently handle the resulting expressions we used partial fractioning to reduce the number of independent integrals to a minimum. In the case of purely real corrections we applied a Mellin-Barnes decomposition to the most intricate denominator structure

$$\frac{1}{(n_i\cdot(k_1+k_2))^\alpha} = \frac{1}{\Gamma(\alpha)}\int_{-i\infty}^{+i\infty}\frac{dz}{2\pi i}\,\frac{1}{(n_i\cdot k_1)^{\alpha+z}(n_i\cdot k_2)^{-z}}\Gamma(\alpha+z)\Gamma(-z) \tag{3.54}$$

in order to disentangle the soft gluon momenta k_i in the eikonal propagators ($n_i = p_i/p_i^0$ corresponds to the normalized hard momentum of a massless eikonal line). This simplified the subsequent angular integrations considerably, which could then be performed with the help of [568]

$$\int d\Omega_{d-1}(k)\,\frac{(k^0)^\alpha}{(n_i\cdot k)^\alpha} = 2^{2-\alpha-2\epsilon}\,\pi^{1-\epsilon}\,\frac{\Gamma(1-\alpha-\epsilon)}{\Gamma(2-\alpha-2\epsilon)}\,,$$

$$\int d\Omega_{d-1}(k)\,\frac{(k^0)^{\alpha+\beta}}{(n\cdot k)^\alpha(\bar{n}\cdot k)^\beta} = 2^{2-\alpha-\beta-2\epsilon}\,\pi^{1-\epsilon}\,\frac{\Gamma(1-\alpha-\epsilon)\,\Gamma(1-\beta-\epsilon)}{\Gamma(1-\epsilon)\Gamma(2-\alpha-\beta-2\epsilon)}\,,$$

$$\begin{aligned}\int d\Omega_{d-1}(k_2)\,\frac{(k_1^0)^\beta(k_2^0)^{\alpha+\beta}}{(n_i\cdot k_2)^\alpha(k_1\cdot k_2)^\beta} &= 2^{2-\alpha-\beta-2\epsilon}\,\pi^{1-\epsilon}\,\frac{1}{\Gamma(\alpha)\,\Gamma(\beta)\,\Gamma(2-\alpha-\beta-2\epsilon)}\\ &\quad\times\int_{-i\infty}^{+i\infty}\frac{dz}{2\pi i}\,\Gamma(-z)\Gamma(z+\alpha)\Gamma(z+\beta)\Gamma(1-\alpha-\beta-\epsilon-z)\left(\frac{n_i\cdot k_1}{2k_1^0}\right)^z\,.\end{aligned} \tag{3.55}$$

[8] The singlet results are also given in arbitrary dimensions, however, in x-space rather than in the Mellin-moment formalism.

The remaining part of the soft-gluon phase space, the energy integrations, could be expressed in terms of the Euler beta function and was thus trivial. In case we had to employ a Mellin-Barnes representation, the resulting integrals were evaluated by means of the MB [541,542], HypExp [569] and Xsummer [540] packages leading to products of Gamma functions and, in more complicated cases, also to hypergeometric functions of the dimensionality parameter ϵ.

The second type of NNLO corrections, the real-virtual contributions, consist of contractions of the diagrams in category (D) with the NLO graphs (not shown in Fig. 3.4). They may, however, be further simplified by utilizing the so-called general eikonal identity Eq. (3.6). Applied to the case of two soft emissions it states that

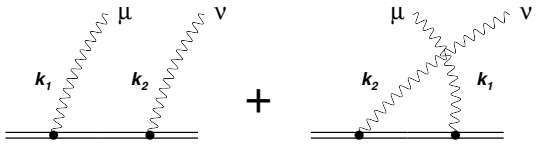

$$= \frac{p_1^\mu}{p_1\cdot k_1}\frac{p_1^\nu}{p_1\cdot(k_1+k_2)} + \frac{p_1^\nu}{p_1\cdot k_2}\frac{p_1^\mu}{p_1\cdot(k_1+k_2)}$$

$$= \frac{p_1^\mu}{p_1\cdot k_1}\frac{p_1^\nu}{p_1\cdot k_2} =$$

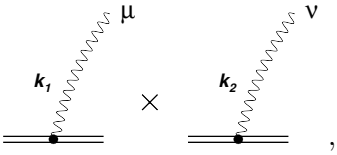

, (3.56)

i. e. the soft momenta are effectively separated leading to a complete factorization of real and virtual contributions, the latter of which are equal to zero due to the arguments presented above. Note, however, that the eikonal identity is actually only valid for commutating currents, as indicated by the photon lines, which is, in fact, the reason why the all-order soft factorization in QED assumes a particularly simple form. In the non-abelian case, on the other hand, there will be an additional term proportional to $i\,f^{abc}\boldsymbol{T}^{(\boldsymbol{R})\,c}$ that prevents a complete separation of real and virtual effects resulting in a non-vanishing contribution to the soft function. Still, the eikonal identity is useful in QCD as well since it allows for the computation of pairs of real-virtual graphs (indicated in Fig. 3.4 by a plus sign) by considering either one of them and treating it with a modified color factor. The resulting loop integrals can then be classified as follows

$$\begin{aligned}
M_1: &\quad \int d^dk\,\frac{1}{[k^2]\,[(k+q)^2]\,[n_i\cdot k]} && \int d^dk\,\frac{1}{[k^2]\,[(k+q)^2]\,[-v\cdot k]} \\
M_2: &\quad \int d^dk\,\frac{1}{[k^2]\,[-n_i\cdot k-n_i\cdot q]\,[-v\cdot k]} && \int d^dk\,\frac{1}{[k^2]\,[v\cdot k+v\cdot q]\,[n\cdot k]} && \int d^dk\,\frac{1}{[k^2]\,[v\cdot k+v\cdot q]\,[-v\cdot k]} \\
M_3: &\quad \int d^dk\,\frac{1}{[k^2]\,[(k+q)^2]\,[-n\cdot k-n\cdot q]\,[\overline{n}\cdot k]} && \int d^dk\,\frac{1}{[k^2]\,[(k+q)^2]\,[v\cdot k-v\cdot q]\,[n_i\cdot k]}\ .
\end{aligned} \tag{3.57}$$

The naming convention of the master integrals, M_1, M_2 and M_3 has been adopted from Ref. [570] where these one-loop functions have already been evaluated in a different context.

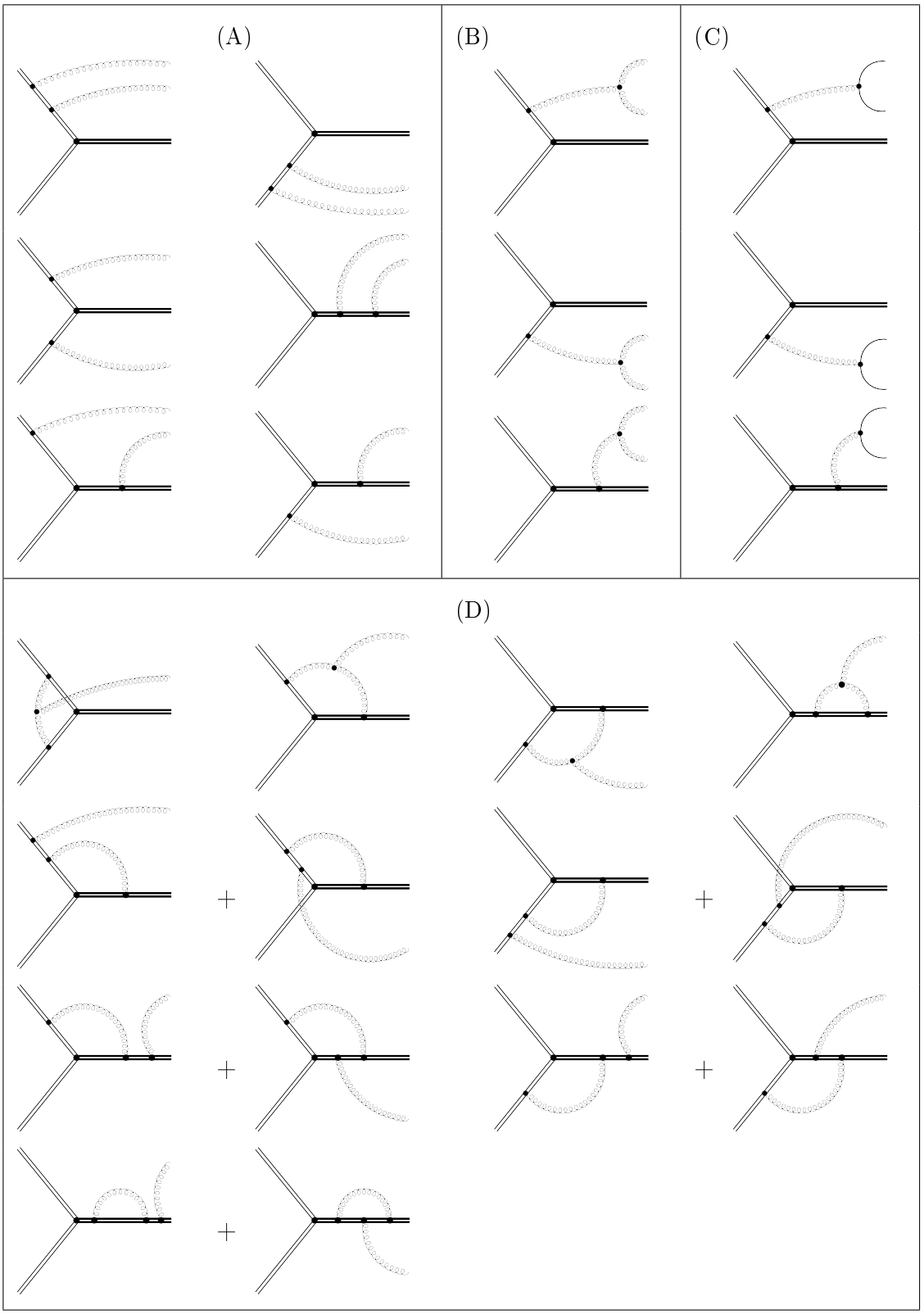

Figure 3.4: *Complete set of eikonal graphs contributing to the NNLO soft function for octet production. The graphs are divided into (A) two emissions from eikonal lines, (B) gluon splitting after emission from an eikonal line, (C) massless quark-pair emission and (D) real-virtual contributions (the pairs of graphs connected by a plus sign can be combined as explained in the text).*

The remaining phase space integration is trivial and did, in particular, not require the introduction of any Mellin-Barnes representations rendering the final expression free of hypergeometric functions. Combining the result with the purely real corrections and applying UV (through Z_{α_s}) and IR renormalization we then arrive at the NNLO soft function for octet production. The relevant coefficients up to $\mathcal{O}\left(\alpha_s^2\right)$ read

$$
\begin{aligned}
S^{(1)}_{\mathbf{R}\otimes\mathbf{R}'|\tilde{\mathbf{R}},\tilde{N}}(L,L_\mu) &= C_{\tilde{R}}\,(L+1) + C_R\left(2\,L^2+\frac{\pi^2}{12}\right) + P^{\mathbf{R},(0)}_{\tilde{N}}\,L_\mu \\
S^{(2)}_{\mathbf{R}\otimes\mathbf{R}'|\tilde{\mathbf{R}},\tilde{N}}(L,L_\mu) &= C_{\tilde{R}}^2\left(\frac{17L^2}{12}+\left(\frac{\zeta(3)}{2}+\frac{151}{36}-\frac{\pi^2}{12}\right)L-\frac{5\zeta(3)}{8}+\frac{13\pi^4}{2880}+\frac{\pi^2}{24}+\frac{223}{54}\right) \\
&+ C_R\,C_{\tilde{R}}\left(2\,L^3+2\,L^2+\frac{\pi^2 L}{12}+\frac{\pi^2}{12}\right)+C_{\tilde{R}}\,T_F\,n_l\left(-\frac{L^2}{3}-\frac{11L}{9}-\frac{40}{27}\right) \\
&+ C_R\,C_A\left(\frac{11L^3}{9}+\left(\frac{67}{18}-\frac{\pi^2}{6}\right)L^2+\left(-\frac{7\zeta(3)}{2}+\frac{101}{27}\right)L\right. \\
&\quad \left.-\frac{11\zeta(3)}{72}-\frac{\pi^4}{48}+\frac{67\pi^2}{864}+\frac{607}{324}\right) \\
&+ C_R\,T_F\,n_l\left(-\frac{4L^3}{9}-\frac{10L^2}{9}-\frac{28L}{27}+\frac{\zeta(3)}{18}-\frac{5\pi^2}{216}-\frac{41}{81}\right) \\
&+ C_R^2\left(2\,L^4+\frac{\pi^2L^2}{6}+\frac{\pi^4}{288}\right)+\left(\frac{P^{\mathbf{R},(1)}_{\tilde{N}}}{2}+P^{\mathbf{R},(0)}_{\tilde{N}}\,S^{(1)}_{\mathbf{R}\otimes\mathbf{R}'|\tilde{\mathbf{R}},\tilde{N}}(L,0)\right)L_\mu \\
&+ \left(\frac{\left(P^{\mathbf{R},(0)}_{\tilde{N}}\right)^2}{2}+\frac{\beta_0 P^{\mathbf{R},(0)}_{\tilde{N}}}{8}\right)L_\mu^2\,.
\end{aligned}
\tag{3.58}
$$

Note that the singlet contributions, $C_{\tilde{R}}=0$, may be naturally included in these results as the corresponding diagrams constitute a subclass of the graphs displayed in Fig. 3.4 and therefore do not lead to any new kinematic dependencies, i. e. they can be described by the same set of master integrals. As expected, the scale dependence $\mu_F \neq \mu_R$ is governed by the expansion coefficients $P^{\mathbf{R},(n)}_{\tilde{N}}$ of the large-N splitting kernels (for explicit expressions see appendix B), which do not distinguish between different final-state representations but only depend on the nature of the initial-state particles. Consequently, this property also holds for the leading L_μ-term of the threshold expansion to all orders in perturbation theory (except for the trivial $\tilde{\mathbf{R}}$-dependence from the factored born cross section). For the leading μ_R-dependence the situation is similar although this cannot be directly concluded from the explicit L-terms quoted above since it involves a delicate cancellation of hard and soft contributions such that the remaining logarithmic dependence of the partonic cross sections for a given expansion order n is at most $\ln^n \frac{\mu_R^2}{m_t^2}$. This, in particular, means that the final threshold result is less sensitive to the actual scale choice than both hard and soft function considered separately.

However, since we are primarily interested in the determination of the unknown functions Eq. (3.42) - (3.44), it is sufficient to consider only the case $L = \ln \frac{N}{2}$ and $L_\mu = 0$ ignoring the general scaling behavior.

With the result for the soft function at hand the only missing ingredient for the determination of the NNLO threshold expansion is the hard function $H^{(2)}_{\mathbf{R}\otimes\mathbf{R}'|\tilde{\mathbf{R}}}$. As mentioned before, it can be evaluated directly in momentum space but due to its definition it requires the knowledge of the two-loop finite remainder functions, which constitute a genuine NNLO contribution and are thus not necessarily available considering the fact that we are ultimately aiming at an approximate NNLO prediction. Fortunately, it is possible to infer the velocity-enhanced terms from the Coulomb resummation formalism, which allows for the inclusion of at least the dominant threshold behavior in the β-expansion. Up to $\mathcal{O}\left(\alpha_s^4\right)$ these potential contributions read [81,230,234,559]

$$\begin{aligned}
H^{\text{pot.}}_{\mathbf{R}\otimes\mathbf{R}'|\tilde{\mathbf{R}}}\left(\alpha_s(\mu_R), \rho, \frac{\mu_R^2}{m_t^2}\right) &= \frac{\alpha_s^2(\mu_R)}{m_t^2}\, H^{(0)}_{\mathbf{R}\otimes\mathbf{R}'|\tilde{\mathbf{R}}}(\rho)\left[1 + \frac{\alpha_s(\mu_R)}{\pi}\, H^{(1),\,\text{match.}}_{\mathbf{R}\otimes\mathbf{R}'|\tilde{\mathbf{R}}}\left(\frac{\mu_R^2}{m_t^2}\right)\right] \\
&\times \left[\left(\frac{\alpha_s(\mu_R)}{\pi}\, D_{\tilde{R}}\, \frac{\pi^2}{\beta}\right) \frac{1}{\exp\left(\frac{\alpha_s(\mu_R)}{\pi}\, D_{\tilde{R}}\, \frac{\pi^2}{\beta}\right) - 1} - 1\right. \\
&- \left(\frac{\alpha_s(\mu_R)}{\pi}\right)^2 D_{\tilde{R}}\, \frac{\pi^2}{\beta}\left(\frac{a_1}{8} - \frac{\beta_0}{4}\ln\frac{2m_t\beta}{\mu_R}\right) \\
&- \left(\frac{\alpha_s(\mu_R)}{\pi}\right)^2 D_{\tilde{R}}\, \pi^2\left(2\, D_{\tilde{R}}\,(1 + v_{\text{spin}}) - C_A\right)\ln\beta \\
&- \left.\left(\frac{\alpha_s(\mu_R)}{\pi}\right)^2 D_{\tilde{R}}\, \frac{\pi^2}{2}\, \delta_{\tilde{R}8}\ln\beta\right] + \mathcal{O}\left(\alpha_s^5(\mu_R)\right) \\
&\equiv \frac{\alpha_s^2(\mu_R)}{m_t^2}\left[\frac{\alpha_s(\mu_R)}{\pi}\, H^{(0),\,\text{pot.}}_{\mathbf{R}\otimes\mathbf{R}'|\tilde{\mathbf{R}}}(\rho) + \left(\frac{\alpha_s(\mu_R)}{\pi}\right)^2 H^{(1),\,\text{pot.}}_{\mathbf{R}\otimes\mathbf{R}'|\tilde{\mathbf{R}}}\left(\rho, \frac{\mu_R^2}{m_t^2}\right)\right]
\end{aligned} \tag{3.59}$$

where $D_{\tilde{R}}$ is the coupling strength of the Coulomb potential in the representation $\tilde{\mathbf{R}}$, with $D_1 = -C_F$ and $D_{8_S} = D_{8_A} = D_8 = -(C_F - C_A/2)$, and $a_1 = \frac{31}{9}\, C_A - \frac{20}{9}\, T_F\, n_l$. The NLO matching coefficients[9] are defined as

$$H^{(1)}_{\mathbf{R}\otimes\mathbf{R}'|\tilde{\mathbf{R}}}\left(\rho, \frac{\mu_R^2}{m_t^2}\right) - H^{(0),\,\text{pot.}}_{\mathbf{R}\otimes\mathbf{R}'|\tilde{\mathbf{R}}}(\rho) \equiv H^{(1),\,\text{match.}}_{\mathbf{R}\otimes\mathbf{R}'|\tilde{\mathbf{R}}}\left(\frac{\mu_R^2}{m_t^2}\right) \times H^{(0)}_{\mathbf{R}\otimes\mathbf{R}'|\tilde{\mathbf{R}}}(\rho)\ , \tag{3.60}$$

i. e. they contain the NLO non-potential hard contributions modulo the Born cross section. While the first rows in Eq. (3.59) contain the corrections due to LO (Sommerfeld factor[10])

[9] Not to be confused with the hard matching coefficients used in the literature usually in context of resummation as explained below.

[10] Due to the close relation of the expansion of the Sommerfeld factor to the Bernoulli numbers, all odd expansion coefficients beyond NLO vanish. This means that the leading power of $1/\beta$ in the NNNLO corrections will also only be $1/\beta^2$.

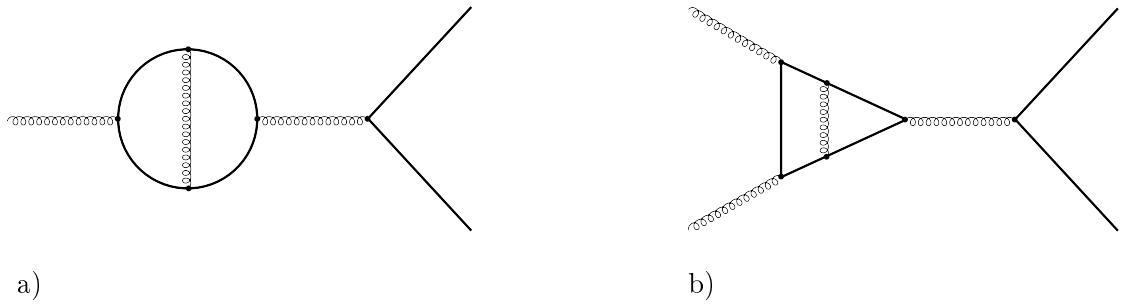

a) b)

Figure 3.5: *Examples of Coulomb exchange between virtual heavy quarks in an octet configuration contributing to the threshold expansion of the two-loop finite remainder.*

and NLO Coulomb interactions, the fourth row describes the effect of additional non-Coulomb potentials on the final-state heavy-quark system. Since they depend on the spin configuration of the $t\bar{t}$ pair, $v_{\text{spin}} = 0$ for a spin-singlet (gluon fusion channel) or $v_{\text{spin}} = -2/3$ for a spin-triplet (quark annihilation channel), they explicitly break the initial-state invariance of the heavy-quark potential.

The same also applies to the last term that effectively only contributes to the quark-induced $t\bar{t}$ cross section. It can be traced back to Coulomb corrections of the gluon propagators as shown in Fig. 3.5 a) and, hence, up to NNLO only occurs in s-channel production. As the original analysis of the non-relativistic threshold enhancements in hadronic collisions was based on a generalization of the singlet heavy-quark potential used in e^+e^- collisions, these contributions were actually missing in the approximate NNLO predictions at that time [230] and only became apparent once the full two-loop virtual corrections were available [234]. In practice, however, their absence had no noticeable consequences since their numerical impact is rather small. In principle, such a virtual Coulomb exchange is also present in the gluon fusion channel, however, exclusively in antisymmetric octet production, which is further suppressed at threshold. Note that in this case there exist an additional contribution from the vertex-type correction depicted in Fig. 3.5 b), which leads to an enhancement of the form $\sim \alpha_s^2(\mu_R)\, \ln \beta\, D_{\tilde{R}}/2$ that completely cancels the propagator-type correction associated with Fig. 3.5 a). In consequence, the effect of potential interactions between virtual heavy-quarks on the gluon-induced $t\bar{t}$ cross sections up to NNLO vanishes at threshold regardless of whether the LO contributions are suppressed or not. It would be interesting to further investigate the origin of this cancellation to clarify whether it is entirely coincidental or has a deeper physical meaning. This is particularly important with regard to the development of a general treatment of these virtual potential effects, which would allow for a systematical inclusion of these corrections in other threshold-enhanced processes as well.

The non-relativistic contributions are not the only available information concerning the NNLO hard function $H^{(2)}_{\mathbf{R}\otimes\mathbf{R}'|\tilde{\mathbf{R}}}$. Its scale dependence can also be predicted in advance from

$$\frac{dH_{\mathbf{R}\otimes\mathbf{R}'|\tilde{\mathbf{R}}}}{d\ln\mu_R^2} = \frac{1}{2}\,\Gamma_H^{\mathbf{R}\otimes\mathbf{R}'|\tilde{\mathbf{R}}}\, H_{\mathbf{R}\otimes\mathbf{R}'|\tilde{\mathbf{R}}} \tag{3.61}$$

such that the dominant gluonic singlet and symmetric octet modes can in general be parametrized

as

$$
\begin{aligned}
H^{(2)}_{\mathbf{8}\otimes\mathbf{8}|\mathbf{1}}\left(\rho,\frac{\mu_R^2}{m_t^2}\right) &= H^{(1),\,\mathrm{pot.}}_{\mathbf{8}\otimes\mathbf{8}|\mathbf{1}}(\rho,1)+\bar{\sigma}^{(0)}_{gg,\mathbf{1}}(\beta)\left\{H^{(2),\,\mathrm{match.}}_{\mathbf{8}\otimes\mathbf{8}|\mathbf{1}}(1)+\frac{C_A^2}{8}\ln^4\left(\frac{\mu_R^2}{m_t^2}\right)\right.\\
&+ \ln^3\left(\frac{\mu_R^2}{m_t^2}\right)\left[C_A^2\left(-\frac{11}{72}-\ln 2\right)+\frac{1}{18}C_A T_F n_l\right]\\
&+ \ln^2\left(\frac{\mu_R^2}{m_t^2}\right)\left[-C_F C_A\frac{\pi^2}{4\beta}+C_A^2\left(-\frac{103}{72}-\frac{\pi^2}{8}+\frac{11}{12}\ln 2+3\ln^2 2\right)\right.\\
&+ \left.C_A\left(C_F\left(\frac{5}{2}-\frac{\pi^2}{8}\right)+T_F n_l\left(\frac{5}{18}-\frac{1}{3}\ln 2\right)\right)\right]\\
&+ \ln\left(\frac{\mu_R^2}{m_t^2}\right)\left[C_F\left(C_A\left(\frac{11}{4}+6\ln 2\right)-T_F n_l\right)\frac{\pi^2}{6\beta}\right.\\
&+ C_A^2\left(-\frac{47}{54}+\frac{55\pi^2}{144}+\frac{\zeta(3)}{4}+\left(\frac{103}{18}+\frac{\pi^2}{2}\right)\ln 2-\frac{11}{6}\ln^2 2-4\ln^3 2\right)\\
&+ C_A\left(C_F\left(-\frac{55}{12}+\frac{11\pi^2}{48}+\left(\frac{\pi^2}{2}-10\right)\ln 2\right)\right.\\
&+ \left.\left.\left.T_F n_l\left(\frac{1}{54}-\frac{5\pi^2}{36}-\frac{10}{9}\ln 2+\frac{2}{3}\ln^2 2\right)\right)+C_F T_F n_l\left(\frac{5}{3}-\frac{\pi^2}{12}\right)\right]\right\}
\end{aligned}
\tag{3.62}
$$

$$
\begin{aligned}
H^{(2)}_{\mathbf{8}\otimes\mathbf{8}|\mathbf{8_S}}\left(\rho,\frac{\mu_R^2}{m_t^2}\right) &= H^{(1),\,\mathrm{pot.}}_{\mathbf{8}\otimes\mathbf{8}|\mathbf{8_S}}(\rho,1)+\bar{\sigma}^{(0)}_{gg,\mathbf{8_S}}(\beta)\left\{H^{(2),\,\mathrm{match.}}_{\mathbf{8}\otimes\mathbf{8}|\mathbf{8_S}}(1)+\frac{C_A^2}{8}\ln^4\left(\frac{\mu_R^2}{m_t^2}\right)\right.\\
&+ \ln^3\left(\frac{\mu_R^2}{m_t^2}\right)\left[C_A^2\left(\frac{7}{72}-\ln 2\right)+\frac{1}{18}C_A T_F n_l\right]\\
&+ \ln^2\left(\frac{\mu_R^2}{m_t^2}\right)\left[-C_A\left(C_F-\frac{C_A}{2}\right)\frac{\pi^2}{4\beta}+C_A^2\left(-\frac{293}{144}-\frac{\pi^2}{16}-\frac{7}{12}\ln 2+3\ln^2 2\right)\right.\\
&+ \left.C_A\left(C_F\left(\frac{5}{2}-\frac{\pi^2}{8}\right)+T_F n_l\left(\frac{13}{36}-\frac{1}{3}\ln 2\right)\right)\right]\\
&+ \ln\left(\frac{\mu_R^2}{m_t^2}\right)\left[\left(C_F-\frac{C_A}{2}\right)\left(C_A\left(\frac{5}{4}+6\ln 2\right)-T_F n_l\right)\frac{\pi^2}{6\beta}\right.\\
&+ C_A^2\left(-\frac{353}{216}+\frac{59\pi^2}{288}+\left(\frac{293}{36}+\frac{\pi^2}{4}\right)\ln 2+\frac{7}{6}\ln^2 2-4\ln^3 2\right)\\
&+ C_A\left(C_F\left(-\frac{25}{12}+\frac{5\pi^2}{48}+\left(\frac{\pi^2}{2}-10\right)\ln 2\right)\right.\\
&+ \left.\left.\left.T_F n_l\left(-\frac{1}{27}-\frac{7\pi^2}{72}-\frac{13}{9}\ln 2+\frac{2}{3}\ln^2 2\right)\right)+C_F T_F n_l\left(\frac{5}{3}-\frac{\pi^2}{12}\right)\right]\right\}
\end{aligned}
\tag{3.63}
$$

whereas the quark-initiated contributions are given as

$$
\begin{aligned}
H^{(2)}_{\mathbf{3}\otimes\bar{\mathbf{3}}|\mathbf{8}}\left(\rho,\frac{\mu_R^2}{m_t^2}\right) &= H^{(1),\,\mathrm{pot.}}_{\mathbf{3}\otimes\bar{\mathbf{3}}|\mathbf{8}}(\rho,1)+\bar{\sigma}^{(0)}_{q\bar{q},\mathbf{8}}(\beta)\left\{H^{(2),\,\mathrm{match.}}_{\mathbf{3}\otimes\bar{\mathbf{3}}|\mathbf{8}}(1)+\frac{C_F^2}{8}\ln^4\left(\frac{\mu_R^2}{m_t^2}\right)\right.\\
&+ \ln^3\left(\frac{\mu_R^2}{m_t^2}\right)\left[C_F^2\left(\frac{3}{4}-\ln 2\right)-\frac{59}{72}C_F\,C_A+\frac{7}{18}C_F\,T_F\,n_l\right]\\
&+ \ln^2\left(\frac{\mu_R^2}{m_t^2}\right)\left[-C_F\left(C_F-\frac{C_A}{2}\right)\frac{\pi^2}{4\beta}+C_F^2\left(\frac{41}{8}-\frac{7\pi^2}{24}-\frac{9}{2}\ln 2+3\ln^2 2\right)\right.\\
&+ C_A\left(\frac{3}{2}C_A+C_F\left(-\frac{307}{48}+\frac{\pi^2}{6}+\frac{55}{12}\ln 2\right)-\frac{17}{12}T_F\,n_l\right)\\
&+ \left.C_F\left(\frac{4}{9}+T_F\,n_l\left(\frac{25}{12}-\frac{7}{3}\ln 2\right)\right)+\frac{1}{3}T_F^2\,n_l^2\right]\\
&+ \ln\left(\frac{\mu_R^2}{m_t^2}\right)\left[\left(C_F-\frac{C_A}{2}\right)\left(\frac{27}{4}C_A+C_F\left(-\frac{9}{2}+6\ln 2\right)-3\,T_F\,n_l\right)\frac{\pi^2}{6\beta}\right.\\
&+ C_F^2\left(\frac{189}{16}-\frac{5\pi^2}{8}-3\zeta(3)+\left(-\frac{41}{2}+\frac{7\pi^2}{6}\right)\ln 2+9\ln^2 2-4\ln^3 2\right)\\
&+ C_F\left(\frac{4}{3}-\frac{16}{9}\ln 2+T_F\,n_l\left(\frac{1055}{108}-\frac{\pi^2}{2}-\frac{25}{3}\ln 2+\frac{14}{3}\ln^2 2\right)\right)\\
&+ C_A^2\left(\frac{953}{72}-\frac{25\pi^2}{48}-\frac{\zeta(3)}{4}-\frac{9}{2}\ln 2\right)\\
&+ C_A\left(C_F\left(-\frac{12337}{432}+\frac{35\pi^2}{24}+\frac{13\zeta(3)}{4}+\left(\frac{295}{12}-\frac{2\pi^2}{3}\right)\ln 2-\frac{17}{2}\ln^2 2\right)\right.\\
&+ \left.\left.T_F\,n_l\left(-\frac{155}{18}+\frac{\pi^2}{4}+5\ln(2)\right)-2\right)+{T_F}^2\,{n_l}^2\left(\frac{10}{9}-\frac{4}{3}\ln 2\right)+\frac{8}{9}T_F\,n_l\right]\Bigg\}\,.
\end{aligned}
\tag{3.64}
$$

Similar to NLO, the unknown matching coefficients $H^{(2),\,\mathrm{match.}}_{\mathbf{R}\otimes\mathbf{R}'|\tilde{\mathbf{R}}}\left(\frac{\mu_R^2}{m_t^2}\right)$ contain the remaining β-independent terms[11] that can only be determined through an explicit calculation of the NNLO virtual corrections, most notably the two-loop finite remainders since the one-loop-squared contributions are, in principle, already known fully analytically from the NLO analysis. The only exception is the antisymmetric octet configuration in gluon fusion production

$$
H^{(2)}_{\mathbf{8}\otimes\mathbf{8}|\mathbf{8_A}}\left(\rho,\frac{\mu_R^2}{m_t^2}\right)=H^{(1),\,\mathrm{pot.}}_{\mathbf{8}\otimes\mathbf{8}|\mathbf{8_A}}(\rho)+\bar{\sigma}^{(0)}_{gg,\mathbf{8_A}}(\beta)\,H^{(2),\,\mathrm{match.}}_{\mathbf{8}\otimes\mathbf{8}|\mathbf{8_A}}(\rho)
\tag{3.65}
$$

whose constant contributions at the two-loop level can be understood as a product of Coulomb corrections and NLO amplitudes and, thus, their evaluation involves virtually no additional

[11] More precisely, they contain the scale-independent, non-potential hard corrections that when combined with the respective Born cross section yield a contribution of $\mathcal{O}(\beta)$ to the threshold expansion.

computational costs. The reason for this lies in the LO suppression of this process, which, in consequence, requires the threshold behavior of the NNLO amplitudes to be only known to $\mathcal{O}(1/\beta)$. This simplifies matters considerably as it means that these contributions are already completely accounted for in the NLO potential function[12]

$$H^{(1),\,\mathrm{pot.}}_{\mathbf{8}\otimes\mathbf{8}|\mathbf{8_A}}(\rho) = \bar{\sigma}^{(0)}_{gg,\mathbf{8_A}}(\beta)\left(C_F - \frac{C_A}{2}\right)^2 \frac{\pi^4}{12\beta^2} \tag{3.66}$$

such that the only terms entering the matching coefficient for antisymmetric octet production stem from the non-potential $\mathcal{O}(\beta^0)$ parts of the NLO finite remainder

$$H^{(2),\,\mathrm{match.}}_{\mathbf{8}\otimes\mathbf{8}|\mathbf{8_A}} \sim$$

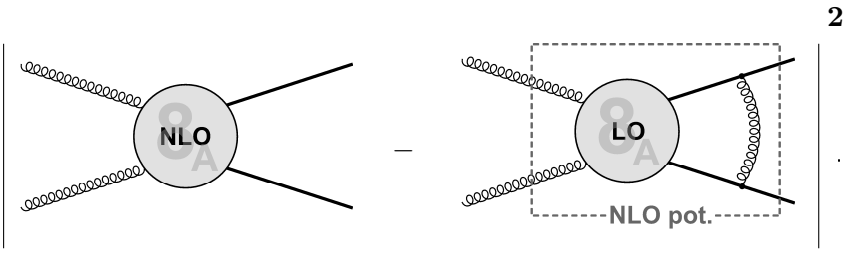

(3.67)

The corresponding potential corrections that need to be subtracted from the full NLO amplitudes may be readily derived by employing the factorization properties of the leading Coulomb behavior

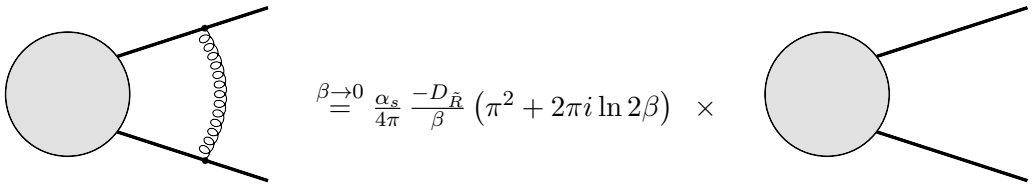

(3.68)

[12] Note that due to the absence of non-relativistic enhancements in the LO partonic cross sections the expansion of Eq. (3.59) starts at order $\mathcal{O}\left(\alpha_s^2 \frac{\alpha_s}{\pi}\right)$, i. e. the ordering convention (LO, NLO, ...) of the potential functions is shifted by one order with respect to the hard functions.

which eventually leads to

$$
\begin{aligned}
H_{\mathbf{8}\otimes\mathbf{8}|\mathbf{8_A}}^{(2),\,\mathrm{match.}}(\rho) \;=\; & \frac{1}{\beta^2}\left[C_F^2\left(\frac{3}{4}-\frac{\pi^2}{2}+\frac{3\pi^4}{16}+\left(6-3\pi^2\right)\ln 2+12\ln^2 2\right)\right. \\
& + C_A^2\left(\frac{25}{48}-\frac{\pi^2}{4}+\frac{3\pi^4}{64}+\left(\frac{5}{4}-\frac{3\pi^2}{8}\right)\ln 2+\frac{3}{4}\ln^2 2\right) \\
& + C_F\,C_A\left(-\frac{5}{4}+\frac{3\pi^2}{4}-\frac{3\pi^4}{16}+\left(-\frac{13}{2}+\frac{9\pi^2}{4}\right)\ln 2-6\ln^2 2\right) \\
& + C_F\left(-\frac{7}{4}+\frac{17\pi^2}{16}-\frac{3\pi^4}{32}+\left(-7+\frac{3\pi^2}{4}\right)\ln 2\right) \\
& + C_A\left(\frac{35}{24}-\frac{19\pi^2}{32}+\frac{3\pi^4}{64}+\left(\frac{7}{4}-\frac{3\pi^2}{16}\right)\ln 2\right) \\
& + C_F\,T_F\,n_l\left(-\frac{1}{2}+\frac{\pi^2}{4}-2\ln 2\right) \\
& + C_A\,T_F\,n_l\left(\frac{5}{12}-\frac{\pi^2}{8}+\frac{1}{2}\ln 2\right) \\
& \left. + T_F\,n_l\left(\frac{7}{12}-\frac{\pi^2}{16}\right)+\frac{1}{12}\,T_F^2\,n_l^2+\frac{49}{48}-\frac{7\pi^2}{32}+\frac{3\pi^4}{256}\right] .
\end{aligned}
\tag{3.69}
$$

In contrast to the matching coefficients of the other color representations the result is velocity-dependent to compensate for the $\mathcal{O}(\beta)$-suppression in the combined Born matrix elements that determine the partonic cross section at leading order. Since this vanishing behavior at threshold relies on a delicate cancellation between contributions from different diagrams, this effect does not persist to NLO as the corresponding quantum corrections do not trivially factorize. Hence, at the amplitude level both potential and non-potential contributions enter the NLO threshold expansion at the same order in β. Interestingly, this does not apply to the resulting NLO cross section where the non-potential terms drop out completely after contraction with the Born matrix elements such that

$$
H_{\mathbf{8}\otimes\mathbf{8}|\mathbf{8_A}}^{(1),\,\mathrm{match.}}(\rho) = 0 \,, \tag{3.70}
$$

which is also the reason why Eq. (3.66) assumes a particularly simple form. Only in the NNLO one-loop-squared corrections these terms finally show up, again accompanied by potential contributions of the same order in the threshold expansion as explained above. Therefore, the antisymmetric octet configuration differs substantially from the remaining representations in the sense that it possesses no clear hierarchy between these sources of velocity enhancements. Another consequence of the LO suppression is the fact that the corresponding threshold expansion up to $\mathcal{O}\left(\alpha_s^4\right)$ is entirely given by $H_{\mathbf{8}\otimes\mathbf{8}|\mathbf{8_A}}^{(2)}$ since all other contributions in Eq. (3.44) involve convolutions with either $H_{\mathbf{8}\otimes\mathbf{8}|\mathbf{8_A}}^{(0)}$ or $H_{\mathbf{8}\otimes\mathbf{8}|\mathbf{8_A}}^{(1)}$. This means that its contribution to

the approximate NNLO predictions can actually be derived without further knowledge of either the NNLO soft function or the two-loop virtual corrections as it is based on pure NLO considerations. This is also the reason why it is the only representation whose threshold behavior is known fully analytically whereas the matching coefficients $H^{(2),\,\text{match.}}_{\mathbf{8}\otimes\mathbf{8}|\mathbf{1}}$, $H^{(2),\,\text{match.}}_{\mathbf{8}\otimes\mathbf{8}|\mathbf{8_S}}$ and $H^{(2),\,\text{match.}}_{\mathbf{3}\otimes\bar{\mathbf{3}}|\mathbf{8}}$ contain contributions that are currently only available in numerical form (albeit with the exact dependence on the number of colors and active flavors) despite the tremendous effort aimed towards the analytical determination of two-loop virtual corrections. Their actual values have, in fact, been for the first time derived in the course of the full NNLO analysis [234] and were thus not included in the original threshold approximation [230]. For $N_c = 3$ and $\mu_R = m_t$ they read

$$\begin{aligned}
H^{(2),\,\text{match.}}_{\mathbf{8}\otimes\mathbf{8}|\mathbf{1}}(1) &= 27.474 + 0.006\,n_l = 27.504\\
H^{(2),\,\text{match.}}_{\mathbf{8}\otimes\mathbf{8}|\mathbf{8_S}}(1) &= 46.957 - 2.311\,n_l = 35.405\\
H^{(2),\,\text{match.}}_{\mathbf{3}\otimes\bar{\mathbf{3}}|\mathbf{8}}(1) &= 56.936 - 1.421\,n_l - 0.268\,n_l^2 = 43.141
\end{aligned} \tag{3.71}$$

where the last values here and below correspond to the case $n_l = 5$. Apart from these coefficients the NNLO threshold expansion is known completely analytically, i. e. all singular terms as $\beta \to 0$ can be predicted from soft and potential factorization [230]. Incorporating these findings in Eq. (3.44), the corresponding threshold functions for gluon fusion production are given by

$$\begin{aligned}
\bar{\sigma}^{(2,0,0)}_{gg,\mathbf{1}}(\beta) &= \frac{C_F^2\pi^2}{12\beta^2} + \frac{C_F}{72\beta}\Big[288C_A\ln^2\beta + 6\big(C_A(-11+48\ln 2)+2n_l\big)\ln\beta\\
&\quad + 9C_F\big(-20+\pi^2\big) + C_A\big(67-66\ln 2+3\pi^2\big) + 2n_l\big(-5+6\ln 2\big)\Big] + \frac{32C_A^2}{\pi^2}\ln^4\beta\\
&\quad + \frac{8C_A}{9\pi^2}\Big[C_A\big(-155+216\ln 2\big)+2n_l\Big]\ln^3\beta + \frac{2C_A}{9\pi^2}\Big[9C_F\big(-20+\pi^2\big)\\
&\quad + C_A\big(1963-2790\ln 2+1872\ln^2 2-96\pi^2\big) + 2n_l\big(-17+18\ln 2\big)\Big]\ln^2\beta\\
&\quad + \frac{1}{27\pi^2}\Big[27C_F\big(-2C_F\pi^2 + C_A(80+6\ln 2(-20+\pi^2)-5\pi^2)\big) + C_A\big(C_A(-23758\\
&\quad + 18\ln 2(1963-96\pi^2) - 24246\ln^2 2 + 10368\ln^3 2 + 1251\pi^2 + 6237\zeta_3)\\
&\quad + 2n_l(218-306\ln 2+162\ln^2 2-9\pi^2)\big)\Big]\ln\beta + \frac{1}{16\pi^2}\,C^{(2)}_{gg,\mathbf{1}}
\end{aligned} \tag{3.72}$$

$$\begin{aligned}
\bar{\sigma}^{(2,0,0)}_{gg,\mathbf{8_S}}(\beta) &= \frac{(2C_F-C_A)^2\pi^2}{48\beta^2}+\frac{(2C_F-C_A)}{288\beta}\Big[576C_A\ln^2\beta+12\big(C_A(-23+48\ln 2)+2n_l\big)\ln\beta \\
&\quad +18C_F\big(-20+\pi^2\big)+C_A\big(278-132\ln 2-3\pi^2\big)+4n_l\big(-5+6\ln 2\big)\Big]+\frac{32C_A^2}{\pi^2}\ln^4\beta \\
&\quad +\frac{8C_A}{9\pi^2}\Big[C_A\big(-173+216\ln 2\big)+2n_l\Big]\ln^3\beta+\frac{C_A}{9\pi^2}\Big[18C_F\big(-20+\pi^2\big) \\
&\quad +C_A\big(4553-6156\ln 2+3744\ln^2 2-201\pi^2\big)+2n_l\big(-37+36\ln 2\big)\Big]\ln^2\beta \\
&\quad +\frac{1}{108\pi^2}\Big[54C_F\big(-4C_F\pi^2+C_A(180+12\ln 2(-20+\pi^2)-7\pi^2)\big)+C_A\big(C_A(-111418 \\
&\quad +36\ln 2(4499-201\pi^2)-105624\ln^2 2+41472\ln^3 2+5823\pi^2+24840\zeta_3) \\
&\quad +4n_l(505-666\ln 2+324\ln^2 2-18\pi^2)\big)\Big]\ln\beta+\frac{1}{16\pi^2}C^{(2)}_{gg,\mathbf{8_S}}
\end{aligned} \tag{3.73}$$

$$\bar{\sigma}^{(2,0,0)}_{gg,\mathbf{8_A}}(\beta) = \frac{\bar{\sigma}^{(0)}_{gg,\mathbf{1}}+\bar{\sigma}^{(0)}_{gg,\mathbf{8_S}}}{16\pi^2\,\bar{\sigma}^{(0)}_{gg,\mathbf{8_A}}}C^{(2)}_{gg,\mathbf{8_A}} \tag{3.74}$$

with coefficients $C^{(2)}_{gg,\tilde{\mathbf{R}}}$ that include the constant behavior of both soft and hard contributions and, hence, are a combination of numerical and analytical inputs. The resulting expressions for the general color dependence are quite lengthy can be found in appendix C (along with the general results for Eq. (3.71)). Here, we focus on the case $N_c = 3$ relevant for SM top-quark pair production yielding [234]

$$\begin{aligned}
C^{(2)}_{gg,\mathbf{1}} &= 37.1457+17.2725\,n_l = 123.508 \\
C^{(2)}_{gg,\mathbf{8_S}} &= 674.517-45.5875\,n_l = 446.58 \\
C^{(2)}_{gg,\mathbf{8_A}} &= 11.2531-2.29745\,n_l+0.142857\,n_l^2 = 3.33731\,.
\end{aligned} \tag{3.75}$$

Since in phenomenological applications one is usually interested in the gluon fusion channel as a whole, i. e. the sum of all three color configurations, it is convenient to define an additional constant

$$C^{(2)}_{gg} = \frac{C^{(2)}_{gg,\mathbf{1}}\,\bar{\sigma}^{(0)}_{gg,\mathbf{1}}+C^{(2)}_{gg,\mathbf{8_S}}\,\bar{\sigma}^{(0)}_{gg,\mathbf{8_S}}}{\bar{\sigma}^{(0)}_{gg,\mathbf{1}}+\bar{\sigma}^{(0)}_{gg,\mathbf{8_S}}}+C^{(2)}_{gg,\mathbf{8_A}} = 503.664-29.9249\,n_l+0.142857\,n_l^2 = 357.611 \tag{3.76}$$

that incorporates all velocity-independent terms that enter Eq. (3.40) and is the reason for the rather peculiar parametrization chosen for $\bar{\sigma}^{(2,0,0)}_{gg,\mathbf{8_A}}$. Note that prior to the threshold analysis it has actually been determined from a fit to the numerical partonic cross section formulae

in Ref. [80] yielding

$$C_{gg}^{(2),\,\mathrm{fit}} = 338.179 - 26.8912\,n_l + 0.142848\,n_l^2 = 207.294\,. \tag{3.77}$$

This determination, however, suffers from sizable numerical uncertainties of up to 50% due to the limited number of fitting points, the freedom of parametrization in the fitting formula and the presence of $1/\beta$ and $\ln\beta$ enhancements that dominate the functional behavior in the small β regime. Still, the agreement for the n_l-dependent terms is quite good $\lesssim 10\%$ and only for $n_l = 0$ one can observe a pronounced difference with respect to the exact result, yet within the stated error estimate.

For the quark annihilation channel the threshold expansion reads

$$\begin{aligned}
\bar{\sigma}_{q\bar{q},\mathbf{8}}^{(2,0,0)}(\beta) \;=\;& \frac{(2C_F - C_A)^2\pi^2}{48\beta^2} + \frac{(2C_F - C_A)}{144\beta}\Big[288C_F\ln^2\beta + 6\big(48C_F\ln 2 - 23C_A + 2n_l\big)\ln\beta \\
& + 12C_F\big(-24 + 9\ln 2 + \pi^2\big) + 3C_A\big(89 - 58\ln 2 - 3\pi^2\big) + 6n_l\big(-5 + 6\ln 2\big) - 32\Big] \\
& + \frac{32C_F^2}{\pi^2}\ln^4\beta + \frac{8C_F}{9\pi^2}\Big[72C_F\big(-2 + 3\ln 2\big) - 29C_A + 2n_l\Big]\ln^3\beta \\
& + \frac{1}{9\pi^2}\Big[2C_F\big(12C_F(120 - 207\ln 2 + 156\ln^2 2 - 7\pi^2) + 3C_A(217 - 198\ln 2 - 4\pi^2) \\
& + 6n_l(-9 + 10\ln 2) - 32\big) + 3C_A(17C_A - 2n_l)\Big]\ln^2\beta \\
& + \frac{1}{108\pi^2}\Big[2C_F\big(36C_F(-960 + \ln 2(1368 - 84\pi^2) - 1140\ln^2 2 + 576\ln^3 2 + 55\pi^2 + 336\zeta_3) \\
& + 2C_A(-7582 + 108\ln 2(115 - 2\pi^2) - 5886\ln^2 2 + 360\pi^2 + 189\zeta_3) \\
& + 4n_l(338 - 630\ln 2 + 378\ln^2 2 - 9\pi^2) + 768 - 1152\ln 2 + 27\pi^2\big) \\
& + 3C_A\big(6C_A(-185 + 126\ln 2 + 6\pi^2 - 6\zeta_3) + 12n_l(11 - 10\ln 2) + 64 - 9\pi^2\big)\Big]\ln\beta \\
& + \frac{1}{16\pi^2}\,C_{q\bar{q}}^{(2)}
\end{aligned} \tag{3.78}$$

with the constant coefficient for $N_c = 3$ given as [234]

$$C_{q\bar{q}}^{(2)} \equiv C_{q\bar{q},\mathbf{8}}^{(2)} = 1104.08 - 42.9666\,n_l - 4.28168\,n_l^2 = 782.208\,. \tag{3.79}$$

The corresponding value from the numerical cross section formulae in Ref. [77] reads

$$C_{q\bar{q}}^{(2),\,\mathrm{fit}} = 1195.82 - 44.1841\,n_l - 4.28168\,n_l^2 = 867.858 \tag{3.80}$$

and qualitatively shows the same behavior as for the gluon fusion result, i. e. the level of agreement increases with the power of n_l. The overall difference is, however, much smaller than in the gluonic case amounting to only about 10% for $n_l = 0$, which again matches the quoted error estimate quite well. The reason why in the $q\bar{q}$ case the fitting procedure seems to yield more precise predictions lies in the parametrization of the partonic cross sections away from threshold. While in the quark annihilation channel one assumes a polynomial β-dependence, in the gluon fusion case also logarithms of β are introduced to the fitting formula reducing the sensitivity to the constant threshold behavior.

Now, in order to employ Eq. (3.75) and Eq. (3.79) as an estimate for the full NNLO partonic cross section, one has to address two central questions, namely how large is the effect of neglecting higher orders in β and how reliable is the theoretical error estimate due to scale variation in the context of kinematic expansions. Both points are strongly connected and aim at establishing approximate NNLO predictions whose error estimate is, on the one hand, significantly improved with regard to the NLO results and, on the other hand, accounts for yet missing contributions in a realistic manner. As already noted above, the partonic fluxes at the Tevatron and the LHC favor top-quark pairs to be produced at larger velocities $\beta \gtrsim 0.3$ such that subleading terms in the expansion may indeed become numerically important. Moreover, the fact that at NLO the β-expansion fails to adequately describe the functional dependence of the full cross sections away from threshold ($\beta \gtrsim 0.1$) suggests that one can expect a similar behavior at NNLO. Therefore, it is crucial to be able to estimate the impact of these missing terms on the approximate predictions quantitatively.

This may be achieved in different ways that are usually complementary and, thus, ideally combined to give the most stringent error estimate. As in the original approach the coefficients $C^{(2)}_{ij,\tilde{\mathbf{R}}}$ were still unknown[13], the most natural method to evaluate the effect of subleading contributions is to assume different values for these constants and compare the resulting cross section predictions. Common values used in the literature include $C^{(2)}_{ij,\tilde{\mathbf{R}}} = 0$ [81,220], $C^{(2)}_{ij,\tilde{\mathbf{R}}} = \overline{C}^{(2)}_{ij,\tilde{\mathbf{R}}}$ [220] and $C^{(2)}_{ij,\tilde{\mathbf{R}}} = \pm|C^{(2),\text{est.}}_{ij,\tilde{\mathbf{R}}}|$ [81] where $\overline{C}^{(2)}_{ij,\tilde{\mathbf{R}}}$ is defined such that it compensates for the constant terms introduced by the Mellin transformation of the soft logarithms[14]

$$\begin{aligned}
\overline{C}^{(2)}_{gg,\mathbf{1}} &= -796.712 + 30.663\, n_l = -643.397 \\
\overline{C}^{(2)}_{gg,\mathbf{8_S}} &= -1519.82 + 37.13\, n_l = -1334.18 \\
\overline{C}^{(2)}_{gg,\mathbf{8_A}} &= 0 \\
\overline{C}^{(2)}_{q\bar{q}} &= -607.594 + 23.685\, n_l = -489.168
\end{aligned} \tag{3.81}$$

and $C^{(2),\text{est.}}_{ij,\tilde{\mathbf{R}}} = \left(C^{(1)}_{ij,\tilde{\mathbf{R}}}\right)^2$ are the squares of the corresponding one-loop constants, a choice that has already proven to yield the correct order of magnitude in other processes. For top-quark

[13] There were partial results available for the one-loop-squared amplitudes [571–574] and two-loop virtual corrections [575–577] as well as the NNLO soft function [566] but they were usually omitted from the threshold analysis as it was not clear to what extent they reflect the full constant behavior.

[14] In principle, one could have also included the Mellin constants related to potential contributions but it is more convenient to consider them separately in case one is interested in resumming these terms.

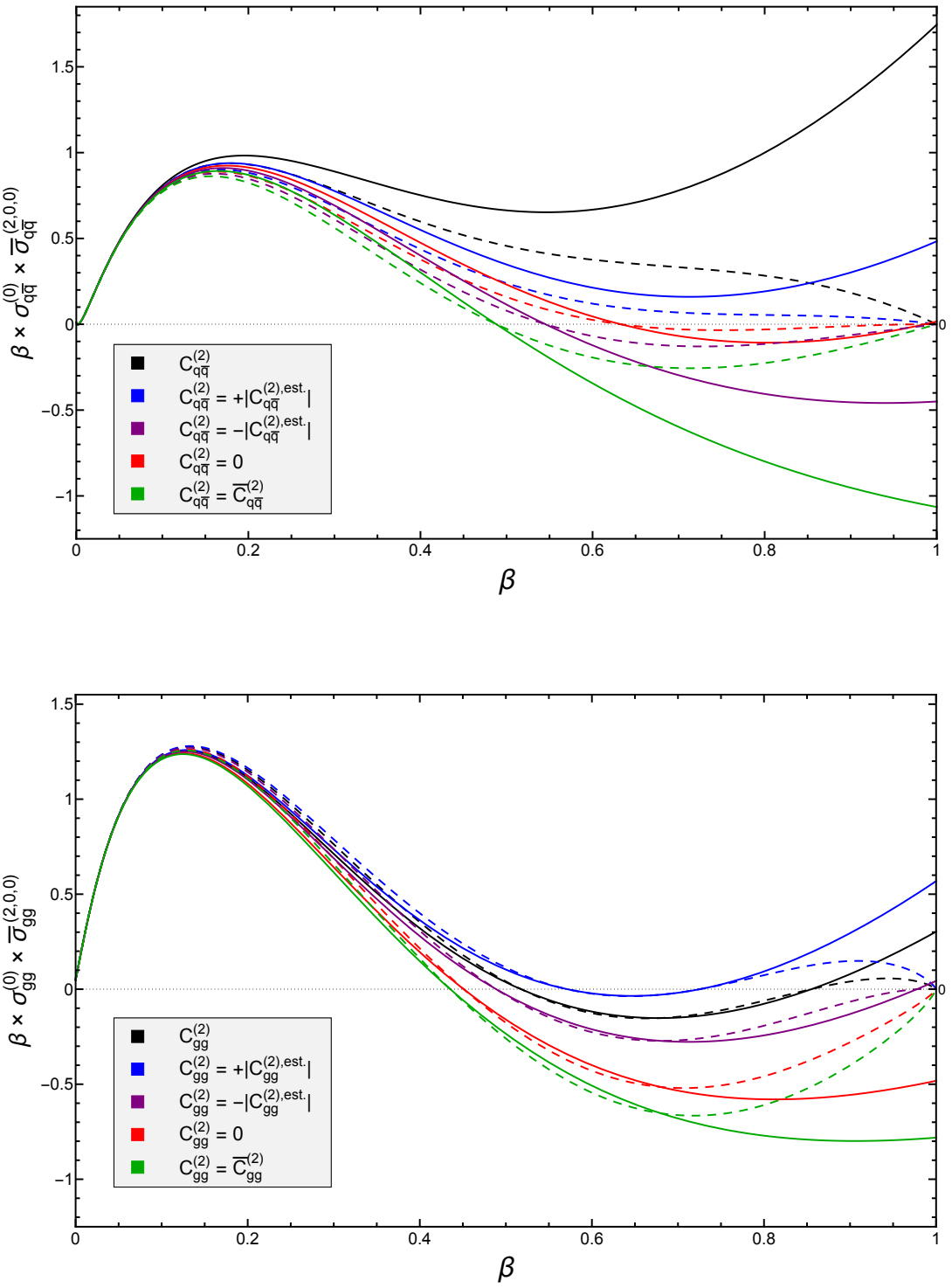

Figure 3.6: *Threshold expansion of the NNLO partonic cross section (multiplied by β for improved visibility) in the quark annihilation (top) and gluon fusion channel (bottom) with different choices of $C^{(2)}_{ij,\tilde{\mathbf{R}}}$. The latter has been constructed as the sum of singlet and octet contributions to yield a physical prediction. For the solid lines only the threshold behavior of the LO prefactor was taken into account while the dashed lines correspond to the case with full LO kinematics.*

pair production they read

$$
\begin{aligned}
C_{gg,\mathbf{1}}^{(2),\text{est.}} &= \left[C_F\left(-20+\pi^2\right)+C_A\left(68-\frac{7\pi^2}{3}-96\ln 2+64\ln^2 2\right)\right]^2 = 196.733\\
C_{gg,\mathbf{8_S}}^{(2),\text{est.}} &= \left[C_F\left(-20+\pi^2\right)+C_A\left(84-\frac{17\pi^2}{6}-104\ln 2+64\ln^2 2\right)\right]^2 = 935.517\\
C_{gg,\mathbf{8_A}}^{(2),\text{est.}} &= 0\\
C_{q\bar{q}}^{(2),\text{est.}} &= \left[C_F\left(32-\frac{4\pi^2}{3}-84\ln 2+64\ln^2 2\right)+C_A\left(\frac{308}{9}-\pi^2-20\ln 2\right)\right.\\
&+ \left. T_F\, n_l\left(-\frac{40}{9}+\frac{16}{3}\ln 2\right)-\frac{32}{9}\right]^2 = 211.156\,.
\end{aligned}
\tag{3.82}
$$

The influence of these constants on the shape of $\bar{\sigma}_{ij,\tilde{\mathbf{R}}}^{(2,0,0)}$ is shown in Fig. 3.6 whereas the corresponding total cross section predictions are given in Tab. 3.1. For the latter only the $\mathcal{O}(\alpha_s^4)$ contributions are treated in the threshold limit while taking into account the full LO and NLO β-dependence. As expected, the impact of $C_{ij,\tilde{\mathbf{R}}}^{(2)}$ on the threshold behavior of the partonic cross sections is marginal, which explicitly confirms the aforementioned difficulties concerning the precision of the fitted values in Eq. (3.77) and Eq. (3.80). For larger values of β, however, one can observe a distinct separation of the various series expansions that gradually increases towards the high-energy regime. For the quark annihilation channel the situation is particularly delicate as, depending on the value of $C_{q\bar{q}}^{(2)}$, the resulting cross section may be positive over the entire β-range or contain large negative contributions that lead to sizable cancellation effects when calculating the total cross section. Interestingly, the curve that corresponds to the true value of $C_{q\bar{q}}^{(2)}$, Eq. (3.79), lies still outside of the parameter space spanned by the various approximate coefficients while in the gluonic case it is contained inside the band bounded by $C_{gg,\tilde{\mathbf{R}}}^{(2),\text{est.}}$ and $\overline{C}_{gg,\tilde{\mathbf{R}}}^{(2)}$. This is, however, irrelevant for the predictive power of the respective total cross section results as the true value does not necessarily yield the best description for the terms of order $\mathcal{O}\left(\beta^2\right)$. Nevertheless, it suggests that the numerical impact of these constant contributions is significant and needs to be properly accounted for. Indeed, the associated cross section predictions vary by about 8% for the LHC and even up to 13% for the Tevatron, which is due to the different weighting of the partonic channels at these colliders. These variations have been employed as a measure for the missing velocity-dependent contributions albeit the actual range of $C_{ij,\tilde{\mathbf{R}}}^{(2)}$-values to be considered in this type of error analysis was interpreted differently at the time. A conservative error estimate would, however, take into account the full spectrum of cross section predictions spanned by the approximate $C_{ij,\tilde{\mathbf{R}}}^{(2)}$-values.

A common strategy to further reduce the uncertainty of the threshold expansion was to replace the functions $\bar{\sigma}_{ij,\tilde{\mathbf{R}}}^{(0)}$ that act as a global prefactor in the threshold formula by the full LO cross sections $\hat{\sigma}_{ij,\tilde{\mathbf{R}}}^{(0)}$. Due to the universal phase space suppression proportional to ρ the different predictions will then eventually move closer together again as β approaches the end of the spectrum (see Fig. 3.6). For the quark-induced cross section this leads to a considerable change in shape above $\beta \gtrsim 0.3$ whereas for the gluonic channels the effect of going to full leading order

$\sigma_{t\bar{t}}^{\mathbf{tot},\,\text{thr.}}$	Tevatron [pb]	LHC			
		7 TeV [pb]	8 TeV [pb]	13 TeV [pb]	14 TeV [pb]
$C_{ij,\tilde{\mathbf{R}}}^{(2)}$	$7.341^{+0.480\,(6.5\%)}_{-0.494\,(6.7\%)}$	$164.5^{+5.0\,(3.1\%)}_{-9.6\,(5.8\%)}$	$234.8^{+6.7\,(2.9\%)}_{-13.1\,(5.6\%)}$	$767.7^{+17.2\,(2.2\%)}_{-36.3\,(4.7\%)}$	$907.9^{+19.6\,(2.2\%)}_{-42.0\,(4.6\%)}$
$C_{ij,\tilde{\mathbf{R}}}^{(2)} = C_{ij,\tilde{\mathbf{R}}}^{(2),\,\text{fit}}$	$7.362^{+0.211\,(2.9\%)}_{-0.424\,(5.8\%)}$	$163.3^{+11.2\,(6.8\%)}_{-11.3\,(6.9\%)}$	$232.9^{+16.4\,(7.0\%)}_{-16.2\,(7.0\%)}$	$761.1^{+58.7\,(7.7\%)}_{-53.8\,(7.1\%)}$	$900.1^{+70.2\,(7.8\%)}_{-63.8\,(7.1\%)}$
$C_{ij,\tilde{\mathbf{R}}}^{(2)} = 0$	$7.061^{+0.237\,(3.4\%)}_{-0.336\,(4.8\%)}$	$161.5^{+10.5\,(6.5\%)}_{11.5\,(7.1\%)}$	$230.7^{+15.5\,(6.7\%)}_{-16.5\,(7.1\%)}$	$755.6^{+55.5\,(7.3\%)}_{-55.6\,(7.4\%)}$	$893.8^{+66.5\,(7.4\%)}_{-66.0\,(7.4\%)}$
$C_{ij,\tilde{\mathbf{R}}}^{(2)} = +\lvert C_{ij,\tilde{\mathbf{R}}}^{(2),\,\text{est.}}\rvert$	$7.154^{+0.225\,(3.1\%)}_{-0.364\,(5.1\%)}$	$165.2^{+10.2\,(6.1\%)}_{-12.6\,(7.6\%)}$	$236.0^{+15.0\,(6.3\%)}_{-18.1\,(7.7\%)}$	$773.6^{+54.4\,(7.0\%)}_{-61.0\,(7.9\%)}$	$915.1^{+65.3\,(7.1\%)}_{-72.4\,(7.9\%)}$
$C_{ij,\tilde{\mathbf{R}}}^{(2)} = -\lvert C_{ij,\tilde{\mathbf{R}}}^{(2),\,\text{est.}}\rvert$	$6.968^{+0.248\,(3.6\%)}_{-0.308\,(4.4\%)}$	$157.9^{+10.9\,(6.9\%)}_{-10.3\,(6.6\%)}$	$225.4^{+15.9\,(7.1\%)}_{-14.9\,(6.6\%)}$	$737.6^{+56.6\,(7.7\%)}_{-50.1\,(6.8\%)}$	$872.4^{+67.7\,(7.8\%)}_{-59.5\,(6.8\%)}$
$C_{ij,\tilde{\mathbf{R}}}^{(2)} = \overline{C}_{ij,\tilde{\mathbf{R}}}^{(2)}$	$6.861^{+0.261\,(3.8\%)}_{-0.370\,(5.4\%)}$	$155.5^{+11.1\,(7.1\%)}_{-9.6\,(6.2\%)}$	$222.0^{+16.2\,(7.3\%)}_{-13.9\,(6.2\%)}$	$726.7^{+57.2\,(7.9\%)}_{-46.8\,(6.4\%)}$	$859.5^{+68.4\,(8.0\%)}_{-55.6\,(6.5\%)}$
$\sigma_{t\bar{t}}^{\mathbf{tot},\,\text{thr.+HE}}$	$7.206^{+0.404\,(5.6\%)}_{-0.450\,(6.2\%)}$	$173.3^{+10.2\,(5.9\%)}_{-13.0\,(7.5\%)}$	$247.8^{+13.8\,(5.6\%)}_{-18.0\,(7.3\%)}$	$811.7^{+38.6\,(4.8\%)}_{-51.7\,(6.4\%)}$	$959.7^{+44.8\,(4.7\%)}_{-59.9\,(6.2\%)}$
$\sigma_{t\bar{t}}^{\mathbf{tot},\,\text{NLO}}$	$6.682^{+0.356\,(5.3\%)}_{-0.752\,(11.3\%)}$	$158.1^{+19.5\,(12.3\%)}_{-21.2\,(13.4\%)}$	$226.3^{+27.8\,(12.3\%)}_{-29.7\,(13.1\%)}$	$746.9^{+90.4\,(12.1\%)}_{-90.4\,(12.1\%)}$	$884.5^{+106.8\,(12.1\%)}_{-105.8\,(12.0\%)}$
$\sigma_{t\bar{t}}^{\mathbf{tot},\,\text{NNLO}}$	$7.009^{+0.259\,(3.7\%)}_{-0.374\,(5.3\%)}$	$167.0^{+6.7\,(4.0\%)}_{-10.7\,(6.4\%)}$	$239.1^{+9.2\,(3.9\%)}_{-14.8\,(6.2\%)}$	$788.1^{+27.1\,(3.4\%)}_{-43.8\,(5.6\%)}$	$933.0^{+31.8\,(3.4\%)}_{-51.0\,(5.5\%)}$

Table 3.1: *Approximate NNLO predictions for $\sigma_{t\bar{t}}^{\mathbf{tot}}$ at the Tevatron and the LHC ($m_t = 173.3\,\text{GeV}$,MSTW2008 PDFs at 68% C.L. [231]) based on the threshold expansion as well as on the combined threshold+high-energy behavior. The given uncertainties are due to the variation of renormalization and factorization scale, however, with the constant scale dependence excluded for the approximate $C_{ij,\tilde{\mathbf{R}}}^{(2)}$-values (lines 3-6) as described below. The threshold+high-energy results were obtained with* HATHOR *[89] where the parametrization error due to the choice of $C_{ij}^{(2)}$ and $r_{ij,x}$ for the different collider setups reads $\{\pm 0.4\%, \pm 2.6\%, \pm 3\%, \pm 4.4\%, \pm 4.6\%\}$ respectively. For comparison, we also quote the full NLO and NNLO results.*

is less pronounced. In consequence, the resulting total cross section at the Tevatron is affected more significantly than the corresponding LHC predictions, decreasing the $C_{ij,\tilde{\mathbf{R}}}^{(2)}$-dependence to $\sim 7\%$ and $\sim 5.5\%$ respectively. The shift of the central value with respect to the NLO results is also collider-dependent amounting to as much as 10% at the Tevatron and 3-4% at the LHC when the constant coefficients are chosen according to Eq. (3.75) and Eq. (3.79). Using the approximate values leads, in the majority of cases, to a smaller cross section even becoming negative (with respect to the NLO prediction) for $\overline{C}_{ij,\tilde{\mathbf{R}}}^{(2)}$ at the LHC, which again stresses the numerical importance of these subleading effects.

In fact, one has to keep in mind that the modification of the LO prefactor is somewhat arbitrary since it involves the inclusion of higher-velocity contributions in a non-systematic fashion[15], i. e. it is not clear to what extent it mimics the true $\mathcal{O}\left(\beta^2\right)$ behavior. Indeed, it is well known from small-x resummation that in the high-energy limit the partonic cross sections will rise as $\ln \rho$ due to diagrams that contain t- or u-channel propagators [555], a feature that cannot be reproduced with this type of threshold approximation.

[15] For the gluon fusion channel it actually already depends on whether this prescription is applied to the individual color representations or the combined threshold cross section (i. e. the weighted sum of the three representations), which leads to a noticeable difference ($\lesssim 1\%$) that may, however, be neglected compared to the $C_{ij,\tilde{\mathbf{R}}}^{(2)}$-dependence.

There have, however, been attempts to combine the information of both these limits to determine improved NNLO approximations that take into account the full kinematic range. To this end, the partonic cross sections are parametrized as [229]

$$\begin{aligned}
\hat{\sigma}^{(2,0,0)}_{gg,\,\text{thr.+HE}} &= \hat{\sigma}^{(0)}_{gg}\left(\frac{\bar{\sigma}^{(0)}_{gg,\mathbf{1}}\,\bar{\sigma}^{(2,0,0)}_{gg,\mathbf{1}}+\bar{\sigma}^{(0)}_{gg,\mathbf{8_S}}\,\bar{\sigma}^{(2,0,0)}_{gg,\mathbf{8_S}}}{\bar{\sigma}^{(0)}_{gg,\mathbf{1}}+\bar{\sigma}^{(0)}_{gg,\mathbf{8_S}}}+\frac{1}{16\pi^2}\,C^{(2)}_{gg,\mathbf{8_A}}\right)\\
&+ \frac{\beta^3}{\pi\,(N_c^2-1)}\left[N_c^3\left(\frac{19696}{3375}-\frac{2\pi^2}{45}\right)-N_c\left(\frac{241}{54}+\frac{7\pi^2}{108}\right)\right]\left(-\ln\rho+r_{x,gg}\,\frac{\eta^\gamma}{C+\eta^\gamma}\right)\\
\hat{\sigma}^{(2,0,0)}_{q\bar{q},\,\text{thr.+HE}} &= \hat{\sigma}^{(0)}_{q\bar{q}}\,\bar{\sigma}^{(2,0,0)}_{q\bar{q},\mathbf{8}}+\frac{\beta^3}{\pi\,N_c^3}\left[N_c^4\left(\frac{2462}{3375}-\frac{\pi^2}{90}\right)-N_c^2\left(\frac{88463}{81000}+\frac{11\pi^2}{2160}\right)+\frac{235}{648}+\frac{7\pi^2}{432}\right]\\
&\times \left(-\ln\rho+r_{x,q\bar{q}}\,\frac{\eta^\gamma}{C+\eta^\gamma}\right)\\
\hat{\sigma}^{(2,0,0)}_{qg,\,\text{thr.+HE}} &= \frac{4N_c^2-6}{192\pi N_c^2}\,(C_F+C_A)\,\rho\,\beta^3\ln^3\left(8\beta^2\right)+\frac{\beta^5}{\pi\,N_c}\left[N_c^2\left(\frac{2462}{1125}-\frac{\pi^2}{45}\right)-\frac{479}{324}-\frac{7\pi^2}{216}\right]\\
&\times \left(-\ln\rho+r_{x,qg}\,\frac{\eta^\gamma}{C+\eta^\gamma}\right)
\end{aligned} \tag{3.83}$$

where $\eta=\frac{1-\rho}{\rho}$ is used to describe the distance from threshold and γ and C are fit parameters obtained from the scale-dependent NNLO contributions. The dependence on the remaining unknown quantities $C^{(2)}_{ij}$ (through $\bar{\sigma}^{(2,0,0)}_{ij,\tilde{\mathbf{R}}}$) and $r_{ij,x}$ serves as an estimate for the deviation from the full NNLO result. Similar to the pure threshold scenario their explicit values are chosen within a reasonable range of the corresponding parameter space (for a typical setup see for instance Ref. [229]). Note that the quark-gluon channel is also included in this approximate NNLO treatment since it shows the same high-energy enhancements as the LO channels. Its leading threshold behavior has been determined in Ref. [578] and, as anticipated, is further suppressed such that its contribution to the total cross section almost exclusively arises from velocities $\beta\sim 1$. The resulting predictions are shown in Tab. 3.1 and it turns out that including the high-energy tails in the analysis leads to quite different consequences at the two colliders. At the Tevatron one can register a modest increase of $\sigma^{\mathbf{tot}}_{t\bar{t}}$ with respect to the threshold scenarios based on approximate $C^{(2)}_{ij,\tilde{\mathbf{R}}}$-values, lying only slightly below the prediction that incorporates the actual constant coefficient results. At the LHC, on the other hand, the cross sections are clearly enhanced ($\sim$5-10%) compared to the pure threshold approximations, which suggests that the integration of the high-energy behavior induces the most significant changes in the gluon fusion channel. Moreover, one can observe an increase of the corresponding parametric uncertainty with center-of-mass energy, indicating a high sensitivity to the $r_{gg,x}$-parameter that governs the subleading ρ-dependence in the high-energy regime. Still, this error remains smaller than the spread of the various threshold-only predictions. At the Tevatron the parametric uncertainty is exceptionally small ($\lesssim$0.5%), which is properly due to accidental cancellation effects related to the chosen input parameters and does not reflect the true uncertainty due to the employed cross section parametrization.

So far, we have ignored the fact that the theoretical error should not only assess the discrepancy with regard to the full NNLO result but also include an estimate for yet missing higher

orders in the strong coupling. As we have learned in the beginning of this chapter, this is usually done via scale variation based on Eq. (2.4), which states that the scale dependence of the total cross section cancels up to $\mathcal{O}\left(\alpha_s^5\right)$ effects. Since this cancellation relies on the interplay of contributions from all available levels of the perturbative expansion, i. e. LO, NLO and NNLO, it crucially depends on the treatment of the scale-controlling functions $\hat{\sigma}_{ij}^{(2,k,l)}$ $(k,l \geq 1)$ whether this method is still valid. There basically exist two possible scenarios. Either one takes into account the full kinematic dependence of these functions, which is known by construction from the lower-order results, or one applies the same kinematic expansion as for the scale-invariant function $\hat{\sigma}_{ij}^{(2,0,0)}$, which leads to a residual dependence of order $\mathcal{O}\left(\alpha_s^4\beta^2\right)$ but seems more consistent from the perturbative point of view.

For the threshold expansion the latter option yields unnaturally small error estimates that, in some cases, are even below 1%, indicating a strong numerical cancellation between these residual terms and the genuine $\mathcal{O}\left(\alpha_s^5\right)$-effects. Therefore, in the original threshold analysis a modified approach was used to determine the combined error due to higher orders in the velocity and the coupling constant. The argument went as follows [220]: since the constant coefficients were not available yet their known scale-dependence should also be excluded from the NNLO contributions. The resulting scale variation was much larger and, moreover, covered the entire cross section range spanned by the different approximations for $C_{ij,\tilde{\mathbf{R}}}^{(2)}$. In consequence, it was employed as an estimate for the combined perturbative error. Still, this method seems rather arbitrary since it implies that, if the constant coefficients had been known at the time, they would have somehow compensated for the accidentally small scale dependence such that the resulting uncertainty would be more realistic, which is certainly not the case.

In order to avoid these conceptual difficulties, it is therefore more convenient to employ the full kinematic dependence of the scale-controlling functions and assess the uncertainty due to missing contributions in $\hat{\sigma}_{ij}^{(2,0,0)}$ otherwise. For the pure threshold approximations this means that one has to include the scale-dependent parts of the NNLO quark-gluon channel as well[16] despite the fact that it vanishes in the limit $\beta \to 0$. In the combined threshold and high-energy predictions, on the other hand, these terms are already implemented due to their non-negligible contribution in the ultra-relativistic regime. Note, however, that the residual scale dependence of these approximate cross sections will still differ from the scaling behavior of the full NNLO results and may, in fact, also suffer from cancellation effects that could lead to an underestimation of the perturbative error. Thus, in Tab. 3.1 the full scale dependence has only been employed for the pure threshold predictions based on the exact $C_{ij,\tilde{\mathbf{R}}}^{(2)}$-values while for the remaining setups the original approach discarding the constant scaling behavior seems more appropriate.

This difficulty to provide a reliable error estimate was one of the main reasons why the determination of the full NNLO corrections became eventually inevitable, at least when aiming at high-precision applications. And indeed, a comparison of the various threshold approximations with the full results shows that the contributions from intermediate and large velocities

[16] In principle, this also applies to the newly emerging $q\tilde{q}$-channel whose overall contribution may, however, be neglected due to its numerical insignificance.

are significant and cannot be simply inferred from the limiting behavior at different ends of the spectrum. Due to its higher center-of-mass energies this discrepancy becomes particularly obvious at the LHC with the full NNLO predictions lying above the range spanned by the different choices of $C^{(2)}_{ij,\tilde{\mathbf{R}}}$. The combined threshold and high-energy analysis, on the other hand, overestimates the actual size of the NNLO corrections, which indicates that the chosen parametrization is not able to describe the shape of $\hat{\sigma}^{(2,0,0)}_{ij}$ in all its details. Nonetheless, these approximate methods constitute a valuable cross-check for the full results and, moreover, may become important again when dealing with new heavy particles in BSM physics.

3.1.2 Soft-gluon resummation

The main idea behind soft-gluon resummation is to improve the predictive power of fixed-order perturbation theory by including the dominant contributions from soft emissions to all orders in QCD. Thus, it may be interpreted as a natural extension of the threshold expansion formalism albeit restricted to the treatment of soft logarithms. As already noted before, it is also possible to resum contributions from potential-gluon exchange but due to their negligible impact on the final cross section predictions [81] we choose to further address them in a fixed-order approach. This has the advantage that one can work in Mellin space leading to a particularly simple form of the resummed cross section formula.

The basis for the resummation of soft enhancements is the fact that they are exclusively confined to the soft function in terms of powers of $\ln N$ and, therefore, always accompanied by a corresponding $\ln \frac{\mu}{Q}$ term as we have learned before. In consequence, the differential equations that govern the scale dependence of the soft function, Eq. (3.51) and Eq. (3.52), can be used to determine the all-order behavior of these soft logarithms through an exponential solution of the form

$$\begin{aligned}
S^{(\mathrm{res})}_{\mathbf{R}\otimes\mathbf{R}'|\tilde{\mathbf{R}},\,N}\left(\alpha_s(\mu_R^2), L, L_\mu\right) &\equiv \tilde{S}_{\mathbf{R}\otimes\mathbf{R}'|\tilde{\mathbf{R}}}\left(\alpha_s(\mu_R^2), L_Q, L_\mu\right)\, \Delta_{\mathbf{R}\otimes\mathbf{R}'|\tilde{\mathbf{R}},\,N}\left(\alpha_s(\mu_R^2), L_Q, L_\mu\right) \\
&= \tilde{S}_{\mathbf{R}\otimes\mathbf{R}'|\tilde{\mathbf{R}}}\left(\alpha_s(\mu_R^2), L_Q, L_\mu\right) \\
&\times \exp\Bigg\{ -\int\limits_{\frac{\mu_R}{N}}^{\mu_R} \frac{d\mu'}{\mu'} \left[\Gamma_H^{\mathbf{R}\otimes\mathbf{R}'|\tilde{\mathbf{R}}} + 4\, P_N^{\mathbf{R}}\right] \left(\alpha_s\left(\mu'^2\right), \frac{\mu' N}{Q}\right) \\
&\qquad - \int\limits_{\frac{\mu_R}{N}}^{\mu_R} \frac{d\mu'}{\mu'}\, G_{\mathbf{R}\otimes\mathbf{R}'|\tilde{\mathbf{R}}}\left(\alpha_s(\mu'^2), L_Q\right) \\
&\qquad + 2 \int\limits_{\mu_F^2}^{\mu_R^2} \frac{d\mu'^2}{\mu'^2}\, \tilde{P}_N^{\mathbf{R}}\left(\alpha_s\left(\mu'^2\right)\right) \Bigg\}
\end{aligned} \tag{3.84}$$

with

$$\tilde{S}_{\mathbf{R}\otimes\mathbf{R}'|\tilde{\mathbf{R}}}\left(\alpha_s(\mu_R^2), L_Q, L_\mu\right) = \lim_{N\to 1} S_{\mathbf{R}\otimes\mathbf{R}'|\tilde{\mathbf{R}},\,N}\left(\alpha_s(\mu_R^2), L, L_\mu\right) \tag{3.85}$$

incorporating the boundary condition at $\ln N = 0$, i. e. the constant behavior obtained from the explicit eikonal cross section calculations in Eq. (3.58). Consequently, the original L-dependence is split into separate $L_Q = \ln \frac{\mu_R e^{\gamma_E}}{Q}$ and $\ln N$ contributions, where the exponential factor e^{γ_E} is due to the fact that we use N instead of $\tilde{N}$ as a Mellin variable now. The function

$$G_{\mathbf{R}\otimes\mathbf{R}'|\tilde{\mathbf{R}}}\left(\alpha_s(\mu_R^2), L_Q\right) = 2\,\beta\left(\alpha_s(\mu_R^2)\right)\left(\frac{1}{\tilde{S}_{\mathbf{R}\otimes\mathbf{R}'|\tilde{\mathbf{R}}}}\frac{d\tilde{S}_{\mathbf{R}\otimes\mathbf{R}'|\tilde{\mathbf{R}}}}{d\alpha_s}\right)\left(\alpha_s(\mu_R^2), L_Q, 0\right) \tag{3.86}$$

has no deeper physical meaning but is chosen such that the coupling constant entering the boundary condition may be evaluated at $\mu = \mu_R$. Note that the splitting kernels $\tilde{P}_N^{\mathbf{R}}$ that control the exponential $\mu_F \neq \mu_R$-dependence contain only the leading logarithms in N, which is necessary to remove subleading contributions from the exponent that could otherwise lead to inconsistencies. The integrals can be evaluated by exploiting the known scale dependence of the strong coupling constant, which is, however, implemented in a different manner for the two exponent structures. While for the $\mu_F \neq \mu_R$ part one usually chooses a strict perturbative treatment, for the first integral the exact one-loop behavior is used and only the higher-order components of the beta function are treated perturbatively. This may be achieved by reparametrizing the running equation in terms of a new variable

$$\tau = 1 + \frac{\alpha_s(\mu_0^2)}{4\pi}\,\beta_0 \ln\frac{\mu^2}{\mu_0^2} \qquad \text{with} \qquad \alpha_s(\tau = 1) = \alpha_s(\mu_0^2) \tag{3.87}$$

such that

$$\mu^2\,\frac{d\alpha_s(\mu^2)}{d\mu^2} = \frac{\alpha_s(\mu_0^2)}{4\pi}\,\beta_0\,\frac{d\alpha_s(\tau)}{d\tau} = -\frac{\alpha_s^2(\tau)}{4\pi}\,\beta_0 - \frac{\alpha_s^3(\tau)}{(4\pi)^2}\,\beta_1 - \frac{\alpha_s^4(\tau)}{(4\pi)^3}\,\beta_2 + \mathcal{O}\left(\alpha_s^5(\tau)\right)\,. \tag{3.88}$$

Solving this equation recursively yields the desired property. Plugging the resulting expression into Eq. (3.84) the exponent can be written as

$$\begin{aligned}
\ln\Delta_{\mathbf{R}\otimes\mathbf{R}'|\tilde{\mathbf{R}},\,N}\left(\alpha_s(\mu_R^2), L_Q, L_\mu\right) &= \ln N\, g^{(1)}_{\mathbf{R}\otimes\mathbf{R}'|\tilde{\mathbf{R}}}\left(\frac{\alpha_s(\mu_R^2)}{4\pi}\,\beta_0 \ln N\right) \\
&+ g^{(2)}_{\mathbf{R}\otimes\mathbf{R}'|\tilde{\mathbf{R}}}\left(\frac{\alpha_s(\mu_R^2)}{4\pi}\,\beta_0 \ln N, L_Q, L_\mu\right) \\
&+ \frac{\alpha_s(\mu_R^2)}{\pi}\, g^{(3)}_{\mathbf{R}\otimes\mathbf{R}'|\tilde{\mathbf{R}}}\left(\frac{\alpha_s(\mu_R^2)}{4\pi}\,\beta_0 \ln N, L_Q, L_{\mu^2}\right) \\
&+ \mathcal{O}\left(\alpha_s^2(\mu_R^2)\left(\alpha_s(\mu_R^2)\ln N\right)^k\right)
\end{aligned} \tag{3.89}$$

where the functions $g^{(k)}_{\mathbf{R}\otimes\mathbf{R}'|\tilde{\mathbf{R}}}$ resum the LL [214,215], NLL [216] and NNLL [220] contributions respectively. Applying the decomposition

$$\left(\Gamma_H^{\mathbf{R}\otimes\mathbf{R}'|\tilde{\mathbf{R}}} + 4\,P_N^{\mathbf{R}}\right) = -\sum_{n=1}^{1}\sum_{m=0}^{n} K^{(n,m)}_{\mathbf{R}\otimes\mathbf{R}'|\tilde{\mathbf{R}}}\left(\frac{\alpha_s(\mu_R^2)}{\pi}\right)^n \ln^m\frac{\mu_R N e^{\gamma_E}}{Q}\,, \tag{3.90}$$

they read

$$
\begin{aligned}
g^{(1)}_{\mathbf{R}\otimes\mathbf{R}'|\tilde{\mathbf{R}}}(\lambda) &= \frac{K^{(1,1)}_{\mathbf{R}\otimes\mathbf{R}'|\tilde{\mathbf{R}}}}{\beta_0\lambda}\left[2\,\lambda+(1-2\,\lambda)\ln(1-2\,\lambda)\right] \\
g^{(2)}_{\mathbf{R}\otimes\mathbf{R}'|\tilde{\mathbf{R}}}(\lambda,L_Q,L_\mu) &= \frac{K^{(1,1)}_{\mathbf{R}\otimes\mathbf{R}'|\tilde{\mathbf{R}}}}{2\beta_0^3}\left\{\beta_1\left[4\lambda+2\ln(1-2\,\lambda)+\ln^2(1-2\,\lambda)\right]-4\beta_0^2\,L_Q\ln(1-2\,\lambda)\right\} \\
&- \frac{2\,K^{(1,0)}_{\mathbf{R}\otimes\mathbf{R}'|\tilde{\mathbf{R}}}}{\beta_0}\ln(1-2\,\lambda)-\frac{4\,K^{(2,1)}_{\mathbf{R}\otimes\mathbf{R}'|\tilde{\mathbf{R}}}}{\beta_0^2}\left[2\lambda+\ln(1-2\,\lambda)\right]+\frac{4\,\tilde{P}_N^{\mathbf{R},(0)}}{\beta_0}\,\lambda\,L_\mu \\
g^{(3)}_{\mathbf{R}\otimes\mathbf{R}'|\tilde{\mathbf{R}}}(\lambda,L_Q,L_\mu) &= \frac{K^{(1,1)}_{\mathbf{R}\otimes\mathbf{R}'|\tilde{\mathbf{R}}}}{8\beta_0^4(1-2\,\lambda)}\left\{\beta_1^2\left[2\,\lambda+\ln(1-2\,\lambda)\right]^2+2\,\beta_0\,\beta_2\left[2(1-\lambda)\lambda+(1-2\,\lambda)\ln(1-2\,\lambda)\right]\right. \\
&- \left.4\,\beta_0^2\,\beta_1 L_Q\left[2\lambda+\ln(1-2\,\lambda)\right]\right\}-\frac{K^{(1,0)}_{\mathbf{R}\otimes\mathbf{R}'|\tilde{\mathbf{R}}}}{2\beta_0^2(1-2\,\lambda)}\,\beta_1\,\left[2\lambda+\ln(1-2\,\lambda)\right] \\
&- \frac{K^{(2,1)}_{\mathbf{R}\otimes\mathbf{R}'|\tilde{\mathbf{R}}}}{\beta_0^3(1-2\,\lambda)}\left\{\beta_1\left[2\lambda(1+\lambda)+\ln(1-2\,\lambda)\right]-4\,\beta_0^2 L_Q\lambda\right\}+\frac{4\,K^{(2,0)}_{\mathbf{R}\otimes\mathbf{R}'|\tilde{\mathbf{R}}}\,\lambda}{\beta_0(1-2\,\lambda)} \\
&+ \frac{8\,K^{(3,1)}_{\mathbf{R}\otimes\mathbf{R}'|\tilde{\mathbf{R}}}\,\lambda^2}{\beta_0^2(1-2\,\lambda)}+\frac{\tilde{P}_N^{\mathbf{R},(0)}}{2}\,\lambda\,L_\mu^2+\frac{2\tilde{P}_N^{\mathbf{R},(1)}}{\beta_0}\,\lambda\,L_\mu \\
&+ \left[C_{\tilde{R}}\,(1+L_Q)+C_R\left(\frac{\pi^2}{12}+2L_Q^2\right)\right]\frac{\lambda}{1-2\,\lambda}\,.
\end{aligned}
\tag{3.91}
$$

The explicit values for the coefficients $K^{(n,m)}_{\mathbf{R}\otimes\mathbf{R}'|\tilde{\mathbf{R}}}$ as well as for β_i can be inferred from appendix A and B. Interestingly, the full NNLL resummation requires the knowledge of the leading logarithmic behavior of $\Gamma_H^{\mathbf{R}\otimes\mathbf{R}'|\tilde{\mathbf{R}}}+4\,P_N^{\mathbf{R}}$ to three-loop order [488], i. e. it cannot be extracted from the result for the NNLO soft function used in the threshold expansion. Indeed, the original resummation formalism does not rely on the explicit fixed-order calculation of these process-dependent soft functions but aims directly at the determination of the anomalous dimensions $A_{\mathbf{R}}$ [488, 579, 580] and $D_{\mathbf{R}\otimes\mathbf{R}'|\tilde{\mathbf{R}}}$ [581] that describe the effect of soft-collinear initial-state radiation and wide-angle soft radiation respectively. In this approach the exponential resummation factor (for $\mu_F=\mu_R=\mu$) is given as

$$
\begin{aligned}
\ln\Delta_{\mathbf{R}\otimes\mathbf{R}'|\tilde{\mathbf{R}},N}\left(\alpha_s(\mu_R^2),L_Q,0\right) &= \int_0^1 dz\,\frac{z^{N-1}-1}{1-z}\left\{\int_{\mu^2}^{Q^2(1-z)^2}\frac{dq_\perp^2}{q_\perp^2}\,2A_{\mathbf{R}}\left(\alpha_s(q_\perp^2)\right)\right. \\
&+ \left.D_{\mathbf{R}\otimes\mathbf{R}'|\tilde{\mathbf{R}}}\left(\alpha_s\left(4m^2(1-z)^2\right)\right)\right\} \\
&+ \mathcal{O}\left(\alpha_s^2(\mu_R^2)\left(\alpha_s(\mu_R^2)\ln N\right)^k\right)\,,
\end{aligned}
\tag{3.92}
$$

which contains an additional integration due to the fact that the Mellin transformation has been shifted into the exponent. Still, it leads to the same expressions as in Eq. (3.91) since both approaches are equivalent. The advantage of this method is that the anomalous dimensions $A_{\mathbf{R}}$ are universal, i. e. independent of the reaction under consideration, such that only the dependence on the non-collinear soft emissions has to be determined process-wise (for the $t\bar{t}$

case see Refs. [219,515]). There exists, however, a slight drawback with regard to the fixed-order approach, which becomes clear when considering the corresponding N-space formula for the resummed partonic cross sections for top-quark pair production

$$\hat{\sigma}^{(\mathrm{res})}_{ij,\,N}(m_t^2,\alpha_s(\mu^2),\frac{\mu^2}{m_t^2}) = \sum_{\tilde{\mathbf{R}}} \hat{\sigma}^{(\mathrm{Coul})}_{\mathbf{R}\otimes\mathbf{R}'|\tilde{\mathbf{R}},\,N}\, \hat{\sigma}^{(\mathrm{Hard})}_{\mathbf{R}\otimes\mathbf{R}'|\tilde{\mathbf{R}}}\, \Delta_{\mathbf{R}\otimes\mathbf{R}'|\tilde{\mathbf{R}},\,N+1} \tag{3.93}$$

where for the gluon fusion channel the sum now runs over $\tilde{\mathbf{R}} \in \{\mathbf{1},\mathbf{8}\}$, i. e. the symmetric and antisymmetric octet configurations are combined into a single color-octet state. In contrast to Eq. (3.10) the threshold-enhanced contributions from potential-gluon exchange have been factorized as well resulting in a new hard matching function $\hat{\sigma}^{(\mathrm{Hard})}_{\mathbf{R}\otimes\mathbf{R}'|\tilde{\mathbf{R}}}$ that is independent of the underlying kinematics and hence also of N. Its expansion up to NNLO in α_s reads

$$\hat{\sigma}^{(\mathrm{Hard})}_{\mathbf{R}\otimes\mathbf{R}'|\tilde{\mathbf{R}}}\left(\alpha_s(\mu^2),\frac{\mu^2}{m_t^2}\right) = \alpha_s^2(\mu^2)\left[1+\frac{\alpha_s(\mu^2)}{\pi}\,\tilde{H}^{(1)}_{\mathbf{R}\otimes\mathbf{R}'|\tilde{\mathbf{R}}}\left(\frac{\mu^2}{m_t^2}\right)+\left(\frac{\alpha_s(\mu^2)}{\pi}\right)^2\tilde{H}^{(2)}_{\mathbf{R}\otimes\mathbf{R}'|\tilde{\mathbf{R}}}\left(\frac{\mu^2}{m_t^2}\right)\right] \tag{3.94}$$

whereas for the Coulomb function it is given by the Mellin transform of

$$\begin{aligned}\hat{\sigma}^{(\mathrm{Coul})}_{\mathbf{R}\otimes\mathbf{R}'|\tilde{\mathbf{R}}}\left(m_t^2,\rho,\alpha_s(\mu^2),\frac{\mu^2}{m_t^2}\right) &= \frac{\hat{\sigma}^{(0)}_{ij,\tilde{\mathbf{R}}}(\rho)}{m_t^2} \\ &\times \left[1+\frac{\alpha_s(\mu^2)}{\pi}\,\tilde{C}^{(1)}_{\mathbf{R}\otimes\mathbf{R}'|\tilde{\mathbf{R}}}(\rho)+\left(\frac{\alpha_s(\mu^2)}{\pi}\right)^2\tilde{C}^{(2)}_{\mathbf{R}\otimes\mathbf{R}'|\tilde{\mathbf{R}}}\left(\rho,\frac{\mu^2}{m_t^2}\right)\right]\end{aligned} \tag{3.95}$$

which corresponds exactly to $H^{\mathrm{pot.}}_{\mathbf{R}\otimes\mathbf{R}'|\tilde{\mathbf{R}}}/\alpha_s^2$ after adding the LO contributions and setting $H^{(1),\,\mathrm{match.}}_{\mathbf{R}\otimes\mathbf{R}'|\tilde{\mathbf{R}}}$ to zero. This also applies to the combined octet configuration as the non-relativistic potentials do not distinguish between the symmetry of the initial-state particles. The corresponding Born cross section is then given through $\hat{\sigma}^{(0)}_{gg,\mathbf{8}} = \hat{\sigma}^{(0)}_{gg,\mathbf{8_S}} + \hat{\sigma}^{(0)}_{gg,\mathbf{8_A}}$. Now, the usual procedure for determining the hard matching coefficients $\tilde{H}^{(n)}_{\mathbf{R}\otimes\mathbf{R}'|\tilde{\mathbf{R}}}$ is to compare Eq. (3.93) to the Mellin transform of the respective partonic cross section at threshold as they are directly related to the constant coefficients $C^{(n)}_{ij,\tilde{\mathbf{R}}}$ (see, for instance, the definition of $\overline{C}^{(2)}_{ij,\tilde{\mathbf{R}}}$). At NLO this is generally not a problem since for most processes that have been considered in the context of soft-gluon resummation analytical results are available. At NNLO, however, it is connected with serious difficulties as we have already seen for the case of $t\bar{t}$ production. Typically, at such a high order in perturbation theory results are only available in numerical form (if at all) in terms of fitting formulae, which can usually not be employed for a high-precision estimate of these constants. The reason for this is that there exists no efficient method for the analytical treatment of contributions that involve real radiation. Due to the fact that the anomalous dimension formalism is not capable of predicting the boundary value $\tilde{S}_{\mathbf{R}\otimes\mathbf{R}'|\tilde{\mathbf{R}}}$ that governs the threshold behavior of these additional emissions, it will thus always rely on input with a finite numerical precision. Hence, in practice an exact determination of the hard matching coefficients beyond NLO requires the calculation of some kind of fixed-order

soft function. Defining a new quantity

$$H^{\text{match.}}_{\mathbf{R}\otimes\mathbf{R}'|\tilde{\mathbf{R}}}\left(\alpha_s(\mu^2),\frac{\mu^2}{m_t^2}\right) = 1+\frac{\alpha_s(\mu^2)}{\pi}\,H^{(1),\,\text{match.}}_{\mathbf{R}\otimes\mathbf{R}'|\tilde{\mathbf{R}}}\left(\frac{\mu^2}{m_t^2}\right)+\left(\frac{\alpha_s(\mu^2)}{\pi}\right)^2 H^{(2),\,\text{match.}}_{\mathbf{R}\otimes\mathbf{R}'|\tilde{\mathbf{R}}}\left(\frac{\mu^2}{m_t^2}\right) \tag{3.96}$$

with coefficients as specified above and

$$\begin{aligned} H^{(1),\,\text{match.}}_{\mathbf{8}\otimes\mathbf{8}|\mathbf{8}}\left(\frac{\mu^2}{m_t^2}\right) &= H^{(1),\,\text{match.}}_{\mathbf{8}\otimes\mathbf{8}|\mathbf{8_S}}\left(\frac{\mu^2}{m_t^2}\right) \\ H^{(2),\,\text{match.}}_{\mathbf{8}\otimes\mathbf{8}|\mathbf{8}}\left(\frac{\mu^2}{m_t^2}\right) &= H^{(2),\,\text{match.}}_{\mathbf{8}\otimes\mathbf{8}|\mathbf{8_S}}\left(\frac{\mu^2}{m_t^2}\right)+\frac{\bar{\sigma}^{(0)}_{gg,\mathbf{8_A}}(\beta)}{\bar{\sigma}^{(0)}_{gg,\mathbf{8_S}}(\beta)}\,H^{(2),\,\text{match.}}_{\mathbf{8}\otimes\mathbf{8}|\mathbf{8_A}}\left(\rho,\frac{\mu^2}{m_t^2}\right) \end{aligned} \tag{3.97}$$

the hard matching function is then given as

$$\hat{\sigma}^{(\text{Hard})}_{\mathbf{R}\otimes\mathbf{R}'|\tilde{\mathbf{R}}}\left(\alpha_s(\mu^2),\frac{\mu^2}{m_t^2}\right) = \alpha_s^2(\mu^2)\,H^{\text{match.}}_{\mathbf{R}\otimes\mathbf{R}'|\tilde{\mathbf{R}}}\left(\alpha_s(\mu^2),\frac{\mu^2}{m_t^2}\right)\,\tilde{S}_{\mathbf{R}\otimes\mathbf{R}'|\tilde{\mathbf{R}}}\left(\alpha_s(\mu^2),L_Q\right)\ . \tag{3.98}$$

Since the two-loop virtual corrections entering $H^{\text{match.}}_{\mathbf{R}\otimes\mathbf{R}'|\tilde{\mathbf{R}}}$ are currently only known numerically, the NNLO hard matching coefficients are only available in a semi-analytical fashion. For $N_c = 3$ and $\mu = m_t$ they read[17]

$$\begin{aligned} \tilde{H}^{(2)}_{\mathbf{8}\otimes\mathbf{8}|\mathbf{1}}(1) &= 52.1161 - 0.836892\,n_l = 47.9316 \\ \tilde{H}^{(2)}_{\mathbf{8}\otimes\mathbf{8}|\mathbf{8}}(1) &= 137.995 - 5.37074\,n_l + 0.0125\,n_l^2 = 111.454 \\ \tilde{H}^{(2)}_{\mathbf{3}\otimes\bar{\mathbf{3}}|\mathbf{8}}(1) &= 106.980 - 4.16574\,n_l - 0.267605\,n_l^2 = 79.4610\ . \end{aligned} \tag{3.99}$$

Due to the absence of the NNLO coefficients $H^{(2),\,\text{match.}}_{\mathbf{R}\otimes\mathbf{R}'|\tilde{\mathbf{R}}}$ and $\tilde{S}^{(2)}_{\mathbf{R}\otimes\mathbf{R}'|\tilde{\mathbf{R}}}$ prior to the full NNLO total cross section analysis these terms were missing in the NNLL resummation formula and one had to resort to approximate $\tilde{H}^{(2)}_{\mathbf{R}\otimes\mathbf{R}'|\tilde{\mathbf{R}}}$-values inspired by the estimates used for $C^{(2)}_{ij,\tilde{\mathbf{R}}}$. Similar to the threshold expansion the impact of these subleading contributions on the final cross section predictions is not negligible and will be discussed below.

The N-space resummation formula for the total cross section can then be expressed in terms of $\hat{\sigma}^{(res)}_{ij,\,N}$ as

$$\begin{aligned} \sigma^{(\text{res})}_{t\bar{t},\,N}(m_t^2) &= \sum_{\substack{ij\,\in\\ \{q\bar{q},gg\}}} \phi_{i/h_1,\,N+1}\,\phi_{j/h_2,\,N+1}\left[\hat{\sigma}^{(res)}_{ij,\,N}(m_t^2,\alpha_s(\mu^2),L_Q) - \left(\hat{\sigma}^{(res)}_{ij,\,N}(m_t^2,\alpha_s(\mu^2),L_Q)\right)_{\alpha_s^p}\right] \\ &+ \sigma^{\mathbf{tot}}_{t\bar{t},\,N}(m_t^2) \end{aligned} \tag{3.100}$$

where $\phi_{k/h_x,\,N+1}$ represents the Mellin transform of the PDF for parton k inside hadron h_x and $\left(\hat{\sigma}^{(res)}_{ij,\,N}\right)_{\alpha_s^p}$ is the perturbative truncation of the resummed partonic cross section at order α_s^p.

[17] The general color dependence of NNLO hard matching coefficients can be found in appendix C.

The actual value of p depends on the chosen precision of the N-space hadronic cross section $\sigma^{\mathbf{tot}}_{t\bar{t},N}$, namely $p = 2,3,4$ at LO, NLO and NNLO respectively. The reason for adding this fixed-order result is to allow for an exact description of the kinematics away from the threshold region. Therefore, all perturbative corrections currently available are completely included in the final predictions and only the orders beyond are approximated via soft-gluon resummation. This is also a major advantage with respect to the threshold expansion as it allows us to incorporate new perturbative results into the resummation formula at any time while the fixed-order analysis of small-velocity enhancements contains, in principle, no additional information once the full result becomes available. The truncation term is hence necessary to avoid double-counting of soft contributions when matching to $\sigma^{\mathbf{tot}}_{t\bar{t},N}$.

In order to obtain physical predictions for the total cross section, one has to transform the resummed results back to x-space, which may be achieved via

$$\sigma^{(\mathrm{res})}_{t\bar{t}}(\rho_{\mathrm{H}}, m_t^2) = \frac{1}{2\pi i} \int_{C_{\mathrm{MP}}-i\infty}^{C_{\mathrm{MP}}+i\infty} dN\, \rho_{\mathrm{H}}^{-N}\, \sigma^{(\mathrm{res})}_{t\bar{t},N}(m_t^2) \tag{3.101}$$

where the constant C_{MP} defining the integration contour in the complex plane has to be carefully chosen to account for possible poles of N in $\sigma^{(\mathrm{res})}_{t\bar{t},N}$. While for a fixed-order expansion the condition $C_{\mathrm{MP}} > 2$ is sufficient to guarantee that this transformation is indeed the correct inverse of the Mellin moments in Eq. (3.36), the integration of the resummed result suffers from additional complications due to cut singularities starting at the branch-point

$$N = N_L = \exp\left(\frac{2\pi}{\beta_0 \alpha_s}\right) . \tag{3.102}$$

They are caused by the integration of the running coupling in Eq. (3.84) down to the Landau pole and thus indicate an increasing influence of non-perturbative effects very close to threshold. The problem with these contributions is that a naive treatment of the corresponding singularities may induce spurious, potentially large power corrections in the resummed x-space cross sections leading to false theoretical predictions. Fortunately, it is possible to avoid the occurrence of these ill-behaved terms by choosing an appropriate integration path in Eq. (3.101) which lies right of all regular singularities and left of N_L. This so-called *Minimal Prescription* [215] provides a consistent, perturbative description of the resummation formalism in x-space as it converges asymptotically to the Mellin inverse of the expanded resummation formula, which is free of such Landau singularities. In practice, the evaluation of the inverse Mellin transformation involves some additional subtleties [215] related to the numerical nature of the PDFs entering $\sigma^{(\mathrm{res})}_{t\bar{t},N}$, which are usually only available in form of interpolation grids that cannot be properly transformed to N-space or back. It is, however, possible to resolve these implementational problems and to incorporate the *Minimal Prescription* into a stable and efficient code that allows for a combined treatment of fixed-order corrections and resummation effects.

The resulting predictions based on the NLO cross section with different levels of resummation are shown in Tab. 3.2. Note that the NNLL-resummed partonic cross sections are formally of order $\mathcal{O}(\alpha_s^4)$ and we thus employ PDFs of NNLO accuracy in the derivation of the corresponding $\sigma^{\mathbf{tot}}_{t\bar{t}}$ predictions to match this increase in perturbative precision. Moreover, we by default

$\sigma_{t\bar{t}}^{\mathbf{tot},\,\mathrm{NLO+res.}}$	A	Tevatron [pb]	LHC			
			7 TeV [pb]	8 TeV [pb]	13 TeV [pb]	14 TeV [pb]
NLL	0	$7.039^{+0.198\,(2.8\%)}_{-0.422\,(6.0\%)}$	$172.0^{+15.4\,(8.9\%)}_{-14.5\,(8.5\%)}$	$245.1^{+22.0\,(9.0\%)}_{-20.9\,(8.5\%)}$	$798.4^{+72.3\,(9.1\%)}_{-70.6\,(8.8\%)}$	$943.9^{+85.6\,(9.1\%)}_{-83.9\,(8.9\%)}$
	2	$6.912^{+0.269\,(3.9\%)}_{-0.497\,(7.2\%)}$	$165.9^{+13.8\,(8.3\%)}_{-15.0\,(9.1\%)}$	$236.5^{+20.0\,(8.5\%)}_{-21.6\,(9.1\%)}$	$772.5^{+69.5\,(9.0\%)}_{-72.6\,(9.4\%)}$	$913.6^{+82.9\,(9.1\%)}_{-86.1\,(9.4\%)}$
NNLL_0	0	$6.844^{+0.180\,(2.6\%)}_{-0.377\,(5.5\%)}$	$164.7^{+15.0\,(9.1\%)}_{-12.8\,(7.8\%)}$	$235.0^{+21.5\,(9.1\%)}_{-18.5\,(7.9\%)}$	$767.7^{+70.7\,(9.2\%)}_{-62.8\,(8.2\%)}$	$907.7^{+83.6\,(9.2\%)}_{-74.7\,(8.2\%)}$
	2	$6.722^{+0.238\,(3.5\%)}_{-0.410\,(6.1\%)}$	$158.7^{+12.2\,(7.7\%)}_{-13.5\,(8.5\%)}$	$226.6^{+17.8\,(7.8\%)}_{-19.4\,(8.6\%)}$	$742.1^{+62.2\,(8.4\%)}_{-65.8\,(8.9\%)}$	$877.8^{+74.2\,(8.5\%)}_{-78.2\,(8.9\%)}$
NNLL	0	$7.405^{+0.033\,(0.4\%)}_{-0.302\,(4.1\%)}$	$178.0^{+10.6\,(6.0\%)}_{-13.5\,(7.6\%)}$	$253.9^{+15.2\,(6.0\%)}_{-19.2\,(7.6\%)}$	$828.7^{+50.5\,(6.1\%)}_{-63.0\,(7.6\%)}$	$979.7^{+59.9\,(6.1\%)}_{-74.6\,(7.6\%)}$
	2	$7.283^{+0.009\,(0.1\%)}_{-0.320\,(4.4\%)}$	$172.0^{+4.7\,(2.7\%)}_{-8.6\,(5.0\%)}$	$245.5^{+6.6\,(2.7\%)}_{-12.4\,(5.1\%)}$	$803.1^{+21.0\,(2.6\%)}_{-42.4\,(5.3\%)}$	$949.8^{+24.9\,(2.6\%)}_{-50.4\,(5.3\%)}$
$\sigma_{t\bar{t}}^{\mathbf{tot},\,\mathrm{NLO}}$	-	$6.682^{+0.356\,(5.3\%)}_{-0.752\,(11.3\%)}$	$158.1^{+19.5\,(12.3\%)}_{-21.2\,(13.4\%)}$	$226.3^{+27.8\,(12.3\%)}_{-29.7\,(13.1\%)}$	$746.9^{+90.4\,(12.1\%)}_{-90.4\,(12.1\%)}$	$884.5^{+106.8\,(12.1\%)}_{-105.8\,(12.0\%)}$
$\sigma_{t\bar{t}}^{\mathbf{tot},\,\mathrm{NNLO}}$	-	$7.009^{+0.259\,(3.7\%)}_{-0.374\,(5.3\%)}$	$167.0^{+6.7\,(4.0\%)}_{-10.7\,(6.4\%)}$	$239.1^{+9.2\,(3.9\%)}_{-14.8\,(6.2\%)}$	$788.1^{+27.1\,(3.4\%)}_{-43.8\,(5.6\%)}$	$933.0^{+31.8\,(3.4\%)}_{-51.0\,(5.5\%)}$
$\sigma_{t\bar{t}}^{\mathbf{tot},\,\mathrm{NNLO+NNLL}}$	0	$7.164^{+0.109\ +0.169}_{-0.200\ -0.122}$	$172.2^{+4.7\ +4.7}_{-5.9\ -4.8}$	$246.0^{+6.6\ +6.2}_{-8.5\ -6.4}$	$806.6^{+20.6\ +14.5}_{-28.6\ -15.7}$	$954.1^{+24.2\ +16.3}_{-34.0\ -17.8}$

Table 3.2: *Resummation-based predictions for $\sigma_{t\bar{t}}^{\mathbf{tot}}$ at the Tevatron and the LHC as well as the corresponding fixed-order results ($m_t = 173.3\,\mathrm{GeV}$, MSTW2008 PDFs at 68% C.L. [231]). The parameter A is defined below while the NNLO hard matching coefficients have been chosen as $\tilde{H}^{(2)}_{\mathbf{R}\otimes\mathbf{R}'|\tilde{\mathbf{R}}}\left(\frac{\mu^2}{m_t^2}\right) = 0$ (NNLL_0) and $\tilde{H}^{(2)}_{\mathbf{R}\otimes\mathbf{R}'|\tilde{\mathbf{R}}} =$ Eq. (3.99) (NNLL). The given uncertainties are due to the variation of renormalization and factorization scale.*

include the two-loop Coulomb contributions $\tilde{C}^{(2)}_{\mathbf{R}\otimes\mathbf{R}'|\tilde{\mathbf{R}}}$ such that the only free parameters in the NNLL resummation formula are the NNLO hard matching coefficients. For comparison we also give the fixed-order NLO and NNLO results as well as the values for the NNLO+NNLL resummed cross sections. As can be seen, including resummation effects in general leads to an increase of the cross section predictions and a reduction of the corresponding theoretical uncertainty due to scale variation. The size of these corrections, however, depends crucially on the chosen precision in the radiative function $\Delta_{\mathbf{R}\otimes\mathbf{R}'|\tilde{\mathbf{R}},\,N+1}$ and the matched fixed-order result as well as on the parameters $\tilde{H}^{(2)}_{\mathbf{R}\otimes\mathbf{R}'|\tilde{\mathbf{R}}}$ and A. The latter has been introduced in Ref. [216] via the replacement[18]

$$\tilde{H}^{(1)}_{\mathbf{R}\otimes\mathbf{R}'|\tilde{\mathbf{R}}} \to \tilde{H}^{(1)}_{\mathbf{R}\otimes\mathbf{R}'|\tilde{\mathbf{R}}}\left(1 - \frac{A}{N+A}\right) \tag{3.103}$$

such that for $A = 0$ one recovers the original resummation formula whereas a value $A \neq 0$ allows for the investigation of power-suppressed effects on the total cross section results. The most common choice is $A = 2$, which is motivated by the observation that the corresponding $\mathcal{O}(\alpha_s^3)$ term of $\hat{\sigma}^{(\mathrm{res})}_{ij,\,N}$ mimics the behavior of the fixed-order NLO result over a wide range in β. Thus, at $\mathcal{O}(\alpha_s^4)$ this definition is obsolete and should be replaced by an analogous prescription for $\tilde{H}^{(2)}_{\mathbf{R}\otimes\mathbf{R}'|\tilde{\mathbf{R}}}$ to ensure a consistent NNLO treatment. Consequently, we

[18] The description in the original publication is somewhat misleading stating that the denominator is of the form $N + A - 1$. While this is true, it has been pointed out in the associated Erratum that the value of N entering this expression should match the value appearing in $\Delta_{\mathbf{R}\otimes\mathbf{R}'|\tilde{\mathbf{R}},\,N+1}$ resulting in the specific form given in Eq. (3.103).

only consider the case $A = 0$ for the respective NNLO+NNLL predictions. At NLO the inclusion of power-suppressed contributions leads to a slight reduction of the total cross section of about 2% at the Tevatron and 3% at the LHC while the scale dependence remains virtually unaffected.

In contrast to this, the value of the other free parameter $\tilde{H}^{(2)}_{\mathbf{R}\otimes\mathbf{R}'|\tilde{\mathbf{R}}}$ has a considerable impact on the NLO+NNLL predictions. For $\tilde{H}^{(2)}_{\mathbf{R}\otimes\mathbf{R}'|\tilde{\mathbf{R}}}\left(\frac{\mu^2}{m_t^2}\right) = 0$ (note that the scale dependence is dropped as well) it actually lies below the NLO+NLL results whereas the hard matching coefficients in Eq. (3.99) induce a significant increase in $\sigma^{(\text{res})}_{t\bar{t}}$ surpassing even the NNLO and NNLO+NNLL results. This is due to the fact that when matching to NLO the effect of including $\tilde{H}^{(2)}_{\mathbf{R}\otimes\mathbf{R}'|\tilde{\mathbf{R}}}$ is formally of $\mathcal{O}(\alpha_s^4)$ similar to the $C^{(2)}_{ij,\tilde{\mathbf{R}}}$-dependence of the threshold expansion. Therefore, matching to NNLO will reduce this dependence to $\mathcal{O}(\alpha_s^5)$ such that the impact on the total cross section will be much less pronounced.

Furthermore, the comparison between the NLO+NNLL and NNLO+NNLL results reveals that

$$\sum_{\substack{ij\,\in\\ \{q\bar{q},gg\}}} \phi_{i/h_1,\,N+1}\,\phi_{j/h_2,\,N+1}\,\hat{\sigma}^{(res)}_{ij,\,N}\bigg|_{\mathcal{O}(\alpha_s^4)\text{ only}} - \sigma^{\mathbf{tot}}_{t\bar{t},\,N}\bigg|_{\mathcal{O}(\alpha_s^4)\text{ only}} > 0\,, \tag{3.104}$$

which is contrary to the threshold analysis where the full corrections are usually larger than the approximate results (except for the quark annihilation channel, see Tab. 3.1). This is the reason why the difference between the NLO+NLL and NNLO+NNLL predictions is negligible while for the corresponding fixed-order results it is quite sizable. But more importantly it implies that both approximation methods, the NNLO threshold expansion as well as the NLO+NNLL analysis, provide only limited control over numerically relevant subleading contributions. This becomes obvious when we recall that both approaches are formally equivalent[19] in the limit $N \to \infty$ (apart from higher-order effects of $\mathcal{O}(\alpha_s^5)$) and yet yield considerably deviating predictions. This, again, stresses the fact that a genuine reduction of the theoretical uncertainty of $\sigma^{\mathbf{tot}}_{t\bar{t}}$ may only be achieved through a full NNLO determination. In the following sections we will describe the main methods needed for such a sophisticated analysis as well as the phenomenological implications of the resulting NNLO and NNLO+NNLL predictions.

3.2 Double-real radiation

The double-real corrections consist of Born diagrams with two additional massless particles in the final state with respect to the LO configuration and can thus be interpreted as a natural extension of the NLO real contributions. In fact, they can be obtained from the latter by inserting a further gluon line or a quark-antiquark splitting in the corresponding diagrams, which in addition to the known NLO channels opens up a new production mode in

[19] This is also the reason why the NNLO threshold expansion should not be employed as a matching term in Eq. (3.100) since it does not provide any new information but rather introduces additional power-suppressed contributions beyond our control [220].

the $\sigma_{t\bar{t}}^{\mathbf{tot}}$ analysis denoted as $q\tilde{q}$-channel (see Eq. (2.9)). It allows for the interaction of pairs of quarks as well as of different quark flavors and, hence, completes the description of QCD-type production processes in hadronic collisions.

In order to regularize the associated IR divergences induced by the four-particle phase space integration we, again, work in CDR such that the corresponding contribution to the partonic cross section is given by

$$\hat{\sigma}_{ij}^{RR}(\beta) = \int dP_4^{(ij)} \; \langle \mathcal{M}_{ijkl}^{(0)} | \mathcal{M}_{ijkl}^{(0)} \rangle \equiv \int d\hat{\sigma}_{n+2}^{RR} \; . \tag{3.105}$$

Due to its complexity this expression can, in practice, not be evaluated analytically but one has to resort to numerical methods that, on the one hand, allow for an efficient integration in a specific, i. e. integer-valued, number of dimensions and, on the other hand, reproduce the correct pole structure needed for the explicit cancellation with remaining NNLO contributions. The most natural solution would be an extension of the well-established NLO subtraction mechanism of the form

$$\hat{\sigma}_{n+2}^{RR} = \int \left(d\hat{\sigma}_{n+2}^{RR} - d\hat{\sigma}_{n+2}^{RR,\,S_{\mathrm{I}}} - d\hat{\sigma}_{n+2}^{RR,\,S_{\mathrm{II}}} \right)_{\epsilon=0} + \int d\hat{\sigma}_{n+1}^{I_{\mathrm{I}}} + \int d\hat{\sigma}_{n}^{I_{\mathrm{II}}} \tag{3.106}$$

where the subtraction terms $d\hat{\sigma}_{n+2}^{RR,\,S_{\mathrm{I}}}$ and $d\hat{\sigma}_{n+2}^{RR,\,S_{\mathrm{II}}}$ regulate the real-emission integrand as one (I) or two (II) massless partons become unresolved. The associated integrated subtraction terms are then defined as

$$\begin{aligned} d\hat{\sigma}_{n+1}^{RR,\,I_{\mathrm{I}}} &= \int\limits_{1} d\hat{\sigma}_{n+2}^{RR,\,S_{\mathrm{I}}} \\ d\hat{\sigma}_{n}^{RR,\,I_{\mathrm{II}}} &= \int\limits_{2} d\hat{\sigma}_{n+2}^{RR,\,S_{\mathrm{II}}} \; . \end{aligned} \tag{3.107}$$

Note that the evaluation of the $d\hat{\sigma}_{n+1}^{RR,\,I_{\mathrm{I}}}$ integral usually requires additional subtractions in order to deal with the remaining soft and collinear divergences in the $n+1$ phase space. This is, however, a task of NLO complexity that can be conveniently performed with the methods discussed in section 2.3.2 and we thus tacitly assume that it has been properly accounted for. The main challenge of such a NNLO subtraction approach is the construction of $d\hat{\sigma}_{n+2}^{RR,\,S_{\mathrm{I}}}$ and $d\hat{\sigma}_{n+2}^{RR,\,S_{\mathrm{II}}}$, which proves to be far more complicated than at NLO owing to the much more involved IR singularity structure. Indeed, the presence of an additional massless parton in the final state may lead to nested and overlapping divergences of up to $1/\epsilon^4$ and, moreover, introduce novel correlation effects in spin and color space due to double emissions from the same external leg. As a result of this advanced complexity it is difficult to derive subtraction terms that meet the same requirements as have been imposed on their NLO counterparts, namely generality and analyticity. Generality means that the resulting subtraction scheme should be applicable to arbitrary NNLO processes regardless of the mass of the participating particles or whether they carry color charge (or, more generally speaking, charge of the underlying gauge group). Analyticity, on the other hand, refers to the property that the integrated

subtraction terms may be evaluated in a closed form similar to the Catani-Seymour dipole operators

$$\begin{aligned} \int d\hat{\sigma}_{n+1}^{RR,\,I_{\mathrm{I}}} &= \int d\hat{\sigma}_{n+1}^{R} \otimes \mathcal{I}^{(\mathrm{I})} \\ \int d\hat{\sigma}_{n}^{RR,\,I_{\mathrm{II}}} &= \int d\hat{\sigma}_{n}^{LO} \otimes \mathcal{I}^{(\mathrm{II})} \,. \end{aligned} \tag{3.108}$$

While this requirement is not essential in the sense that it constraints the number of possible physical applications, it is still important from the implementational perspective. On the one hand, it facilitates the construction of a stable and well-converging algorithm and on the other hand it makes the corresponding subtraction method easily accessible to a wider public.

Despite the fact that there have been many proposals to solve the problem of NNLO subtraction (or, to be more general, the integration of NNLO real radiation), there currently exists no method that is both general and analytical such that one has to drop one of these prerequisites in order to do NNLO phenomenology. Thus, the proper treatment of double-real radiation remains an active field of research and it might be possible that a further improvement of one of the existing concepts will ultimately succeed in combining these requirements. In the following we will summarize the most promising of these approaches and briefly explain their basic concept as well as their advantages and potential drawbacks before we in detail discuss Stripper (SecToR Improved Phase sPacE for real Radiation), the scheme employed in NNLO $t\bar{t}$ production.

3.2.1 Antenna subtraction

The Antenna subtraction scheme was originally invented for NLO calculations [582, 583] as an alternative to the Catani-Seymour dipole formalism and has later been extended to NNLO [584]. Thus, it is completely general in the class of processes it can be applied to. It is based on the use of so-called color-ordered amplitudes $|\mathfrak{M}_k^{(l)}\rangle$ which are defined in terms of regular l-loop, n-particle amplitudes via [585, 586]

$$|\mathcal{M}_n^{(l)}\rangle = \sum_k C_{n,k}^{(l)}(N_c)\ |\mathfrak{M}_k^{(l)}\rangle \tag{3.109}$$

where k runs over $(n-1)!$ non-cyclic permutations of the external parton indices (spin and momentum indices have been suppressed for readability), which means that the ordering of the external legs in the color-stripped matrix elements is fixed. All color information is contained in the coefficients $C_{n,k}^{(l)}$ allowing for a separate treatment of kinematic and gauge group contributions. In consequence, the subtraction terms have to only be constructed for the QED-like amplitudes $|\mathfrak{M}_k^{(l)}\rangle$, which is considerably simpler than for the full matrix elements as the singular behavior is confined to combinations of resolved and unresolved partons that are color-connected, i. e. adjacent in the ordering of external legs. Especially at NNLO, this is a major advantage since the case where the two unresolved partons are unconnected can be reduced to an iterative application of the NLO formula. The actual form of the subtractions

terms is determined by so-called three- and four-parton antenna functions (the latter only contributes at NNLO) that are proportional to a ratio of color-ordered amplitudes

$$\begin{aligned} X^0_{ijk}(p_i,p_j,p_k) &\propto \frac{|\mathfrak{M}^{(0)}_{ijk}|^2}{|\mathfrak{M}^{(0)}_{IK}|^2} \\ X^0_{ijkl}(p_i,p_j,p_k,p_l) &\propto \frac{|\mathfrak{M}^{(0)}_{ijkl}|^2}{|\mathfrak{M}^{(0)}_{IL}|^2} \,. \end{aligned} \tag{3.110}$$

As indicated, these Antennae depend only on the momenta of the corresponding partons and their specific nature $i,j,k,l,I,K,L \in \{q,\bar{q},g\}$. An advantage of this parametrization is the fact that the integration over the unresolved phase space can be performed analytically [587] allowing for an explicit pole cancellation. Interestingly, however, these functions are non-local meaning that they do not mimic the IR-singular behavior of the respective real-emission amplitudes in a point-wise manner but only after integrating over parts of phase space. The reason for this is the absence of spin correlations in the treatment of collinear limits due to the construction of X^0_{ijk} and X^0_{ijkl} in terms of squared matrix elements. In order to still allow for a stable and efficient implementation of this method, one has to compensate this non-locality by either adding a suitable local counterterm or by combining several phase space points such that the correlation effects drop out [588].

There exists, however, a more severe drawback related to the chosen parametrization in Eq. (3.110) that has not been completely resolved yet, namely the description of subleading color effects. The problem with these contributions is that they are usually given in terms of incoherent interferences of color-ordered amplitudes, which can consequently not be approximated by the squared matrix elements that enter X^0_{ijk} and X^0_{ijkl}. Adjusting the antennae accordingly turns out to be highly non-trivial and has so far only been accomplished for the purely gluonic case [589]. Thus, for most processes an antenna-based treatment of double-real radiation is currently merely possible in the leading-color limit.

3.2.2 CoLoRFulNNLO (Completely Local subtRactions for Fully differential Predictions at NNLO)

This subtraction scheme has been conceived for NNLO calculations of processes with colorless initial state [590–600] and is, hence, only of limited phenomenological use at hadron colliders such as the Tevatron or the LHC. The main idea is to employ a decomposition of subtraction terms as proposed in Eq. (3.106), however, with the additional subtraction term for the remaining IR divergences in $d\hat{\sigma}^{RR,S_\mathrm{I}}_{n+2}$ made explicit such that one obtains three distinct contributions [590]. Subsequently, one uses the well-known soft and collinear behavior of QCD amplitudes to determine the actual form of theses local subtraction terms, carefully accounting for overlapping limits in order to avoid multiple subtractions in the unresolved region of phase space. Moreover, the chosen parametrization has to allow for an exact factorization of $d\Phi_{n+2}$ into resolved and unresolved contributions while still maintaining the delicate cancellation structure among the various subtraction terms. The resulting subtraction formula then

provides a fully differential description of double-real radiation with the complete color and spin dependence explicitly included.

A further advantage of this approach is that the integration over the unresolved phase space can be performed analytically even though such an analysis, in practice, requires a tedious effort on the computational side. The basic strategy for the determination of these integrated subtraction terms consists of a reduction to master integrals by means of algebraic and symmetry relations as well as IBP methods [595] and a consecutive evaluation with different well-established computational techniques as, for instance, Mellin-Barnes representations [597]. The result can be expressed in terms of multiple polylogarithms of the kinematic variables involved in the scattering process [595]. In actual implementations it is, however, more convenient to approximate the finite part of the integrated subtraction terms (the poles are needed in analytic form to allow for an explicit cancellation with the other NNLO contributions) by interpolation functions in order to increase the overall computational efficiency [595,597].

A first application of this approach relevant for the LHC is the description of the differential Higgs decay $H \to b\bar{b}$ at NNLO [601]. While this is an impressive demonstration of the potential inherent to this method it would be highly desirable to extend it to colored initial states as well in order to make it applicable to a broader spectrum of QCD processes. There, in fact, exists such a formulation for hadronic collision scenarios [596] but it yet remains to be seen whether this improved version is really applicable to any physical processes.

3.2.3 Resummation-based approaches

Over the last years a class of conceptually entirely different subtraction schemes has been developed that are more oriented towards the traditional phase space slicing methods. The basic idea is to parametrize the divergent behavior of a higher-order differential cross section $d\sigma_X^{(N)NLO}$ in terms of a single variable κ that describes all IR soft and collinear limits simultaneously as $\kappa \to 0$. In order to guarantee the highest possible degree of generality, this quantity should be determined exclusively from kinematics, i.e. it should be constructed from the momenta and energies of the partons participating in the scattering process. Furthermore, there has to exist a resummation formalism that describes the leading logarithmic enhancements as κ vanishes. The integrated cross section is then given as [602]

$$\sigma_X^{(N)NLO} = \int d\kappa \, \frac{d\sigma_X^{(N)NLO}}{d\kappa} = \underbrace{\int_0^{\kappa_{cut}} d\kappa \, \frac{d\sigma_X^{(N)NLO}}{d\kappa}}_{\equiv \sigma_X^{(N)NLO,\,\text{sing.}}(\kappa_{cut})} + \underbrace{\int_{\kappa_{cut}} d\kappa \, \frac{d\sigma_X^{(N)NLO}}{d\kappa}}_{\equiv \sigma_X^{(N)NLO,\,\text{int.}}} \tag{3.111}$$

where the cutoff κ_{cut} has been introduced to separate the leading IR-singular from the IR-integrable region. The latter is defined by at least one of the unresolved partons becoming observable, which at NLO results in a completely finite integral whereas at NNLO the integration can be performed by an iterated use of NLO subtractions. Thus, the problem is reduced to the evaluation of $\sigma_X^{(N)NLO,\,\text{sing.}}$ which is exactly where resummation comes into play. Indeed, for a sufficiently small cutoff $\kappa_{cut} \to 0$ the integration range is entirely restricted

to the regime where such an approach is valid allowing for the following approximation

$$\sigma_X^{(N)NLO,\,\text{sing.}}(\kappa_{cut}) \approx \int_0^{\kappa_{cut}} d\kappa \, \frac{d\sigma_X^{(N)NLO,\,\text{res.}}}{d\kappa} + \mathcal{O}(\kappa_{cut}) = \sigma_X^{(N)NLO,\,\text{res.}}(\kappa_{cut}) + \mathcal{O}(\kappa_{cut}) \; . \tag{3.112}$$

Here, $d\sigma_X^{(N)NLO,\,\text{res.}}$ corresponds to an fixed-order expansion of the resummation formula truncated at NLO or NNLO respectively. Since such a formula is generally composed of convolutions of various factorized contributions, e. g. Hard, Soft or Jet functions, this means that all of these components have to match the required accuracy.

As the hard contributions entering the resummation procedure usually contain virtual corrections, these terms are naturally included in this subtraction formalism leading to a complete description of the corresponding cross section and not just the real-emission part. This in particular means that the pole cancellation between real and virtual (and, at NNLO, real-virtual) contributions is implicitly contained in this approach. Due to the parametrization in terms of a single quantity it is, however, maximally non-local, i. e. the cancellation only occurs after integration over the remaining phase space variables. In practice, a naive implementation of this method is therefore likely to suffer from large numerical instabilities. This is even more so as a small cutoff required for the use of Eq. (3.112) will induce additional IR-enhancements in $\sigma_X^{(N)NLO,\,\text{int.}}$ that may cause further computational problems. The solution to these problems is the introduction of an intermediate cutoff parameter κ_{off} such that [602]

$$\sigma_X^{(N)NLO} = \sigma_X^{(N)NLO,\,\text{res.}}(\kappa_{cut}) + \int_{\kappa_{cut}} d\kappa \left[\frac{d\sigma_X^{(N)NLO,\,\text{int.}}}{d\kappa} - \frac{d\sigma_X^{(N)NLO,\,\text{res.}}}{d\kappa} \Theta(\kappa_{off} - \kappa) \right] + \mathcal{O}(\kappa_{cut}) \; . \tag{3.113}$$

The additional subtraction renders the integrand point-wise convergent in κ leading to a significant improvement in stability and efficiency and making it, thus, applicable to actual physical processes. Nonetheless, there already exist proposals for a further optimization of the numerics by either increasing the locality of the subtractions through the introduction of an additional variable κ' [602] (resulting in double differential expressions in Eq. (3.113)) or by extending the resummation formula to include also subleading power corrections such that the residual uncertainty is reduced to $\mathcal{O}(\kappa_{cut}^2)$ [602–604].

The first successful application of such a resummation-based subtraction scheme was NNLO hadronic Higgs production, which employed $\kappa = p_T$, the transverse momentum of the Higgs, as a suitable variable for dividing the phase space [605, 606]. In fact, the corresponding transverse momentum resummation formula [607,608] may be used to compute NNLO results for any process that at LO contains only colorless particles in the final state, e. g. $Z\gamma$ [609,610], ZZ [611] or WW [612].

In order to also address the production of colored final states[20], one has to resort to a different variable $\kappa = \mathcal{T}_N$ defined via [602, 616]

$$\mathcal{T}_N = \sum_k \min_i \left\{ \frac{2q_i \cdot p_k}{Q_i} \right\} \tag{3.114}$$

where p_k are the momenta of the final-state partons, q_i ($i = a, b, 1, \ldots, N$ where a, b denote the initial state) are the so-called jet-axes obtained from an arbitrary IR-safe jet algorithm and Q_i are the corresponding normalization factors. One can convince oneself that this choice leads to a proper separation of resolved and unresolved kinematics since at LO the number of final-state jets corresponds to the number of final-state partons such that $\mathcal{T}_N = 0$. Only at higher orders several partons are clustered into a single jet resulting in $\mathcal{T}_N \geq 0$. The required resummation formula for this quantity can be derived in the framework of SCET and is currently known to NNLO accuracy for $\mathcal{T}_0$ and $\mathcal{T}_1$ [617–622]. In consequence, this variable can so far only be applied to the NNLO determination of processes with one colored final-state parton, e. g. the associated production of Higgs, W-boson or Z-boson with one jet [623–625]. A further drawback of this variable is the fact that it is limited to massless partons. There exist, however, proposals to include massive partons as well [602] such that the number of possible applications is likely to further increase in the near future.

3.2.4 Stripper

The subtraction scheme employed for the calculation of double-real radiation in $t\bar{t}$ production, Stripper, differs from the methods discussed so far in the sense that it drops the analyticity requirement aiming at a fully numerical treatment in terms of a Laurent expansion in ϵ. In consequence, an explicit verification of the pole cancellation is only achieved at the numerical level and, thus, subject to the available precision of the utilized integration routines. This will, however, not diminish the quality of the resulting physical predictions as the correctness of this approach is guaranteed by the KLN theorem as well as the subtraction prescriptions outlined below. A key aspect of this method is that it is completely general, i. e. it can be applied to arbitrary processes with massless and massive final states taking into account the full spin and color dependence. Apart from top-quark pair production [77–80, 385] it has so far been successfully employed in calculations of t-channel single top production [285], fully differential top decays [13], inclusive semileptonic charmless b-quark decays [626], $H + j$ production [627, 628] and the spin asymmetry in muon decays [629] as well as for the NNLO QED corrections to the decay of Z bosons into massless lepton pairs [630]. Nevertheless, we will in the following focus on the kinematic configuration relevant for the case of NNLO $t\bar{t}$ production

$$p_1 + p_2 \longrightarrow \underbrace{q_1 + q_2}_{q_i^2 = m_t^2} + \underbrace{k_1 + k_2}_{k_i^2 = 0} \tag{3.115}$$

[20] There exist proposals for an extension of the p_T-subtraction method to colored final states [613–615] as well but these novel concepts are not fully developed yet.

giving a concise summary of the detailed description in Refs. [232,233] to illustrate the main features of this subtraction method. Moreover we discuss its actual implementation based on multi-dimensional MC methods that has been used for derivation of the double-real corrections to $\sigma_{t\bar{t}}^{\mathbf{tot}}$.

Parametrization of the phase space

The main idea behind STRIPPER is to mix different aspects from FKS subtraction [550] and *Sector Decomposition* [631] to disentangle the overlapping divergences such that they completely factorize allowing for a simple regularization in terms of plus distributions. To this end, the phase space is decomposed into various sectors according to the underlying collinear singularity structure by introducing so-called selector functions θ_1, θ_2 and θ_3 satisfying the following requirements:

1. $\theta_1(k) = 1$ if $k||p_1$ and $\theta_1(k) = 0$ if $k||p_2$ where k is the momentum of an arbitrary massless final-state parton.
2. $\theta_2(k)$ corresponds to $\theta_1(k)$ with p_1 and p_2 interchanged such that $\theta_1 + \theta_2 = 1$.
3. $\theta_3(k_1, k_2) = 1$ if $k_1||k_2$ with the assumption that it cancels all divergences due to $k_{1,2}||p_{1,2}$.
4. All selector functions have to vanish fast enough to regulate the collinear divergences in the respective limits.

The resulting partition of the phase space reads

$$
\begin{aligned}
1 \;=\; & \left.\begin{aligned} &+\theta_1(k_1)\theta_1(k_2) \\ &+\theta_2(k_1)\theta_2(k_2) \end{aligned}\right\} \text{triple-collinear sector} \\
& \left.\begin{aligned} &+\theta_1(k_1)\theta_2(k_2)(1-\theta_3(k_1,k_2)) \\ &+\theta_2(k_1)\theta_1(k_2)(1-\theta_3(k_1,k_2)) \end{aligned}\right\} \text{double-collinear sector} \\
& \left.\begin{aligned} &+(\theta_1(k_1)\theta_2(k_2)+\theta_2(k_1)\theta_1(k_2))\theta_3(k_1,k_2) \end{aligned}\right\} \text{single-collinear sector}
\end{aligned}
\tag{3.116}
$$

where the first and third sector can actually be treated together as they contain the same single-collinear divergences. The double-collinear sector, on the other hand, allows only for collinear emissions from different legs and can, hence, be regarded as an iterated NLO problem. The next step consists of choosing a suitable parametrization of the phase space

$$
\begin{aligned}
d\Phi_4 \;&=\; \frac{d^{d-1}k_1}{(2\pi)^{d-1}2k_1^0}\,\frac{d^{d-1}k_2}{(2\pi)^{d-1}2k_2^0} \\
&\times\; \frac{d^{d-1}q_1}{(2\pi)^{d-1}2q_1^0}\,\frac{d^{d-1}q_2}{(2\pi)^{d-1}2q_2^0}\,(2\pi)^d\,\delta^{(d)}(q_1+q_2-Q) \\
&\equiv\; d\tilde{\Phi}_3(s;k_1,k_2)\times d\Phi_2(Q;q_1,q_2)
\end{aligned}
\tag{3.117}
$$

with

$$Q = p_1 + p_2 - k_1 - k_2 \tag{3.118}$$

and $d\tilde{\Phi}_3$ is obtained from the regular three-particle phase space $d\Phi_3$ by omitting the delta function for momentum conservation, i. e. it is only constrained by the condition $Q^2 \geq 4\,m_t^2$. For the massless system spanned by the three vectors $\vec{p}_1$, $\vec{k}_1$ and $\vec{k}_2$ ($\vec{p}_2 = -\vec{p}_1$ by definition) one can exploit rotational invariance and space inversion invariance to eliminate the additional ϵ-dimensional components such that

$$\begin{aligned}
p_1^\mu &= \frac{\sqrt{s}}{2}(1,0,0,1) \\
p_2^\mu &= \frac{\sqrt{s}}{2}(1,0,0,-1) \\
n_1^\mu &= \frac{\sqrt{s}}{2}\beta^2(1,0,\sin\theta_1,\cos\theta_1) \\
n_2^\mu &= \frac{\sqrt{s}}{2}\beta^2(1,\sin\phi\sin\theta_2,\cos\phi\sin\theta_2,\cos\theta_2) \\
k_1^\mu &= \hat{\xi}_1\, n_1^\mu \\
k_2^\mu &= \hat{\xi}_2\, n_2^\mu
\end{aligned} \tag{3.119}$$

where the angles are restricted to $\phi, \theta_{1,2} \in [0,\pi]$ and the auxiliary vectors $n_{1,2}^\mu$ are necessary for an unambiguous definition of soft limits. The energies are remapped to the variables $\hat{\xi}_{1,2}$ whose integration range is further decomposed into two non-overlapping regions

$$\left\{(\hat{\xi}_1,\hat{\xi}_2):\ 0 \leq \hat{\xi}_1 \leq 1\ ,\ 0 \leq \hat{\xi}_2 \leq \hat{\xi}_1\,\xi_{max}(\hat{\xi}_1)\right\} \tag{3.120}$$

$$\left\{(\hat{\xi}_1,\hat{\xi}_2):\ 0 \leq \hat{\xi}_2 \leq 1\ ,\ 0 \leq \hat{\xi}_1 \leq \hat{\xi}_2\,\xi_{max}(\hat{\xi}_2)\right\} \tag{3.121}$$

with momentum conservation

$$2(p_1+p_2)(k_1+k_2) - 2k_1k_2 = s - Q^2 \tag{3.122}$$

implying that

$$\xi_{max}(\xi) = \min\left(1,\ \frac{1}{\xi}\frac{1-\xi}{1-\beta^2\eta_3\xi}\right) \leq 1\ . \tag{3.123}$$

For the later use of *Sector Decomposition* it is convenient to remap the angular variables as well by introducing a set of new variables $\hat{\eta}_{1,2}, \eta_3 \in [0,1]$ via

$$\hat{\eta}_{1,2} = \frac{1}{2}(1-\cos\theta_{1,2}) \tag{3.124}$$

$$\begin{aligned}
\eta_3 &= \frac{1}{2}(1-\cos\theta_3) \\
&= \frac{1}{2}(1-\cos\phi\sin\theta_1\sin\theta_2-\cos\theta_1\cos\theta_2) \\
&= \frac{1}{2}(1-\cos(\theta_1-\theta_2)+(1-\cos\phi)\sin\theta_1\sin\theta_2)\ .
\end{aligned} \tag{3.125}$$

An inspection of the potentially divergent propagators

$$\begin{aligned}
(p_1-k_i)^2 &= -s\beta^2\hat{\xi}_i\hat{\eta}_i \\
(p_2-k_i)^2 &= -s\beta^2\hat{\xi}_i(1-\hat{\eta}_i) \\
(k_1+k_2)^2 &= s\beta^4\hat{\xi}_1\hat{\xi}_2\eta_3 \\
(p_1-k_1-k_2)^2 &= -s\beta^2(\hat{\xi}_1\hat{\eta}_1+\hat{\xi}_2\hat{\eta}_2-\beta^2\hat{\xi}_1\hat{\xi}_2\eta_3) \\
(p_2-k_1-k_2)^2 &= -s\beta^2(\hat{\xi}_1(1-\hat{\eta}_1)+\hat{\xi}_2(1-\hat{\eta}_2)-\beta^2\hat{\xi}_1\hat{\xi}_2\eta_3) \\
(q_i+k_j)^2-m_t^2 &= 2\hat{\xi}_j\; q_i\cdot n_j \\
(q_i+k_1+k_2)^2-m_t^2 &= 2(\hat{\xi}_1\; q_i\cdot n_1+\hat{\xi}_2\; q_i\cdot n_2+\hat{\xi}_1\hat{\xi}_2\; n_1\cdot n_2)
\end{aligned} \tag{3.126}$$

reveals that η_3 may induce a singularity at $\hat{\eta}_1=\hat{\eta}_2$ and $\phi=0$. This parametrization in terms of three variables is, however, impractical as the actual divergence structure corresponds to a line singularity that can be described by $\hat{\eta}_1$ and $\hat{\eta}_2$ alone. This may be achieved with the help of the non-linear variable transformation

$$\zeta=\frac{1}{2}\frac{(1-\cos(\theta_1-\theta_2))(1+\cos\phi)}{1-\cos(\theta_1-\theta_2)+(1-\cos\phi)\sin\theta_1\sin\theta_2}\in[0,1] \tag{3.127}$$

such that the final expression for the phase space measure of the massless system is given as

$$\begin{aligned}
d\tilde{\Phi}_3(s;k_1,k_2) &= \left.\begin{aligned}&\frac{\pi^{2\epsilon}}{8(2\pi)^5\Gamma(1-2\epsilon)}s^{2-2\epsilon}\beta^{8-8\epsilon}\,(\zeta(1-\zeta))^{-\frac{1}{2}-\epsilon}\,d\zeta\\ &\times(\hat{\eta}_1(1-\hat{\eta}_1))^{-\epsilon}(\hat{\eta}_2(1-\hat{\eta}_2))^{-\epsilon}\frac{\eta_3^{1-2\epsilon}}{|\hat{\eta}_1-\hat{\eta}_2|^{1-2\epsilon}}\\ &\times\hat{\xi}_1^{1-2\epsilon}\hat{\xi}_2^{1-2\epsilon}\,d\hat{\eta}_1\,d\hat{\eta}_2\,d\hat{\xi}_1\,d\hat{\xi}_2\end{aligned}\right\}\equiv\mu_\zeta\,d\zeta\\
&\qquad\equiv\mu_{\eta\xi}\,d\hat{\eta}_1\,d\hat{\eta}_2\,d\hat{\xi}_1\,d\hat{\xi}_2\,.
\end{aligned} \tag{3.128}$$

Note that despite the fact that the massless vectors are chosen to lie in the four physical dimensions the measure has to still be considered in d dimensions to regulate the singular behavior of the matrix elements.

The massive system is best described in the center-of-mass frame of Q with momenta $q'_{1,2}$ related to the original heavy-quark momenta via

$$\begin{aligned}
q_i^0 &= \frac{Q^0q_i'^0+\overrightarrow{Q}\cdot\overrightarrow{q_i'}}{\sqrt{Q^2}}\\
\overrightarrow{q_i} &= \overrightarrow{q_i'}+\left(q_i'^0+\frac{\overrightarrow{Q}\cdot\overrightarrow{q_i'}}{Q^0+\sqrt{Q^2}}\right)\frac{\overrightarrow{Q}}{\sqrt{Q^2}}\qquad i=1,2\,.
\end{aligned} \tag{3.129}$$

As the three spatial dimensions are already fixed by the massless vectors, it is no longer possible to remove the ϵ-dimensional components of the heavy-quark system by rotational invariance. Since the momenta in the center-of-mass frame are back-to-back, it is, however, sufficient to add one additional spatial component and discard the remaining $(d-5)$-dimensional

contributions such that

$$\begin{aligned} {q_1'}^0 &= {q_2'}^0 = \tfrac{1}{2}\sqrt{Q^2} \\ \overrightarrow{q_1'} &= -\overrightarrow{q_2'} = \tfrac{1}{2}\sqrt{Q^2+\beta^2-1} \\ &\times \left(\sin\rho_Q \sin\phi_Q \sin\theta_Q\, \vec{n}^{(d-4)}, \cos\rho_Q \sin\phi_Q \sin\theta_Q, \cos\phi_Q \sin\theta_Q, \cos\theta_Q\right) . \end{aligned} \tag{3.130}$$

The angles, though in principle lying in the range $[0,\pi]$, can be chosen as $\phi_Q \in [0,2\pi]$ and $\rho_Q \in [0,\pi/2]$ provided that one exploits the independence of the final results from the sign of the ϵ-dimensional component. The corresponding phase space measure is then given by

$$\begin{aligned} d\Phi_2(Q;q_1,q_2) &= \frac{(4\pi)^\epsilon \Gamma(1-\epsilon)}{8(2\pi)^2\Gamma(1-2\epsilon)} \left(Q^2\right)^{-\epsilon} \left(\sqrt{1-\frac{4m^2}{Q^2}}\right)^{1-2\epsilon} (1-\cos^2\theta_Q)^{-\epsilon} \left(\sin^2\phi_Q\right)^{-\epsilon} \\ &\times \frac{4^{1+\epsilon}\Gamma(-2\epsilon)}{\Gamma^2(-\epsilon)(1-\cos^2\rho_Q)^{1+\epsilon}}\, d\cos\theta_Q\, d\phi_Q\, d\cos\rho_Q \\ &= \mu_2\, d\cos\theta_Q\, d\phi_Q\, d\cos\rho_Q \end{aligned} \tag{3.131}$$

with the contributions from the additional spatial dimension suppressed by a power of ϵ as becomes clear when applying the identity

$$\frac{4^{1+\epsilon}\Gamma(-2\epsilon)}{\Gamma^2(-\epsilon)(1-\cos^2\rho_Q)^{1+\epsilon}} = \delta(1-\cos\rho_Q) + \frac{4^{1+\epsilon}\Gamma(-2\epsilon)}{\Gamma^2(-\epsilon)} \left[\frac{1}{(1-\cos^2\rho_Q)^{1+\epsilon}}\right]_+ \tag{3.132}$$

with the plus distribution defined via

$$\int_0^1 d\cos\rho_Q \left[\frac{1}{(1-\cos^2\rho_Q)^{1+\epsilon}}\right]_+ f(\cos\rho_Q) = \int_0^1 d\cos\rho_Q \frac{1}{(1-\cos^2\rho_Q)^{1+\epsilon}} \Big(f(\cos\rho_Q) - f(1)\Big) . \tag{3.133}$$

Consequently, the phase space can be divided into a four-dimensional part

$$d\Phi_2^{(d|\epsilon)} = \frac{(4\pi)^\epsilon \Gamma(1-\epsilon)}{8(2\pi)^2\Gamma(1-2\epsilon)} \left(Q^2\right)^{-\epsilon} \left(\sqrt{1-\frac{4m^2}{Q^2}}\right)^{1-2\epsilon} (1-\cos^2\theta_Q)^{-\epsilon} \left(\sin^2\phi_Q\right)^{-\epsilon} d\cos\theta_Q\, d\phi_Q \tag{3.134}$$

and an ϵ-dimensional part

$$\begin{aligned} d\Phi_2^{(\epsilon)} &= d\Phi_2 - d\Phi_2^{(d|\epsilon)} \\ &= \frac{(16\pi)^\epsilon}{4(2\pi)^2\Gamma(-\epsilon)} \left(Q^2\right)^{-\epsilon} \left(\sqrt{1-\frac{4m^2}{Q^2}}\right)^{1-2\epsilon} (1-\cos^2\theta_Q)^{-\epsilon} \left(\sin^2\phi_Q\right)^{-\epsilon} \\ &\times \left[\frac{1}{(1-\cos^2\rho_Q)^{1+\epsilon}}\right]_+ d\cos\theta_Q\, d\phi_Q\, d\cos\rho_Q \end{aligned} \tag{3.135}$$

that only contributes when the integrand contains poles and, hence, is expected to be small in practice. The parametrization of the singular propagators in terms of these phase space

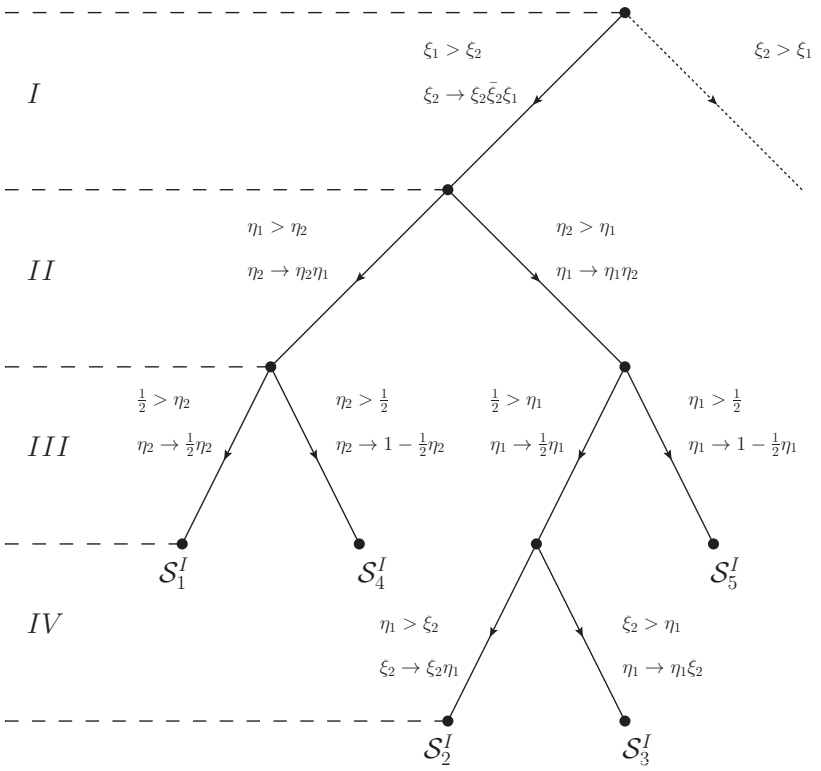

Figure 3.7: *Schematic representation of the Sector Decomposition employed in the triple-collinear phase space region taken from Ref. [233]. Apart from the definition of the individual sectors also the corresponding variable transformation with respect to $\hat{\eta}_{1,2}$, $\hat{\xi}_{1,2}$ are given where $\hat{\xi}_2 = \xi_{max}(\hat{\xi}_1)$. Note that the second branch indicated by the dashed line is symmetric to the first one and has thus been omitted.*

variables reveals the true nature of the overlapping IR-singularities still present in the problem despite the partitioning into collinear sectors. In order to be able to extract the explicit pole structure of the phase space integrals, these singularities have to be factorized, which is conveniently done with the help of *Sector Decomposition* as we will see now.

Factorization of divergences and construction of integrable cross sections

Sector Decomposition is a technique not specifically designed for the treatment of singular phase space integrals but it allows for the disentanglement of overlapping divergences in arbitrary multi-dimensional integrals. The general strategy is quite simple and may be best illustrated through an explicit example. Suppose we have a two-dimensional integral of the form

$$I = \int_0^1 dx \int_0^1 dy\, x^{-1+b_1\epsilon}\, y^{-1+b_2\epsilon}\, \frac{1}{x+(1-x)y}\,, \tag{3.136}$$

which is finite except for the region where x and y vanish simultaneously. To isolate the singular behavior we decompose the integration range into two sectors and subsequently remap

the new bounds to the unit square again

$$\begin{aligned} I &= \int_0^1 dx \int_0^x dy\, x^{-1+b_1\epsilon}\, y^{-1+b_2\epsilon}\, \frac{1}{x+(1-x)y} + \int_0^1 dy \int_0^y dx\, x^{-1+b_1\epsilon}\, y^{-1+b_2\epsilon}\, \frac{1}{x+(1-x)y} \\ &= \int_0^1 dx \int_0^1 dy\, x^{-2+(b_1+b_2)\epsilon}\, y^{-1+b_2\epsilon}\, \frac{1}{1+(1-x)y} + \int_0^1 dx \int_0^1 dy\, x^{-1+b_1\epsilon}\, y^{-2+(b_1+b_2)\epsilon}\, \frac{1}{1+(1-y)x}\,. \end{aligned} \tag{3.137}$$

The polynomial denominator is now finite for $x, y \to 0$ and the singular behavior is completely encoded in the monomials of the integration variables, which can be extracted by using the identity

$$\frac{1}{\lambda^{1-b\epsilon}} = \frac{1}{b}\frac{\delta(\lambda)}{\epsilon} + \sum_{n=0}^{\infty} \frac{(b\epsilon)^n}{n!} \left[\frac{\ln^n(\lambda)}{\lambda}\right]_+ \tag{3.138}$$

with the plus distribution defined via

$$\int_0^1 d\lambda \left[\frac{\ln^n(\lambda)}{\lambda}\right]_+ f(\lambda) = \int_0^1 \frac{\ln^n(\lambda)}{\lambda}(f(\lambda) - f(0))\,. \tag{3.139}$$

As this concept can be easily extended to higher dimensional integrals through an iterative application of the phase space partitioning and remapping, it is perfectly suited for the evaluation of the singular $\hat{\eta}_{1,2}$ and $\hat{\xi}_{1,2}$ integrations of the massless final-state system. The corresponding decomposition trees for the triple- and double-collinear sectors are shown in Fig. 3.7 and Fig. 3.8 respectively resulting in a final total of seven phase space sectors. The different tree levels have a direct physical interpretation since they each factorize a certain type of IR divergence:

(I) Factorization of soft divergences

(II) Factorization of collinear divergences

(III) Factorization of collinear divergences for the case $k_1 || k_2$

(IV) Factorization of soft-collinear divergences

Note that due to the less complex singularity structure in the double-collinear sector the levels (II) and (III) can be safely omitted for these contributions. Moreover, the variable transformation in Eq. (3.127) is, in principle, no longer needed as there are no singularities induced by η_3. In practice, however, it is more convenient to utilize the same parametrization in all sectors since it simplifies the actual implementation into an efficient algorithm.

As the factorization procedure establishes a sector-dependent relation between the variables $\eta_{1,2}$, $\xi_{1,2}$ and the original kinematic variables $\hat{\eta}_{1,2}$, $\hat{\xi}_{1,2}$, the phase space measure becomes sector-specific as well such that the total contribution of double-real radiation to the partonic cross section is given as

$$\hat{\sigma}_{ij}^{RR} = \frac{\rho}{8} \left(\frac{e^{\gamma_E}\mu_R^2}{4\pi}\right)^{3\epsilon} \sum_{\mathcal{S}} \sigma_{ij}^{RR,(\mathcal{S})} \tag{3.140}$$

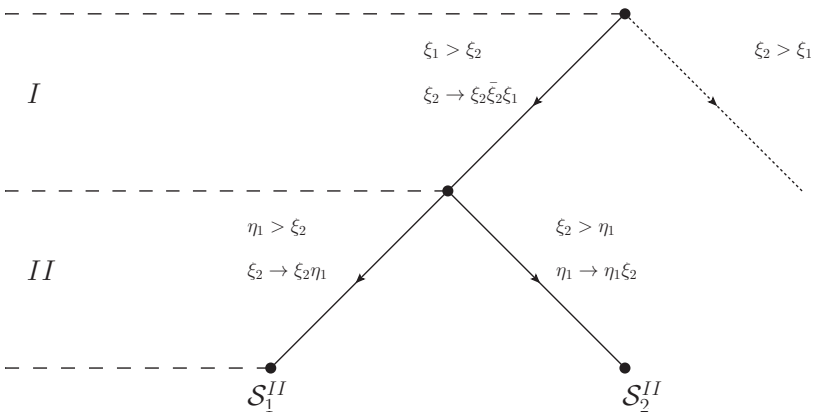

Figure 3.8: *Schematic representation of the Sector Decomposition employed in the double-collinear phase space region taken from Ref. [233] with the same notation as in Fig. 3.8.*

where

$$\sigma_{ij}^{RR,(\mathcal{S})} = \int d\zeta\, d\eta_1\, d\eta_2\, d\xi_1\, d\xi_2\, d\cos\theta_Q\, d\phi_Q\, d\cos\rho_Q\, \mu_2\, \mu_\zeta\, \Sigma_{ij}^{(\mathcal{S})} \,. \tag{3.141}$$

The entire sector dependence and process-specific information are contained in the integrand

$$\Sigma_{ij}^{(\mathcal{S})} = \frac{1}{s_i s_j c_i c_j}\, \mu_{\mathcal{S}}^{\text{reg}}\, \theta_{\mathcal{S}}\, F_J \frac{1}{\eta_1^{1-b_1\epsilon}} \frac{1}{\eta_2^{1-b_2\epsilon}} \frac{1}{\xi_1^{1-b_3\epsilon}} \frac{1}{\xi_2^{1-b_4\epsilon}}\, \mathfrak{M}_{ij}^{(\mathcal{S})} \tag{3.142}$$

where s_k and c_k are the spin and color-averaging factors introduced in Eq. (2.38), $\mu_{\mathcal{S}}^{\text{reg}}$ is the finite part of the phase space measure $\mu_{\eta\xi}$ (see Tab. 3.3) and $\theta_{\mathcal{S}}$ is a selector function that defines the corresponding sector. Note that the sectors may be overlapping, i. e. several sectors may contribute to the same momentum configuration. The jet function F_J equals unity for an inclusive quantity such as $\sigma_{t\bar{t}}^{\text{tot}}$ but will be used later to construct more differential observables by applying additional cuts on the four-particle phase space (see chapter 4).

The crucial point why the STRIPPER approach is so successful is the last term of the integrand that parametrizes the singular behavior. Indeed, it is QCD itself that fixes the power of the sector variables in the denominator to $1 - b_i\epsilon$ as it contains at most logarithmic singularities of IR nature, which can be explicitly checked by employing the factorization properties of the soft and collinear limits. In consequence, the function

$$\mathfrak{M}_{ij}^{(\mathcal{S})} = \eta_1^{1+a_1} \eta_2^{1+a_2} \xi_1^{1+a_3} \xi_2^{1+a_4}\, \langle \mathcal{M}_{ijkl}^{(0)} | \mathcal{M}_{ijkl}^{(0)} \rangle \tag{3.143}$$

is regular by IR power counting in all singular regions of phase space characterized by any of the sector variables vanishing. The corresponding powers a_i needed to regulate the squared matrix element are also sector-dependent and can be found in Tab. 3.3. Having factorized the divergent behavior, the construction of suitable subtraction terms is rather simple. First of all, the identity in Eq. (3.138) to derive a Laurent expansion of the integrand $\Sigma_{ij}^{(\mathcal{S})}$, where the contributions proportional to the delta distributions may by interpreted as integrated subtraction terms while the plus distributions generate the actual subtractions for the squared matrix element. Due to the presence of overlapping singularities the integrated subtraction terms

sector	regulator	$\mu_{\mathcal{S}}^{\text{reg}}$
$\mathcal{S}_1^I$	$\eta_1^{1-2\epsilon}\eta_2^{-\epsilon}\xi_1^{3-4\epsilon}\xi_2^{1-2\epsilon}$	$((1-\eta_1)(2-\eta_1\eta_2))^{-\epsilon}\,\bar{\xi}_2^{\,2-2\epsilon}\left(\frac{\eta_{31}(\eta_1,\eta_2)}{2-\eta_2}\right)^{1-2\epsilon}$
$\mathcal{S}_2^I$	$\eta_1^{2-3\epsilon}\eta_2^{1-2\epsilon}\xi_1^{3-4\epsilon}\xi_2^{1-2\epsilon}$	$((1-\eta_2)(2-\eta_1\eta_2))^{-\epsilon}\,\bar{\xi}_2^{\,2-2\epsilon}\left(\frac{\eta_{31}(\eta_2,\eta_1)}{2-\eta_1}\right)^{1-2\epsilon}$
$\mathcal{S}_3^I$	$\eta_1^{-\epsilon}\eta_2^{1-2\epsilon}\xi_1^{3-4\epsilon}\xi_2^{2-3\epsilon}$	$((1-\eta_2)(2-\eta_1\eta_2\xi_2))^{-\epsilon}\,\bar{\xi}_2^{\,2-2\epsilon}\left(\frac{\eta_{31}(\eta_2,\eta_1\xi_2)}{2-\eta_1\xi_2}\right)^{1-2\epsilon}$
$\mathcal{S}_4^I$	$\eta_1^{1-2\epsilon}\eta_2^{1-2\epsilon}\xi_1^{3-4\epsilon}\xi_2^{1-2\epsilon}$	$((1-\eta_1)(2-\eta_2)(2-\eta_1(2-\eta_2)))^{-\epsilon}\,\bar{\xi}_2^{\,2-2\epsilon}\eta_{32}^{1-2\epsilon}(\eta_1,\eta_2)$
$\mathcal{S}_5^I$	$\eta_1^{1-2\epsilon}\eta_2^{1-2\epsilon}\xi_1^{3-4\epsilon}\xi_2^{1-2\epsilon}$	$((1-\eta_2)(2-\eta_1)(2-\eta_2(2-\eta_1)))^{-\epsilon}\,\bar{\xi}_2^{\,2-2\epsilon}\eta_{32}^{1-2\epsilon}(\eta_2,\eta_1)$
$\mathcal{S}_1^{II}$	$\eta_1^{2-3\epsilon}\eta_2^{-\epsilon}\xi_1^{3-4\epsilon}\xi_2^{1-2\epsilon}$	$((1-\eta_1)(1-\eta_2))^{-\epsilon}\,\bar{\xi}_2^{\,2-2\epsilon}\left(\frac{\eta_3}{\lvert 1-\eta_1-\eta_2\rvert}\right)^{1-2\epsilon}$
$\mathcal{S}_2^{II}$	$\eta_1^{-\epsilon}\eta_2^{-\epsilon}\xi_1^{3-4\epsilon}\xi_2^{2-3\epsilon}$	$((1-\eta_2)(1-\eta_1\xi_2))^{-\epsilon}\,\bar{\xi}_2^{\,2-2\epsilon}\left(\frac{\eta_3}{\lvert 1-\eta_2-\eta_1\xi_2\rvert}\right)^{1-2\epsilon}$

Table 3.3: *The integration measure $\mu_{\eta\xi}$ of the massless system expressed in terms of the sector variables $\eta_{1,2}, \xi_{1,2}$ adopted from Ref. [233]. The respective components are split into a product of regulators and a regular function, $\mu_{\mathcal{S}}^{reg}$, which can be expanded in ϵ.*

usually themselves require appropriate subtractions to be integrable, which are, however, produced automatically in this approach. Hence, the final integrand contains, in fact, 16 different terms corresponding to all possible combinations of setting the variables $\{\eta_1, \eta_2, \xi_1, \xi_2\}$ to zero. The next step is the determination of $\mathfrak{M}_{ij}^{(\mathcal{S})}$ in these limits, which due to the chosen parametrization in terms of energies and angles is particularly simple since the vanishing of the sector variables corresponds to the well-known limits of QCD amplitudes. Consequently, all subtraction terms are maximally local and apart from the underlying hard scattering amplitudes completely process-independent. Note, however, that in contrast to NLO where we only have the single soft and collinear limits defined through the operators in Eq. (2.94) and Eq. (2.98) respectively, one now has to consider two additional cases, namely the triple-collinear and the double-soft limit [547]. For the latter one has to distinguish between two scenarios, the emission of a soft $q\bar{q}$-pair or of two soft gluons. While the first case can be expressed entirely in terms of LO eikonal current operators

$$\begin{aligned}&\langle \mathcal{M}_{n+2}^{(0)}(p_1,\ldots,p_n,q_1,q_2)\,|\mathcal{M}_{n+2}^{(0)}(p_1,\ldots,p_i,q_1,q_2)\rangle \xrightarrow{q_{1,2}\to 0}\\ &\quad \left(4\pi\,{\mu_R}^{2\epsilon}\,\alpha_s\right)^2 \langle \mathcal{M}_n^{(0)}(p_1,\ldots,p_n)\,|\mathbf{J}_\mu^{(0)\,\dagger}(q_1+q_2)\cdot\mathbf{J}_\nu^{(0)}(q_1+q_2)\,\Pi^{\mu\nu}(q_1,q_2)|\mathcal{M}_n^{(0)}(p_1,\ldots,p_n)\rangle\end{aligned} \tag{3.144}$$

with

$$\Pi^{\mu\nu}(q_1,q_2) = \frac{T_F}{(q_1\cdot q_2)^2}\,\left(-g^{\mu\nu}\,q_1\cdot q_2 + q_1^\mu q_2^\nu + q_2^\mu q_1^\nu\right)\,, \tag{3.145}$$

the second case requires the introduction of the two-gluon soft current

$$\begin{aligned}\mathbf{J}_{ab}^{\mu\nu}(q_1,q_2) \;=\; &\frac{1}{2}\{\mathbf{J}_a^\mu(q_1),\mathbf{J}_b^\nu(q_2)\} + i f_{abc}\sum_{i=1}^{n}\mathbf{T}_i^c\left\{\frac{p_i^\mu q_1^\nu - p_i^\nu q_2^\mu}{(q_1\cdot q_2)\,[p_i\cdot(q_1+q_2)]}\right.\\ &\left.-\frac{p_i\cdot(q_1-q_2)}{2\,[p_i\cdot(q_1+q_2)]}\left[\frac{p_i^\mu p_i^\nu}{(p_i\cdot q_1)(p_i\cdot q_2)}+\frac{g^{\mu\nu}}{q_1\cdot q_2}\right]\right\}\end{aligned} \tag{3.146}$$

such that

$$\begin{aligned}&\langle \mathcal{M}_{n+2}^{(0)}(p_1,\ldots,p_n,q_1,q_2)\,|\mathcal{M}_{n+2}^{(0)}(p_1,\ldots,p_i,q_1,q_2)\rangle \xrightarrow{q_{1,2}\to 0}\\ &\qquad \left(4\pi\,{\mu_R}^{2\epsilon}\,\alpha_s\right)^2 \langle \mathcal{M}_n^{(0)}(p_1,\ldots,p_n)\,|\left[\mathbf{J}_{\mu\nu}^{ab}(q_1,q_2)\right]^\dagger\,\mathbf{J}_{ab}^{\mu\nu}(q_1,q_2)|\mathcal{M}_n^{(0)}(p_1,\ldots,p_n)\rangle\,.\end{aligned} \tag{3.147}$$

This expression contains contributions from up to four charge operators $\mathbf{T}_i^a$, which may, however, again be reduced to a smaller subset of independent correlator structures by employing color conservation. In order to extract the behavior of the triple-collinear limit, one can use the Sudakov parametrization

$$p_i^\mu = x_i p^\mu + k_{\perp i}^\mu - \frac{k_{\perp i}^2}{x_i}\frac{n^\mu}{2p\cdot n}\,,\qquad i=1,2,3\quad\text{with}\quad p^2=n^2=p\cdot k_{\perp i}=n\cdot k_{\perp i}=0 \tag{3.148}$$

such that for $k_{\perp i}^\mu \to 0$ the squared matrix element is given as

$$\begin{aligned}&\langle \mathcal{M}_{n+2}^{(0)}(p_1,p_2,p_3,\ldots)\,|\mathcal{M}_{n+2}^{(0)}(p_1,p_2,p_3,\ldots)\rangle \xrightarrow{k_{\perp i}^\mu\to 0}\\ &\qquad \left(4\pi\,{\mu_R}^{2\epsilon}\,\alpha_s\right)^2 \langle \mathcal{M}_n^{(0)}(x\,p,\ldots)\,|\frac{4\hat{P}_{a_1a_2a_3}^{ss'}}{s_{123}^2}|\mathcal{M}_n^{(0)}(x\,p,\ldots)\rangle\end{aligned} \tag{3.149}$$

where $s_{123} = (p_1 + p_2 + p_3)^2$ and $x = x_1 + x_2 + x_3$. The corresponding splitting functions depending on the parton indices $a_i \in \{q, \bar{q}, g\}$ contain up to two spin correlators and can be found in Refs. [547,632]. As usual, the soft-collinear behavior can be obtained by taking the soft limit of the collinear splitting functions and vice versa, i.e. the limits commute. Still, for the determination of the collinear behavior of the double-soft limit it is convenient to use a specific ordering to avoid unnecessary complications [233]. This may be achieved by first taking the collinear limit of the two relevant partons ($q\bar{q}$ or gg) and subsequently performing the soft limit of the combined gluonic state that is the origin of the splitting leading to the following factorization formula

$$\begin{aligned}\langle \mathcal{M}^{(0)}_{n+2}(p_1,\ldots,p_n,q_1,q_2)\,|\mathcal{M}^{(0)}_{n+2}(p_1,\ldots,p_i,q_1,q_2)\rangle \xrightarrow{q_1||q_2,\,q_{1,2}\to 0} \\ \left(4\pi\,{\mu_R}^{2\epsilon}\,\alpha_s\right)^2 \langle \mathcal{M}^{(0)}_{n}(p_1,\ldots,p_n)\,|\frac{\mathbf{J}^{(0)\,\dagger}_{\mu,\,a}\,2\hat{P}^{\mu\nu\,(0)}_{a_1a_2}\,\mathbf{J}^{(0)}_{\nu,\,a}}{(q_1+q_2)^2}|\mathcal{M}^{(0)}_{n}(p_1,\ldots,p_n)\rangle\ .\end{aligned} \tag{3.150}$$

Implementation

With these additional QCD limits we now have all ingredients at hand to calculate the NNLO double-real corrections to top-quark pair production. For an inclusive observable such as the total cross section it is convenient to take into account the inherent symmetries of the corresponding matrix elements, namely charge conjugation invariance and rotational invariance, to further reduce the computational effort. The main idea is to find a selector function that fulfills all the requirements mentioned above and at the same time restricts the necessary integration regime to a fraction of the full phase space. In our implementation we have used the following decomposition parametrized in terms of the auxiliary vectors $n^\mu_{1,2}$ defined in Eq. (3.119):

1. $n_1^z > 0 \ \wedge\ n_2^z > -\alpha\, n_2^0$ (triple-collinear sector)
2. $n_1^z > 0 \ \wedge\ n_2^z < -\alpha\, n_2^0$ (double-collinear sector) .

Moreover, we ignore the second branch $\xi_2 > \xi_1$ in Fig. 3.7 and Fig. 3.8. Due to the underlying symmetries the missing contributions can be restored afterwards by multiplying the result by a suitable global correction factor. For some channels it is, however, not possible to recover the full result through symmetry operations, for instance the qg-channel. In this case we still employ the same phase space slicing and, for a fixed flavor assignment of initial-state and (massless) final-state partons, consider all possible parton permutations which compensates for the phase space restrictions in the individual integrals induced by the above selector function.

The actual numerical integration is performed with the help of MC techniques, which are particularly suited for the evaluation of higher-dimensional integrals. The main idea is to use the mean-value theorem to estimate an integral

$$F = \int_R d\vec{x}\, f(\vec{x}) \tag{3.151}$$

over the region R by evaluating the integrand at a large number of randomly selected points $\vec{x}_i$ such that

$$F \approx \frac{A}{N} \sum_i^N f(\vec{x}_i)\, \theta(\vec{x}_i) \tag{3.152}$$

where A is the rectangular (higher-dimensional) area enclosing R and $\theta(\vec{x})$ is a selector function equal to unity if $\vec{x} \in R$ and zero otherwise. The advantage of this approach is that the integration error, i. e. the standard deviation from this mean value, decreases as $1/\sqrt{N}$ irrespective of the number of dimensions, which is superior to other numerical methods for sufficiently high dimension. In our specific case we have $\vec{x} = (\eta_1, \eta_2, \xi_1, \xi_2, \zeta, \cos\theta_Q, \phi_Q, \cos\rho_Q)$ with the corresponding integration ranges all remapped to the interval $[0, 1]$ such that $A = \theta(\vec{x}) = 1$. In a more recent implementation of Stripper employed in the calculation of differential NNLO $t\bar{t}$ predictions (see chapter 4) we also included the convolution with the PDFs in the integration routine increasing the number of integration variables by two. However, since in the original calculation we were aiming at the determination of a fitting function for the partonic cross sections, we have kept the dependence on the partonic fluxes separate. Of course, both implementations ultimately yield the same predictions for $\sigma_{t\bar{t}}^{\mathbf{tot}}$.

In order to further increase the efficiency of the MC algorithm we use so-called adaptive importance sampling. Importance sampling means that the random values for $\vec{x}$ are generated according to a probability distribution that mimics the functional behavior of the integrand as close as possible such that the deviation from the mean value is significantly reduced. The integral in Eq. (3.151) is then given by ($A = \theta(\vec{x}) = 1$)

$$F \approx \frac{1}{N} \sum_i^N w(\vec{x}_i)\, f(\vec{x}_i) \tag{3.153}$$

where the weight $w(\vec{x})$ is the inverse of the chosen probability density. In practice, it is difficult to predict this quantity in advance owing to the increased complexity of the integrand in actual applications. This led to the development of adaptive methods that use the integrand itself to construct an appropriate distribution for the random number generation. In our implementation we used Ranlux [633, 634] as a classical random number generator and Parni [635] for the optimization via importance sampling. Note that the run time per MC point $\vec{x}_i$ will increase when using importance sampling but due to the significant reduction of total points needed to obtain a certain precision there still is an overall gain in efficiency.

Apart from the MC error that can be made arbitrarily small by using a sufficiently large number of integration points (the actual value depends on the respective parton channels) there exists another source of numerical uncertainty, namely the dependence on the cutoff parameter Δ_{cut}. This parameter is needed to avoid numerical instabilities occurring in the subtracted integrands in the singular regions of phase space induced by the well-known inverse square root behavior of collinear limits. Even though these inverse square roots are integrable, their numerical evaluation involves the cancellation of a large number of digits and, thus, can only to a certain extent be cured by using a higher numerical precision. In fact, we perform the whole calculation in quadruple precision (see appendix E) to minimize the occurrence of numerical instabilities. Since the matrix elements in the potentially dangerous region of phase

space grow as $1/(\eta_1\eta_2\xi_1\xi_2)$ we choose a cutoff of the form

$$\Delta_{cut} < \eta_1\,\eta_2\,\xi_1\,\xi_2\ , \tag{3.154}$$

which leads to an estimated size of the missing phase space of

$$\delta\Phi_4(\Delta_{cut}) = \Delta_{cut}\sum_{n=0}^{3}\frac{1}{n!}\ln^n\left(\frac{1}{\Delta_{cut}}\right)\ . \tag{3.155}$$

It does, however, not serve as a reliable error estimate for the total cross section due to the presence of square root and logarithmic enhancements and, therefore, in practice the cutoff dependence is usually assessed from an explicit comparison of evaluations with two different values for Δ_{cut}. Indeed, it turns out that for our particular problem a value of $\Delta_{cut} = 10^{-8}$ leads to an uncertainty that is smaller than the MC integration error but other processes might require a different value.

The numerical impact of the double-real corrections on the partonic and hadronic cross section results depends crucially on the chosen normalization and, hence, does by itself not represent a meaningful physical quantity. In our calculation, for instance, we choose to multiply all cross section contributions by $\beta^{10\epsilon}$ to remove the dominant threshold logarithms in β, which leads to a substantial reduction of $\hat{\sigma}_{ij}^{RR}$ while other parts are strongly enhanced. This allows for an improved error control as the absolute impact of the cross section components with less numerical precision can be effectively suppressed. While this is important in practice, it also shows that considering the individual contributions from different final-state multiplicities to the predictions for $\sigma_{t\bar{t}}^{\mathbf{tot}}$ (or, in fact, any physical observable) does not provide any deeper physical insights. We, thus, refrain from showing explicit partial results here and refer the reader to the combined cross section results presented in section 3.5.

3.3 Real-Virtual contributions

The real-virtual corrections consist of one-loop diagrams with an additional massless parton in the final state compared to the Born configuration. Thus, they can be obtained from the NLO diagrams by either dressing the real-emission graphs with a quantum loop or, alternatively, by equipping the loop diagrams with another external gluon line/$q\bar{q}$ splitting. As a consequence, the real-virtual contributions involve the same partonic production modes as the NLO corrections, namely the quark annihilation channel, the gluon fusion channel and the qg-channel. However, in contrast to the NLO case, loop and phase space divergences can no longer be treated separately requiring the combination of various computational methods for the evaluation of real and virtual components to be able to derive meaningful results.

The first step is the determination of the loop-induced corrections, which in CDR may be written as

$$\mathcal{A}_{ij}(p_1,\ldots,p_5;\epsilon) = 2\,\mathrm{Re}\,\langle\mathcal{M}_{ijk}^{(0)}|\mathcal{M}_{ijk}^{(1)}\rangle\ . \tag{3.156}$$

They consist of the bare one-loop amplitudes contracted with the $n+1$ Born matrix elements and a renormalization part proportional to the NLO real-emission integrand $\langle\mathcal{M}_{ijk}^{(0)}|\mathcal{M}_{ijk}^{(0)}\rangle$.

While the combination of these pieces is UV-finite, it still contains IR poles such that $\mathcal{A}_{ij}$ will be usually given in terms of a Laurent expansion in ϵ. However, unlike the virtual corrections at NLO the coefficients of this expansion may become singular in certain corners of phase space, i. e. they implicitly contain additional poles of soft and collinear origin such that the overall degree of divergence of the real-virtual contributions is $\mathcal{O}(1/\epsilon^4)$. A common strategy to determine these coefficients is to decompose $\mathcal{A}_{ij}$ into independent building blocks, for example tensor structures or spin and color structures, such that the generic loop integrals are projected onto a smaller set of scalar integrals. This would, in principle, allow for an entirely analytical evaluation of the virtual part by computing these master integrals as an expansion in ϵ and, afterwards, summing up the individual contributions. Such an approach is, however, impractical in actual calculations as the resulting expressions can usually not be efficiently translated into a numerical algorithm needed for the subsequent phase space integration.

Since this integration is based on MC methods, it requires the evaluation of $\mathcal{A}_{ij}$ at a large number of distinct phase space points rendering its proper implementation a highly non-trivial task. In general, the most effective strategy is to adhere to a block-wise treatment computing each decomposition structure individually such that the final summation can be performed numerically. This has the further advantage that potentially dangerous terms that may lead to instabilities in exceptional regions of phase space are under better numerical control because they can be easily located and properly adjusted. Note that this concerns, in fact, only the finite part of $\mathcal{A}_{ij}$ as the entire pole structure can be predicted from IR renormalization

$$\mathcal{A}_{ij} = 2\,\mathrm{Re}\left(\langle \mathcal{M}^{(0)}_{ijk} | \mathcal{F}^{(1)}_{ijk} \rangle + \langle \mathcal{M}^{(0)}_{ijk} | Z^{t\bar{t}j,\,(1)}_{\mathcal{F}} | \mathcal{M}^{(0)}_{ijk} \rangle\right) \equiv \mathcal{A}^{\mathrm{Fin}}_{ij} + \mathcal{A}^{\mathrm{Div}}_{ij} \tag{3.157}$$

where $Z^{t\bar{t}j,\,(1)}_{\mathcal{F}}$ is the $\mathcal{O}(\alpha_s)$ coefficient of the IR renormalization operator introduced in section 3.1 that, however, now involves five independent color correlators $\mathbf{T}_i \cdot \mathbf{T}_j$ due to the additional parton in the final state. Still, the calculation of $\mathcal{A}^{\mathrm{Div}}_{ij}$ does not cause any numerical complications as it effectively corresponds to a modified NLO process that can be handled with the well-established subtraction methods presented in section 2.3.2. For $\mathcal{A}^{\mathrm{Fin}}_{ij}$, on the other hand, the situation is different and we had to use a highly-efficient code[21] originally developed and employed in the analysis of the NLO corrections to $p\bar{p} \to t\bar{t} + j$ [115, 116] to cope with more extensive computational effort. Note, however, that we had to modify this code in order to be able to run it in quad-double precision (see appendix E), which guaranteed a higher numerical stability and allowed us to utilize an NLO version of Stripper to perform the actual phase space integration. As a result, the total contribution from the real-virtual corrections to $\sigma^{\mathrm{tot}}_{t\bar{t}}$ is given by

$$\hat{\sigma}^{RV}_{ij}(\beta) = \int dP^{(ij)}_3\, F_J\, \theta_{\mathcal{S}} \left[\mathcal{A}_{ij} - \mathcal{A}^{\mathrm{Sub}}_{ij}\right] + \int dP^{(ij)}_2\, F_J\, \mathcal{A}^{\mathrm{Int}}_{ij}\ . \tag{3.158}$$

As all potentially divergent propagators (the subset of propagators in Eq. (3.126) involving only k_1) are already completely factorized, we may this time refrain from applying *Sector*

[21] We thank S. Dittmaier for kindly providing us with his code for the evaluation of the corresponding one-loop virtual corrections.

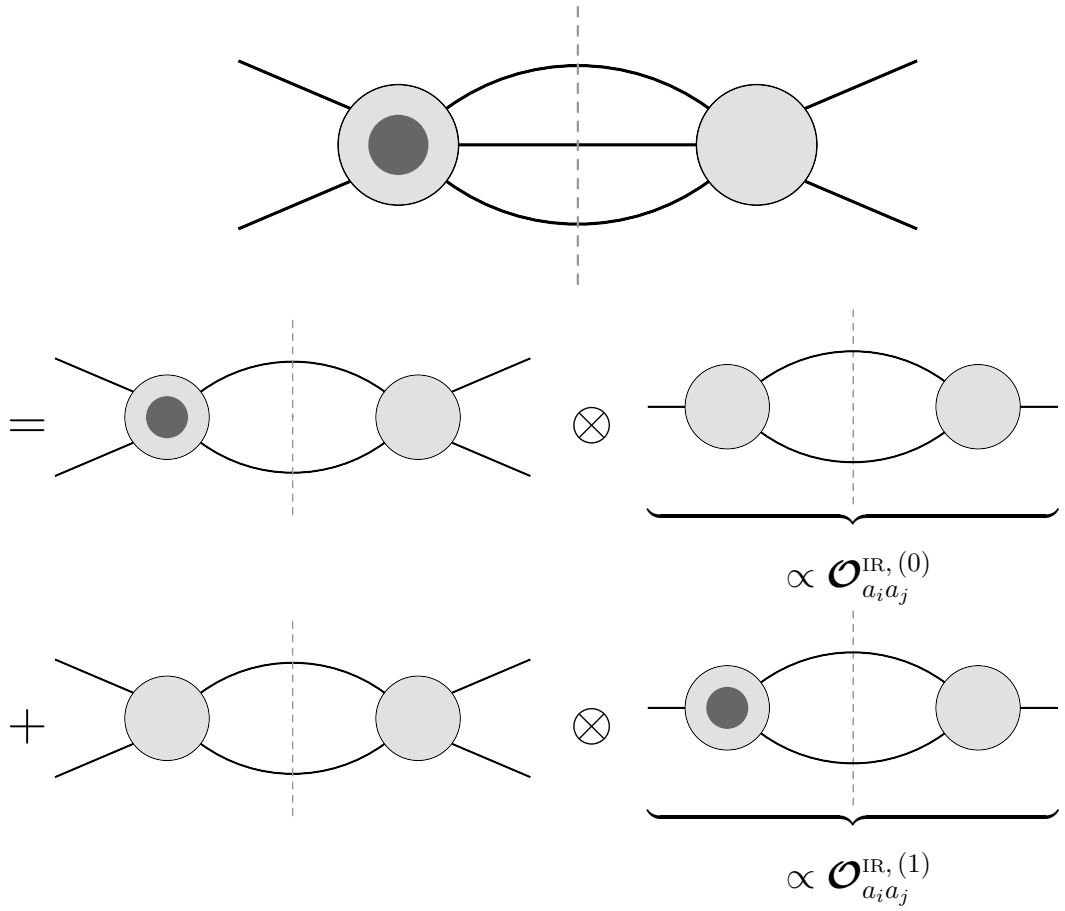

Figure 3.9: *Factorization of the real-virtual corrections in the IR limit represented through cut diagrams. The blobs correspond to generic Born processes while the dotted blobs indicate the presence of a quantum loop. The symbol $\otimes$ denotes correlation effects in spin and color space.*

Decomposition, which simplifies the actual calculation considerably. In consequence, there only exists a single collinear sector selected by the function $\theta_{\mathcal{S}}$ defined as

$$\theta_{\mathcal{S}} = \begin{cases} n^z \geq 0 & 1 \\ n^z < 0 & 0 \end{cases} \tag{3.159}$$

where similar to the double-real emissions n^μ denotes an auxiliary vector specifying the (four-dimensional) direction of the unresolved parton. For the total cross section, $F_J = 1$, the missing phase space can again be recovered by exploiting the underlying symmetries and various flavor permutations.

Interestingly, for the construction of the subtraction terms it is not sufficient to know the IR-singular behavior of the squared matrix elements given in Eq. (2.92) (see also Eq. (2.94) and Eq. (2.98)). The reason for this is the presence of loop corrections that are not exclusively confined to the underlying hard scattering process but may also occur in the factorized three-parton correlations that govern the soft and collinear limits as indicated in Fig. 3.9. Hence, the

modified IR factorization formula accounting also for virtual effects reads [570,590,636–641]

$$\begin{aligned} 2\,\mathrm{Re}\,\langle \mathcal{M}^{(0)}_{n+1}\left(\ldots,p_i,p_j,\ldots\right)|\mathcal{M}^{(1)}_{n+1}\left(\ldots,p_i,p_j,\ldots\right)\rangle \xrightarrow{\mathrm{IR}} \\ 4\pi\,{\mu_R}^{2\epsilon}\,\alpha_s\Big[2\,\mathrm{Re}\,\langle \mathcal{M}^{(0)}_{n}\left(\ldots,p_i+p_j,\ldots\right)|\boldsymbol{\mathcal{O}}^{\mathrm{IR},\,(0)}_{a_i a_j}|\mathcal{M}^{(1)}_{n}\left(\ldots,p_i+p_j,\ldots\right)\rangle \\ +\frac{\alpha_s}{4\pi}\,\langle \mathcal{M}^{(1)}_{n}\left(\ldots,p_i+p_j,\ldots\right)|\boldsymbol{\mathcal{O}}^{\mathrm{IR},\,(1)}_{a_i a_j}|\mathcal{M}^{(0)}_{n}\left(\ldots,p_i+p_j,\ldots\right)\rangle\Big] \end{aligned} \tag{3.160}$$

with

$$\begin{aligned} \boldsymbol{\mathcal{O}}^{\mathrm{Soft},\,(1)}_{a_i a_j} &= 2\,\mathrm{Re}\,\frac{\mathbf{J}^{(0)\,\dagger}_a\cdot\mathbf{J}^{(1)}_a}{\lambda^2} \\ \boldsymbol{\mathcal{O}}^{\mathrm{Col.},\,(1)}_{a_i a_j} &= \frac{\hat{P}^{ss'\,(1)}_{a_i a_j}(z,k_\perp,\epsilon)}{p_i\cdot p_j} \end{aligned} \tag{3.161}$$

where we have used the same parametrization for the soft and collinear limits as in section 2.3.2. These operators are not finite (despite applying UV renormalization) but contain single and double poles in ϵ as could have been anticipated from the known IR structure of one-loop amplitudes. Explicit results for the NLO soft current $\mathbf{J}^{\mu,\,(1)}_a$ and the NLO splitting functions $\hat{P}^{ss'\,(1)}_{a_i a_j}$ are collected in appendix E of Ref [632].

Using these information we are now able to perform the numerical phase space integration to determine $\hat{\sigma}^{RV}_{ij}$ in terms of a Laurent series in ϵ. There is, however, one subtle point that we need to address, namely the presence of $\mathcal{O}(\epsilon)$-terms in the matrix elements that enter the integrated subtraction term in Eq. (3.158). To this end, we split $\mathcal{A}_{ij}$ according to the loop order of the underlying amplitudes such that

$$\mathcal{A}^{\mathrm{Int}}_{ij} = 2\,\mathrm{Re}\left(\langle \mathcal{M}^{(0)}_{ij}|\boldsymbol{\mathcal{I}}^{(0)}|\mathcal{M}^{(1)}_{ij}\rangle + \langle \mathcal{M}^{(0)}_{ij}|\boldsymbol{\mathcal{I}}^{(1)}|\mathcal{M}^{(0)}_{ij}\rangle\right) \tag{3.162}$$

where the $\boldsymbol{\mathcal{I}}^{(n)}$ are operators[22] in spin and color space that collect all contributions generated by $\boldsymbol{\mathcal{O}}^{\mathrm{IR},\,(n)}_{a_i a_j}$. Apart from the poles present in the one-loop soft current and the one-loop splitting kernels they contain additional powers of $1/\epsilon$ produced through the subtraction mechanism resulting in the leading singular behavior indicated above. In consequence, the squared LO matrix elements have to be known to $\mathcal{O}(\epsilon^4)$ whereas for the one-loop amplitudes one still has to provide two additional orders in ϵ beyond the finite part. Especially for the latter this is highly unsatisfactory as it increases the computational effort substantially due to the fact that these contributions can usually not be found in the literature and have to be recalculated from scratch. Moreover, these extra orders usually exhibit a more complex dependence on the kinematic variables, which may lead to numerical complications as, for instance, prolonged runtimes in the MC integration or, at worst, stability problems.

[22] Note that, due to the presence of collinear divergences, the $\boldsymbol{\mathcal{I}}^{(n)}$ operators may, in fact, also change the parton indices of the corresponding amplitudes in Eq. (3.162) which makes, however, conceptually no difference for our discussion.

There exists, however, an elegant method to circumvent the computation of these higher-order terms [642]. The main idea is to work with finite remainders (see Eq. (3.157)) instead of renormalized amplitudes, which allows for a systematic combination of virtual contributions from different parts of the NNLO calculation such that the dependence on terms of $\mathcal{O}(\epsilon)$ in the matrix elements drops out completely. To this end, consider the following decomposition

$$\begin{aligned}\mathcal{A}_{ij}^{\text{Int}} &= \langle \mathcal{M}_{ij}^{(0)} | \boldsymbol{\mathcal{I}}_{\text{Div}}^{(1)} | \mathcal{M}_{ij}^{(0)} \rangle + 2\,\text{Re}\,\langle \mathcal{M}_{ij}^{(0)} | \boldsymbol{\mathcal{I}}^{(0)}\, Z_{\mathcal{F}}^{t\bar{t}j,\,(1)} | \mathcal{M}_{ij}^{(0)} \rangle \\ &+ \langle \mathcal{M}_{ij}^{(0)} | \boldsymbol{\mathcal{I}}_{\text{Fin}}^{(1)} | \mathcal{M}_{ij}^{(0)} \rangle + 2\,\text{Re}\,\langle \mathcal{M}_{ij}^{(0)} | \boldsymbol{\mathcal{I}}^{(0)} | \mathcal{F}_{ij}^{(1)} \rangle\end{aligned} \tag{3.163}$$

where the first line corresponds to the integrated subtraction term of $\mathcal{A}_{ij}^{\text{Div}}$ while the second line is generated by the subtractions to $\mathcal{A}_{ij}^{\text{Fin}}$. Note that the separation of divergent and finite parts in $\boldsymbol{\mathcal{I}}^{(1)}$ is performed at the level of IR operators, i. e. for $\mathbf{J}_a^{\mu,\,(1)}$ and $\hat{P}_{a_i a_j}^{ss'\,(1)}$, which means that both $\boldsymbol{\mathcal{I}}_{\text{Div}}^{(1)}$ and $\boldsymbol{\mathcal{I}}_{\text{Fin}}^{(1)}$ contain poles in ϵ. Now the crucial point is that in the double-virtual corrections as well as in the expressions generated by collinear renormalization there exist additional terms proportional to $|\mathcal{F}_{ij}^{(1)}\rangle$ (see section 3.4) such that the overall contribution of this function to the NNLO partonic cross sections is given by

$$\hat{\sigma}_{ij,\mathcal{F}}^{(2)} = \int dP_2^{(ij)}\, 2\,\text{Re}\,\langle \mathcal{M}_{ij}^{(0)} | \underbrace{Z_{\mathcal{F}}^{t\bar{t},\,(1)} + \left(Z_{\mathcal{F}}^{t\bar{t},\,(1)}\right)^{\dagger} + \mathcal{C}_{ij}^{(0)} + \boldsymbol{\mathcal{I}}^{(0)}}_{=\mathcal{O}(\epsilon^0)} | \mathcal{F}_{ij}^{(1)} \rangle \tag{3.164}$$

with $Z_{\mathcal{F}}^{t\bar{t},\,(1)}$ defined in Eq. (3.15) and

$$\mathcal{C}_{ij}^{(0)} = \frac{1-\beta^2}{\pi\epsilon}\, \frac{2\,P_{ij}^{(0)} \otimes \text{Re}\,\langle \mathcal{M}_{ij}^{(0)} | \mathcal{F}_{ij}^{(1)} \rangle}{2\,\text{Re}\,\langle \mathcal{M}_{ij}^{(0)} | \mathcal{F}_{ij}^{(1)} \rangle}\,. \tag{3.165}$$

As indicated, the various poles cancel in the combined operator structure rendering an evaluation of higher-order terms in the finite remainder unnecessary. Interestingly, this cancellation only works if one uses azimuthally-averaged splitting functions in $\boldsymbol{\mathcal{I}}^{(0)}$ defined via

$$\left[\int_{\mathbb{S}_1^{d-3}} d\Omega\right]^{-1} \int_{\mathbb{S}_1^{d-3}} d\Omega\, \hat{P}_{a_i a_j}^{ss'\,(0)} \equiv \bar{P}_{a_i a_j}^{(0)}\, \delta_{ss'} \tag{3.166}$$

where $\mathbb{S}_1^{d-3}$ denotes the $d-3$ dimensional unit sphere and $d\Omega$ is the corresponding azimuthal phase space measure. In our case, the average amounts to the simple replacement $k_\perp^\mu k_\perp^\nu \to k_\perp^2\, g^{\mu\nu}/(2-2\epsilon)$ and the extraction of an overall delta in spin space ($-g^{\mu\nu}$ for gluon splittings). This modified treatment is necessary to avoid contractions of objects with different dimensionality, namely transverse vectors (d-dim.) and finite remainders (4-dim.). Indeed, the fact that the pole structure of virtual amplitudes predicted by the anomalous dimension matrix $\boldsymbol{\Gamma}_{\mathcal{F}}$ (see Eq. (3.13)) is free of spin correlations suggests that the dependence on these transverse directions is somewhat spurious and, thus, can be safely eliminated by the above prescription. Note, however, that this only applies to the *integrated* subtraction terms whereas for $\mathcal{A}_{ij}^{\text{Sub}}$ the full spin correlations have to be taken into account in order to maintain the locality of the subtraction.

In our calculation we have actually implemented both scenarios, on the one hand, utilizing common one-loop matrix elements to $\mathcal{O}(\epsilon^2)$ and, on the other hand, four-dimensional finite remainders. While the contributions of the partial real-virtual and double-virtual results as well as of the collinear counterterms differ by construction, we find full agreement when combining these types of NNLO corrections. This successful and simplified treatment of loop-induced amplitudes provided the inspiration for the development of an improved formulation of STRIPPER [632] where all resolved states, i. e. also Born-level matrix elements, are handled in four dimensions. This corresponds to the use of the so-called 't Hooft-Veltman regularization scheme, which, in contrast to CDR, is characterized by treating only unresolved degrees of freedom, i. e. internal loops and additional external soft and collinear partons, in d dimensions.

Such a differentiation between four-dimensional and d-dimensional quantities makes the formulation of a NNLO subtraction mechanism a highly non-trivial task as it involves a delicate interplay of all parts of the partonic cross sections not just the virtual corrections. In particular, the average over azimuthal angles has to be performed with great care accounting for the various collinear limits and sectors present in the decomposition of the double-real-emission phase space. Apart from rendering the evaluation of higher ϵ-orders unnecessary, there exists a second major advantage compared to the original STRIPPER approach related to the explicit treatment of higher dimensions in the phase space parametrization. As we have learned in the discussion of the massive $t\bar{t}$ system, the number of independent momentum vectors requires the introduction of an additional non-vanishing spatial component in order to ensure a complete coverage of the four-particle phase space. This implies that for processes with a higher Born-level multiplicity the number of explicit dimensions needs to be increased even further, which, in practice, leads to a substantial increase of the computational costs. As the novel formulation of STRIPPER relies only on four-dimensional (external) momenta and polarizations, it does not suffer from this implementational drawback effectively extending the number of potentially accessible processes. It is, thus, perfectly suited for automation and is currently incorporated into a general-purpose MC tool that will eventually be made publicly available [632]. Nonetheless, for the calculation of $\sigma_{t\bar{t}}^{\text{tot}}$ and the more differential top-quark observables presented in chapter 4 it was sufficient to work with the original version of STRIPPER restricting the use of four-dimensional finite remainders to the case of one-loop and, as we will see, two-loop amplitudes.

3.4 Double-virtual corrections

3.4.1 The one-loop-squared contributions

At NNLO the purely virtual corrections consist of LO cut diagrams dressed with two additional quantum loops and, hence, only affect the quark annihilation and the gluon fusion channel. They can be divided into two conceptually different categories, the two-loop virtual and the one-loop-squared contributions, depending on whether both loops are on the same side of the unitarity cut or equally distributed to either side. While the determination of the former involves the use of sophisticated numerical methods, the results for the one-loop-

squared corrections can be derived in an entirely analytical fashion. This is due to the fact that the actual calculation is rather of NLO complexity as the matrix elements involved are, in principle, known from the analysis of the $\mathcal{O}(\alpha_s^3)$ virtual corrections. The only additional complication can be attributed to the more involved contraction with their complex conjugates instead of the Born amplitudes, for the first time allowing for imaginary parts to contribute to the partonic cross section predictions[23]

$$\hat{\sigma}_{ij}^{1\text{LS}}(\beta) = \int dP_2^{(ij)}\, F_J\, \langle \mathcal{M}_{ij}^{(1)} | \mathcal{M}_{ij}^{(1)} \rangle \ . \tag{3.167}$$

The foundation for the evaluation of this expression was the calculation of the respective one-loop scalar integrals that act as a master basis for this problem. They have been provided up to $\mathcal{O}(\epsilon^2)$ in Refs. [571,572] and were employed in the subsequent publications containing the results for the quark annihilation and gluon fusion channel at the integrand level [573,574], i. e. prior to the phase space integration. In our analysis of NNLO top-quark pair production we, however, computed the one-loop-squared corrections in a different manner based on the use of finite remainders thus rendering the additional ϵ-orders irrelevant as explained in the previous section. Moreover, the results in Refs. [573,574] did not allow for a decomposition of $\hat{\sigma}_{ij}^{1\text{LS}}$ into irreducible color representations required for the determination of the NNLO hard matching coefficients (see section 3.1.2) inevitably calling for an independent calculation of these contributions.

To this end, we constructed color-projected one-loop amplitudes by utilizing the operator basis defined in Eq. (2.46) and Eq. (2.47). After applying UV renormalization, we used *Passarino-Veltman reduction* [643] to separate the tensor structure from the underlying scalar integrals, which are subsequently mapped to the set of master integrals provided in Ref. [571]. In consequence, the one-loop matrix elements may be written as

$$|\mathcal{M}_{ij}^{(1)}\rangle = \sum_\alpha \mathcal{S}_\alpha \otimes \mathcal{T}_\alpha \ , \tag{3.168}$$

i. e. as a vector in tensor-color-space with basis vectors $\mathcal{T}_\alpha$ that consist of a product of independent Lorentz structures and color states defining the singlet/octet basis, and coefficient functions $\mathcal{S}_\alpha$ that are linear combinations of the scalar master integrals. The construction of the finite remainders as well as the one-loop-squared integrands in Eq. (3.167) may then be simply interpreted as operations on this vector space. The final expression for the latter reads

$$\begin{aligned} \langle \mathcal{M}_{ij}^{(1)} | \mathcal{M}_{ij}^{(1)} \rangle \ &= \ \langle \mathcal{M}_{ij}^{(0)} | \left(Z_{\mathcal{F}}^{t\bar{t},\,(1)} \right)^\dagger \, Z_{\mathcal{F}}^{t\bar{t},\,(1)} | \mathcal{M}_{ij}^{(0)} \rangle + 2\,\text{Re}\, \langle \mathcal{M}_{ij}^{(0)} | \left(Z_{\mathcal{F}}^{t\bar{t},\,(1)} \right)^\dagger | \mathcal{F}_{ij}^{(1)} \rangle \\ &+ \ \langle \mathcal{F}_{ij}^{(1)} | \mathcal{F}_{ij}^{(1)} \rangle \end{aligned} \tag{3.169}$$

where the contraction of the correlated matrix elements and/or finite remainders has the following generic form

$$\langle \mathcal{X} | \mathcal{Y} \rangle = \sum_\alpha \sum_\beta \mathcal{S}_\alpha^* \, \left(\mathcal{T}^* \mathcal{T} \right)_{\alpha\beta} \, \mathcal{S}_\beta \ . \tag{3.170}$$

[23] As indicated by the use of cut diagrams, we in this chapter only consider the fully inclusive case $F_J = 1$. The calculation of one-looped-squared corrections for more differential observables is discussed in chapter 4.

The matrix $(\mathcal{T}^*\mathcal{T})_{\alpha\beta}$ is diagonal in color due to the orthogonality of the singlet/octet configurations but contains off-diagonal entries in the subspace spanned by the tensor structures. The major advantage of this representation is the fact that by summing over spin and evaluating the corresponding traces over Lorentz structures these terms can now be reduced to simple combinations of the dimensionality parameter $d = 4-2\epsilon$ and the kinematic invariants. Expanding all quantities with respect to ϵ, we arrive at a Laurent series for Eq. (3.169) that can be subsequently integrated order by order over the two-particle phase space yielding the final expression for the partonic cross section contribution $\hat{\sigma}_{ij}^{\text{1LS}}$.

In practice, we chose two different strategies for this integration. For the determination of the NNLO hard matching coefficients we considered only the last term in Eq. (3.169), divided into distinct color configurations, and applied an additional expansion in the velocity β keeping only the leading threshold behavior. The corresponding phase space integration is trivial and can be performed completely analytically (see appendix C). For the total cross section, we first summed over all color states and then carried out the phase space integration numerically. Such a treatment is sufficient for our purposes as the other parts of the NNLO analysis are also only available in numerical fashion. Yet, let us stress that due to the use of finite remainders we are able to avoid the most complicated functional dependencies at the integrand level in form of multiple polylogarithms suggesting that a closed solution for $\hat{\sigma}_{ij}^{\text{1LS}}$ in terms of harmonic polylogarithms might be possible. Such an analysis would, however, go beyond the scope of this work and we, therefore, postpone it to a future study.

3.4.2 The two-loop virtual contributions

The evaluation of the two-loop virtual corrections

$$\hat{\sigma}_{ij}^{\text{2L}}(\beta) = \int dP_2^{(ij)}\, F_J\, 2\,\text{Re}\,\langle \mathcal{M}_{ij}^{(0)} | \mathcal{M}_{ij}^{(2)} \rangle \tag{3.171}$$

was one of the main aspects of this thesis and we will therefore discuss them in greater detail than the other parts of the NNLO analysis. The inclusive results $F_J = 1$ have meanwhile been published in Ref. [234]. In contrast to the one-loop-squared corrections their determination relies on purely numerical methods owing not only to the increased complexity but also quantity of the relevant Feynman diagrams that form the basis of the NNLO virtual amplitudes. For the gluon fusion channel we have, for instance, generated a total of 726 diagrams (compared to 33 at NLO) whereas the evaluation of the quark annihilation channel still involved as many as 190 diagrams (10 at NLO). When constructing the corresponding two-loop matrix elements, we again make use of projection operators to be able to distinguish between singlet and octet configurations as required for the determination of the NNLO hard matching coefficients described in section 3.1.2. After contracting the resulting expressions with the corresponding Born amplitudes we can eliminate the existing Dirac structure by explicitly evaluating the associated traces over γ-matrices such that we are merely left with a linear combination of scalar integrals.

All information on color and the number of active flavors are then contained in the respective prefactors suggesting the following decomposition [644,645]

$$\begin{aligned}
\tilde{\mathcal{A}}_{q\bar{q}}^{(n_f)}(\beta,\cos\theta,\epsilon) &\equiv \frac{1}{2}\,\mathrm{Re}\,\langle\mathcal{M}_{q\bar{q}}^{(0)}|\mathcal{M}_{q\bar{q}}^{(2)}\rangle \\
&= 2(N_c^2-1)\Bigg(N_c^2\,A^{(q)} + B^{(q)} + \frac{1}{N_c^2}\,C^{(q)} + N_c\,n_l\,D_l^{(q)} + N_c\,n_h\,D_h^{(q)} \\
&+ \frac{n_l}{N_c}\,E_l^{(q)} + \frac{n_h}{N_c}\,E_h^{(q)} + n_l^2\,F_l^{(q)} + n_l\,n_h\,F_{lh}^{(q)} + n_h^2\,F_h^{(q)}\Bigg) \\
\tilde{\mathcal{A}}_{gg}^{(n_f)}(\beta,\cos\theta,\epsilon) &\equiv \frac{1}{2}\,\mathrm{Re}\,\langle\mathcal{M}_{gg}^{(0)}|\mathcal{M}_{gg}^{(2)}\rangle \\
&= (N_c^2-1)\Bigg(N_c^3\,A^{(g)} + N_c\,B^{(g)} + \frac{1}{N_c}\,C^{(g)} + \frac{1}{N_c^3}\,D^{(g)} + N_c^2\,n_l\,E_l^{(g)} \\
&+ N_c^2\,n_h\,E_h^{(g)} + n_l\,F_l^{(g)} + n_h\,F_h^{(g)} + \frac{n_l}{N_c^2}\,G_l^{(g)} + \frac{n_h}{N_c^2}\,G_h^{(g)} + N_c\,n_l^2\,H_l^{(g)} \\
&+ N_c\,n_l\,n_h\,H_{lh}^{(g)} + N_c\,n_h^2\,H_h^{(g)} + \frac{n_l^2}{N_c}\,I_l^{(g)} + \frac{n_l\,n_h}{N_c}\,I_{lh}^{(g)} + \frac{n_h^2}{N_c}\,I_h^{(g)}\Bigg)
\end{aligned} \tag{3.172}$$

where n_h is an additional parameter indicating the number of heavy-quark flavors (in our case $n_h = 1$) and the color coefficients $A^{(i)}$, $B^{(i)}$, $C^{(i)}$,$D_{l,h}^{(q)}$, $D^{(g)}$, $E_{l,h}^{(i)}$, $F_{l,h}^{(i)}$, $F_{lh}^{(q)}$, $G_{l,h}^{(g)}$, $H_{l,h,lh}^{(g)}$ and $I_{l,h,lh}^{(g)}$ are functions that solely depend on $d = 4-2\epsilon$ and the kinematic invariants t and β. Note that we have already applied UV renormalization, which may be accomplished by equipping the bare two-loop contributions ($\mu_R = m_t$)

$$\tilde{\mathcal{A}}_{ij}^{B} \equiv 2\left(\frac{e^{\gamma_E} m_t^2}{4\pi}\right)^{2\epsilon} \mathrm{Re}\,\langle\widetilde{\mathcal{M}}_{ij}^{(0)}|\widetilde{\mathcal{M}}_{ij}^{(2)}\rangle \tag{3.173}$$

with an appropriate counterterm of the form

$$\begin{aligned}
C_{q\bar{q}}^{\mathrm{UV}} &= \frac{1}{2\pi^2}\left(Z_q^{(2)} + Z_Q^{(2)} + Z_{\alpha_s}^{(2)} + Z_Q^{(1)}\,Z_{\alpha_s}^{(1)}\right)\langle\widetilde{\mathcal{M}}_{q\bar{q}}^{(0)}|\widetilde{\mathcal{M}}_{q\bar{q}}^{(0)}\rangle \\
&+ \frac{1}{\pi}\left(\frac{e^{\gamma_E} m_t^2}{4\pi}\right)^{\epsilon}\left[\left(Z_Q^{(1)} + 2\,Z_{\alpha_s}^{(1)}\right)\mathrm{Re}\,\langle\widetilde{\mathcal{M}}_{q\bar{q}}^{(0)}|\widetilde{\mathcal{M}}_{q\bar{q}}^{(1)}\rangle + Z_m^{(1)}\,\mathrm{Re}\,\langle\widetilde{\mathcal{M}}_{q\bar{q}}^{(0)}|\widetilde{\mathcal{M}}_{q\bar{q}}^{(1),\,Z_m}\rangle\right] \\
C_{gg}^{\mathrm{UV}} &= \frac{1}{2\pi^2}\left[Z_g^{(2)} + Z_Q^{(2)} + Z_{\alpha_s}^{(2)} + Z_g^{(1)}\,Z_Q^{(1)} + Z_{\alpha_s}^{(1)}\,Z_Q^{(1)} + Z_{\alpha_s}^{(1)}\,Z_g^{(1)}\right]\langle\widetilde{\mathcal{M}}_{gg}^{(0)}|\widetilde{\mathcal{M}}_{gg}^{(0)}\rangle \\
&+ \frac{1}{2\pi^2}\left[Z_m^{(2)} + \left(Z_g^{(1)} + Z_Q^{(1)} + Z_{\alpha_s}^{(1)}\right)Z_m^{(1)}\right]\langle\widetilde{\mathcal{M}}_{gg}^{(0)}|\widetilde{\mathcal{M}}_{gg}^{(0),\,Z_m}\rangle \\
&+ \frac{1}{2\pi^2}\left(Z_m^{(1)}\right)^2\mathrm{Re}\,\langle\widetilde{\mathcal{M}}_{gg}^{(0)}|\widetilde{\mathcal{M}}_{gg}^{(0),\,Z_m^2}\rangle \\
&+ \frac{1}{\pi}\left(\frac{e^{\gamma_E} m_t^2}{4\pi}\right)^{\epsilon}\left[\left(Z_g^{(1)} + Z_Q^{(1)} + 2\,Z_{\alpha_s}^{(1)}\right)\mathrm{Re}\,\langle\widetilde{\mathcal{M}}_{gg}^{(0)}|\widetilde{\mathcal{M}}_{gg}^{(1)}\rangle + Z_m^{(1)}\,\mathrm{Re}\,\langle\widetilde{\mathcal{M}}_{gg}^{(0)}|\widetilde{\mathcal{M}}_{gg}^{(1),\,Z_m}\rangle\right].
\end{aligned} \tag{3.174}$$

The amplitudes with superscript Z_m and Z_m^2 responsible for the mass renormalization are constructed from the subclass of diagrams with internal heavy-quark propagators by utilizing

the replacements

$$\begin{aligned} \frac{i}{\not{p}-m_t+i\epsilon} &\xrightarrow{Z_m} \frac{i\,m_t}{(\not{p}-m_t+i\epsilon)^2} \\ \frac{i}{\not{p}-m_t+i\epsilon} &\xrightarrow{Z_m^2} \frac{i\,m_t^2}{(\not{p}-m_t+i\epsilon)^3}\,. \end{aligned} \tag{3.175}$$

One should stress that due to the singular nature of the renormalization constants (for explicit results see appendix A) all amplitudes entering the UV renormalization procedure have to be provided to higher orders in ϵ. In particular, the one-loop contributions need to be known to $\mathcal{O}(\epsilon)$, which may this time not be compensated by a suitable rearrangement of terms from different parts of the cross section calculation owing to the irregular distribution of UV divergences among them. In order to be able to adequately combine the two-loop corrections with the partonic fluxes, one still has to decouple the renormalized amplitudes[24] with the help of Eq. (2.27),

$$\tilde{\mathcal{A}}_{ij}^{(n_l)} = 4\,\tilde{\mathcal{A}}_{ij}^{(n_f)} + C_{ij}^{\text{Decoup.}}\,, \tag{3.176}$$

which, in contrast to the NLO virtual corrections, now leads to non-vanishing contributions even when setting $\mu_R = m_t$ as can be inferred from

$$\begin{aligned} C_{q\bar{q}}^{\text{Decoup.}} &= \frac{1}{2\pi^2}\left[2\left(Z_Q^{(1)}+Z_{\alpha_s}^{(1)}\right)\zeta_{\alpha_s}^{(1)}+\zeta_{\alpha_s}^{(2)}\right]\langle\widetilde{\mathcal{M}}_{q\bar{q}}^{(0)}|\widetilde{\mathcal{M}}_{q\bar{q}}^{(0)}\rangle \\ &+ \frac{2}{\pi}\left(\frac{e^{\gamma_E}m_t^2}{4\pi}\right)^{\epsilon}\zeta_{\alpha_s}^{(1)}\,\text{Re}\,\langle\widetilde{\mathcal{M}}_{q\bar{q}}^{(0)}|\widetilde{\mathcal{M}}_{q\bar{q}}^{(1)}\rangle \\ C_{gg}^{\text{Decoup.}} &= \frac{1}{2\pi^2}\left[2\left(Z_g^{(1)}+Z_Q^{(1)}+Z_{\alpha_s}^{(1)}\right)\zeta_{\alpha_s}^{(1)}+\zeta_{\alpha_s}^{(2)}\right]\langle\widetilde{\mathcal{M}}_{gg}^{(0)}|\widetilde{\mathcal{M}}_{gg}^{(0)}\rangle \\ &+ \frac{1}{\pi^2}\zeta_{\alpha_s}^{(1)}\,Z_m^{(1)}\,\langle\widetilde{\mathcal{M}}_{gg}^{(0)}|\widetilde{\mathcal{M}}_{gg}^{(0),\,Z_m}\rangle + \frac{2}{\pi}\left(\frac{e^{\gamma_E}m_t^2}{4\pi}\right)^{\epsilon}\zeta_{\alpha_s}^{(1)}\,\text{Re}\,\langle\widetilde{\mathcal{M}}_{gg}^{(0)}|\widetilde{\mathcal{M}}_{gg}^{(1)}\rangle\,. \end{aligned} \tag{3.177}$$

Apart from the novel $\zeta_{\alpha_s}^{(2)}$-dependence this may be attributed to scale-independent terms appearing at higher orders in ϵ in the perturbative coefficient $\zeta_{\alpha_s}^{(1)}$. They can be traced back to the fact that the decoupling constant only acts as a global prefactor for the collinearly unrenormalized cross sections[25] such that the remaining initial-state divergences lead to an admixture of d-dimensional contributions to the finite part of the two-loop amplitudes. Note, however, that due to the inherent finiteness of the decoupling relation this only applies to the $\mathcal{O}(\epsilon)$ terms of ζ_{α_s} itself and not to the corresponding Born or one-loop amplitudes.

Having applied the color decomposition in Eq. (3.172), the next step in the calculation of $\hat{\sigma}_{ij}^{\text{2L}}$ is the determination of a set of master integrals. To this end, we employ IBP relations

[24] Note that, in order to allow for a direct comparison with the available analytic two-loop results, the prefactor in Eq. (3.172) has been chosen such that it compensates for the differences in the $\alpha_s^{(n_f)}$ expansion. For the decoupled result we, however, return to our original notation, i. e. $\hat{\sigma}_{ij}^{\text{2L}}(\beta) = \int dP_2^{(ij)}\,F_J\,\tilde{\mathcal{A}}_{ij}^{(n_l)}$.

[25] In consequence, there are also scale-independent decoupling contributions to the real-virtual and one-loop-squared corrections, which we have, however, omitted in the previous discussion since they are conceptually irrelevant for the evaluation strategies presented above.

# of prop.	masters	masters $t \leftrightarrow u$	highest pole
2	1	1	-3
3	17	12	-3
4	47	34	-2
5	145	90	-2
6	86 (16)	52 (12)	0
6 NP	37 (19)	26 (8)	0
7	126 (22)	71 (11)	0
7 NP	60 (6)	38 (3)	0
Total	422 (38)	260 (23)	

Table 3.4: *Internal structure of the master basis relevant for the evaluation of the two-loop virtual corrections organized according to the number of internal propagators. For completeness we also give the number of independent masters after employing $t \leftrightarrow u$ symmetry and the highest spurious pole for each class of integrals. For the most complicated six and seven line integrals we also indicate the number of masters with non-planar (NP) topologies. In parenthesis we provide the number of masters that has been previously determined in Ref. [646] such that the total number of new integrals evaluated in this work amounts to* 100.

implemented in a Laporta-based algorithm that allows for a reduction of the two-loop scalar integrals to a basis of 422 masters in the gluonic case and 145 masters for the quark-initiated corrections. The latter are, however, included in the gluon master basis as the internal properties of QCD, i. e. the composition of the underlying interaction vertices, allow for gluons to form the same topological structures as quarks (but not vice versa). Thus, both production modes can be described by a single set of master integrals, which constitutes a considerable simplification from the computational perspective. Nevertheless, this basis is not yet minimal in the sense that some of the masters are connected via $t \leftrightarrow u$ transformations. Hence, it would, in principle, be sufficient to evaluate only one representative of such related integrals, effectively reducing the number of independent masters as shown in Tab. 3.4. For the subsequent use of differential equations it is, however, more convenient to maintain the explicit $t - u$-dependence and work with the complete set of 422 scalar two-loop integrals. A further advantage of this approach is that the $t \leftrightarrow u$ symmetry may serve as an additional cross-check at various stages of the calculation as we will see later.

A crucial aspect in choosing an appropriate basis is the presence of spurious poles in the color coefficients entering Eq. (3.172) that require the evaluation of the masters to higher orders in ϵ (see Tab. 3.4), which depending on the complexity of the affected integrals may cause serious computational difficulties. Since there exists no systematic prescription to avoid these poles, we adopt the following strategy. For the masters with the most complicated topologies

involving six or seven internal propagators we, by hand, perform a change of basis such that all spurious contributions are eliminated. For the less complex masters such a treatment would be too cumbersome and is, in fact, not necessary as they can usually be evaluated to sufficiently high orders at virtually no additional computational cost. Indeed, most of them can be either considered as textbook examples or found in the literature oftentimes in an entirely analytical form. In practice, however, we refrain from using any external input in terms of precalculated results and evaluate the complete basis from scratch.

As already indicated, our method of choice in this context is the use of differential equations outlined in section 2.3.2 since it allows for a uniform treatment of arbitrary topologies and, thus, is perfectly suited for automation. As we are dealing with a 2-to-2 process, the full kinematic dependence is described by two systems of homogeneous linear first-order partial differential equations

$$\widetilde{m}^2 \frac{\partial}{\partial \widetilde{m}^2} M_k(\widetilde{m}, \tilde{t}, \epsilon) = \sum_l J_{kl}^{(\widetilde{m})}(\widetilde{m}, \tilde{t}, \epsilon)\, M_l(\widetilde{m}, \tilde{t}, \epsilon) \tag{3.178}$$

$$\tilde{t} \frac{\partial}{\partial \tilde{t}} M_k(\widetilde{m}, \tilde{t}, \epsilon) = \sum_l J_{kl}^{(\tilde{t})}(\widetilde{m}, \tilde{t}, \epsilon)\, M_l(\widetilde{m}, \tilde{t}, \epsilon) \tag{3.179}$$

where the kinematic variables are given by the dimensionless ratios $\widetilde{m}^2 = m_t^2/s$ and $\tilde{t} = t/s$ (t defined in Eq. (2.36)). Since we are solely interested in a solution in terms of a Laurent expansion, we replace all quantities with their respective series representations (see Eq. (2.72)) resulting in a new system of differential equations

$$\widetilde{m}^2 \frac{\partial}{\partial \widetilde{m}^2} \widetilde{M}_k(\widetilde{m}, \tilde{t}) = \sum_l \tilde{J}_{kl}^{(\widetilde{m})}(\widetilde{m}, \tilde{t})\, \widetilde{M}_l(\widetilde{m}, \tilde{t}) \tag{3.180}$$

$$\tilde{t} \frac{\partial}{\partial \tilde{t}} \widetilde{M}_k(\widetilde{m}, \tilde{t}) = \sum_l \tilde{J}_{kl}^{(\tilde{t})}(\widetilde{m}, \tilde{t})\, \widetilde{M}_l(\widetilde{m}, \tilde{t})\ . \tag{3.181}$$

Note that due to the presence of poles in the Jacobi matrices $J^{(\widetilde{m})}$ and $J^{(\tilde{t})}$ some masters need to be determined to higher orders in ϵ than originally required by the spurious pole structure at the amplitude level. Fortunately, this does in our case not introduce any additional contributions beyond $\mathcal{O}(\epsilon^0)$ in the six or seven line integrals.

Despite the fact that the two systems of differential equations are only weakly coupled in the sense that they can be decomposed into smaller subsystems, they are still too complex for an analytical evaluation such that we have to rely on purely numerical methods as already mentioned above. The main idea is to approximate the exact functional behavior of the master integral components $\widetilde{M}_k(\widetilde{m}, \tilde{t})$ through an interpolation function obtained from a fit to a discrete set of phase space points. To this end, we parametrize the underlying kinematics in terms of the velocity and the scattering angle and subsequently divide the corresponding physical phase space into a grid of 80×42 sampling points (see Fig. 3.10) chosen as follows

$$\begin{aligned} \beta_i &= \frac{i}{80}\ , \qquad i = 1, ..., 79 \qquad \beta_{80} = 0.999 \\ \cos\theta_i^{\pm} &= \pm\, x_i^{\mathrm{GK}}\ , \qquad i = 1, ..., 21\ . \end{aligned} \tag{3.182}$$

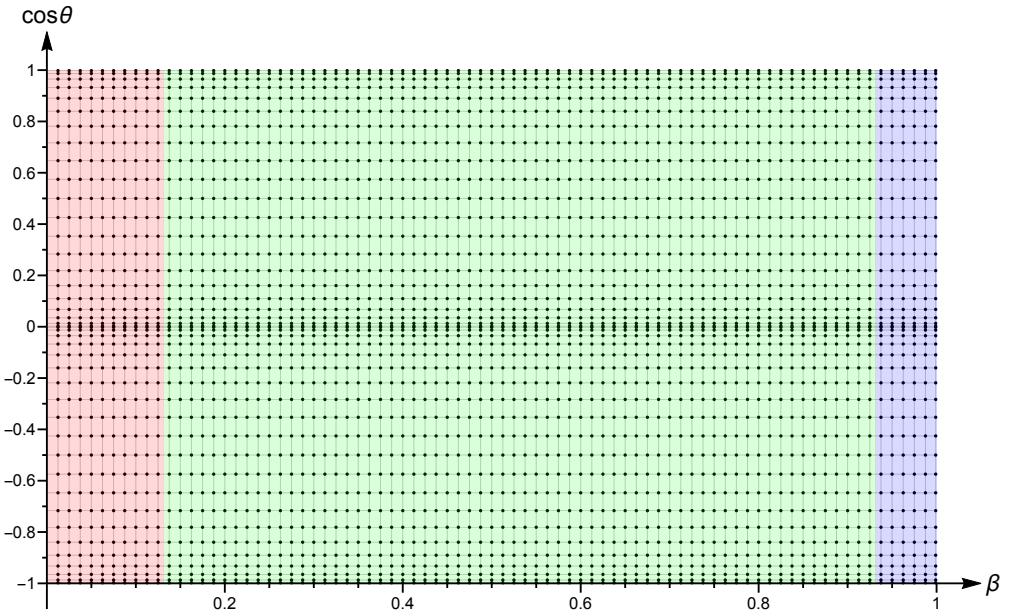

Figure 3.10: *Phase space grid spanned by the* 80 *velocity values and* 42 *Gauss-Kronrod points defined in Eq. (3.182). The colored regions correspond to the threshold (red), intermediate (green) and high-energy (blue) regime whose evaluation requires different computational strategies as described below.*

While the β-values are only constrained by the condition that they cover the entire velocity range accessible at the Tevatron and the LHC, for $\cos\theta$ we impose an additional criterium, namely its values should allow for an efficient and precise numerical integration needed for the determination of reliable partonic cross section predictions.

In order to avoid possible complications induced by the use of numerical fitting routines, we choose to employ a so-called deterministic integration rule that allows for the approximation of an integral over a well-behaved, i. e. smooth and finite, function in terms of a weighted sum

$$\int_a^b f(x)\,dx \approx \sum_{i=1}^{n} w_i\, f(x_i)\;, \qquad x_i \in [a,b] \tag{3.183}$$

where both the weights w_i and the abscissas x_i depend on the specific integration rule as well as on the chosen order n. A well-known example of such an integration rule is the Gaussian quadrature formalism, which is constructed such that it yields exact results for polynomial integrands of degree $2n-1$ or less. For our particular problem we use an extension of this method, the Gauss-Kronrod rule, which increases the number of evaluation points with respect to the standard Gaussian quadrature by $n+1$ allowing for an exact description of even higher degree polynomials of up to order $3n+1$. The crucial point is that, since the original Gaussian abscissas are embedded in this new set of points, one can actually apply two integration rules simultaneously without having to perform additional integrand evaluations. This is a tremendous computational advantage as the difference between the approximate results provided by these rules can be taken as an estimate of the overall integration error.

In our particular case, we first divide the phase space integral into two separate domains according to the sign of $\cos\theta$ and then apply a Gauss-Kronrod rule of order $n = 10$ to each of these partial integrals such that

$$\begin{aligned}\int dP_2^{(ij)}\, \tilde{\mathcal{A}}_{ij}^{(n_l)}(\beta,\cos\theta,\epsilon) &= N_\epsilon \frac{1}{s_i s_j c_i c_j} \frac{\beta(1-\beta^2)}{128\pi} \left[\int_{-1}^{0} d\cos\theta\, \sin^{-2\epsilon}\theta\, \tilde{\mathcal{A}}_{ij}^{(n_l)}(\beta,\cos\theta,\epsilon) \right. \\ &+ \left. \int_{0}^{1} d\cos\theta\, \sin^{-2\epsilon}\theta\, \tilde{\mathcal{A}}_{ij}^{(n_l)}(\beta,\cos\theta,\epsilon) \right] \\ &\approx N_\epsilon \frac{1}{s_i s_j c_i c_j} \frac{\beta(1-\beta^2)}{128\pi} \sum_{i=1}^{2n+1} w_i^{\mathrm{GK}} \left\{ \left[1-(x_i^{\mathrm{GK}})^2\right]^{-\epsilon} \right. \\ &\times \left. \left[\tilde{\mathcal{A}}_{ij}^{(n_l)}(\beta,-x_i^{\mathrm{GK}},\epsilon) + \tilde{\mathcal{A}}_{ij}^{(n_l)}(\beta,x_i^{\mathrm{GK}},\epsilon) \right] \right\}\end{aligned} \tag{3.184}$$

where the process-independent normalization factor is given as

$$N_\epsilon = \frac{\left(e^{\gamma_E}\, \frac{\mu_R^2}{m_t^2}\, \frac{\rho}{\beta^2}\right)^\epsilon}{\Gamma(1-\epsilon)} \overset{\epsilon\to 0}{=} 1 + \mathcal{O}(\epsilon)\,. \tag{3.185}$$

The respective Gauss-Kronrod weights w_i^{GK} and abscissa x_i^{GK} are related to certain classes of orthogonal polynomials and can be obtained with any major algebraic/numeric software package, for instance MATHEMATICA. The reason for splitting the integration range lies in the system of differential equations itself, which, as we will see, contains various physical and unphysical singularities that constrain the computationally accessible phase space region. As a consequence, employing the Gauss-Kronrod method for the full $\cos\theta$-regime is no longer possible owing to the fact that the midpoint abscissa at $x_{\mathrm{mid}}^{\mathrm{GK}} \equiv (a+b)/2 = (-1+1)/2 = 0$, which is always present in the above summation formula regardless of n, coincides with one of these singularities. Nevertheless, for the gluon fusion channel there is, indeed, a positive side effect of having to split the phase space integration, namely the explicit validation of the underlying $\cos\theta \leftrightarrow -\cos\theta$ symmetry. Due to the indistinguishability of the initial-state partons there exists no distinctive direction required for the unique definition of the scattering angle beyond $\pi/2$ such that $\tilde{\mathcal{A}}_{gg}^{(n_l)}$ (but not necessarily the individual masters) does, in fact, not depend on the sign of $\cos\theta$. As a result, the comparison of the contributions from the two separate regions of phase space may serve as an additional error estimate for the quality of our integration method.

Having specified the phase space grid, we can now translate the discrete $(\beta,\cos\theta)$-coordinates to the kinematic variables $(\widetilde{m},\tilde{t})$ used in the differential equations . The actual evaluation of the full phase space grid is then performed in three subsequent steps graphically summarized in Fig. 3.11. Note that we only consider the case $\mu_R = m_t$ here since the full scale dependence can be restored afterwards with help of the normalization factor in Eq. (3.185), which is, in turn, a direct consequence of the scale invariance of the bare amplitudes.

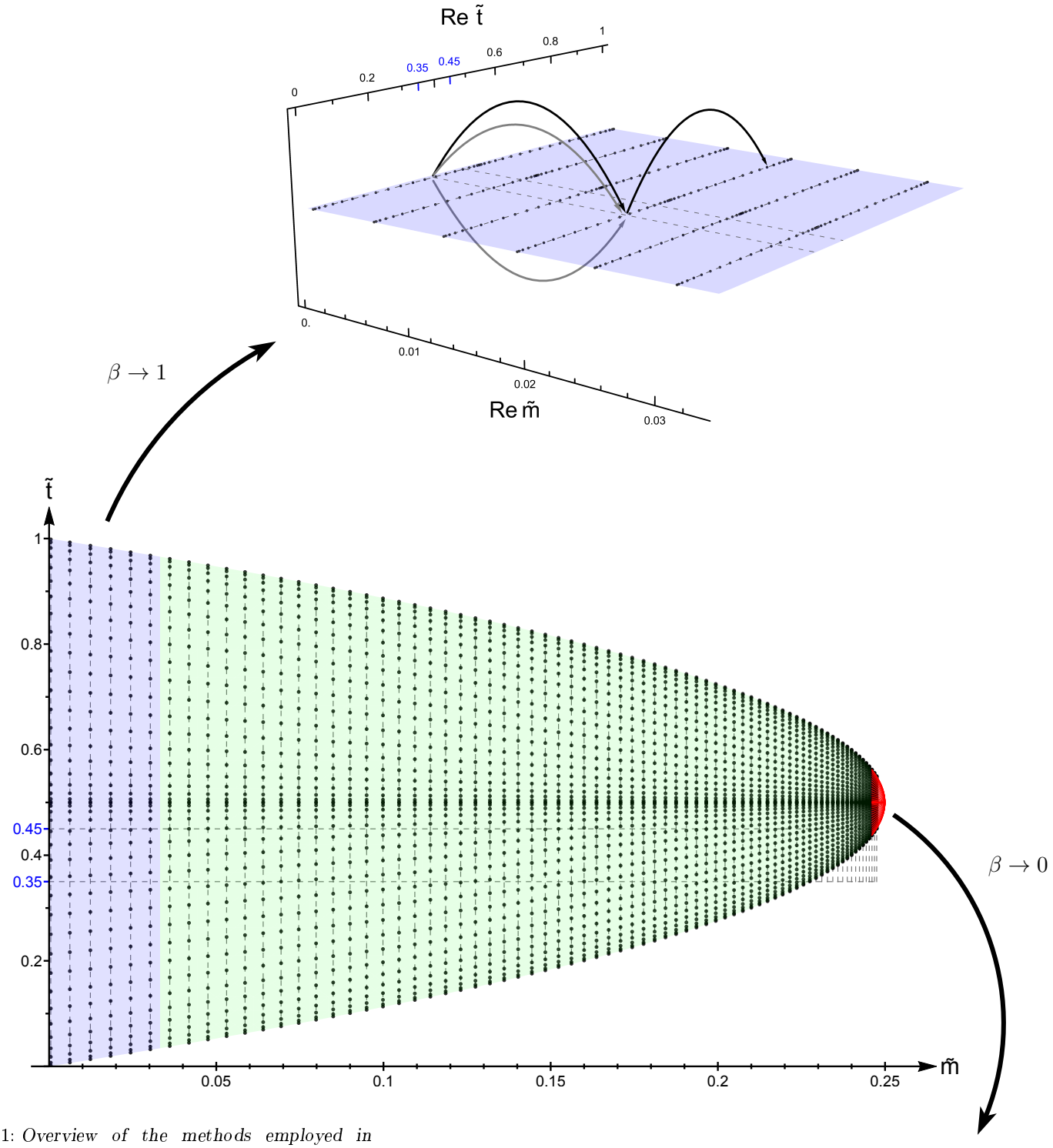

Figure 3.11: *Overview of the methods employed in the evaluation of the two-loop master integrals. Parametrizing the phase space grid (black dots) in terms of $\widetilde{m}$ and $\tilde{t}$, the variables of the differential equations , the projected integration paths are denoted by the dashed lines whereas the actual integration is performed on elliptic contours in the complex plane (alternative contours for error estimate in gray). As indicated, the boundaries for the $\widetilde{m}$-integration lie in the high-energy regime (blue) at $\tilde{t}_0 \in \{\frac{7}{20}, \frac{9}{20}\}$. The resulting output then serves as boundary condition for the numerical solution in $\tilde{t}$ in the complete intermediate range (green) down to the threshold regime (red). There, we utilize power-logarithmic expansions in β along fixed values of $\cos\theta$ (red lines) where the unknown constants are determined through matching to the numerical results at $\beta \in \{\frac{1}{10}, \frac{1}{8}\}$.*

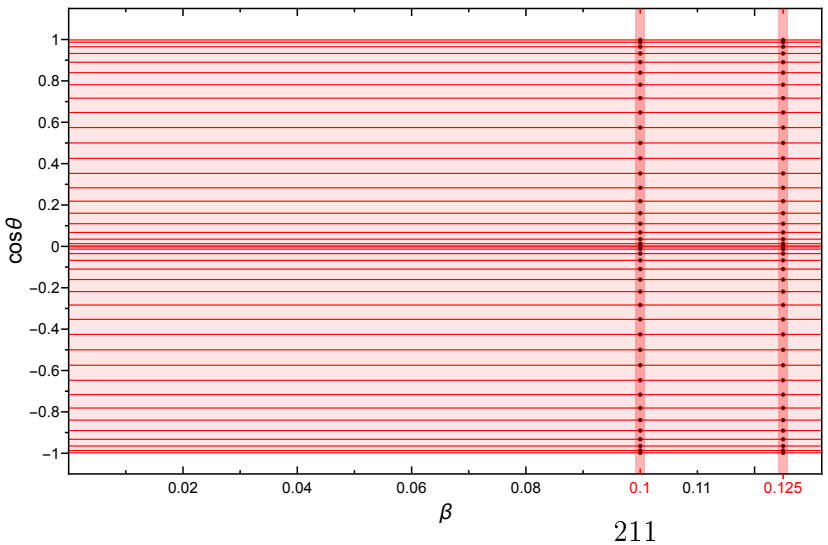

Determination of the boundary conditions

While the analytic structure of the master integrals is completely determined by the system of differential equations , the boundary values are a priori unknown and have to be derived otherwise. This task is further complicated by the fact that the integration routines, employed in the subsequent solution of the masters for arbitrary kinematics, rely on high-precision numerical inputs. Thus, one has to discard the possibility of a direct calculation at a fixed point in phase space even with the help of specialized tools such as SecDec [647–650] or Fiesta [651–653]. These tools, in principle, allow for the evaluation of multi-loop integrals for arbitrary momentum configurations but unfortunately they are not able to provide results with a sufficiently large number of digits, in some cases with complex integrand structures even failing to produce results at all. Hence, we are forced to pursue a different strategy based on the expansion of the scalar integrals in a well-accessible kinematic limit such as the regular high-energy regime $\widetilde{m} \to 0$. Regular in this context means that the value of $\tilde{t}$ should be chosen such that there exists a clear hierarchy between the two kinematic variables, i. e.

$$\frac{\widetilde{m}}{\tilde{t}} \ll 1 \quad \text{and} \quad \frac{\widetilde{m}}{1-\tilde{t}} \ll 1 \,. \tag{3.186}$$

The functional behavior of the master basis in this limit can be described in terms of a power-logarithmic series in $\widetilde{m}$

$$\widetilde{M}_k(\widetilde{m}, \tilde{t}) = \sum_{n=n_0} \sum_{m=0}^{M} \mathcal{K}_k^{(n,m)}(\tilde{t})\, \widetilde{m}^n \, \ln^m \widetilde{m} \tag{3.187}$$

with coefficients $\mathcal{K}_k^{(n,m)}$ whose dependence on $\tilde{t}$ can be determined exactly. In order to guarantee an adequate numerical precision of the thus obtained boundaries, these expansions have to be performed to sufficiently high orders, in our particular case up to $(\widetilde{m}^{50})$, which represents a serious computational challenge. Note that the maximum power of the logarithms M in Eq. (3.187) is in practice bounded from above by the internal properties of the master integrals such that for a fixed expansion order we are always able to derive the full logarithmic dependence.

In general, our strategy can be divided into two consecutive steps. First we use Mellin-Barnes techniques to deduce the leading behavior of the master integrals analytically. Such an analysis requires the evaluation of multiple Mellin-Barnes representations, which could be efficiently handled by extensive use of the tools included in the MB package [541, 542]. Still, there exists no standard procedure for an automated treatment of the full master basis calling for a tedious computation on an integral-by-integral basis with specifically tailored solution strategies. Yet, in a few cases a pure Mellin-Barnes approach was not successful such that the exact $\tilde{t}$-dependence could only be recovered by utilizing the known kinematic structure encoded in Eq. (3.181). The corresponding boundary condition at $\tilde{t} = 0$ has been obtained from a simultaneous expansion of the Mellin-Barnes integrals in $\widetilde{m}$ and $\tilde{t}$ with coefficients that could be subsequently resummed either analytically with the Xsummer package [540] or semi-analytically by means of the Pslq algorithm [654]. The latter is essentially a fitting routine that expresses any given numerical input in terms of a predefined basis of real-valued

constants with rational coefficients. In our case this basis[26] consists of $\zeta(2)$, $\zeta(3)$, $\zeta(4)$ and $\zeta(5)$ as well as of the combinations $\zeta(2)\ln 2$ and $\zeta(2)\,\zeta(3)$. Despite the fact that there exists no strict proof for the correctness of this conversion from numerical to analytical expressions, it is exceedingly unlikely that a certain input value can be adequately described by a different set of irrational constants at such a high level of accuracy. Therefore, we may safely interpret the thus obtained results as analytical within the overall precision of our calculation.

Having fixed the leading coefficients in Eq. (3.187) the next step is to extend the power-logarithmic expansion to a sufficiently high order in $\widetilde{m}$. As one might expect, a direct, i. e. order-by-order, evaluation is not feasible in this context considering the enormous computational effort already put into the determination of the leading behavior. Instead, we make use of the fact that the entire kinematic dependence in the high-energy limit can be inferred from Eq. (3.180) by expanding the Jacobian $\tilde{J}_{kl}^{(\widetilde{m})}$ in a Laurent series in $\widetilde{m}$. Assuming a solution for the masters in form of Eq. (3.187) the whole system of differential equations is effectively reduced to an ordinary matrix equation for the coefficients $\mathcal{K}_k^{(n,m)}$. This equation may be further decomposed into well-ordered subsystems that can then be solved recursively in terms of a set of general boundary coefficients

$$\mathcal{K}_k^{(n,m)}(\tilde{t}) = M_{kl}^{(n,m)}(\tilde{t})\,\mathcal{B}_l(\tilde{t})\;. \tag{3.188}$$

The actual values for $\mathcal{B}_l$ are determined afterwards by matching the power-logarithmic solution to the results of the Mellin-Barnes analysis. This is possible since the boundaries of the differential equations lie at low powers of $\widetilde{m}$ such that their explicit form can be completely deduced from the leading high-energy behavior. The matrices $M_{kl}^{(n,m)}$ depend on the Laurent coefficients of $\tilde{J}_{kl}^{(\widetilde{m})}$ and are thus solely governed by the algebraic structure of the individual subsystems. In practice, one has to distinguish between two different cases. If the Jacobian of a particular subsystem contains no inverse powers of $\widetilde{m}$, i. e. it can be simply Taylor-expanded, the corresponding solution can be obtained by using only fundamental matrix operations, namely addition and multiplication, which simplifies the computational effort tremendously. Otherwise the situation becomes more involved as the solution procedure requires the construction of so-called generalized matrix inverses, an extension of the regular inverse to matrices with vanishing determinants. From the computational point of view this is substantially more demanding leading to the development of a novel algorithm for the determination of power-logarithmic solutions for arbitrary systems of coupled linear first-order differential equations.

While in principle it would be possible to implement this algorithm such that the explicit $\tilde{t}$-dependence in $\mathcal{K}_k^{(n,m)}$ is preserved, it is far more efficient to work with prespecified values $\tilde{t} = \tilde{t}_0$ as they allow for a purely numerical treatment. However, in order to retain a maximum of analyticity, these values should be rational numbers such that the numerical precision of the power-logarithmic series is completely governed by its expansion depth without further limitations due to the finite number of digits in $\tilde{t}_0$. In our particular case we choose $\tilde{t}_0 \in \{\frac{7}{20}, \frac{9}{20}\}$ allowing for the determination of two independent sets of boundary conditions

[26] Note that even though they are present in the solution of the individual masters, constants (or products of constants) with transcendality weight ≥ 4 drop out in the final expression for the physical amplitude.

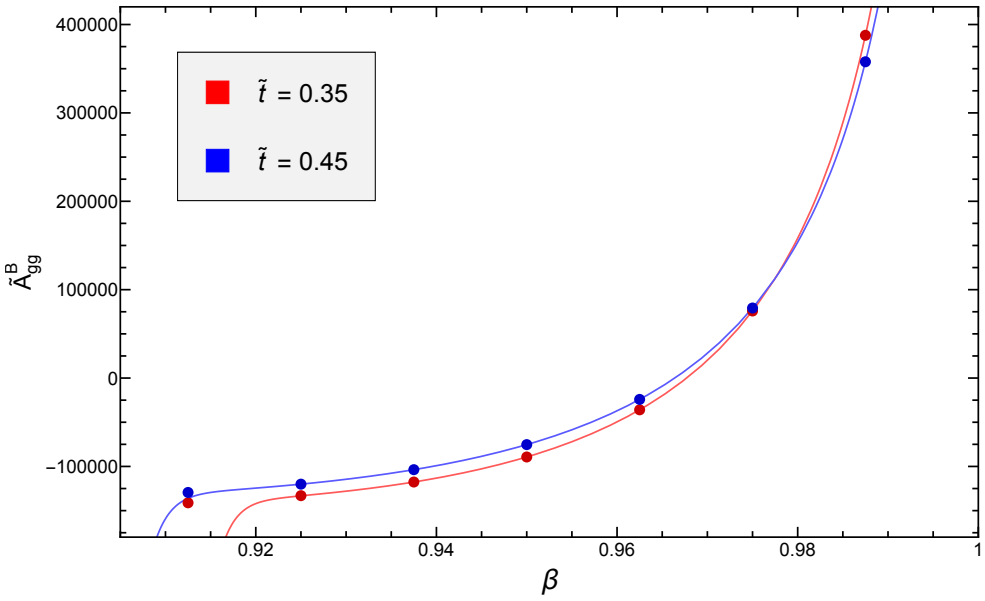

Figure 3.12: *Finite part of the bare two-loop contributions $\tilde{\mathcal{A}}^B_{gg}$ evaluated for fixed values of $\tilde{t}$ both through numerical integration of the differential equations Eq. (3.180) (dots) and a power-logarithmic series in $\widetilde{m}$ (lines) indicating the radius of convergence of the latter.*

that serve as starting points for the numerical integration and, hence, provide an additional means of estimating the overall numerical precision of our approach.

Note that the matching procedure itself can also be considered as a test of the kinematic structure of our results since it involves a comparison of two completely independent calculations. In this context it is important to check whether the number of free parameters in $\mathcal{B}_l$ is equal to the number of differential equations (assuming that all masters can be represented by a power-logarithmic series), which guarantees that the most general solution is employed in the matching. Interestingly it turns out that the leading $\widetilde{m} \to 0$ behavior in the Mellin-Barnes results is not solely restricted to integer powers but for some masters may also exhibit a square-root dependence that persists even at the amplitude level. This shows that the most general solution involves arbitrary rational powers of n, which have to be properly accounted for in the ansatz in Eq. (3.187) in order to be able to identify the full set boundary conditions $\mathcal{B}_l$.

The computational power of our method may raise the question whether it might not be possible to extend it to a larger fraction of the β-spectrum beyond the high-energy regime by increasing the expansion depth of the power-logarithmic series to even higher orders. Unfortunately, the radius of convergence of the two-loop amplitudes with respect to $\widetilde{m}$ is rather small such that the expansion is only valid up to $\beta \gtrsim 0.92$ as can be inferred from Fig. 3.12. This forces us to resort to a purely numerical treatment for the bulk of the two-loop virtual corrections taking into account the exact form of the differential equations as we will see next. Note, however, that we will encounter the method of series expansions again when dealing with the evaluation of the master basis in the threshold region greatly profiting from the experience gained in the determination of the high-energy behavior.

Numerical integration

As the master integrals are smooth functions of $\widetilde{m}$ and $\tilde{t}$, they can, in principle, be evaluated at any point in phase space by solving Eq. (3.180) and Eq. (3.181) numerically provided that the boundary conditions are known. In practice, however, the situation becomes a little more complex due to the presence of singular denominators in $\tilde{J}_{kl}^{(\widetilde{m})}$ and $\tilde{J}_{kl}^{(\tilde{t})}$ (see, for instance, Fig. 3.13) that have a significant impact on the efficiency and stability of the numerical integration routines. These terms can be characterized according to their origin as physical and spurious singularities and have to be addressed differently in the actual calculation. Physical singularities appear at points in phase space that correspond to an intrinsic singular limit of the underlying two-loop amplitudes, e. g. the threshold limit $\beta \to 0$ or the production of ultra-relativistic top quarks at large/small scattering angle $\tilde{t} = 0, 1$. Even though this divergent behavior will be ultimately compensated by the phase space integration and the convolution with the partonic fluxes, it cannot be avoided at the amplitude level rendering an evaluation of points in the immediate vicinity of these singularities by standard methods impossible. The spurious divergence structure, on the other hand, is a specific property of the chosen master basis and could hence, in principle, be removed by an appropriate basis transformation. There exists, however, no clear prescription on how to construct such a (kinematically) finite basis forcing us to pursue a different strategy. The main idea is to circumvent the problematic regions of phase space by shifting the path of integration to the complex plane as indicated in Fig. 3.11. The fact that this is possible is a direct consequence of the Cauchy integral theorem and the unphysical nature of the spurious singularities, which in combination with the physical boundaries do not lead to any branch cuts in the $\widetilde{m}$-$\tilde{t}$-plane.

This method grants us access to a large portion of the kinematically-allowed phase space without having to worry about potential numerical complications. The only case that could still be problematic is the endpoint of the integration lying too close to a spurious singularity, which can, however, in practice be coped with by using an increased number of digits in the integration routine. To this end, we had to modify the original Adams-Moulton-type algorithm that performs the actual numerical evaluation [655] such that it works in quad-double precision (for further details see appendix E). The algorithm itself is based on so-called variable multi-step methods that solve an initial-value problem of the form

$$\frac{d}{dz}\,\vec{y}(z) = \vec{f}\,(z, \vec{y}(z))\,, \qquad \vec{y}(z_0) = \vec{y}_0, \qquad z, z_0 \in \mathbb{C} \tag{3.189}$$

by integrating both sides of the equation with respect to z and approximating the resulting expression by decomposing the integration path into small intervals of flexible size that can be consecutively evaluated through interpolation. Hence, the value of $\vec{y}(z)$ after n integration steps is given as

$$\begin{aligned} \vec{y}(z_n) &= \vec{y}(z_{n-1}) + \int\limits_{z_{n-1}}^{z_n} dz\, \vec{f}\,(z, \vec{y}(z)) \\ &= \vec{y}(z_{n-1}) + h_n \sum_{i=0}^{i_{max}} b_{n,i}\, \vec{f}\,(z_{n-i}, \vec{y}(z_{n-i})) \end{aligned} \tag{3.190}$$

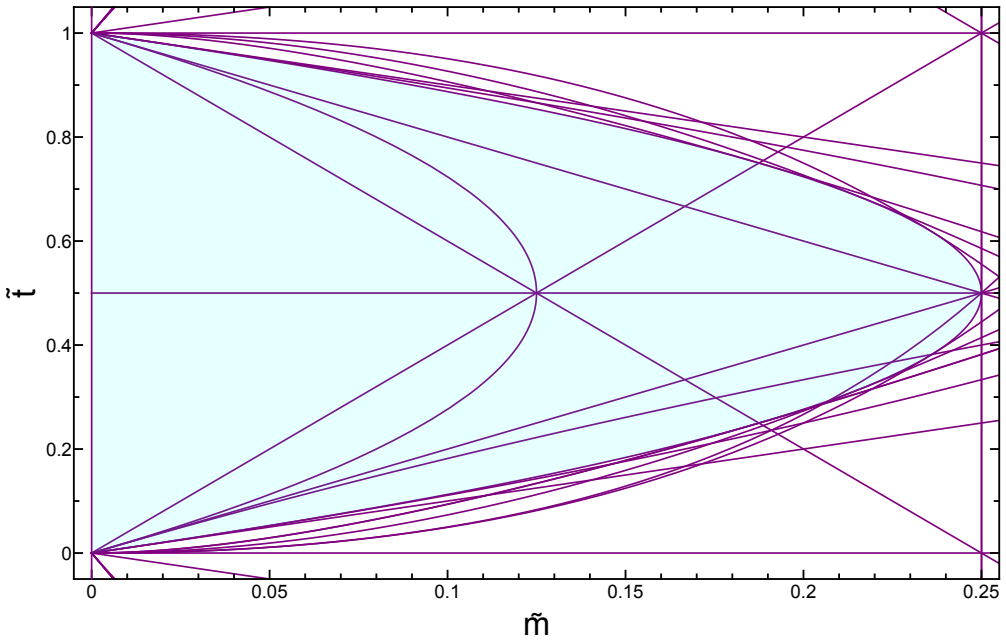

Figure 3.13: *Singularity structure (purple) of the two systems of differential equations in $\widetilde{m}$ and $\tilde{t}$ describing the full master basis of the two-loop gluon fusion amplitudes. Divergent contributions not touching the physical phase space (light blue) have been excluded.*

where i_{max} varies between $\{0, \ldots, 11\}$ and the coefficients $b_{n,i}$ are computed from the current and past step sizes $h_k = z_k - z_{k-1}$ $(k = n - i_{max}, \ldots, n)$. Note that this equation depends implicitly on $\vec{y}(z_n)$ in the sense that its value cannot be simply read off but has to actually be determined iteratively due to the additional contribution from $\vec{f}\,(z_n, \vec{y}(z_n))$. While at first glance this seems to increase the computational effort, it in practice leads to a far more stable evaluation with improved convergence properties. In our particular case the number of steps (and, consequently, the runtime) depends crucially on the phase space point under consideration but lies typically at the order of 10^3 to 10^4 ($\sim$ 1-10 h runtime). As this approach allows for a simultaneous treatment of the complete master basis it is perfectly suited for automation. Moreover, since the individual grid points are independent, an additional speed-up may be achieved by evaluating multiple points on the phase space grid in parallel.

In practice, however, the possible integration order is already restricted by the form of the differential equations Eq. (3.180) and Eq. (3.181) and we thus proceed as follows. First, for a fixed value of $\tilde{t}_0 \in \left\{\frac{7}{20}, \frac{9}{20}\right\}$, we integrate along the $\widetilde{m}$-direction to the corresponding β-values defined in Eq. (3.182). The results then serve as new boundary conditions for the integration in $\tilde{t}$-direction to the individual Gauss-Kronrod points. Note that near threshold $\widetilde{m} \to \frac{1}{4}$ these boundaries may lie outside the physically-allowed phase space as indicated in Fig. 3.11, which, however, conceptually makes no difference as the integration procedure does not rely on physical background conditions but solely on the mathematical content of the differential equations . Unfortunately it is not possible to cover the entire phase space grid in this manner due to the fact that there are still physical divergences remaining in the system

as already noted above. In consequence, all points in the region $\widetilde{m} > \frac{99}{400}$ ($\beta < \frac{1}{10}$) as well as some single points close to $\tilde{t} = 1$ are inaccessible with this method even when improving our implementation by employing higher-precision floating point data formats (see appendix E). While the missing points in the high-energy regime may be recovered by exploiting the $t \leftrightarrow u$ symmetry and the exact results obtained from MB techniques, the evaluation of the master integrals in the threshold domain requires a different strategy.

However, before we discuss our solution to this problem in detail let us briefly address the error estimate for the integration output. Since we have derived two independent sets of boundary conditions, the most natural method of quantifying the numerical precision of our results is a comparison of the corresponding phase space grids. Moreover, we have performed the integration on different elliptic contours as well as in different hemispheres of the complex $\widetilde{m}$-$\tilde{t}$-space (see Fig. 3.11). As previously explained, for a subset of master integrals it was also possible to estimate the overall precision by explicitly checking the equality under $t \leftrightarrow u$ exchange. The result of these analyses is a relative error induced by the numerical integration of about 10^{-8} for points close to the singularities of the Jacobi matrices whereas in the regular parts of phase space it is usually further suppressed by several orders of magnitude. While this superb precision can be interpreted as a clear proof for the numerical correctness of our implementation, it does not rule out the possibility that the numerical values themselves, despite their high accuracy, are erroneous. As an additional cross-check we therefore compared our findings to the master- integral results obtained with SecDec. The major advantage of such a comparison is that it does not only represent a valuable check of the numerical integration routine itself but also of the boundary conditions determined in the previous step of the calculation. Naturally, this procedure does not cover the entire master basis but for those integrals that are assessable by this alternative evaluation method we find full agreement within the provided numerical precision.

Threshold expansions

As could have been anticipated from the discussion of threshold enhancements in section 3.1, in the limit $\widetilde{m} \to \frac{1}{4}$ the integration routine suffers from considerable numerical instabilities. They are mainly induced by the singular Coulomb contributions, which for the individual masters may be even more pronounced, in some cases reaching down to $\mathcal{O}\left(\frac{1}{\beta^9}\right)$. In consequence, the integration algorithm ultimately fails to converge for values $\widetilde{m} > \frac{99}{400}$ ($\beta < \frac{1}{10}$) forcing us to employ a different approach in this region of phase space. Motivated by the successful application of power-logarithmic expansions in the high-energy regime, we decide to pursue a similar strategy also in the threshold limit, namely determine a general solution for the master basis in terms of a series in β and subsequently fix the unknown boundary coefficients through a suitable matching condition.

Fortunately, the latter can be obtained without any additional computational effort since the radius of convergence of the threshold expansion is sufficiently large such that it is valid well beyond $\beta = \frac{1}{10}$ as shown in Fig. 3.14. Thus, we are able to match directly to the high-precision results of the numerical integration in the intermediate range where both the expansion and the numerical solution provide reliable estimates for the true functional dependence of the

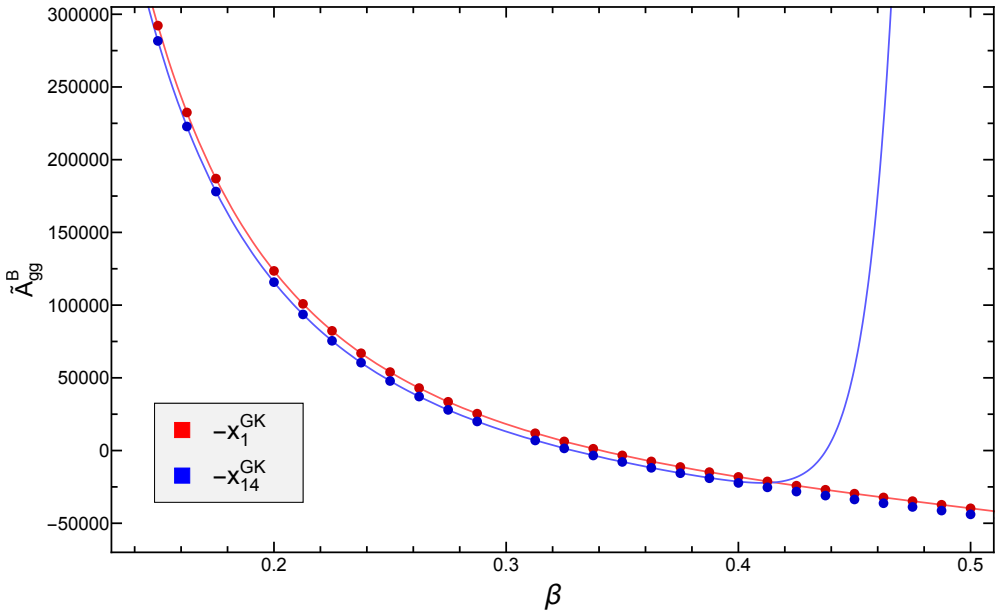

Figure 3.14: *Finite part of the bare two-loop contributions $\tilde{\mathcal{A}}^B_{gg}$ evaluated for two different values of $\cos\theta = -x_i^{GK}$ both through numerical integration of the differential equations Eq. (3.192) (dots) and a power-logarithmic series in β (lines) indicating the radius of convergence of the latter.*

master integrals. This, however, requires the determination of 42 separate power-logarithmic series of the form

$$\widetilde{M}_k(\beta, \pm x_i^{\mathrm{GK}}) = \sum_{n=n_0} \sum_{m=0}^{M} \tilde{\mathcal{K}}_k^{(n,m)}(\pm x_i^{\mathrm{GK}})\, \beta^n\, \ln^m \beta \tag{3.191}$$

in order to cover the full range of Gauss-Kronrod points. Note that due to their dependence on $\pm x_i^{\mathrm{GK}} \in \mathbb{R}$ the coefficients $\tilde{\mathcal{K}}_k^{(n,m)}$ are in general real-valued now, which may in practice lead to considerable numerical complications associated with the finite number of digits involved in the calculation. We therefore had to modify our original implementation of the algorithm that determines the power-logarithmic solutions to be able to handle floating point numbers of arbitrary precision.

Yet, before we can apply our novel solution routine to the system of differential equations, we have to express it in terms of β rather than $\widetilde{m}$ or $\tilde{t}$. To this end, we have to take into account that both of the latter variables depend on the velocity such that the new Jacobian is given as a combination of the original matrices $\tilde{J}_{kl}^{(\widetilde{m})}$ and $\tilde{J}_{kl}^{(\tilde{t})}$,

$$\begin{aligned}
\frac{d}{d\beta}\widetilde{M}_k(\beta, \pm x_i^{\mathrm{GK}}) &= \left(\frac{\partial \tilde{t}}{\partial \beta}\frac{\partial \widetilde{M}_k}{\partial \tilde{t}} + \frac{\partial \widetilde{m}}{\partial \beta}\frac{\partial \widetilde{M}_k}{\partial \widetilde{m}}\right)(\beta, \pm x_i^{\mathrm{GK}}) \\
&= \left(\frac{\mp x_i^{\mathrm{GK}}}{1 \mp x_i^{\mathrm{GK}}\beta}\,\tilde{J}_{kl}^{(\tilde{t})} - \frac{2\beta}{1-\beta^2}\,\tilde{J}_{kl}^{(\widetilde{m})}\right)(\beta, \pm x_i^{\mathrm{GK}})\; \widetilde{M}_l(\beta, \pm x_i^{\mathrm{GK}}) \\
&\equiv \tilde{J}_{kl}^{(\beta)}(\beta, \pm x_i^{\mathrm{GK}})\; \widetilde{M}_l(\beta, \pm x_i^{\mathrm{GK}})\,.
\end{aligned} \tag{3.192}$$

In order to allow for an accurate description of the master basis in the threshold limit, we solve this equation with an ansatz for $\widetilde{M}_k(\beta, \pm x_i^{\mathrm{GK}})$ up to $\mathcal{O}(\beta^{39})$, the result displaying some peculiar features that were a priori unexpected. First of all, it involves extremely high inverse powers of β reaching as far as $\mathcal{O}\left(\frac{1}{\beta^{12}}\right)$, which goes significantly beyond the known Coulomb behavior of the renormalized two-loop amplitude. Furthermore, the power-logarithmic expansion for certain master integrals contains rational powers of the velocity of type $\beta^{\frac{n}{4}}$ ($n \in \mathbb{Z}$), which do, however, not survive the consecutive matching procedure. Still, they have to be thoroughly accounted for to guarantee that $\widetilde{M}_k(\beta, \pm x_i^{\mathrm{GK}})$ assumes the most general form consistent with Eq. (3.192), which apart from the explicit evaluation of the new system of differential equations through resubstitution represents the most important cross-check of our findings.

For the subsequent matching procedure we choose two different velocity values $\beta \in \left\{\frac{1}{10}, \frac{1}{8}\right\}$ allowing for an estimate of the numerical precision through a comparison of the thus obtained boundary coefficients. In addition to that we also vary the expansion depth of the power-logarithmic series to assess the impact of missing higher-order contributions. Due to large cancellation effects such an analysis, however, only makes sense at the amplitude level, i. e. after substituting the matched results back into the bare expression $\tilde{\mathcal{A}}_{gg}^{B}$. It turns out that the corresponding error estimate depends crucially on the actual value of x_i^{GK} revealing an additional problem concerning the scattering angles close to $\pi/2$. In this case the numerical precision of the matching conditions is not sufficient to cope with these sizable cancellations rendering the resulting predictions unusable. Indeed, by taking a look at the singularity structures in Fig. 3.13 the origin of these numerical instabilities can be easily identified. For values of $\widetilde{m}$ close to threshold there are additional spurious divergences in the vicinity of $\cos\theta \approx 0$, which ultimately spoil the attainable precision of our approach.

There exists, however, a simple solution to this problem that enables us to recover the missing points on the phase space grid. Since the functional dependence of the amplitudes $\tilde{\mathcal{A}}_{ij}^{B}$ on the scattering angle is very smooth, as can be explicitly checked for the results with $\beta \geq \frac{1}{10}$, it may be well described polynomially (otherwise the Gauss-Kronrod integration rule would not be applicable). Hence, we can restore the full kinematic dependence to sufficiently high precision by performing a fit to the available grid points for fixed value of β. The corresponding interpolation function can be constructed from Legendre polynomials and, after the determination of the free parameters, is valid over the entire $\cos\theta$-range. The resulting relative precision, estimated from varying the order of the Legendre polynomials in the fitting ansatz as well as from the use of different matching points and expansion depths discussed above, is $\geq 10^{-7}$ which is by far enough for any practical application. Note, however, that for the determination of the hard matching coefficients we performed a separate fit where we kept the β-dependence explicit albeit restricted to the leading threshold behavior allowing for an even higher accuracy.

Results for the two-loop virtual corrections

Once we have evaluated the master basis over the entire phase space grid, we are able to derive explicit results for the renormalized two-loop amplitudes $\tilde{\mathcal{A}}_{ij}^{(n_f)}$. As an example we show in Tab. 3.5 the numerical values of the color coefficients defined in Eq. (3.172) computed at the

	ϵ^{-4}	ϵ^{-3}	ϵ^{-2}	ϵ^{-1}	ϵ^{0}
$A^{(g)}$	10.74942557	18.69389337	−156.8237244	262.1482588	12.72180680
$B^{(g)}$	−21.28599123	−55.99039551	−235.0412564	1459.833288	−509.6019155
$C^{(g)}$		−6.199051597	−68.70297402	−268.1060373	804.0981895
$D^{(g)}$			94.08660818	−130.9619794	−283.3496755
$E_l^{(g)}$		−12.54099650	18.20646589	27.95708293	−112.6060988
$E_h^{(g)}$			0.012907497	11.79259573	−47.68412574
$F_l^{(g)}$		24.83365643	−26.60868620	−50.75380859	125.0537955
$F_h^{(g)}$			0.0	−23.32918072	132.5618962
$G_l^{(g)}$			3.099525798	67.04300456	−214.1081462
$G_h^{(g)}$				0.0	−179.3374874
$H_l^{(g)}$			2.388761238	−5.452031425	3.632861953
$H_{lh}^{(g)}$				−0.004302499	−3.945712447
$H_h^{(g)}$					0.00439856
$I_l^{(g)}$			−4.730220272	10.81032548	−7.182940516
$I_{lh}^{(g)}$				0.0	7.780900470
$I_h^{(g)}$					0.0
$A^{(q)}$	0.22625	1.391733154	−2.298174307	−4.145752449	17.37136599
$B^{(q)}$	−0.4525	−1.323646320	8.507455541	6.035611156	−35.12861106
$C^{(q)}$	0.22625	−0.06808683395	−18.00716652	6.302454931	3.524044913
$D_l^{(q)}$		−0.22625	0.2605057339	−0.7250180282	−1.935417247
$D_h^{(q)}$			0.5623350684	0.1045606449	−1.704747998
$E_l^{(q)}$		0.22625	−0.3323207300	7.904121951	2.848697837
$E_h^{(q)}$			−0.5623350684	4.528240788	12.73232424
$F_l^{(q)}$					−1.984228442
$F_{lh}^{(q)}$					−2.442562819
$F_h^{(q)}$					−0.07924540546

Table 3.5: *Values of the color coefficients defined in Eq. (3.172) of the renormalized two-loop virtual amplitudes with $n_f = n_l + n_h$ active flavors for the gluon fusion and quark annihilation channels at $\tilde{m} = \frac{1}{5}$, $\tilde{t} = \frac{9}{20}$ with $\mu_R = m_t$. The gray shaded values are only known numerically, whereas the remaining ones have been obtained analytically in Refs. [564, 575–577, 656, 657].*

benchmark point $(\widetilde{m}, \tilde{t}) = (\frac{1}{5}, \frac{9}{20})$, which allows for a direct comparison with the analytical results provided in Refs. [575–577,656,657] for the leading-color and various closed fermion-loop contributions. We find full numerical agreement within the previously quoted error estimates, which constitutes a strong validation of the computational methods employed in the course of this analysis. Note that the pole structure for the individual color coefficients may also be derived fully analytically [564] with the help of Eq. (3.11) relying solely on lower-order 2-to-2 top-quark amplitudes. Since our approach does not differentiate between singular and finite contributions, which becomes particularly evident in the systems of coupled differential equations Eq. (3.180), Eq. (3.181) and Eq. (3.192) that mix various orders of the ϵ-expansion, the prediction of the correct pole structure serves as an important check for the correctness of our implementation. Apart from that, there exists an additional result for $\tilde{\mathcal{A}}_{ij}^{(n_f)}$ in the high-energy limit [644,645] based on a conceptually entirely different evaluation method that allows for a further test of the Mellin-Barnes results derived in step one of our calculation. Unfortunately, this independent analysis incorporates only the leading $t, u \gg m_t^2$ behavior and, thus, does not provide a comparison for the full set boundary conditions that enter the numerical integration. For the accessible boundaries we, however, find full agreement.

Since in our evaluation of the NNLO partonic cross sections we (at higher-loop level) choose to work with finite remainders rather than renormalized amplitudes, we still have to apply IR renormalization. This may be accomplished by first decoupling the heavy degrees of freedom and then decomposing the resulting expressions according to

$$\begin{aligned}\tilde{\mathcal{A}}_{ij}^{(n_l)} &= \langle \mathcal{M}_{ij}^{(0)} | 2\,\mathrm{Re} Z_{\mathcal{F}}^{t\bar{t},\,(2)} | \mathcal{M}_{ij}^{(0)} \rangle + 2\,\mathrm{Re}\,\langle \mathcal{M}_{ij}^{(0)} | Z_{\mathcal{F}}^{t\bar{t},\,(1)} | \mathcal{F}_{ij}^{(1)} \rangle \\ &+ 2\,\mathrm{Re}\,\langle \mathcal{M}_{ij}^{(0)} | \mathcal{F}_{ij}^{(2)} \rangle \end{aligned} \tag{3.193}$$

where the two-loop finite remainder is conveniently normalized such that the subsequent integration over the scattering angle corresponds directly to the respective partonic cross section contribution

$$\tilde{F}_{ij} = \tilde{F}_{ij}^{(0)} + n_l\,\tilde{F}_{ij}^{(1)} + n_l^2\,\tilde{F}_{ij}^{(2)} \equiv \frac{1}{s_i s_j c_i c_j}\,\frac{\beta(1-\beta^2)}{128\pi}\,2\,\mathrm{Re}\,\langle \mathcal{M}_{ij}^{(0)} | \mathcal{F}_{ij}^{(2)} \rangle\ . \tag{3.194}$$

The pole structure of the two-loop virtual corrections is then completely encoded in the remaining terms proportional to $Z_{\mathcal{F}}^{t\bar{t},\,(n)}$ that are at most of NLO complexity and can hence be, in principle, determined in analytical form.

After evaluating $\tilde{F}_{ij}$ on the entire phase space grid the resulting numerical expressions may be used to construct interpolation functions for $\tilde{F}_{ij}^{(n)}$ that allow for an extension of the two-loop analysis to arbitrary kinematics. The result is depicted in Fig. 3.15 revealing the true complexity of these double-virtual contributions. Apart from the overall smoothness of the functional dependence, which serves as a further justification for the validity of the subsequent Gauss-Kronrod integration, one can observe some distinct kinematic features already present at lower orders in perturbation theory. As required by parity conservation the result for the

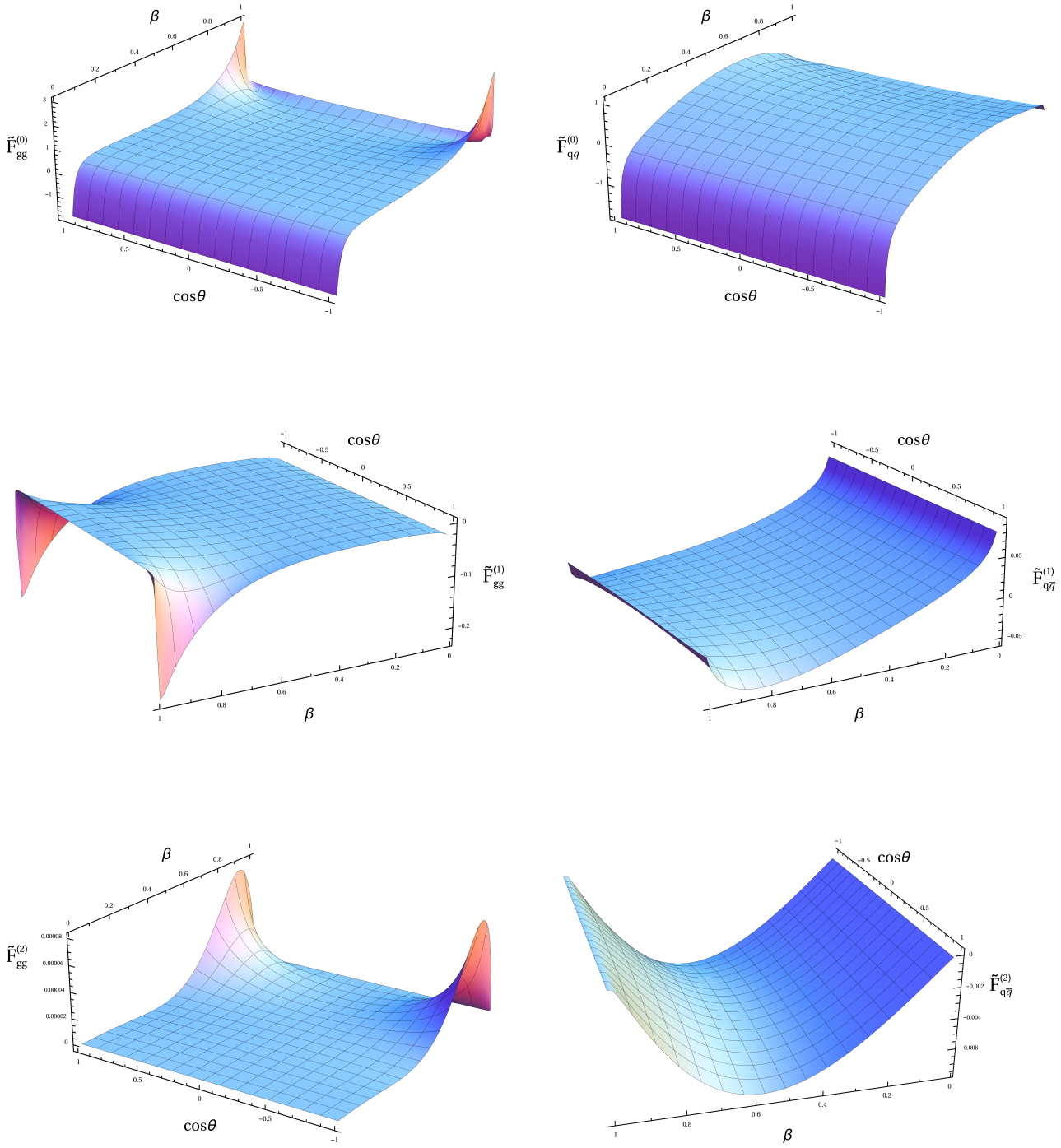

Figure 3.15: *Finite remainder functions of the gluon-fusion (left) and quark-annihilation (right) channel for different powers of n_l normalized according to Eq. (3.194).*

gluon fusion channel is symmetric in $\cos\theta$ whereas the quark annihilation channel displays a slight tendency towards positive values of the scattering angle in the intermediate β-range and negative values in the high-energy regime. In the threshold regime both $\tilde{F}_{q\bar{q}}^{(0)}$ and $\tilde{F}_{gg}^{(0)}$ show the characteristic $1/\beta$ drop associated with potential-gluon exchange that will eventually be compensated by the corresponding partonic fluxes. As anticipated from our discussion of the leading threshold enhancements in section 3.1, for higher powers of n_l this behavior is less pronounced. Furthermore, in the gluonic results there exist additional enhancements close to the corners of the physical phase space at $\beta \approx 1$ and $\cos\theta \approx \pm 1$. This effect can be traced back to the LO spectrum in Fig. 2.6 as it involves the same type of t/u-channel heavy-quark exchange albeit dressed with additional loop corrections that further increase the divergent behavior. In consequence, the Gauss-Kronrod integration in this part of phase space will be less accurate, which is, however, irrelevant in practical applications since on the cross section level the high-energy regime is dominated by real radiation. For the remainder of the phase space the Gauss-Kronrod rule yields very precise results with a relative error of order 10^{-5}, which can be safely neglected considering the other sources of uncertainty entering the NNLO cross section analysis.

Another important aspect of the two-loop finite remainders is their use in the determination of the dominant threshold behavior, in particular the hard matching coefficients that cannot be predicted from soft-gluon or Coulomb resummation. To this end, we decompose $\tilde{F}_{ij}$ in terms of irreducible representations of the final-state heavy-quark system, which may, as usual, be achieved with the help of the projection operators defined in Eq. (2.46) and Eq. (2.47). The $\beta \to 0$ expansion can then be obtained by employing the results of the explicit Legendre fit described above such that the color-projected finite remainders $\tilde{F}_{ij}^{\tilde{\mathbf{R}}}$ at threshold read

$$
\begin{aligned}
\tilde{F}_{q\bar{q}}^{\mathbf{8}}(\beta,\cos\theta) \overset{\beta\to 0}{=}\; & \frac{1}{4}\,\frac{d\bar{\sigma}_{q\bar{q}}^{(0)}}{d\cos\theta}\left(C_F-\frac{C_A}{2}\right) \\
&\times\Bigg\{-\frac{1}{\beta^2}\left(C_F-\frac{C_A}{2}\right)\left[\ln^2\beta+2\,\ln 2\,\ln\beta+\ln^2 2-\frac{\pi^2}{12}\right]+\frac{1}{\beta}\Bigg[\Bigg(C_A\left(-\frac{31}{6}+2\,\ln 2\right) \\
&\quad +C_F\,(3-4\,\ln 2)+\frac{4}{3}\,n_l\Bigg)\ln\beta+C_A\left(\frac{131}{18}-\frac{43}{6}\,\ln 2+2\,\ln^2 2-\frac{\pi^2}{4}\right) \\
&\quad +C_F\left(-8+6\,\ln 2-6\,\ln^2 2+\frac{7\pi^2}{12}\right)-\frac{8}{9}\,n_h+n_l\left(-\frac{10}{9}+2\,\ln 2\right)\Bigg] \\
&\quad -\frac{1}{2}\left(C_F-\frac{C_A}{2}\right)(3+\cos^2\theta)\ln^2\beta+\left(C_A\left(-\frac{41}{12}+\frac{3}{2}\,\ln 2\right)+C_F\left(-\frac{7}{6}-3\,\ln 2\right)\right. \\
&\quad \left.+3\,n_h+\left(-2\,C_A+\frac{16}{3}\,C_F\right)\cos\theta+\frac{1}{2}\left(C_F-\frac{C_A}{2}\right)(1-2\ln 2)\cos^2\theta\right)\ln\beta\Bigg\} \\
&+\frac{\beta}{512\pi}\,\frac{1}{N_c^2}\left(\Delta_{q\bar{q}}^{(\mathbf{8},0)}+\Delta_{q\bar{q}}^{(\mathbf{8},1)}\cos\theta+\Delta_{q\bar{q}}^{(\mathbf{8},2)}\cos^2\theta\right)
\end{aligned}
\tag{3.195}
$$

$$
\begin{aligned}
\tilde{F}_{gg}^{\mathbf{1}}(\beta,\cos\theta) &\overset{\beta\to 0}{=} \frac{1}{4}\,\frac{d\bar{\sigma}_{gg,\mathbf{1}}^{(0)}}{d\cos\theta}\,C_F \\
&\times\Bigg\{-\frac{1}{\beta^2}C_F\left[\ln^2\beta+2\,\ln 2\,\ln\beta+\ln^2 2-\frac{\pi^2}{12}\right]+\frac{1}{\beta}\Bigg[\left(C_A\left(-\frac{11}{3}-4\,\ln 2\right)+\frac{2}{3}\,n_l\right)\ln\beta \\
&\quad +C_A\left(\frac{49}{18}-\frac{11}{3}\,\ln 2-6\,\ln^2 2+\frac{\pi^2}{3}\right)+C_F\left(-5+\frac{\pi^2}{4}\right)+n_l\left(-\frac{5}{9}+\frac{2}{3}\,\ln 2\right)\Bigg] \\
&\quad -4\,C_F\,\ln^2\beta-\left(4\,C_A+C_F\,(4+8\ln 2)+C_F\,\cos^2\theta\right)\ln\beta\Bigg\} \\
&+\frac{\beta}{512\pi}\,\frac{1}{(N_c^2-1)^2}\,\left(\Delta_{gg}^{(\mathbf{1},0)}+\Delta_{gg}^{(\mathbf{1},2)}\cos^2\theta\right)
\end{aligned}
$$

$$
\begin{aligned}
\tilde{F}_{gg}^{\mathbf{8_S}}(\beta,\cos\theta) &\overset{\beta\to 0}{=} \frac{1}{4}\,\frac{d\bar{\sigma}_{gg,\mathbf{8_S}}^{(0)}}{d\cos\theta}\,\left(C_F-\frac{C_A}{2}\right) \\
&\times\Bigg\{-\frac{1}{\beta^2}\left(C_F-\frac{C_A}{2}\right)\left[\ln^2\beta+2\,\ln 2\,\ln\beta+\ln^2 2-\frac{\pi^2}{12}\right]+\frac{1}{\beta}\Bigg[\left(C_A\left(-\frac{11}{3}-2\,\ln 2\right)\right. \\
&\quad \left.+\frac{2}{3}\,n_l\right)\ln\beta+C_A\left(\frac{67}{18}-\frac{8}{3}\,\ln 2-4\,\ln^2 2+\frac{5\pi^2}{24}\right)+C_F\left(-5+\frac{\pi^2}{4}\right) \\
&\quad +n_l\left(-\frac{5}{9}+\frac{2}{3}\,\ln 2\right)\Bigg]-4\left(C_F-\frac{C_A}{2}\right)\ln^2\beta-\Bigg(C_A\,(2-4\,\ln 2)+C_F\,(4+8\,\ln 2) \\
&\quad +\left(C_F-\frac{C_A}{2}\right)\cos^2\theta\Bigg)\ln\beta\Bigg\} \\
&+\frac{\beta}{512\pi}\,\frac{1}{(N_c^2-1)^2}\,\left(\Delta_{gg}^{(\mathbf{8_S},0)}+\Delta_{gg}^{(\mathbf{8_S},2)}\cos^2\theta\right)
\end{aligned}
$$

$$
\begin{aligned}
\tilde{F}_{gg}^{\mathbf{8_A}}(\beta,\cos\theta) &\overset{\beta\to 0}{=} \frac{1}{4}\,\frac{d\bar{\sigma}_{gg,\mathbf{8_A}}^{(0)}}{d\cos\theta}\,\left(C_F-\frac{C_A}{2}\right)^2 \\
&\times\frac{1}{\beta^2}\left[-\ln^2\beta+2\,(1-\ln 2)\ln\beta+\ln 2\,(2-\ln 2)+\frac{\pi^2}{12}\right]
\end{aligned}
\tag{3.196}
$$

while the corresponding Born contributions are given by

$$
\frac{d\bar{\sigma}_{q\bar{q}}^{(0)}}{d\cos\theta}=\frac{1}{N_c^2}\,\frac{\beta}{512\pi}\,\left\langle\mathcal{M}_{q\bar{q}}^{(0)}|\mathcal{M}_{q\bar{q}}^{(0)}\right\rangle\Big|_{\beta^0}=\frac{\pi\,\beta}{16}\,\frac{N_c^2-1}{N_c^2}
\tag{3.197}
$$

$$\frac{d\bar{\sigma}^{(0)}_{gg,\,\mathbf{1}}}{d\cos\theta} = \frac{1}{(N_c^2-1)^2}\,\frac{\beta}{512\pi}\,\langle\mathcal{M}^{(0)}_{gg,\,\mathbf{1}}|\mathcal{M}^{(0)}_{gg,\,\mathbf{1}}\rangle\,\Big|_{\beta^0} = \frac{\pi\,\beta}{8}\,\frac{1}{N_c\,(N_c^2-1)}$$

$$\frac{d\bar{\sigma}^{(0)}_{gg,\,\mathbf{8_S}}}{d\cos\theta} = \frac{1}{(N_c^2-1)^2}\,\frac{\beta}{512\pi}\,\langle\mathcal{M}^{(0)}_{gg,\,\mathbf{8_S}}|\mathcal{M}^{(0)}_{gg,\,\mathbf{8_S}}\rangle\,\Big|_{\beta^0} = \frac{\pi\,\beta}{16}\,\frac{N_c^2-4}{N_c\,(N_c^2-1)}$$

$$\frac{d\bar{\sigma}^{(0)}_{gg,\,\mathbf{8_A}}}{d\cos\theta} = \frac{1}{(N_c^2-1)^2}\,\frac{\beta}{512\pi}\,\langle\mathcal{M}^{(0)}_{gg,\,\mathbf{8_A}}|\mathcal{M}^{(0)}_{gg,\,\mathbf{8_A}}\rangle\,\Big|_{\beta^2} = \frac{\pi\,\beta^3}{16}\,\frac{N_c}{N_c^2-1}\,\cos^2\theta\,. \tag{3.198}$$

The constant coefficients $\Delta_{ij}^{(\tilde{\mathbf{R}},k)}$ are only known numerically and can be found in appendix C. Note that our evaluation strategy for the two-loop virtual corrections may only provide numerical results for the singular terms in $\tilde{F}_{ij}^{\tilde{\mathbf{R}}}$. They have, however, been thoroughly checked against the analytic expressions quoted above, which can be obtained with the methods described in section 3.1.1. Such a comparison represents a highly non-trivial test of our entire evaluation strategy as it takes into account every single aspect of the numerical analysis explained above. In consequence, we can now safely combine our findings with the other parts of the NNLO calculation to derive actual physical predictions.

3.5 Results for the partonic and hadronic cross sections

In order to derive theory predictions for the NNLO partonic cross sections $\hat{\sigma}_{ij}^{\mathrm{NNLO}}$ and subsequently $\sigma_{t\bar{t}}^{\mathbf{tot}}$, we employ the following strategy. At the parton level we specify a set of discrete evaluation points in the interval $\beta_i \in [0,1]$ (defined in Eq. (3.182)), which form the basis of a numerical fit that allows for a reliable theoretical description of $t\bar{t}$ production for arbitrary velocity values. Treating the scale-controlling terms separately , the functions $\hat{\sigma}_{ij}^{(2,0,0)}$ can be evaluated with the methods presented in sections 3.2-3.4 where we choose to keep only the dependence on the number of light flavors explicit while otherwise working completely numerically such that

$$\hat{\sigma}_{ij}^{(2,0,0)}(\beta) = F_{ij}^{(0)}(\beta) + F_{ij}^{(1)}(\beta)\,n_l + F_{ij}^{(2)}(\beta)\,n_l^2\,. \tag{3.199}$$

Note that this is the most general decomposition whereas in practice the maximum power of n_l hinges on the particular channel under consideration, i. e. $F_{ij}^{(1,2)}$ may vanish for certain initial-state configurations ij. The contributions from collinear renormalization, needed to obtain finite cross section results, are also derived in a fully numerical fashion, which is fairly straightforward using Eq. (2.31) and the definition of the convolution integrals in Eq. (2.3). Since we choose to work in CDR, the corresponding LO and NLO cross sections entering the collinear counterterms have to be, in general, provided to higher orders in ϵ increasing the complexity of the respective integrand structures. This does, however, not apply to the one-loop amplitudes as the decomposition into singular terms and finite remainders renders the

inclusion of these $\mathcal{O}(\epsilon)$ parts redundant as explained in section 3.3. Hence, in our calculation we treat the NLO real and virtual corrections separately allowing for an explicit numerical check of this property.

After combining the individual pieces of the partonic cross sections we observe a complete cancellation of IR singularities well within the numerical precision of our evaluation. This may be regarded as a strong test for the correctness of our approach since the various contributions have been computed with conceptually very different methods. The remaining finite corrections can then be employed for the determination of the partonic interpolation functions in Eq. (3.199). The resulting precision, on the one hand, depends on the error of the individual β-points and, on the other hand, on the chosen parametrization for $F_{ij}^{(n)}$ entering the fit, both of which are discussed separately for each channel below. Let us stress, however, that our predictions are in general rather limited by the precision of the discrete values $F_{ij}^{(n)}(\beta_i)$ than the quality of subsequent fit, the most dominant contributions coming from the double-real and real-virtual corrections. To further reduce the numerical impact of these components, we include in our calculation a common normalization factor $\beta^{10\epsilon}$, which shifts the dominant threshold logarithms of β to parts of the cross section that are under better numerical control. Alternatively, one could also increase the statistics of the MC integration of the real-emission matrix elements. This would, however, cause additional unnecessary computational costs and we thus settle for the first option. Finally, the scale dependence can be restored by using the well-known LO and NLO cross section results presented in section 2.3 and, for the non-trivial parts of $\hat{\sigma}_{ij}^{(2,k,l)}$ $(k,l>0)$ involving convolutions, the previously derived collinear counterterms since these contributions are directly related.

In the following we now discuss the partonic results for the different channels contributing to NNLO top-quark pair production as well as their implications for the total cross section. Afterwards we examine the perturbative behavior of $\sigma_{t\bar{t}}^{\mathbf{tot}}$, the different sources of uncertainty entering the theoretical predictions and the phenomenological impact of going to full NNLO. Note, however, that some of the possible applications of $\sigma_{t\bar{t}}^{\mathbf{tot}}$, in particular the use in α_s and top-mass measurements as well as PDF analyses, have already been presented in section 1.2.1 and 1.3.1 and we therefore refer the reader to these parts of the thesis for further details.

3.5.1 The qg- and $q\tilde{q}$-channels

The NNLO results for the qg- and $q\tilde{q}$-channels have been derived in Ref. [79] and Ref. [78] respectively. As can be inferred from Eq. (2.8) and Eq. (2.9), they are both radiation-induced meaning that the final-state top-quark pair is always accompanied by additional massless partons. Consequently, the corresponding partonic cross sections vanish at threshold and the dominant contributions to $\sigma_{t\bar{t}}^{\mathbf{tot}}$ stem from intermediate and large velocities β. Note, however, that while the calculation of the former involves only double-real emissions (apart from collinear-renormalization effects), the latter, being present already at NLO, also receives virtual corrections. In order to be able to adequately constrain the high-energy behavior of $F_{ij}^{(n)}$, the general strategy described above has to be slightly modified by incorporating additional evaluation points in the fitting procedure, namely $\beta = 0.99375$ and $\beta = 0.9999$ for the qq-subchannel and $\beta = 0.99999$ for the n_l-dependent part of the qg-channel.

Moreover, the known leading high-energy behavior

$$\hat{\sigma}_{ij}^{(2,0,0)}\Big|_{\rho\to 0} \approx c_1^{ij}\ln\rho + c_0^{ij} + \mathcal{O}(\rho) \tag{3.200}$$

has been employed in the construction of a suitable fitting function[27] albeit currently only [555]

$$\begin{aligned} c_1^{qg} &= -1.689571450230512 \\ c_1^{q\tilde{q}} &= -0.4768323995789214 \end{aligned} \tag{3.201}$$

can be predicted exactly (for the analytic expressions see, for instance, Eq. (3.83)) while c_0^{ij} remains a free parameter of the fit. The corresponding parton level results are then given by [78, 79]

$$\begin{aligned} F_{qg}^{(0)} &= 28.0998\beta^2 + 24.1753\beta^3 - 12.3211\beta^5 - 49.909\beta^7 + 11.7853\beta^3\mathrm{L}_\beta + 28.6697\beta^6\mathrm{L}_\beta^2 \\ &+ \left(-1.68957 + 30.6335\rho^2\right)\mathrm{L}_\rho + \left(-9.80339\rho - 76.7407\rho^2\right)\mathrm{L}_\rho^2 - 3.82993\rho\mathrm{L}_\rho^3 \\ F_{qg}^{(1)} &= 0.363838\beta^2 - 1.44391\beta^3 + 1.1146\beta^7 - 0.309165\beta^3\mathrm{L}_\beta + 0.990057\beta^4\mathrm{L}_\beta^2 \\ &+ 0.362183\rho^2\mathrm{L}_\rho + \left(0.194867\rho + 1.57274\rho^2\right)\mathrm{L}_\rho^2 + 0.0401411\rho\mathrm{L}_\rho^3 \\ F_{qq'}^{(0)} &= c_1^{q\tilde{q}}\,\mathrm{L}_\rho - \beta^2\exp\left[-0.740558 - 23.4518\beta^2 - 0.193073\beta^3 - 5.97215\beta^4 - 0.541402\beta^5\right. \\ &+ \left. 31.8227\beta^6 + \mathrm{L}_\rho^2\left(-3.29162\rho + 15.9932\rho^2\right) + \mathrm{L}_\rho\left(-21.3725\rho - 11.1642\rho^2 + 8.64746\rho^3\right)\right] \\ F_{q\bar{q}'}^{(0)} &= c_1^{q\tilde{q}}\,\mathrm{L}_\rho - \beta^2\exp\left[-0.740572 - 31.2117\beta^2 - 0.31495\beta^3 + 15.8601\beta^4 - 1.64639\beta^5\right. \\ &+ \left. 18.9767\beta^6 + \mathrm{L}_\rho^2\left(-3.16565\rho + 12.3828\rho^2\right) + \mathrm{L}_\rho\left(-19.6977\rho - 16.1386\rho^2 + 4.17707\rho^3\right)\right] \\ F_{qq}^{(0)} &= c_1^{q\tilde{q}}\,\mathrm{L}_\rho - \beta^2\exp\left[-0.740558 - 22.8129\beta^2 - 0.191648\beta^3 - 6.58031\beta^4 - 0.537669\beta^5\right. \\ &+ \left. 31.7872\beta^6 + \mathrm{L}_\rho^2\left(-3.25313\rho + 15.8988\rho^2\right) + \mathrm{L}_\rho\left(-21.0783\rho - 10.8176\rho^2 + 8.64557\rho^3\right)\right] \end{aligned}$$

where $\mathrm{L}_\rho \equiv \ln\rho$, $\mathrm{L}_\beta \equiv \ln\beta$ and we have kept explicit the various sub-processes contributing to the $q\tilde{q}$-channel. In Fig. 3.16 these functions have been plotted together with the discrete results from the calculations at fixed velocity. Apart from the fact that the shape of these curves reproduces the expected functional dependence in the threshold and high-energy limits, it can be seen that they are in good agreement with the computed data points, which reflects the excellent quality of the derived interpolating functions. Only for small values of β one can observe larger deviations between the fits and the original evaluations compared to the respective numerical uncertainty. This is also the reason why for the quark-gluon channel Eq. (3.202) does not reproduce the correct threshold behavior specified in Eq. (3.83). Note, however, that the absolute size of these deviations as well as of the partonic cross sections themselves is negligible for this part of the spectrum, especially when considering the additional screening effect of the partonic fluxes for $\beta \to 0$. Therefore, these potential discrepancies do not lead to any practical implications in phenomenological applications and, thus, may be safely ignored.

[27] It has been previously checked that an unconstrained fit reproduces the high-energy dependence in Eq. (3.200).

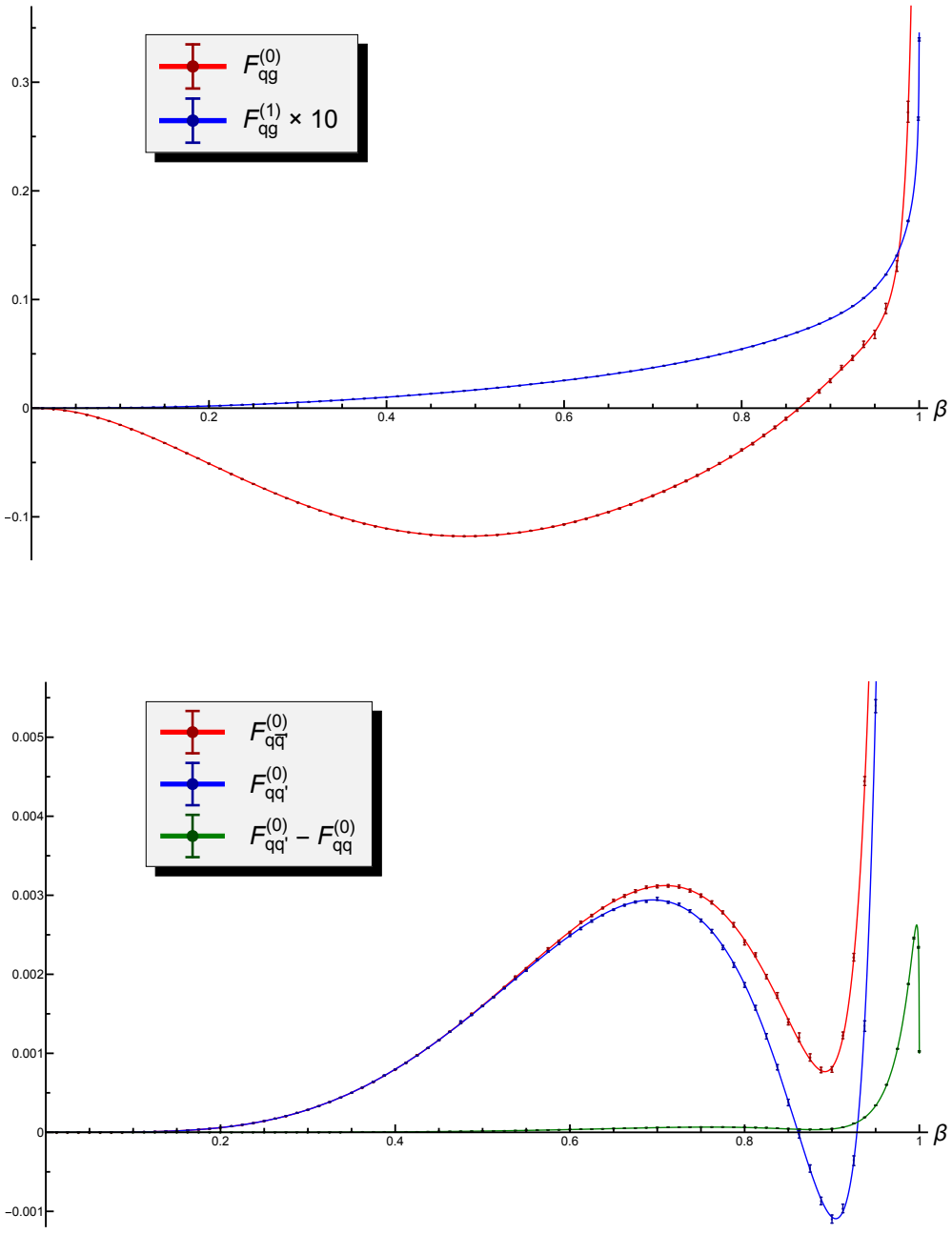

Figure 3.16: *The NNLO partonic cross section results for the qg-channel (top) and the various sub-processes contributing to the $q\tilde{q}$-channel (bottom). For an improved visibility, the n_l-dependent quark-gluon contributions have been rescaled and the qq-result is plotted in form of a difference relation with respect to the qq'-channel. For comparison, we also show the set of discrete data points that form the basis for the analytical fits where the error bars indicate the corresponding numerical uncertainty.*

Channel	c_0^{ij}	$c_0^{ij,\,\text{approx.}}$
qq'	-2.4037	$\{-1.4305, -2.4318\}$
$q\bar{q}'$	-2.4134	
qq	-2.5196	
qg	$-9.96 + 0.0345\,n_l$ $n_l = 5 \;\Rightarrow -9.79$	$\{-9.46, -13.01\}$

Table 3.6: *Results for the constant high-energy coefficients c_0^{ij} determined from a fit to full NNLO data points [78, 79] compared to the estimate from Ref. [229]. The authors of the latter publication do not provide a central prediction but, as indicated, an approximate range of values. The error from the fit cannot be accurately quantified but is potentially large.*

A straightforward application of the findings in Eq. (3.202) is the numerical determination of the yet unknown constant high-energy coefficients c_0^{ij} defined in Eq. (3.200). The result of such an analysis has been summarized in Tab. 3.6 allowing for a direct comparison with the numerical estimates derived in Ref. [229]. Note that for the qq'- and $q\bar{q}'$-subchannels the quoted values have actually not been taken from the global expression in Eq. (3.202) but extracted with a separate fit disregarding the imprecise low β region. This explains their larger deviation from the determination in the qq-subchannel despite the fact that these quantities are formally equal. The difference between these results can, hence, be regarded as a measure for the numerical uncertainty of this analysis. For the qg-channel such an error estimate is not available and one has to assume a sizable uncertainty of possibly a few tens of percent, at least on the n_l-independent part. The reason for this the position of the high-energy endpoint $\beta = 0.999$ entering the corresponding $F_{qg}^{(0)}$ fit that does not lie close enough to the region where the expansion Eq. (3.200) dominates. Shifting the endpoint as has been done for $F_{qg}^{(1)}$, however, involves a tremendous computational effort and, thus, this potentially more accurate analysis has been temporarily suspended. Nevertheless, one finds good agreement with the results in Ref. [229] obtained by completely different means which represents an important, non-trivial check for both setups. In practice, the high-energy expansion is currently irrelevant for top quarks since the available center-of-mass energies are not sufficient to advance to the region where Eq. (3.200) is valid.

Another interesting feature of the quark-gluon channel is the similarity of the size and shape of $\hat{\sigma}_{qg}^{(2,0,0)}$ to the $\mathcal{O}(\alpha_s^3)$ contributions $\hat{\sigma}_{qg}^{(1,0,0)}$. Since this channel only starts at NLO, the NNLO results are actually the first perturbative correction to this production process indicating that the next order in α_s might also be sizable. The phenomenological implications induced by these similarities may, however, only be reliably assessed by moving to the hadronic level as shown in Fig. 3.17 where we combined partonic cross sections and fluxes taking into account the relative difference in the strong coupling. At the Tevatron, NLO and NNLO contributions remain quite similar whereas at the LHC one can observe a large discrepancy between the respective curves, which will clearly lead to substantially different corrections to $\sigma_{t\bar{t}}^{\mathbf{tot}}$.

		Tevatron [pb]	LHC			
			7 TeV [pb]	8 TeV [pb]	13 TeV [pb]	14 TeV [pb]
qg	NLO	$-0.068^{+0.079}_{-0.050}$	$-0.88^{+13.77}_{-8.58}$	$-0.48^{+20.03}_{-12.53}$	$6.55^{+67.57}_{-43.09}$	$9.02^{+79.98}_{-51.17}$
	$\text{NNLO}_{\text{thr.+HE}}$	$0.040^{+0.130\ +0.009}_{-0.093\ -0.009}$	$5.77^{+6.59\ +2.71}_{-8.17\ -2.71}$	$8.11^{+8.61\ +4.13}_{-11.31\ -4.13}$	$23.68^{+20.66\ +16.26}_{-32.60\ -16.26}$	$27.36^{+24.11\ +19.67}_{-37.78\ -19.67}$
	NNLO	$-0.057^{+0.056}_{-0.068}$	$-1.82^{+4.53}_{-6.10}$	$-2.25^{+6.38}_{-8.53}$	$-3.89^{+20.21}_{-25.93}$	$-4.07^{+23.84}_{-30.34}$
$q\tilde{q}$		$0.0012^{+0.0026}_{-0.0009}$	$0.0972^{+0.4542}_{-0.0294}$	$0.1482^{+0.6988}_{-0.0448}$	$0.609^{+2.711}_{-0.184}$	$0.742^{+3.260}_{-0.224}$
$\sum_{ij}$ NNLO		$0.551^{+0.326}_{-0.129}$	$18.11^{+8.62}_{-10.88}$	$25.64^{+12.24}_{-15.85}$	$81.16^{+38.85}_{-54.59}$	$95.51^{+45.65}_{-64.90}$
$\sigma_{t\bar{t}}^{\mathbf{tot},\,\text{NNLO}}$		$7.009^{+0.259\ +0.169}_{-0.374\ -0.121}$	$167.0^{+6.7\ +4.6}_{-10.7\ -4.7}$	$239.1^{+9.2\ +6.1}_{-14.8\ -6.2}$	$788.1^{+27.1\ +14.3}_{-43.8\ -15.5}$	$933.0^{+31.8\ +16.1}_{-51.0\ -17.6}$

Table 3.7: *Theoretical predictions for the qg- and $q\tilde{q}$-channels at the Tevatron and the LHC ($m_t = 173.3\,\text{GeV}$, MSTW2008 PDFs at 68% C.L. [231]). For comparison, we also present results for the full NNLO corrections from all channels ($\sum_{ij}$) and the total cross section as well as, for the qg-channel, the NLO contributions (NNLO PDFs) and the NNLO approximations from Refs. [89,229]. The quoted uncertainties are due to the variation of renormalization and factorization scale and, for the total cross section, the choice of PDFs. The approximate result receives an additional parametrization error due to the choice of $r_{qg,x}$ as explained in section 3.1.1.*

Indeed, a quantitative comparison in Tab. 3.7 reveals the full extent of these contrary shapes allowing for the absolute size of the NNLO contributions to become even larger than the NLO term. This does, however, not necessarily signal a breakdown of the perturbative expansion as the reason for this anomalous behavior is an accidental cancellation of positive and negative cross section contributions controlled by the partonic fluxes.

With regard to the full NNLO result, i. e. with the NNLO corrections for all channels included, the impact of the NNLO qg corrections is only moderate $\lesssim 1\%$. Its value for the theoretical predictions lies, hence, rather in the reduction of the scale uncertainty, which is quite important considering the progress in the experimental determination of $\sigma_{t\bar{t}}^{\mathbf{tot}}$ along with the need for ever more precise predictions. The impact of the $q\tilde{q}$-channel on the total cross section is, on the other hand, completely negligible lying at the sub-permille level regardless of the concrete collider setup as the absolute size of the respective partonic cross sections is too small to profit from the enhanced flux factors (see Fig. 2.1). For a possible future higher-energy hadron collider or the production of lighter quarks such as bottom or charm pairs these findings may still become relevant since their theoretical description involves fluxes that are peaked towards even higher values of β, putting more emphasis on the logarithmic high-energy behavior.

Having previously stressed the importance of going to full NNLO in order to reduce the rather sizable theoretical uncertainty inherent to the approximate treatment of NNLO effects, the numerical cross section formulae in Eq. (3.202) now allow for an explicit assessment of the quality of these approximations. For the qg-channel such a comparison is shown in Fig. 3.17 where we have plotted the full NNLO result together with the predictions from Ref. [229] (see also section 3.1.1), which are based on a combination of the known threshold and

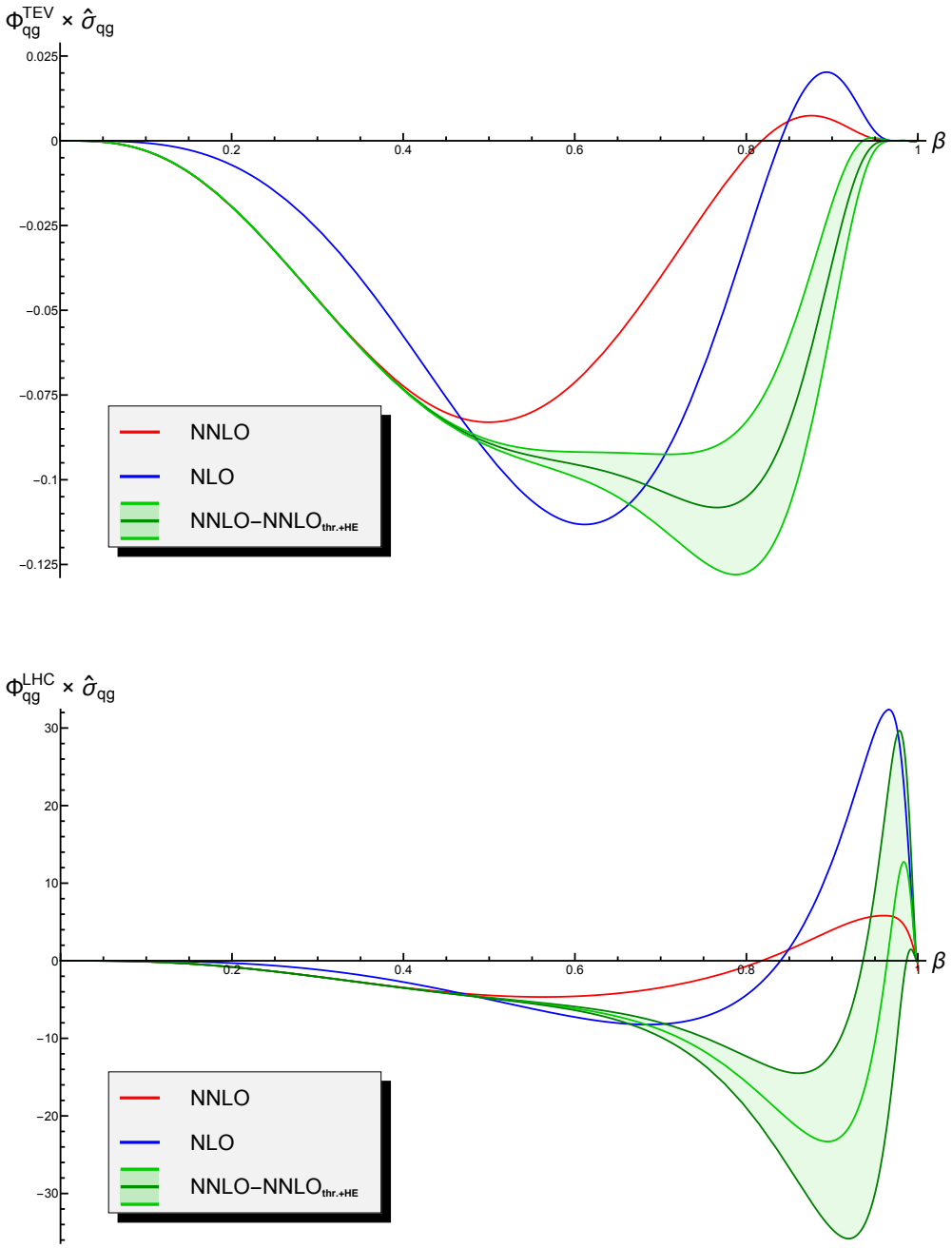

Figure 3.17: *Product of the partonic cross section and flux for the qg-channel at NLO (rescaled by $1/\alpha_s$) and NNLO in QCD for the Tevatron (top) and the LHC (bottom) at 8 TeV (NNLO PDF* MSTW2008 *at 68% C.L. [231], $\mu_R = \mu_F = m_t = 173.3\,\text{GeV}$, $n_l = 5$). For comparison, we also show the difference of the exact NNLO result with respect to the combined threshold+high-energy analysis presented in Ref. [229] where the error band is due to the choice of $r_{qg,x}$ as explained in section 3.1.1.*

high-energy behavior. It becomes obvious that, apart from the velocity ranges where these limits apply, the shape of the approximation differs quite considerably from the genuine NNLO behavior, which for the most part lies even outside the quoted error band. This suggests that there will be significant deviations in the corresponding numerical predictions for $\sigma_{t\bar{t}}^{\mathbf{tot}}$. Indeed, when inspecting the results in Tab. 3.7, one can see that the difference can amount to almost 5% at the LHC, which is comparable to the size of the total theoretical uncertainty. Considering the fact that such a large effect is already present in a subleading production mode, it confirms our original assumption that a reliable NNLO analysis requires an exact treatment of the respective partonic cross sections.

3.5.2 The quark annihilation channel

The NNLO corrections to the quark annihilation channel have actually been derived in two subsequent publications, Ref. [77] and Ref. [78], the latter containing the so-called non-singlet double-real contributions $q\bar{q} \to t\bar{t} + q\bar{q}\big|_{\mathrm{NS}}$ stemming from squared diagrams where the final-state light-quark pair is not produced by a pure gluon splitting. These contributions behave very similar to the $q\bar{q}'$ corrections discussed in the previous section and have, thus, been determined in form of a difference relation with respect to Eq. (3.202) yielding [78]

$$F_{q\bar{q},\mathrm{NS}}^{(0)} = F_{q\bar{q}'}^{(0)} + \Delta F_{q\bar{q},\mathrm{NS}}^{(0)}$$

$$\begin{aligned}\Delta F_{q\bar{q},\mathrm{NS}}^{(0)} = {} & \left(1.53647\beta^3 + 10.7411\beta^4\right)\rho - 24.3298\beta^4\rho^2 + \left(-4.50719\beta^3 + 15.4975\beta^4\right)\rho^3 \\ & + \left(2.90068\beta^3 - 4.98808\beta^4\right)\rho^4 - 1.26644\beta^{20}\mathrm{L}_\beta \\ & + \mathrm{L}_\rho^2\left(0.327143\rho - 10.7669\rho^2\right) + \mathrm{L}_\rho\left(3.86236\rho - 21.332\rho^2 + 17.4705\rho^3\right) .\end{aligned} \tag{3.202}$$

In consequence, they show the same threshold and high-energy dependence, in particular the characteristic logarithmic enhancement defined in Eq. (3.200) with $c_0^{q\bar{q}} = c_0^{q\tilde{q}}$. This, however, also means that the impact of these non-singlet corrections on $\sigma_{t\bar{t}}^{\mathbf{tot}}$ is negligible and only when taking into account the remaining $q\bar{q}$ contributions are we able to assess the true extent of going to full NNLO.

In contrast to the production modes discussed so far, the evaluation of the quark annihilation channel involves the complete spectrum of real and virtual corrections, i. e. one has to employ the entire collection of computational methods present above. Note, however, that for the contributions proportional to n_l^2 such an advanced analysis is, in fact, not necessary as they are solely associated with LO cut diagrams that contain two additional insertions of the one-loop vacuum polarization. The situation may be simplified even further by exploiting the

factorization properties of these (renormalized) one-loop subdiagrams

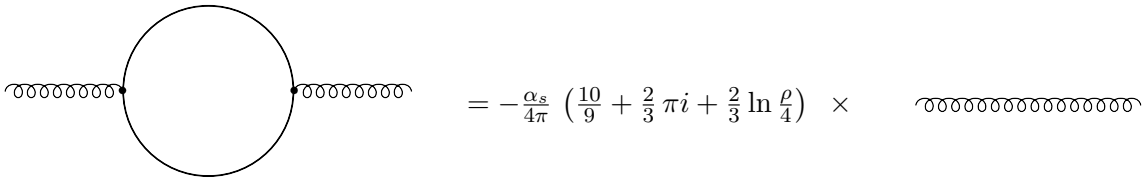

$$= -\tfrac{\alpha_s}{4\pi}\left(\tfrac{10}{9} + \tfrac{2}{3}\pi i + \tfrac{2}{3}\ln\tfrac{\rho}{4}\right) \times \tag{3.203}$$

which allows for a completely analytical derivation of these terms yielding [77]

$$F_{q\bar{q}}^{(2)} = \frac{\hat{\sigma}_{q\bar{q}}^{(0)}}{108\pi^2}\left(25 - 3\pi^2 + 30\ln\frac{\rho}{4} + 9\ln^2\frac{\rho}{4}\right) . \tag{3.204}$$

For the determination of the remaining parts of the partonic cross section, however, one has to rely on purely numerical methods except for the strict threshold region where the leading functional behavior can be inferred from soft-gluon and Coulomb resummation. Therefore, it is advantageous to separate this singular velocity dependence from $F_{q\bar{q}}^{(0,1)}$ such that the numerical results describe only the effect of going beyond the known threshold approximation:

$$\begin{aligned} F_{q\bar{q}}^{(0)} &= F_{q\bar{q},\,\beta}^{(0)} + F_{q\bar{q},\mathrm{NS}}^{(0)} + F_{q\bar{q},\,\mathrm{fit}}^{(0)} \\ F_{q\bar{q}}^{(1)} &= F_{q\bar{q},\,\beta}^{(1)} + F_{q\bar{q},\,\mathrm{fit}}^{(1)} \, . \end{aligned} \tag{3.205}$$

Note that the n_l-independent function receives additional contributions from non-singlet double-real emissions, which have been determined in a separate calculation as explained above.

The explicit expressions for the remaining functions read[28] [77]

$$\begin{aligned} F^{(0)}_{q\bar{q},\,\beta} &= \hat{\sigma}^{(0)}_{q\bar{q}}\,\big[0.0228463/\beta^2 + (-0.0333905 + 0.342203\mathrm{L}_\beta \\ &\quad -0.888889\mathrm{L}_\beta^2)/\beta + 1.58109\mathrm{L}_\beta + 6.62693\mathrm{L}_\beta^2 \\ &\quad -9.53153\mathrm{L}_\beta^3 + 5.76405\mathrm{L}_\beta^4\big] \\ F^{(1)}_{q\bar{q},\,\beta} &= \hat{\sigma}^{(0)}_{q\bar{q}}\,\big[(0.0116822 - 0.0277778\mathrm{L}_\beta)/\beta \\ &\quad +0.353207\mathrm{L}_\beta - 0.575239\mathrm{L}_\beta^2 + 0.240169\mathrm{L}_\beta^3\big] \end{aligned} \tag{3.206}$$

$$\begin{aligned} F^{(0)}_{q\bar{q},\,\mathrm{fit}} &= (-2.32235\beta + 44.3522\beta^2 - 24.6747\beta^3)\rho \\ &\quad +(2.92101\beta + 224.311\beta^2 + 21.5307\beta^3)\rho^2 \\ &\quad +(2.05531\beta + 945.506\beta^2 + 36.1101\beta^3 \\ &\quad -176.632\beta^4)\rho^3 + 7.68918\beta^4\rho^4 + \mathrm{L}_\rho(3.11129\rho \\ &\quad +100.125\rho^2 + 563.1\rho^3 + 568.023\rho^4) \\ F^{(1)}_{q\bar{q},\,\mathrm{fit}} &= (0.90756\beta - 6.75556\beta^2 + 9.18183\beta^3)\rho \\ &\quad +(-0.99749\beta + 27.7454\beta^2 - 12.9055\beta^3)\rho^2 \\ &\quad +(-0.0077383\beta - 4.49375\beta^2 + 3.86854\beta^3)\rho^3 \\ &\quad -0.380386\beta^4\rho^4 + \mathrm{L}_\rho(1.3894\rho + 6.13693\rho^2 \\ &\quad +8.78276\rho^3 - 0.0504095\rho^4) + \mathrm{L}_\rho^2\,0.137881\rho\,. \end{aligned} \tag{3.207}$$

As can be seen in Fig. 3.19, the fitted results, as expected, vanish at either end of the spectrum and describe the distinct evaluation points in the intermediate interval $\beta \in [\frac{1}{80}, \frac{999}{1000}]$ exceptionally well. Only in the high-energy limit very close to $\beta \approx 1$, i. e. beyond the last computed point, the fits become potentially unreliable, which is, however, irrelevant in practice since the numerical contribution of this region to any $t\bar{t}$ observable at the Tevatron or LHC is negligible. Moreover, this part of the partonic cross section is dominated by $F^{(0)}_{q\bar{q},\mathrm{NS}}$ such that even for the description of lighter quarks this loss of precision is probably still acceptable.

A first application of Eq. (3.207) was the determination of the constant coefficient in the NNLO threshold expansion [77]

$$C^{(2),\,\mathrm{fit}}_{q\bar{q}} = 1195.82 - 44.1841\,n_l - \frac{4}{27}\left(25 - 3\pi^2 - 60\ln 2 + 36\ln^2 2\right) n_l^2 = 867.858 \tag{3.208}$$

which, in fact, was the only reliable approximation of this quantity prior to the exact numerical evaluation in Ref. [234]. As indicated, the n_l^2 term is known fully analytically while for the other powers of n_l one has to assume a certain, non-negligible numerical uncertainty. Due to the fact that the interpolating functions display a polynomial β-dependence near threshold, this uncertainty for the complete expression ($n_l = 5$) is conservatively estimated to lie around 10%, which matches the difference to the exact result in Eq. (3.79) quite well.

[28] As explained in section 3.1.1, parts of the $\ln\beta$ corrections were missing in the original threshold analysis [230] and, hence, also in the expression for $F^{(0)}_{q\bar{q},\,\beta}$ employed in the fit. We have, however, checked that using the corrected version has only a negligible impact on $F^{(0)}_{q\bar{q},\,\mathrm{fit}}$ and, thus, quote the result given in Ref. [77].

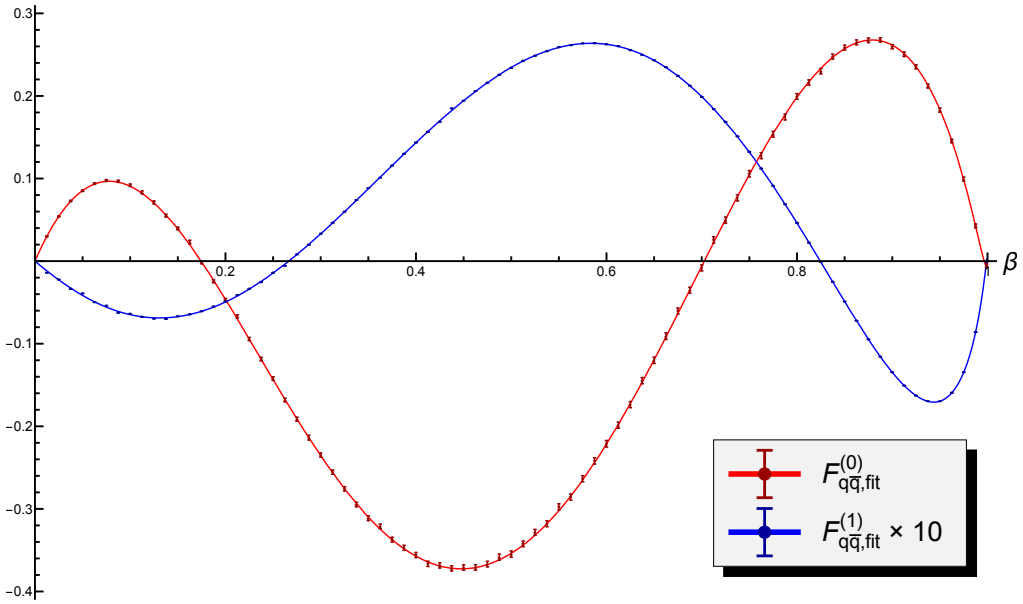

Figure 3.18: *The functions $F^{(0,1)}_{q\bar{q},\,\mathrm{fit}}$ (n_l-dependent contributions rescaled for improved visibility) that describe the full NNLO behavior beyond the known threshold approximation compared to the set of discrete data points (with numerical errors) that form the basis of the fitting formulae in Eq. (3.207).*

In order to assess the phenomenological impact of the findings in Eq. (3.207), in particular with respect to the theory predictions for $\sigma^{\mathrm{tot}}_{t\bar{t}}$, we in Fig. 3.19 show the product of the $q\bar{q}$ partonic cross section and flux at the Tevatron[29] and compare the exact result to the NNLO threshold approximation. As one can see, there are sizable corrections away from the strict threshold regime, whose relative sign, however, depends crucially on the actual values for the constant threshold coefficient and the velocity. Interestingly, using the exact threshold expansion, i. e. with $C^{(2)}_{q\bar{q}}$ set to the value given in Eq. (3.79), leads to a much worse description of the true NNLO behavior than keeping only the singular terms in $\hat{\sigma}^{(2,0,0)}_{q\bar{q}}$ as $\beta \to 0$. This implies a strong dependence of the approximate NNLO predictions on subleading effects which somewhat spoil a reliable estimate of the functional behavior for $\beta \gtrsim 0.1$. This becomes even more obvious when plotting the difference between the full and approximate results (see Fig. 3.19) revealing the presence of potentially large cancellation effects when integrating over the entire physical velocity range. This means that while the discrepancy between the approximate and exact NNLO predictions may indeed be small, this apparent agreement is entirely coincidental as it is completely controlled by the specific value for $C^{(2)}_{q\bar{q}}$ employed in the threshold analysis. Note that the situation is not improved by incorporating the known high-energy behavior into the approximate NNLO treatment as has been done in Ref. [229]. Similar to the pure threshold expansion this approach fails to adequately reproduce the true

[29] At the LHC the situation is similar but has less influence on the total cross section predictions due to the suppression by the gluon fusion channel.

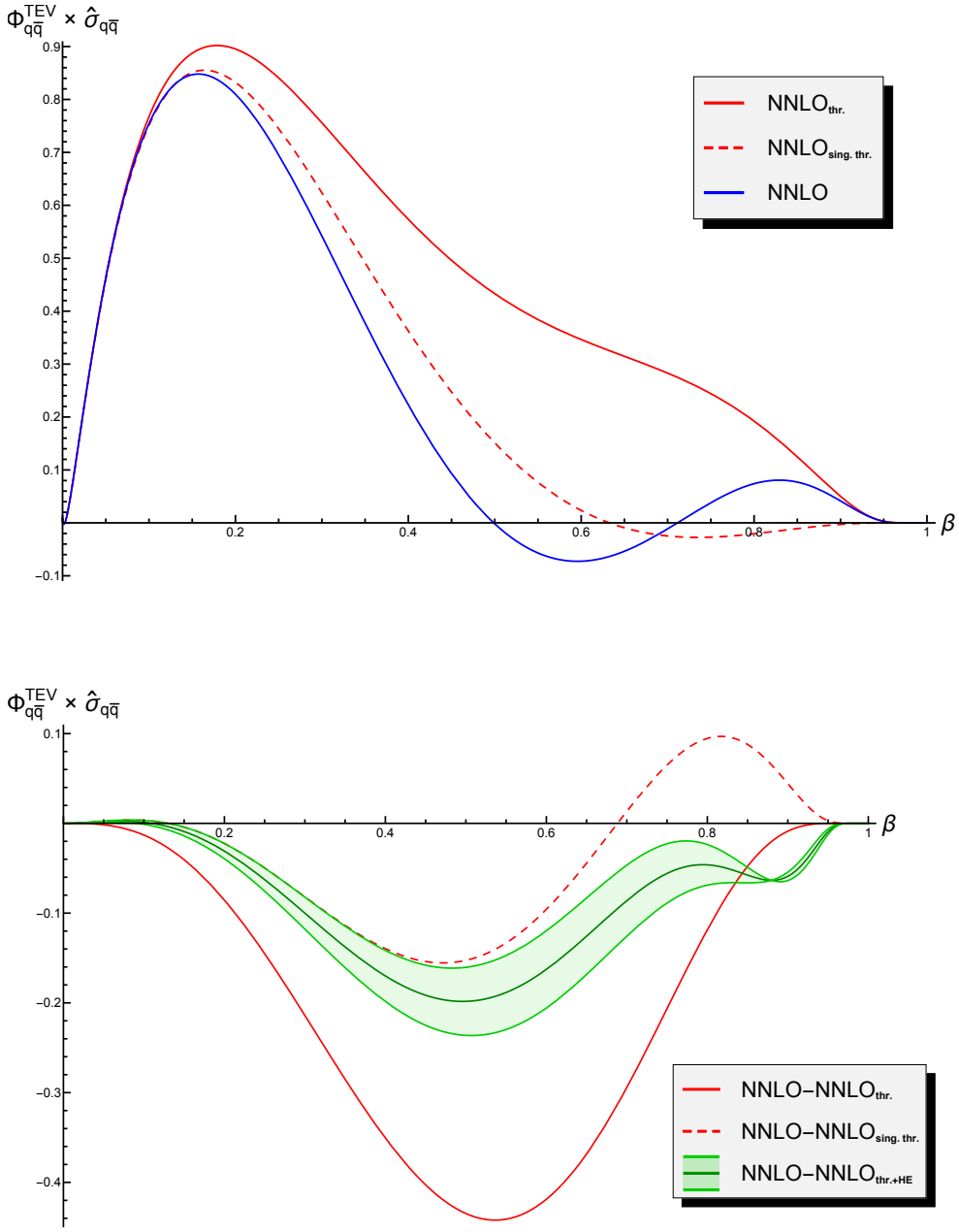

Figure 3.19: *Product of the $q\bar{q}$ partonic cross section and flux at the Tevatron (*MSTW2008 *at 68% C.L. [231], $\mu_R = \mu_F = m_t = 173.3\,\text{GeV}$, $n_l = 5$) for the exact NNLO result and two different threshold scenarios ($NNLO_{thr.}$: $C_{q\bar{q}}^{(2)} = Eq.\,(3.79)$, $NNLO_{sing.\ thr.}$: $C_{q\bar{q}}^{(2)} = 0$). While the upper plot shows the full cross section contributions, the lower plot shows the impact of going beyond the known threshold behavior. For comparison, we in the latter also present the difference between the exact NNLO result and the combined threshold+high-energy analysis presented in Ref. [229] where the error band is due to the choice of $C_{q\bar{q}}^{(2)}$ and $r_{q\bar{q},x}$ as explained in section 3.1.1.*

	Tevatron [pb]	LHC			
		7 TeV [pb]	8 TeV [pb]	13 TeV [pb]	14 TeV [pb]
NNLO$_{\text{thr.}}$ $C_{q\bar{q}}^{(2)}=0$	$0.468^{+0.414}_{-0.415}$	$1.84^{+2.03}_{-1.69}$	$2.28^{+2.56}_{-2.09}$	$4.65^{+5.63}_{-4.32}$	$5.15^{+6.32}_{-4.79}$
NNLO$_{\text{thr.}}$	$0.739^{+0.240}_{-0.051}$	$3.17^{+1.09}_{-0.33}$	$3.97^{+1.39}_{-0.42}$	$8.39^{+3.01}_{-0.92}$	$9.33^{+3.36}_{-1.03}$
NNLO$_{\text{thr.+HE}}$	$0.550^{+0.229\ +0.033}_{-0.071\ -0.033}$	$2.47^{+1.00\ +0.11}_{-0.34\ -0.11}$	$3.13^{+1.24\ +0.13}_{-0.41\ -0.13}$	$6.85^{+2.59\ +0.14}_{-0.85\ -0.13}$	$7.65^{+2.88\ +0.12}_{-0.94\ -0.12}$
NNLO	$0.408^{+0.282}_{-0.090}$	$1.71^{+1.26}_{-0.37}$	$2.14^{+1.57}_{-0.45}$	$4.51^{+3.32}_{-0.86}$	$5.02^{+3.72}_{-0.95}$
$\sum_{ij}$ NNLO	$0.551^{+0.326}_{-0.129}$	$18.11^{+8.62}_{-10.88}$	$25.64^{+12.24}_{-15.85}$	$81.16^{+38.85}_{-54.59}$	$95.51^{+45.65}_{-64.90}$
$\sigma_{t\bar{t}}^{\text{tot, NLO}}$	$6.682^{+0.356\ +0.182}_{-0.752\ -0.125}$	$158.1^{+19.5\ +4.2}_{-21.2\ -5.3}$	$226.3^{+27.8\ +5.6}_{-29.7\ -7.0}$	$746.9^{+90.4\ +14.1}_{-90.4\ -17.1}$	$884.5^{+106.8\ +16.1}_{-105.8\ -19.4}$
$\sigma_{t\bar{t}}^{\text{tot, NNLO}}$	$7.009^{+0.259\ +0.169}_{-0.374\ -0.121}$	$167.0^{+6.7\ +4.6}_{-10.7\ -4.7}$	$239.1^{+9.2\ +6.1}_{-14.8\ -6.2}$	$788.1^{+27.1\ +14.3}_{-43.8\ -15.5}$	$933.0^{+31.8\ +16.1}_{-51.0\ -17.6}$
$\sigma_{t\bar{t}}^{\text{tot, NLO+NNLL}_0}$	$6.844^{+0.180\ +0.162}_{-0.377\ -0.116}$	$164.7^{+15.0\ +4.5}_{-11.9\ -4.5}$	$235.0^{+21.5\ +5.8}_{-18.5\ -6.0}$	$767.7^{+70.7\ +13.7}_{-62.8\ -14.9}$	$907.7^{+83.6\ +15.4}_{-74.7\ -16.9}$
$\sigma_{t\bar{t}}^{\text{tot, NNLO+NNLL}_0}$	$7.091^{+0.175\ +0.168}_{-0.218\ -0.121}$	$169.7^{+4.5\ +4.7}_{-6.9\ -4.7}$	$242.6^{+6.4\ +6.1}_{-10.0\ -6.3}$	$797.3^{+20.6\ +14.4}_{-33.0\ -15.6}$	$943.4^{+24.3\ +16.1}_{-39.1\ -17.7}$
$\sigma_{t\bar{t}}^{\text{tot, NNLO+NNLL}}$	$7.164^{+0.109\ +0.169}_{-0.200\ -0.122}$	$172.2^{+4.7\ +4.7}_{-5.9\ -4.8}$	$246.0^{+6.6\ +6.2}_{-8.5\ -6.4}$	$806.6^{+20.6\ +14.5}_{-28.6\ -15.7}$	$954.1^{+24.2\ +16.3}_{-34.0\ -17.8}$

Table 3.8: *Theoretical predictions for the quark annihilation channel at the Tevatron and the LHC (m_t = 173.3 GeV, MSTW2008 PDFs at 68% C.L. [231]) in approximate (threshold expansion, threshold+HE analysis [89, 229]) and full NNLO . For comparison, we also present results for the full NNLO corrections from all channels ($\sum_{ij}$) as well as for the total cross section at different orders in QCD and soft-gluon resummation ($A=0$, NNLL$_0$ corresponds to $\tilde{H}^{(2)}_{\mathbf{R}\otimes\mathbf{R}'|\tilde{\mathbf{R}}}=0$). The quoted uncertainties are due to the variation of renormalization and factorization scale and, for the $\sigma_{t\bar{t}}^{\text{tot}}$ predictions, the choice of PDFs. The approximate threshold+HE result receives an additional parametrization error due to the choice of $C_{q\bar{q}}^{(2)}$ and $r_{q\bar{q},x}$ as explained in section 3.1.1.*

functional dependence of $\hat{\sigma}_{q\bar{q}}^{(2,0,0)}$ in the intermediate and large β-range (except, of course, very close to $\beta\approx 1$). For the most part of the spectrum, the exact result lies even outside the quoted error band (see Fig. 3.19) stressing again the necessity of going to full NNLO.

The resulting hadronic cross section predictions have been summarized in Tab. 3.8 confirming our previous conclusions also quantitatively. Indeed, the various approximate NNLO results tend to overestimate the size of the full NNLO contributions up to the level of tens of percent, which, however, only at the Tevatron, where the quark annihilation channel is the dominant source of $t\bar{t}$ pairs, leads to an actual reduction of $\sigma_{t\bar{t}}^{\text{tot}}$ compared to these approximations. At the LHC, this effect is completely compensated by the corresponding gluonic corrections as we will see in the next section. For the resummed cross section predictions the implications of going to full NNLO are, in fact, twofold. On the one hand, the precision in the matching procedure is further improved presumably reducing the sensitivity to subleading effects. On the other hand, the full result allows for an at least approximate determination of the NNLO $q\bar{q}$ hard matching coefficient through $C_{q\bar{q}}^{(2),\text{fit}}$, which raises the perturbative precision of the hard function to the same level as the remaining components in the resummation formula. While the numerical impact of this adjustment on the central predictions amounts to only about 1%, it is of great significance for the determination of the theoretical uncertainty due to missing

higher-order contributions since it allows for a consistent treatment of the scale dependence. Otherwise an error estimate via scale variation may suffer from accidental cancellation effects, as for instance described in section 3.1.2, which render this method unreliable.

Thus, when focusing solely on the reduction of the perturbative uncertainty, the NNLO result should be rather compared to the NLO prediction than to the various NNLO approximations. At the Tevatron, the relevant collider for the $q\bar{q}$-channel, one can observe a significant gain in precision, the error decreasing by about 50% with respect to the NLO result. Moreover, the uncertainty becomes more symmetric which seems more natural since there a priori exists no particular reason why the contributions from higher orders should favor a specific sign, i. e. enhance or decrease $\sigma_{t\bar{t}}^{\mathbf{tot}}$. Including resummation effects further reduces the error to the level of 3%, a precision so high the theory predictions are no longer dominated by this particular source of uncertainty as we will see in section 3.5.4. For the LHC, due to the pp initial state, the numerical impact of the NNLO quark annihilation results is rather small $\lesssim 1\%$ and we, hence, have to turn to the corrections for the gluon fusion channel to assess the true extent of going to full NNLO.

3.5.3 The gluon fusion channel

The evaluation of the gluon fusion channel was by far the most challenging part of the NNLO $t\bar{t}$ program since it not only involved the full spectrum of real and virtual corrections but, due to the self-interacting nature of gluons, also a significantly larger number of diagrams with additional topologies not present in the theoretical description of the other production modes. Therefore, it was the last piece of the NNLO analysis to be completed, the results being finally published in Ref. [80]. Nevertheless, with the recent shutdown of the Tevatron it represents the most important ingredient for high-precision top-quark phenomenology at current collider experiments, gluon fusion being the dominant source of $t\bar{t}$ pairs at the LHC regardless of the operating energy (see Tab. 2.1).

Similar to the $q\bar{q}$ case, the partonic results are conveniently parametrized in terms of the known threshold behavior (modulo the constant coefficients $C_{gg,\tilde{\mathbf{R}}}^{(2)}$) and some interpolating functions quantifying the effect of going to full NNLO

$$F_{gg}^{(n)} \equiv F_{gg,\beta}^{(n)} + F_{gg,\text{fit}}^{(n)} \,, \qquad n = 0, 1(, 2) \tag{3.209}$$

with [80]

$$\begin{aligned}
F_{gg,\beta}^{(2)} &= 0 \\
F_{gg,\beta}^{(1)} &= \hat{\sigma}_{gg}^{(0)} \left[(-0.00611924 + 0.0436508\mathrm{L}_\beta)/\beta \right. \\
&\quad \left. +0.139124\mathrm{L}_\beta - 0.755826\mathrm{L}_\beta^2 + 0.54038\mathrm{L}_\beta^3\right] \\
F_{gg,\beta}^{(0)} &= \hat{\sigma}_{gg}^{(0)} \left[0.43408/\beta^2 + 14.8618\mathrm{L}_\beta - 1.99838\mathrm{L}_\beta^2 \right. \\
&\quad -14.7016\mathrm{L}_\beta^3 + 29.1805\mathrm{L}_\beta^4 \\
&\quad \left. +(-0.0240072 + 1.81537\mathrm{L}_\beta + 3.14286\mathrm{L}_\beta^2)/\beta\right] \,.
\end{aligned} \tag{3.210}$$

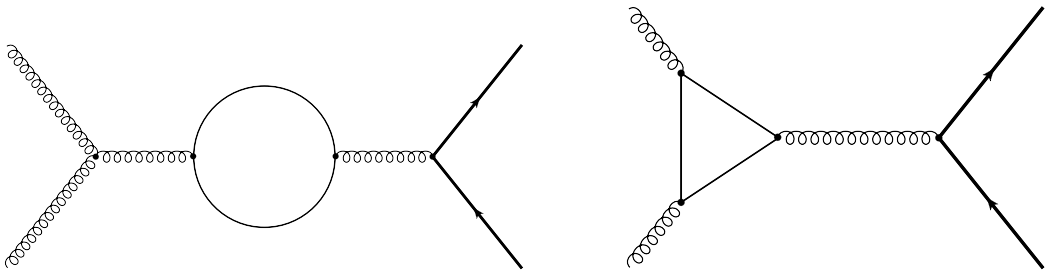

Figure 3.20: *NLO closed fermion-loop diagrams that form the basis for the calculation of the NNLO n_l^2 contributions in the gluon fusion channel.*

As indicated, the n_l^2 contributions, even though they have originally been treated in a fully numerical fashion, may in fact be excluded from the fitting procedure and evaluated completely analytically. Note, however, that the corresponding analysis is more complicated than for the quark annihilation channel since it, apart from an additional loop structure, involves contributions from collinear renormalization as well as modified factorization properties. The latter is due to the fact that the LO matrix element consists of several diagrams, which are affected quite differently by loop corrections, the origin of the n_l^2-dependence. A great computational advantage in this context is the decomposition of the virtual amplitudes into the singlet/octet basis as the relevant light-fermion loops occur only in the antisymmetric octet configuration[30]. The main building block of the actual calculation is then given by the sum of diagrams displayed in Fig. 3.20, which is known entirely analytically from the NLO analysis and, in fact, turns out to be completely finite due to a cancellation of UV divergences between the individual graphs. It may be used to construct the bare one-loop-squared and two-loop corrections (the latter with the help of Eq. (3.203)) as well as the corresponding counterterms from UV and collinear renormalization. Note that in this particular case the convolutions usually present in the latter contributions can be reduced to regular products since the n_l-dependent parts of the respective splitting kernels are proportional to a delta function. Due to the multiplicative nature of the renormalization constants, interference terms of pure LO diagrams then completely drop out (which we have explicitly checked) as they would otherwise lead to a n_l^2-dependence for the other color configurations as well. Combining these findings, we finally arrive at

$$F_{gg}^{(2)} = \frac{\rho\, N_c}{3456\,(N_c^2-1)\pi}\left[\beta\,(2+21\,\rho) - 10\,\rho \ln\frac{1+\beta}{1-\beta} + 6\,\rho\left(2\,\beta - \ln\frac{1+\beta}{1-\beta}\right)\ln\frac{\rho}{4}\right]. \tag{3.211}$$

[30] There exist additional light-fermion loop contributions in the two-loop virtual corrections of the singlet and symmetric octet states but they are only of order n_l.

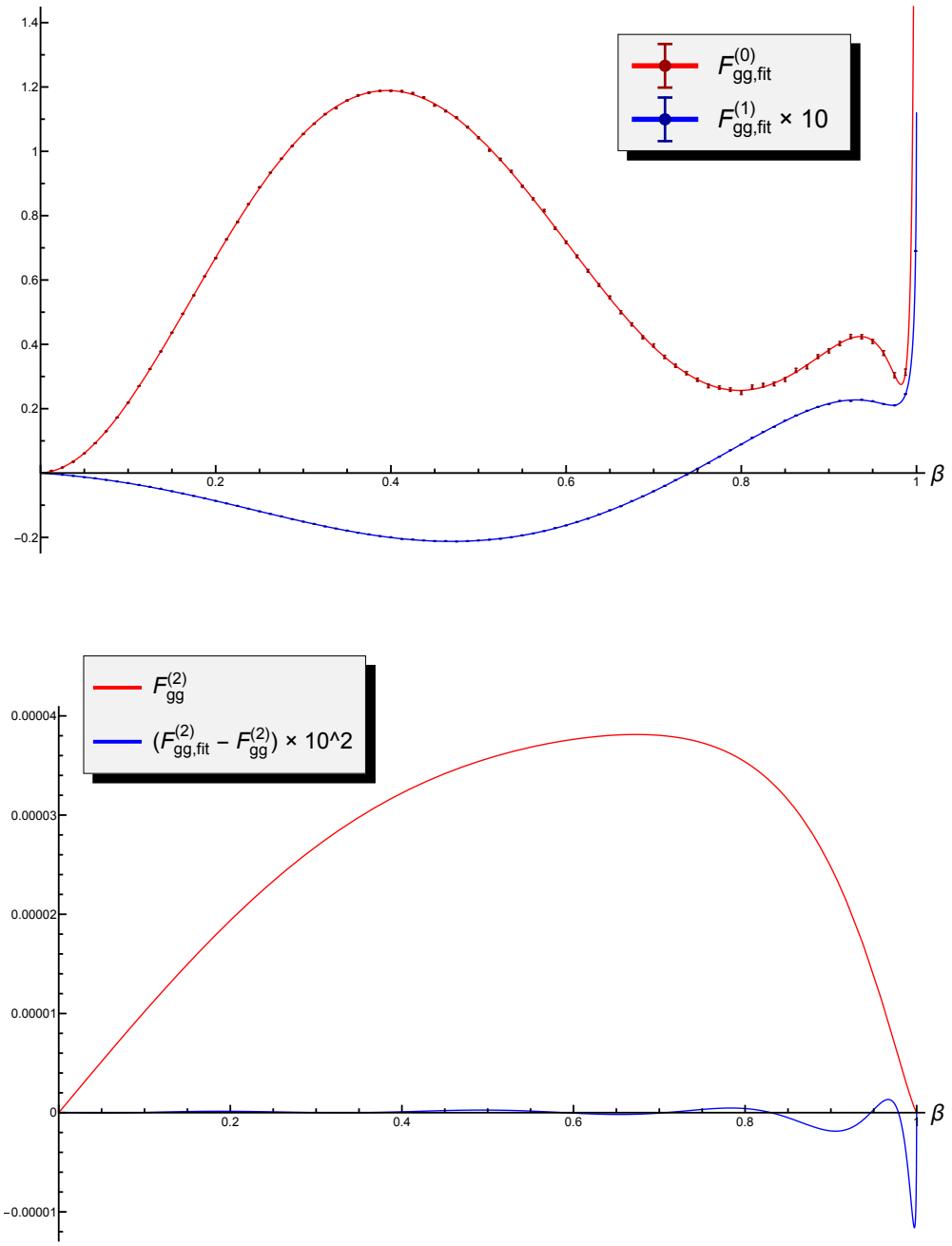

Figure 3.21: *The functions $F^{(0,1)}_{gg,\,fit}$ (top) and $F^{(2)}_{gg}$ (bottom) that describe the full NNLO behavior beyond the known threshold approximation. While the latter is compared to the fitted result in Eq. (3.212), for the contributions from lower powers of n_l we present the set of discrete data points (with numerical errors) that form the basis of the corresponding interpolation formulae in Eq. (3.213). As indicated, some functions have been rescaled for improved visibility.*

As shown in Fig. 3.21, the n_l^2 contributions vanish both at threshold and in the ultra-relativistic limit whereas the bulk of the corrections stems from intermediate velocities with a slight tendency towards larger values of β. For comparison we also plotted the difference of the original n_l^2 function obtained from a numerical fit [80]

$$\begin{aligned} F^{(2)}_{gg,\,\mathrm{fit}} &= 10^{-4}\left[(6.44022\beta - 4.8664\beta^2 - 0.0324653\mathrm{L}_\rho^2)\rho\right. \\ &\quad +(-13.8424\beta + 4.7366\beta^2 - 2.91398\mathrm{L}_\rho)\rho^2 \\ &\quad \left.+(8.43828\beta - 2.78748\beta^2 + 2.38971\beta^3)\rho^3\right] \end{aligned} \tag{3.212}$$

and the exact result, which may be interpreted as an estimate for the quality of our fitting routine. As can be seen, the absolute deviation from the analytic solution lies below 10^{-8} for the major part of the spectrum and only for $\beta \to 1$ becomes more pronounced, however still bounded by 1.2×10^{-7}. This difference is numerically insignificant for actual phenomenological applications such that the use of the fitted result will not change the corresponding theoretical predictions and, hence, can be regarded as a viable alternative to the exact expression.

For the lower powers of n_l contributing to the partonic cross section $\hat{\sigma}_{gg}^{(2,0,0)}$ such an analysis is, of course, not possible and we have to rely on a comparison to the computed data points in order to assess the quality of the fitted results, which are given by [80]

$$\begin{aligned} F^{(1)}_{gg,\,\mathrm{fit}} &= -0.0195046\beta - 1.4717\beta^2 - 0.223616\beta^3 \\ &\quad +0.499196\beta^5 + 1.32756\beta^7 + 0.00466872\beta^3\mathrm{L}_\beta \\ &\quad +0.0321469\beta^6\mathrm{L}_\beta^2 + (0.579781\mathrm{L}_\rho^2 + 0.166646\mathrm{L}_\rho^3)\rho \\ &\quad +(-1.36644\mathrm{L}_\rho + 2.24909\mathrm{L}_\rho^2)\rho^2 \\ F^{(0)}_{gg,\,\mathrm{fit}} &= 581.27542\beta + 1251.4057\beta^2 - 60.478096\beta^3 \\ &\quad +1101.2272\beta^4 - 2905.3858\beta^5 + 629.9128\beta^4\mathrm{L}_\beta \\ &\quad -5.1891075\mathrm{L}_\rho + (1200.741\mathrm{L}_\rho + 162.50333\mathrm{L}_\rho^2)\rho \\ &\quad +(36.074524\mathrm{L}_\rho - 1192.8918\mathrm{L}_\rho^2 - 1810.2849\beta)\rho^2 \\ &\quad +1568.7591\beta\rho^3 - 461.21326\beta\rho^4 + 121.6379\beta\rho^5\,. \end{aligned} \tag{3.213}$$

As can be inferred from the corresponding curves in Fig. 3.21, the interpolating functions describe the underlying discrete results exceptionally well, vanishing at threshold and showing the characteristic logarithmic rise as $\beta \to 1$. Note that for an improved determination of this high-energy behavior we have actually imposed on $F^{(0)}_{gg,\,\mathrm{fit}}$ the exact logarithmic dependence $\sim c_1^{gg} \ln\rho$ implied by Eq. (3.200) with [555]

$$c_1^{gg} = -5.189107503169016 \tag{3.214}$$

resulting in a numerical prediction for the constant high-energy coefficient of [80]

$$c_0^{gg} = -31.96 + 0.1119\,n_l \tag{3.215}$$

which is well within the estimated range quoted in Ref. [229]. Still, one has to assume a sizable numerical uncertainty on this value as the region that is most sensitive to the ultra-relativistic expansion lies beyond our last evaluation point $\beta = 0.999$ such that it cannot be

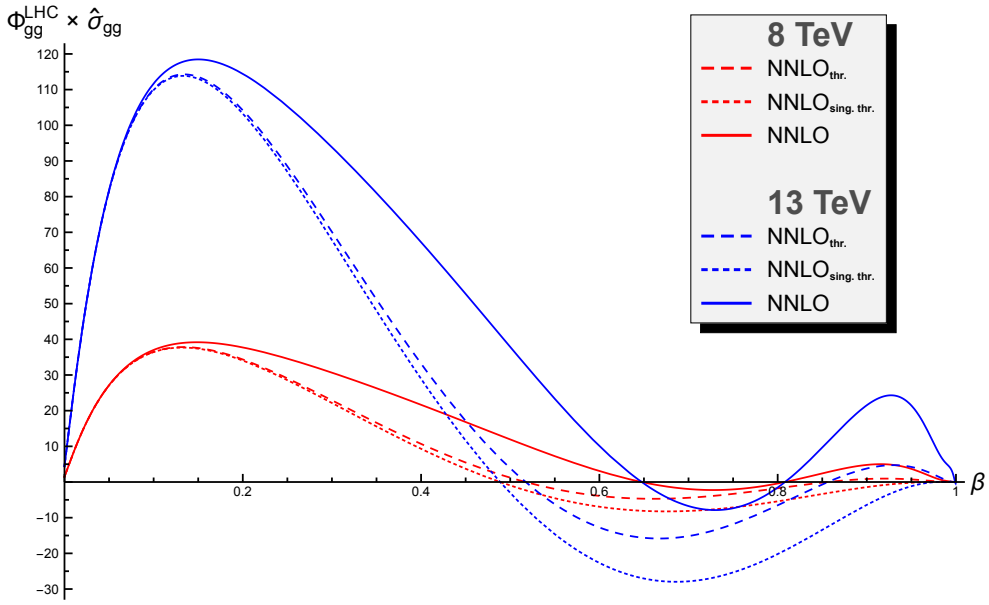

Figure 3.22: *Product of the gg partonic cross section and flux at the LHC* (MSTW2008 *at 68% C.L. [231],* $\mu_R = \mu_F = m_t = 173.3\,\text{GeV}$, $n_l = 5$*) with* 8 TeV *and* 13 TeV *center-of-mass energy for the exact NNLO result and two different threshold scenarios (NNLO$_{thr.}$:* $C_{gg}^{(2)} =$ *Eq.* (3.76), *NNLO$_{sing.\ thr.}$:* $C_{gg}^{(2)} = 0$*).*

adequately constrained. This is also the reason why the fitting formulae in Eq. (3.213) are potentially unreliable beyond this point , which is, however, irrelevant for any of the present collider setups.

At the other end of the spectrum for $\beta \to 0$, the fitted result may be employed for the determination of the color-averaged constant term of the threshold expansion (see Eq. (3.76)) yielding [80]

$$C_{gg}^{(2),\text{fit}} = 338.179 - 26.8912\, n_l + 0.142848\, n_l^2 = 207.294\,. \tag{3.216}$$

A consecutive estimate of the corresponding numerical uncertainty at $n_l = 5$ amounts to as much as 50%, which is substantially larger than for the $q\bar{q}$ case and can be traced back to the presence of $\ln\beta$ terms in $F_{gg,\text{fit}}^{(0,1)}$ that spoil the numerical sensitivity. A comparison with the exact value for $C_{gg}^{(2)}$ in Eq. (3.76) reveals that this error estimate was indeed reasonable with the largest deviation, as expected, stemming from the constant contribution $n_l = 0$.

The impact of the partonic NNLO corrections on the final cross section predictions is again most conveniently assessed by multiplying $\hat{\sigma}_{gg}^{(2,0,0)}$ with the respective partonic fluxes. Focusing on the LHC, it becomes clear that the full NNLO result leads to sizable positive enhancements on top of the pure threshold approximation that affect the entire β-range as can be seen in Fig. 3.22. Thus, one can also expect a much larger numerical impact on $\sigma_{t\bar{t}}^{\text{tot}}$ than for the quark annihilation channel since these contributions cannot be suppressed by cancellation effects. This becomes particularly obvious when looking at the respective differences of full and approximate results in Fig. 3.23 which display a qualitatively similar shape

	Tevatron [pb]	LHC			
		7 TeV [pb]	8 TeV [pb]	13 TeV [pb]	14 TeV [pb]
NNLO$_{\text{thr.}}$ $C^{(2)}_{gg,\tilde{\mathbf{R}}} = 0$	$0.139^{+0.110}_{-0.132}$	$10.74^{+14.23}_{-13.06}$	$14.92^{+20.66}_{-18.42}$	$43.95^{+70.07}_{-56.68}$	$51.14^{+83.11}_{-66.32}$
NNLO$_{\text{thr.}}$	$0.149^{+0.116}_{-0.177}$	$12.37^{+14.88}_{-17.39}$	$17.32^{+21.30}_{-24.77}$	$52.34^{+68.65}_{-80.26}$	$61.13^{+80.81}_{-94.79}$
NNLO$_{\text{thr.+HE}}$	$0.161^{+0.111\ +0.003}_{-0.165\ -0.003}$	$16.15^{+13.42\ +1.99}_{-14.72\ -1.99}$	$23.05^{+19.12\ +3.45}_{-20.84\ -3.45}$	$74.11^{+60.94\ +19.63}_{-66.99\ -19.64}$	$87.24^{+71.67\ +24.86}_{-79.18\ -24.87}$
NNLO	$0.198^{+0.095}_{-0.133}$	$18.13^{+12.76}_{-13.64}$	$25.60^{+18.29}_{-19.53}$	$79.93^{+59.25}_{-64.49}$	$93.81^{+69.78}_{-76.39}$
$\sum_{ij}$ NNLO	$0.551^{+0.326}_{-0.129}$	$18.11^{+8.62}_{-10.88}$	$25.64^{+12.24}_{-15.85}$	$81.16^{+38.85}_{-54.59}$	$95.51^{+45.65}_{-64.90}$
$\sigma^{\mathbf{tot},\,\text{NLO}}_{t\bar{t}}$	$6.682^{+0.356\ +0.182}_{-0.752\ -0.125}$	$158.1^{+19.5\ +4.2}_{-21.2\ -5.3}$	$226.3^{+27.8\ +5.6}_{-29.7\ -7.0}$	$746.9^{+90.4\ +14.1}_{-90.4\ -17.1}$	$884.5^{+106.8\ +16.1}_{-105.8\ -19.4}$
$\sigma^{\mathbf{tot},\,\text{NNLO}}_{t\bar{t}}$	$7.009^{+0.259\ +0.169}_{-0.374\ -0.121}$	$167.0^{+6.7\ +4.6}_{-10.7\ -4.7}$	$239.1^{+9.2\ +6.1}_{-14.8\ -6.2}$	$788.1^{+27.1\ +14.3}_{-43.8\ -15.5}$	$933.0^{+31.8\ +16.1}_{-51.0\ -17.6}$
$\sigma^{\mathbf{tot},\,\text{NLO+NNLL}_0}_{t\bar{t}}$	$6.844^{+0.180\ +0.162}_{-0.377\ -0.116}$	$164.7^{+15.0\ +4.5}_{-11.9\ -4.5}$	$235.0^{+21.5\ +5.8}_{-18.5\ -6.0}$	$767.7^{+70.7\ +13.7}_{-62.8\ -14.9}$	$907.7^{+83.6\ +15.4}_{-74.7\ -16.9}$
$\sigma^{\mathbf{tot},\,\text{NNLO+NNLL}_0}_{t\bar{t}}$	$7.091^{+0.175\ +0.168}_{-0.218\ -0.121}$	$169.7^{+4.5\ +4.7}_{-6.9\ -4.7}$	$242.6^{+6.4\ +6.1}_{-10.0\ -6.3}$	$797.3^{+20.6\ +14.4}_{-33.0\ -15.6}$	$943.4^{+24.3\ +16.1}_{-39.1\ -17.7}$
$\sigma^{\mathbf{tot},\,\text{NNLO+NNLL}}_{t\bar{t}}$	$7.164^{+0.109\ +0.169}_{-0.200\ -0.122}$	$172.2^{+4.7\ +4.7}_{-5.9\ -4.8}$	$246.0^{+6.6\ +6.2}_{-8.5\ -6.4}$	$806.6^{+20.6\ +14.5}_{-28.6\ -15.7}$	$954.1^{+24.2\ +16.3}_{-34.0\ -17.8}$

Table 3.9: *Theoretical predictions for the gluon fusion channel at the Tevatron and the LHC ($m_t = 173.3\,\text{GeV}$, MSTW2008 PDFs at 68% C.L. [231]) in approximate (threshold expansion, threshold+HE analysis [89, 229]) and full NNLO . For comparison, we also present results for the full NNLO corrections from all channels ($\sum_{ij}$) as well as for the total cross section at different orders in QCD and soft-gluon resummation ($A = 0$, NNLL$_0$ corresponds to $\tilde{H}^{(2)}_{\mathbf{R}\otimes\mathbf{R}'|\tilde{\mathbf{R}}} = 0$). The quoted uncertainties are due to the variation of renormalization and factorization scale and, for the $\sigma^{tot}_{t\bar{t}}$ predictions, the choice of PDFs. The approximate threshold+HE result receives an additional parametrization error due to the choice of $C^{(2)}_{gg}$ and $r_{gg,x}$ as explained in section 3.1.1.*

regardless of center-of-mass energy or choice of $C^{(2)}_{gg,\tilde{\mathbf{R}}}$. Moreover, we again compare the exact NNLO predictions to the combined threshold+high-energy approximation from Ref. [229]. As for the qg- and $q\bar{q}$-channel the approximate result fails to reproduce the actual functional dependence of $\hat{\sigma}^{(2,0,0)}_{gg}$ away from the two fixed kinematic limits at $\beta \to 0, 1$. Note, however, that the alternating sign of the deviation from the full result will lead to cancellations when performing the integration over velocities such that the numerical difference for the total cross section will be less pronounced. The actual size of the discrepancy will thus be governed by the fluxes suggesting that for larger collision energies there will be a better agreement between the approximate and the full result.

This observation is eventually confirmed by the respective $\sigma^{\mathbf{tot}}_{t\bar{t}}$ predictions collected in Tab. 3.9, which reveal that the various approximations differ from the exact analysis by several tens of percent. This difference is, indeed, quite significant considering the fact that the theoretical uncertainty due to scale variation has dramatically decreased to the level of $\sim$5% as well. Including resummation effects the precision may be improved even further down to $\sim$3% whereas the central values are shifted up by around 2-3%. Note, however, that an exact treatment of the resummed cross section requires additional input that goes beyond the color-averaged analysis described above relying strongly on the methods and results discussed

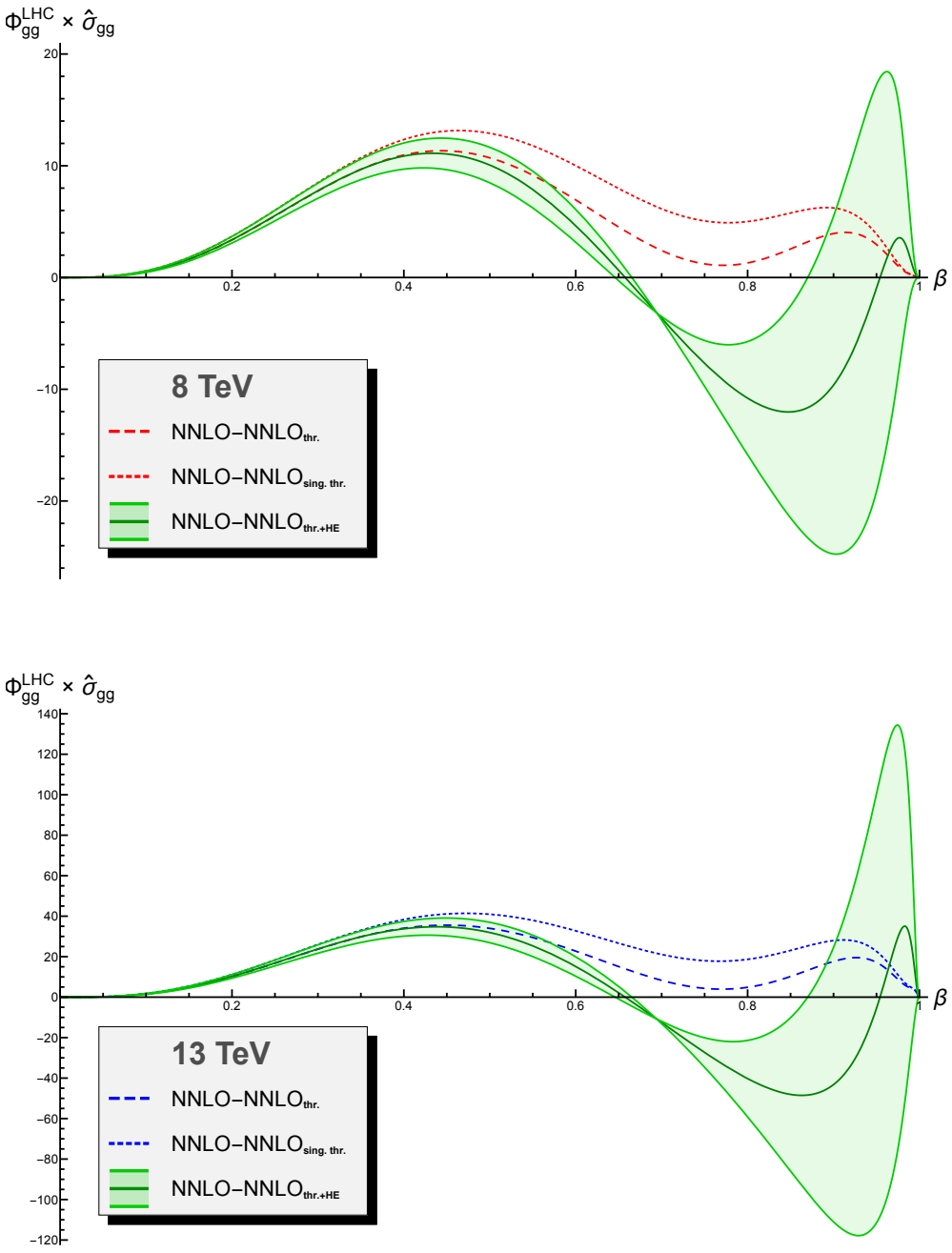

Figure 3.23: *Difference plot for the product of the gg partonic cross section and flux at the LHC* (MSTW2008 *at 68% C.L. [231],* $\mu_R = \mu_F = m_t = 173.3\,\text{GeV}$, $n_l = 5$*) with* 8 TeV *(top) and* 13 TeV *(bottom) center-of-mass energy. The exact NNLO result is compared to two different threshold scenarios (*$NNLO_{thr.}$*:* $C_{gg}^{(2)} = Eq.\,(3.76)$, $NNLO_{sing.\ thr.}$*:* $C_{gg}^{(2)} = 0$*) as well as the combined threshold+high-energy analysis presented in Ref. [229] where the error band of the latter is due to the choice of* $C_{gg}^{(2)}$ *and* $r_{gg,x}$ *as explained in section 3.1.1.*

in section 3.1.2. Finally, at the Tevatron the NNLO contributions of the gluon fusion channel amount to about half of the $q\bar{q}$ corrections. Yet, the actual increase with respect to the various approximate NNLO predictions is much smaller such that the numerical impact on $\sigma_{t\bar{t}}^{\mathbf{tot}}$ is less pronounced. Still, the full NNLO gg results render the theoretical description of the total cross section more reliable, especially since they allow for a systematic inclusion of scale dependent terms eliminating potential inconsistencies inherent to an approximate treatment (see, for instance, the discussion at the end of section 3.1.1).

At this high level of precision, there are other sources of theoretical uncertainty that become important and that we have not yet properly addressed, e. g. the PDF error or the finite precision of the input parameters α_s and m_t. However, since they are not specific to a certain channel, we will discuss them separately in the next section giving a complete picture of the theory error affecting the predictions for $\sigma_{t\bar{t}}^{\mathbf{tot}}$.

3.5.4 Theory error and comparison to experimental data

As the theoretical description of the total cross section for top-quark pair production relies on a perturbative treatment in form of an expansion in the strong coupling, it suffers from a few conceptual drawbacks that need to be properly addressed to guarantee the reliability of the corresponding theory predictions. First of all, it is a priori not clear whether the resulting perturbative series is well converging or if it will, at worst, eventually break down. Moreover, there will, even in the former case, always remain a residual uncertainty connected to our lack of knowledge regarding the size (and sign) of yet undetermined higher-order contributions. While we are able to estimate this uncertainty through a variation of renormalization and factorization scales, there actually exists no solid proof that this procedure can correctly reproduce the approximate impact of these missing terms.

Having at hand three orders of the α_s-expansion now, we are finally able to investigate the perturbative behavior of $\sigma_{t\bar{t}}^{\mathbf{tot}}$ more thoroughly which allows us to ultimately resolve these concerns. To this end, we have in Fig. 3.24 plotted the perturbative uncertainty, i. e. the restricted scale variation defined in Eq. (2.5), of the total cross section at different orders in perturbation theory both for the Tevatron and the LHC. As one can see, there is a significant reduction of the scale dependence with each successive order of the α_s-expansion, the overlap between the respective scale bands indicating that our error estimate indeed consistently describes the approximate size of the yet missing terms of the perturbative series.

A more quantitative comparison based on the results in Tab. 2.2, Tab. 2.3 and Tab. 3.10 shows that even the central values of each successive cross section order are contained in the uncertainty bands of the corresponding previous-order predictions. In the latter table we also present the results for the NLO and NNLO K-factors, $K_{\mathrm{NLO}} = \sigma_{t\bar{t}}^{\mathbf{tot},\mathrm{NLO}}/\sigma_{t\bar{t}}^{\mathbf{tot},\mathrm{LO}}$ and $K_{\mathrm{NNLO}} = \sigma_{t\bar{t}}^{\mathbf{tot},\mathrm{NNLO}}/\sigma_{t\bar{t}}^{\mathbf{tot},\mathrm{NLO}}$, derived from different PDF sets illustrating the universality of these observations. Despite the fact that the absolute numerical values for these ratios may indeed be quite different, the inclusion of higher-order corrections has always a stabilizing effect on the $\sigma_{t\bar{t}}^{\mathbf{tot}}$ predictions regardless of the details concerning the modeling of the proton content. Moreover, the difference between the results from the various PDF sets gradually decreases with each successive order of the perturbative expansion such that at NNLO they all

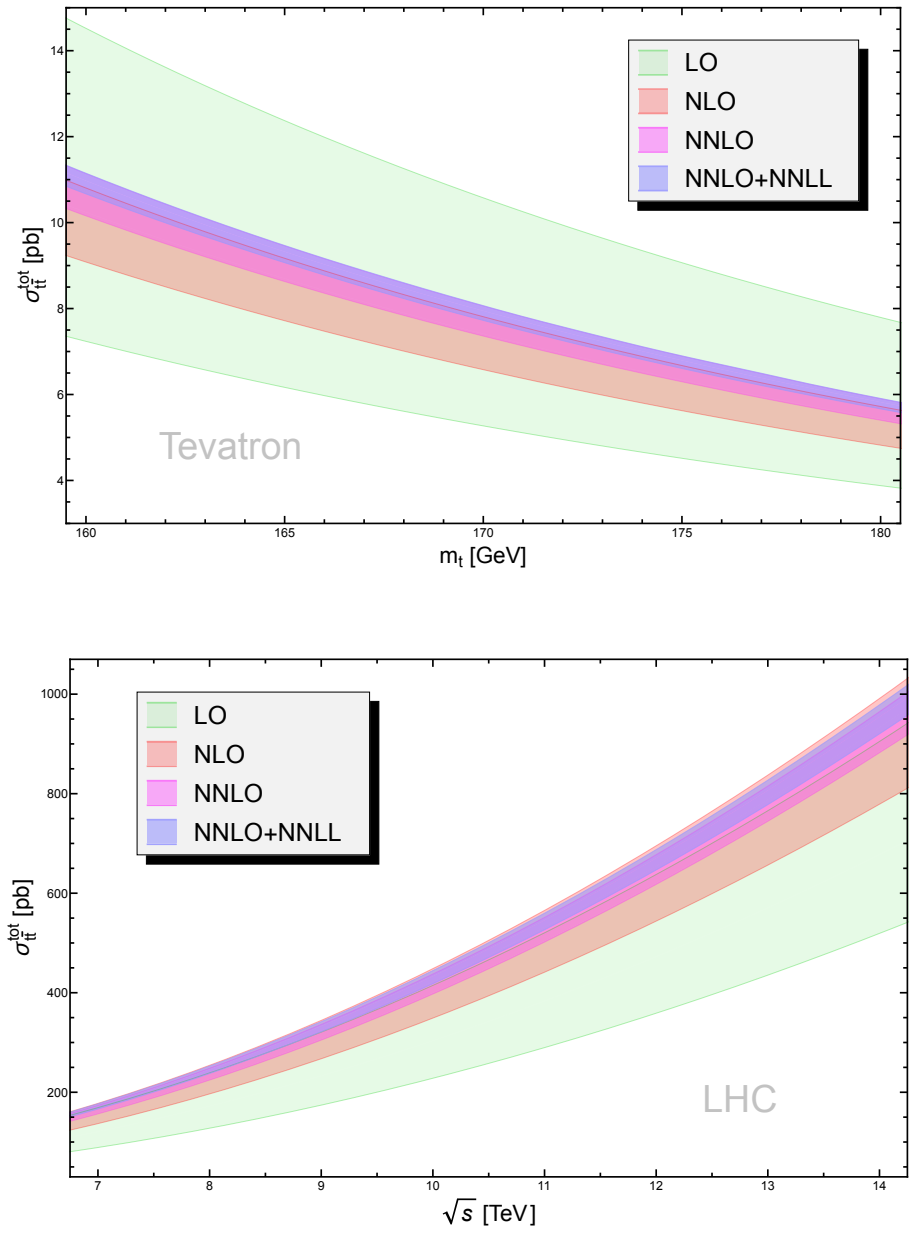

Figure 3.24: *Scale variation for the total cross section at the Tevatron (top) and the LHC (bottom) at different orders in perturbation theory* (MSTW2008 *at 68% C.L. [231],* $m_t = 173.3\,\text{GeV}$, $n_l = 5$*).*

lie within a few percent (except for the ABM11-based LHC predictions, see below). The corresponding perturbative errors, for a long time the dominant source of theoretical uncertainty in $t\bar{t}$ total cross section analyses, are all at the level of $\sim 5\%$ now. This leads to an entirely new situation where for a reliable description of $\sigma_{t\bar{t}}^{\text{tot}}$ one eventually has to take into account additional sources of uncertainty, in particular from the fundamental input parameters that cannot be predicted from theory: the PDFs, the top-quark mass and the strong coupling constant. While this, in practice, leads to a higher computational effort for the determination

	Tevatron [pb]	LHC			
		7 TeV [pb]	8 TeV [pb]	13 TeV [pb]	14 TeV [pb]
K_{NLO}					
MSTW2008	$1.009^{+0.237\ +0.034}_{-0.273\ -0.028}$	$1.309^{+0.231\ +0.036}_{-0.259\ -0.035}$	$1.314^{+0.225\ +0.033}_{-0.250\ -0.032}$	$1.309^{+0.199\ +0.026}_{-0.216\ -0.024}$	$1.305^{+0.195\ +0.026}_{-0.210\ -0.023}$
HERAPDF1.5	$1.023^{+0.230\ +0.040}_{-0.263\ -0.017}$	$1.365^{+0.232\ +0.040}_{-0.256\ -0.034}$	$1.370^{+0.228\ +0.038}_{-0.249\ -0.036}$	$1.360^{+0.206\ +0.029}_{-0.217\ -0.039}$	$1.355^{+0.201\ +0.028}_{-0.212\ -0.039}$
NNPDF3.0	$1.216^{+0.225\ +0.077}_{-0.281\ -0.077}$	$1.472^{+0.213\ +0.233}_{-0.251\ -0.187}$	$1.470^{+0.206\ +0.217}_{-0.241\ -0.176}$	$1.455^{+0.178\ +0.179}_{-0.201\ -0.147}$	$1.451^{+0.174\ +0.175}_{-0.195\ -0.144}$
K_{NNLO}					
MSTW2008	$1.049^{+0.070\ +0.037}_{-0.024\ -0.036}$	$1.056^{+0.086\ +0.042}_{-0.079\ -0.034}$	$1.057^{+0.084\ +0.039}_{-0.079\ -0.032}$	$1.055^{+0.079\ +0.029}_{-0.082\ -0.027}$	$1.055^{+0.078\ +0.028}_{-0.082\ -0.026}$
ABM11	$1.050^{+0.064\ +0.033}_{-0.019\ -0.033}$	$1.069^{+0.085\ +0.079}_{-0.075\ -0.079}$	$1.068^{+0.085\ +0.073}_{-0.077\ -0.073}$	$1.059^{+0.081\ +0.054}_{-0.080\ -0.054}$	$1.056^{+0.080\ +0.051}_{-0.080\ -0.051}$
CT10	$1.075^{+0.066\ +0.055}_{-0.022\ -0.041}$	$1.128^{+0.085\ +0.075}_{-0.079\ -0.063}$	$1.128^{+0.083\ +0.066}_{-0.080\ -0.056}$	$1.120^{+0.078\ +0.042}_{-0.082\ -0.037}$	$1.119^{+0.077\ +0.039}_{-0.082\ -0.035}$
HERAPDF1.5	$1.185^{+0.064\ +0.061}_{-0.019\ -0.039}$	$1.268^{+0.094\ +0.047}_{-0.087\ -0.055}$	$1.250^{+0.093\ +0.044}_{-0.088\ -0.053}$	$1.190^{+0.086\ +0.032}_{-0.087\ -0.046}$	$1.182^{+0.084\ +0.030}_{-0.087\ -0.045}$
NNPDF3.0	$1.079^{+0.067\ +0.031}_{-0.023\ -0.030}$	$1.086^{+0.084\ +0.039}_{-0.077\ -0.038}$	$1.087^{+0.082\ +0.036}_{-0.078\ -0.035}$	$1.088^{+0.077\ +0.028}_{-0.080\ -0.028}$	$1.088^{+0.076\ +0.028}_{-0.080\ -0.027}$
$\sigma_{t\bar{t}}^{\mathbf{tot},\,\mathrm{NNLO}}$					
MSTW2008	$7.009^{+0.259\ +0.169}_{-0.374\ -0.121}$	$167.0^{+6.7\ +4.6}_{-10.7\ -4.7}$	$239.1^{+9.2\ +6.1}_{-14.8\ -6.2}$	$788.1^{+27.1\ +14.3}_{-43.8\ -15.5}$	$933.0^{+31.8\ +16.1}_{-51.0\ -17.6}$
ABM11	$6.765^{+0.201\ +0.151}_{-0.295\ -0.151}$	$131.8^{+5.1\ +6.1}_{-8.1\ -6.1}$	$193.1^{+7.3\ +8.3}_{-11.6\ -8.3}$	$682.1^{+22.9\ +21.4}_{-37.0\ -21.4}$	$814.1^{+26.8\ +24.4}_{-43.4\ -24.4}$
CT10	$7.232^{+0.272\ +0.257}_{-0.391\ -0.195}$	$167.4^{+6.8\ +7.9}_{-10.8\ -6.4}$	$239.5^{+9.4\ +9.9}_{-15.0\ -8.1}$	$787.4^{+27.6\ +20.2}_{-44.1\ -17.6}$	$931.8^{+32.3\ +22.2}_{-51.3\ -19.7}$
HERAPDF1.5	$7.459^{+0.272\ +0.130}_{-0.263\ -0.151}$	$172.1^{+6.6\ +3.9}_{-9.3\ -6.2}$	$245.8^{+9.0\ +5.2}_{-12.9\ -8.4}$	$803.1^{+27.4\ +13.3}_{-37.4\ -22.0}$	$949.5^{+32.1\ +15.1}_{-43.4\ -25.3}$
NNPDF3.0	$7.138^{+0.267\ +0.138}_{-0.384\ -0.132}$	$170.0^{+6.9\ +4.4}_{-11.0\ -4.4}$	$243.5^{+9.6\ +5.8}_{-15.3\ -5.8}$	$802.5^{+28.2\ +14.6}_{-45.3\ -14.6}$	$949.8^{+33.0\ +16.9}_{-52.7\ -16.9}$

Table 3.10: *Theoretical predictions for the NLO and NNLO K-factors, K_{NLO} and K_{NNLO}, at the Tevatron and the LHC based on different PDF sets. The quoted uncertainties are due to the variation of renormalization and factorization scale as well as the parametric PDF error. In case of the* CT10 *and* HERAPDF1.5 *sets the PDF error on the NNLO K-factor has been derived from the individual errors on $\sigma_{t\bar{t}}^{\mathbf{tot},\,\mathrm{NLO}}$ and $\sigma_{t\bar{t}}^{\mathbf{tot},\,\mathrm{NNLO}}$ neglecting potential correlation effects while the remaining PDF errors are obtained using the prescriptions given in section 2.2. For comparison we also provide the corresponding absolute NNLO cross section results.*

of a comprehensive error estimate, it also offers the unique opportunity to reverse the line of thought and directly study these quantities in $t\bar{t}$ data thus increasing the number of possible phenomenological applications.

In order to assess the numerical impact of these novel uncertainty contributions on the $\sigma_{t\bar{t}}^{\mathbf{tot}}$ predictions at the Tevatron and the LHC, we in the following focus on the currently most advanced theoretical calculations available working exclusively at NNLO+NNLL accuracy. For a more general picture we again extend our analysis beyond our default PDF set, MSTW2008 [231], to include the NNPDF3.0 [90], CT10 [499], ABM11 [501] and HERAPDF1.5 [497] sets as well. The corresponding cross section results have been summarized in Tab. 3.11 and Tab. 3.12, providing a detailed account of the individual sources of uncertainty as well as the respective total theory error. For the central predictions the strong coupling

Tevatron						
PDF set	$\sigma_{t\bar{t}}^{\mathbf{tot}}$ [pb]	δ_{scale} [pb]	δ_{PDF} [pb]	δ_{α_s} [pb]	δ_{m_t} [pb]	δ_{tot} [pb]
MSTW2008	7.164	$^{+0.109\ (+1.5\%)}_{-0.200\ (-2.8\%)}$	$^{+0.169\ (+2.4\%)}_{-0.122\ (-1.7\%)}$	$^{+0.098\ (+1.4\%)}_{-0.098\ (-1.4\%)}$	$^{+0.228\ (+3.2\%)}_{-0.220\ (-3.1\%)}$	$^{+0.409\ (+5.7\%)}_{-0.470\ (-6.6\%)}$
ABM11	6.867	$^{+0.103\ (+1.5\%)}_{-0.174\ (-2.5\%)}$	$^{+0.157\ (+2.3\%)}_{-0.157\ (-2.3\%)}$	–	$^{+0.207\ (+3.0\%)}_{-0.201\ (-2.9\%)}$	$^{+0.363\ (+5.3\%)}_{-0.429\ (-6.2\%)}$
CT10	7.395	$^{+0.115\ (+1.6\%)}_{-0.210\ (-2.8\%)}$	$^{+0.270\ (+3.7\%)}_{-0.203\ (-2.7\%)}$	$^{+0.088\ (+1.2\%)}_{-0.088\ (-1.2\%)}$	$^{+0.235\ (+3.2\%)}_{-0.227\ (-3.1\%)}$	$^{+0.484\ (+6.5\%)}_{-0.527\ (-7.1\%)}$
HERAPDF1.5	7.623	$^{+0.115\ (+1.5\%)}_{-0.073\ (-1.0\%)}$	$^{+0.135\ (+1.8\%)}_{-0.154\ (-2.0\%)}$	$^{+0.140\ (+1.8\%)}_{-0.140\ (-1.8\%)}$	$^{+0.241\ (+3.2\%)}_{-0.233\ (-3.1\%)}$	$^{+0.425\ (+5.6\%)}_{-0.385\ (-5.1\%)}$
NNPDF3.0	7.298	$^{+0.114\ (+1.6\%)}_{-0.207\ (-2.8\%)}$	$^{+0.141\ (+1.9\%)}_{-0.135\ (-1.8\%)}$	$^{+0.081\ (+1.1\%)}_{-0.081\ (-1.1\%)}$	$^{+0.231\ (+3.2\%)}_{-0.223\ (-3.1\%)}$	$^{+0.396\ (+5.4\%)}_{-0.480\ (-6.6\%)}$
CDF +DØ [163]	7.60	–	–	–	–	$^{+0.41\ (+5.4\%)}_{-0.41\ (-5.4\%)}$

Table 3.11: *The NNLO+NNLL total cross section predictions for top-quark pair production at the Tevatron based on different PDF sets and including all major sources of theoretical uncertainty. For comparison we also present the most precise cross section measurement by* CDF *and* DØ *where the total experimental error is a combination of statistical, systematic and luminosity uncertainties.*

constant has been set to the preferred value employed by each of the PDF collaborations (for a comparison of the respective reference values $\alpha_s(M_Z)$ see Fig. 2.4) whereas for the mass and central scales we, again, used $\mu_F = \mu_R = m_t = 173.3\,\text{GeV}$. Similarly, the PDF errors were obtained from the individual prescriptions described in section 2.2, i. e. Eq. (2.15) for NNPDF3.0, Eq. (2.16) for MSTW2008, HERAPDF1.5 and CT10 (rescaled to 68% C.L.) and Eq. (2.17) for ABM11. The perturbative uncertainty as well as the parametric α_s and m_t errors are, on the other hand, independent of the actual PDF implementations and were thus evaluated in an identical manner for all PDF sets. Note that there exists no standard procedure for estimating the latter uncertainties and we therefore adopted the strategies presented in Ref. [262], which contains a similar kind of cross section analysis, however, still based on the approximate results for the hard matching coefficients $\tilde{H}^{(2)}_{\mathbf{R}\otimes\mathbf{R}'|\tilde{\mathbf{R}}}$ and not on the more recent determinations in Ref. [234]. In consequence, the results in Tab. 3.11 and Tab. 3.12 may, in fact, be interpreted as an update[31] of the numbers provided in Ref. [262].

For the evaluation of the α_s error one assigns a common uncertainty of $\Delta\alpha_s = 0.00007$ to the central $\alpha_s(M_Z)$-values employed by the various PDF collaborations, which then propagates to the total cross section results both via the partonic fluxes and cross sections. For each PDF set, it can be reliably estimated from a linear fit of $\sigma_{t\bar{t}}^{\mathbf{tot}}(\mu_F = \mu_R = m_t)$ in the range $\alpha_s(M_Z) \in [0.116, 0.120]$ close to the current world average where all PDF groups provide additional predictions beyond their default choices for the strong coupling constant. Note, however, that the ABM11 set is excluded from this analysis as the α_s error is, by construction, already contained in the total PDF uncertainty. For the uncertainty related to the finite precision of the top-quark mass we use an analogous approach assuming the experimental error on m_t to be $\Delta m_t = \pm 1\,\text{GeV}$, which is consistent with the latest top-mass measurements at the Tevatron and the LHC as well as with the combined world average (see Fig. 1.4). Yet, in

[31] This does not apply to the NNPDF predictions since in Ref. [262] an older version of this PDF set, namely NNPDF2.3, has been used.

LHC						
PDF set	$\sigma_{t\bar{t}}^{\mathrm{tot}}$ [pb]	δ_{scale} [pb]	δ_{PDF} [pb]	δ_{α_s} [pb]	δ_{m_t} [pb]	δ_{tot} [pb]
7 TeV						
MSTW2008	172.2	$^{+4.7\ (+2.7\%)}_{-5.9\ (-3.4\%)}$	$^{+4.7\ (+2.7\%)}_{-4.8\ (-2.8\%)}$	$^{+3.0\ (+1.7\%)}_{-3.0\ (-1.7\%)}$	$^{+5.3\ (+3.1\%)}_{-5.1\ (-3.0\%)}$	$^{+12.4\ (+7.2\%)}_{-13.5\ (-7.8\%)}$
ABM11	135.9	$^{+3.7\ (+2.7\%)}_{-4.2\ (-3.1\%)}$	$^{+6.4\ (+4.7\%)}_{-6.4\ (-4.7\%)}$	–	$^{+4.3\ (+3.2\%)}_{-4.2\ (-3.1\%)}$	$^{+11.4\ (+8.4\%)}_{-11.9\ (-8.7\%)}$
CT10	172.6	$^{+4.9\ (+2.8\%)}_{-6.0\ (-3.5\%)}$	$^{+8.0\ (+4.6\%)}_{-6.5\ (-3.8\%)}$	$^{+2.9\ (+1.7\%)}_{-2.9\ (-1.7\%)}$	$^{+5.3\ (+3.1\%)}_{-5.1\ (-3.0\%)}$	$^{+14.9\ (+8.6\%)}_{-14.8\ (-8.6\%)}$
HERAPDF1.5	177.3	$^{+5.0\ (+2.8\%)}_{-4.5\ (-2.5\%)}$	$^{+4.0\ (+2.3\%)}_{-6.4\ (-3.6\%)}$	$^{+3.8\ (+2.1\%)}_{-3.8\ (-2.1\%)}$	$^{+5.4\ (+3.1\%)}_{-5.2\ (-2.9\%)}$	$^{+12.7\ (+7.2\%)}_{-13.6\ (-7.7\%)}$
NNPDF3.0	175.3	$^{+4.9\ (+2.8\%)}_{-6.1\ (-3.5\%)}$	$^{+4.5\ (+2.6\%)}_{-4.5\ (-2.6\%)}$	$^{+1.9\ (+1.1\%)}_{-1.9\ (-1.1\%)}$	$^{+5.4\ (+3.1\%)}_{-5.2\ (-3.0\%)}$	$^{+12.2\ (+7.0\%)}_{-13.2\ (-7.5\%)}$
ATLAS [85]	182.9	–	–	–	–	$^{+6.3\ (+3.5\%)}_{-6.3\ (-3.5\%)}$
CMS [86]	173.6	–	–	–	–	$^{+6.3\ (+3.6\%)}_{-5.9\ (-3.4\%)}$
8 TeV						
MSTW2008	246.0	$^{+6.6\ (+2.7\%)}_{-8.5\ (-3.4\%)}$	$^{+6.2\ (+2.5\%)}_{-6.4\ (-2.6\%)}$	$^{+4.0\ (+1.6\%)}_{-4.0\ (-1.6\%)}$	$^{+7.4\ (+3.0\%)}_{-7.1\ (-2.9\%)}$	$^{+17.0\ (+6.9\%)}_{-18.9\ (-7.7\%)}$
ABM11	198.8	$^{+5.2\ (+2.6\%)}_{-6.3\ (-3.2\%)}$	$^{+8.5\ (+4.3\%)}_{-8.5\ (-4.3\%)}$	–	$^{+6.1\ (+3.1\%)}_{-5.9\ (-3.0\%)}$	$^{+15.7\ (+7.9\%)}_{-16.6\ (-8.4\%)}$
CT10	246.4	$^{+6.8\ (+2.8\%)}_{-8.6\ (-3.5\%)}$	$^{+10.0\ (+4.1\%)}_{-8.2\ (-3.3\%)}$	$^{+4.0\ (+1.6\%)}_{-4.0\ (-1.6\%)}$	$^{+7.4\ (+3.0\%)}_{-7.1\ (-2.9\%)}$	$^{+19.9\ (+8.1\%)}_{-20.2\ (-8.2\%)}$
HERAPDF1.5	252.8	$^{+6.8\ (+2.7\%)}_{-6.3\ (-2.5\%)}$	$^{+5.4\ (+2.1\%)}_{-8.6\ (-3.4\%)}$	$^{+5.0\ (+2.0\%)}_{-5.0\ (-2.0\%)}$	$^{+7.5\ (+3.0\%)}_{-7.3\ (-2.9\%)}$	$^{+17.3\ (+6.8\%)}_{-18.6\ (-7.4\%)}$
NNPDF3.0	250.6	$^{+6.9\ (+2.8\%)}_{-8.8\ (-3.5\%)}$	$^{+5.9\ (+2.3\%)}_{-5.9\ (-2.3\%)}$	$^{+2.6\ (+1.0\%)}_{-2.6\ (-1.0\%)}$	$^{+7.5\ (+3.0\%)}_{-7.3\ (-2.9\%)}$	$^{+16.8\ (+6.7\%)}_{-18.5\ (-7.4\%)}$
ATLAS +CMS [182]	241.5	–	–	–	–	$^{+8.5\ (+3.5\%)}_{-8.5\ (-3.5\%)}$
13 TeV						
MSTW2008	806.6	$^{+20.6\ (+2.6\%)}_{-28.6\ (-3.6\%)}$	$^{+14.5\ (+1.8\%)}_{-15.7\ (-1.9\%)}$	$^{+11.1\ (+1.4\%)}_{-11.1\ (-1.4\%)}$	$^{+22.3\ (+2.8\%)}_{-21.6\ (-2.7\%)}$	$^{+49.4\ (+6.1\%)}_{-57.5\ (-7.1\%)}$
ABM11	697.9	$^{+16.8\ (+2.4\%)}_{-23.0\ (-3.3\%)}$	$^{+22.0\ (+3.2\%)}_{-22.0\ (-3.2\%)}$	–	$^{+19.8\ (+2.8\%)}_{-19.2\ (-2.7\%)}$	$^{+46.4\ (+6.6\%)}_{-52.2\ (-7.5\%)}$
CT10	806.1	$^{+21.2\ (+2.6\%)}_{-29.1\ (-3.6\%)}$	$^{+20.3\ (+2.5\%)}_{-17.8\ (-2.2\%)}$	$^{+11.1\ (+1.4\%)}_{-11.1\ (-1.4\%)}$	$^{+22.3\ (+2.8\%)}_{-21.6\ (-2.7\%)}$	$^{+53.3\ (+6.6\%)}_{-59.2\ (-7.3\%)}$
HERAPDF1.5	821.9	$^{+19.8\ (+2.4\%)}_{-19.9\ (-2.4\%)}$	$^{+13.5\ (+1.6\%)}_{-22.4\ (-2.7\%)}$	$^{+12.4\ (+1.5\%)}_{-12.4\ (-1.5\%)}$	$^{+22.7\ (+2.8\%)}_{-21.9\ (-2.7\%)}$	$^{+49.0\ (+6.0\%)}_{-53.6\ (-6.5\%)}$
NNPDF3.0	821.6	$^{+21.4\ (+2.6\%)}_{-29.7\ (-3.6\%)}$	$^{+14.9\ (+1.8\%)}_{-14.9\ (-1.8\%)}$	$^{+7.5\ (+0.9\%)}_{-7.5\ (-0.9\%)}$	$^{+22.7\ (+2.8\%)}_{-22.0\ (-2.7\%)}$	$^{+49.6\ (+6.0\%)}_{-57.3\ (-7.0\%)}$
ATLAS [197]	818	–	–	–	–	$^{+34\ (+4.2\%)}_{-34\ (-4.2\%)}$
CMS [187]	835	–	–	–	–	$^{+33\ (+3.9\%)}_{-33\ (-3.9\%)}$
14 TeV						
MSTW2008	954.1	$^{+24.2\ (+2.5\%)}_{-34.0\ (-3.6\%)}$	$^{+16.3\ (+1.7\%)}_{-17.8\ (-1.9\%)}$	$^{+12.8\ (+1.3\%)}_{-12.8\ (-1.3\%)}$	$^{+26.1\ (+2.7\%)}_{-25.3\ (-2.7\%)}$	$^{+57.5\ (+6.0\%)}_{-67.5\ (-7.1\%)}$
ABM11	832.5	$^{+19.9\ (+2.4\%)}_{-27.5\ (-3.3\%)}$	$^{+25.1\ (+3.0\%)}_{-25.1\ (-3.0\%)}$	–	$^{+23.3\ (+2.8\%)}_{-22.6\ (-2.7\%)}$	$^{+54.1\ (+6.5\%)}_{-61.3\ (-7.4\%)}$
CT10	953.2	$^{+24.9\ (+2.6\%)}_{-34.6\ (-3.6\%)}$	$^{+22.4\ (+2.3\%)}_{-19.9\ (-2.1\%)}$	$^{+12.8\ (+1.3\%)}_{-12.8\ (-1.3\%)}$	$^{+26.1\ (+2.7\%)}_{-25.2\ (-2.6\%)}$	$^{+61.6\ (+6.5\%)}_{-69.2\ (-7.3\%)}$
HERAPDF1.5	971.0	$^{+23.0\ (+2.4\%)}_{-23.5\ (-2.4\%)}$	$^{+15.4\ (+1.6\%)}_{-25.7\ (-2.6\%)}$	$^{+14.1\ (+1.5\%)}_{-14.1\ (-1.5\%)}$	$^{+26.5\ (+2.7\%)}_{-25.6\ (-2.6\%)}$	$^{+56.7\ (+5.8\%)}_{-62.4\ (-6.4\%)}$
NNPDF3.0	971.7	$^{+25.1\ (+2.6\%)}_{-35.3\ (-3.6\%)}$	$^{+17.2\ (+1.8\%)}_{-17.2\ (-1.8\%)}$	$^{+8.7\ (+0.9\%)}_{-8.7\ (-0.9\%)}$	$^{+26.6\ (+2.7\%)}_{-25.8\ (-2.7\%)}$	$^{+57.9\ (+6.0\%)}_{-67.5\ (-6.9\%)}$

Table 3.12: *The NNLO+NNLL total cross section predictions for top-quark pair production at the LHC based on different PDF sets and including all major sources of theoretical uncertainty. For comparison we also present the most precise cross section measurements by* CMS *and* ATLAS *where the total experimental error is a combination of statistical, systematic and luminosity uncertainties.*

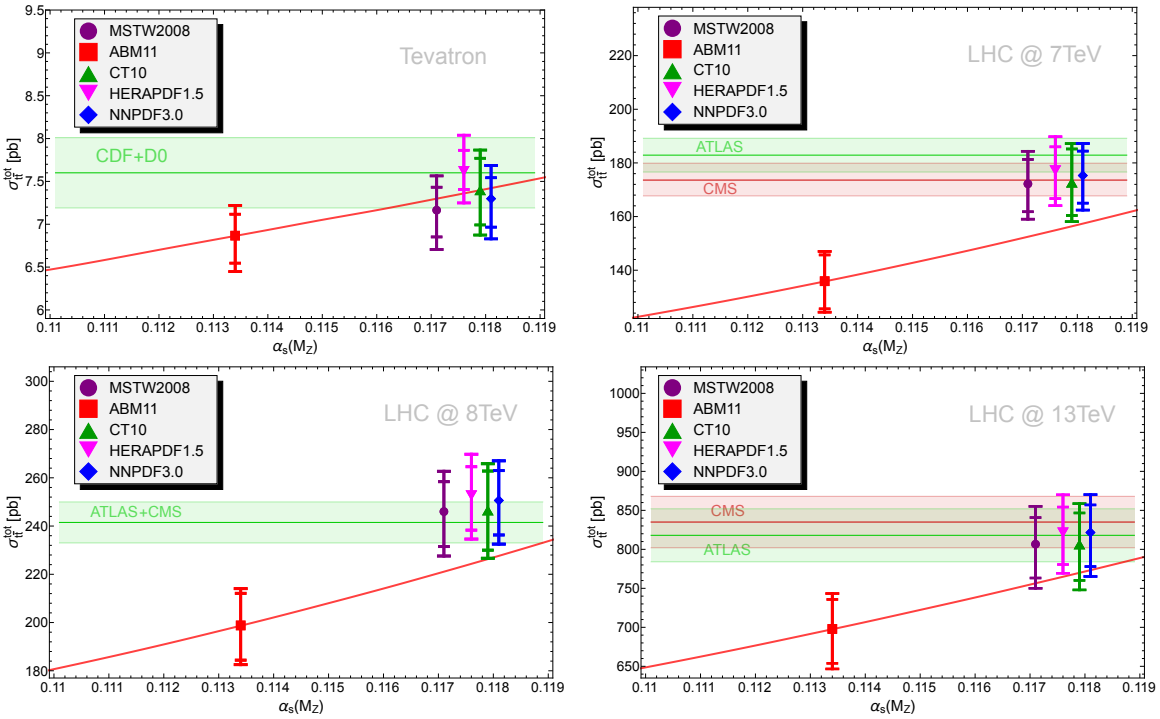

Figure 3.25: *The NNLO+NNLL total cross section predictions for the Tevatron and the LHC obtained from various PDF sets compared to experimental data [85, 86, 163, 182, 187, 197], as a function of the default $\alpha_s(M_Z)$-value. The inner error bars denote the linear sum of scale and PDF uncertainties (including α_s errors for the* Abm11 *results) whereas the outer error bars correspond to the total theory uncertainty. For the central* Abm11 *predictions we extended our analysis to cover a larger range of the strong coupling parameter.*

contrast to the α_s error, it is in this case sufficient to consider only the default PDF members, i. e. without the need to interpolate between different $\sigma_{t\bar{t}}^{\mathbf{tot}}$ results, allowing for a direct calculation of the corresponding deviations from the central cross section predictions. Following the recommendations of the Higgs Cross Section Working Group [658], the total parametric uncertainty on $\sigma_{t\bar{t}}^{\mathbf{tot}}$ is then given by the quadratic sum of the resulting top-mass error and the uncertainties associated with the PDFs and strong coupling constant. Finally, the total theory uncertainty is defined as the linear combination of this parametric uncertainty and the perturbative error due to scale variation.

In general, the total cross section predictions at the Tevatron and the LHC, shown in Tab. 3.11 and Tab. 3.12 respectively, are in good agreement for the various PDF sets employed in this analysis (see also Fig. 3.25), both for the central values and the theoretical uncertainties. Only the Abm11-based LHC results are somewhat out of line lying about 1-2σ below the predictions derived from the other sets. This behavior could have already been anticipated from our discussion in section 2.2 and has been thoroughly investigated in previous publications [262,494]. On the one hand, it can be traced back to a significantly lower value of α_s (see Fig. 2.4), which affects both the PDF evolution and the perturbative expansion of the partonic cross sections. Indeed, as indicated in Fig. 3.25, using a value similar to the ones employed by

the other PDF groups would lead to a sizable enhancement of the ABM11 predictions moving them much closer to the other cross section results. On the other hand, the deviations may be attributed to the use of a softer large-x gluon PDF, which is the reason why they are most pronounced for the LHC at 7 Tev and 8 TeV center-of-mass energy whereas at the Tevatron these reduction effects can be partly compensated by the larger $q\bar{q}$ fluxes such that all PDF predictions lie actually within 1σ.

The total theory uncertainty at both colliders varies between $\sim$5-8% comparable to the precision of the latest experimental determinations, which for the LHC lies at about 4% while for the Tevatron it is slightly larger $\sim$5.5% owing to the lower statistics. The same level of agreement can also be observed for the corresponding central values, i. e. the total cross section predictions are fully consistent with the $t\bar{t}$ data collected by the CDF , DØ, ATLAS and CMS experiments (even though the ABM11 results tend to underestimate the measured cross sections as well). This implies that our precise knowledge of this observable may conversely be used to acquire additional information on its input parameters, namely the top-quark mass, the strong coupling constant and the PDFs, especially the poorly constrained large-x gluon PDF. For the determination of the former it turns out to be quite handy to have some sort of simplified interpolation formula that parametrizes the top-mass dependence of the NNLO+NNLL cross section as well as its various theory uncertainties over a larger range of m_t-values than employed in the evaluation of δ_{m_t}. To this end, we performed a number of supplementary $\sigma_{t\bar{t}}^{\mathbf{tot}}$ calculations in the regime $m_t \in [150\,\text{GeV}, 190\,\text{GeV}]$ as shown in Fig. 3.26 that are subsequently employed as data points in a general top-mass fit of the form[32]

$$\sigma_{t\bar{t}}^{\mathbf{tot}}(m_t) = \sigma_{t\bar{t}}^{\mathbf{tot}}(m_{ref}) \left(\frac{m_{ref}}{m_t}\right)^5 \left[1 + a_1 \frac{m_t - m_{ref}}{m_{ref}} + a_2 \left(\frac{m_t - m_{ref}}{m_{ref}}\right)^2\right] . \tag{3.217}$$

The leading functional behavior in terms of a power law can be inferred from the approximate sensitivity relation in Eq. (1.18) whereas the polynomial correction factor has been introduced to account for possible deviations from the idealized top-mass dependence further away from its reference value, which has in our case been set to $m_{ref} = 173.3\,\text{GeV}$. Consequently, the corresponding reference cross sections $\sigma_{t\bar{t}}^{\mathbf{tot}}(m_{ref})$ as well as their respective uncertainties are given by the results in Tab. 3.11 and Tab. 3.12 leaving only the coefficients a_1 and a_2 as free parameters of the fit. Their explicit values depend on the actual collider setup and can be found in Tab. 3.13.

Note that due to the considerable computational effort associated with the determination of these interpolation formulae, especially with regard to the PDF uncertainties, we restrict our analysis to the MSTW2008 set only. The good agreement of the m_t-related uncertainties among the different PDF sets in Tab. 3.11 and Tab. 3.12, however, suggests that, at least for the central values, the top-mass dependence of the various PDF predictions is indeed quite similar. Moreover, we have neglected the α_s-related uncertainty in our theory error budget since it is usually the smallest parametric uncertainty affecting $\sigma_{t\bar{t}}^{\mathbf{tot}}$ while its determination is rather costly involving an additional fitting procedure, as explained above. Thus, the total

[32] A similar analysis has already been performed in Ref. [80], however, still based on a somewhat approximate treatment of the NNLO hard matching coefficients.

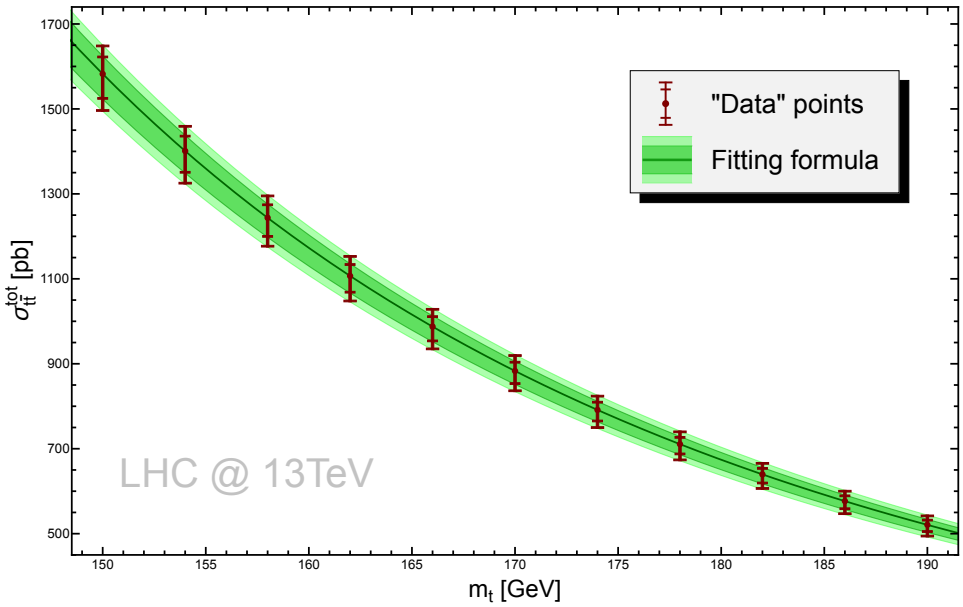

Figure 3.26: *Interpolation function (Eq. (3.217)) describing the top-mass dependence of the NNLO+NNLL total cross section prediction at the LHC with* 13 TeV *center-of-mass energy compared to the discrete set of* $\sigma_{t\bar{t}}^{\mathbf{tot}}$ *evaluations entering the fitting procedure. The inner error bars (dark-shaded band) correspond to mere scale uncertainties while the outer error bars (light-shaded band) represent the total theory uncertainty given by the linear sum of scale and PDF uncertainties. As explained in the text, the* α_s *error has not been considered here.*

theory uncertainty of the interpolation functions will be given by the linear sum of scale and PDF uncertainties, which for the parameters in Tab. 3.13 amounts to

$$\begin{aligned} \delta_{\text{tot}}^{\sigma,\pm} &= \delta_{\text{scale}}^{\sigma,\pm} + \delta_{\text{PDF}}^{\sigma,\pm} \\ \delta_{\text{tot}}^{a_i,\pm} &= \frac{\left(\sigma_{t\bar{t}}^{\mathbf{tot}}(m_{ref}) + \delta_{\text{scale}}^{\sigma,\pm}\right)\,\delta_{\text{scale}}^{a_i,\pm} + \left(\sigma_{t\bar{t}}^{\mathbf{tot}}(m_{ref}) + \delta_{\text{PDF}}^{\sigma,\pm}\right)\,\delta_{\text{PDF}}^{a_i,\pm}}{\sigma_{t\bar{t}}^{\mathbf{tot}}(m_{ref}) + \delta_{\text{tot}}^{\sigma,\pm}} \end{aligned} \tag{3.218}$$

where $\delta_{\text{scale}}^{\sigma,\pm}$, $\delta_{\text{PDF}}^{\sigma,\pm}$, $\delta_{\text{tot}}^{\sigma,\pm}$ and $\delta_{\text{scale}}^{a_i,\pm}$, $\delta_{\text{PDF}}^{a_i,\pm}$, $\delta_{\text{tot}}^{a_i,\pm}$ describe the individual shifts that have to be applied to $\sigma_{t\bar{t}}^{\mathbf{tot}}(m_{ref})$ and a_i, $i = 1, 2$, respectively to obtain the corresponding error bounds $\sigma_{t\bar{t}}^{\mathbf{tot}}(m_t) + \delta_{\text{scale/PDF/tot}}^{\pm}$. Note that for the coefficients a_1 and a_2 the sign of these shifts is not necessarily equal to the sign of the final cross section shifts $\delta_{\text{scale/PDF/tot}}^{\pm}$ as the correction factor in Eq. (3.217) rather determines the shape of $\sigma_{t\bar{t}}^{\mathbf{tot}}(m_t)$ than its overall normalization.

In section 1.2.1 we have already explained how this kind of interpolation formula can be used to extract the top-quark mass from measurements of the total $t\bar{t}$ production cross section, which has the advantage that one can avoid possible scheme ambiguities inherent to the more standard measurement techniques. Nevertheless, the precision of such an extraction can usually not compete with the results attainable with the latter methods calling for a further reduction of the theoretical uncertainty on $\sigma_{t\bar{t}}^{\mathbf{tot}}$, especially with regard to the potential exper-

$m_{ref} = 173.3\,\text{GeV}$		Tevatron	LHC			
			7 TeV	8 TeV	13 TeV	14 TeV
$\sigma_{t\bar{t}}^{\text{tot}}(m_{ref})$ [pb]	Central	7.16368	172.155	245.968	806.575	954.134
	$\delta_{\text{scale}}^{\sigma,+}$	+0.10931	+4.723	+6.635	+20.622	+24.219
	$\delta_{\text{scale}}^{\sigma,-}$	−0.19978	−5.870	−8.470	−28.642	−34.019
	$\delta_{\text{PDF}}^{\sigma,+}$	+0.16926	+4.709	+6.176	+14.485	+16.250
	$\delta_{\text{PDF}}^{\sigma,-}$	−0.12163	−4.800	−6.356	−15.712	−17.832
a_1	Central	−0.412930	−0.216228	−0.094524	0.282939	0.332916
	$\delta_{\text{scale}}^{a_1,+}$	−0.002184	−0.005493	−0.005598	−0.006544	−0.007096
	$\delta_{\text{scale}}^{a_1,-}$	+0.007146	+0.015363	+0.015141	+0.014611	+0.014660
	$\delta_{\text{PDF}}^{a_1,+}$	+0.022259	+0.016059	+0.015620	+0.012550	+0.012045
	$\delta_{\text{PDF}}^{a_1,-}$	−0.010478	−0.014879	−0.014344	−0.010954	−0.010321
a_2	Central	−0.627040	−0.390638	−0.435527	−0.487734	−0.484500
	$\delta_{\text{scale}}^{a_2,+}$	+0.012045	+0.008183	+0.005524	+0.002790	+0.001977
	$\delta_{\text{scale}}^{a_2,-}$	+0.007748	−0.013004	−0.012601	−0.006365	−0.004733
	$\delta_{\text{PDF}}^{a_2,+}$	+0.010911	−0.010276	−0.007342	+0.007878	+0.004981
	$\delta_{\text{PDF}}^{a_2,-}$	−0.001380	+0.010952	+0.007076	−0.002050	−0.003355

Table 3.13: *Parameters of the NNLO+NNLL cross section fit defined in Eq. (3.217) for the Tevatron and the LHC, including scale and PDF uncertainties. The results for $\sigma_{t\bar{t}}^{\text{tot}}(m_{ref})$ are equivalent to the findings in Tab. 3.11 and Tab. 3.12, however, in this case provided at a higher numerical precision to ensure that the accuracy of the fitting formulae lies within a few permille in the* 130-210 GeV *top-mass range.*

imental advances anticipated for the current and upcoming LHC runs. The same also applies to the cross-section-based determination of α_s, which is complementary to other measurement techniques and thus represents an important consistency check of the SM but still lacks precision (see Fig. 1.11). Considering the fact that the different sources of theoretical uncertainty contribute almost in equal parts to the total theory error, a significant improvement seems, however, not feasible within the near future since it would require substantial progress both on the theoretical (higher-order corrections) and experimental (more precise measurements of input parameters) side.

The determination of the large-x gluon PDF, on the other hand, already profits from the available total cross section results, in particular from the detailed comparison of LHC top-quark data with the NNLO+NNLL theory predictions. Indeed, due to the serious improvement with respect to previous PDF analyses most collaborations have meanwhile included $t\bar{t}$ cross section measurements in their global PDF fits. The NNPDF3.0 set, for instance, already contains an early batch of inclusive $t\bar{t}$ data collected by ATLAS and CMS at both 7 TeV and 8 TeV,

[33] Using uncorrelated systematic uncertainties will increase the total experimental error by about 40-50%.

LHC cross section ratios						
PDF set	$R_{t\bar{t}}^{\sqrt{s_1}/\sqrt{s_2}}$	δ_{scale}	δ_{PDF}	δ_{α_s}	δ_{m_t}	δ_{tot}
8 TeV/7 TeV						
MSTW2008	1.429	$^{+0.001\ (+0.1\%)}_{-0.001\ (-0.1\%)}$	$^{+0.004\ (+0.3\%)}_{-0.004\ (-0.3\%)}$	$^{+0.001\ (+0.1\%)}_{-0.001\ (-0.1\%)}$	$^{+0.001\ (+0.1\%)}_{-0.001\ (-0.1\%)}$	$^{+0.005\ (+0.4\%)}_{-0.005\ (-0.4\%)}$
ABM11	1.463	$^{+0.001\ (+0.1\%)}_{-0.002\ (-0.1\%)}$	$^{+0.006\ (+0.4\%)}_{-0.006\ (-0.4\%)}$	–	$^{+0.001\ (+0.1\%)}_{-0.001\ (-0.1\%)}$	$^{+0.007\ (+0.5\%)}_{-0.008\ (-0.6\%)}$
CT10	1.428	$^{+0.001\ (+0.1\%)}_{-0.001\ (-0.1\%)}$	$^{+0.008\ (+0.5\%)}_{-0.010\ (-0.7\%)}$	$^{+0.001\ (+0.1\%)}_{-0.001\ (-0.1\%)}$	$^{+0.001\ (+0.1\%)}_{-0.001\ (-0.1\%)}$	$^{+0.009\ (+0.7\%)}_{-0.011\ (-0.8\%)}$
HERAPDF1.5	1.426	$^{+0.001\ (+0.0\%)}_{-0.002\ (-0.1\%)}$	$^{+0.003\ (+0.2\%)}_{-0.003\ (-0.2\%)}$	$^{+0.002\ (+0.2\%)}_{-0.002\ (-0.2\%)}$	$^{+0.001\ (+0.1\%)}_{-0.001\ (-0.1\%)}$	$^{+0.005\ (+0.3\%)}_{-0.006\ (-0.4\%)}$
NNPDF3.0	1.429	$^{+0.001\ (+0.1\%)}_{-0.001\ (-0.1\%)}$	$^{+0.005\ (+0.3\%)}_{-0.005\ (-0.3\%)}$	$^{+0.001\ (+0.1\%)}_{-0.001\ (-0.1\%)}$	$^{+0.001\ (+0.1\%)}_{-0.001\ (-0.1\%)}$	$^{+0.006\ (+0.4\%)}_{-0.006\ (-0.4\%)}$
ATLAS [85]	1.326	–	–	–	–	$^{+0.057\ (+4.3\%)}_{-0.057\ (-4.3\%)}$
CMS [86, 186]	1.41	–	–	–	–	$^{+0.06\ (+4.3\%)}_{-0.06\ (-4.3\%)}$
	1.43	–	–	–	–	$^{+0.09\ (+6.6\%)}_{-0.09\ (-6.6\%)}$
13 TeV/7 TeV						
MSTW2008	4.685	$^{+0.009\ (+0.2\%)}_{-0.012\ (-0.3\%)}$	$^{+0.050\ (+1.1\%)}_{-0.052\ (-1.1\%)}$	$^{+0.015\ (+0.3\%)}_{-0.015\ (-0.3\%)}$	$^{+0.014\ (+0.3\%)}_{-0.014\ (-0.3\%)}$	$^{+0.063\ (+1.3\%)}_{-0.068\ (-1.5\%)}$
ABM11	5.136	$^{+0.013\ (+0.3\%)}_{-0.024\ (-0.5\%)}$	$^{+0.082\ (+1.6\%)}_{-0.082\ (-1.6\%)}$	–	$^{+0.016\ (+0.3\%)}_{-0.017\ (-0.3\%)}$	$^{+0.097\ (+1.9\%)}_{-0.108\ (-2.1\%)}$
CT10	4.670	$^{+0.010\ (+0.2\%)}_{-0.013\ (-0.3\%)}$	$^{+0.097\ (+2.1\%)}_{-0.126\ (-2.7\%)}$	$^{+0.014\ (+0.3\%)}_{-0.014\ (-0.3\%)}$	$^{+0.014\ (+0.3\%)}_{-0.014\ (-0.3\%)}$	$^{+0.109\ (+2.3\%)}_{-0.141\ (-3.0\%)}$
HERAPDF1.5	4.635	$^{+0.008\ (+0.2\%)}_{-0.017\ (-0.4\%)}$	$^{+0.046\ (+1.0\%)}_{-0.037\ (-0.8\%)}$	$^{+0.028\ (+0.6\%)}_{-0.028\ (-0.6\%)}$	$^{+0.013\ (+0.3\%)}_{-0.013\ (-0.3\%)}$	$^{+0.063\ (+1.4\%)}_{-0.065\ (-1.4\%)}$
NNPDF3.0	4.686	$^{+0.009\ (+0.2\%)}_{-0.013\ (-0.3\%)}$	$^{+0.062\ (+1.3\%)}_{-0.060\ (-1.3\%)}$	$^{+0.008\ (+0.2\%)}_{-0.008\ (-0.2\%)}$	$^{+0.014\ (+0.3\%)}_{-0.014\ (-0.3\%)}$	$^{+0.073\ (+1.5\%)}_{-0.075\ (-1.6\%)}$
ATLAS [85, 197]	4.47	–	–	–	–	$^{+0.17\ (+3.8\%)}_{-0.17\ (-3.8\%)}$
CMS [86, 659]	4.57	–	–	–	–	$^{+0.20\ (+4.4\%)}_{-0.20\ (-4.4\%)}$
13 TeV/8 TeV						
MSTW2008	3.279	$^{+0.005\ (+0.1\%)}_{-0.006\ (-0.2\%)}$	$^{+0.027\ (+0.8\%)}_{-0.028\ (-0.9\%)}$	$^{+0.008\ (+0.2\%)}_{-0.008\ (-0.2\%)}$	$^{+0.007\ (+0.2\%)}_{-0.007\ (-0.2\%)}$	$^{+0.034\ (+1.0\%)}_{-0.037\ (-1.1\%)}$
ABM11	3.511	$^{+0.007\ (+0.2\%)}_{-0.012\ (-0.3\%)}$	$^{+0.042\ (+1.2\%)}_{-0.042\ (-1.2\%)}$	–	$^{+0.009\ (+0.2\%)}_{-0.009\ (-0.2\%)}$	$^{+0.050\ (+1.4\%)}_{-0.055\ (-1.6\%)}$
CT10	3.271	$^{+0.005\ (+0.1\%)}_{-0.007\ (-0.2\%)}$	$^{+0.051\ (+1.6\%)}_{-0.066\ (-2.0\%)}$	$^{+0.008\ (+0.2\%)}_{-0.008\ (-0.2\%)}$	$^{+0.007\ (+0.2\%)}_{-0.007\ (-0.2\%)}$	$^{+0.057\ (+1.8\%)}_{-0.074\ (-2.2\%)}$
HERAPDF1.5	3.250	$^{+0.004\ (+0.1\%)}_{-0.009\ (-0.3\%)}$	$^{+0.025\ (+0.8\%)}_{-0.019\ (-0.6\%)}$	$^{+0.015\ (+0.5\%)}_{-0.015\ (-0.5\%)}$	$^{+0.007\ (+0.2\%)}_{-0.007\ (-0.2\%)}$	$^{+0.034\ (+1.0\%)}_{-0.034\ (-1.1\%)}$
NNPDF3.0	3.278	$^{+0.005\ (+0.1\%)}_{-0.007\ (-0.2\%)}$	$^{+0.032\ (+1.0\%)}_{-0.031\ (-1.0\%)}$	$^{+0.004\ (+0.1\%)}_{-0.004\ (-0.1\%)}$	$^{+0.007\ (+0.2\%)}_{-0.007\ (-0.2\%)}$	$^{+0.038;(+1.2\%)}_{-0.039\ (-1.2\%)}$
ATLAS [85, 197]	3.37	–	–	–	–	$^{+0.14\ (+4.2\%)}_{-0.14\ (-4.2\%)}$
CMS [86, 659]	3.24	–	–	–	–	$^{+0.15\ (+4.6\%)}_{-0.15\ (-4.6\%)}$

Table 3.14: *Results for the LHC total cross section ratios including all possible combinations of Run 1 and Run 2 collision energies. The theory predictions at NNLO+NNLL accuracy are based on different PDF sets and account for all major sources of theoretical uncertainty. The experimental results have been either provided directly by* ATLAS *and* CMS *or, for* $R_{t\bar{t}}^{13/7}$ *and* $R_{t\bar{t}}^{13/8}$*, estimated from the most precise absolute cross section measurements in the* $e\mu$ *dilepton channel. The total experimental error is a combination of statistical, systematic and luminosity uncertainties where for the naive ratio estimates we assumed that all systematic effects are fully correlated*[33] *while the contributions from statistics and the luminosity may vary independently.*

which is presumably the reason why the corresponding PDF errors for the LHC predictions in Tab. 3.12 are slightly reduced with respect to the results of the other sets, at least for lower collider energies. Similar to the extraction of m_t or α_s a further reduction of this uncertainty seems to rely on additional improvements in the theoretical description of $\sigma_{t\bar{t}}^{\mathbf{tot}}$. There exists, however, a promising alternative that comes at virtually no additional computational cost while leading to a dramatic increase of the theoretical precision, namely the investigation of LHC cross section ratios $R_{t\bar{t}}^{\sqrt{s_1}/\sqrt{s_2}} \equiv \sigma_{t\bar{t}}^{\mathbf{tot},\sqrt{s_1}}/\sigma_{t\bar{t}}^{\mathbf{tot},\sqrt{s_2}}$.

The corresponding NNLO+NNLL predictions for all possible combinations of Run 1 and Run 2 collision energies are shown in Tab. 3.14 where the individual sources of theoretical uncertainty have been evaluated in the same manner as for $\sigma_{t\bar{t}}^{\mathbf{tot}}$, i. e. $R_{t\bar{t}}^{\sqrt{s_1}/\sqrt{s_2}}$ is treated as an independent observable rather than the ratio of the results in Tab. 3.12. Note that, in contrast to the total cross section, the theory error is now clearly dominated by the PDF uncertainty already indicating the phenomenological potential for further constraining this input parameter. Moreover, we in Tab. 3.14 also present the latest experimental determinations of the cross section ratios albeit only for $R_{t\bar{t}}^{8/7}$ there actually exist explicit results provided directly by ATLAS [85] and CMS [86, 186] whereas for the ratios involving 13 TeV data we derived our own estimates based on the most precise absolute cross section measurements in the $e\mu$ dilepton channel [85, 86, 197, 659]. As has been noticed in Refs. [261, 262], the large degree of correlation of both experimental and theoretical uncertainties between different center-of-mass energies renders $R_{t\bar{t}}^{\sqrt{s_1}/\sqrt{s_2}}$ particularly suited for high-precision SM studies. Indeed, the LHC ratios in Tab. 3.14 display a similar sensitivity to the gluon PDF as the corresponding absolute cross section results [262] while the total theory error has dropped to the level of 1-3% or even below. In consequence, the relative deviation of the various PDF predictions is much more pronounced, especially for the ABM11 set, implying that $R_{t\bar{t}}^{\sqrt{s_1}/\sqrt{s_2}}$ might have a substantially higher discriminating power in the relevant large-x regime than $\sigma_{t\bar{t}}^{\mathbf{tot}}$. Considering the fact that the experimental precision is approximately the same for both of these observables, it would be worth thinking about incorporating $t\bar{t}$ total cross section ratios in future PDF fits.

As can be inferred from the corresponding uncertainties δ_{α_s} and δ_{m_t} the sensitivity of $R_{t\bar{t}}^{\sqrt{s_1}/\sqrt{s_2}}$ to the remaining input parameters α_s and m_t is strongly suppressed such that their determination cannot profit from the improved theoretical precision in this quantity. In fact, for the top-quark mass this could have already been expected from the functional form of the fitting formula in Eq. (3.217), which implies that the leading m_t-dependence will always cancel out in this kind of cross section ratio. Note, however, that there exist another possible application for this class of observables, namely the search for contributions from BSM physics which might otherwise be inaccessible through an analysis of the absolute cross sections. To this end, one assumes that the total cross section at center-of-mass energy $\sqrt{s}$ is given as $\sigma_{t\bar{t}}^{\mathbf{tot}} \equiv \sigma_{t\bar{t}}^{\mathbf{SM},\sqrt{s}} + \sigma_{t\bar{t}}^{\mathbf{BSM},\sqrt{s}}$ such that the cross section ratio can be decomposed as follows [261]

$$R_{t\bar{t}}^{\sqrt{s_1}/\sqrt{s_2}} = \frac{\sigma_{t\bar{t}}^{\mathbf{SM},\sqrt{s_1}} + \sigma_{t\bar{t}}^{\mathbf{BSM},\sqrt{s_1}}}{\sigma_{t\bar{t}}^{\mathbf{SM},\sqrt{s_2}} + \sigma_{t\bar{t}}^{\mathbf{BSM},\sqrt{s_2}}} \approx \frac{\sigma_{t\bar{t}}^{\mathbf{SM},\sqrt{s_1}}}{\sigma_{t\bar{t}}^{\mathbf{SM},\sqrt{s_2}}} \left(1 + \frac{\sigma_{t\bar{t}}^{\mathbf{BSM},\sqrt{s_1}}}{\sigma_{t\bar{t}}^{\mathbf{SM},\sqrt{s_1}}} - \frac{\sigma_{t\bar{t}}^{\mathbf{BSM},\sqrt{s_2}}}{\sigma_{t\bar{t}}^{\mathbf{SM},\sqrt{s_2}}}\right) . \tag{3.219}$$

An essential requirement for this method to work is that $\sigma_{t\bar{t}}^{\mathbf{BSM},\sqrt{s}}$ evolves differently with energy than $\sigma_{t\bar{t}}^{\mathbf{SM},\sqrt{s}}$. If this is the case, the precise knowledge of the SM prediction $R_{t\bar{t}}^{\mathrm{SM},\sqrt{s_1}/\sqrt{s_2}} \equiv \sigma_{t\bar{t}}^{\mathbf{SM},\sqrt{s_1}}/\sigma_{t\bar{t}}^{\mathbf{SM},\sqrt{s_2}}$ will allow us to probe the measured LHC cross section ratios for hidden BSM contaminations down to the percent level even though the effective detection potential will certainly depend on the specific new-physics scenario under consideration. However, since so far all measurements are consistent with the various theory predictions in Tab. 3.14, $R_{t\bar{t}}^{\sqrt{s_1}/\sqrt{s_2}}$ can currently only be used to further constrain the parameter space of possible BSM models and set exclusion limits. It remains to be seen whether the situation will change once the gluon PDF has been further improved and additional measurements at 13 TeV and 14 TeV become available.

Still, the total cross section for top-quark pair production has proven to be a powerful phenomenological tool in SM physics and beyond, in particular with the inclusion of the full NNLO QCD corrections. The possible benefits of studying more exclusive quantities related to the top quark have already been outlined in sections 1.3.3 and 1.3.4 and will be discussed in greater detail in the next chapter focusing, however, primarily on the Tevatron where most of these differential observables have first been measured.

Chapter 4

Differential NNLO $t\bar{t}$ production at the Tevatron

The determination of the NNLO QCD corrections for the inclusive $t\bar{t}$ production cross section were an important step towards a more detailed understanding of top-quark physics at modern hadron colliders offering access to a large variety of phenomenological applications as illustrated in section 3.5. Nevertheless, there is still room for improvement considering the fact that the sensitivity to certain SM parameters as well as potential BSM contributions may be further enhanced by focusing our attention on more exclusive regions of the heavy-quark phase space. Thus, it would be advantageous to be able to also describe differential top-quark observables of the form

$$\frac{d^n\sigma}{d\mathcal{Q}_1\cdots d\mathcal{Q}_n} = \sum_{ij}\int_0^1\int_0^1 dx_1 dx_2\, f_i^A(x_1,\mu_F) f_j^B(x_2,\mu_F)\,\frac{d^n\hat{\sigma}_{ij\to t\bar{t}+X}}{d\mathcal{Q}_1\cdots d\mathcal{Q}_n}\left(\mu_R,\mu_F,\alpha_s(\mu_R)\right) \quad (4.1)$$

at this high level of theoretical precision in order to allow for an in-depth comparison with the experimental data collected at the Tevatron and the LHC. Indeed, the necessary ingredients for such a differential NNLO analysis in terms of the kinematic variables $\mathcal{Q}_i$ are already available from the calculation of $\sigma_{t\bar{t}}^{\text{tot}}$ since the only difference with respect to fully inclusive top-quark production lies in the presence of additional kinematic cuts in the two- to four-particle phase space integrations.

Consequently, by relying on the same computational framework outlined in chapter 3, we were able to present the first-ever theoretical predictions for various exclusive top-quark observables at exact $\mathcal{O}(\alpha_s^4)$ accuracy. Note that the corresponding results, which have meanwhile been published in Refs. [385, 406], refer solely to the Tevatron as the primary objective of these early NNLO studies was to resolve the tension between the measured $t\bar{t}$ forward-backward asymmetry and its computed SM expectation as we will discuss in more detail below (see also section 1.3.3). Moreover, the CDF and DØ collaborations were the first to provide solid experimental results for the main kinematic top-quark distributions and, for the time being, the data collected by these experiments remains the only source of investigating the kinematic properties of the top quark in quark-dominated $t\bar{t}$ production. Hence, the comparison with the corresponding NNLO QCD predictions presented in this chapter will offer phenomenological insights that are complementary to the conclusions drawn from LHC data[1] (see section 1.3.4) despite the fact that the latter is generally far more precise. However, since the calculation of the differential $\mathcal{O}(\alpha_s^4)$ corrections involves some minor modifications with regard to the total

[1] The differential NNLO QCD predictions for the LHC [427–429] have been derived with the help of the four-dimensional formulation of STRIPPER [632] and, thus, differ in the implementational details from the strategy outlined below.

inclusive scenario, we first of all specify the details of the computational setup used in the derivation of these NNLO Tevatron distributions.

The most notable innovation is certainly the treatment of the PDF convolution, which in case of $\sigma_{t\bar{t}}^{\mathbf{tot}}$ was parametrized as the (integrated) product of a collider-dependent partonic flux factor with a universal partonic cross section. At the differential level, such an approach is no longer feasible since the computational effort for a separate determination of the relevant NNLO corrections to $d^n\hat{\sigma}_{ij\to t\bar{t}+X}/d\mathcal{Q}_1\cdots d\mathcal{Q}_n$ is by current standards unmanageable. Our solution to this problem is to include the PDF convolution in the MC framework employed in the evaluation of the phase space integrals such that the resulting outputs correspond directly to the hadronic cross section contributions. To this end, we return to the original formulation of the convolution shown in Eq. (4.1) in terms of the momentum fractions x_1 and x_2, which are subsequently remapped to an alternative set of variables $x'_{1,2} \in [0,1]$ via

$$\begin{aligned} x_1 &= \rho_{\mathrm{H}}^{x'_1(1-x'_2)} \\ x_2 &= \rho_{\mathrm{H}}^{x'_1 x'_2} \end{aligned} \tag{4.2}$$

to facilitate their implementation into the MC integration routines. Note that this will introduce an additional Jacobian factor of the form $x'_1\,\rho_{\mathrm{H}}^{x'_1}\,\ln^2\rho_{\mathrm{H}}$ into the convolution integrals, which has to be properly accounted for to guarantee the numerical correctness of the final cross section predictions. In practice, such a non-trivial modification of the functional dependence may become problematic, namely, when it artificially increases the complexity of the integrand and thus spoils the numerical convergence. In our case, however, the Jacobian has no noticeable impact on the performance of integration algorithm stressing the effectiveness of the chosen mapping in Eq. (4.2).

Another important aspect is in this context the implementation of the collinear-renormalization procedure, which indeed turns out to be crucial for a successful numerical evaluation of the corresponding convolutions of the LO and NLO exclusive cross sections with the splitting kernels in Eq. (2.29). In contrast to the total cross section where these additional integrations could be performed at the level of analytically known functions, in the differential case such a treatment is due to the absence of the relevant analytic expressions (at least at NLO) no longer possible. In consequence, these convolutions have also become part of the MC framework, which increases the number of integration variables by up to two and, moreover, introduces further Jacobian factors into the integrand. For the final hadronic cross section results the order[2] in which the various convolutions (PDFs + splitting functions) are evaluated is irrelevant since these contributions commute by definition. In practice, however, it proves to be by far most efficient to chose an integrand representation that corresponds to the scenario where first the splitting functions are combined with the PDFs and only afterwards the resulting expressions are convoluted with the partonic cross sections. Thus, the required computational demand for the evaluation of the NNLO collinear-renormalization contributions remains comparable to an NLO-type calculation even at the differential level.

[2] Within the MC formalism all integrations are performed simultaneously, which may be achieved by remapping the integration domain to the unit hypercube. Still, this remapping procedure is not unique and to some extend reflects an ordering of the underlying convolution integrals.

The determination of the other parts of the partonic cross section is on the contrary quite straightforward. While again working in CDR, we now fully exploit the advantages associated with the simplified treatment of virtual contributions described in section 3.3 by parametrizing the one- and two-loop amplitudes in terms of finite remainders. The thus removed spurious $\mathcal{O}(\epsilon)$ terms would otherwise lead to an unnecessary increase of the computational costs and introduce additional numerical uncertainties in the final cross section results. Note, however, that, in order to allow for a completely general description of the two-loop virtual corrections, the corresponding finite remainder grids derived in section 3.4.2 have to be continued to arbitrary kinematics with the help of a suitable interpolation function. This is particularly important as the subsequent integral over the two-particle phase space is no longer evaluated by means of a deterministic integration rule but also via MC methods using the four-dimensional parametrization of the heavy-quark system given in Eq. (3.134). This, in fact, applies to the entire class of 2-to-2 cross section contributions such that now all phase space integrals required for the derivation of the differential NNLO Tevatron predictions can be treated within the same STRIPPER-based MC framework.

The additional constraints induced by the dependence on the kinematic (top-quark) variables $\mathcal{Q}_i$ are conveniently implemented by means of the jet function F_J introduced in Eq. (3.142) (see also Eq. (3.158), Eq. (3.167) and Eq. (3.171)), which for the generic cross section in Eq. (4.1) assumes the following form

$$F_J = \prod_{i=1}^{n} \delta(Q_i(p_t, p_{\bar{t}}) - \mathcal{Q}_i) \; . \tag{4.3}$$

Here, $Q_i(p_t, p_{\bar{t}})$ denotes the corresponding functional definition of $\mathcal{Q}_i$ expressed in terms of the top and anti-top four-momenta in the laboratory frame as can, for instance, be seen in Tab. 4.1 for the single and double differential distributions evaluated in the course of this thesis. Note that these observables are in general not invariant under the symmetry operations utilized for the recovery of the omitted phase space regions in the total inclusive case. Thus, in order to still be able to employ the same selector functions for the separation of collinear sectors, we have to apply some sort of momentum reassignment that compensates for the kinematic restrictions in the construction of the partonic final-state systems. This "de-symmetrization" procedure is based on the use of randomly selected rotation and charge conjugation operations and in principle allows for the calculation of the $\mathcal{O}(\alpha_s^4)$ corrections to any (stable-)top-related quantity accessible in hadronic collisions.

In practice, however, a continuous treatment in terms of arbitrary values of $\mathcal{Q}_i$ as implied by Eq. (4.3) is usually not feasible. From the theory point of view this is due to the fact that there currently exists no straightforward method to incorporate the kinematic conditions encoded in the respective delta functions into a MC-based numerical integration routine regardless of the underlying subtraction scheme. Moreover, the measurement of these differential observables naturally involves only a finite number of $t\bar{t}$ events, which, as is generally known, are subsequently grouped into a small set of discrete data bins in order to minimize the impact of statistical fluctuations. Therefore, a meaningful comparison of theory and experiment is usually only possible at the level of binned distributions suggesting that the definition of the

jet function should be modified as follows

$$\begin{aligned}\delta(Q_i(p_t,p_{\bar{t}})-\mathcal{Q}_i) \quad &\longrightarrow \quad \left\{\frac{\theta(Q_i-\mathcal{b}_i^{(0)})\theta(\mathcal{b}_i^{(1)}-Q_i)}{\mathcal{b}_i^{(1)}-\mathcal{b}_i^{(0)}};\ldots;\frac{\theta(Q_i-\mathcal{b}_i^{(m_i-1)})\theta(\mathcal{b}_i^{(m_i)}-Q_i)}{\mathcal{b}_i^{(m_i)}-\mathcal{b}_i^{(m_i-1)}}\right\} \\ &\equiv \quad \left\{\theta_{\mathrm{bin}_1}(Q_i);\ldots;\theta_{\mathrm{bin}_{m_i}}(Q_i)\right\}\ .\end{aligned} \tag{4.4}$$

The binning functions $\theta_{\mathrm{bin}_k}(Q_i)$ restrict the kinematics of the $t\bar{t}$ pair to the range spanned by the bin edges $\mathcal{b}_i^{(k-1)}$ and $\mathcal{b}_i^{(k)}$ ($\mathcal{b}_i^{(k)}>\mathcal{b}_i^{(k-1)}$). They may, in principle, be assigned freely allowing for an utmost degree of flexibility in the description of differential cross sections despite the discretised treatment of their kinematic dependencies. The resulting theory predictions will then be given in terms of n-dimensional histograms[3]

$$\frac{d^n\sigma}{d\mathcal{Q}_1\cdots d\mathcal{Q}_n}=\left\{\left\{\sigma_{\mathrm{bin}_1,\ldots,\mathrm{bin}_1}(Q_1,\ldots,Q_n);\ldots;\sigma_{\mathrm{bin}_{m_1},\ldots,\mathrm{bin}_{m_n}}(Q_1,\ldots,Q_n)\right\}\right\}\ , \tag{4.5}$$

where

$$\sigma_{\mathrm{bin}_{k_1},\ldots,\mathrm{bin}_{k_n}}(Q_1,\ldots,Q_n)=\int d\sigma\ \theta_{\mathrm{bin}_{k_1}}(Q_1)\cdots\theta_{\mathrm{bin}_{k_n}}(Q_n)\ . \tag{4.6}$$

The normalization in Eq. (4.4) has been chosen such that

$$\begin{aligned}\sigma_{t\bar{t}}^{\mathrm{tot}} \quad &= \quad \int d\mathcal{Q}_1\cdots d\mathcal{Q}_n\,\frac{d^n\sigma}{d\mathcal{Q}_1\cdots d\mathcal{Q}_n} \\ &\simeq \quad \sum_{k_1=1}^{m_1}\cdots\sum_{k_n=1}^{m_n}\sigma_{\mathrm{bin}_{k_1},\ldots,\mathrm{bin}_{k_n}}(Q_1,\ldots,Q_n)\left(\mathcal{b}_1^{(k_1)}-\mathcal{b}_1^{(k_1-1)}\right)\cdots\left(\mathcal{b}_n^{(k_n)}-\mathcal{b}_n^{(k_n-1)}\right)\ ,\end{aligned} \tag{4.7}$$

i. e. the area under the binned curve still corresponds to the total cross section provided that the outer edges $\mathcal{b}_i^{(0)}$ and $\mathcal{b}_i^{(m_i)}$ cover the entire physical domain of the variables $\mathcal{Q}_i$. For some observables, e. g. the top-quark rapidity y_t, this will, however, lead to bin sizes $\mathcal{w}_i^{(k)}\equiv\mathcal{b}_i^{(k)}-\mathcal{b}_i^{(k-1)}$ that diverge in certain corners of phase space effectively setting the respective bin entries to zero. To solve this issue, one usually imposes a finite cutoff on these singular normalization factors while leaving the integration bounds in the numerator of the affected binning functions unchanged. The resulting integral in Eq. (4.6) will then contain so-called overflow entries, i. e. contributions from kinematic configurations beyond the nominal bin size set by the chosen cutoff edge. Note that, in practice, this strategy is also applied to distributions that are already restricted through some sort of physical constraint, for instance the available center-of-mass energy, since it allows for the use of a reasonably fine binning while still covering the entire cross section range. This is particularly advantageous for the description of the tails of kinematic distributions as they usually suffer from larger statistical fluctuations, both in experiment and in the MC integration employed for the derivation of the theoretical predictions. The resulting uncertainties can hence be further reduced by working with a single bin including overflow events rather than several separate bins.

[3] As indicated by the double parentheses, in practice, these histograms may be represented by multidimensional arrays (vectors, matrices, etc.) of order $m_1\times\ldots\times m_n$.

Single differential observables		
$\mathcal{Q}_1$	$Q_1(p_t, p_{\bar{t}})$	Binning
$p_{T,t}$	$\sqrt{p_{t,x}^2 + p_{t,y}^2}$	$[0; 45; 90; 140; 200; 300; 500; \mathbf{965}]$ GeV
$\lvert y_t \rvert$	$\left\lvert \frac{1}{2} \ln \frac{E_t + p_{t,z}}{E_t - p_{t,z}} \right\rvert$	$[0; 0.25; 0.5; 0.75; 1; 1.25; 1.5; \boldsymbol{\infty}]$
$\cos\theta$	$\frac{(p_t \cdot p_{t\bar{t}})(p_p \cdot p_{t\bar{t}}) - m_{t\bar{t}}^2 p_t \cdot p_p}{p_p \cdot p_{t\bar{t}} \sqrt{(p_t \cdot p_{t\bar{t}})^2 - m_{t\bar{t}}^2 m_t^2}}$	$[-1; -0.8; -0.6; -0.4; -0.2; 0; 0.2; 0.4; 0.6; 0.8; 1]$
$m_{t\bar{t}}$	$\sqrt{(p_t + p_{\bar{t}})^2}$	$[240; 412.5; 505; 615; 750; 1200; \mathbf{1960}]$ GeV
Δy	$\frac{1}{2} \ln \frac{(E_t + p_{t,z})(E_{\bar{t}} - p_{\bar{t},z})}{(E_t - p_{t,z})(E_{\bar{t}} + p_{\bar{t},z})}$	$[-2; -1.5; -1; -0.5; 0; 0.5; 1; 1.5; 2]$

Double differential observables	
$\mathcal{Q}_1; \mathcal{Q}_2$	Binning
$m_{t\bar{t}}; \Delta y$	$[250; 350; 450; 550; 650; 750]$ GeV $\times [-1; 0; 1]$
$p_{T,t\bar{t}}; \Delta y$	$[0; 10; 20; 30; 40; 50; 60; 70; 80]$ GeV $\times [-1; 0; 1]$

Table 4.1: *Summary of the kinematic variables employed in the exclusive NNLO $t\bar{t}$ analysis at the Tevatron. Apart from the functional definitions in terms of the top-quark momenta p_t, $p_{\bar{t}}$ and $p_{t\bar{t}} \equiv p_t + p_{\bar{t}}$ (and analogously $p_{T,t\bar{t}} \equiv |\vec{p}_{T,t} + \vec{p}_{T,\bar{t}}|$) as well as the proton momentum p_p we also present the explicit binning $\left[\mathcal{b}_1^{(0)}; \ldots; \mathcal{b}_1^{(m_1)}\right]$ and $\left[\mathcal{b}_1^{(0)}; \ldots; \mathcal{b}_1^{(m_1)}\right] \times \left[\mathcal{b}_2^{(0)}; \ldots; \mathcal{b}_2^{(m_2)}\right]$ used in the calculation of the respective single and double differential cross sections. For an improved visibility, the bins associated with the edges in bold print are omitted from the plots shown in the subsequent sections whereas the bins corresponding to italicized edges contain overflow events.*

Another potential problem related to the discretised treatment of differential observables is the impairment of the subtraction mechanism for the evaluation of real radiation contributions when choosing a too fine binning. The reason for this is the increased probability for kinematic configurations of the real-emission matrix element and the corresponding subtraction term(s) to lie in different bins such that the delicate cancellation structure regulating the IR-singular behavior is no longer effective. The consequence is the emergence of numerical instabilities in the MC phase space integration, an aspect that is, in fact, already known from NLO calculations, leading to a reduced numerical convergence or, at worst, even to a complete breakdown of the integration procedure. A possible solution to this mis-binning problem is the use of so-called smearing techniques which allow for a certain overlap at the boundary of adjacent bins. Thereby, parts of the MC weights are shifted between the real-emission and subtraction kinematics, which to some extend restores the original cancellation mechanism. For the top-quark distributions evaluated in the course of this thesis such a smeared treatment is, however, not necessary as the corresponding bin widths are sufficiently large to render potential mis-binning effects irrelevant. The positions of the respective bin edges are shown in Tab. 4.1 both for the single and double differential cross sections. They have been adopted from the experimental analyses in Refs. [388, 392, 459, 660] in order to allow for a direct comparison of the NNLO theory predictions with the latest CDF and DØ data. Apart from this explicit binning, no further kinematic cuts have been imposed.

Similar to the total cross section analysis, the actual calculation is performed for central scales $\mu_F = \mu_R = m_t$ where again we choose $m_t = 173.3\,\text{GeV}$ as the default value for the top-quark mass. Although it has been argued in section 1.3.4 that the use of dynamic scales in general leads to a much more reliable theoretical description of differential top-quark observables, for the limited kinematic range accessible at the Tevatron it is presumably sufficient to work with such a fixed scale choice. For the future, it might still be worth reassessing the NNLO distributions presented in this work with the PFPC scale setting procedure proposed in Eq. (1.62) especially with regard to more advanced phenomenological applications such as PDF or top-mass determinations that rely on a precise theory error estimate. The perturbative uncertainty due to missing higher-order contributions is usually dominating in this context. For each bin specified in Tab. 4.1 it is evaluated separately by employing the restricted scale variation in Eq. (2.5), which is assumed to hold also at the differential level. This similarly applies to any derived quantities such as normalized distributions or differential asymmetries. Note, however, that, since these observables are constructed in the form of cross section ratios, the resulting theory errors are subject to strong correlation effects, i. e. the corresponding numerators and denominators are not varied independently but rather treated as a single scale-dependent quantity. In consequence, one should be alerted to the possibility of underestimating the true size of missing higher-order effects in these ratios, an aspect that we will thoroughly investigate in the following discussions.

For the determination of the second major source of theoretical uncertainty, the PDF error, we pursue a two-fold strategy. As a first handle on the PDF dependence we compare the central NNLO QCD predictions for our default PDF choice MSTW2008 [231] to the results derived from three additional PDF sets, namely HERAPDF1.5 [497], CT10 [499] and NNPDF2.3 [263]. Such an analysis is sensitive to differences in the PDF parametrization and might thus help to further improve the functional description of the partonic momentum spectra inside the proton in regions that are so far only insufficiently constrained through data. Yet, for a more robust error estimate it would be advantageous to also have the individual PDF uncertainties based on the prescriptions given in section 2.2 available. Due to the large computational effort associated with the combined treatment of partonic fluxes and cross sections at the differential level, a direct evaluation of the respective NNLO PDF errors is, however, no longer feasible and we therefore have to resort to an approximate error estimation procedure. To this end, we assume that the shapes of the differential top-quark distributions are only moderately affected by the $\mathcal{O}(\alpha_s^4)$ corrections such that the hadronic cross section ratio[4]

$$\frac{\frac{d^n\sigma^{(i)}_{\text{NNLO}}}{d\mathcal{Q}_1\cdots d\mathcal{Q}_n}}{\frac{d^n\sigma^{(i)}_{NLO}}{d\mathcal{Q}_1\cdots d\mathcal{Q}_n}} = \frac{ff^{(i)}_{\text{NNLO}} \otimes \frac{d^n\hat{\sigma}_{\text{NNLO}}}{d\mathcal{Q}_1\cdots d\mathcal{Q}_n}}{ff^{(i)}_{\text{NNLO}} \otimes \frac{d^n\hat{\sigma}_{\text{NLO}}}{d\mathcal{Q}_1\cdots d\mathcal{Q}_n}} \tag{4.8}$$

constructed from the NNLO partonic flux $ff^{(i)}_{\text{NNLO}}$ of a specific PDF member $i \geq 0$ is effectively independent of i. Consequently, the NNLO predictions for the entire set of eigenvectors can

[4] Note that the *NLO* differential cross section in the denominator differs from the usual definition which is based on a convolution with PDFs of NLO accuracy.

be conveniently expressed in terms of the central PDF member $i = 0$ via

$$ff^{(i)}_{\text{NNLO}} \otimes \frac{d^n\hat{\sigma}_{\text{NNLO}}}{d\mathcal{Q}_1 \cdots d\mathcal{Q}_n} \approx ff^{(i)}_{\text{NNLO}} \otimes \frac{d^n\hat{\sigma}_{\text{NLO}}}{d\mathcal{Q}_1 \cdots d\mathcal{Q}_n} \times \frac{ff^{(0)}_{\text{NNLO}} \otimes \frac{d^n\hat{\sigma}_{\text{NNLO}}}{d\mathcal{Q}_1 \cdots d\mathcal{Q}_n}}{ff^{(0)}_{\text{NNLO}} \otimes \frac{d^n\hat{\sigma}_{\text{NLO}}}{d\mathcal{Q}_1 \cdots d\mathcal{Q}_n}} \,. \tag{4.9}$$

Focusing solely on the MSTW2008 set, the resulting approximations for $d^n\sigma^{(i)}_{\text{NNLO}}/d\mathcal{Q}_1 \cdots d\mathcal{Q}_n$ can then be further processed with the help of the standard Hessian error prescription in Eq. (2.16), which de facto reduces the determination of the NNLO PDF uncertainty to a problem of mere NLO complexity (provided that the central predictions are already known). While there exists no formal proof for the validity of such an approximate treatment, it may be somewhat justified by the observation that the corresponding PDF uncertainties for the distributions specified in Tab. 4.1 are always significantly smaller than the respective scale errors. Thus, for the phenomenological implications derived in the following sections the exact knowledge of the PDF uncertainty will most likely be irrelevant.

The other sources of parametric uncertainty known from the discussion of the total cross section (see section 3.5.4), namely the experimental errors on α_s and m_t, are not considered here[5]. Note, however, that for certain normalized distributions the sensitivity to these parameters, in particular the top-quark mass, may be strongly enhanced. For the future it might therefore be worth thinking about including the corresponding uncertainties in the total theory error estimate[6] of these observables not only at the Tevatron but also at the LHC where one can expect a similar behavior.

Another potential source of uncertainty albeit of rather technical nature is the MC integration error. Ideally, it can be completely eliminated from the theoretical description of differential NNLO $t\bar{t}$ production but due to the finite computational resources available for such an analysis it still has to be taken into account. It turns out that for all observables considered below the MC error is generally small even for the double differential cross sections, which are certainly the computationally most demanding quantities in this context. In particular for the NNLO predictions that can be compared to actual data the MC error amounts to about 1% or less and can hence be safely neglected. Only for some bins in the tails of the kinematic distributions where the cross sections are very small, the MC errors could become sizable. We, however, refrain from making any additional effort towards a further improvement of the MC errors in such bins as they are insignificant for the physical conclusions presented in this chapter.

Still, these high-energy tails cannot be completely omitted since they contribute to the normalization condition in Eq. (4.7), which apart from the explicit pole cancellation represents the most important internal consistency check of our computational setup. As a further test of the MC implementation we, moreover, verified that both the α_s^2- and α_s^3-parts of our NNLO differential cross section results are in perfect agreement with an independent evaluation using MCFM [110]. Indeed, also the LO and NLO QCD predictions shown below have been

[5] As usual, the strong coupling constant has been set to the default value employed by each of the considered PDF sets.

[6] Unless specifically noted otherwise, the total theory uncertainty for all quantities discussed in this chapter is defined as the sum of scale and PDF errors added in quadrature.

derived with the same MC framework that has been utilized for the calculation of the NNLO corrections. The only difference lies in the determination of the PDF uncertainty as for the lower perturbative orders one can directly resort to the common Hessian error prescription relevant for the MSTW2008 set. In order to also validate the proper "de-symmetrization" of the 2-to-4 kinematics, we performed a separate analysis of the related LO process $pp \to t\bar{t}jj$ comparing our setup to the results obtained with the help of the self-contained MC package HELAC-NLO [433]. By choosing a set of characteristic top-quark observables that goes far beyond the distributions defined in Tab. 4.1 we were hence able to establish the correctness of our approach even in more exotic corners of the four-particle phase space.

Finally, we also performed a comparison of the NNLO $p_{T,t\bar{t}}$ spectrum as well as the corresponding differential asymmetry with the respective NLO predictions in $t\bar{t}j$ production [115, 117, 661, 662]. This transverse-momentum analysis probably represents the most important cross-check of our MC implementation as it is the only non-trivial comparison at $\mathcal{O}(\alpha_s^4)$ accuracy. The main idea is to exploit the fact that, once the top-quark pair has a non-vanishing transverse momentum (in our case $p_{T,t\bar{t}} \geq 10\,\text{GeV}$), there always exists at least one resolved parton that recoils against the $t\bar{t}$ system such that for this observable the $\text{N}^{\text{k}}\text{LO}$ corrections in the $t\bar{t}j$ final state are formally equal to the $\text{N}^{\text{k+1}}\text{LO}$ contributions in regular $t\bar{t}$ production. Indeed, we find that our NNLO calculation is fully consistent with the findings in Refs. [117,661,662] and, moreover, perfectly agrees with an additional evaluation based on the HELAC-NLO package. Thus, our MC framework may be readily applied to the remaining observables in Tab. 4.1 as well, the result of which will be discussed in the following. The corresponding numerical cross section values through NNLO QCD are collected in appendix D.

4.1 Forward-backward asymmetry

Ever since its first measurement the forward-backward asymmetry, i. e. the imbalance in the number of top and anti-top quarks produced in complementary hemispheres $\pm\Delta y > 0$, has certainly become one of the most influential quantities studied within the Tevatron physics program. The reason for this lay in the long-persisting discrepancy between the SM theory predictions at NLO QCD, possibly augmented with EW corrections [377, 382, 384] and higher-order contributions from soft-gluon resummation [383,399–401], and the available data collected by the CDF [386–389] and DØ [390–393] collaborations. Only lately, by means of the full NNLO corrections derived in the course of this thesis, we were finally able to reconcile this gap between theory and experiment. The main features of this analysis as well as the corresponding phenomenological implications have already been thoroughly discussed in section 1.3.3. In the following we will thus rather focus on the technical details of the NNLO calculation and elaborate a little more on the kinematic dependence of A_{FB} in terms of Δy, $m_{t\bar{t}}$ and $p_{T,t\bar{t}}$. This will help to further clarify the origin of the unexpectedly large $\mathcal{O}(\alpha_s^4)$ corrections and illustrate why they could not be properly assessed in terms of approximate NNLO methods.

part.	$\alpha_s^3 N_3$		$\alpha_s^4 N_4$			
channel	R	V	RR	RV	VV	FAC
$q\bar{q}$	0.661	0.056	1.499	−1.090	0.009	−0.131
qg	0.0004	–	0.005	−0.010	–	
$q\tilde{q}$	–	–	0.0001	–	–	
Σ	0.662	0.056	1.504	−1.100	0.009	−0.131

Table 4.2: *Relative contributions of the fermion-induced partonic production modes to the NNLO QCD asymmetric numerator* $\sigma_{t\bar{t}}^{+} - \sigma_{t\bar{t}}^{-} \equiv \alpha_s^3 N_3 + \alpha_s^4 N_4$. *The different channels are further decomposed according to final-state multiplicities into real (R), virtual (V), double-real (RR), real-virtual (RV) and double-virtual (VV) corrections. The contributions from collinear factorization*[7] *(FAC), on the other hand, are treated collectively, i. e. as the sum over all multiplicities and partonic channels.*

As described in section 1.3.3, the inclusive asymmetry is defined as

$$\mathrm{A_{FB}}(\Delta y) = \frac{\sigma_{t\bar{t}}^{+}(\Delta y) - \sigma_{t\bar{t}}^{-}(\Delta y)}{\sigma_{t\bar{t}}^{\mathbf{tot}}} \tag{4.10}$$

where the contributions from the two rapidity hemispheres $\pm\Delta y > 0$ are given by

$$\sigma_{t\bar{t}}^{\pm}(\Delta y) = \int \theta\left(\pm\Delta y\right)\, d\sigma \simeq \sum_k \sigma_{\mathrm{bin}_k}(\Delta y)\; w_{\Delta y}^{(k)}\; \theta_{\mathrm{Asym}}\; \theta(\pm|\mathcal{b}_{\Delta y}^{(k)}| \mp |\mathcal{b}_{\Delta y}^{(k-1)}|)\;. \tag{4.11}$$

Note that, from the perturbative point of view, this cross section ratio may also be expanded in terms of the α_s giving rise to two formally equivalent representations of $\mathrm{A_{FB}}$, shown in Eq. (1.49) and Eq. (1.50) respectively, that only differ in their subleading behavior beyond NNLO accuracy. The numerical difference of the resulting asymmetry predictions thus serves as an estimate for the impact of yet unknown higher-order terms in the perturbative expansion. As indicated in Eq. (4.11), the relevant contributions to the numerator of $\mathrm{A_{FB}}$ have in practice been calculated from the rapidity distribution $d\sigma/d\Delta y$ specified in Tab. 4.1, which saves us some unnecessary computational effort. Indeed, within our MC framework such a differential approach is completely equivalent to a direct integration over the full Δy-hemispheres since it in principle corresponds to a simple re-binning of the original distribution. Note, however, that we have introduced an additional selector function θ_{Asym} whose purpose is to remove the main symmetric contributions from the differential cross section predictions entering $\sigma_{t\bar{t}}^{\pm}$. While these symmetric pieces must, by construction, cancel in the difference of the numerator functions, their finite numerical precision may still generate spurious numerical artifacts in Eq. (4.10) that could eventually spoil a reliable extraction of the NNLO asymmetric behavior. In our case it turns out to be sufficient to exclude all gg-initiated reactions as well as the LO $q\bar{q}$ cross section from the calculation of $\mathrm{A_{FB}}$ whereas the remaining symmetric contributions, which are numerically subdominant, can be safely retained.

[7] The contributions from collinear factorization to $\alpha_s^3 N_3$ vanish since they are proportional to the LO partonic cross sections and hence completely symmetric.

In consequence, the asymmetry analysis can be organized according to the same building blocks as a regular cross section calculation, namely partonic production channels and final-state multiplicities. The relative contributions of these components to the NNLO inclusive numerator in Eq. (4.10) (see also Eq. (1.49)) are shown in Tab. 4.2. Despite the fact that such a decomposition is by no means unique, this comparison still gives us a general idea of what are the driving forces behind the asymmetric behavior of the top quark. It turns out that similar to $\sigma_{t\bar{t}}^{\mathbf{tot}}$ also the NLO and NNLO numerators $\alpha_s^3 N_3$ and $\alpha_s^4 N_4$ are clearly dominated by $q\bar{q}$ annihilation whereas the contributions from the qg-channel and the remaining $q\tilde{q}$-type reactions are further suppressed by several orders of magnitudes. Irrespective of the particular production mode, real radiation (R, RR, RV) can be identified as the primary source of $\mathrm{A_{FB}}$. The purely virtual corrections (V, VV), on the other hand, are rather small. Interestingly, at NLO all contributions, both real and virtual, are positive amounting to about 72% of the total NNLO asymmetric numerator while for the $\mathcal{O}(\alpha_s^4)$ corrections one can observe a strong cancellation between double-real and real-virtual contributions. Collinear factorization also favors negative values of Δy leading to a further reduction of $\alpha_s^4 N_4$, which due to the presence of the NLO real-radiation cross sections is indeed quite sizable. Still, the overall contribution of the NNLO corrections remains positive resulting in a $\sim 33\%$ increase of the NNLO numerator with respect to the NLO evaluation[8].

Nevertheless, in order to be able to assess the full impact of the $\mathcal{O}(\alpha_s^4)$ corrections, one also has to consider the denominator in Eq. (4.10), which is constructed as the sum of the two hemisphere functions $\sigma_{t\bar{t}}^{\pm}$. Therefore, it can, in principle, be computed in a similar fashion as the numerator, i. e. from the integral over the $d\sigma/d\Delta y$ distribution (albeit this time including also the symmetric cross section contributions). In practice, however, it is far more efficient to exploit the inclusiveness of the denominator and work with the total cross section results presented in chapter 3. Apart from the obvious computational savings, this allows us to profit from the advanced numerical precision of the NNLO $\sigma_{t\bar{t}}^{\mathbf{tot}}$ predictions, which, in combination with the exclusion of symmetric numerator contributions described above, reduces the MC error on $\mathrm{A_{FB}}$ to the permille level. Consequently, it can be safely neglected in any practical application.

Due to the positive sign of the $\mathcal{O}(\alpha_s^4)$ cross section corrections, the actual shift of the NNLO asymmetry predictions with respect to the NLO analysis is less pronounced than for the numerator itself. Moreover, it depends on the particular definition employed for $\mathrm{A_{FB}}$ ranging from $\sim 27\%$ for the unexpanded ratio in Eq. (1.49) to $\sim 14\%$ for the expanded expression in Eq. (1.50). This, however, only concerns the pure QCD contributions. Including also EW effects, which, as is well known, are essential to a reliable description of asymmetric top-quark production, the relative shift from NLO+EW to NNLO+EW amounts to $\sim 21\%$ and $\sim 7\%$ respectively. The rather modest impact on the expanded $\mathrm{A_{FB}}$ indicated by the latter value is somewhat artificial and, hence, does not reflect the true significance of extending the asymmetry analysis to NNLO accuracy. It can be explained with a different power counting of

[8] Naively, the numbers in Tab. 4.2 suggest that the increase of going from NLO to NNLO is even higher. One, however, also has to take into account the numerical differences of the corresponding NLO and NNLO PDF sets, which lead to an additional $\sim$-4% shift in $\alpha_s^3 N_3$ that somewhat softens the NNLO asymmetric behavior.

the α_s-dependent terms in the EW numerator N_{EW}, which incorporates the joint contributions from several types of EW interactions (see section 1.3.3). While its explicit value can be inferred from Tab. 2 of Ref. [377], in our calculation we adapted an alternative definition

$$N_{\mathrm{EW}} \equiv \mathrm{A}_{\mathrm{FB}}^{\mathrm{EW},\,[377]} \times \sigma_{t\bar{t}}^{\mathbf{tot},\,LO} = 0.088^{+0.030}_{-0.020} \tag{4.12}$$

in terms of the EW asymmetry ratio

$$\mathrm{A}_{\mathrm{FB}}^{\mathrm{EW},\,[377]} \equiv \frac{N_{\mathrm{EW}}^{[377]}}{\sigma_{t\bar{t}}^{\mathbf{tot},\,LO\;[377]}} \,. \tag{4.13}$$

This allows us to minimize the impact of the different PDF set and top-quark mass used in the direct evaluation of $N_{\mathrm{EW}}^{[377]}$. Note that, following the prescriptions for the expanded A_{FB}, the LO cross sections $\sigma_{t\bar{t}}^{\mathbf{tot},\,LO\;[377]}$(likewise adopted from Tab. 2 of Ref. [377]) and $\sigma_{t\bar{t}}^{\mathbf{tot},\,LO}$(based on the computational setup described above) have been constructed from NLO PDFs instead of the usual LO fluxes. Moreover, for the EW and combined QCD+EW predictions we have to resort to a slightly adjusted scale variation procedure restricted to the case $\mu_F = \mu_R$ presented in Ref. [377]. We have, however, checked that for the pure QCD corrections to the inclusive asymmetry the corresponding uncertainty estimates are only marginally affected by this modification and thus expect them to still provide a reliable projection of missing higher-order contributions.

An aspect that has so far not been quantitatively addressed within the NNLO asymmetry analysis is the explicit PDF dependence of the corresponding theory predictions. While for an inclusive, ratio-like quantity such as A_{FB} it is generally assumed to be small, the presence of additional symmetric contributions in the denominator of Eq. (4.10), especially from gluon fusion production, might in principle spoil this naive picture. Therefore, it may be instructive to determine not only the individual PDF error of our default PDF choice MSTW2008, which indeed turns out to be suppressed by at least a factor of 3 with respect to the scale uncertainty, but to also investigate the impact of using different PDF sets in the derivation of the unexpanded and expanded asymmetry results.

To this end, consider the various PDF predictions shown in Tab. 4.3 based on the theoretically most advanced treatment of A_{FB} at NNLO and NNLO+EW accuracy. As can be seen, they are in almost perfect agreement, the central values lying within a few percent ($\lesssim 1\%$ if the NNPDF2.3 set is excluded) regardless of the particular asymmetry definition. For the individual numerators and denominators, on the other hand, the difference between the various PDF sets is more pronounced signaling the presence of strong cancellation effects between these two components. A closer examination reveals that there, in fact, exists a subtle interplay between the fermionic and bosonic degrees of freedom in the partonic fluxes. In consequence, the inclusion of the gg-initiated contributions in the denominator may either decrease (CT10) or enhance (HERAPDF1.5, NNPDF2.3) the relative deviation with regard to the MSTW2008 set. Yet, it is not clear whether this is an accidental effect specific to this observable or if this correlation has a deeper physical reason. We will further investigate this point at the differential level where the sensitivity to the choice of PDFs is potentially higher and might thus provide additional insights on the PDF dependence of the A_{FB} predictions. Nevertheless, we

	Numerator [pb]	Denominator [pb]	A_{FB}[%] (Eq. (1.49))	A_{FB}[%] (Eq. (1.50))
NNLO				
MSTW2008	$0.525^{+0.055}_{-0.085}$	$7.009^{+0.259}_{-0.374}$	$7.50^{+0.50}_{-0.86}$	$8.36^{+0.21}_{-0.27}$
CT10	$0.546^{+0.058}_{-0.089}$	$7.232^{+0.272}_{-0.391}$	$7.55^{+0.51}_{-0.87}$	$8.43^{+0.22}_{-0.27}$
HERAPDF1.5	$0.567^{+0.059}_{-0.079}$	$7.459^{+0.272}_{-0.263}$	$7.60^{+0.51}_{-0.81}$	$8.47^{+0.22}_{-0.20}$
NNPDF2.3	$0.549^{+0.058}_{-0.089}$	$7.104^{+0.266}_{-0.371}$	$7.73^{+0.52}_{-0.90}$	$8.61^{+0.23}_{-0.29}$
NNLO+EW				
MSTW2008	$0.613^{+0.085}_{-0.105}$	$7.009^{+0.259}_{-0.374}$	$8.75^{+0.86}_{-1.09}$	$9.64^{+0.61}_{-0.61}$
CT10	$0.635^{+0.088}_{-0.109}$	$7.232^{+0.272}_{-0.391}$	$8.78^{+0.85}_{-1.10}$	$9.69^{+0.60}_{-0.61}$
HERAPDF1.5	$0.652^{+0.086}_{-0.096}$	$7.459^{+0.272}_{-0.263}$	$8.74^{+0.81}_{-1.02}$	$9.64^{+0.55}_{-0.49}$
NNPDF2.3	$0.637^{+0.087}_{-0.109}$	$7.104^{+0.266}_{-0.371}$	$8.97^{+0.86}_{-1.13}$	$9.88^{+0.62}_{-0.63}$
CDF [388, 389]	–	–	$16.4^{+4.7}_{-4.7}$	
	–	–	$16.0^{+4.5}_{-4.5}$	
DØ [392, 393]	–	–	$10.6^{+3.0}_{-3.0}$	
	–	–	$11.8^{+2.8}_{-2.8}$	

Table 4.3: *Comparison of the NNLO and NNLO+EW inclusive asymmetry predictions derived from different PDF sets with the latest experimental results by* CDF *and* DØ*. The EW contributions have been adopted from Ref. [377] applying the rescaling procedure in Eq. (4.12) for each PDF set separately. The quoted uncertainties are due to scale variation only ($\mu_F \neq \mu_R$ for pure QCD, $\mu_F = \mu_R$ for QCD+EW).*

can conclude that currently for most asymmetry-related applications the PDF errors can be safely neglected. In case of a future reduction of the perturbative uncertainties, for instance through the inclusion of soft-gluon resummation, the PDF dependence might, however, need to be revisited.

4.1.1 Rapidity dependence

In general the kinematic dependence of the forward-backward asymmetry can be expressed in terms of a one-dimensional distribution of the form

$$A_{FB}(\Delta y, \mathcal{Q}') = \left\{ \left\{ A_{FB}^{\text{bin}_1}(\Delta y, Q'); \ldots; A_{FB}^{\text{bin}_m}(\Delta y, Q') \right\} \right\} \tag{4.14}$$

where

$$A_{FB}^{\text{bin}_k}(\Delta y, Q') = \frac{\sigma_{\text{bin}_k,+}(\Delta y, Q')\,\theta_{\text{Asym}} - \sigma_{\text{bin}_k,-}(\Delta y, Q')\,\theta_{\text{Asym}}}{\sigma_{\text{bin}_k,+}(\Delta y, Q') + \sigma_{\text{bin}_k,-}(\Delta y, Q')}\,, \tag{4.15}$$

and

$$\sigma_{\text{bin}_k,\pm}(\Delta y, Q') = \int d\sigma\; \theta_{\text{bin}_k}(Q')\; \theta(\pm\Delta y) \tag{4.16}$$

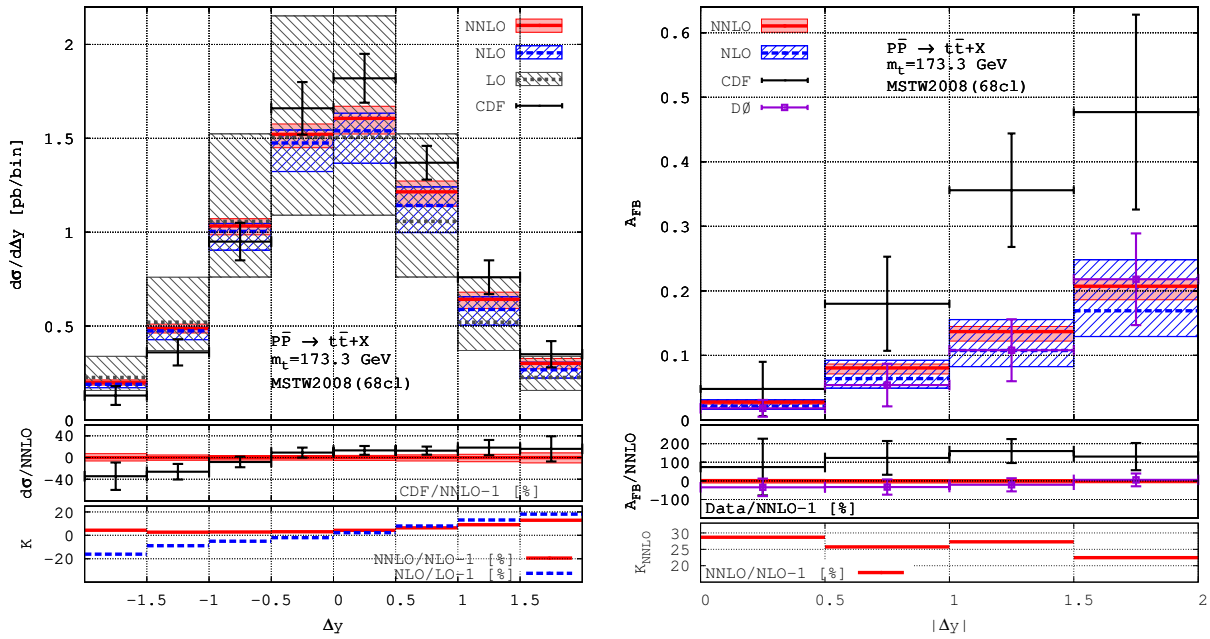

Figure 4.1: *Comparison of the SM theory predictions through NNLO QCD for the differential distribution*[9] $d\sigma/d\Delta y$ *(left) and the related differential asymmetry* $A_{FB}(\Delta y, |\Delta y|)$ *(right) with data [388, 392, 663]. The corresponding theory error is derived from scale and PDF variation. The end bins* $|\Delta y| \geq 1.5$ *contain overflow events.*

are the entries of a double differential cross section $d^2\sigma/d\mathcal{Q}'\,d\Delta y$ with the rapidity binning chosen such that it spans the entire positive/negative Δy-hemisphere. The case $\mathcal{Q}' = |\Delta y|$ is, however, somewhat special in this context as it involves the same variable used to distinguish between the forward and backward regime of the $t\bar{t}$ pair. Thus, employing the identity

$$\theta_{\text{bin}_k}(\Delta y) = \theta_{\text{bin}_k}(|\Delta y|)\;[\theta(+\Delta y) + \theta(-\Delta y)] \tag{4.17}$$

the kinematic dependence $A_{FB}(\Delta y, |\Delta y|)$ can, in fact, be inferred from the single differential distribution $d\sigma/d\Delta y$ shown in Fig. 4.1. With the inclusion of the $\mathcal{O}(\alpha_s^4)$ corrections the theoretical description of this observable is under good perturbative control now, the errors of the NNLO analysis lying significantly (by about a factor of two) below the NLO results. Moreover, the NNLO K-factor appears to be much flatter and less pronounced than at NLO indicating that the NNLO corrections have an important stabilizing effect on the predicted rapidity spectrum. A comparison with the latest CDF measurement shows that also the agreement between theory and data has been further improved such that now merely in a few bins one can actually observe a (small) deviation from the SM expectation.

This is indeed quite remarkable considering the fact that for the related differential asymmetry the discrepancy between the NNLO theory prediction and CDF data is much larger ($\sim$1-2σ) affecting all but the central rapidity bins (see Fig. 4.1). This implies that the symmetric

[9] Due to their intended use in the construction of a differential asymmetry, the differential cross sections $d\sigma/d\Delta y$, $d^2\sigma/dm_{t\bar{t}}\,d\Delta y$ and $d^2\sigma/dp_{T,t\bar{t}}\,d\Delta y$ have not been divided by their respective bin widths as prescribed by Eq. (4.4) since this normalization factor drops out of the ratio in Eq. (4.15).

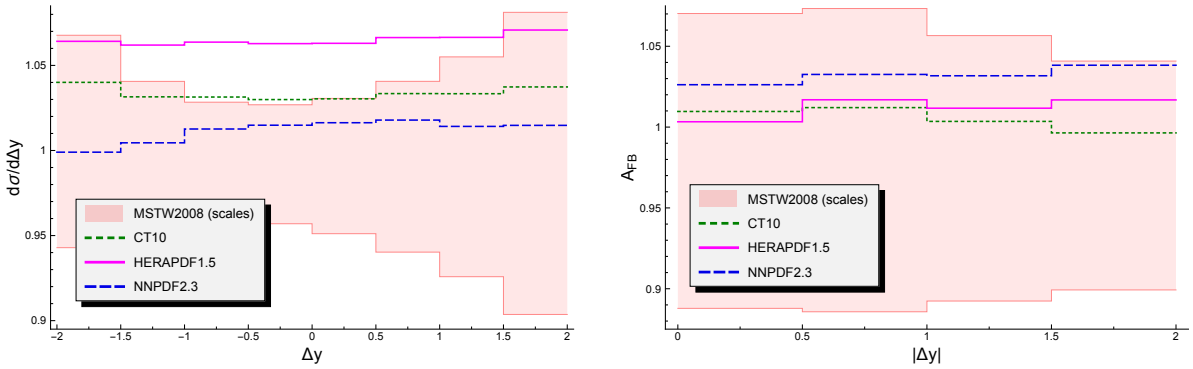

Figure 4.2: *The NNLO QCD predictions for $d\sigma/d\Delta y$ (left) and $A_{FB}(\Delta y, |\Delta y|)$ (right) derived from four different PDF sets. Given are the ratios of the* HERAPDF1.5, CT10 *and* NNPDF2.3 *based predictions with respect to the default* MSTW2008 *result. For reference we also show the scale dependence of the latter prediction (red band).*

contributions to $d\sigma/d\Delta y$ are able to partly compensate for the differences in the asymmetric behavior such that this discrepancy can, to a great extent, be attributed to deviations in the numerator of Eq. (4.15). Thus, one may conjecture that the inclusion of EW corrections, which most notably contribute to this asymmetric numerator, might help to further resolve the tension between theory and experiment. Unfortunately, the available EW results for $A_{FB}(\Delta y, |\Delta y|)$ (as well as the other differential asymmetries) come in a different format (binning, PDFs, m_t) and are, hence, currently not compatible with our pure QCD determination such that we have to postpone this combined NNLO+EW treatment to a future analysis. The DØ measurement, on the other hand, is already in good agreement with the NNLO QCD prediction, which is in line with the findings of the inclusive A_{FB} analysis where a significant excess above the SM expectation could only be detected in CDF data.

Due to the steady increase of the asymmetric behavior with $|\Delta y|$, an alternative method of presenting the kinematic dependence of A_{FB} is through a linear relation of the form

$$A_{FB}(\Delta y, |\Delta y|) = \alpha_y \, |\Delta y| + \underbrace{\beta_y}_{=0} \tag{4.18}$$

where, as indicated, the intercept β_y has to vanish assuming that $d\sigma/d\Delta y$ is a continuous function over the whole rapidity range. Thus, the differential asymmetry may be compactly described in terms of a single variable α_y, which, in practice, has been obtained from a least-squares fit to the discrete NLO and NNLO theory predictions in Fig. 4.1 yielding

$$\begin{aligned} \alpha_y^{\text{NLO}} &= 0.092^{+0.042}_{-0.022} \\ \alpha_y^{\text{NNLO}} &= 0.114^{+0.006}_{-0.012} \,. \end{aligned} \tag{4.19}$$

The relative difference between these slopes of about 25% could have actually already been inferred from the K-factors in Fig. 4.1, which are of similar size and, moreover, nearly constant with $|\Delta y|$. While this is indeed a quite sizable enhancement, we notice that the NNLO result

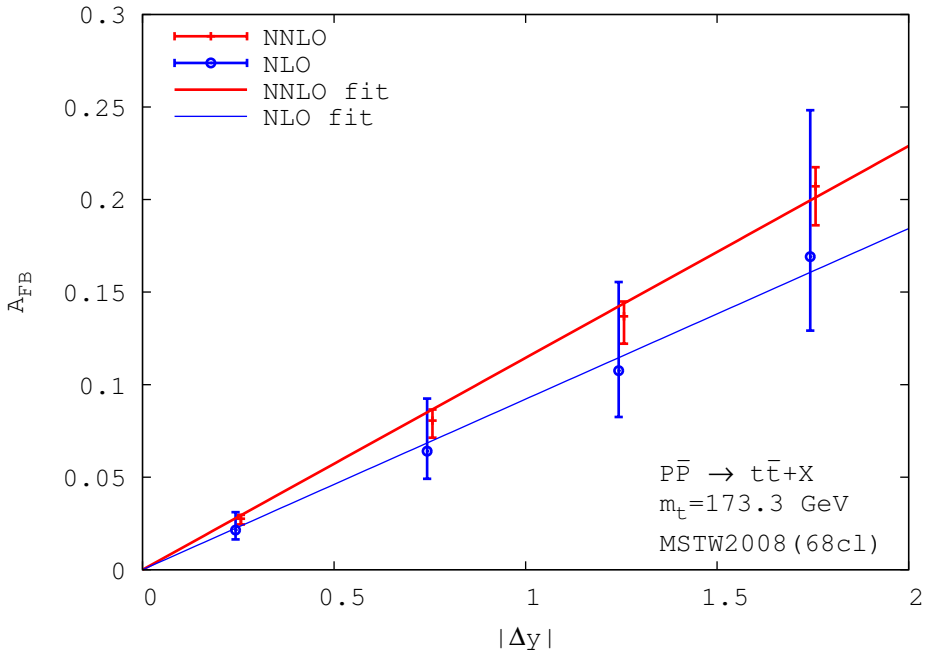

Figure 4.3: *Result for the least-squares linear fit in Eq. (4.18) at NLO and NNLO QCD versus the discrete* $A_{FB}(\Delta y, |\Delta y|)$ *calculations in all available rapidity bins including their respective total theory uncertainties.*

is still completely contained within the NLO error band demonstrating the good perturbative convergence of this observable. The error itself has significantly decreased by roughly a factor of three from the NLO to NNLO differential asymmetry, a fact that is also reflected by the uncertainties on α_y in Eq. (4.19). They include contributions from both scale and PDF variation whereas the MC error on $A_{FB}(\Delta y, |\Delta y|)$ of $\lesssim 1\%$ has been consequently neglected in the fitting procedure. Interestingly, the impact of the PDF error on the asymmetry is only marginal (its omission would only change the "+"-error of α_y^{NNLO} from 0.006 to 0.005) in contrast to the original $d\sigma/d\Delta y$ distribution where, in some bins, it can become as large as the scale uncertainty. This, again, signals the presence of strong cancellation effects between the numerator and denominator known already from the inclusive A_{FB} analysis. Similarly, also the spread between the predictions from different PDF sets is considerably reduced when moving from $d\sigma/d\Delta y$ to $A_{FB}(\Delta y, |\Delta y|)$ as can be seen in Fig. 4.2. In fact, for the latter all PDF predictions (and consequently also the resulting slopes) are fully contained within the error band due to NNLO scale variation indicating that for this observable the perturbative uncertainty serves as a good estimate of the total theory error. This particularly applies to the comparison with CDF and DØ data, which is clearly dominated by experimental uncertainties and, therefore, insensitive to the details of the theory error analysis.

The corresponding results for the measured slopes α_y^{CDF} and $\alpha_y^{\text{D}\emptyset}$ have already been discussed in section 1.3.3 (see especially Eq. (1.56)). Here, we will only note that, as expected, the DØ measurement is fully consistent with the NNLO theory prediction while the CDF evaluation lies significantly above the SM expectation. There exists, however, an additional aspect of

this slope analysis that we have not properly addressed yet, namely the validity of the linear approximation in Eq. (4.18). Indeed, any deviation from linearity could seriously hamper the comparison between theory and data, in particular when it is hidden underneath sizable theoretical or experimental uncertainties. Hence, in order to give a better perspective for the quality of the linear fit, we in Fig. 4.3 compare the central NLO and NNLO slopes of Eq. (4.19) with the actual calculated bin values for $A_{FB}(\Delta y, |\Delta y|)$ including their respective theory errors. As one can see, the predicted asymmetry displays a similar functional behavior at NLO and NNLO QCD albeit this kinematic dependence is presumably not linear. This becomes particularly evident when varying the rapidity range that enters the fitting procedure suggesting that the deviation from linearity is gradually increasing with $|\Delta y|$. While at NLO this anomalous behavior could, due to the relatively large uncertainty on α_y^{NLO}, still be ignored, at NNLO it is actually comparable to the size of the theory error. Thus, such a simplified treatment of the differential asymmetry, unless it is further refined beyond the linear approximation, may only serve as a rough estimate of the exact kinematic dependence. In practice, one should therefore rather resort to the original $A_{FB}(\Delta y, |\Delta y|)$ distribution when drawing any physical conclusions from a comparison of theory and data.

4.1.2 Invariant-mass dependence

As outlined in Eq. (4.15) and Eq. (4.16), the $m_{t\bar{t}}$-dependence of A_{FB} can be obtained from the double differential cross section $d^2\sigma/dm_{t\bar{t}}\,d\Delta y$ plotted in Fig. 4.4 where we have exploited the fact that the binning in Δy can be absorbed into a simple sign factor allowing for a one-dimensional representation of this quantity. In contrast to $d\sigma/d\Delta y$, there has been no separate measurement of this distribution published by any of the Tevatron experiments such that it is not clear how well the newly derived NNLO QCD predictions compare to actual data or whether any discrepancies in $A_{FB}(\Delta y, m_{t\bar{t}})$ might already be discernible at the cross section level. From the theory perspective one may, however, note that this observable exhibits good perturbative convergence over the full kinematic range as can be inferred from the similar shapes of the NLO and NNLO K-factors combined with the substantially smaller size of K_{NNLO}. Moreover, the NNLO theory uncertainty has been reduced by about a factor of two with respect to the NLO analysis, both predictions being consistent within their error estimates. This indicates the robustness of our theoretical description of $d^2\sigma/dm_{t\bar{t}}\,d\Delta y$, a feature that can also be observed for the resulting differential asymmetry in Fig. 4.4.

There, the NNLO theory uncertainty has decreased even more lying at least a factor of three below the NLO error estimate. Similar to $A_{FB}(\Delta y, |\Delta y|)$, it is dominated by the scale error whereas the PDF uncertainty (and likewise the MC error of $\lesssim 1\%$) can, in principle, be neglected. This is also in line with the findings in Fig. 4.5 where we show the relative difference of the $d^2\sigma/dm_{t\bar{t}}\,d\Delta y$ and $A_{FB}(\Delta y, m_{t\bar{t}})$ predictions from various PDF sets. Again, the differential asymmetry proves to be far less sensitive to the choice of PDFs than the original cross section it is based upon such that in the following discussion of the $m_{t\bar{t}}$-dependence it is sufficient to work exclusively with the MSTW2008 set. Further indication for the good perturbative behavior of $A_{FB}(\Delta y, m_{t\bar{t}})$ is given by the fact that the NNLO prediction is completely contained within the NLO error band (except for a small overhang in the first bin),

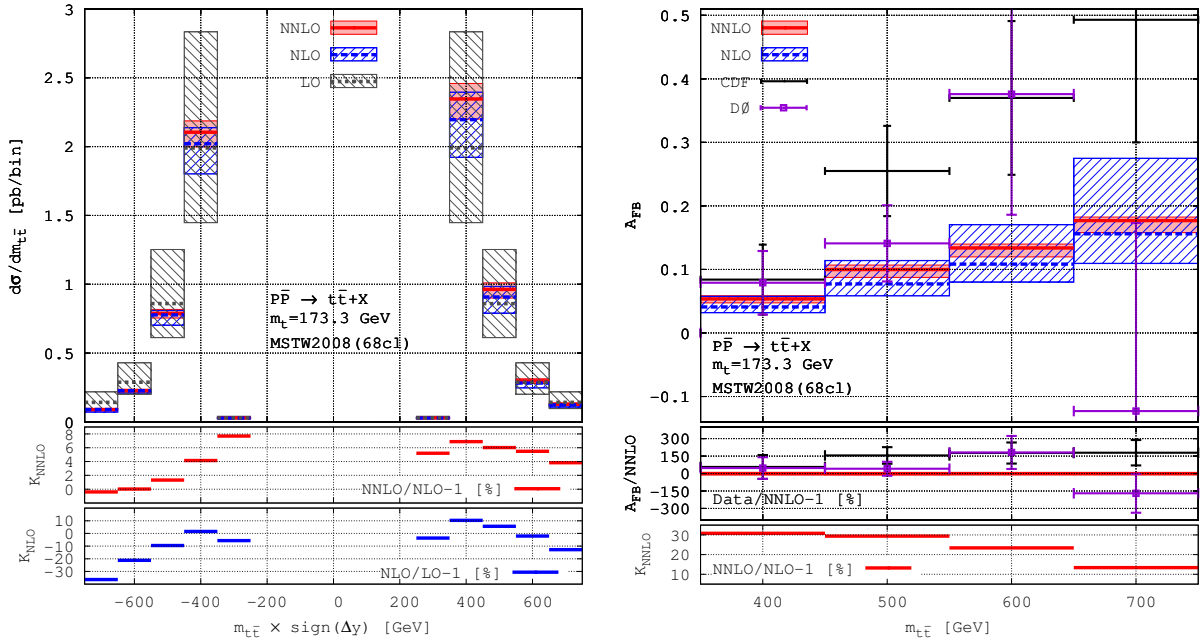

Figure 4.4: *Comparison of the SM theory predictions through NNLO QCD for the double differential distribution $d^2\sigma/dm_{t\bar{t}}\,d\Delta y$ (left) and the related differential asymmetry $\mathrm{A_{FB}}(\Delta y, m_{t\bar{t}})$ (right) with data [388, 392, 663]. The corresponding theory error is derived from scale and PDF variation. The end bins of both distributions contain overflow events whereas for the asymmetry the bin $450\,\mathrm{GeV} \geq m_{t\bar{t}} \geq 350\,\mathrm{GeV}$ also contains underflow contributions.*

which is quite remarkable considering the relatively large K-factor amounting to $\sim$30% close to threshold and decreasing steadily to around 10% in the highest $m_{t\bar{t}}$ bin. Note that, in order to match the binning of the experimental asymmetry analyses, we have absorbed the contributions of the leading bin at $250\,\mathrm{GeV} \leq m_{t\bar{t}} \leq 350\,\mathrm{GeV}$ into the $350\,\mathrm{GeV} \leq m_{t\bar{t}} \leq 450\,\mathrm{GeV}$ bin such that now $\mathrm{A_{FB}}(\Delta y, m_{t\bar{t}})$ contains both over- and underflow events.

The explicit comparison between the corresponding NNLO theory predictions and data has already been presented in section 1.3.3 displaying a similar behavior as the inclusive asymmetry, i. e. the DØ measurement is consistent with the SM expectation whereas the CDF data tends to be 1-2σ higher. As was the case for $\mathrm{A_{FB}}(\Delta y, |\Delta y|)$, a compact way of illustrating these results is through their respective slopes obtained from a linear fit of the form

$$\mathrm{A_{FB}}(\Delta y, m_{t\bar{t}}) = \alpha_M\, m_{t\bar{t}} + \beta_M\ . \tag{4.20}$$

Note, however, that this time the intercept can no longer be constrained by continuity arguments since the asymmetric behavior at absolute threshold $m_{t\bar{t}} = 2m_t$ is a priori completely unknown. In consequence, the kinematic dependence is now described by a pair of coefficients, α_M and β_M, whose values at NLO and NNLO QCD are shown in Tab. 4.4.

It turns out that the inclusion of the $\mathcal{O}(\alpha_s^4)$ corrections has a rather moderate impact on the functional behavior of $\mathrm{A_{FB}}(\Delta y, m_{t\bar{t}})$ affecting the central slope and intercept by only a few percent. Indeed, the main benefit lies in the dramatic reduction of the corresponding uncertainties, which at NLO could be as large as 100% while at NNLO they are constantly

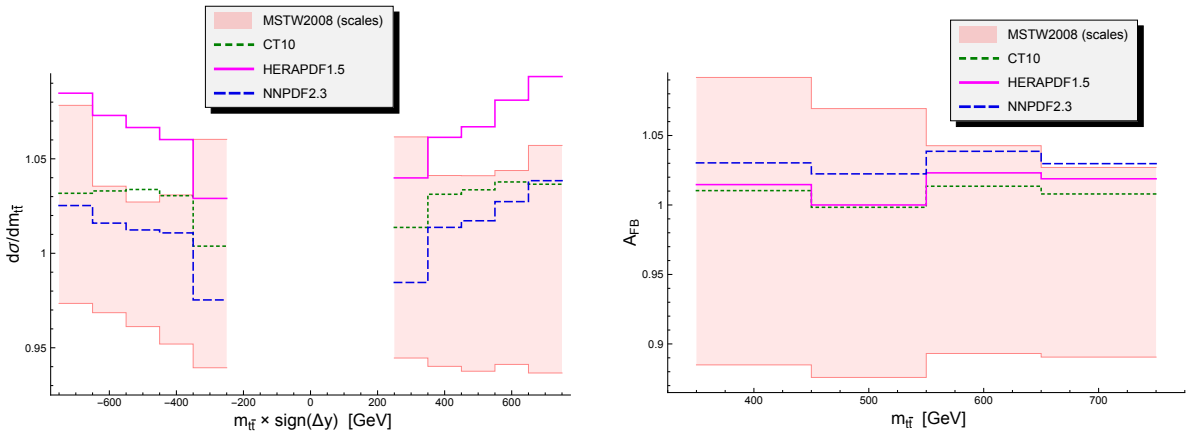

Figure 4.5: *The NNLO QCD predictions for* $d^2\sigma/dm_{t\bar{t}}\,d\Delta y$ *(left) and* $\mathrm{A_{FB}}(\Delta y, m_{t\bar{t}})$ *(right) derived from four different PDF sets. Given are the ratios of the* HERAPDF1.5, CT10 *and* NNPDF2.3 *based predictions with respect to the default* MSTW2008 *result. For reference we also show the scale dependence of the latter prediction (red band).*

below 10% both for α_M and β_M. In order to give a better perspective for quality of the linear approximation, we in Fig. 4.6 show the fitted asymmetries at NLO and NNLO accuracy together with the respective bin values of the discrete $\mathrm{A_{FB}}$ evaluation. In contrast to the NLO result where a possible deviation from linearity could be easily concealed beneath the large theory errors, the NNLO curve clearly suggests that the $m_{t\bar{t}}$ functional dependence of $\mathrm{A_{FB}}$ is consistent with being linear in the invariant-mass range considered here.

	$\mathrm{NLO_{cent}}$	$\mathrm{NLO_{min}}$	$\mathrm{NLO_{max}}$	$\mathrm{NNLO_{cent}}$	$\mathrm{NNLO_{min}}$	$\mathrm{NNLO_{max}}$
$\alpha_M \times 10^3\,\mathrm{GeV}$	0.377	0.255	0.709	0.404	0.364	0.405
β_M	-0.111	-0.070	-0.235	-0.106	-0.097	-0.101

Table 4.4: *Values of the pairs of coefficients* (α_M, β_M) *defined in Eq. (4.20) derived from the central and maximal/minimal (central* $\pm$ *total theory uncertainty)* $\mathrm{A_{FB}}(\Delta y, m_{t\bar{t}})$ *bin values at NLO and NNLO QCD.*

Further evidence for this hypothesis also comes from the measured slopes in Eq. (1.54), which, even though they might be numerically incompatible (CDF) with the SM theory prediction, still show the same monotonic rise towards larger values of $m_{t\bar{t}}$. A notable exception from this general pattern is the last bin $m_{t\bar{t}} > 650\,\mathrm{GeV}$ of the DØ analysis whose central value does not only underestimate the presumed linear dependence of $\mathrm{A_{FB}}(\Delta y, m_{t\bar{t}})$, it has, in fact, even become negative implying an inverse asymmetric behavior of the $t\bar{t}$ pair in this region of phase space. This observation has recently led to a proposal for an alternative evaluation strategy of $\mathrm{A_{FB}}$ based on the so-called PMC/BLM scale setting procedure [396,397,450–454].

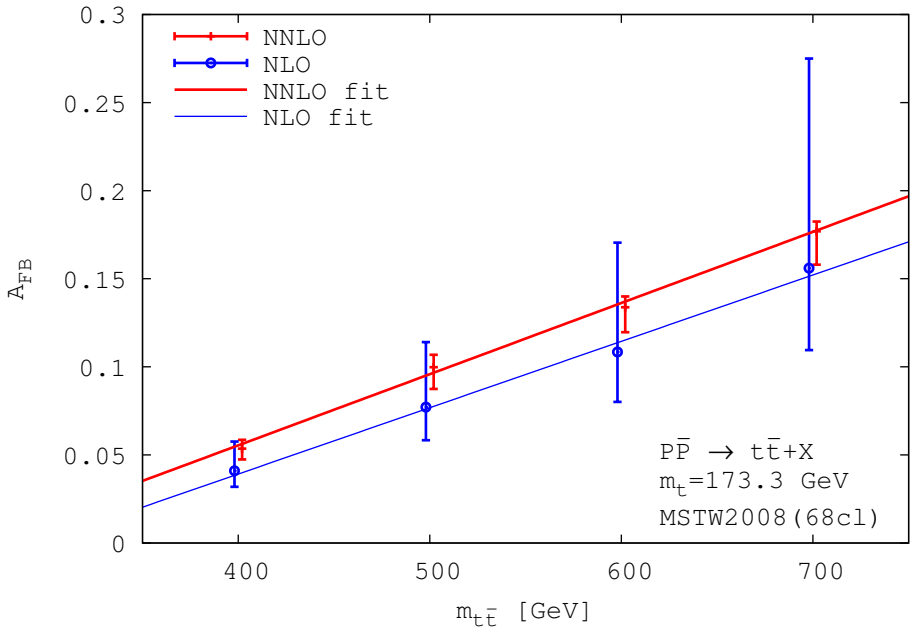

Figure 4.6: *Result for the least-squares linear fit in Eq. (4.20) at NLO and NNLO QCD versus the discrete* $A_{FB}(\Delta y, m_{t\bar{t}})$ *calculations in all available* $m_{t\bar{t}}$ *bins including their respective total theory uncertainties.*

To that end, one considers a slightly modified asymmetry definition

$$\hat{A}_{FB}(\Delta y, m_{t\bar{t}} > m_{t\bar{t}}^{\text{cut}}) = \frac{\sigma_+^c(\Delta y, m_{t\bar{t}}^{\text{cut}})\,\theta_{\text{Asym}} - \sigma_-^c(\Delta y, m_{t\bar{t}}^{\text{cut}})\,\theta_{\text{Asym}}}{\sigma_+^c(\Delta y, m_{t\bar{t}}^{\text{cut}}) + \sigma_-^c(\Delta y, m_{t\bar{t}}^{\text{cut}})} \tag{4.21}$$

expressed in terms of the cumulative cross sections

$$\sigma_\pm^c(\Delta y, m_{t\bar{t}}^{\text{cut}}) = \int d\sigma\; \theta(m_{t\bar{t}} - m_{t\bar{t}}^{\text{cut}})\; \theta(\pm\Delta y)\;, \tag{4.22}$$

which sum up all contributions above a certain cutoff parameter $m_{t\bar{t}}^{\text{cut}}$ thus allowing for a simultaneous study of both inclusive ($m_{t\bar{t}}^{\text{cut}} = 350\,\text{GeV}$ including underflow events) and differential ($m_{t\bar{t}}^{\text{cut}} > 350\,\text{GeV}$) asymmetry properties.

The corresponding theory predictions at NLO and NNLO QCD obtained from the computational setup described above are shown in Fig. 4.7 displaying a similar linear behavior as the fully differential asymmetry despite a quite opposite $m_{t\bar{t}}$-dependence of the individual numerators and denominators. As indicated by the NLO+EW prediction of Ref. [664] presented in the same figure, the inclusion of EW corrections does not seem to alter this picture. Being also based on the conventional scale setting $\mu_F = \mu_R = m_t$, the functional form of this prediction is compatible with the pure QCD analysis where the differences in the overall normalization may, apart from the presence of EW effects, be attributed to the use of an expanded asymmetry definition as well as different values for m_t and the PDFs. Hence, one can conclude that, within the SM, a pronounced "increasing-decreasing" behavior of $\hat{A}_{FB}(\Delta y, m_{t\bar{t}} > m_{t\bar{t}}^{\text{cut}})$

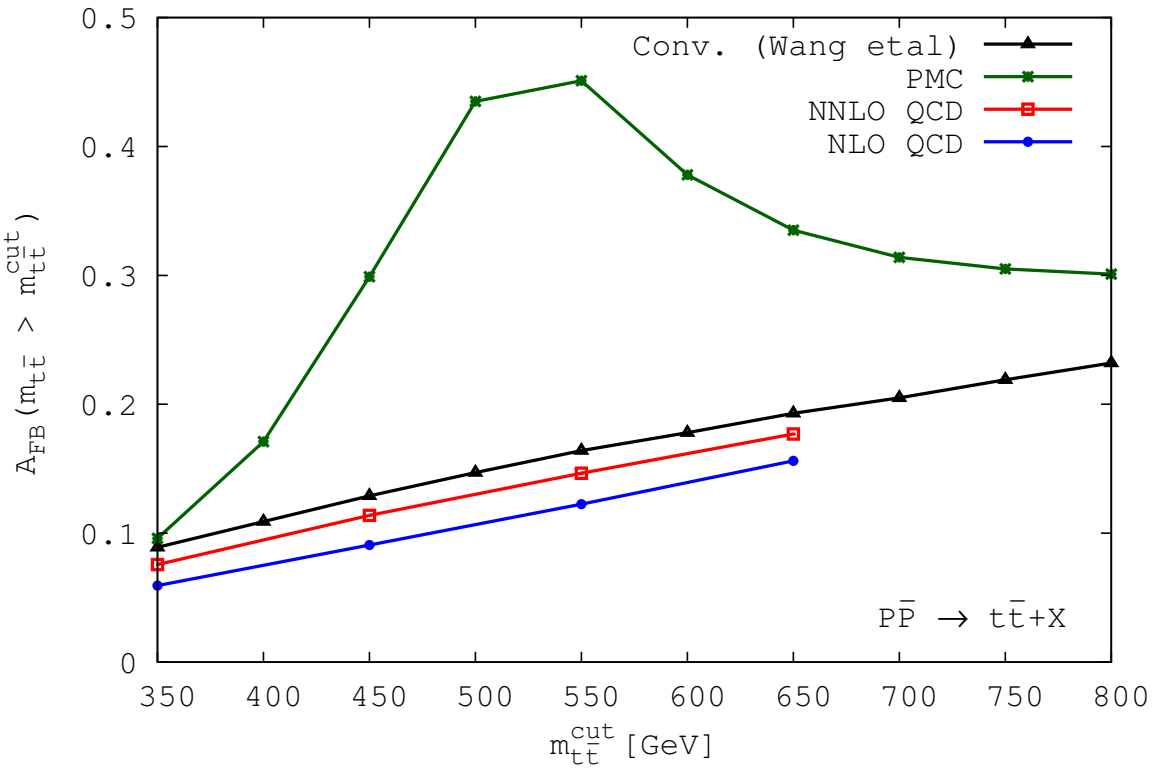

Figure 4.7: *Comparison of the NLO and NNLO $m_{t\bar{t}}$ cumulative asymmetry predictions derived in this work with the NLO+EW results from Ref. [664]. The latter contains both, a prediction based on conventional scale setting as well as the PMC scale-setting procedure, and apart from a different top mass and PDF set ($m_t = 173.1\,\text{GeV}$, CTEQ6.6M) uses an expanded definition of $\hat{A}_{FB}(\Delta y, m_{t\bar{t}} > m_{t\bar{t}}^{cut})$.*

as suggested by the DØ measurement cannot be reproduced from standard perturbative evaluation techniques. Note that this is expected to also hold in case of dynamic scales since in the limited range of $m_{t\bar{t}}$ used for the calculation of the above predictions, the fixed and dynamic treatment of $\mu_{R/F}$ should lead to consistent results within scale errors.

In contrast, the cumulative asymmetry prediction based on the PMC/BLM scale setting procedure [664] shows a substantially different behavior, strongly increasing for $350\,\text{GeV} \leq m_{t\bar{t}}^{cut} \leq 550\,\text{GeV}$ while gradually declining towards the end of the spectrum (see Fig. 4.7). Moreover, the overall level of asymmetry is much higher and thus potentially in better agreement with the observed excess of asymmetric $t\bar{t}$ events in CDF data. The origin of this modified kinematic dependence is the qualitatively different scale at which the renormalized coupling is evaluated in the PMC approach. Starting from threshold μ_R first strongly decreases reaching its minimum at around $m_{t\bar{t}} \sim 500\,\text{GeV}$ before it begins to grow again assuming its maximum value in the high-energy regime at $m_{t\bar{t}} \sim 800\,\text{GeV}$. While the latter lies still below our default scale choice $\mu_R = m_t$, it is more than a factor of five times bigger than the minimum value illustrating the large variations associated with this alternative scale setting procedure. In practice, it should therefore not be difficult to distinguish between the cumulative $\hat{A}_{FB}$ predictions

based on the PMC prescription or a conventional scale setting especially in the region around $m_{t\bar{t}} \sim 500\,\text{GeV}$ where the former results are clearly enhanced. The necessary experimental analysis of $\hat{\text{A}}_{\text{FB}}(\Delta y, m_{t\bar{t}} > m_{t\bar{t}}^{\text{cut}})$ in the intermediate range $350\,\text{GeV} < m_{t\bar{t}}^{\text{cut}} < 650\,\text{GeV}$ is, however, still missing such that a more conclusive separation of these scale setting approaches through actual data is currently not possible. It thus remains to be seen whether there exists a true deviation from linearity in the invariant-mass dependence of A_{FB} or if the anomalous DØ measurement at high $m_{t\bar{t}}$ is merely a statistical effect.

4.1.3 Pair-transverse-momentum dependence

The kinematic dependence of the forward-backward asymmetry on the transverse momentum of the $t\bar{t}$ system is of special theoretical interest since it allows for a separate examination of virtual contributions and real-radiation effects. Indeed, as explained in the beginning of this chapter, the $\mathcal{O}(\alpha_s^4)$ corrections to the latter can be derived from pure NLO considerations by employing the well-known results for related $t\bar{t}j$ final state provided in Refs. [115,117,661,662]. Thus, the shape of the transverse-momentum spectrum beyond $p_{T,t\bar{t}} \geq 10\,\text{GeV}$ is already fixed such that the true value of our NNLO calculation lies in the determination of the functional behavior at $p_{T,t\bar{t}} = 0$. The corresponding theory predictions for $d^2\sigma/dp_{T,t\bar{t}}\,d\Delta y$ as well as the resulting asymmetry $\text{A}_{\text{FB}}(\Delta y, p_{T,t\bar{t}})$ are shown in Fig. 4.8 where for the double differential distribution we again made use of the fact that the rapidity dependence may be expressed in terms of a simple sign factor. Unlike for the Δy or $m_{t\bar{t}}$ analyses presented above, a comparison to experimental data is, however, not possible for these observables since so far no parton-level results have been made available by the CDF and DØ collaborations. In consequence, we will in the following restrict our discussion to the theoretical description of the $p_{T,t\bar{t}}$-dependence focusing in particular on the impact of radiative corrections on the asymmetric behavior.

For the $d^2\sigma/dp_{T,t\bar{t}}\,d\Delta y$ distribution, we notice that the inclusion of the NNLO contributions leads to a considerably harder transverse-momentum spectrum as indicated by the large K-factors of up to $\sim 40\%$ for $p_{T,t\bar{t}} \geq 10\,\text{GeV}$. For the central bins $p_{T,t\bar{t}} < 10\,\text{GeV}$, on the other hand, the effect of going to NNLO is rather moderate ($K_{\text{NNLO}} \sim -10\%$) profiting from the presence of three non-vanishing orders of the perturbative expansion. Thus, it is not surprising that the corresponding theory error is affected by both scale and PDF uncertainties whereas for the bins involving purely radiative contributions the scale error, being effectively of NLO accuracy, is clearly dominating. Similarly, as can be inferred from Fig. 4.9, the significance of the employed PDF set is much more pronounced in the soft region of the transverse-momentum spectrum while for larger $p_{T,t\bar{t}}$ the various PDF predictions are readily contained within the error band due to scale variation. In all bins regardless of $p_{T,t\bar{t}}$, the relative MC error lies below 4 permille and may hence be safely neglected.

For the related differential asymmetry, the impact of going to NNLO is qualitatively similar to the original $d^2\sigma/dp_{T,t\bar{t}}\,d\Delta y$ distribution, i. e. $\text{A}_{\text{FB}}(\Delta y, p_{T,t\bar{t}})$ receives sizable corrections for $p_{T,t\bar{t}} \geq 10\,\text{GeV}$ whereas for the lowest $p_{T,t\bar{t}}$ bin the corresponding K-factor is rather small. Note, however, that the sign of these corrections is now positive in all bins leading to an increase of forward-produced top quarks over the entire transverse-momentum spectrum. Interestingly, in the purely radiative regime $p_{T,t\bar{t}} \geq 10\,\text{GeV}$ the shift between NLO and NNLO QCD seems to be almost independent of $p_{T,t\bar{t}}$, a pattern that is consistent with the analysis

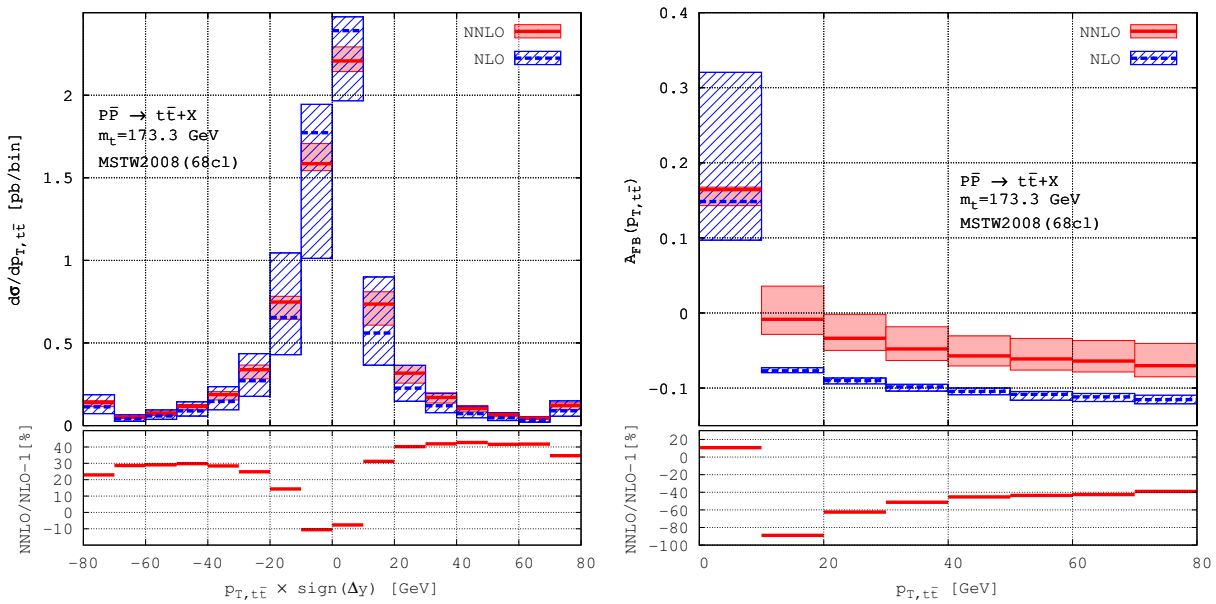

Figure 4.8: *The SM theory predictions through NNLO QCD for the double differential distribution* $d^2\sigma/dp_{T,t\bar{t}}\,d\Delta y$ *(left) and the related differential asymmetry* $\mathrm{A_{FB}}(\Delta y, p_{T,t\bar{t}})$ *(right). The corresponding theory error is derived from scale and PDF variation. The end bins contain overflow events.*

in Ref. [665] and has, moreover, been observed in reconstruction-level CDF data [388]. One may thus conjecture that the inclusion of the NNLO corrections will lead to a better agreement with data also at the parton level.

The corresponding theory errors are again dominated by the scale uncertainty while the PDF dependence is in principle negligible (see also Fig. 4.9). Indeed, away from the point $p_{T,t\bar{t}} = 0$ the NNLO scale variation is the first reliable estimate for the size of missing higher-order contributions to $\mathrm{A_{FB}}(\Delta y, p_{T,t\bar{t}})$, hence being significantly larger than the respective NLO errors. The reason for this peculiar behavior lies in the fact that at NLO both the numerator and denominator of the asymmetry are effectively of $\mathcal{O}(\alpha_s^3)$ such that the scale dependence is exclusively confined to the partonic fluxes, which themselves are subject to further cancellation effects. In consequence, the standard scale variation procedure is only valid for this type of observable when combining at least two non-vanishing orders of the perturbative expansion. For $p_{T,t\bar{t}} < 10\,\mathrm{GeV}$, on the other hand, both the NLO and NNLO error appears to provide a realistic estimate of the total theory uncertainty at that respective order despite the apparently asymmetric form of the latter.

The relative MC error is again below 1% for each of the central bin values of $\mathrm{A_{FB}}(\Delta y, p_{T,t\bar{t}})$. In some of the bins and for certain scale choices, however, the predicted asymmetry becomes very close to zero (see Fig. 4.8) and, as can be anticipated, in such cases the relative MC errors turn out to be much larger. Still, their absolute impact on the error estimates in the corresponding bins remains small, especially with respect to the sizable scale uncertainties. They can therefore be considered as harmless and, consequently, be further neglected in the total theory error budget of the differential asymmetry.

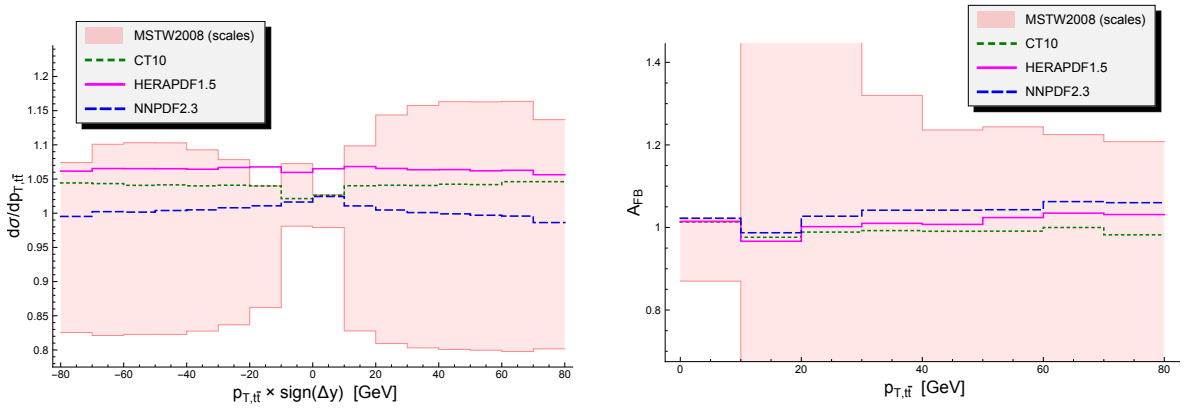

Figure 4.9: *The NNLO QCD predictions for* $d^2\sigma/dp_{T,t\bar{t}}\,d\Delta y$ *(left) and* $\mathrm{A_{FB}}(\Delta y, p_{T,t\bar{t}})$ *(right) derived from four different PDF sets. Given are the ratios of the* HERAPDF1.5, CT10 *and* NNPDF2.3 *based predictions with respect to the default* MSTW2008 *result. For reference we also show the scale dependence of the latter prediction (red band).*

An alternative way of studying the $p_{T,t\bar{t}}$-dependence of $\mathrm{A_{FB}}$ is through a cumulative approach of the form

$$\hat{\mathrm{A}}_{\mathrm{FB}}(\Delta y, p_{T,t\bar{t}} < p_{T,t\bar{t}}^{\mathrm{cut}}) = \frac{\hat{N}}{\hat{D}} = \frac{\sigma_+^c(\Delta y, p_{T,t\bar{t}}^{\mathrm{cut}})\,\theta_{\mathrm{Asym}} - \sigma_-^c(\Delta y, p_{T,t\bar{t}}^{\mathrm{cut}})\,\theta_{\mathrm{Asym}}}{\sigma_+^c(\Delta y, p_{T,t\bar{t}}^{\mathrm{cut}}) + \sigma_-^c(\Delta y, p_{T,t\bar{t}}^{\mathrm{cut}})} \tag{4.23}$$

where now the corresponding cross sections entering the numerator $\hat{N}$ and denominator $\hat{D}$ are defined via

$$\sigma_\pm^c(\Delta y, p_{T,t\bar{t}}^{\mathrm{cut}}) = \int d\sigma\;\theta(p_{T,t\bar{t}}^{\mathrm{cut}} - p_{T,t\bar{t}})\;\theta(\pm\Delta y)\;, \tag{4.24}$$

i. e. they contain all contributions *below* a certain cutoff parameter $p_{T,t\bar{t}}^{\mathrm{cut}}$. This has the advantage that each bin of the $\hat{\mathrm{A}}_{\mathrm{FB}}(\Delta y, p_{T,t\bar{t}} < p_{T,t\bar{t}}^{\mathrm{cut}})$ distribution receives corrections from all relevant perturbative orders rendering this observable potentially more stable against large higher-order effects. Apart from that, the simultaneous treatment of inclusive and differential asymmetry properties is fully maintained albeit the former case now corresponds to the rightmost bin $p_{T,t\bar{t}}^{\mathrm{cut}} = 80\,\mathrm{GeV}$ (taking into account also overflow events with $p_{T,t\bar{t}} \geq 80\,\mathrm{GeV}$) whereas a cut at $p_{T,t\bar{t}}^{\mathrm{cut}} = 10\,\mathrm{GeV}$ is equal to the first bin of the regular asymmetry distribution $\mathrm{A_{FB}}(\Delta y, p_{T,t\bar{t}})$.

The results for the cumulative numerator, denominator and asymmetry at NLO and NNLO QCD are shown in Fig. 4.10 and Tab. 4.5 confirming the observation made in the beginning of this section: for $p_{T,t\bar{t}} \leq 10\,\mathrm{GeV}$ the numerator $\hat{N}$ is only marginally affected by NNLO corrections such that the difference in $\hat{\mathrm{A}}_{\mathrm{FB}}$ is solely due to the change in the denominator $\hat{D}$. Once one moves to higher $p_{T,t\bar{t}}$ the NNLO corrections to $\hat{N}$ quickly become quite pronounced while the rate of change in the denominator $\hat{D}$ is much more moderate. From this we conclude that the difference between the inclusive $\mathrm{A_{FB}}$ computed in NLO and NNLO QCD to a large extent originates from events that are accompanied by hard radiation.

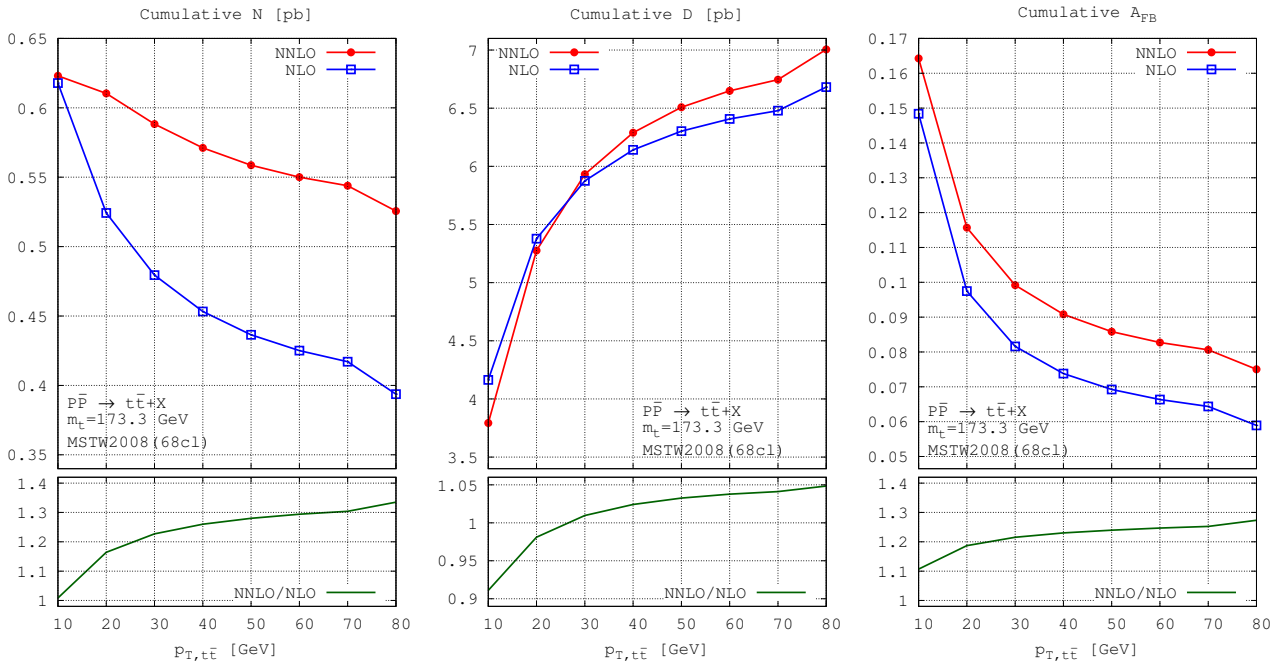

Figure 4.10: *Results for the NLO and NNLO QCD corrections to the cumulative numerator, denominator and asymmetry defined in Eq. (4.23). The calculation is based on the same* 10 GeV *binning used in the underlying* $A_{FB}(\Delta y, p_{T,t\bar{t}})$ *distribution, i. e. the highest bin at* $p_{T,t\bar{t}}^{\text{cut}} = 80\,\text{GeV}$ *contains overflow events.*

The significance of this statement becomes clear when we recall that prior to the full NNLO asymmetry analysis (most) approximate A_{FB} predictions based on soft-gluon resummation or equivalent parton shower approaches failed to generate large perturbative corrections beyond NLO (see section 1.3.3). This discrepancy can now be at least partly understood in terms of the outlined transverse-momentum dependence: as we have learned in section 3.1, soft-gluon resummation in $t\bar{t}$ production applies to kinematic configurations which are of almost 2-to-2 type, i. e. where the final-state heavy-quark system takes virtually all the available energy of the partonic reaction leaving only room for very soft radiation. Since the initial state has zero transverse momentum, one thus necessarily ends up with $t\bar{t}$ pairs that carry only very little $p_{T,t\bar{t}}$. It is difficult to quantify on purely theoretical grounds how small that $p_{T,t\bar{t}}$ would be, but as a rough indication one can use the fact that the transverse-momentum spectrum of the top pair is, at the Tevatron, peaked below 10 GeV [614, 666]. Consequently, we expect that the bulk of the contributions from soft-gluon resummation is presumably confined to the first bin $p_{T,t\bar{t}} \leq 10\,\text{GeV}$ and will be rapidly decreasing with growing $p_{T,t\bar{t}}$.

It is thus not surprising that these approaches were unable to predict the true size of the NNLO corrections to A_{FB}, which, as we have established above, are governed by harder radiation. One should, however, keep in mind that, in practice, implementations of soft-gluon resummation may typically generate noticeable contributions even in kinematic regions away from the relevant partonic threshold. For a more detailed comparison between the NNLO fixed order results and the resummation-based predictions it would therefore be beneficial to

$p_{T,t\bar{t}}$ [GeV]	10	20	30	40	50	60	70	≥ 80
$\hat{N}^{\text{NLO}}$ [pb]	0.618	0.524	0.479	0.453	0.436	0.425	0.417	0.394
$\hat{N}^{\text{NNLO}}$ [pb]	0.623	0.610	0.588	0.571	0.559	0.550	0.544	0.526
$\hat{D}^{\text{NLO}}$ [pb]	4.164	5.378	5.876	6.142	6.303	6.407	6.479	6.682
$\hat{D}^{\text{NNLO}}$ [pb]	3.793	5.276	5.932	6.290	6.508	6.649	6.745	7.005
$\hat{\text{A}}_{\text{FB}}^{\text{NLO}}$	0.148	0.097	0.082	0.074	0.069	0.066	0.064	0.059
$\hat{\text{A}}_{\text{FB}}^{\text{NNLO}}$	0.164	0.116	0.099	0.091	0.086	0.083	0.081	0.075

Table 4.5: *Values for the cumulative numerator, denominator and asymmetry appearing in Fig. 4.10.*

also have the $p_{T,t\bar{t}}$-dependence of the latter available. In addition, this will ultimately allow for a merged NNLO+NNLL treatment which, similar to the total cross section, incorporates the major part of the purely QCD-induced corrections.

4.1.4 Angular dependence and Legendre moments

As explained in section 1.3.3, the forward-backward asymmetry does not have to be exclusively defined through Δy but may, in fact, be parametrized by any kinematic variable that divides the underlying reference frame into two separate hemispheres. A further example of such a variable, which has been recently employed in a measurement by the CDF collaboration [660,667], is $\cos\theta$ where θ is the angle between the top quark and the incoming proton in the $t\bar{t}$ rest frame. The corresponding asymmetry

$$\text{A}_{\text{FB}}(\cos\theta) = \frac{1}{\sigma_{t\bar{t}}^{\text{tot}}}\frac{d\sigma}{d\cos\theta}(\cos\theta > 0) - \frac{1}{\sigma_{t\bar{t}}^{\text{tot}}}\frac{d\sigma}{d\cos\theta}(\cos\theta < 0) \tag{4.25}$$

represents an independent observable and only for vanishing $p_{T,t\bar{t}}$ coincides with the definition in Eq. (4.10). It can thus be used for a complementary analysis of the available Tevatron $t\bar{t}$ data offering additional insights on the asymmetric behavior of the top quark.

As indicated in Eq. (4.25), the basis for such an analysis is the normalized distribution $(1/\sigma_{t\bar{t}}^{\text{tot}})d\sigma/d\cos\theta$, which can be consistently evaluated through NNLO QCD using the computational setup described above. Note, however, that in order to assess in more detail the angular dependence of the top quark, we decided to choose a finer binning than is actually required for the determination of $\text{A}_{\text{FB}}(\cos\theta)$. Moreover, we do not account for the finite bin width as suggested by Eq. (4.4) but rather treat the value in each bin such that it corresponds to the integral of the cross-section over that bin. In consequence, the sum over all bin values equals unity, which simplifies the subsequent calculation of $\text{A}_{\text{FB}}(\cos\theta)$ considerably since it involves no further re-binning. This prescription also matches the normalization employed in the experimental analysis of Refs. [660,667] allowing for a direct comparison of the NNLO theory predictions with data.

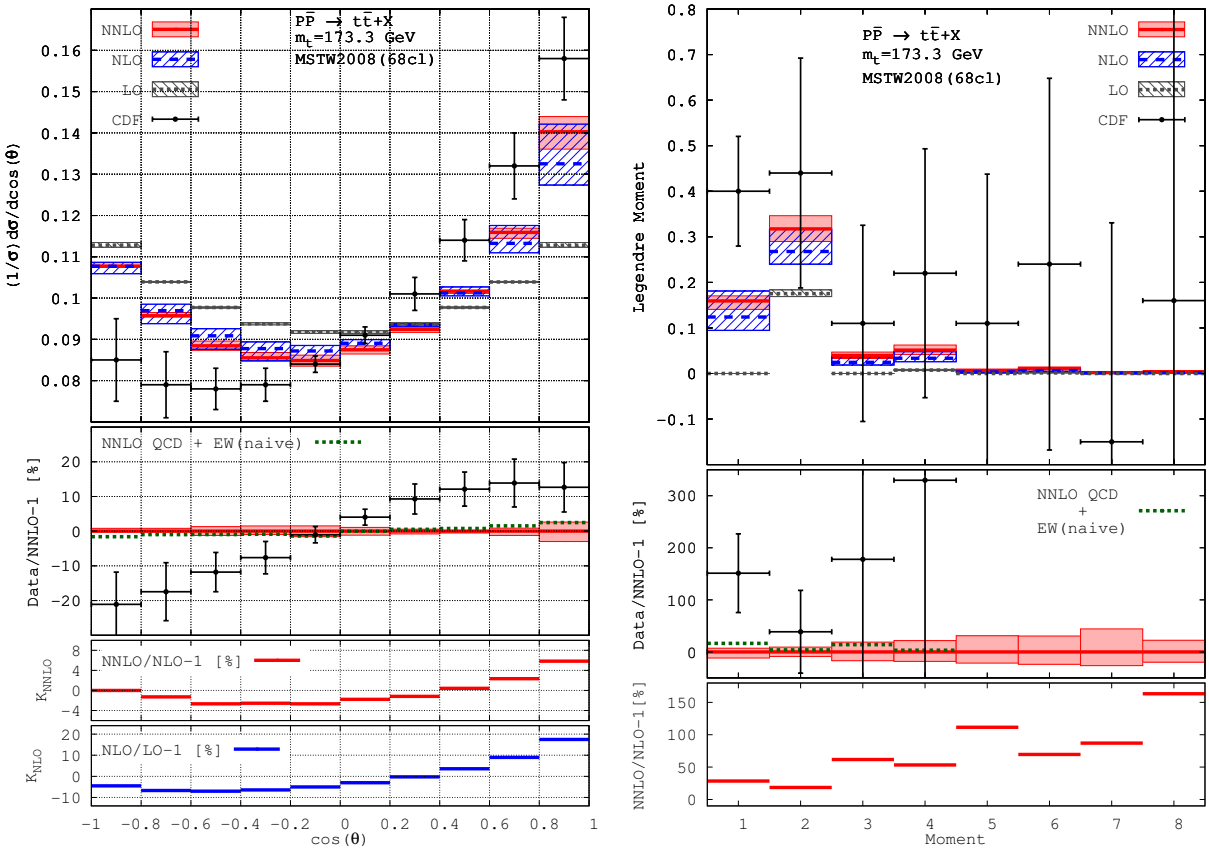

Figure 4.11: *Theoretical predictions for the normalized* $\cos\theta$ *distribution (left) and the related Legendre moments (right) compared to the available data from Refs. [660, 667]. Apart from the pure QCD results through NNLO derived in this thesis, we also show a naive estimate of EW corrections (see text) as well as the K-factors* K_{NNLO} *and* K_{NLO}*. The theory error of the pure QCD predictions is based on scale variation only whereas for the combined NNLO QCD+EW(naive) evaluation we merely provide the central cross section values.*

The corresponding result is shown in Fig. 4.11 where we have plotted the different theoretical and experimental findings for $(1/\sigma_{t\bar{t}}^{\text{tot}})d\sigma/d\cos\theta$ both in terms of absolute numbers and as a ratio of data to NNLO QCD. While the deviation between the measured angular distribution and theory never exceeds 2.3σ, especially the latter figure illustrates the clear tendency of CDF data to under-/overestimate the SM expectation at large negative/positive $\cos\theta$. This is in line with the known $\sim 2\sigma$ discrepancy for the unexpanded $\text{A}_{\text{FB}}(\Delta y)$ at NNLO QCD presented in section 1.3.3 (see in particular Tab. 1.4) already hinting at the approximate equivalence of the two asymmetry definitions.

Analogous to $\text{A}_{\text{FB}}(\Delta y)$ the inclusion of the NNLO corrections helps to reduce the gap between theory and experiment in $(1/\sigma_{t\bar{t}}^{\text{tot}})d\sigma/d\cos\theta$ and, moreover, leads to a decreased scale dependence[10]. Further indication for the good perturbative convergence of this observable

[10] Note that, similar to $\text{A}_{\text{FB}}(\Delta y, p_{T,t\bar{t}})$, the LO scale dependence of $(1/\sigma_{t\bar{t}}^{\text{tot}})d\sigma/d\cos\theta$ is subject to huge cancellation effects and thus does not serve as a reliable estimate of the theoretical uncertainty due to missing higher-order contributions.

also comes from the NLO and NNLO K-factors, which are of similar shape but differ in their overall size with K_{NNLO} being significantly smaller than K_{NLO}. Note that we have, for the sake of simplicity, neglected the PDF dependence of theoretical cross section predictions. For a ratio-like quantity such as $(1/\sigma_{t\bar{t}}^{\text{tot}})d\sigma/d\cos\theta$ the corresponding errors are expected to be small albeit at NNLO they could be of the same order as the scale uncertainty. Since the comparison with the measured $\cos\theta$ distribution is dominated by experimental uncertainties, it will, however, for the following discussions be sufficient to consider only the latter contributions to the total theory uncertainty.

A type of correction that can, on the other hand, not be neglected in the theoretical description of $(1/\sigma_{t\bar{t}}^{\text{tot}})d\sigma/d\cos\theta$ are EW effects. Given the important role these contributions play in the analysis of A_{FB}, it can be anticipated that they will also have a noticeable impact on the angular dependence of the top quark itself. Unfortunately, the relevant EW corrections are not available in a form that is readily combinable with our QCD calculation forcing us to pursue an approximate strategy for the evaluation of these effects. Utilizing the known NLO+EW result given in Refs. [660,667] (which has, in turn, been provided by the authors of Ref. [377]) we assume that the difference with respect to our NLO calculation can be attributed to pure non-QCD corrections such that a naive combination with the NNLO predictions may be achieved via

NNLO QCD + EW(naive) = NNLO QCD + NLO(QCD+EW) [377] - NLO QCD (this work).

While the computational setup in this work differs in several aspects (PDF set, m_t, $\alpha_s(M_Z)$) from the analysis in Ref. [377], we have verified that the respective results at pure NLO QCD are in reasonable agreement with each other[11]. Thus, we expect that such an approximate treatment is able to adequately reproduce the main features of the exact NNLO+EW angular dependence.

Restricting our discussion solely to the central theory predictions we in Fig. 4.11 show the corresponding ratio (NNLO QCD+EW(naive))/NNLO and compare it to data. We observe that the EW corrections are comparable to the size of the NNLO scale error shifting the theoretical $(1/\sigma_{t\bar{t}}^{\text{tot}})d\sigma/d\cos\theta$ distribution closer to the measured results. Still, they are not able to fully resolve the discrepancy between SM expectation and data suggesting that this anomalous behavior will also persist for the associated asymmetry $\text{A}_{\text{FB}}(\cos\theta)$, which we will analyze next.

To this end, we do, however, not employ the direct approach in Eq. (4.25) but rather resort to a more exotic evaluation method in terms of so-called Legendre moments defined as

$$a_\ell = (2\ell+1)\int_{-1}^{1} P_\ell(\cos\theta)\,\frac{1}{\sigma_{t\bar{t}}^{\text{tot}}}\,\frac{d\sigma}{d\cos\theta}\,d\cos\theta\,. \tag{4.26}$$

[11] We wish to thank Werner Bernreuther for his help with this comparison.

Here, we exploited the fact that, using the orthogonality and completeness relations

$$\begin{aligned} \int_{-1}^{1} P_k(\cos\theta)\, P_\ell(\cos\theta)\, d\cos\theta &= \frac{2}{2\ell+1}\,\delta_{k\ell} \\ \sum_{\ell=0}^{\infty} \frac{2\ell+1}{2}\, P_\ell(\cos\theta)\, P_\ell(\cos\theta') &= \delta(\cos\theta-\cos\theta')\,, \end{aligned} \tag{4.27}$$

the normalized angular distribution can be decomposed into a series of Legendre polynomials

$$\frac{1}{\sigma_{t\bar{t}}^{\mathbf{tot}}}\,\frac{d\sigma}{d\cos\theta} = \frac{1}{2}\sum_{\ell=0}^{\infty} a_\ell\, P_\ell(\cos\theta) \tag{4.28}$$

with the expansion coefficients a_ℓ normalized such that $a_0 = 1$. The advantage of such an approach is that the analytically unknown (at least at NNLO) and supposedly complicated kinematic dependence can be completely described in terms of a few numerical coefficients provided that Eq. (4.28) converges fast enough. In case of $(1/\sigma_{t\bar{t}}^{\mathbf{tot}})d\sigma/d\cos\theta$, we find that already with the first four non-trivial moments $a_1,\ldots,a_4$ it is possible to reproduce the binned NNLO predictions in Fig. 4.11 to better than 1%. Indeed, even the experimental data presented in Refs. [660, 667] is based on such a Legendre decomposition, i.e. the corresponding $\cos\theta$ distribution has been obtained by integrating a series of measured Legendre moments[12] over the bin ranges specified in Tab. 4.1. This, in principle, allows for the use of arbitrary binnings in the experimental analysis offering a much higher degree of flexibility in the actual application of the available data.

A comparison of the experimental result for the first eight Legendre moments with the SM theory prediction through NNLO QCD is shown in Fig. 4.11. As one can see, with the exception of a_1 all of the computed moments are in good agreement with the measurement albeit the significance of this comparison is, especially for the higher moments $\ell \geq 5$, somewhat hampered by the large experimental uncertainties. For the first moment the measured value lies notably above the SM expectation even though with the inclusion of the NNLO corrections the deviation has been reduced to under 2σ. In general, the impact of the NNLO contributions is sizable with K-factors ranging between 20-160% with a clear tendency towards larger corrections for the higher moments. Still, the NNLO predictions are consistently contained within the error band of the NLO evaluation, which indicates the perturbative stability present in the theoretical description of these observables.

Similar to $(1/\sigma_{t\bar{t}}^{\mathbf{tot}})d\sigma/d\cos\theta$ we have again neglected the PDF-related uncertainty since it is expected to be small. The MC error, on the other hand, plays a much greater role in the Legendre analysis than for the other kinematic distributions where it can be safely omitted.

[12] For the experimental results of $(1/\sigma_{t\bar{t}}^{\mathbf{tot}})d\sigma/d\cos\theta$ [660, 667] in Fig. 4.11 actually only the first moment is obtained from data while the moments with $\ell \geq 2$ have been set to their respective SM values at NLO(QCD+EW) [377]. Using the full batch of measured moments would result in a much larger experimental uncertainty bringing the corresponding data into full agreement with theory even without considering NNLO QCD corrections.

ℓ	$A_{FB}(\cos\theta)$[%]			
	NLO	NNLO	NNLO QCD+EW(naive)	CDF [660, 667]
1	$6.20^{+2.85}_{-1.47}$	$7.96^{+0.56}_{-0.93}$	9.26	$20.0^{+6.0}_{-6.0}$
3	$-0.31^{+0.08}_{-0.15}$	$-0.50^{+0.08}_{-0.09}$	−0.56	$-1.4^{+2.7}_{-2.7}$
5	$0.02^{+0.01}_{-0.00}$	$0.04^{+0.01}_{-0.01}$	–	$0.7^{+2.1}_{-2.1}$
7	$-0.00^{+0.00}_{-0.00}$	$-0.01^{+0.00}_{-0.00}$	–	$0.6^{+1.9}_{-1.9}$
Σ	$5.91^{+2.71}_{-1.40}$	$7.50^{+0.49}_{-0.86}$	8.70	$19.9^{+5.7}_{-5.7}$

Table 4.6: *Various SM theory predictions for the contribution of the odd Legendre moments $a_{1,3,5,7}$ to the inclusive asymmetry $A_{FB}(\cos\theta)$ (see Eq. (4.29)). For comparison also the corresponding experimental results are shown based on the measured moments in Refs. [660, 667]. The theory error of the pure QCD predictions is based on scale variation only whereas for the combined NNLO QCD+EW(naive) evaluation we merely provide the central asymmetry values for the leading moments a_1 and a_3 (see text).*

For $a_{1,2,3}$ it is below five permille while for a_4 it lies around 2%. For the higher moments it grows even further such that for a_8 it exceeds 30% and thus actually becomes the dominant source of uncertainty on the theory side. Nevertheless, compared to the experimental errors the size of the MC error is still moderate and, hence, its inclusion (or omission) does not significantly affect the comparison of SM theory with data.

In Fig. 4.11 we also present a naive estimate of the EW corrections to a_ℓ following the approximate evaluation strategy for the $\cos\theta$ distribution explained above. Note, however, that the relevant NLO(QCD+EW) contributions have been computed from a binned $\cos\theta$ spectrum whereas our calculation of the Legendre moments is based on a fully continuous treatment of the angular dependence, i. e. the corresponding integrals in Eq. (4.26) have been evaluated within the same MC framework used for the derivation of the other differential quantities discussed in this chapter. In consequence, we restrict the combined NNLO QCD+EW(naive) analysis to the first four moments only since for $\ell \geq 5$ the numerical differences between these two approaches due to finite bin-size effects would render the respective predictions increasingly unreliable. We observe that the EW corrections are particularly relevant for the odd moments where they amount to $\sim 15\%$ of the NNLO QCD results. Still, for a_1 their size is not sufficient to close the gap between theory and experiment as could have been anticipated from the corresponding NNLO QCD+EW(naive) analysis of $(1/\sigma_{t\bar{t}}^{\mathbf{tot}})d\sigma/d\cos\theta$.

In order to assess the impact of the various Legendre moments on the inclusive asymmetry $A_{FB}(\cos\theta)$, we apply the decomposition in Eq. (4.28) also to the angular cross sections in the two hemispheres $\pm\cos\theta > 0$ entering Eq. (4.25) yielding

$$A_{FB}(\cos\theta) = \frac{1}{2}\sum_{\ell=0}^{\infty} a_\ell \left(P_\ell^+ - P_\ell^-\right) = \frac{1}{2}\sum_{n=0}^{\infty} a_{2n+1}\,\frac{(-1)^n\,(2n)!}{(n+1)\,(2^n\,n!)^2}\,. \tag{4.29}$$

As one can see, only the odd moments survive in the difference $P_\ell^+ - P_\ell^-$, which follows directly from the symmetry properties of the Legendre polynomials under $\cos\theta \leftrightarrow -\cos\theta$

transformations

$$P_\ell^\pm = \int_0^1 P_\ell(\pm\cos\theta)\, d\cos\theta = \begin{cases} \int_0^1 P_\ell(\cos\theta)\, d\cos\theta & \text{for } \ell = \text{even} \\ \pm\int_0^1 P_\ell(\cos\theta)\, d\cos\theta & \text{for } \ell = \text{odd}\,. \end{cases} \tag{4.30}$$

The remaining integrals can be evaluated with the help of recurrence relations and, as indicated in Eq. (4.29), brought into a closed analytical form depending solely on the summation index $n = \frac{\ell-1}{2}$. Since this coefficient factor is rapidly decreasing for increasing n, the contribution from higher moments is further suppressed such that the dominant part of the asymmetry is determined by a_1 and a_3 as can be inferred from Tab. 4.6. There, we show the individual contributions to $A_{FB}(\cos\theta)$ from all odd moments up to $\ell = 7$ at different orders in QCD as well as NNLO QCD+EW(naive)[13] and compare them to the experimental results by CDF [660, 667]. Due to the large discrepancy between the predicted and the measured value of a_1, one can observe a similar gap between theory and data of $\sim 2\sigma$ also for $A_{FB}(\cos\theta)$.

In order to explain this deviation, in Refs. [660, 667] the possibility of new-physics contributions has been considered as well. The advantage of knowing not only the inclusive asymmetry itself but its actual Legendre decomposition is that it allows us to distinguish between different BSM scenarios since their impact on the various Legendre moments can be quite different. It turns out that since the observed asymmetry excess is exclusively confined to the first moment, the most promising candidate for a BSM-based asymmetry description is a s-channel model governed by the exchange of a heavy, gluon-like particle with axial-vector couplings to quarks. Additional t-channel contributions mediated, for instance through a new, heavy vector boson, are on the other hand rather disfavored. For a more conclusive identification of possible new-physics contributions to $A_{FB}(\cos\theta)$ it would, however, be beneficial to extend the Legendre analysis also to DØ data, which is generally in better agreement with the SM predictions. Only then it will be possible to decide whether the discrepancy in a_1 is indeed driven by BSM effects.

4.2 Differential top-quark distributions

Apart from the inclusive and differential asymmetries discussed above, the CDF and DØ collaborations also studied the kinematic properties of the top quark in regular differential distributions, most notably $d\sigma/d|y_t|$, $d\sigma/dm_{t\bar{t}}$ and $d\sigma/dp_{T,t}$. The corresponding comparison between data and the relevant SM predictions at NNLO QCD has already been presented in section 1.3.4. The main features of this analysis are the improved theoretical control over the shape of the differential distributions through the inclusion of the $\mathcal{O}(\alpha_s^4)$ corrections and, consequently, a generally better agreement between theory and experiment. However, as in virtually all bins the measured central values lie above the predicted cross section, it would be

[13] Note that the difference of these predictions to the unexpanded results for $A_{FB}(\Delta y)$ in Tab. 1.4 is well below 1% stressing the close correspondence of these asymmetry definitions at the Tevatron collider.

interesting to extend this comparison also to the level of normalized distributions eliminating some of the experimental and theoretical uncertainties affecting the absolute cross section analysis. While experimental results in the required format are currently not available, we will in the following provide the necessary theory predictions through NNLO QCD and discuss their basic perturbative behavior as well as their main kinematic properties. Moreover, we will investigate in greater detail the dependence of the differential distributions on the PDFs and the top-quark mass giving a more complete picture of the parametric uncertainties in exclusive $t\bar{t}$ production. Besides, these parameter studies might be helpful in assessing the potential for a future use of differential top-quark observables in PDF fits or top-mass measurements.

4.2.1 Top-quark rapidity

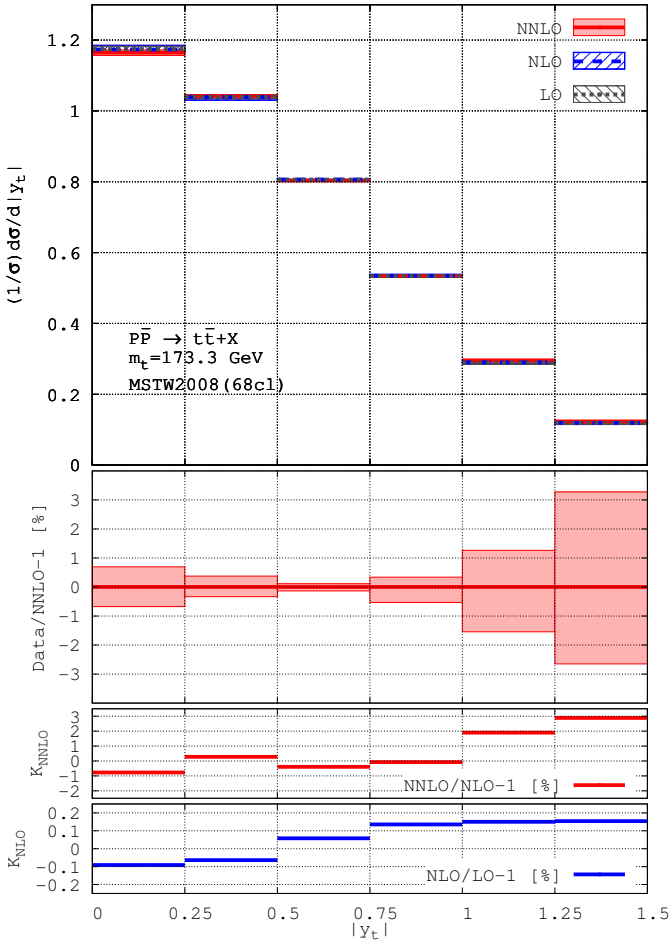

Figure 4.12: *The SM theory prediction for the normalized differential distribution* $(1/\sigma_{t\bar{t}}^{tot})d\sigma/d|y_t|$ *through NNLO QCD as well as the respective NNLO/NLO and NLO/LO K-factors* $K_{\rm NNLO}$ *and* $K_{\rm NLO}$*. The corresponding theory error at NLO and NNLO is derived from scale and PDF variation while at LO it is based on scale variation only.*

In Fig. 4.12 we show the normalized rapidity distribution of the top quark where, in order to allow for a combined treatment of t and $\bar{t}$, one usually uses the absolute value $|y_t|$ rather than the original definition employed in the asymmetry analysis (through Δy). Indeed, we

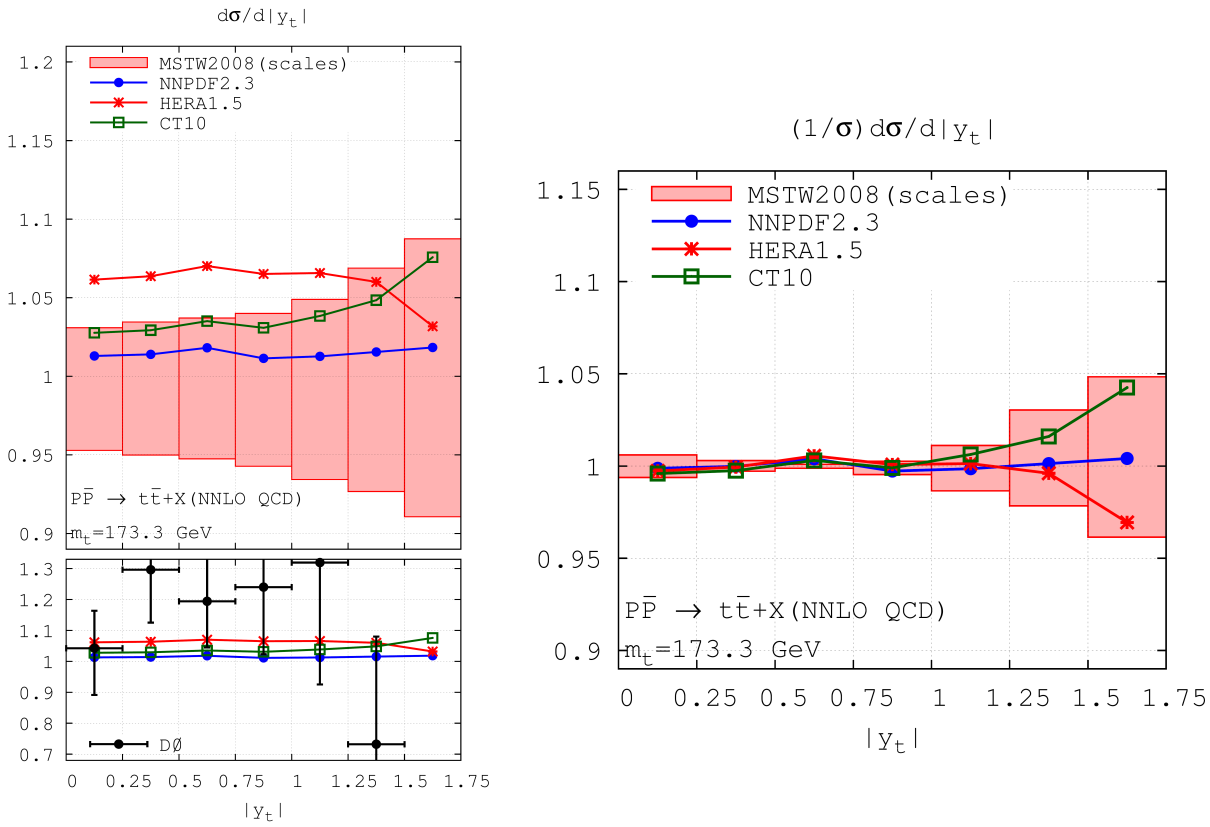

Figure 4.13: *The NNLO QCD predictions for the absolute rapidity spectrum $d\sigma/d|y_t|$ (left) as well as the corresponding normalized distribution $(1/\sigma_{t\bar{t}}^{\mathbf{tot}})d\sigma/d|y_t|$ (right) derived from four different PDF sets. Given are the ratios of the* HERAPDF1.5, CT10 *and* NNPDF2.3 *based predictions with respect to the default* MSTW2008 *result. For reference we also show the scale dependence of the latter prediction (red band). In case of the absolute $|y_t|$ distribution we moreover compare the different PDF results with the available data from the* DØ *Collaboration [459].*

have checked that the top and anti-top $|y|$ distributions agree within MC errors, which are of the order of $\lesssim 1\%$, such that we can in the following restrict our discussion solely to the case of top quarks. As could have been anticipated from the result for the absolute rapidity distribution in Fig. 1.26, the shape of $(1/\sigma_{t\bar{t}}^{\mathbf{tot}})d\sigma/d|y_t|$ is monotonically decreasing towards the end of the spectrum with the higher-order corrections slightly favoring the production of top quarks in the forward/backward regime $|y_t| \geq 1$.

Due to the quite small K-factors, which at most amount to about 3%, the higher-order predictions lie consistently within the error bands of the lower order calculations (except for the extremely small error in $0.75 \geq |y_t| \geq 0.5$) indicating the good perturbative convergence of this quantity. Interestingly, K_{NNLO} may still be up to 20 times larger than K_{NLO} while the corresponding perturbative uncertainty due to scale variation is only marginally reduced from LO to NNLO. This stresses the particular importance of extending the theoretical description of this observable to NNLO accuracy since the resulting shift of the central bin values is comparable to the NLO scale errors.

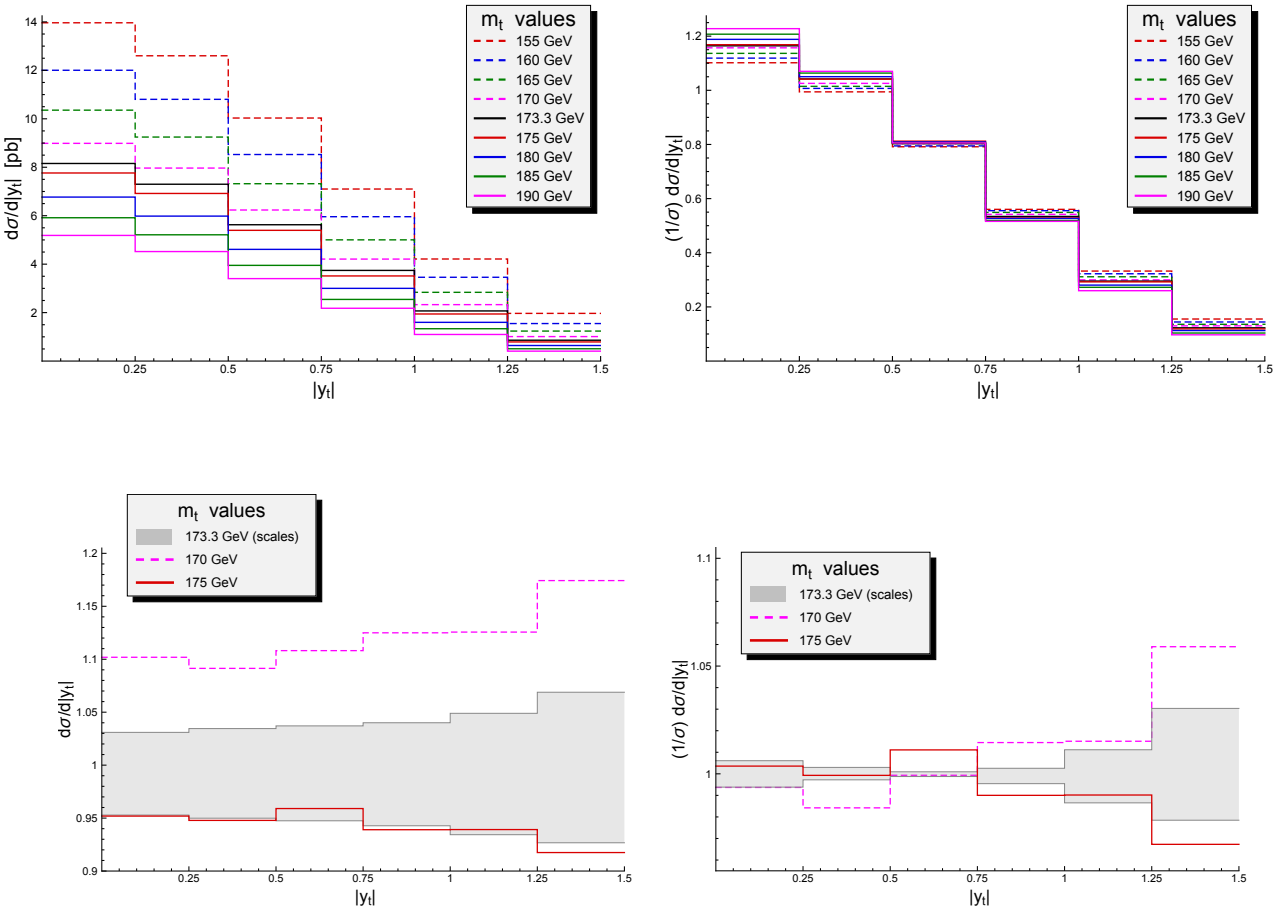

Figure 4.14: *The top-mass dependence of the NNLO QCD predictions for the absolute rapidity spectrum* $d\sigma/d|y_t|$ *(left) as well as the corresponding normalized distribution* $(1/\sigma_{t\bar{t}}^{\mathbf{tot}})d\sigma/d|y_t|$ *(right). The corresponding parametric uncertainties associated with an experimental error on* m_t *of about* $\Delta m_t = \pm 1\,\mathrm{GeV}$ *may be assessed from the lower plots where we present the results for the three top-mass values closest to the world average normalized to our default prediction at* $m_t = 173.3\,\mathrm{GeV}$*. For reference we, in the latter case, also show the NNLO scale dependence (gray band).*

The PDF errors are usually smaller than the relevant scale uncertainties albeit at NNLO they are not always negligible, especially towards the end of the $(1/\sigma_{t\bar{t}}^{\mathbf{tot}})d\sigma/d|y_t|$ spectrum. Further evidence for this observation comes from the PDF analysis in Fig. 4.13 where we have plotted the ratio of HERAPDF1.5, CT10 and NNPDF2.3 differential cross section predictions to our default calculation based on the MSTW2008 set. As one can see, the various results are in good agreement and only above $|y_t| \geq 1$ start to diverge from each other. While the resulting spread of PDF predictions is still compatible with the NNLO scale error, this behavior hints at a possible ambiguity in the functional dependence of the different PDF sets and one might speculate whether this observable has the power to constrain it.

For the absolute distribution $d\sigma/d|y_t|$ the situation is quite different, the spread between the various PDF sets being much more pronounced. In particular the HERAPDF1.5 result

lies significantly above our default prediction, in most bins even surpassing the corresponding NNLO scale error. This suggests that the PDF error estimates of the individual PDF sets may not be fully compatible with the differences in the central predictions signaling the potential of this observable for the use in PDF fits. It is, however, not clear if this discrepancy is due to approximate treatment of PDF errors in Eq. (4.9) or whether it would also persist when these uncertainties are evaluated exactly. Moreover, owing to the large experimental uncertainties all PDF sets are in agreement with the available data such that the constraining power of the absolute distribution might, in practice, not be sufficient to reliably distinguish between different PDF scenarios.

The dependence of the rapidity distribution on the value of top-quark mass can be inferred from Fig. 4.14. As one can see, the spread of the various m_t predictions is dramatically reduced when moving from $d\sigma/d|y_t|$ to the normalized spectrum. Still, in most bins the corresponding parametric uncertainty due to a shift of order $\Delta m_t = \pm 1\,\text{GeV}$ appears to be compatible with the NNLO scale error. In fact, the impact of the top-mass error seems to be more significant for the normalized distribution since its scale dependence has also been substantially reduced. Nevertheless, one may conclude that both the absolute and the normalized $|y_t|$ spectra are presumably not very well suited for a future use in top-mass determinations since their sensitivity to m_t is rather limited.

4.2.2 Invariant mass of the $t\bar{t}$ pair

In Fig. 4.15 we present the theoretical prediction for the normalized invariant-mass spectrum $(1/\sigma_{t\bar{t}}^{\text{tot}})d\sigma/dm_{t\bar{t}}$ through NNLO QCD. While the shape, of course, remains identical to the absolute case, the theoretical uncertainty has been significantly reduced lying at the low percent-level now. In fact, at LO the corresponding error estimate clearly underestimates the size of missing higher-order contributions, which can again be traced back to the cancellation of the leading α_s-dependence. In consequence, the scale variation is completely determined by the limited scale dependence of the partonic fluxes in numerator and denominator, which is unable to reliably predict the true impact of the NLO and NNLO corrections.

As indicated by the respective K-factors, K_{NLO} and K_{NNLO}, these higher-order effects tend to favor the production of $t\bar{t}$ pairs close to threshold $m_{t\bar{t}} \sim 2m_t$ whereas for higher values of $m_{t\bar{t}}$ they lead to a further reduction of the normalized cross section. In this context, the shift from LO to NLO is quite sizable while the addition of the NNLO corrections results in a much smaller K-factor of at most $\sim 2\%$ such that the NNLO prediction is consistently contained within the error band of the NLO result. In combination with the decreased NNLO scale error, this illustrates the improved theoretical robustness of our NNLO evaluation.

As for the PDF dependence shown in Fig. 4.16, the situation is similar to the rapidity distributions, i. e. for $d\sigma/dm_{t\bar{t}}$ the difference between the various PDF sets is comparable to or larger than the NNLO scale variation whereas in the normalized case one can observe a much better agreement with deviations occurring only at the upper end of the spectrum. Note, however, that the large spread of PDF predictions in the last bin of the latter distribution should be interpreted with care considering the fact that the corresponding MC errors are around 4-5% ($\lesssim 1\%$ for all other bins). For the absolute distribution a comparison with data shows that

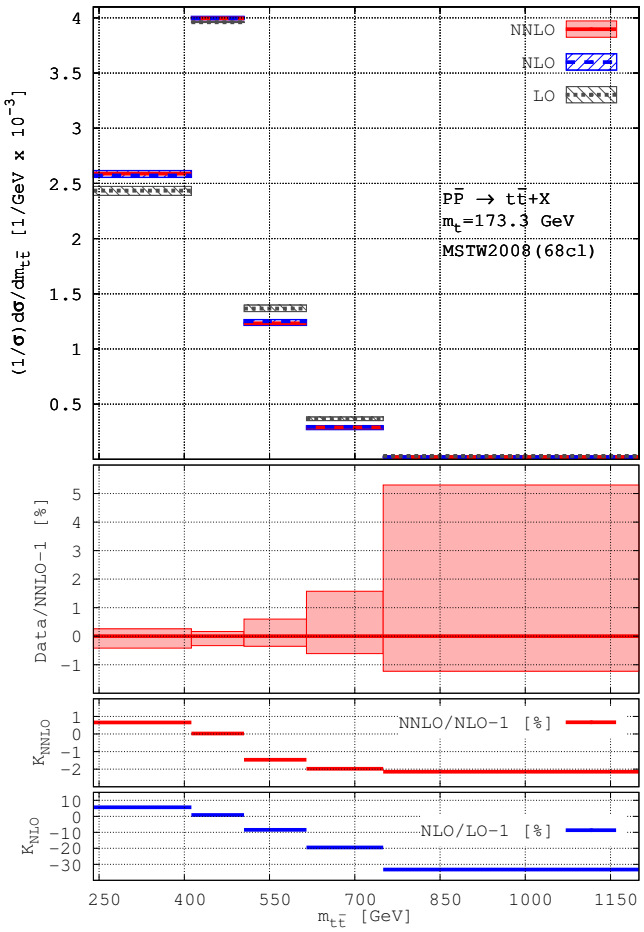

Figure 4.15: *The SM theory prediction for the normalized differential distribution* $(1/\sigma_{t\bar{t}}^{\mathrm{tot}})d\sigma/dm_{t\bar{t}}$ *through NNLO QCD as well as the respective NNLO/NLO and NLO/LO K-factors* K_{NNLO} *and* K_{NLO}*. The corresponding theory error at NLO and NNLO is derived from scale and PDF variation while at LO it is based on scale variation only.*

all PDF sets are able to adequately describe the measured $m_{t\bar{t}}$ spectrum. Thus, a further discrimination of the functional form of the PDFs from this observable will be difficult, which can be mainly attributed to the large experimental uncertainties.

For a use in top-mass determinations, on the other hand, the invariant-mass distribution seems to be far more suited. As indicated in Fig. 4.17, especially in the first bin the sensitivity to the value of m_t is highly pronounced since the lower bin edge is directly affected by the position of the production threshold $m_{t\bar{t}} = 2\,m_t$. For the absolute spectrum the top-mass dependence at higher values of $m_{t\bar{t}}$ dramatically decreases such that the corresponding parametric uncertainty lies actually well below the scale error. For $(1/\sigma_{t\bar{t}}^{\mathrm{tot}})d\sigma/dm_{t\bar{t}}$, however, the sensitivity remains high, in particular since the other sources of theoretical uncertainty have been further reduced. It will thus be interesting to see how these different m_t predictions compare to experimental data.

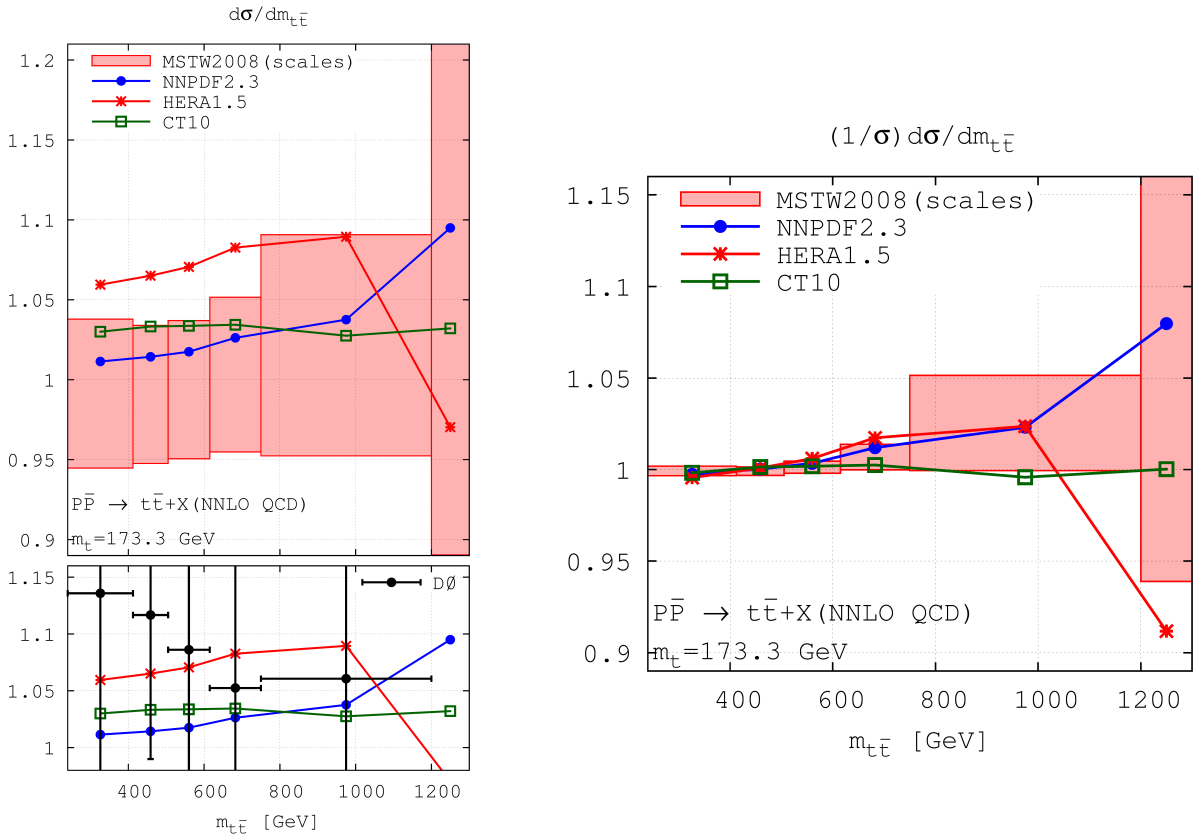

Figure 4.16: *The NNLO QCD predictions for the absolute invariant-mass spectrum $d\sigma/dm_{t\bar{t}}$ (left) as well as the corresponding normalized distribution $(1/\sigma_{t\bar{t}}^{tot})d\sigma/dm_{t\bar{t}}$ (right) derived from four different PDF sets. Given are the ratios of the* HERAPDF1.5, CT10 *and* NNPDF2.3 *based predictions with respect to the default* MSTW2008 *result. For reference we also show the scale dependence of the latter prediction (red band). In case of the absolute $m_{t\bar{t}}$ distribution we moreover compare the different PDF results with the available data from the* DØ *Collaboration [459].*

Another consequence of the significant top-mass dependence of the normalized distribution is a presumably large m_t-related uncertainty that is not properly accounted for in Fig. 4.15. Therefore, one has to be careful when using the combined scale and PDF uncertainty as an estimate for the total theory error on this observable. Certainly, for the future it would be advantageous to also include the uncertainty due to a $\Delta m_t = \pm 1\,\text{GeV}$ shift in the corresponding theory predictions but due to the increased computational effort of such an advanced error estimate we, for now, have to postpone this type of analysis.

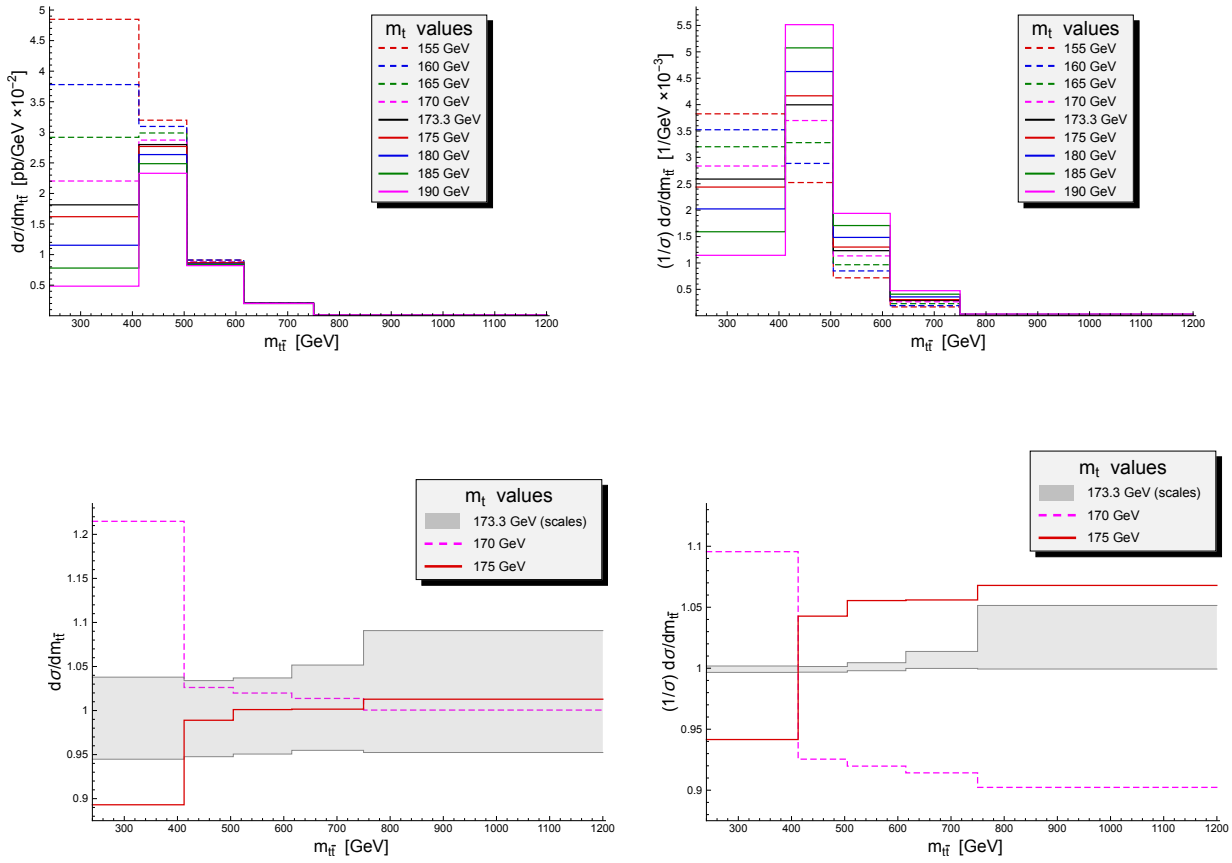

Figure 4.17: *The top-mass dependence of the NNLO QCD predictions for the absolute invariant-mass spectrum* $d\sigma/dm_{t\bar{t}}$ *(left) as well as the corresponding normalized distribution* $(1/\sigma_{t\bar{t}}^{\mathbf{tot}})d\sigma/dm_{t\bar{t}}$ *(right). The corresponding parametric uncertainties associated with an experimental error on* m_t *of about* $\Delta m_t = \pm 1\,\mathrm{GeV}$ *may be assessed from the lower plots where we present the results for the three top-mass values closest to the world average normalized to our default prediction at* $m_t = 173.3\,\mathrm{GeV}$*. For reference we, in the latter case, also show the NNLO scale dependence (gray band).*

4.2.3 Transverse momentum of the top quark

In contrast to the rapidity and invariant mass, the transverse momentum of the individual top or anti-top quarks has not been considered in the course of the asymmetry analysis and may thus offer some complementary insights on the kinematic properties of these particles. While for the experimental determination one usually averages over the t and $\bar{t}$ spectra, in the following we will only focus on $p_{T,t}$ having checked that the difference with respect to the $p_{T,\bar{t}}$ distribution lies within the MC error.

The corresponding theory result for $(1/\sigma_{t\bar{t}}^{\mathbf{tot}})d\sigma/dp_{T,t}$ through NNLO QCD is shown in Fig. 4.18. Profiting again from large cancellation effects, the theoretical uncertainty has been significantly reduced with respect to the absolute cross section at all available orders of the perturbative expansion. While at LO this leads to the known underestimation of higher-order effects, the NLO and NNLO predictions are consistent within their error bands, which in the

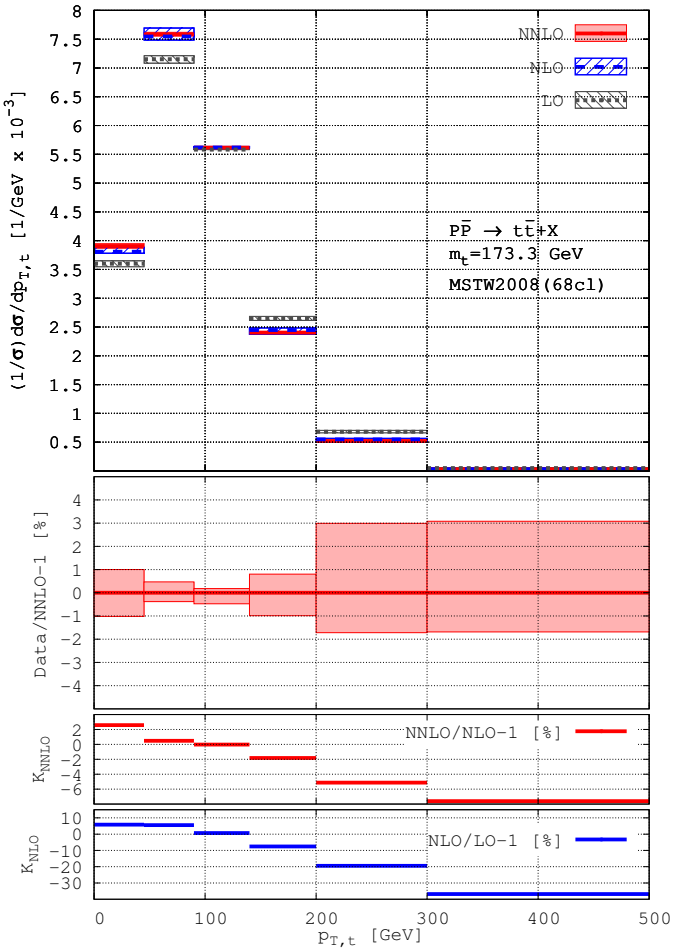

Figure 4.18: *The SM theory prediction for the normalized differential distribution* $(1/\sigma_{t\bar{t}}^{tot})d\sigma/dp_{T,t}$ *through NNLO QCD as well as the respective NNLO/NLO and NLO/LO K-factors* K_{NNLO} *and* K_{NLO}*. The corresponding theory error at NLO and NNLO is derived from scale and PDF variation while at LO it is based on scale variation only.*

latter case amounts to merely $\lesssim 3\%$. This is in line with the rather moderate size of the NNLO K-factors, which have a similar shape as K_{NLO} but are at least a factor 2-5 times smaller illustrating the perturbative convergence firmly present in this observable.

The PDF dependence of the normalized distribution is again substantially improved with respect to the absolute cross section showing a similar diverging behavior in the end bins as $|y_t|$ and $m_{t\bar{t}}$. However, since the MC error in these bins is relatively large, i. e. for $300 \leq p_{T,t} \leq 500\,\mathrm{GeV}$ it is close to 2% while for the overflow bin $p_{T,t} \geq 500\,\mathrm{GeV}$ it is around 5% (in the remaining bins the MC error lies below 1%), one once more has to be careful when drawing any deeper conclusion from this part of the spectrum. For $d\sigma/dp_{T,t}$ we observe a good agreement of the different PDF predictions with the DØ measurement. Due to the fact that the cross section results from HERAPDF1.5, CT10 and NNPDF2.3 are generally higher than the default calculation based on the MSTW2008 set, in the two bins where

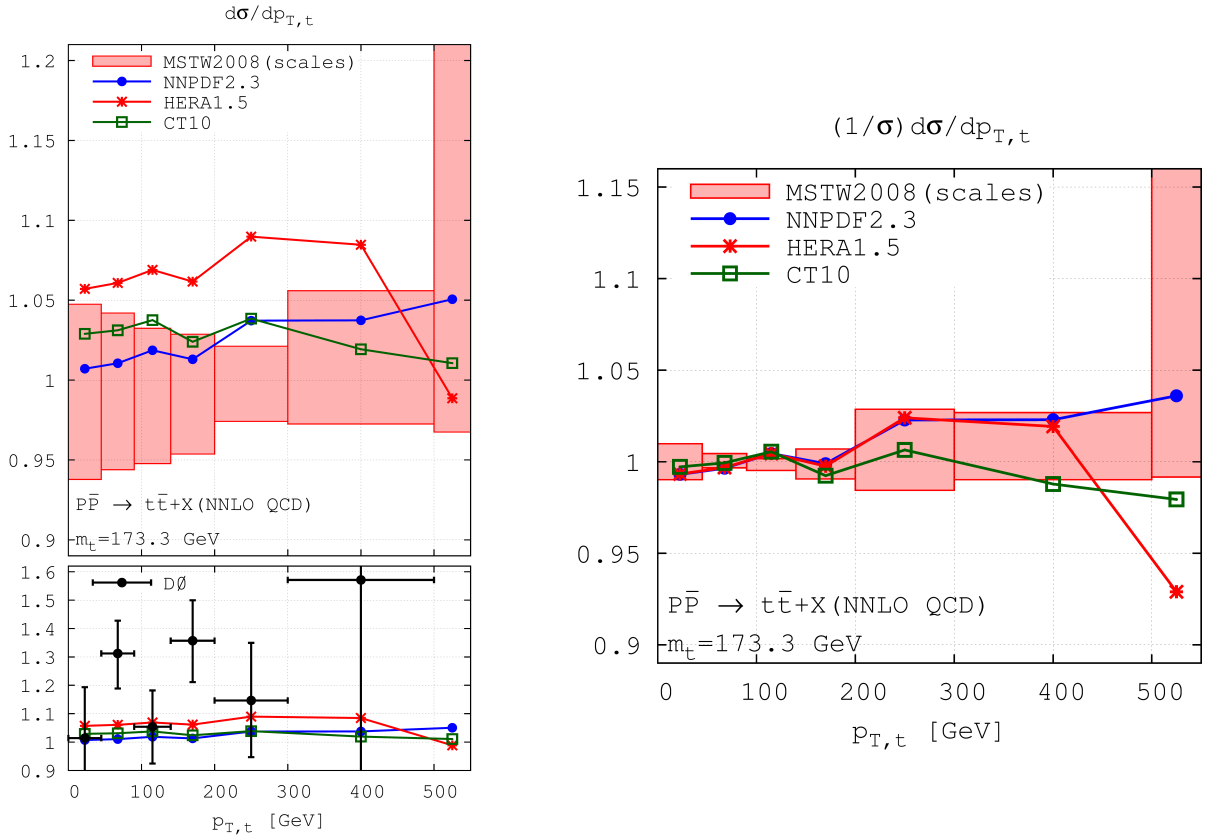

Figure 4.19: *The NNLO QCD predictions for the absolute transverse-momentum spectrum $d\sigma/dp_{T,t}$ (left) as well as the corresponding normalized distribution $(1/\sigma_{t\bar{t}}^{tot})d\sigma/dp_{T,t}$ (right) derived from four different PDF sets. Given are the ratios of the* HERAPDF1.5, CT10 *and* NNPDF2.3 *based predictions with respect to the default* MSTW2008 *result. For reference we also show the scale dependence of the latter prediction (red band). In case of the absolute $p_{T,t}$ distribution we moreover compare the different PDF results with the available data from the* DØ *Collaboration [459].*

data exceeds theory the deviation between the measured values and the SM expectation is actually slightly reduced. Since this discrepancy is to a large extent related to differences in the total cross section, it will be interesting to see how the various PDF predictions compare to normalized data.

The top-mass dependence of the transverse-momentum spectrum is shown in Fig. 4.20. As one can see, the spread between the various m_t predictions is significantly reduced when moving from the absolute distribution to the normalized cross section $(1/\sigma_{t\bar{t}}^{tot})d\sigma/dp_{T,t}$. Still, the latter appears to be more suited for a possible application in top-mass measurements since the relative deviation of the different predictions with respect to the theoretical (scale) error is much more pronounced. Indeed, the parametric uncertainty of the absolute transverse-momentum spectrum $d\sigma/dp_{T,t}$, estimated through a variation of the top mass of about $\Delta m_t = \pm 1\,\text{GeV}$, seems to be quite compatible with the NNLO scale error.

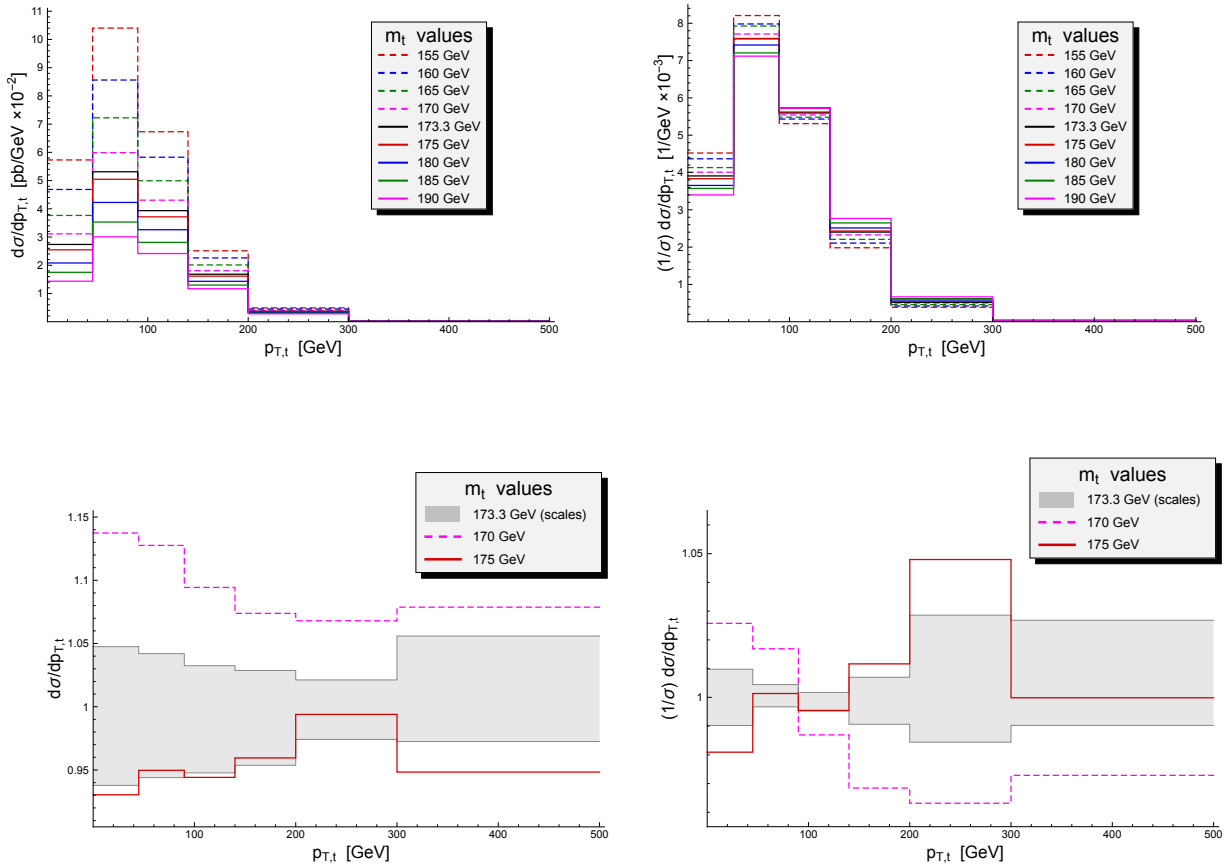

Figure 4.20: *The top-mass dependence of the NNLO QCD predictions for the absolute transverse-momentum spectrum* $d\sigma/dp_{T,t}$ *(left) as well as the corresponding normalized distribution* $(1/\sigma_{t\bar{t}}^{\mathbf{tot}})d\sigma/dp_{T,t}$ *(right). The corresponding parametric uncertainties associated with an experimental error on* m_t *of about* $\Delta m_t = \pm 1\,\text{GeV}$ *may be assessed from the lower plots where we present the results for the three top-mass values closest to the world average normalized to our default prediction at* $m_t = 173.3\,\text{GeV}$*. For reference we, in the latter case, also show the NNLO scale dependence (gray band).*

Note that the rather odd mass dependence in the bins $45 \leq p_{T,t} \leq 90\,\text{GeV}$ and $90 \leq p_{T,t} \leq 140\,\text{GeV}$ of the normalized distribution is probably due to binning effects, which could be easily clarified by recalculating the corresponding differential cross sections with a different, i. e. shifted or even finer, binning. It, however, remains to be seen to which extent this behavior affects an actual comparison with data or whether it has any impact on a possible top-mass extraction.

Chapter 5

Epilogue: Conclusions and perspectives

In this thesis we have presented all ingredients necessary for the theoretical description of inclusive and differential top-quark pair production in hadronic collisions at NNLO accuracy. We have applied our findings to provide high-precision SM predictions for the Tevatron and the LHC and, where possible, compared them to the available data. Furthermore, we demonstrated the phenomenological potential of our cross section results in applications that go beyond a simple comparison between theory and experiment, for example PDF determinations or top-mass measurements.

The foundation for a NNLO treatment of top-quark pair production has already been laid in Refs. [232, 233] with the development of a novel subtraction scheme for double-real radiation called Stripper, which has been subsequently employed to calculate the $\mathcal{O}(\alpha_s^4)$ contributions to the quark annihilation [77] and quark-gluon [79] reactions as well as the remaining fermionic scattering channels [78]. However, for the gluon fusion channel, which is particularly important for the LHC, the evaluation of the two-loop virtual corrections turned out to be the true bottleneck of the NNLO analysis. With the help of a novel approach based on power-logarithmic expansions in the kinematic variables $\tilde{t} = t/s$ and β, we were finally able to determine precise numerical solutions for the relevant set of master integrals at different points of the physical phase space, thus allowing for the construction of a suitable interpolation function for the adequate description of these contributions. This not only enabled us to complete the inclusive NNLO $t\bar{t}$ program through the provision of the missing gluon fusion results [80], it also allowed for a determination of the constant terms in the threshold expansion of the two-loop virtual corrections [234], which were previously unknown. Moreover, we were able to identify an additional contribution to the singular threshold behavior of the quark annihilation channel due to virtual Coulomb exchange [234].

The threshold constants, which are distinguished according to their final-state color configuration, are important since they are related to the NNLO hard matching coefficients in the NNLL resummation formula for the all-order treatment of soft-gluon effects. The second ingredient required for the determination of these coefficients is the knowledge of the NNLO soft functions that describe the interaction of low-energetic radiation through eikonal currents. While for the singlet case these contributions were already available [566], the corresponding expressions for color-octet production have been derived in the course of this thesis [558]. This eventually put us into the position to eliminate all approximate constituents from the NNLL resummation formula improving the theoretical predictions for the total $t\bar{t}$ production cross section to full NNLO+NNLL accuracy.

The theory error on these predictions including the parametric top-mass and α_s uncertainties is at the low percent-level now, comparable to but usually still above the currently available experimental precision. A further reduction of the theoretical uncertainty in the near future is, however, rather unlikely since it would require a combined effort at various levels of the theory analysis. So far, all measurements performed at the Tevatron and the LHC are in good agreement with the SM expectation such that the NNLO(+NNLL) cross section results have been used to further constrain the parameter space of possible BSM extensions [205] as well as to improve on some of the less well measured quantities within the SM, for instance the large-x gluon PDF [84,88,90,262,264]. Alternatively, the precise knowledge of the total cross section has been employed in extractions of the top-quark mass [34,63,83–86] and the strong coupling constant [83], which, despite the higher uncertainty associated with such a determination, offers a valuable cross-check with regard to the standard measurement techniques since it eliminates some of the theoretical ambiguities present in these approaches.

The second major accomplishment of this thesis was the modification of the available NNLO methods such that they would also allow for a calculation of differential top-quark observables. To this end, we incorporated the various elements of the inclusive $t\bar{t}$ analysis into a unified, STRIPPER-based MC framework, which allowed for the evaluation of phase space integrals of different multiplicity as well as the convolution with the PDFs. In a first application of this generalized NNLO implementation we computed the $\mathcal{O}(\alpha_s^4)$ contributions to the $t\bar{t}$ forward-backward asymmetry at the Tevatron, both inclusive and as a function of the kinematic variables Δy, $m_{t\bar{t}}$ and $p_{T,t\bar{t}}$ [385,406]. This helped to resolve most of the tension between theory and experimental data for a long time present in this observable.

Furthermore, we derived NNLO predictions for the main kinematic distributions studied within the CDF and DØ top-quark-physics programs, namely $|y_t|$, $m_{t\bar{t}}$ and $p_{T,t}$, and compared them to the available measurements [406]. Again, we observed a good agreement between the SM expectation and data profiting from the enhanced theoretical precision and perturbative stability related to the inclusion of the $\mathcal{O}(\alpha_s^4)$ corrections. For a possible use of these observables in future PDF or top-mass extractions we also examined the parametric dependence of the differential cross section predictions on these quantities. Indeed, we found that, for the absolute distributions, the spread between the considered PDF sets may not be fully compatible with the individual PDF error estimates signaling the potential to constrain PDF, provided that the experimental uncertainties are further reduced. For a measurement of the top-quark mass the normalized invariant-mass spectrum appears to be the most promising candidate since it shows the highest sensitivity to m_t compared to the underlying theory error.

For the future it would be desirable to merge the fixed-order NNLO treatment of differential top-quark pair production with the available resummation-based approaches at NNLL accuracy [223–226,399,437–440]. As demonstrated for the inclusive asymmetry, for some observables also the inclusion of EW effects might be advantageous to guarantee a more reliable theoretical description. Indeed, the methods presented in this thesis may even be employed to extend the current NLO EW results to NNLO accuracy as well. Similarly, they might be applicable to other processes with strongly-interacting and/or massive final-state particles.

Another important step is the derivation of NNLO differential top-quark predictions for the LHC. It has meanwhile been accomplished [427,428] by means of the four-dimensional formulation of STRIPPER [632], which allows for a even more efficient and stable implementation. Apart from the comparison with ATLAS and CMS data, it has so far been used to design new search strategies for hidden BSM resonances [429] as well as for advanced PDF studies [668] already indicating the tremendous phenomenological potential of these NNLO results. However, in order to allow for a even more realistic description of exclusive $t\bar{t}$ production, one has to abandon the stable-top approximation and also include top-quark decays in the theoretical analysis. In fact, the necessary ingredients for a treatment in the narrow-width approximation are already available from Refs. [12,13] such that soon also the kinematic properties of leptons and jets in particle-level $t\bar{t}$ events may be reliably predicted at NNLO accuracy.

Appendix

A. UV renormalization

In this appendix we provide all necessary ingredients required to obtain UV-finite results for the dimensionally regularized $t\bar{t}$ amplitudes up to the two-loop level. Note that the one-loop contributions to the corresponding renormalization and decoupling constants have to be expanded to $\mathcal{O}(\epsilon^2)$ since at NNLO they will multiply one-loop amplitudes which contain $1/\epsilon^2$ poles of soft-collinear origin.

For the external gluon (g), light quark (q) and heavy-quark (Q) fields the respective on-shell renormalization constants have been adopted from Refs. [644,645,669] and read

$$
\begin{aligned}
Z_g &= 1 + \left(\frac{\alpha_s^{(n_f)}}{2\pi}\right) T_F\, n_h \left\{-\frac{2}{3\epsilon} - \frac{2}{3}\,L_m - \frac{1}{3}\,\epsilon\,L_m^2 - \frac{\pi^2}{18}\,\epsilon - \frac{1}{9}\,\epsilon^2\,L_m^3 - \frac{\pi^2}{18}\,\epsilon^2\,L_m + \frac{2}{9}\,\epsilon^2\,\zeta_3\right\} \\
&+ \left(\frac{\alpha_s^{(n_f)}}{2\pi}\right)^2 T_F\, n_h \left\{T_F\, n_h \left[\frac{4}{9\epsilon}\,L_m + \frac{2}{3}\,L_m^2 + \frac{\pi^2}{27}\right] + T_F\, n_l \left[-\frac{4}{9\epsilon^2} - \frac{4}{9\epsilon}\,L_m - \frac{2}{9}\,L_m^2 - \frac{\pi^2}{27}\right]\right. \\
&\left. + C_F \left[-\frac{1}{2\epsilon} - L_m - \frac{15}{4}\right] + C_A \left[\frac{35}{36\epsilon^2} + \frac{13}{18\epsilon}\,L_m - \frac{5}{8\epsilon} - \frac{5}{4}\,L_m + \frac{1}{9}\,L_m^2 + \frac{13}{48} + \frac{13\pi^2}{216}\right]\right\} \\
Z_q &= 1 + \left(\frac{\alpha_s^{(n_f)}}{2\pi}\right)^2 C_F\, T_F\, n_h \left[\frac{1}{4\epsilon} + \frac{1}{2}\,L_m - \frac{5}{24}\right] \\
Z_Q &= 1 + \left(\frac{\alpha_s^{(n_f)}}{2\pi}\right) C_F \left\{-\frac{3}{2\epsilon} - 2 - \frac{3}{2}\,L_m - 4\,\epsilon - 2\,\epsilon\,L_m - \frac{3}{4}\,\epsilon\,L_m^2 - \frac{\pi^2}{8}\,\epsilon - 8\,\epsilon^2 - 4\,\epsilon^2\,L_m - \epsilon^2\,L_m^2\right. \\
&\left. - \frac{1}{4}\,\epsilon^2\,L_m^3 - \frac{\pi^2}{6}\,\epsilon^2 - \frac{\pi^2}{8}\,\epsilon^2\,L_m + \frac{1}{2}\,\epsilon^2\,\zeta_3\right\} + \left(\frac{\alpha_s^{(n_f)}}{2\pi}\right)^2 C_F \left\{T_F\, n_h \left[\frac{1}{4\epsilon} + \frac{1}{\epsilon}\,L_m + \frac{947}{72} + \frac{11}{6}\,L_m\right.\right. \\
&\left. + \frac{3}{2}\,L_m^2 - \frac{5\pi^2}{4}\right] + T_F\, n_l \left[-\frac{1}{2\epsilon^2} + \frac{11}{12\epsilon} + \frac{113}{24} + \frac{19}{6}\,L_m + \frac{1}{2}\,L_m^2 + \frac{\pi^2}{3}\right] + C_F \left[\frac{9}{8\epsilon^2} + \frac{51}{16\epsilon}\right. \\
&\left. + \frac{9}{4\epsilon}\,L_m + \frac{433}{32} + \frac{51}{8}\,L_m + \frac{9}{4}\,L_m^2 - \frac{49\pi^2}{16} + 4\,\ln 2\,\pi^2 - 6\,\zeta_3\right] + C_A \left[\frac{11}{8\epsilon^2} - \frac{127}{48\epsilon} - \frac{1705}{96}\right. \\
&\left.\left. - \frac{215}{24}\,L_m - \frac{11}{8}\,L_m^2 + \frac{5\pi^2}{4} - 2\,\ln 2\,\pi^2 + 3\,\zeta_3\right]\right\}
\end{aligned}
\tag{A.1}
$$

whereas the pole mass is renormalized via [669]

$$
\begin{aligned}
Z_m = 1 &+ \left(\frac{\alpha_s^{(n_f)}}{2\pi}\right) C_F \left\{-\frac{3}{2\epsilon} - 2 - \frac{3}{2} L_m - 4\,\epsilon - 2\,\epsilon\, L_m - \frac{3}{4}\,\epsilon\, L_m^2 - \frac{\pi^2}{8}\,\epsilon - 8\,\epsilon^2 - 4\,\epsilon^2\, L_m - \epsilon^2\, L_m^2 \right. \\
&\left. - \frac{1}{4}\,\epsilon^2\, L_m^3 - \frac{\pi^2}{6}\,\epsilon^2 - \frac{\pi^2}{8}\,\epsilon^2\, L_m + \frac{1}{2}\,\epsilon^2\,\zeta_3 \right\} + \left(\frac{\alpha_s^{(n_f)}}{2\pi}\right)^2 C_F \left\{ T_F\, n_h \left[-\frac{1}{2\epsilon^2} + \frac{5}{12\epsilon} + \frac{143}{24} \right.\right. \\
&\left. + \frac{13}{6} L_m + \frac{1}{2} L_m^2 - \frac{2\pi^2}{3} \right] + T_F\, n_l \left[-\frac{1}{2\epsilon^2} + \frac{5}{12\epsilon} + \frac{71}{24} + \frac{13}{6} L_m + \frac{1}{2} L_m^2 + \frac{\pi^2}{3} \right] \\
&+ C_F \left[\frac{9}{8\epsilon^2} + \frac{45}{16\epsilon} + \frac{9}{4\epsilon} L_m + \frac{199}{32} + \frac{45}{8} L_m + \frac{9}{4} L_m^2 - \frac{17\pi^2}{16} + 2\,\ln 2\,\pi^2 - 3\,\zeta_3 \right] \\
&\left. + C_A \left[\frac{11}{8\epsilon^2} - \frac{97}{48\epsilon} - \frac{1111}{96} - \frac{185}{24} L_m - \frac{11}{8} L_m^2 + \frac{\pi^2}{3} - \ln 2\,\pi^2 + \frac{3}{2}\,\zeta_3 \right] \right\} .
\end{aligned}
\tag{A.2}
$$

Due to the physical nature of the on-shell renormalization scheme, the explicit scale dependence of these constants in terms of $L_m = \ln \mu_R^2/m_t^2$ is indeed only spurious and cancels with the scale dependence of the renormalized strong coupling.

The corresponding $\overline{\text{MS}}$ renormalization constant for $n_f = n_l + n_h$ active quark flavors can be directly inferred from the respective evolution equation for $\alpha_s^{(n_f)}$ and is, up to the two-loop level, given by

$$
Z_{\alpha_s}^{(n_f)} = 1 - \left(\frac{\alpha_s^{(n_f)}}{2\pi}\right) \frac{\beta_0^{(n_f)}}{2\epsilon} + \left(\frac{\alpha_s^{(n_f)}}{2\pi}\right)^2 \left(\frac{\left(\beta_0^{(n_f)}\right)^2}{4\epsilon^2} - \frac{\beta_1^{(n_f)}}{8\epsilon} \right) , \tag{A.3}
$$

where

$$
\beta_0^{(n_f)} = \frac{11}{3}\, C_A - \frac{4}{3}\, T_F\, n_f , \qquad \beta_1^{(n_f)} = \frac{34}{3}\, C_A^2 - \frac{20}{3}\, C_A\, T_F\, n_f - 4\, C_F\, T_F\, n_f . \tag{A.4}
$$

In order to account for non-logarithmic top-mass effects, in the calculation of hadronic cross sections we prefer to work with n_l active flavors, which is achieved by removing the heavy degrees of freedom from the running of the strong coupling constant (see Eq. (2.27)). The required two-loop decoupling parameter has been derived in Ref. [513] yielding

$$
\begin{aligned}
\zeta_{\alpha_s} = 1 &+ \left(\frac{\alpha_s}{2\pi}\right) T_F\, n_h \left\{ \frac{2}{3} L_m + \frac{1}{3}\,\epsilon\, L_m^2 + \frac{\pi^2}{18}\,\epsilon + \frac{1}{9}\,\epsilon^2\, L_m^3 + \frac{\pi^2}{18}\,\epsilon^2\, L_m - \frac{2}{9}\,\epsilon^2\,\zeta_3 \right\} \\
&+ \left(\frac{\alpha_s}{2\pi}\right)^2 T_F\, n_h \left\{ \frac{4}{9}\, T_F\, n_h\, L_m^2 + C_F \left[\frac{15}{4} + L_m \right] + C_A \left[-\frac{8}{9} + \frac{5}{3} L_m \right] \right\} .
\end{aligned}
\tag{A.5}
$$

The corresponding coefficients $\beta_i \equiv \beta_i^{(n_l)}$, governing the evolution of the effective coupling α_s, may be obtained from Eq. (A.4) by setting the number of heavy quarks to zero such that

$n_f = n_l$ while at three-loop order the contribution to the light-quark beta function is given by [670,671]

$$\begin{aligned}\beta_2 = &\frac{2857}{54} C_A^3 - \frac{1415}{27} C_A^2 T_F n_l + \frac{158}{27} C_A T_F^2 n_l^2 + \frac{44}{9} C_F T_F^2 n_l^2 \\ &- \frac{205}{9} C_F C_A T_F n_l + 2 C_F^2 T_F n_l \,.\end{aligned} \tag{A.6}$$

Note that the latter expression is, in fact, not needed in the NNLO renormalization procedure as indicated in Eq. (A.3). The reason we still provide it here is that it contributes to the NNLL resummed exponents in Eq. (3.91) and thus eventually also to the NNLO+NNLL total cross section predictions. Moreover, it is employed in the NNLO PDF evolution thereby essentially affecting all $\mathcal{O}(\alpha_s^4)$ corrections, inclusive and differential, derived in the course of this thesis.

B. IR renormalization

In this appendix we list the anomalous dimensions occurring in Eq. (3.13) necessary to construct the one- and two-loop finite remainders. The corresponding expressions related to a single parton (collinear in origin for massless partons and soft in origin for massive partons) read [561,562]

$$\begin{aligned}
\gamma^g\left(\alpha_s\right) &= \left(\frac{\alpha_s}{2\pi}\right)\left\{-\frac{11}{6}\,C_A+\frac{2}{3}\,T_F\,n_l\right\}+\left(\frac{\alpha_s}{2\pi}\right)^2\left\{C_A^2\left[-\frac{173}{27}+\frac{11\pi^2}{72}+\frac{1}{2}\,\zeta_3\right]\right.\\
&\left.+\,C_A\,T_F\,n_l\left[\frac{64}{27}-\frac{\pi^2}{18}\right]+C_F\,T_F\,n_l\right\}\\
\gamma^q\left(\alpha_s\right) &= -\left(\frac{\alpha_s}{2\pi}\right)\frac{3}{2}\,C_F+\left(\frac{\alpha_s}{2\pi}\right)^2 C_F\left\{C_A\left[-\frac{961}{216}-\frac{11\pi^2}{24}+\frac{13}{2}\,\zeta_3\right]\right.\\
&\left.+\,C_F\left[-\frac{3}{8}+\frac{\pi^2}{2}-6\,\zeta_3\right]+T_F\,n_l\left[\frac{65}{54}+\frac{\pi^2}{6}\right]\right\}\\
\gamma^Q\left(\alpha_s\right) &= -\left(\frac{\alpha_s}{2\pi}\right)C_F+\left(\frac{\alpha_s}{2\pi}\right)^2 C_F\left\{C_A\left[-\frac{49}{18}+\frac{\pi^2}{6}-\zeta_3\right]+\frac{10}{9}\,T_F\,n_l\right\},
\end{aligned} \tag{B.1}$$

whereas the cusp anomalous dimensions are given by [672,673]

$$\gamma_{\text{cusp}}\left(\alpha_s\right) = \frac{\alpha_s}{\pi}+\left(\frac{\alpha_s}{2\pi}\right)^2\left\{C_A\left[\frac{67}{9}-\frac{\pi^2}{3}\right]-\frac{20}{9}\,T_F\,n_l\right\}$$

$$\begin{aligned}
\gamma_{\text{cusp}}\left(\beta,\alpha_s\right) &= \gamma_{\text{cusp}}\left(\alpha_s\right)\beta\coth\beta\\
&+\left(\frac{\alpha_s}{2\pi}\right)^2 2\,C_A\left\{\coth^2\beta\left[\text{Li}_3(e^{-2\beta})+\beta\,\text{Li}_2(e^{-2\beta})-\zeta_3+\frac{\pi^2}{6}\,\beta+\frac{1}{3}\,\beta^3\right]\right.\\
&+\coth\beta\left[\text{Li}_2(e^{-2\beta})-2\,\beta\ln(1-e^{-2\beta})-\frac{\pi^2}{6}\,(1+\beta)-\beta^2-\frac{1}{3}\,\beta^3\right]\\
&\left.+\frac{\pi^2}{6}+\zeta_3+\beta^2\right\}.
\end{aligned} \tag{B.2}$$

In addition, we also provide the anomalous dimensions necessary to determine the renormalization constants of the hard functions $H_{\mathbf{R}\otimes\mathbf{R}'|\tilde{\mathbf{R}}}$. For color-octet production, they have been originally derived in Refs. [219,515]

$$
\begin{aligned}
\Gamma_H^{\mathbf{3}\otimes\bar{\mathbf{3}}|\mathbf{1}}\left(\frac{\mu}{Q}\right) &= \frac{\alpha_s}{\pi} C_F \left(-4\ln\left(\frac{\mu}{Q}\right) - 3\right) + \left(\frac{\alpha_s}{\pi}\right)^2 \left(C_F^2 \left(-6\zeta(3) - \frac{3}{8} + \frac{\pi^2}{2}\right)\right. \\
&\quad + C_A C_F \left(\ln\left(\frac{\mu}{Q}\right)\left(\frac{\pi^2}{3} - \frac{67}{9}\right) + \frac{13\zeta(3)}{2} - \frac{11\pi^2}{24} - \frac{961}{216}\right) \\
&\quad \left. + C_F T_F n_l \left(\frac{20}{9}\ln\left(\frac{\mu}{Q}\right) + \frac{\pi^2}{6} + \frac{65}{54}\right)\right) \\
\Gamma_H^{\mathbf{3}\otimes\bar{\mathbf{3}}|\mathbf{8}}\left(\frac{\mu}{Q}\right) &= \frac{\alpha_s}{\pi}\left(C_F\left(-4\ln\left(\frac{\mu}{Q}\right) - 3\right) - C_A\right) + \left(\frac{\alpha_s}{\pi}\right)^2 \left(C_A^2\left(-\frac{\zeta(3)}{2} - \frac{49}{36} + \frac{\pi^2}{12}\right)\right. \\
&\quad + C_A C_F \left(\ln\left(\frac{\mu}{Q}\right)\left(\frac{\pi^2}{3} - \frac{67}{9}\right) + \frac{13\zeta(3)}{2} - \frac{11\pi^2}{24} - \frac{961}{216}\right) \\
&\quad \left. + C_F^2\left(-6\zeta(3) - \frac{3}{8} + \frac{\pi^2}{2}\right) + \frac{5}{9} C_A T_F n_l + C_F T_F n_l \left(\frac{20}{9}\ln\left(\frac{\mu}{Q}\right) + \frac{\pi^2}{6} + \frac{65}{54}\right)\right) \\
\Gamma_H^{\mathbf{8}\otimes\mathbf{8}|\mathbf{1}}\left(\frac{\mu}{Q}\right) &= \frac{\alpha_s}{\pi}\left(C_A\left(-4\ln\left(\frac{\mu}{Q}\right) - \frac{11}{3}\right) + \frac{4}{3} T_F n_l\right) \\
&\quad + \left(\frac{\alpha_s}{\pi}\right)^2 \left(C_A^2\left(\ln\left(\frac{\mu}{Q}\right)\left(\frac{\pi^2}{3} - \frac{67}{9}\right) + \frac{11\pi^2}{72} + \frac{\zeta(3)}{2} - \frac{173}{27}\right)\right. \\
&\quad \left. + C_A T_F n_l \left(\frac{20}{9}\ln\left(\frac{\mu}{Q}\right) - \frac{\pi^2}{18} + \frac{64}{27}\right) + C_F T_F n_l\right) \\
\Gamma_H^{\mathbf{8}\otimes\mathbf{8}|\mathbf{8}_{A,S}}\left(\frac{\mu}{Q}\right) &= \frac{\alpha_s}{\pi}\left(C_A\left(-4\ln\left(\frac{\mu}{Q}\right) - \frac{14}{3}\right) + \frac{4}{3} T_F n_l\right) \\
&\quad + \left(\frac{\alpha_s}{\pi}\right)^2 \left(C_A^2\left(\ln\left(\frac{\mu}{Q}\right)\left(\frac{\pi^2}{3} - \frac{67}{9}\right) + \frac{17\pi^2}{72} - \frac{839}{108}\right)\right. \\
&\quad \left. + C_A T_F n_l \left(\frac{20}{9}\ln\left(\frac{\mu}{Q}\right) - \frac{\pi^2}{18} + \frac{79}{27}\right) + C_F T_F n_l\right) \,.
\end{aligned}
\tag{B.3}
$$

Note that for an initial state in the adjoint representation, i. e. the gluon fusion channel, the anomalous dimensions for the symmetric and antisymmetric octet configurations are identical. This means that the differences in the respective pole structures of $H^0_{\mathbf{8}\otimes\mathbf{8}|\mathbf{8}_A}$ and $H^0_{\mathbf{8}\otimes\mathbf{8}|\mathbf{8}_S}$ are solely due to the corresponding lower-order matrix elements entering Eq. (3.22).

For the renormalization of the soft functions we also need to know the soft limit of the Altarelli-Parisi splitting functions in Mellin space. Up to $\mathcal{O}\left(\alpha_s^2\right)$ the corresponding expressions are textbook material and read

$$\begin{aligned}
P_{\tilde{N}}^{\mathbf{3}} &= \frac{\alpha_s}{2\pi} C_F \left(-2\ln N + \frac{3}{2}\right) + \left(\frac{\alpha_s}{2\pi}\right)^2 \left(C_A C_F \left(\left(\frac{\pi^2}{3} - \frac{67}{9}\right)\ln N - 3\zeta(3) + \frac{11\pi^2}{18} + \frac{17}{24}\right)\right. \\
&\quad \left. + C_F^2 \left(6\zeta(3) + \frac{3}{8} - \frac{\pi^2}{2}\right) + C_F T_F n_l \left(\frac{20}{9}\ln N - \frac{2\pi^2}{9} - \frac{1}{6}\right)\right) \\
P_{\tilde{N}}^{\mathbf{8}} &= \frac{\alpha_s}{2\pi} \left(C_A \left(-2\ln N + \frac{11}{6}\right) - \frac{2}{3} T_F n_l\right) + \left(\frac{\alpha_s}{2\pi}\right)^2 \left(C_A^2 \left(\left(\frac{\pi^2}{3} - \frac{67}{9}\right)\ln N + 3\zeta(3) + \frac{8}{3}\right)\right. \\
&\quad \left. + C_A T_F n_l \left(\frac{20}{9}\ln N - \frac{4}{3}\right) - C_F T_F n_l\right) .
\end{aligned} \tag{B.4}$$

The respective splitting kernels $P_N^{\mathbf{R}}$, used in the resummation formalism, can be obtained from these functions by setting $\ln N \to \ln N + \gamma_E$ whereas the leading-singular kernels $\tilde{P}_N^{\mathbf{R}}$ contain only the terms proportional to $\ln N$.

C. Color dependence of threshold and resummation results

While the color dependence of the soft functions is explicitly contained in Eq. (3.58), we here present the corresponding general color results for the NNLO hard functions consisting of one-loop-squared and two-loop contributions. The analytic expressions for the leading threshold behavior of the latter have already been shown in Eq. (3.196) and Eq. (3.196). The numerical values for the constant coefficients $\Delta_{ij}^{(\tilde{\mathbf{R}},k)}$, on the other hand, can be found in Tab. C.1 and Tab. C.2 where we use the same color decomposition as for the renormalized two-loop functions $\tilde{\mathcal{A}}_{q\bar{q}}^{(n_f)}$ and $\tilde{\mathcal{A}}_{gg}^{(n_f)}$, i. e.

$$\begin{aligned}
\Delta_{q\bar{q}}^{(\tilde{\mathbf{R}},k)} &= 2(N_c^2-1)\bigg(N_c^2\,A^{(q)} + B^{(q)} + \frac{1}{N_c^2}\,C^{(q)} + N_c\,n_l\,D_l^{(q)} + N_c\,n_h\,D_h^{(q)} \\
&\quad + \frac{n_l}{N_c}\,E_l^{(q)} + \frac{n_h}{N_c}\,E_h^{(q)} + n_l^2\,F_l^{(q)} + n_l\,n_h\,F_{lh}^{(q)} + n_h^2\,F_h^{(q)}\bigg) \\
\Delta_{gg}^{(\tilde{\mathbf{R}},k)} &= (N_c^2-1)\bigg(N_c^3\,A^{(g)} + N_c\,B^{(g)} + \frac{1}{N_c}\,C^{(g)} + \frac{1}{N_c^3}\,D^{(g)} + N_c^2\,n_l\,E_l^{(g)} \\
&\quad + N_c^2\,n_h\,E_h^{(g)} + n_l\,F_l^{(g)} + n_h\,F_h^{(g)} + \frac{n_l}{N_c^2}\,G_l^{(g)} + \frac{n_h}{N_c^2}\,G_h^{(g)} + N_c\,n_l^2\,H_l^{(g)} \\
&\quad + N_c\,n_l\,n_h\,H_{lh}^{(g)} + N_c\,n_h^2\,H_h^{(g)} + \frac{n_l^2}{N_c}\,I_l^{(g)} + \frac{n_l\,n_h}{N_c}\,I_{lh}^{(g)} + \frac{n_h^2}{N_c}\,I_h^{(g)}\bigg)\,.
\end{aligned} \tag{C.1}$$

Analogous to the two-loop finite remainders, the one-loop-squared results are defined via

$$\tilde{F}'_{ij} = \tilde{F}'^{(0)}_{ij} + n_l\,\tilde{F}'^{(1)}_{ij} + n_l^2\,\tilde{F}'^{(2)}_{ij} \equiv \frac{1}{s_i s_j c_i c_j}\,\frac{\beta(1-\beta^2)}{128\pi}\,\langle \mathcal{F}_{ij}^{(1)} | \mathcal{F}_{ij}^{(1)} \rangle \tag{C.2}$$

such that the corresponding color-projected threshold expansions are given as

$$\begin{aligned}
\tilde{F}'^{\mathbf{1}}_{gg}(\beta,\cos\theta) &\overset{\beta\to 0}{=} \frac{1}{4}\frac{d\bar{\sigma}^{(0)}_{gg,\mathbf{1}}}{d\cos\theta}\,C_F \\
&\quad\times\bigg\{\frac{1}{\beta^2}\,C_F\left[\ln^2\beta + 2\,\ln 2\,\ln\beta + \ln^2 2 + \frac{\pi^2}{4}\right] + \frac{1}{\beta}\bigg[\left(4\,C_A\,\ln 2\right)\ln\beta \\
&\qquad + C_A\left(1 + 2\,\ln^2 2 + \frac{\pi^2}{3}\right) + C_F\left(-5 + \frac{\pi^2}{4}\right)\bigg] + 4\,C_F\,\ln^2\beta \\
&\qquad - \left(C_F\,(-4 + 8\,\ln 2) + C_F\,\cos^2\theta\right)\ln\beta\bigg\} \\
&\quad + \frac{\beta}{512\pi}\,\frac{1}{(N_c^2-1)^2}\left(\Delta'^{(\mathbf{1},0)}_{gg} + \Delta'^{(\mathbf{1},2)}_{gg}\cos^2\theta\right)
\end{aligned} \tag{C.3}$$

	$\Delta_{gg}^{(\mathbf{1},0)}$	$\Delta_{gg}^{(\mathbf{1},2)}$	$\Delta_{gg}^{(\mathbf{8_S},0)}$	$\Delta_{gg}^{(\mathbf{8_S},2)}$
$\mathrm{A}^{(g)}$			50.58973335	
$\mathrm{B}^{(g)}$	−547.4522400	−66.84277146	−33.27055329	
$\mathrm{C}^{(g)}$	100.8789935	133.6855429	−719.3971740	−33.42138573
$\mathrm{D}^{(g)}$	−86.08730702	−66.84277146	172.1746140	133.6855429
$\mathrm{E}_l^{(g)}$			−23.04935002	
$\mathrm{E}_h^{(g)}$			5.003909657	
$\mathrm{F}_l^{(g)}$	0.7180516443		77.83333496	
$\mathrm{F}_h^{(g)}$	26.52886661		−44.29728915	
$\mathrm{G}_l^{(g)}$	−5.327023282		57.45626045	
$\mathrm{G}_h^{(g)}$	−27.86040273		97.12660208	
	$\Delta'^{(\mathbf{1},0)}_{gg}$	$\Delta'^{(\mathbf{1},2)}_{gg}$	$\Delta'^{(\mathbf{8_S},0)}_{gg}$	$\Delta'^{(\mathbf{8_S},2)}_{gg}$
$\mathrm{A}^{(g)}$			$2-\frac{8\pi^2}{3}+\frac{8\pi^4}{9}-\left(8-\frac{16\pi^2}{3}\right)\ln 2$ $+\left(24-\frac{8\pi^2}{3}\right)\ln^2 2-32\ln^3 2$ $+32\ln^4 2$	
$\mathrm{B}^{(g)}$	$36-10\,\pi^2+\frac{265\pi^4}{36}-16\,\pi^2\ln 2$ $+\left(96+\frac{152\pi^2}{3}\right)\ln^2 2+64\ln^4 2$	$-4\,\pi^2\,(2-\ln 2)$	$-28+25\,\pi^2-\frac{38\pi^4}{9}+\left(72-\frac{70\pi^2}{3}\right)$ $\ln 2-\left(176-\frac{44\pi^2}{3}\right)\ln^2 2$ $+128\ln^3 2-128\ln^4 2$	
$\mathrm{C}^{(g)}$	$-120+\frac{56\pi^2}{3}-\frac{59\pi^4}{6}+32\,\pi^2\ln 2$ $-\left(160+24\,\pi^2\right)\ln^2 2$	$8\,\pi^2\,(2-\ln 2)$	$130-\frac{169\pi^2}{3}+\frac{115\pi^4}{24}-160\ln 2$ $+\left(320-8\,\pi^2\right)\ln^2 2$	$-2\,\pi^2\,(2-\ln 2)$
$\mathrm{D}^{(g)}$	$100+2\,\pi^2+\frac{17\pi^4}{4}-16\,\pi^2\ln 2$ $+16\,\pi^2\ln^2 2$	$-4\,\pi^2\,(2-\ln 2)$	$-200-4\,\pi^2-\frac{17\pi^4}{2}+32\,\pi^2\ln 2$ $-32\,\pi^2\ln^2 2$	$8\,\pi^2\,(2-\ln 2)$

Table C.1: *Values for the constant coefficients of the β-expansion of the one-loop-squared and two-loop finite remainders $\tilde{F}'^{\mathbf{1},\mathbf{8_S}}_{gg}$ and $\tilde{F}^{\mathbf{1},\mathbf{8_S}}_{gg}$. The coefficients of the unlisted color structures vanish.*

$$
\begin{aligned}
\tilde{F}'^{\mathbf{8_S}}_{gg}(\beta,\cos\theta) \overset{\beta\to 0}{=}\; & \frac{1}{4}\frac{d\bar{\sigma}^{(0)}_{gg,\,\mathbf{8_S}}}{d\cos\theta}\left(C_F-\frac{C_A}{2}\right) \\
& \times\left\{\frac{1}{\beta^2}\left(C_F-\frac{C_A}{2}\right)\left[\ln^2\beta+2\,\ln 2\,\ln\beta+\ln^2 2+\frac{\pi^2}{4}\right]+\frac{1}{\beta}\left[\left(2\,C_A\,\ln 2\right)\ln\beta\right.\right. \\
& \quad +C_A\left(2+\ln 2+\frac{5\pi^2}{24}\right)+C_F\left(-5+\frac{\pi^2}{4}\right)\Big]+4\left(C_F-\frac{C_A}{2}\right)\ln^2\beta \\
& \quad \left.-\left[4\left(C_F-\frac{C_A}{2}\right)(1-2\ln 2)-\left(C_F-\frac{C_A}{2}\right)\cos^2\theta\right]\ln\beta\right\} \\
& +\frac{\beta}{512\pi}\,\frac{1}{(N_c^2-1)^2}\left(\Delta'^{(\mathbf{8_S},0)}_{gg}+\Delta'^{(\mathbf{8_S},2)}_{gg}\cos^2\theta\right)
\end{aligned}
\tag{C.4}
$$

$$
\begin{aligned}
\tilde{F}'^{\mathbf{8}}_{q\bar{q}}(\beta,\cos\theta) \overset{\beta\to 0}{=}\; & \frac{1}{4}\frac{d\bar{\sigma}^{(0)}_{q\bar{q}}}{d\cos\theta}\left(C_F-\frac{C_A}{2}\right) \\
& \times\left\{\frac{1}{\beta^2}\left(C_F-\frac{C_A}{2}\right)\left[\ln^2\beta+2\,\ln 2\,\ln\beta+\ln^2 2+\frac{\pi^2}{4}\right]+\frac{1}{\beta}\left[\left(C_A\left(\frac{3}{2}-2\,\ln 2\right)\right.\right. \\
& \quad -C_F\,(3-4\ln 2)-\frac{2}{3}\,n_l\Big)\ln\beta+C_A\left(\frac{50}{9}-\frac{1}{2}\,\ln 2-2\,\ln^2 2-\frac{\pi^2}{4}\right) \\
& \quad +C_F\left(-8+2\,\ln^2 2+\frac{7\pi^2}{12}\right)-\frac{8}{9}\,n_h-\frac{5}{9}\,n_l\Big] \\
& \quad +\frac{1}{2}\left(C_F-\frac{C_A}{2}\right)(3+\cos^2\theta)\ln^2\beta+\left(-\frac{3}{2}\left(C_F-\frac{C_A}{2}\right)(1-2\ln 2)\right. \\
& \quad \left.\left.-n_h+\left(2\,C_A-\frac{16}{3}\,C_F\right)\cos\theta-\frac{1}{2}\left(C_F-\frac{C_A}{2}\right)(1-2\ln 2)\cos^2\theta\right)\ln\beta\right\} \\
& +\frac{\beta}{512\pi}\,\frac{1}{N_c^2}\left(\Delta'^{(\mathbf{8},0)}_{q\bar{q}}+\Delta'^{(\mathbf{8},1)}_{q\bar{q}}\cos\theta+\Delta'^{(\mathbf{8},2)}_{q\bar{q}}\cos^2\theta\right)\,.
\end{aligned}
\tag{C.5}
$$

Note that the expression for the antisymmetric octet configuration is not presented here as it can be inferred from the result of the NNLO matching coefficient in Eq. (3.69) and the known two-loop behavior in Eq. (3.196). In contrast to $\tilde{F}_{ij}$, the constant coefficients $\Delta'^{(\tilde{\mathbf{R}},k)}_{ij}$ are available in entirely analytical form and can be found in Tab. C.1 and Tab. C.2 (using again the color decomposition of Eq. (C.1)).

The general color dependence of the NNLO matching coefficients in Eq. (3.71) is then given by

$$
H^{(2),\,\mathrm{match.}}_{\mathbf{R}\otimes\mathbf{R}'|\tilde{\mathbf{R}}}(1)=\pi^2\,\frac{\left(\Delta^{(\tilde{\mathbf{R}},0)}_{ij}+\Delta'^{(\tilde{\mathbf{R}},0)}_{ij}\right)+\frac{1}{3}\,\left(\Delta^{(\tilde{\mathbf{R}},2)}_{ij}+\Delta'^{(\tilde{\mathbf{R}},2)}_{ij}\right)}{\langle\mathcal{M}^{(0)}_{ij,\tilde{\mathbf{R}}}|\mathcal{M}^{(0)}_{ij,\tilde{\mathbf{R}}}\rangle\Big|_{\beta^0}}
\tag{C.6}
$$

where the leading threshold behavior of the Born contributions $\langle\mathcal{M}^{(0)}_{ij,\tilde{\mathbf{R}}}|\mathcal{M}^{(0)}_{ij,\tilde{\mathbf{R}}}\rangle$ can be obtained from Eq. (3.197) and Eq. (3.198). In consequence, the β-independent terms of the

	$\Delta_{q\bar{q}}^{(\mathbf{8},0)}$	$\Delta_{q\bar{q}}^{(\mathbf{8},1)}$	$\Delta_{q\bar{q}}^{(\mathbf{8},2)}$
$\mathrm{A}^{(q)}$	85.56106806		
$\mathrm{B}^{(q)}$	167.5535816	−76.93782458	
$\mathrm{C}^{(q)}$	−215.4820001	307.7512983	3.463381701
$\mathrm{D}_l^{(q)}$	−6.945827165		
$\mathrm{D}_h^{(q)}$	−9.807111102		
$\mathrm{E}_l^{(q)}$	−2.093392127		
$\mathrm{E}_h^{(q)}$	−53.85221126		
$\mathrm{F}_l^{(q)}$	−8.703107352		
$\mathrm{F}_{lh}^{(q)}$	1.329172411		
$\mathrm{F}_h^{(q)}$	6.320987654		
	$\Delta'^{(\mathbf{8},0)}_{q\bar{q}}$	$\Delta'^{(\mathbf{8},1)}_{q\bar{q}}$	$\Delta'^{(\mathbf{8},2)}_{q\bar{q}}$
$\mathrm{A}^{(q)}$	$\frac{784}{81} + \frac{14\pi^2}{27} + \frac{\pi^4}{144} - \left(\frac{56}{9} + \frac{\pi^2}{6}\right) \ln 2$ $- \left(\frac{103}{9} + \frac{\pi^2}{3}\right) \ln^2 2 + 4 \ln^3 2 + 4 \ln^4 2$		
$\mathrm{B}^{(q)}$	$\frac{448}{9} - \frac{62\pi^2}{27} - \frac{7\pi^4}{72} - \left(\frac{104}{3} - \frac{2\pi^2}{3}\right) \ln 2$ $- \left(\frac{122}{9} - \frac{8\pi^2}{3}\right) \ln^2 2 + 8 \ln^3 2 - 8 \ln^4 2$	$-\frac{2\pi^2}{3} (1 - 3 \ln 2)$	
$\mathrm{C}^{(q)}$	$64 - \frac{85\pi^2}{12} + \frac{103\pi^4}{144} - \left(48 + 4\pi^2\right) \ln 2$ $+ \left(41 + \frac{19\pi^2}{6}\right) \ln^2 2 - 12 \ln^3 2 + 4 \ln^4 2$	$\frac{8\pi^2}{3} (1 - 3 \ln 2)$	$\frac{\pi^2}{8} \left(\pi^2 - 4 \ln 2 + 4 \ln^2 2\right)$
$\mathrm{D}_l^{(q)}$	$-\frac{560}{81} - \frac{5\pi^2}{27} + \left(\frac{284}{27} + \frac{2\pi^2}{9}\right) \ln 2$ $+\frac{16}{9} \ln^2 2 - \frac{16}{3} \ln^3 2$		
$\mathrm{D}_h^{(q)}$	$-\frac{896}{81} - \frac{8\pi^2}{27} + \frac{32}{9} \ln 2 + \frac{64}{9} \ln^2 2$		
$\mathrm{E}_l^{(q)}$	$-\frac{160}{9} - \frac{19\pi^2}{27} + \left(28 + \frac{10\pi^2}{9}\right) \ln 2$ $-\frac{112}{9} \ln^2 2 + \frac{16}{3} \ln^3 2$		
$\mathrm{E}_h^{(q)}$	$-\frac{256}{9} + \frac{56\pi^2}{27} + \left(\frac{32}{3} + 2\pi^2\right) \ln 2 - \frac{64}{9} \ln^2 2$		
$\mathrm{F}_l^{(q)}$	$\frac{100}{81} + \frac{4\pi^2}{9} - \frac{80}{27} \ln 2 + \frac{16}{9} \ln^2 2$		
$\mathrm{F}_{lh}^{(q)}$	$\frac{320}{81} - \frac{128}{27} \ln 2$		
$\mathrm{F}_h^{(q)}$	$\frac{256}{81}$		

Table C.2: *Values for the constant coefficients of the β-expansion of the one-loop-squared and two-loop finite remainder $\tilde{F}'^{\mathbf{8}}_{q\bar{q}}$ and $\tilde{F}^{\mathbf{8}}_{q\bar{q}}$. The coefficients of the unlisted color structures vanish.*

NNLO threshold expansions read

$$
\begin{aligned}
C_{q\bar{q}}^{(2)} = {} & N_c^2 \left(\frac{146218}{27} - \frac{33677\pi^2}{108} - \frac{491\pi^4}{240} - \frac{11773\zeta(3)}{9} + \left(-8044 + \frac{815\pi^2}{2} + 1404\zeta(3) \right) \ln 2 \right. \\
& \left. + \left(\frac{50585}{9} - 209\pi^2 \right) \ln^2 2 - 2252 \ln^3 2 + 508 \ln^4 2 \right) \\
& + N_c \left(-\frac{13568}{81} + \frac{56\pi^2}{9} + \frac{1952}{9} \ln 2 - \frac{1088}{9} \ln^2 2 \right) \\
& + \left(-\frac{588430}{81} + \frac{43709\pi^2}{108} + \frac{467\pi^4}{72} + \frac{19891\zeta(3)}{9} + \left(\frac{97336}{9} - 604\pi^2 - 2772\zeta(3) \right) \ln 2 \right. \\
& \left. + \left(-\frac{70286}{9} + 372\pi^2 \right) \ln^2 2 + 3584 \ln^3 2 - 1016 \ln^4 2 \right) \\
& + \frac{1}{N_c} \left(\frac{256}{3} - \frac{40\pi^2}{9} + \left(-160 + 2\pi^2 \right) \ln 2 + \frac{1088}{9} \ln^2 2 \right) \\
& + \frac{1}{N_c^2} \left(2624 - \frac{1525\pi^2}{12} - \frac{533\pi^4}{144} - 896\zeta(3) + \left(-3696 + \frac{1253\pi^2}{6} + 1344\zeta(3) \right) \ln 2 \right. \\
& \left. + \left(2505 - \frac{472\pi^2}{3} \right) \ln^2 2 - 1332 \ln^3 2 + 508 \ln^4 2 \right) \\
& + n_l \left(N_c \left(-\frac{23380}{81} + \frac{685\pi^{\ 2}}{54} + \frac{226\zeta(3)}{9} + \left(\frac{13940}{27} - \frac{38\pi^2}{3} \right) \ln 2 - \frac{3584}{9} \ln^2 2 \right. \right. \\
& \left. + \frac{416}{3} \ln^3 2 \right) + \left(\frac{320}{81} - \frac{128}{27} \ln 2 \right) + \frac{1}{N_c} \left(\frac{14948}{81} - \frac{661\pi^2}{54} - \frac{226\zeta(3)}{9} \right. \\
& \left. \left. + \left(-\frac{3220}{9} + 14\pi^2 \right) \ln 2 + \frac{2984}{9} \ln^2 2 - \frac{416}{3} \ln^3 2 \right) \right) \\
& + n_l^2 \left(\frac{100}{81} + \frac{4\pi^2}{9} - \frac{80}{27} \ln 2 + \frac{16}{9} \ln^2 2 \right) + \frac{1}{2(N_c^2 - 1)} \left(\Delta_{q\bar{q}}^{(\mathbf{8},0)} + \frac{1}{3} \Delta_{q\bar{q}}^{(\mathbf{8},2)} \right)
\end{aligned}
\tag{C.7}
$$

$$
\begin{aligned}
C_{gg,\mathbf{1}}^{(2)} = {} & N_c^2 \left(\frac{1091701}{81} - \frac{19414\pi^2}{27} - \frac{1895\pi^4}{144} - \frac{35750\zeta(3)}{9} \right. \\
& + \left(-\frac{181424}{9} + \frac{3181\pi^2}{3} + 5544\zeta(3) \right) \ln 2 + \left(14496 - 690\pi^2 \right) \ln^2 2 - 6672 \ln^3 2 \\
& \left. + 2032 \ln^4 2 \right) + \left(610 - \frac{188\pi^2}{3} - \frac{5\pi^4}{8} + \left(-960 + \frac{166\pi^2}{3} \right) \ln 2 + \left(680 - 42\pi^2 \right) \ln^2 2 \right) \\
& + \frac{1}{N_c^2} \left(25 - \frac{\pi^2}{6} + \frac{17\pi^4}{16} - \frac{11}{3}\pi^2 \ln 2 + 4\pi^2 \ln^2 2 \right) \\
& + n_l N_c \left(-\frac{21256}{81} + \frac{403\pi^2}{27} + \frac{452\zeta(3)}{9} + \left(\frac{3488}{9} - 16\pi^2 \right) \ln 2 - 272 \ln^2 2 + 96 \ln^3 2 \right) \\
& + \frac{N_c}{4(N_c^2 - 1)} \left(\Delta_{gg}^{(\mathbf{1},0)} + \frac{1}{3} \Delta_{gg}^{(\mathbf{1},2)} \right)
\end{aligned}
\tag{C.8}
$$

$$
\begin{aligned}
C^{(2)}_{gg,\mathbf{8_S}} = N_c^2 \Bigg(& \frac{1285909}{81} - \frac{46937\pi^2}{54} - \frac{253\pi^4}{20} - \frac{39728\zeta(3)}{9} \\
& + \left(-\frac{210416}{9} + 1228\pi^2 + 5520\zeta(3) \right) \ln 2 + \left(16464 - 740\pi^2\right) \ln^2 2 - 7168 \ln^3 2 \\
& + 2032 \ln^4 2 \Big) + \left(750 - \frac{135\pi^2}{2} + \frac{3\pi^4}{2} + \left(-1060 + 53\pi^2\right) \ln 2 + \left(680 - 34\pi^2\right) \ln^2 2 \right) \\
& + \frac{1}{N_c^2} \left(25 - \frac{\pi^2}{6} + \frac{17\pi^4}{16} - \frac{11}{3}\pi^2 \ln 2 + 4\pi^2 \ln^2 2 \right) \\
& + n_l\, N_c \left(-\frac{25528}{81} + \frac{439\pi^2}{27} + \frac{452\zeta(3)}{9} + \left(\frac{4040}{9} - 16\pi^2 \right) \ln 2 - 296 \ln^2 2 + 96 \ln^3 2 \right) \\
& + \frac{N_c}{2(N_c^2-1)(N_c^2-4)} \left(\Delta_{gg}^{(\mathbf{8_S},0)} + \frac{1}{3}\, \Delta_{gg}^{(\mathbf{8_S},2)} \right)
\end{aligned}
\tag{C.9}
$$

While these constants contain contributions from both the hard and the soft function, the antisymmetric octet configuration is completely determined by the NNLO double-virtual corrections

$$
C^{(2)}_{gg,\mathbf{8_A}} = \frac{16}{3}\, \frac{N_c^2}{N_c^2 - 2} \left[\left(C_F - \frac{C_A}{2} \right)^2 \frac{\pi^4}{12} + \beta^2\, H^{(2),\,\text{match.}}_{\mathbf{8}\otimes\mathbf{8}|\mathbf{8_A}}(\rho) \right] . \tag{C.10}
$$

Note that due to the suppression of the associated LO cross section it involves also Coulomb effects, which for the other color configurations affect only the singular threshold behavior. The NNLO hard matching coefficients $\tilde{H}^{(2)}_{\mathbf{R}\otimes\mathbf{R}'|\tilde{\mathbf{R}}}\left(\frac{\mu^2}{m_t^2}\right)$, used in the resummation formalism described in section 3.1.2, are related to these threshold constants via Mellin transform, i. e. they receive additional contributions from the conversion of the soft logarithms in the β-expansion to N-space. The general color dependence of these matching coefficients in the gluon fusion channel is then given by

$$
\begin{aligned}
\tilde{H}^{(2)}_{\mathbf{8}\otimes\mathbf{8}|\mathbf{1}}(1) = N_c^2 \Bigg(& \frac{3157}{1296} - \frac{53\pi^2}{216} + \frac{313\pi^4}{2304} - \frac{11\zeta(3)}{72} + \left(\frac{101}{27} - \frac{7\zeta(3)}{2} \right) \gamma_E + \left(\frac{13}{18} + \frac{11\pi^2}{12} \right) \gamma_E^2 + \frac{11\gamma_E^3}{9} \\
& + 2\,\gamma_E^4 - \left(\frac{101}{27} + \frac{11\pi^2}{48} - \frac{7\zeta(3)}{2} + \left(\frac{13}{9} + \frac{11\pi^2}{6} \right) \gamma_E + \frac{11\gamma_E^2}{3} + 8\,\gamma_E^3 \right) \ln 2 + \left(\frac{20}{9} + \frac{37\pi^2}{24} \right. \\
& \left. + \frac{11\gamma_E}{3} + 8\,\gamma_E^2 \right) \ln^2 2 - \frac{11}{9} \ln^3 2 - \ln^4 2 \Big) + \left(-\frac{15}{8} + \frac{7\pi^2}{12} - \frac{21\pi^4}{128} + \left(5 - \frac{\pi^2}{4} \right) \gamma_E^2 + \left(\frac{11\pi^2}{24} \right. \right. \\
& \left. \left. - \left(10 - \frac{\pi^2}{2} \right) \gamma_E \right) \ln 2 + \left(\frac{5}{2} - \frac{5\pi^2}{8} \right) \ln^2 2 \right) + \frac{1}{N_c^2} \left(\frac{25}{16} - \frac{\pi^2}{96} + \frac{17\pi^4}{256} - \frac{11}{48}\pi^2 \ln 2 + \frac{\pi^2}{4} \ln^2 2 \right) \\
& + n_l\, N_c \left(-\frac{41}{162} - \frac{5\pi^2}{432} + \frac{\zeta(3)}{36} - \frac{14\gamma_E}{27} - \frac{5\gamma_E^2}{9} - \frac{2\gamma_E^3}{9} + \left(\frac{14}{27} + \frac{10\gamma_E}{9} + \frac{2\gamma_E^2}{3} \right) \ln 2 \right. \\
& \left. - \left(\frac{5}{9} + \frac{2\gamma_E}{3} \right) \ln^2 2 + \frac{2}{9} \ln^3 2 \right) + \frac{N_c}{64(N_c^2-1)} \left(\Delta_{gg}^{(\mathbf{1},0)} + \frac{1}{3}\, \Delta_{gg}^{(\mathbf{1},2)} \right)
\end{aligned}
\tag{C.11}
$$

$$\begin{aligned}\tilde{H}^{(2)}_{\mathbf{8}\otimes\mathbf{8}|\mathbf{8}}(1) = {}& \frac{N_c^3}{N_c^2-4}\left(\frac{7}{36}-\frac{\pi^2}{48}\right)(1-3\ln 2) + N_c^2\left(\frac{7249}{1296}+\frac{355\pi^2}{864}+\frac{41\pi^4}{960}-\frac{7\zeta(3)}{9}\right.\\
&+\left(\frac{803}{108}+\frac{\pi^2}{3}-3\,\zeta(3)\right)\gamma_E+\left(\frac{221}{36}+\frac{2\pi^2}{3}\right)\gamma_E^2+\frac{29\gamma_E^3}{9}+2\,\gamma_E^4+\left(-\frac{185}{27}-\frac{\pi^2}{12}+3\zeta(3)\right.\\
&\left.-\left(\frac{203}{18}+\frac{4\pi^2}{3}\right)\gamma_E-\frac{23\gamma_E^2}{3}-8\,\gamma_E^3\right)\ln 2+\left(\frac{149}{36}+\frac{5\pi^2}{12}+\frac{11\gamma_E}{3}+8\,\gamma_E^2\right)\ln^2 2-\frac{2}{9}\ln^3 2\\
&\left.-\ln^4 2\right)+\frac{N_c}{N_c^2-4}\left(\frac{7}{24}-\frac{17\pi^2}{96}+\frac{\pi^4}{64}+\left(\frac{7}{6}-\frac{\pi^2}{8}\right)\ln 2\right)+\left(\frac{347}{144}+\frac{5\pi^2}{12}-\frac{7\pi^4}{256}\right.\\
&+\left(\frac{5}{2}-\frac{\pi^2}{8}\right)\gamma_E+\left(5-\frac{\pi^2}{4}\right)\gamma_E^2+\frac{1}{N_c^2-4}\left(\frac{317}{144}-\frac{\pi^2}{2}+\frac{\pi^4}{32}\right)+\left(-\frac{11}{6}+\frac{3\pi^2}{16}\right.\\
&\left.\left.-\left(10-\frac{\pi^2}{2}\right)\gamma_E-\frac{1}{N_c^2-4}\left(\frac{11}{6}-\frac{\pi^2}{4}\right)\right)\ln 2+\left(\frac{5}{2}-\frac{\pi^2}{8}+\frac{1}{N_c^2-4}\right)\ln^2 2\right)\\
&+\frac{1}{N_c^2}\left(\frac{25}{16}-\frac{\pi^2}{96}+\frac{17\pi^4}{256}-\frac{11}{48}\pi^2\ln 2+\frac{\pi^2}{4}\ln^2 2\right)+\frac{n_l\,N_c^2}{N_c^2-4}\left(\frac{7}{72}-\frac{\pi^2}{96}\right)\\
&+n_l\,N_c\left(-\frac{313}{324}-\frac{5\pi^2}{432}+\frac{\zeta(3)}{36}-\frac{61\gamma_E}{54}-\frac{13\gamma_E^2}{18}-\frac{2\gamma_E^3}{9}+\frac{1}{N_c^2-4}\left(\frac{11}{72}-\frac{\pi^2}{48}\right)+\left(\frac{113}{108}\right.\right.\\
&\left.\left.+\frac{13\gamma_E}{9}+\frac{2\gamma_E^2}{3}-\frac{1}{6(N_c^2-4)}\right)\ln 2-\left(\frac{13}{18}+\frac{2\gamma_E}{3}\right)\ln^2 2+\frac{2}{9}\ln^3 2\right)+\frac{n_l^2\,N_c^2}{144(N_c^2-4)}\\
&+\frac{N_c}{32(N_c^2-1)(N_c^2-4)}\left(\Delta_{gg}^{(\mathbf{8_S},0)}+\frac{1}{3}\,\Delta_{gg}^{(\mathbf{8_S},2)}\right)\,.\end{aligned} \tag{C.12}$$

The rather odd color structure in the octet configuration is due to the fact that it is a combination of symmetric and antisymmetric contributions (see Eq. (3.97)). In contrast to $C^{(2)}_{gg,\mathbf{8_A}}$, it however only takes into account the non-Coulombic part of the hard function $H^{(2)}_{\mathbf{8}\otimes\mathbf{8}|\mathbf{8_A}}\left(\rho,\frac{\mu^2}{m_t^2}\right)$ such that $\tilde{H}^{(2)}_{\mathbf{8}\otimes\mathbf{8}|\mathbf{8}}\left(\frac{\mu^2}{m_t^2}\right)$ is not directly proportional to the corresponding combined octet constant

$$C^{(2)}_{gg,\mathbf{8}} = C^{(2)}_{gg,\mathbf{8_S}} + \frac{\bar{\sigma}^{(0)}_{gg,\mathbf{1}}(\beta)+\bar{\sigma}^{(0)}_{gg,\mathbf{8_S}}(\beta)}{\bar{\sigma}^{(0)}_{gg,\mathbf{8_S}}(\beta)}\,C^{(2)}_{gg,\mathbf{8_A}} \tag{C.13}$$

of the NNLO threshold expansion. For the quark annihilation channel up to NNLL accuracy only the color-octet configuration contributes to the resummation formula. The corresponding

NNLO hard matching coefficient reads

$$
\begin{aligned}
\tilde{H}^{(2)}_{\mathbf{3}\otimes\bar{\mathbf{3}}|\mathbf{8}}(1) = N_c^2 \Bigg(& \frac{1561}{216} + \frac{451\pi^2}{1728} - \frac{11\pi^4}{3840} - \frac{101\zeta(3)}{144} + \left(\frac{823}{108} - \frac{5\zeta(3)}{4}\right)\gamma_E + \frac{35\gamma_E^2}{6} + \frac{29\gamma_E^3}{18} + \frac{\gamma_E^4}{2} \\
& - \left(\frac{919}{108} + \frac{\pi^2}{32} - \frac{5\zeta(3)}{4} + \frac{73\gamma_E}{6} + \frac{16\gamma_E^2}{3} + 2\,\gamma_E^3\right)\ln 2 + \left(\frac{665}{144} - \frac{\pi^2}{16} + \frac{29\gamma_E}{6} + 2\,\gamma_E^2\right)\ln^2 2 \\
& - \frac{31}{36}\ln^3 2 - \frac{1}{4}\ln^4 2\Bigg) - N_c\left(\frac{128}{81} + \frac{\pi^2}{18} + \frac{8\gamma_E}{9} + \frac{8\gamma_E^2}{9} - \left(\frac{10}{9} + \frac{16\gamma_E}{9}\right)\ln 2 + \frac{4}{9}\ln^2 2\right) \\
& + \left(\frac{4129}{648} - \frac{715\pi^2}{1728} - \frac{13\pi^4}{1152} + \frac{11\zeta(3)}{144} + \left(\frac{115}{54} - \frac{\pi^2}{3} + \frac{7\zeta(3)}{4}\right)\gamma_E - \left(\frac{5}{12} + \frac{\pi^2}{3}\right)\gamma_E^2 - \frac{29\gamma_E^3}{18} - \gamma_E^4\right. \\
& \left. + \left(-\frac{313}{54} + \frac{\pi^2}{3} - \frac{7\zeta(3)}{4} - \left(\frac{2}{3} - \frac{2\pi^2}{3}\right)\gamma_E + \frac{23\gamma_E^2}{6} + 4\,\gamma_E^3\right)\ln 2\right. \\
& \left. + \left(\frac{89}{72} - \frac{\pi^2}{12} - \frac{11\gamma_E}{6} - 4\,\gamma_E^2\right)\ln^2 2 + \frac{1}{9}\ln^3 2 + \frac{1}{2}\ln^4 2\right) \\
& - \frac{1}{N_c}\left(\frac{16}{9} - \frac{\pi^2}{6} - \frac{8\gamma_E^2}{9} - \left(\frac{2}{3} + \frac{\pi^2}{8} - \frac{16\gamma_E}{9}\right)\ln 2 - \frac{4}{9}\ln^2 2\right) \\
& + \frac{1}{N_c^2}\left(4 - \frac{39\pi^2}{64} + \frac{139\pi^4}{2304} - \left(4 - \frac{\pi^2}{3}\right)\gamma_E^2 + \frac{\gamma_E^4}{2} - \left(3 + \frac{19\pi^2}{96} - \left(8 - \frac{2\pi^2}{3}\right)\gamma_E\right.\right. \\
& \left.\left. - \frac{3\gamma_E^2}{2} + 2\,\gamma_E^3\right)\ln 2 - \left(\frac{23}{16} - \frac{\pi^2}{2} + 3\,\gamma_E - 2\,\gamma_E^2\right)\ln^2 2 + \frac{3}{4}\ln^3 2 - \frac{1}{4}\ln^4 2\right) \\
& + n_l\left(N_c\left(-\frac{601}{324} - \frac{35\pi^{\,2}}{864} + \frac{\zeta(3)}{72} - \frac{77\gamma_E}{54} - \gamma_E^2 - \frac{\gamma_E^3}{9} + \left(\frac{11}{4} + \frac{\pi^2}{24} + \frac{8\gamma_E}{3} + \gamma_E^2\right)\ln 2\right.\right. \\
& \left.\left. - \left(\frac{14}{9} + \frac{5\gamma_E}{3}\right)\ln^2 2 + \frac{4}{9}\ln^3 2\right) + \left(\frac{20}{81} - \frac{8}{27}\ln 2\right) + \frac{1}{N_c}\left(-\frac{319}{324} - \frac{13\pi^2}{864} - \frac{\zeta(3)}{72} + \frac{7\gamma_E}{27}\right.\right. \\
& \left.\left. + \frac{5\gamma_E^2}{6} + \frac{\gamma_E^3}{9} + \left(\frac{161}{108} + \frac{\pi^2}{24} - \frac{5\gamma_E}{3} - \gamma_E^2\right)\ln 2 + \left(\frac{1}{18} + \frac{5\gamma_E}{3}\right)\ln^2 2 - \frac{4}{9}\ln^3 2\right)\right) \\
& + n_l^2\left(\frac{25}{324} + \frac{\pi^2}{36} - \frac{5}{27}\ln 2 + \frac{1}{9}\ln^2 2\right) + \frac{1}{32(N_c^2-1)}\left(\Delta^{(\mathbf{8},0)}_{q\bar{q}} + \frac{1}{3}\,\Delta^{(\mathbf{8},2)}_{q\bar{q}}\right) .
\end{aligned}
\tag{C.14}
$$

D. Differential cross section predictions for the Tevatron

Δy	$d\sigma/d\Delta y$ [pb/bin]		
	LO	NLO	NNLO
[-2 ; -1.5]	$2.26^{+1.13}_{-0.69} \times 10^{-1}$	$1.90^{+0.06+0.06+0.08}_{-0.18-0.05-0.18} \times 10^{-1}$	$1.98^{+0.13+0.05+0.14}_{-0.11-0.05-0.12} \times 10^{-1}$
[-1.5 ; -1]	$5.21^{+2.40}_{-1.51} \times 10^{-1}$	$4.74^{+0.14+0.13+0.19}_{-0.46-0.10-0.47} \times 10^{-1}$	$4.87^{+0.20+0.12+0.23}_{-0.22-0.08-0.24} \times 10^{-1}$
[-1 ; -0.5]	$1.06^{+0.47}_{-0.30} \times 10^{0}$	$1.00^{+0.03+0.03+0.04}_{-0.10-0.02-0.10} \times 10^{0}$	$1.03^{+0.03+0.03+0.04}_{-0.04-0.02-0.05} \times 10^{0}$
[-0.5 ; 0]	$1.51^{+0.65}_{-0.41} \times 10^{0}$	$1.48^{+0.06+0.04+0.07}_{-0.15-0.03-0.15} \times 10^{0}$	$1.52^{+0.04+0.04+0.06}_{-0.07-0.03-0.07} \times 10^{0}$
[0 ; 0.5]	$1.51^{+0.65}_{-0.41} \times 10^{0}$	$1.54^{+0.08+0.04+0.09}_{-0.17-0.03-0.17} \times 10^{0}$	$1.61^{+0.05+0.04+0.06}_{-0.08-0.03-0.08} \times 10^{0}$
[0.5 ; 1]	$1.06^{+0.47}_{-0.30} \times 10^{0}$	$1.14^{+0.09+0.03+0.10}_{-0.14-0.02-0.14} \times 10^{0}$	$1.21^{+0.05+0.03+0.06}_{-0.07-0.02-0.08} \times 10^{0}$
[1 ; 1.5]	$5.20^{+2.40}_{-1.51} \times 10^{-1}$	$5.89^{+0.65+0.15+0.67}_{-0.83-0.13-0.84} \times 10^{-1}$	$6.42^{+0.35+0.16+0.39}_{-0.48-0.12-0.49} \times 10^{-1}$
[1.5 ; 2]	$2.26^{+1.13}_{-0.69} \times 10^{-1}$	$2.67^{+0.40+0.08+0.41}_{-0.44-0.05-0.44} \times 10^{-1}$	$3.01^{+0.24+0.08+0.26}_{-0.29-0.06-0.30} \times 10^{-1}$

Table D.1: *Differential distribution in the rapidity difference Δy between t and $\bar{t}$ at LO, NLO and NNLO QCD. The format is central $\pm$ scales $\pm$ pdf $\pm$ total where for the total error the scale and PDF uncertainties are added in quadrature. At LO only the scale error is given. The end bins contain overflow events. Note that, in order to allow for a simple rebinning, the normalization for all tables provided in this appendix is chosen per bin and not according to Eq. (4.4).*

$\lvert\Delta y\rvert$	$A_{FB}(\Delta y, \lvert\Delta y\rvert)$	
	NLO	NNLO
[0 ; 0.5]	$2.14^{+0.96+0.06+0.97}_{-0.50-0.02-0.50} \times 10^{-2}$	$2.76^{+0.19+0.09+0.21}_{-0.31-0.01-0.31} \times 10^{-2}$
[0.5 ; 1]	$6.41^{+2.84+0.07+2.84}_{-1.47-0.24-1.49} \times 10^{-2}$	$8.06^{+0.59+0.10+0.59}_{-0.92-0.16-0.93} \times 10^{-2}$
[1 ; 1.5]	$1.08^{+0.48+0.03+0.48}_{-0.25-0.03-0.25} \times 10^{-1}$	$1.37^{+0.08+0.02+0.08}_{-0.15-0.03-0.15} \times 10^{-1}$
[1.5 ; 2]	$1.69^{+0.79+0.07+0.79}_{-0.40-0.04-0.40} \times 10^{-1}$	$2.07^{+0.08+0.06+0.10}_{-0.21-0.04-0.21} \times 10^{-1}$

Table D.2: *Rapidity-dependent A_{FB} at NLO and NNLO QCD. The format is central $\pm$ scales $\pm$ pdf $\pm$ total. The highest bin contains overflow events.*

$m_{t\bar{t}} \times \text{sign}(\Delta y)$ [GeV]	$d^2\sigma/dm_{t\bar{t}}\,d\Delta y$ [pb/bin]		
	LO	NLO	NNLO
[-750 ; -650]	$1.42^{+0.76}_{-0.46} \times 10^{-1}$	$9.04^{+0.03+0.30+0.30}_{-1.85-0.20-1.86} \times 10^{-2}$	$9.01^{+0.71+0.24+0.75}_{-0.24-0.22-0.32} \times 10^{-2}$
[-650 ; -550]	$2.88^{+1.41}_{-0.87} \times 10^{-1}$	$2.27^{+0.03+0.06+0.07}_{-0.17-0.06-0.18} \times 10^{-1}$	$2.27^{+0.08+0.06+0.10}_{-0.07-0.05-0.09} \times 10^{-1}$
[-550 ; -450]	$8.60^{+3.93}_{-2.47} \times 10^{-1}$	$7.78^{+0.22+0.22+0.31}_{-0.74-0.15-0.75} \times 10^{-1}$	$7.88^{+0.21+0.21+0.30}_{-0.31-0.14-0.34} \times 10^{-1}$
[-450 ; -350]	$1.99^{+0.84}_{-0.54} \times 10^{0}$	$2.02^{+0.10+0.05+0.12}_{-0.22-0.03-0.22} \times 10^{0}$	$2.10^{+0.06+0.05+0.08}_{-0.10-0.04-0.11} \times 10^{0}$
[-350 ; -250]	$2.93^{+1.18}_{-0.77} \times 10^{-2}$	$2.77^{+0.08+0.08+0.11}_{-0.24-0.04-0.24} \times 10^{-2}$	$2.98^{+0.18+0.07+0.19}_{-0.18-0.04-0.18} \times 10^{-2}$
[250 ; 350]	$2.93^{+1.18}_{-0.77} \times 10^{-2}$	$2.83^{+0.08+0.05+0.10}_{-0.26-0.07-0.26} \times 10^{-2}$	$2.97^{+0.18+0.07+0.20}_{-0.16-0.04-0.17} \times 10^{-2}$
[350 ; 450]	$1.99^{+0.84}_{-0.54} \times 10^{0}$	$2.20^{+0.19+0.06+0.20}_{-0.27-0.04-0.27} \times 10^{0}$	$2.35^{+0.10+0.06+0.11}_{-0.14-0.04-0.15} \times 10^{0}$
[450 ; 550]	$8.59^{+3.93}_{-2.47} \times 10^{-1}$	$9.08^{+0.72+0.23+0.76}_{-1.16-0.22-1.18} \times 10^{-1}$	$9.62^{+0.40+0.25+0.47}_{-0.60-0.18-0.63} \times 10^{-1}$
[550 ; 650]	$2.88^{+1.41}_{-0.87} \times 10^{-1}$	$2.82^{+0.17+0.10+0.20}_{-0.36-0.05-0.36} \times 10^{-1}$	$2.98^{+0.13+0.08+0.15}_{-0.18-0.06-0.19} \times 10^{-1}$
[650 ; 750]	$1.42^{+0.76}_{-0.46} \times 10^{-1}$	$1.24^{+0.05+0.04+0.06}_{-0.15-0.03-0.15} \times 10^{-1}$	$1.29^{+0.07+0.04+0.08}_{-0.08-0.03-0.09} \times 10^{-1}$

Table D.3: *Double differential distribution in the rapidity difference and invariant mass of the $t\bar{t}$ pair at LO, NLO and NNLO QCD. The format is central ± scales ± pdf ± total. At LO only the scale error is given. The end bins contain overflow events.*

$m_{t\bar{t}}$ [GeV]	$A_{FB}(\Delta y, m_{t\bar{t}})$	
	NLO	NNLO
[350 ; 450]	$4.10^{+1.66+0.07+1.66}_{-0.90-0.10-0.91} \times 10^{-2}$	$5.36^{+0.49+0.09+0.50}_{-0.61-0.07-0.62} \times 10^{-2}$
[450 ; 550]	$7.71^{+3.69+0.09+3.69}_{-1.85-0.34-1.88} \times 10^{-2}$	$9.98^{+0.68+0.15+0.70}_{-1.23-0.17-1.24} \times 10^{-2}$
[550 ; 650]	$1.08^{+0.61+0.09+0.62}_{-0.28-0.00-0.28} \times 10^{-1}$	$1.34^{+0.06+0.03+0.06}_{-0.14-0.02-0.14} \times 10^{-1}$
[650 ; 750]	$1.56^{+1.19+0.03+1.19}_{-0.46-0.03-0.47} \times 10^{-1}$	$1.77^{+0.04+0.03+0.06}_{-0.19-0.02-0.19} \times 10^{-1}$

Table D.4: *Invariant-mass-dependent A_{FB} at NLO and NNLO QCD. The format is central±scales±pdf±total. The lowest and highest bins contain spillover events.*

$p_{T,t\bar{t}} \times \mathrm{sign}(\Delta y)$ [GeV]	$d^2\sigma/dp_{T,t\bar{t}}\,d\Delta y$ [pb/bin]		
	LO	NLO	NNLO
[-80 ; -70]	0	$1.13^{+0.74+0.04+0.74}_{-0.41-0.03-0.41} \times 10^{-1}$	$1.39^{+0.10+0.04+0.11}_{-0.24-0.03-0.24} \times 10^{-1}$
[-70 ; -60]	0	$3.98^{+2.49+0.13+2.49}_{-1.41-0.07-1.41} \times 10^{-2}$	$5.12^{+0.52+0.13+0.53}_{-0.92-0.11-0.92} \times 10^{-2}$
[-60 ; -50]	0	$5.81^{+3.61+0.17+3.61}_{-2.05-0.13-2.06} \times 10^{-2}$	$7.50^{+0.77+0.18+0.79}_{-1.33-0.15-1.34} \times 10^{-2}$
[-50 ; -40]	0	$8.89^{+5.47+0.28+5.47}_{-3.12-0.17-3.12} \times 10^{-2}$	$1.15^{+0.12+0.03+0.12}_{-0.20-0.02-0.21} \times 10^{-1}$
[-40 ; -30]	0	$1.46^{+0.89+0.05+0.89}_{-0.51-0.03-0.51} \times 10^{-1}$	$1.88^{+0.17+0.04+0.18}_{-0.32-0.04-0.33} \times 10^{-1}$
[-30 ; -20]	0	$2.71^{+1.64+0.08+1.64}_{-0.94-0.05-0.94} \times 10^{-1}$	$3.39^{+0.27+0.08+0.28}_{-0.55-0.06-0.56} \times 10^{-1}$
[-20 ; -10]	0	$6.54^{+3.91+0.18+3.91}_{-2.25-0.13-2.26} \times 10^{-1}$	$7.48^{+0.30+0.18+0.35}_{-1.03-0.13-1.04} \times 10^{-1}$
[-10 ; 0]	$3.31^{+1.47}_{-0.93}$	$1.77^{+0.16+0.05+0.17}_{-0.76-0.03-0.76} \times 10^{0}$	$1.59^{+0.11+0.04+0.12}_{-0.03-0.03-0.04} \times 10^{0}$
[0 ; 10]	$3.31^{+1.47}_{-0.93}$	$2.39^{+0.04+0.07+0.08}_{-0.42-0.05-0.43} \times 10^{0}$	$2.21^{+0.06+0.06+0.09}_{-0.05-0.05-0.06} \times 10^{0}$
[10 ; 20]	0	$5.60^{+3.39+0.18+3.39}_{-1.94-0.11-1.95} \times 10^{-1}$	$7.35^{+0.72+0.18+0.75}_{-1.27-0.14-1.27} \times 10^{-1}$
[20 ; 30]	0	$2.26^{+1.39+0.07+1.39}_{-0.79-0.05-0.79} \times 10^{-1}$	$3.17^{+0.46+0.08+0.46}_{-0.61-0.06-0.61} \times 10^{-1}$
[30 ; 40]	0	$1.20^{+0.74+0.04+0.74}_{-0.42-0.03-0.42} \times 10^{-1}$	$1.70^{+0.27+0.05+0.27}_{-0.34-0.03-0.34} \times 10^{-1}$
[40 ; 50]	0	$7.21^{+4.51+0.24+4.52}_{-2.56-0.15-2.56} \times 10^{-2}$	$1.03^{+0.17+0.03+0.17}_{-0.20-0.02-0.21} \times 10^{-1}$
[50 ; 60]	0	$4.68^{+2.95+0.13+2.96}_{-1.67-0.15-1.67} \times 10^{-2}$	$6.62^{+1.08+0.18+1.09}_{-1.33-0.13-1.33} \times 10^{-2}$
[60 ; 70]	0	$3.18^{+2.03+0.11+2.03}_{-1.14-0.07-1.14} \times 10^{-2}$	$4.50^{+0.74+0.11+0.74}_{-0.91-0.11-0.92} \times 10^{-2}$
[70 ; *80*]	0	$8.96^{+5.95+0.34+5.96}_{-3.30-0.25-3.31} \times 10^{-2}$	$1.21^{+0.17+0.04+0.17}_{-0.24-0.03-0.24} \times 10^{-1}$

Table D.5: *Double differential distribution in the rapidity difference and transverse momentum of the $t\bar{t}$ pair at LO, NLO and NNLO QCD. The format is central $\pm$ scales $\pm$ pdf $\pm$ total. At LO only the scale error is given. The end bins contain overflow events.*

$p_{T,t\bar{t}}$ [GeV]	$A_{FB}(\Delta y, p_{T,t\bar{t}})$	
	NLO	NNLO
[0 ; 10]	$+1.48^{+1.72+0.02+1.72}_{-0.51-0.02-0.52} \times 10^{-1}$	$+1.64^{+0.03+0.02+0.03}_{-0.21-0.02-0.21} \times 10^{-1}$
[10 ; 20]	$-7.71^{+0.22+0.35+0.41}_{-0.19-0.18-0.26} \times 10^{-2}$	$-8.52^{+44.2+0.19+44.2}_{-20.1-0.22-20.1} \times 10^{-3}$
[20 ; 30]	$-9.00^{+0.27+0.18+0.33}_{-0.23-0.41-0.47} \times 10^{-2}$	$-3.37^{+3.19+0.11+3.19}_{-1.61-0.07-1.62} \times 10^{-2}$
[30 ; 40]	$-9.85^{+0.30+0.18+0.35}_{-0.25-0.51-0.57} \times 10^{-2}$	$-4.79^{+2.95+0.18+2.95}_{-1.53-0.09-1.53} \times 10^{-2}$
[40 ; 50]	$-1.04^{+0.03+0.03+0.04}_{-0.03-0.04-0.05} \times 10^{-1}$	$-5.72^{+2.65+0.14+2.66}_{-1.34-0.16-1.35} \times 10^{-2}$
[50 ; 60]	$-1.08^{+0.03+0.01+0.04}_{-0.03-0.07-0.08} \times 10^{-1}$	$-6.12^{+2.72+0.21+2.72}_{-1.48-0.13-1.49} \times 10^{-2}$
[60 ; 70]	$-1.12^{+0.04+0.03+0.04}_{-0.03-0.05-0.06} \times 10^{-1}$	$-6.41^{+2.74+0.15+2.74}_{-1.43-0.21-1.45} \times 10^{-2}$
[70 ; *80*]	$-1.15^{+0.04+0.04+0.06}_{-0.03-0.05-0.06} \times 10^{-1}$	$-7.03^{+2.95+0.24+2.96}_{-1.46-0.21-1.47} \times 10^{-2}$

Table D.6: *Transverse-momentum-dependent* A_{FB} *at NLO and NNLO QCD. The format is central* $\pm$ *scales* $\pm$ *pdf* $\pm$ *total. The highest bin contains overflow events.*

$\cos\theta$	$(1/\sigma_{t\bar{t}}^{\text{tot}}) d\sigma/d\cos\theta$ [1/bin]		
	LO	NLO	NNLO
[-1 ; -0.8]	$1.13^{+0.01}_{-0.00} \times 10^{-1}$	$1.08^{+0.01}_{-0.02} \times 10^{-1}$	$1.08^{+0.01}_{-0.00} \times 10^{-1}$
[-0.8 ; -0.6]	$1.04^{+0.00}_{-0.00} \times 10^{-1}$	$9.69^{+0.16}_{-0.31} \times 10^{-2}$	$9.57^{+0.08}_{-0.03} \times 10^{-2}$
[-0.6 ; -0.4]	$9.77^{+0.01}_{-0.01} \times 10^{-2}$	$9.09^{+0.17}_{-0.33} \times 10^{-2}$	$8.84^{+0.12}_{-0.11} \times 10^{-2}$
[-0.4 ; -0.2]	$9.38^{+0.02}_{-0.03} \times 10^{-2}$	$8.78^{+0.16}_{-0.30} \times 10^{-2}$	$8.55^{+0.13}_{-0.08} \times 10^{-2}$
[-0.2 ; 0]	$9.18^{+0.03}_{-0.04} \times 10^{-2}$	$8.72^{+0.13}_{-0.24} \times 10^{-2}$	$8.49^{+0.13}_{-0.13} \times 10^{-2}$
[0 ; 0.2]	$9.18^{+0.03}_{-0.04} \times 10^{-2}$	$8.90^{+0.09}_{-0.15} \times 10^{-2}$	$8.75^{+0.09}_{-0.10} \times 10^{-2}$
[0.2 ; 0.4]	$9.38^{+0.02}_{-0.03} \times 10^{-2}$	$9.35^{+0.03}_{-0.03} \times 10^{-2}$	$9.24^{+0.05}_{-0.07} \times 10^{-2}$
[0.4 ; 0.6]	$9.77^{+0.01}_{-0.01} \times 10^{-2}$	$1.01^{+0.01}_{-0.01} \times 10^{-1}$	$1.02^{+0.00}_{-0.01} \times 10^{-1}$
[0.6 ; 0.8]	$1.04^{+0.00}_{-0.00} \times 10^{-1}$	$1.13^{+0.04}_{-0.02} \times 10^{-1}$	$1.16^{+0.01}_{-0.01} \times 10^{-1}$
[0.8 ; 1]	$1.13^{+0.01}_{-0.00} \times 10^{-1}$	$1.33^{+0.10}_{-0.05} \times 10^{-1}$	$1.40^{+0.04}_{-0.04} \times 10^{-1}$

Table D.7: *Normalized differential distribution in* $\cos\theta$ *at LO, NLO and NNLO QCD. The format is central* $\pm$ *scales.*

ℓ	Legendre Moment a_ℓ		
	LO	NLO	NNLO
1		$1.24^{+0.57}_{-0.29} \times 10^{-1}$	$1.59^{+0.11}_{-0.19} \times 10^{-1}$
2	$1.75^{+0.08}_{-0.06} \times 10^{-1}$	$2.68^{+0.49}_{-0.28} \times 10^{-1}$	$3.17^{+0.29}_{-0.28} \times 10^{-1}$
3		$2.45^{+1.17}_{-0.60} \times 10^{-2}$	$3.96^{+0.74}_{-0.67} \times 10^{-2}$
4	$7.47^{+1.68}_{-1.22} \times 10^{-3}$	$3.34^{+1.45}_{-0.78} \times 10^{-2}$	$5.12^{+1.11}_{-0.93} \times 10^{-2}$
5		$3.25^{+1.58}_{-0.76} \times 10^{-3}$	$6.88^{+2.14}_{-1.48} \times 10^{-3}$
6	$1.27^{+0.33}_{-0.23} \times 10^{-3}$	$6.35^{+3.06}_{-1.67} \times 10^{-3}$	$1.08^{+0.33}_{-0.26} \times 10^{-2}$
7		$9.69^{+4.17}_{-2.39} \times 10^{-4}$	$1.81^{+0.80}_{-0.48} \times 10^{-3}$
8	$5.15^{+8.31}_{-5.66} \times 10^{-5}$	$1.47^{+0.79}_{-0.39} \times 10^{-3}$	$3.87^{+0.86}_{-0.76} \times 10^{-3}$

Table D.8: *First eight Legendre moments a_ℓ of the normalized angular distribution $(1/\sigma_{t\bar{t}}^{tot})d\sigma/d\cos\theta$ at LO, NLO and NNLO QCD. The format is central $\pm$ scales.*

$\lvert y_t\rvert$	$d\sigma/d\lvert y_t\rvert$ [pb/bin]		
	LO	NLO	NNLO
[0 ; 0.25]	$1.94^{+0.84}_{-0.54} \times 10^{0}$	$1.96^{+0.09+0.06+0.11}_{-0.21-0.03-0.21} \times 10^{0}$	$2.04^{+0.06+0.05+0.08}_{-0.10-0.04-0.10} \times 10^{0}$
[0.25 ; 0.5]	$1.72^{+0.75}_{-0.48} \times 10^{0}$	$1.74^{+0.08+0.04+0.09}_{-0.19-0.04-0.19} \times 10^{0}$	$1.82^{+0.06+0.05+0.08}_{-0.09-0.03-0.10} \times 10^{0}$
[0.5 ; 0.75]	$1.33^{+0.59}_{-0.37} \times 10^{0}$	$1.35^{+0.07+0.04+0.08}_{-0.15-0.03-0.15} \times 10^{0}$	$1.41^{+0.05+0.04+0.06}_{-0.07-0.02-0.08} \times 10^{0}$
[0.75 ; 1]	$8.83^{+4.01}_{-2.53} \times 10^{-1}$	$8.93^{+0.55+0.23+0.59}_{-1.06-0.18-1.07} \times 10^{-1}$	$9.35^{+0.37+0.23+0.44}_{-0.54-0.16-0.56} \times 10^{-1}$
[1 ; 1.25]	$4.79^{+2.25}_{-1.40} \times 10^{-1}$	$4.84^{+0.35+0.16+0.39}_{-0.61-0.07-0.62} \times 10^{-1}$	$5.17^{+0.25+0.12+0.28}_{-0.34-0.09-0.35} \times 10^{-1}$
[1.25 ; 1.5]	$1.97^{+0.97}_{-0.60} \times 10^{-1}$	$1.99^{+0.18+0.05+0.18}_{-0.28-0.05-0.28} \times 10^{-1}$	$2.15^{+0.15+0.05+0.16}_{-0.16-0.05-0.16} \times 10^{-1}$
[1.5 ; ∞]	$6.18^{+3.27}_{-1.96} \times 10^{-2}$	$6.22^{+0.69+0.23+0.73}_{-0.96-0.16-0.98} \times 10^{-2}$	$6.67^{+0.58+0.22+0.62}_{-0.60-0.19-0.63} \times 10^{-2}$

$\lvert y_t\rvert$	$(1/\sigma^{\mathrm{tot}}_{t\bar{t}})d\sigma/d\lvert y_t\rvert$ [1/bin]		
	LO	NLO	NNLO
[0 ; 0.25]	$2.94^{+0.02}_{-0.02} \times 10^{-1}$	$2.93^{+0.02+0.02+0.03}_{-0.02-0.00-0.02} \times 10^{-1}$	$2.91^{+0.02+0.01+0.02}_{-0.02-0.01-0.02} \times 10^{-1}$
[0.25 ; 0.5]	$2.60^{+0.01}_{-0.01} \times 10^{-1}$	$2.60^{+0.01+0.00+0.01}_{-0.01-0.02-0.02} \times 10^{-1}$	$2.61^{+0.01+0.01+0.01}_{-0.01-0.00-0.01} \times 10^{-1}$
[0.5 ; 0.75]	$2.01^{+0.00}_{-0.00} \times 10^{-1}$	$2.02^{+0.00+0.00+0.00}_{-0.00-0.00-0.00} \times 10^{-1}$	$2.01^{+0.00+0.00+0.00}_{-0.00-0.00-0.00} \times 10^{-1}$
[0.75 ; 1]	$1.33^{+0.01}_{-0.01} \times 10^{-1}$	$1.34^{+0.01+0.00+0.01}_{-0.01-0.01-0.01} \times 10^{-1}$	$1.34^{+0.00+0.00+0.00}_{-0.01-0.00-0.01} \times 10^{-1}$
[1 ; 1.25]	$7.24^{+0.14}_{-0.12} \times 10^{-2}$	$7.25^{+0.13+0.09+0.16}_{-0.11-0.02-0.11} \times 10^{-2}$	$7.38^{+0.08+0.04+0.09}_{-0.10-0.06-0.11} \times 10^{-2}$
[1.25 ; 1.5]	$2.98^{+0.10}_{-0.09} \times 10^{-2}$	$2.98^{+0.10+0.02+0.10}_{-0.09-0.06-0.10} \times 10^{-2}$	$3.07^{+0.09+0.04+0.10}_{-0.07-0.05-0.08} \times 10^{-2}$
[1.5 ; ∞]	$9.33^{+0.56}_{-0.47} \times 10^{-3}$	$9.31^{+0.51+0.20+0.55}_{-0.44-0.23-0.50} \times 10^{-3}$	$9.52^{+0.46+0.23+0.51}_{-0.37-0.27-0.45} \times 10^{-3}$

Table D.9: *Absolute and normalized differential distribution in the rapidity of the top quark $|y_t|$ at LO, NLO and NNLO QCD. The format is central $\pm$ scales $\pm$ pdf $\pm$ total. At LO only the scale error is given.*

$m_{t\bar{t}}$ [GeV]	$d\sigma/dm_{t\bar{t}}$ [pb/bin]		
	LO	NLO	NNLO
[240 ; 412.5]	$2.78^{+1.16}_{-0.75} \times 10^{0}$	$2.96^{+0.21+0.07+0.22}_{-0.34-0.06-0.35} \times 10^{0}$	$3.13^{+0.12+0.07+0.14}_{-0.17-0.05-0.18} \times 10^{0}$
[412.5 ; 505]	$2.43^{+1.08}_{-0.68} \times 10^{0}$	$2.47^{+0.14+0.07+0.16}_{-0.28-0.05-0.29} \times 10^{0}$	$2.59^{+0.09+0.07+0.11}_{-0.14-0.05-0.14} \times 10^{0}$
[505 ; 615]	$9.95^{+4.74}_{-2.94} \times 10^{-1}$	$9.20^{+0.31+0.28+0.42}_{-0.99-0.18-1.00} \times 10^{-1}$	$9.50^{+0.35+0.26+0.44}_{-0.47-0.18-0.50} \times 10^{-1}$
[615 ; 750]	$3.27^{+1.68}_{-1.02} \times 10^{-1}$	$2.66^{+0.06+0.09+0.11}_{-0.25-0.05-0.25} \times 10^{-1}$	$2.73^{+0.14+0.08+0.16}_{-0.12-0.06-0.14} \times 10^{-1}$
[750 ; 1200]	$9.21^{+5.26}_{-3.08} \times 10^{-2}$	$6.20^{+0.00+0.23+0.23}_{-0.88-0.14-0.89} \times 10^{-2}$	$6.36^{+0.58+0.20+0.61}_{-0.30-0.15-0.34} \times 10^{-2}$
[1200 ; 1960]	$2.82^{+2.12}_{-1.12} \times 10^{-4}$	$1.07^{+0.10}_{-0.78} \times 10^{-4}$	$1.27^{+0.47}_{-0.14} \times 10^{-4}$

$m_{t\bar{t}}$ [GeV]	$(1/\sigma^{\mathrm{tot}}_{t\bar{t}})d\sigma/dm_{t\bar{t}}$ [1/bin]		
	LO	NLO	NNLO
[240 ; 412.5]	$4.20^{+0.07}_{-0.07} \times 10^{-1}$	$4.44^{+0.08+0.00+0.08}_{-0.03-0.02-0.03} \times 10^{-1}$	$4.47^{+0.01+0.01+0.01}_{-0.02-0.01-0.02} \times 10^{-1}$
[412.5 ; 505]	$3.66^{+0.00}_{-0.00} \times 10^{-1}$	$3.70^{+0.02+0.01+0.02}_{-0.01-0.00-0.01} \times 10^{-1}$	$3.70^{+0.01+0.00+0.01}_{-0.01-0.00-0.01} \times 10^{-1}$
[505 ; 615]	$1.50^{+0.03}_{-0.03} \times 10^{-1}$	$1.38^{+0.01+0.01+0.02}_{-0.04-0.00-0.04} \times 10^{-1}$	$1.36^{+0.01+0.01+0.01}_{-0.00-0.00-0.00} \times 10^{-1}$
[615 ; 750]	$4.94^{+0.24}_{-0.21} \times 10^{-2}$	$3.98^{+0.11+0.04+0.12}_{-0.33-0.01-0.33} \times 10^{-2}$	$3.90^{+0.05+0.03+0.06}_{-0.00-0.02-0.02} \times 10^{-2}$
[750 ; 1200]	$1.39^{+0.12}_{-0.10} \times 10^{-2}$	$9.28^{+0.49+0.14+0.51}_{-1.71-0.10-1.72} \times 10^{-3}$	$9.08^{+0.47+0.12+0.48}_{-0.01-0.11-0.11} \times 10^{-3}$
[1200 ; 1960]	$4.25^{+0.91}_{-0.68} \times 10^{-5}$	$1.61^{+0.31}_{-1.19} \times 10^{-5}$	$1.82^{+0.58}_{-0.11} \times 10^{-5}$

Table D.10: *Absolute and normalized differential distribution in the invariant mass of the $t\bar{t}$ pair at LO, NLO and NNLO QCD. The format is central $\pm$ scales $\pm$ pdf $\pm$ total. At LO as well as for the last bins only the scale error is shown.*

$p_{T,t}$ [GeV]	$d\sigma/dp_{T,t}$ [pb/bin]		
	LO	NLO	NNLO
[0 ; 45]	$1.07^{+0.45}_{-0.29} \times 10^{0}$	$1.15^{+0.09+0.03+0.09}_{-0.13-0.02-0.14} \times 10^{0}$	$1.23^{+0.06+0.03+0.07}_{-0.08-0.02-0.08} \times 10^{0}$
[45 ; 90]	$2.13^{+0.91}_{-0.59} \times 10^{0}$	$2.27^{+0.17+0.05+0.18}_{-0.27-0.05-0.27} \times 10^{0}$	$2.39^{+0.10+0.06+0.12}_{-0.13-0.04-0.14} \times 10^{0}$
[90 ; 140]	$1.85^{+0.82}_{-0.52} \times 10^{0}$	$1.88^{+0.11+0.05+0.12}_{-0.21-0.04-0.22} \times 10^{0}$	$1.97^{+0.06+0.05+0.08}_{-0.10-0.04-0.11} \times 10^{0}$
[140 ; 200]	$1.05^{+0.49}_{-0.31} \times 10^{0}$	$9.81^{+0.32+0.35+0.47}_{-1.02-0.14-1.03} \times 10^{-1}$	$1.01^{+0.03+0.03+0.04}_{-0.05-0.02-0.05} \times 10^{0}$
[200 ; 300]	$4.51^{+2.23}_{-1.37} \times 10^{-1}$	$3.67^{+0.07+0.13+0.14}_{-0.31-0.07-0.32} \times 10^{-1}$	$3.65^{+0.08+0.11+0.14}_{-0.09-0.08-0.12} \times 10^{-1}$
[300 ; 500]	$6.59^{+3.68}_{-2.18} \times 10^{-2}$	$4.20^{+0.00+0.12+0.12}_{-0.81-0.15-0.82} \times 10^{-2}$	$4.07^{+0.23+0.14+0.27}_{-0.11-0.10-0.15} \times 10^{-2}$
[500 ; 965]	$5.54^{+3.88}_{-2.11} \times 10^{-4}$	$2.21^{+0.18}_{-1.51} \times 10^{-4}$	$2.25^{+0.54}_{-0.07} \times 10^{-4}$

$p_{T,t}$ [GeV]	$(1/\sigma^{\mathrm{tot}}_{t\bar{t}})d\sigma/dp_{T,t}$ [1/bin]		
	LO	NLO	NNLO
[0 ; 45]	$1.62^{+0.02}_{-0.02} \times 10^{-1}$	$1.71^{+0.03+0.00+0.03}_{-0.01-0.01-0.01} \times 10^{-1}$	$1.76^{+0.02+0.00+0.02}_{-0.02-0.01-0.02} \times 10^{-1}$
[45 ; 90]	$3.22^{+0.03}_{-0.03} \times 10^{-1}$	$3.40^{+0.07+0.00+0.07}_{-0.02-0.02-0.03} \times 10^{-1}$	$3.41^{+0.02+0.01+0.02}_{-0.01-0.01-0.01} \times 10^{-1}$
[90 ; 140]	$2.79^{+0.00}_{-0.00} \times 10^{-1}$	$2.81^{+0.01+0.00+0.01}_{-0.00-0.00-0.01} \times 10^{-1}$	$2.81^{+0.00+0.00+0.01}_{-0.01-0.00-0.01} \times 10^{-1}$
[140 ; 200]	$1.59^{+0.02}_{-0.02} \times 10^{-1}$	$1.47^{+0.02+0.02+0.02}_{-0.04-0.00-0.04} \times 10^{-1}$	$1.44^{+0.01+0.01+0.01}_{-0.01-0.00-0.01} \times 10^{-1}$
[200 ; 300]	$6.81^{+0.25}_{-0.22} \times 10^{-2}$	$5.49^{+0.17+0.07+0.18}_{-0.50-0.03-0.50} \times 10^{-2}$	$5.20^{+0.15+0.05+0.16}_{-0.08-0.04-0.09} \times 10^{-2}$
[300 ; 500]	$9.96^{+0.79}_{-0.67} \times 10^{-3}$	$6.29^{+0.47+0.06+0.48}_{-1.46-0.16-1.47} \times 10^{-3}$	$5.81^{+0.16+0.09+0.18}_{-0.06-0.08-0.10} \times 10^{-3}$
[500 ; 965]	$8.38^{+1.49}_{-1.15} \times 10^{-5}$	$3.30^{+0.66}_{-2.32} \times 10^{-5}$	$3.21^{+0.62}_{-0.03} \times 10^{-5}$

Table D.11: *Absolute and normalized differential distribution in the transverse momentum of the top quark at LO, NLO and NNLO QCD. The format is central ± scales ± pdf ± total. At LO as well as for the last bins only the scale error is given. Note that the upper bound of the highest bin depends on the value of the top-quark mass, in this case* $m_t = 173.3\,\mathrm{GeV}$.

E. Software

Due to their high complexity the calculations performed in the course of this thesis have required the use of numerous software systems, most notably:

- DiaGen/IdSolver [674], a private code for the generation and evaluation of Feynman diagrams used in the construction of the $t\bar{t}$ amplitudes through NNLO accuracy. The latter package has been employed to perform the IBP reduction of the one- and two-loop integrals as well as the higher multiplicity phase space integrals to a smaller set of master integrals. For the efficient manipulation of the large number of IBP relations it uses the rational-function algebra library Fermat [675].

- Form [676] is a symbolic manipulation system employed for the algebraic simplification of regular Feynman diagrams as well as eikonal graphs. It has been proven particularly useful in the evaluation of the underlying Dirac and color algebra, the latter of which has been efficiently treated with the help of the Color.h package.

- FormCalc [677], a Mathematica package used for the low-level generation and formatting of Fortran code.

- Gmm++ [678], a C++ package for the efficient performance of basic linear-algebra operations. It has been used in the determination of the deep power-logarithmic expansions in the evaluation of the two-loop master integrals.

- Helac-Nlo [433]/Mcfm [110]/SecDec [647–650], different stand-alone software packages used for numerous checks of our computational framework. While Helac-Nlo has been primarily employed for testing the correctness of the numerical integration routines, the results obtained with Mcfm served as an independent cross-check for the α_s^2- and α_s^3-parts of our total and differential cross section calculations. The program SecDec, on the other hand, has been used to check a large fraction of the bare two-loop scalar master integrals contributing to the NNLO double-virtual corrections.

- HypExp/Hpl [569,679], Mathematica packages for the manipulation and simplification of hypergeometric functions occurring in the evaluation of the NNLO soft functions.

- Intel Fortran Compiler has been used to extend the internal precision of our Stripper-based MC framework to quadruple level, which leads to an improved stability of our numerical integration routines.

- Lhapdf [502–504] is a general purpose Fortran/C++ interpolator allowing for the evaluation of PDFs from discretised data files. It has been used to construct the partonic fluxes in section 2.2 as well as in the determination of the total and differential cross section predictions presented throughout this thesis.

- Mathematica, a major algebraic/numeric computer system employed for the largest part of the symbolic calculations performed in the course of this thesis. It also serves as an interface between different branches of the NNLO $t\bar{t}$ analysis and has been used in the interpretation and graphical representation of our various findings.

- MB package/MB Tools [541, 542]/Xsummer [540], a collection of Mathematica tools designed for the manipulation and evaluation of Mellin-Barnes integrals. In particular, it has been used in the calculation of the NNLO soft functions as well as in the determination of the high-energy boundary conditions entering the system of differential equations for the two-loop master integrals.

- Parni [635], an adaptive MC random-number generation optimizer that has been used to improve the performance of the numerical integration routines via importance sampling.

- QD/Arprec [680], two high-level Fortran/C++ packages allowing for the extension of our numerical integration routines to quad-double and arbitrary precision respectively. The former has been used in cases where the default quadruple precision provided by the Intel Fortran Compiler was no longer sufficient to guarantee a stable and efficient evaluation, i.e. the integration of the real-virtual finite remainders as well as the system of differential equations determining the kinematic behavior of the two-loop master integrals. The Arprec library, on the other hand, has been primarily used for numerical tests. Moreover, it has been employed in the determination of high-precision boundary conditions for the calculation of the two-loop threshold expansions described in section 3.4.2.

- Ranlux [633, 634], a classic random-number generator and the basis of our MC integration routines.

- Top++ [87], a program for the calculation of $t\bar{t}$ total cross section predictions at hadron colliders. It incorporates the findings derived in this thesis and published in Ref. [80] (in addition to the previous results of Refs. [77–79, 220]) and has been employed to compute the various fixed-order and resummed total cross section predictions presented in chapters 2 and 3. Note, however, that, in order to be able to study in detail the NNLO threshold expansions, we used a modified version of Top++ that also includes results from previous implementations.

- Zvode [655] is a general purpose Fortran solver for initial-value problems of systems of ordinary differential equations. It has been used for the numerical integration of the system of scalar two-loop master integrals, however modified such that it works in quad-double and even arbitrary precision. As input one has to provide a subroutine that calculates the right-hand side of the differential equation, which may be crucial for the numerical performance of the underlying algorithm. Since in our case the dependence on the kinematic variables is given in terms of fractions of polynomials, we applied a so-called Horner decomposition, i.e. we rearranged the corresponding polynomials in the numerators and denominators via

$$c_0 + c_1 x + c_2 x^2 + \cdots + c_n x^n = c_0 + x(c_1 + x(c_2 + \cdots + x(c_{n-1} + c_n x))) \,. \tag{E.1}$$

  This considerably reduces the amount of arithmetic operations needed to evaluate these expressions and thus leads to a numerically highly-efficient subroutine.

Bibliography

[1] M. Kobayashi and T. Maskawa, *CP Violation in the Renormalizable Theory of Weak Interaction*, *Prog. Theor. Phys.* **49** (1973) 652–657.

[2] J. H. Christenson, J. W. Cronin, V. L. Fitch and R. Turlay, *Evidence for the 2 pi Decay of the k(2)0 Meson*, *Phys. Rev. Lett.* **13** (1964) 138–140.

[3] H. Harari, *A New Quark Model for Hadrons*, *Phys. Lett.* **B57** (1975) 265–269.

[4] M. L. Perl et al., *Evidence for Anomalous Lepton Production in e+ - e- Annihilation*, *Phys. Rev. Lett.* **35** (1975) 1489–1492.

[5] S. W. Herb et al., *Observation of a Dimuon Resonance at 9.5-GeV in 400-GeV Proton-Nucleus Collisions*, *Phys. Rev. Lett.* **39** (1977) 252–255.

[6] SLD Electroweak Group, DELPHI, ALEPH, SLD, SLD Heavy Flavour Group, OPAL, LEP Electroweak Working Group, L3 collaboration, S. Schael et al., *Precision electroweak measurements on the Z resonance*, *Phys. Rept.* **427** (2006) 257–454, [hep-ex/0509008].

[7] CDF collaboration, F. Abe et al., *Observation of top quark production in $\bar{p}p$ collisions*, *Phys. Rev. Lett.* **74** (1995) 2626–2631, [hep-ex/9503002].

[8] D0 collaboration, S. Abachi et al., *Observation of the top quark*, *Phys. Rev. Lett.* **74** (1995) 2632–2637, [hep-ex/9503003].

[9] CDF collaboration, T. Aaltonen et al., *First Observation of Electroweak Single Top Quark Production*, *Phys. Rev. Lett.* **103** (2009) 092002, [0903.0885].

[10] D0 collaboration, V. M. Abazov et al., *Observation of Single Top Quark Production*, *Phys. Rev. Lett.* **103** (2009) 092001, [0903.0850].

[11] ATLAS, CDF, CMS, D0 collaboration, *First combination of Tevatron and LHC measurements of the top-quark mass*, 1403.4427.

[12] J. Gao, C. S. Li and H. X. Zhu, *Top Quark Decay at Next-to-Next-to Leading Order in QCD*, *Phys. Rev. Lett.* **110** (2013) 042001, [1210.2808].

[13] M. Brucherseifer, F. Caola and K. Melnikov, *$\mathcal{O}(\alpha_s^2)$ corrections to fully-differential top quark decays*, *JHEP* **04** (2013) 059, [1301.7133].

[14] ILC collaboration, G. Aarons et al., *International Linear Collider Reference Design Report Volume 2: Physics at the ILC*, 0709.1893.

[15] TLEP Design Study Working Group collaboration, M. Bicer et al., *First Look at the Physics Case of TLEP*, *JHEP* **01** (2014) 164, [1308.6176].

[16] B. Fuks, *Opportunities with top quarks at future circular colliders*, in *Proceedings, 7th International Workshop on Top Quark Physics (TOP2014): Cannes, France, September 28-October 3, 2014*, 2014. 1412.1685.

[17] Gfitter Group collaboration, M. Baak, J. CÃºth, J. Haller, A. Hoecker, R. Kogler, K. Moenig et al., *The global electroweak fit at NNLO and prospects for the LHC and ILC*, *Eur. Phys. J.* **C74** (2014) 3046, [1407.3792].

[18] M. J. G. Veltman, *Limit on Mass Differences in the Weinberg Model*, *Nucl. Phys.* **B123** (1977) 89–99.

[19] K. G. Chetyrkin, M. Faisst, J. H. Kuhn, P. Maierhofer and C. Sturm, *Four-Loop QCD Corrections to the Rho Parameter*, *Phys. Rev. Lett.* **97** (2006) 102003, [hep-ph/0605201].

[20] Y. Schroder and M. Steinhauser, *Four-loop singlet contribution to the rho parameter*, *Phys. Lett.* **B622** (2005) 124–130, [hep-ph/0504055].

[21] R. Boughezal and M. Czakon, *Single scale tadpoles and O(G(F m(t)**2 alpha(s)**3)) corrections to the rho parameter*, *Nucl. Phys.* **B755** (2006) 221–238, [hep-ph/0606232].

[22] M. Faisst, P. Maierhoefer and C. Sturm, *Standard and epsilon-finite Master Integrals for the rho-Parameter*, *Nucl. Phys.* **B766** (2007) 246–268, [hep-ph/0611244].

[23] J. J. van der Bij, K. G. Chetyrkin, M. Faisst, G. Jikia and T. Seidensticker, *Three loop leading top mass contributions to the rho parameter*, *Phys. Lett.* **B498** (2001) 156–162, [hep-ph/0011373].

[24] M. Faisst, J. H. Kuhn, T. Seidensticker and O. Veretin, *Three loop top quark contributions to the rho parameter*, *Nucl. Phys.* **B665** (2003) 649–662, [hep-ph/0302275].

[25] G. F. Giudice, P. Paradisi and A. Strumia, *Indirect determinations of the top quark mass*, *JHEP* **11** (2015) 192, [1508.05332].

[26] M. Awramik, M. Czakon, A. Freitas and G. Weiglein, *Precise prediction for the W boson mass in the standard model*, *Phys. Rev.* **D69** (2004) 053006, [hep-ph/0311148].

[27] M. Awramik, M. Czakon and A. Freitas, *Electroweak two-loop corrections to the effective weak mixing angle*, *JHEP* **11** (2006) 048, [hep-ph/0608099].

[28] M. Awramik, M. Czakon, A. Freitas and B. A. Kniehl, *Two-loop electroweak fermionic corrections to sin**2 theta**b anti-b(eff)*, *Nucl. Phys.* **B813** (2009) 174–187, [0811.1364].

[29] S. Heinemeyer, W. Hollik and G. Weiglein, *Electroweak precision observables in the minimal supersymmetric standard model*, *Phys. Rept.* **425** (2006) 265–368, [hep-ph/0412214].

[30] D. Buttazzo, G. Degrassi, P. P. Giardino, G. F. Giudice, F. Sala, A. Salvio et al., *Investigating the near-criticality of the Higgs boson*, *JHEP* **12** (2013) 089, [1307.3536].

[31] J. Ellis, J. R. Espinosa, G. F. Giudice, A. Hoecker and A. Riotto, *The Probable Fate of the Standard Model*, *Phys. Lett.* **B679** (2009) 369–375, [0906.0954].

[32] G. Degrassi, S. Di Vita, J. Elias-Miro, J. R. Espinosa, G. F. Giudice, G. Isidori et al., *Higgs mass and vacuum stability in the Standard Model at NNLO*, *JHEP* **08** (2012) 098, [1205.6497].

[33] F. Bezrukov, M. Yu. Kalmykov, B. A. Kniehl and M. Shaposhnikov, *Higgs Boson Mass and New Physics*, *JHEP* **10** (2012) 140, [1205.2893].

[34] S. Alekhin, A. Djouadi and S. Moch, *The top quark and Higgs boson masses and the stability of the electroweak vacuum*, *Phys. Lett.* **B716** (2012) 214–219, [1207.0980].

[35] I. Masina, *Higgs boson and top quark masses as tests of electroweak vacuum stability*, *Phys. Rev.* **D87** (2013) 053001, [1209.0393].

[36] I. Yu. Kobzarev, L. B. Okun and M. B. Voloshin, *Bubbles in Metastable Vacuum*, *Sov. J. Nucl. Phys.* **20** (1975) 644–646.

[37] S. R. Coleman, *The Fate of the False Vacuum. 1. Semiclassical Theory*, *Phys. Rev.* **D15** (1977) 2929–2936.

[38] C. G. Callan, Jr. and S. R. Coleman, *The Fate of the False Vacuum. 2. First Quantum Corrections*, *Phys. Rev.* **D16** (1977) 1762–1768.

[39] ATLAS, CDF, CMS, D0 collaboration, R. Y. Peters, *Tevatron Top-Quark Combinations and World Top-Quark Mass Combination*, in *Proceedings, 7th International Workshop on Top Quark Physics (TOP2014): Cannes, France, September 28-October 3, 2014*, 2014. 1411.0820.

[40] M. Beneke, P. Marquard, P. Nason and M. Steinhauser, *On the ultimate uncertainty of the top quark pole mass*, 1605.03609.

[41] M. Beneke, *Renormalons*, *Phys. Rept.* **317** (1999) 1–142, [hep-ph/9807443].

[42] M. C. Smith and S. S. Willenbrock, *Top quark pole mass*, *Phys. Rev. Lett.* **79** (1997) 3825–3828, [hep-ph/9612329].

[43] R. Hempfling and B. A. Kniehl, *On the relation between the fermion pole mass and MS Yukawa coupling in the standard model*, *Phys. Rev.* **D51** (1995) 1386–1394, [hep-ph/9408313].

[44] P. A. Baikov, K. G. Chetyrkin and J. H. Kuehn, *Quark Mass and Field Anomalous Dimensions to $\mathcal{O}(\alpha_s^5)$*, *JHEP* **10** (2014) 076, [1402.6611].

[45] K. Melnikov and T. v. Ritbergen, *The Three loop relation between the MS-bar and the pole quark masses*, *Phys. Lett.* **B482** (2000) 99–108, [hep-ph/9912391].

[46] P. Marquard, A. V. Smirnov, V. A. Smirnov and M. Steinhauser, *Quark Mass Relations to Four-Loop Order in Perturbative QCD*, *Phys. Rev. Lett.* **114** (2015) 142002, [1502.01030].

[47] A. H. Hoang and T. Teubner, *Top quark pair production at threshold: Complete next-to-next-to-leading order relativistic corrections*, *Phys. Rev.* **D58** (1998) 114023, [hep-ph/9801397].

[48] K. Melnikov and A. Yelkhovsky, *Top quark production at threshold with O(alpha-s**2) accuracy*, *Nucl. Phys.* **B528** (1998) 59–72, [hep-ph/9802379].

[49] O. I. Yakovlev, *Top quark production near threshold: NNLO QCD correction*, *Phys. Lett.* **B457** (1999) 170–176, [hep-ph/9808463].

[50] M. Beneke, *A Quark mass definition adequate for threshold problems*, *Phys. Lett.* **B434** (1998) 115–125, [hep-ph/9804241].

[51] M. Beneke, A. Signer and V. A. Smirnov, *Top quark production near threshold and the top quark mass*, *Phys. Lett.* **B454** (1999) 137–146, [hep-ph/9903260].

[52] A. H. Hoang, Z. Ligeti and A. V. Manohar, *B decays in the upsilon expansion*, *Phys. Rev.* **D59** (1999) 074017, [hep-ph/9811239].

[53] A. H. Hoang and T. Teubner, *Top quark pair production close to threshold: Top mass, width and momentum distribution*, *Phys. Rev.* **D60** (1999) 114027, [hep-ph/9904468].

[54] K. Seidel, F. Simon, M. Tesar and S. Poss, *Top quark mass measurements at and above threshold at CLIC*, *Eur. Phys. J.* **C73** (2013) 2530, [1303.3758].

[55] T. Horiguchi, A. Ishikawa, T. Suehara, K. Fujii, Y. Sumino, Y. Kiyo et al., *Study of top quark pair production near threshold at the ILC*, 1310.0563.

[56] W. Fischler, *Quark - anti-Quark Potential in QCD*, *Nucl. Phys.* **B129** (1977) 157–174.

[57] A. Billoire, *How Heavy Must Be Quarks in Order to Build Coulombic q anti-q Bound States*, *Phys. Lett.* **B92** (1980) 343–347.

[58] M. Peter, *The Static potential in QCD: A Full two loop calculation*, *Nucl. Phys.* **B501** (1997) 471–494, [hep-ph/9702245].

[59] Y. Schroder, *The Static potential in QCD to two loops*, *Phys. Lett.* **B447** (1999) 321–326, [hep-ph/9812205].

[60] A. H. Hoang, A. Jain, I. Scimemi and I. W. Stewart, *Infrared Renormalization Group Flow for Heavy Quark Masses*, *Phys. Rev. Lett.* **101** (2008) 151602, [0803.4214].

[61] A. H. Hoang and I. W. Stewart, *Top Mass Measurements from Jets and the Tevatron Top-Quark Mass*, *Nucl. Phys. Proc. Suppl.* **185** (2008) 220–226, [0808.0222].

[62] A. B. Galtieri, F. Margaroli and I. Volobouev, *Precision measurements of the top quark mass from the Tevatron in the pre-LHC era*, *Rept. Prog. Phys.* **75** (2012) 056201, [1109.2163].

[63] S. Moch et al., *High precision fundamental constants at the TeV scale*, 1405.4781.

[64] D0 collaboration, Useful Diagrams of Top Signals and Backgrounds, http://www-d0.fnal.gov/Run2Physics/top/top_public_web_pages/top_feynman_diagrams.html.

[65] Particle Data Group collaboration, K. A. Olive et al., *Review of Particle Physics*, *Chin. Phys.* **C38** (2014) 090001.

[66] CMS collaboration, V. Khachatryan et al., *Measurement of the top quark mass using proton-proton data at* $\sqrt{(s)} = 7$ *and 8 TeV*, *Phys. Rev.* **D93** (2016) 072004, [1509.04044].

[67] CMS collaboration, *Projected improvement of the accuracy of top-quark mass measurements at the upgraded LHC*, .

[68] A. Buckley et al., *General-purpose event generators for LHC physics*, *Phys. Rept.* **504** (2011) 145–233, [1101.2599].

[69] J. M. Campbell, R. K. Ellis, P. Nason and E. Re, *Top-pair production and decay at NLO matched with parton showers*, *JHEP* **04** (2015) 114, [1412.1828].

[70] T. Jezo and P. Nason, *On the Treatment of Resonances in Next-to-Leading Order Calculations Matched to a Parton Shower*, *JHEP* **12** (2015) 065, [1509.09071].

[71] R. Frederix, S. Frixione, A. S. Papanastasiou, S. Prestel and P. Torrielli, *Off-shell single-top production at NLO matched to parton showers*, *JHEP* **06** (2016) 027, [1603.01178].

[72] C. S. Hill, J. R. Incandela and J. M. Lamb, *A Method for measurement of the top quark mass using the mean decay length of b hadrons in* $t\bar{t}$ *events*, *Phys. Rev.* **D71** (2005) 054029, [hep-ex/0501043].

[73] CDF collaboration, T. Aaltonen et al., *Measurements of the top-quark mass using charged particle tracking*, *Phys. Rev.* **D81** (2010) 032002, [0910.0969].

[74] CMS collaboration, *Measurement of the top quark mass using the B-hadron lifetime technique*, .

[75] ATLAS collaboration, *Measurement of the top quark mass in topologies enhanced with single top-quarks produced in the t-channel in* $\sqrt{s} = 8\,\text{TeV}$ *ATLAS data*, .

[76] CMS collaboration, *Measurement of the top quark mass from single-top production events*, .

[77] P. Baernreuther, M. Czakon and A. Mitov, *Percent Level Precision Physics at the Tevatron: First Genuine NNLO QCD Corrections to $q\bar{q} \to t\bar{t} + X$*, *Phys. Rev. Lett.* **109** (2012) 132001, [1204.5201].

[78] M. Czakon and A. Mitov, *NNLO corrections to top-pair production at hadron colliders: the all-fermionic scattering channels*, *JHEP* **12** (2012) 054, [1207.0236].

[79] M. Czakon and A. Mitov, *NNLO corrections to top pair production at hadron colliders: the quark-gluon reaction*, *JHEP* **01** (2013) 080, [1210.6832].

[80] M. Czakon, P. Fiedler and A. Mitov, *Total Top-Quark Pair-Production Cross Section at Hadron Colliders Through $O(\alpha_s^4)$*, *Phys. Rev. Lett.* **110** (2013) 252004, [1303.6254].

[81] M. Beneke, P. Falgari, S. Klein and C. Schwinn, *Hadronic top-quark pair production with NNLL threshold resummation*, *Nucl. Phys.* **B855** (2012) 695–741, [1109.1536].

[82] D0 collaboration, V. M. Abazov et al., *Determination of the pole and $\overline{MS}$ masses of the top quark from the $t\bar{t}$ cross section*, *Phys. Lett.* **B703** (2011) 422–427, [1104.2887].

[83] CMS collaboration, S. Chatrchyan et al., *Determination of the top-quark pole mass and strong coupling constant from the t t-bar production cross section in pp collisions at $\sqrt{s} = 7$ TeV*, *Phys. Lett.* **B728** (2014) 496–517, [1307.1907].

[84] S. Alekhin, J. Blumlein and S. Moch, *The ABM parton distributions tuned to LHC data*, *Phys. Rev.* **D89** (2014) 054028, [1310.3059].

[85] ATLAS collaboration, G. Aad et al., *Measurement of the $t\bar{t}$ production cross-section using $e\mu$ events with b -tagged jets in pp collisions at $\sqrt{s} = 7$ and 8 TeV with the ATLAS detector*, *Eur. Phys. J.* **C74** (2014) 3109, [1406.5375].

[86] CMS collaboration, V. Khachatryan et al., *Measurement of the $\mathrm{t\bar{t}}$ production cross section in the $\mathrm{e\mu}$ channel in proton-proton collisions at $\sqrt{s} = 7$ and 8 TeV*, *JHEP* **08** (2016) 029, [1603.02303].

[87] M. Czakon and A. Mitov, *Top++: A Program for the Calculation of the Top-Pair Cross-Section at Hadron Colliders*, *Comput. Phys. Commun.* **185** (2014) 2930, [1112.5675].

[88] M. Beneke, P. Falgari, S. Klein, J. Piclum, C. Schwinn, M. Ubiali et al., *Inclusive Top-Pair Production Phenomenology with TOPIXS*, *JHEP* **07** (2012) 194, [1206.2454].

[89] M. Aliev, H. Lacker, U. Langenfeld, S. Moch, P. Uwer and M. Wiedermann, *HATHOR: HAdronic Top and Heavy quarks crOss section calculatoR*, *Comput. Phys. Commun.* **182** (2011) 1034–1046, [1007.1327].

[90] NNPDF collaboration, R. D. Ball et al., *Parton distributions for the LHC Run II*, *JHEP* **04** (2015) 040, [1410.8849].

[91] W. Bernreuther, M. Fuecker and Z.-G. Si, *Weak interaction corrections to hadronic top quark pair production*, *Phys. Rev.* **D74** (2006) 113005, [hep-ph/0610334].

[92] F. Jegerlehner, M. Yu. Kalmykov and B. A. Kniehl, *On the difference between the pole and the $\overline{MS}$ masses of the top quark at the electroweak scale*, *Phys. Lett.* **B722** (2013) 123–129, [1212.4319].

[93] M. Beneke, Y. Kiyo, P. Marquard, A. Penin, J. Piclum and M. Steinhauser, *Next-to-Next-to-Next-to-Leading Order QCD Prediction for the Top Antitop S-Wave Pair Production Cross Section Near Threshold in e^+e^- Annihilation*, *Phys. Rev. Lett.* **115** (2015) 192001, [1506.06864].

[94] M. Burns, K. Kong, K. T. Matchev and M. Park, *Using Subsystem MT2 for Complete Mass Determinations in Decay Chains with Missing Energy at Hadron Colliders*, *JHEP* **03** (2009) 143, [0810.5576].

[95] P. Konar, K. Kong, K. T. Matchev and M. Park, *Superpartner Mass Measurement Technique using 1D Orthogonal Decompositions of the Cambridge Transverse Mass Variable M_{T2}*, *Phys. Rev. Lett.* **105** (2010) 051802, [0910.3679].

[96] K. T. Matchev and M. Park, *A General method for determining the masses of semi-invisibly decaying particles at hadron colliders*, *Phys. Rev. Lett.* **107** (2011) 061801, [0910.1584].

[97] CMS collaboration, S. Chatrchyan et al., *Measurement of masses in the $t\bar{t}$ system by kinematic endpoints in pp collisions at $\sqrt{s} = 7$ TeV*, *Eur. Phys. J.* **C73** (2013) 2494, [1304.5783].

[98] M. Beneke et al., *Top quark physics*, in *1999 CERN Workshop on standard model physics (and more) at the LHC, CERN, Geneva, Switzerland, 25-26 May: Proceedings*, pp. 419–529, 2000. hep-ph/0003033.

[99] D. Chakraborty, J. Konigsberg and D. L. Rainwater, *Review of top quark physics*, *Ann. Rev. Nucl. Part. Sci.* **53** (2003) 301–351, [hep-ph/0303092].

[100] W. Wagner, *Top quark physics in hadron collisions*, *Rept. Prog. Phys.* **68** (2005) 2409–2494, [hep-ph/0507207].

[101] A. Quadt, *Top quark physics at hadron colliders*, *Eur. Phys. J.* **C48** (2006) 835–1000.

[102] W. Bernreuther, *Top quark physics at the LHC*, *J. Phys.* **G35** (2008) 083001, [0805.1333].

[103] A. Kharchilava, *Top mass determination in leptonic final states with J/ψ*, *Phys. Lett.* **B476** (2000) 73–78, [hep-ph/9912320].

[104] R. Chierici and A. Dierlamm, *Determination of the top mass with exclusive events t —> W b —> l nu J/psi X*, .

[105] CMS collaboration, V. Khachatryan et al., *Measurement of the mass of the top quark in decays with a J/psi meson in pp collisions at 8 TeV*, 1608.03560.

[106] G. Corcella, M. L. Mangano and M. H. Seymour, *Jet activity in t anti-t events and top mass reconstruction at hadron colliders*, *JHEP* **07** (2000) 004, [hep-ph/0004179].

[107] G. Corcella and F. Mescia, *A Phenomenological Study of Bottom Quark Fragmentation in Top Quark Decay*, *Eur. Phys. J.* **C65** (2010) 171–180, [0907.5158].

[108] S. Biswas, K. Melnikov and M. Schulze, *Next-to-leading order QCD effects and the top quark mass measurements at the LHC*, *JHEP* **08** (2010) 048, [1006.0910].

[109] CMS collaboration, *Determination of the top-quark mass from the m(lb) distribution in dileptonic ttbar events at sqrt(s) = 8 TeV*, .

[110] J. M. Campbell and R. K. Ellis, *MCFM for the Tevatron and the LHC*, *Nucl. Phys. Proc. Suppl.* **205-206** (2010) 10–15, [1007.3492].

[111] S. Badger, R. Sattler and V. Yundin, *One-Loop Helicity Amplitudes for $t\bar{t}$ Production at Hadron Colliders*, *Phys. Rev.* **D83** (2011) 074020, [1101.5947].

[112] J. Alwall, M. Herquet, F. Maltoni, O. Mattelaer and T. Stelzer, *MadGraph 5 : Going Beyond*, *JHEP* **06** (2011) 128, [1106.0522].

[113] T. Sjostrand, S. Mrenna and P. Z. Skands, *PYTHIA 6.4 Physics and Manual*, *JHEP* **05** (2006) 026, [hep-ph/0603175].

[114] S. Alioli, P. Fernandez, J. Fuster, A. Irles, S.-O. Moch, P. Uwer et al., *A new observable to measure the top-quark mass at hadron colliders*, *Eur. Phys. J.* **C73** (2013) 2438, [1303.6415].

[115] S. Dittmaier, P. Uwer and S. Weinzierl, *NLO QCD corrections to t anti-t + jet production at hadron colliders*, *Phys. Rev. Lett.* **98** (2007) 262002, [hep-ph/0703120].

[116] S. Dittmaier, P. Uwer and S. Weinzierl, *Hadronic top-quark pair production in association with a hard jet at next-to-leading order QCD: Phenomenological studies for the Tevatron and the LHC*, *Eur. Phys. J.* **C59** (2009) 625–646, [0810.0452].

[117] K. Melnikov and M. Schulze, *NLO QCD corrections to top quark pair production in association with one hard jet at hadron colliders*, *Nucl. Phys.* **B840** (2010) 129–159, [1004.3284].

[118] S. Alioli, S.-O. Moch and P. Uwer, *Hadronic top-quark pair-production with one jet and parton showering*, *JHEP* **01** (2012) 137, [1110.5251].

[119] A. Kardos, C. Papadopoulos and Z. Trocsanyi, *Top quark pair production in association with a jet with NLO parton showering*, *Phys. Lett.* **B705** (2011) 76–81, [1101.2672].

[120] ATLAS collaboration, G. Aad et al., *Determination of the top-quark pole mass using $t\bar{t}$ + 1-jet events collected with the ATLAS experiment in 7 TeV pp collisions*, *JHEP* **10** (2015) 121, [1507.01769].

[121] CMS collaboration, *Determination of the normalised invariant mass distribution of $t\bar{t}$+jet and extraction of the top quark mass*, .

[122] D0 collaboration, V. M. Abazov et al., *Direct measurement of the mass difference between top and antitop quarks*, *Phys. Rev.* **D84** (2011) 052005, [1106.2063].

[123] CDF collaboration, T. Aaltonen et al., *Measurement of the mass difference between top and antitop quarks*, *Phys. Rev.* **D87** (2013) 052013, [1210.6131].

[124] CMS collaboration, S. Chatrchyan et al., *Measurement of the mass difference between top and antitop quarks*, *JHEP* **06** (2012) 109, [1204.2807].

[125] ATLAS collaboration, G. Aad et al., *Measurement of the mass difference between top and anti-top quarks in pp collisions at $\sqrt(s) = 7$ TeV using the ATLAS detector*, *Phys. Lett.* **B728** (2014) 363–379, [1310.6527].

[126] CMS collaboration, *Measurement of the top - antitop mass difference in pp collisions at sqrt(s) = 8 TeV*, .

[127] D0 collaboration, V. M. Abazov et al., *Precision measurement of the ratio $B(t \to Wb)/B(t \to Wq)$ and Extraction of V_{tb}*, *Phys. Rev. Lett.* **107** (2011) 121802, [1106.5436].

[128] CDF collaboration, T. Aaltonen et al., *Measurement of $R = \mathcal{B}(t \to Wb)/\mathcal{B}(t \to Wq)$ in Top-quark-pair Decays using Lepton+jets Events and the Full CDF Run II Data set*, *Phys. Rev.* **D87** (2013) 111101, [1303.6142].

[129] CDF collaboration, T. A. Aaltonen et al., *Measurement of $B(t \to Wb)/B(t \to Wq)$ in Top-Quark-Pair Decays Using Dilepton Events and the Full CDF Run II Data Set*, *Phys. Rev. Lett.* **112** (2014) 221801, [1404.3392].

[130] CMS collaboration, V. Khachatryan et al., *Measurement of the ratio $\mathcal{B}(t \to Wb)/\mathcal{B}(t \to Wq)$ in pp collisions at $\sqrt{s} = 8$ TeV*, *Phys. Lett.* **B736** (2014) 33–57, [1404.2292].

[131] M. Jezabek and J. H. Kuhn, *The Top width: Theoretical update*, *Phys. Rev.* **D48** (1993) R1910–R1913, [hep-ph/9302295].

[132] A. Denner and T. Sack, *The Top width*, *Nucl. Phys.* **B358** (1991) 46–58.

[133] G. Eilam, R. R. Mendel, R. Migneron and A. Soni, *Radiative corrections to top quark decay*, *Phys. Rev. Lett.* **66** (1991) 3105–3108.

[134] M. Jezabek and J. H. Kuhn, *QCD Corrections to Semileptonic Decays of Heavy Quarks*, *Nucl. Phys.* **B314** (1989) 1–6.

[135] A. Czarnecki and K. Melnikov, *Two loop QCD corrections to top quark width*, *Nucl. Phys.* **B544** (1999) 520–531, [hep-ph/9806244].

[136] K. G. Chetyrkin, R. Harlander, T. Seidensticker and M. Steinhauser, *Second order QCD corrections to Gamma(t —> W b)*, *Phys. Rev.* **D60** (1999) 114015, [hep-ph/9906273].

[137] I. R. Blokland, A. Czarnecki, M. Slusarczyk and F. Tkachov, *Heavy to light decays with a two loop accuracy*, *Phys. Rev. Lett.* **93** (2004) 062001, [hep-ph/0403221].

[138] CDF collaboration, T. Aaltonen et al., *First Direct Bound on the Total Width of the Top Quark in $p\bar{p}$ Collisions at $\sqrt{s} = 1.96$-TeV*, *Phys. Rev. Lett.* **102** (2009) 042001, [0808.2167].

[139] CDF collaboration, T. A. Aaltonen et al., *Direct Measurement of the Total Decay Width of the Top Quark*, *Phys. Rev. Lett.* **111** (2013) 202001, [1308.4050].

[140] C. P. Yuan, *Physics of top quark at the Tevatron*, *AIP Conf. Proc.* **359** (1996) 383–390, [hep-ph/9604434].

[141] D0 collaboration, V. M. Abazov et al., *An Improved determination of the width of the top quark*, *Phys. Rev.* **D85** (2012) 091104, [1201.4156].

[142] CDF, D0 collaboration, T. Aaltonen et al., *Combination of CDF and D0 measurements of the W boson helicity in top quark decays*, *Phys. Rev.* **D85** (2012) 071106, [1202.5272].

[143] ATLAS collaboration, *Combination of the ATLAS and CMS measurements of the W-boson polarization in top-quark decays*, .

[144] CMS collaboration, S. Chatrchyan et al., *Measurement of the W-boson helicity in top-quark decays from $t\bar{t}$ production in lepton+jets events in pp collisions at $\sqrt{s} = 7$ TeV*, *JHEP* **10** (2013) 167, [1308.3879].

[145] CMS collaboration, V. Khachatryan et al., *Measurement of the W boson helicity in events with a single reconstructed top quark in pp collisions at $\sqrt{s} = 8$ TeV*, *JHEP* **01** (2015) 053, [1410.1154].

[146] A. Czarnecki, J. G. Korner and J. H. Piclum, *Helicity fractions of W bosons from top quark decays at NNLO in QCD*, *Phys. Rev.* **D81** (2010) 111503, [1005.2625].

[147] W. J. Stirling and E. Vryonidou, *Effect of spin-3/2 top quark excitation on $t\bar{t}$ production at the LHC*, *JHEP* **01** (2012) 055, [1110.1565].

[148] D. Chang, W.-F. Chang and E. Ma, *Alternative interpretation of the Tevatron top events*, *Phys. Rev.* **D59** (1999) 091503, [hep-ph/9810531].

[149] D. Choudhury, T. M. P. Tait and C. E. M. Wagner, *Beautiful mirrors and precision electroweak data*, *Phys. Rev.* **D65** (2002) 053002, [hep-ph/0109097].

[150] CDF collaboration, T. Aaltonen et al., *Exclusion of exotic top-like quarks with -4/3 electric charge using jet-charge tagging in single-lepton ttbar events at CDF*, *Phys. Rev.* **D88** (2013) 032003, [1304.4141].

[151] D0 collaboration, V. M. Abazov et al., *Measurement of the Electric Charge of the Top Quark in $t\bar{t}$ Events*, *Phys. Rev.* **D90** (2014) 051101, [1407.4837].

[152] CMS collaboration, *Constraints on the Top-Quark Charge from Top-Pair Events*, .

[153] ATLAS collaboration, G. Aad et al., *Measurement of the top quark charge in pp collisions at $\sqrt{s} = 7$ TeV with the ATLAS detector*, *JHEP* **11** (2013) 031, [1307.4568].

[154] CDF collaboration, T. Aaltonen et al., *Evidence for $t\bar{t}\gamma$ Production and Measurement of $\sigma_{t\bar{t}\gamma}/\sigma_{t\bar{t}}$*, *Phys. Rev.* **D84** (2011) 031104, [1106.3970].

[155] ATLAS collaboration, *Measurement of the inclusive t tbar gamma cross section with the ATLAS detector*, .

[156] CMS collaboration, *Measurement of the inclusive top-quark pair + photon production cross section in the muon + jets channel in pp collisions at 8 TeV*, .

[157] ATLAS collaboration, G. Aad et al., *Observation of top-quark pair production in association with a photon and measurement of the $t\bar{t}\gamma$ production cross section in pp collisions at $\sqrt{s} = 7$ TeV using the ATLAS detector*, *Phys. Rev.* **D91** (2015) 072007, [1502.00586].

[158] CMS collaboration, S. Chatrchyan et al., *Measurement of associated production of vector bosons and top quark-antiquark pairs at sqrt(s) = 7 TeV*, *Phys. Rev. Lett.* **110** (2013) 172002, [1303.3239].

[159] CMS collaboration, V. Khachatryan et al., *Measurement of top quark-antiquark pair production in association with a W or Z boson in pp collisions at $\sqrt{s} = 8$ TeV*, *Eur. Phys. J.* **C74** (2014) 3060, [1406.7830].

[160] CMS collaboration, V. Khachatryan et al., *Observation of top quark pairs produced in association with a vector boson in pp collisions at $\sqrt{s} = 8$ TeV*, *JHEP* **01** (2016) 096, [1510.01131].

[161] ATLAS collaboration, G. Aad et al., *Measurement of the $t\bar{t}W$ and $t\bar{t}Z$ production cross sections in pp collisions at $\sqrt{s} = 8$ TeV with the ATLAS detector*, *JHEP* **11** (2015) 172, [1509.05276].

[162] D. Schaile and P. M. Zerwas, *Measuring the weak isospin of B quarks*, *Phys. Rev.* **D45** (1992) 3262–3265.

[163] CDF, D0 collaboration, T. A. Aaltonen et al., *Combination of measurements of the top-quark pair production cross section from the Tevatron Collider*, *Phys. Rev.* **D89** (2014) 072001, [1309.7570].

[164] CDF collaboration, T. Aaltonen et al., *Measurement of the Top Quark Mass and $p\bar{p}$ -> $t\bar{t}$ Cross Section in the All-Hadronic Mode with the CDFII Detector*, *Phys. Rev.* **D81** (2010) 052011, [1002.0365].

[165] CDF collaboration, T. Aaltonen et al., *First Measurement of the Ratio $\sigma_(t\bar{t})/\sigma_(Z/\gamma * * \to \ell\ell)$ and Precise Extraction of the $t\bar{t}$ Cross Section*, *Phys. Rev. Lett.* **105** (2010) 012001, [1004.3224].

[166] CDF collaboration, T. Aaltonen et al., *Measurements of the Top-quark Mass and the $t\bar{t}$ Cross Section in the Hadronic τ+ Jets Decay Channel at $\sqrt{s} = 1.96$ TeV*, *Phys. Rev. Lett.* **109** (2012) 192001, [1208.5720].

[167] CDF collaboration, T. Aaltonen et al., *Measurement of the top-quark pair production cross-section in events with two leptons and bottom-quark jets using the full CDF data set*, *Phys. Rev.* **D88** (2013) 091103, [1304.7961].

[168] CDF collaboration, T. A. Aaltonen et al., *Study of Top-Quark Production and Decays involving a Tau Lepton at CDF and Limits on a Charged-Higgs Boson Contribution*, *Phys. Rev.* **D89** (2014) 091101, [1402.6728].

[169] D0 collaboration, V. M. Abazov et al., *Measurement of the $t\bar{t}$ cross section using high-multiplicity jet events*, *Phys. Rev.* **D82** (2010) 032002, [0911.4286].

[170] D0 collaboration, V. M. Abazov et al., *Measurement of $t\bar{t}$ production in the tau + jets topology using $p\bar{p}$ collisions at sqrts = 1.96 TeV*, *Phys. Rev.* **D82** (2010) 071102, [1008.4284].

[171] D0 collaboration, V. M. Abazov et al., *Measurement of the top quark pair production cross section in the lepton+jets channel in proton-antiproton collisions at $\sqrt{s}$=1.96 TeV*, *Phys. Rev.* **D84** (2011) 012008, [1101.0124].

[172] D0 collaboration, V. M. Abazov et al., *Measurement of the $t\bar{t}$ production cross section using dilepton events in $p\bar{p}$ collisions*, *Phys. Lett.* **B704** (2011) 403–410, [1105.5384].

[173] CMS collaboration, V. Khachatryan et al., *First Measurement of the Cross Section for Top-Quark Pair Production in Proton-Proton Collisions at $\sqrt{s} = 7$ TeV*, *Phys. Lett.* **B695** (2011) 424–443, [1010.5994].

[174] ATLAS collaboration, G. Aad et al., *Measurement of the top quark-pair production cross section with ATLAS in pp collisions at $\sqrt{s} = 7$ TeV*, *Eur. Phys. J.* **C71** (2011) 1577, [1012.1792].

[175] CMS collaboration, S. Chatrchyan et al., *Measurement of the top quark pair production cross section in pp collisions at $\sqrt{s} = 7$ TeV in dilepton final states containing a τ*, *Phys. Rev.* **D85** (2012) 112007, [1203.6810].

[176] CMS collaboration, S. Chatrchyan et al., *Measurement of the $t\bar{t}$ production cross section in the dilepton channel in pp collisions at $\sqrt{s} = 7$ TeV*, *JHEP* **11** (2012) 067, [1208.2671].

[177] CMS collaboration, S. Chatrchyan et al., *Measurement of the $t\bar{t}$ production cross section in pp collisions at $\sqrt{s} = 7$ TeV with lepton + jets final states*, *Phys. Lett.* **B720** (2013) 83–104, [1212.6682].

[178] CMS collaboration, S. Chatrchyan et al., *Measurement of the top-antitop production cross section in the tau+jets channel in pp collisions at sqrt(s) = 7 TeV*, *Eur. Phys. J.* **C73** (2013) 2386, [1301.5755].

[179] CMS collaboration, S. Chatrchyan et al., *Measurement of the $t\bar{t}$ production cross section in the all-jet final state in pp collisions at $\sqrt{s} = 7$ TeV*, *JHEP* **05** (2013) 065, [1302.0508].

[180] CMS collaboration, S. Chatrchyan et al., *Measurement of the $t\bar{t}$ production cross section in the dilepton channel in pp collisions at $\sqrt{s} = 8$ TeV*, *JHEP* **02** (2014) 024, [1312.7582].

[181] CMS collaboration, V. Khachatryan et al., *Measurement of the $t\bar{t}$ production cross section in pp collisions at $\sqrt{s} = 8$ TeV in dilepton final states containing one τ lepton*, *Phys. Lett.* **B739** (2014) 23–43, [1407.6643].

[182] CMS collaboration, *Combination of ATLAS and CMS top quark pair cross section measurements in the emu final state using proton-proton collisions at 8 TeV*, .

[183] CMS collaboration, *Measurement of the inclusive and differential tt production cross sections in lepton + jets final states at 13 TeV*, .

[184] CMS collaboration, V. Khachatryan et al., *Measurement of the $\mathrm{t\bar{t}}$ production cross section in the all-jets final state in pp collisions at $\sqrt{s} = 8$ TeV*, *Eur. Phys. J.* **C76** (2016) 128, [1509.06076].

[185] CMS collaboration, V. Khachatryan et al., *Measurement of the top quark pair production cross section in proton-proton collisions at $\sqrt{(s)} = 13$ TeV*, *Phys. Rev. Lett.* **116** (2016) 052002, [1510.05302].

[186] CMS collaboration, V. Khachatryan et al., *Measurements of the $\mathrm{t\bar{t}}$ production cross section in lepton+jets final states in pp collisions at 8 TeV and ratio of 8 to 7 TeV cross sections*, *Submitted to: Eur. Phys. J. C* (2016) , [1602.09024].

[187] CMS collaboration, *A measurement of the inclusive tbart production cross section in proton-proton collisions at sqrts=13 TeV using events with one isolated charged lepton and at least one jet*, .

[188] CMS collaboration, *Measurement of the $\mathrm{t\bar{t}}$ production cross section at 13 TeV in the all-jets final state*, .

[189] ATLAS collaboration, G. Aad et al., *Measurement of the cross section for top-quark pair production in pp collisions at $\sqrt{s} = 7$ TeV with the ATLAS detector using final states with two high-pt leptons*, *JHEP* **05** (2012) 059, [1202.4892].

[190] ATLAS collaboration, *Measurement of the $t\bar{t}$ production cross section in the all-hadronic channel in ATLAS with $\sqrt{s} = 7$ TeV data*, .

[191] ATLAS collaboration, *Measurement of the top quark pair production cross-section with ATLAS in pp collisions at $\sqrt{s} = 7$ TeV in the single-lepton channel using semileptonic b decays*, .

[192] ATLAS collaboration, G. Aad et al., *Measurement of the top quark pair cross section with ATLAS in pp collisions at $\sqrt{s} =$ 7 TeV using final states with an electron or a muon and a hadronically decaying τ lepton*, *Phys. Lett.* **B717** (2012) 89–108, [1205.2067].

[193] ATLAS collaboration, G. Aad et al., *Measurement of the ttbar production cross section in the tau+jets channel using the ATLAS detector*, *Eur. Phys. J.* **C73** (2013) 2328, [1211.7205].

[194] ATLAS collaboration, G. Aad et al., *Simultaneous measurements of the $t\bar{t}$, W^+W^-, and $Z/\gamma^* \to \tau\tau$ production cross-sections in pp collisions at $\sqrt{s} = 7$ TeV with the ATLAS detector*, *Phys. Rev.* **D91** (2015) 052005, [1407.0573].

[195] ATLAS collaboration, G. Aad et al., *Measurement of the top pair production cross section in 8 TeV proton-proton collisions using kinematic information in the lepton+jets final state with ATLAS*, *Phys. Rev.* **D91** (2015) 112013, [1504.04251].

[196] ATLAS collaboration, *Measurements of the $t\bar{t}$ production cross-section in the dilepton and lepton-plus-jets channels and of the ratio of the $t\bar{t}$ and Z boson cross-sections in pp collisions at $\sqrt{s} = 13$ TeV with the ATLAS detector*, .

[197] ATLAS collaboration, M. Aaboud et al., *Measurement of the $t\bar{t}$ production cross-section using $e\mu$ events with b-tagged jets in pp collisions at $\sqrt{s}$=13 TeV with the ATLAS detector*, 1606.02699.

[198] CDF collaboration, A. Abulencia et al., *Search for charged Higgs bosons from top quark decays in $p\bar{p}$ collisions at $\sqrt{s} =$ 1.96-TeV.*, *Phys. Rev. Lett.* **96** (2006) 042003, [hep-ex/0510065].

[199] D0 collaboration, V. M. Abazov et al., *Combination of t anti-t cross section measurements and constraints on the mass of the top quark and its decays into charged Higgs bosons*, *Phys. Rev.* **D80** (2009) 071102, [0903.5525].

[200] ATLAS collaboration, G. Aad et al., *Search for charged Higgs bosons through the violation of lepton universality in $t\bar{t}$ events using pp collision data at $\sqrt{s} = 7$ TeV with the ATLAS experiment*, *JHEP* **03** (2013) 076, [1212.3572].

[201] CMS collaboration, S. Chatrchyan et al., *Search for a light charged Higgs boson in top quark decays in pp collisions at $\sqrt{s} = 7$ TeV*, *JHEP* **07** (2012) 143, [1205.5736].

[202] ATLAS collaboration, G. Aad et al., *Search for charged Higgs bosons decaying via $H^+ \to \tau\nu$ in top quark pair events using pp collision data at $\sqrt{s} = 7$ TeV with the ATLAS detector*, *JHEP* **06** (2012) 039, [1204.2760].

[203] ATLAS collaboration, G. Aad et al., *Search for a light charged Higgs boson in the decay channel $H^+ \to c\bar{s}$ in $t\bar{t}$ events using pp collisions at $\sqrt{s} = 7$ TeV with the ATLAS detector*, *Eur. Phys. J.* **C73** (2013) 2465, [1302.3694].

[204] ATLAS collaboration, G. Aad et al., *Search for charged Higgs bosons decaying via $H^\pm \to \tau^\pm\nu$ in fully hadronic final states using pp collision data at $\sqrt{s} = 8$ TeV with the ATLAS detector*, *JHEP* **03** (2015) 088, [1412.6663].

[205] M. Czakon, A. Mitov, M. Papucci, J. T. Ruderman and A. Weiler, *Closing the stop gap*, *Phys. Rev. Lett.* **113** (2014) 201803, [1407.1043].

[206] CMS collaboration, V. Khachatryan et al., *Search for a charged Higgs boson in pp collisions at $\sqrt{s} = 8$ TeV*, *JHEP* **11** (2015) 018, [1508.07774].

[207] CMS collaboration, V. Khachatryan et al., *Search for a light charged Higgs boson decaying to $c\bar{s}$ in pp collisions at $\sqrt{s} = 8$ TeV*, *JHEP* **12** (2015) 178, [1510.04252].

[208] V. N. Gribov and L. N. Lipatov, *Deep inelastic e p scattering in perturbation theory*, *Sov. J. Nucl. Phys.* **15** (1972) 438–450.

[209] Y. L. Dokshitzer, *Calculation of the Structure Functions for Deep Inelastic Scattering and e+ e- Annihilation by Perturbation Theory in Quantum Chromodynamics.*, *Sov. Phys. JETP* **46** (1977) 641–653.

[210] G. Altarelli and G. Parisi, *Asymptotic Freedom in Parton Language*, *Nucl. Phys.* **B126** (1977) 298–318.

[211] P. Nason, S. Dawson and R. K. Ellis, *The Total Cross-Section for the Production of Heavy Quarks in Hadronic Collisions*, *Nucl. Phys.* **B303** (1988) 607–633.

[212] W. Beenakker, H. Kuijf, W. L. van Neerven and J. Smith, *QCD Corrections to Heavy Quark Production in p anti-p Collisions*, *Phys. Rev.* **D40** (1989) 54–82.

[213] M. Czakon and A. Mitov, *Inclusive Heavy Flavor Hadroproduction in NLO QCD: The Exact Analytic Result*, *Nucl. Phys.* **B824** (2010) 111–135, [0811.4119].

[214] S. Catani, M. L. Mangano, P. Nason and L. Trentadue, *The Top cross-section in hadronic collisions*, *Phys. Lett.* **B378** (1996) 329–336, [hep-ph/9602208].

[215] S. Catani, M. L. Mangano, P. Nason and L. Trentadue, *The Resummation of soft gluons in hadronic collisions*, *Nucl. Phys.* **B478** (1996) 273–310, [hep-ph/9604351].

[216] R. Bonciani, S. Catani, M. L. Mangano and P. Nason, *NLL resummation of the heavy quark hadroproduction cross-section*, *Nucl. Phys.* **B529** (1998) 424–450, [hep-ph/9801375].

[217] M. Czakon and A. Mitov, *On the Soft-Gluon Resummation in Top Quark Pair Production at Hadron Colliders*, *Phys. Lett.* **B680** (2009) 154–158, [0812.0353].

[218] S. Moch and P. Uwer, *Theoretical status and prospects for top-quark pair production at hadron colliders*, *Phys. Rev.* **D78** (2008) 034003, [0804.1476].

[219] M. Czakon, A. Mitov and G. F. Sterman, *Threshold Resummation for Top-Pair Hadroproduction to Next-to-Next-to-Leading Log*, *Phys. Rev.* **D80** (2009) 074017, [0907.1790].

[220] M. Cacciari, M. Czakon, M. Mangano, A. Mitov and P. Nason, *Top-pair production at hadron colliders with next-to-next-to-leading logarithmic soft-gluon resummation*, *Phys. Lett.* **B710** (2012) 612–622, [1111.5869].

[221] N. Kidonakis, E. Laenen, S. Moch and R. Vogt, *Sudakov resummation and finite order expansions of heavy quark hadroproduction cross-sections*, *Phys. Rev.* **D64** (2001) 114001, [hep-ph/0105041].

[222] N. Kidonakis and R. Vogt, *The Theoretical top quark cross section at the Tevatron and the LHC*, *Phys. Rev.* **D78** (2008) 074005, [0805.3844].

[223] N. Kidonakis, *Next-to-next-to-leading soft-gluon corrections for the top quark cross section and transverse momentum distribution*, *Phys. Rev.* **D82** (2010) 114030, [1009.4935].

[224] N. Kidonakis, *NNLL threshold resummation for top-pair and single-top production*, *Phys. Part. Nucl.* **45** (2014) 714–722, [1210.7813].

[225] V. Ahrens, A. Ferroglia, M. Neubert, B. D. Pecjak and L. L. Yang, *Renormalization-Group Improved Predictions for Top-Quark Pair Production at Hadron Colliders*, *JHEP* **09** (2010) 097, [1003.5827].

[226] V. Ahrens, A. Ferroglia, M. Neubert, B. D. Pecjak and L.-L. Yang, *RG-improved single-particle inclusive cross sections and forward-backward asymmetry in $t\bar{t}$ production at hadron colliders*, *JHEP* **09** (2011) 070, [1103.0550].

[227] V. Ahrens, A. Ferroglia, M. Neubert, B. D. Pecjak and L. L. Yang, *Precision predictions for the t+t(bar) production cross section at hadron colliders*, *Phys. Lett.* **B703** (2011) 135–141, [1105.5824].

[228] N. Kidonakis and B. D. Pecjak, *Top-quark production and QCD*, *Eur. Phys. J.* **C72** (2012) 2084, [1108.6063].

[229] S. Moch, P. Uwer and A. Vogt, *On top-pair hadro-production at next-to-next-to-leading order*, *Phys. Lett.* **B714** (2012) 48–54, [1203.6282].

[230] M. Beneke, M. Czakon, P. Falgari, A. Mitov and C. Schwinn, *Threshold expansion of the gg(qq-bar) —> QQ-bar + X cross section at O(alpha(s)**4)*, *Phys. Lett.* **B690** (2010) 483–490, [0911.5166].

[231] A. D. Martin, W. J. Stirling, R. S. Thorne and G. Watt, *Parton distributions for the LHC*, *Eur. Phys. J.* **C63** (2009) 189–285, [0901.0002].

[232] M. Czakon, *A novel subtraction scheme for double-real radiation at NNLO*, *Phys. Lett.* **B693** (2010) 259–268, [1005.0274].

[233] M. Czakon, *Double-real radiation in hadronic top quark pair production as a proof of a certain concept*, *Nucl. Phys.* **B849** (2011) 250–295, [1101.0642].

[234] P. Baernreuther, M. Czakon and P. Fiedler, *Virtual amplitudes and threshold behaviour of hadronic top-quark pair-production cross sections*, *JHEP* **02** (2014) 078, [1312.6279].

[235] N. Kidonakis, *NNNLO soft-gluon corrections for the top-antitop pair production cross section*, *Phys. Rev.* **D90** (2014) 014006, [1405.7046].

[236] C. Muselli, M. Bonvini, S. Forte, S. Marzani and G. Ridolfi, *Top Quark Pair Production beyond NNLO*, *JHEP* **08** (2015) 076, [1505.02006].

[237] W. Hollik and M. Kollar, *NLO QED contributions to top-pair production at hadron collider*, *Phys. Rev.* **D77** (2008) 014008, [0708.1697].

[238] W. Beenakker, A. Denner, W. Hollik, R. Mertig, T. Sack and D. Wackeroth, *Electroweak one loop contributions to top pair production in hadron colliders*, *Nucl. Phys.* **B411** (1994) 343–380.

[239] W. Bernreuther, M. Fuecker and Z. G. Si, *Mixed QCD and weak corrections to top quark pair production at hadron colliders*, *Phys. Lett.* **B633** (2006) 54–60, [hep-ph/0508091].

[240] J. H. Kuhn, A. Scharf and P. Uwer, *Electroweak corrections to top-quark pair production in quark-antiquark annihilation*, *Eur. Phys. J.* **C45** (2006) 139–150, [hep-ph/0508092].

[241] J. H. Kuhn, A. Scharf and P. Uwer, *Electroweak effects in top-quark pair production at hadron colliders*, *Eur. Phys. J.* **C51** (2007) 37–53, [hep-ph/0610335].

[242] S. Moretti, M. R. Nolten and D. A. Ross, *Weak corrections to gluon-induced top-antitop hadro-production*, *Phys. Lett.* **B639** (2006) 513–519, [hep-ph/0603083].

[243] W. Bernreuther, M. Fucker and Z.-G. Si, *Weak interaction corrections to hadronic top quark pair production: Contributions from quark-gluon and b anti-b induced reactions*, *Phys. Rev.* **D78** (2008) 017503, [0804.1237].

[244] A. Denner, S. Dittmaier, M. Roth and D. Wackeroth, *Predictions for all processes e+ e- —> 4 fermions + gamma*, *Nucl. Phys.* **B560** (1999) 33–65, [hep-ph/9904472].

[245] A. Denner, S. Dittmaier, M. Roth and L. H. Wieders, *Electroweak corrections to charged-current e+ e- —> 4 fermion processes: Technical details and further results*, *Nucl. Phys.* **B724** (2005) 247–294, [hep-ph/0505042].

[246] A. Denner and J.-N. Lang, *The Complex-Mass Scheme and Unitarity in perturbative Quantum Field Theory*, *Eur. Phys. J.* **C75** (2015) 377, [1406.6280].

[247] A. Denner, S. Dittmaier, S. Kallweit and S. Pozzorini, *NLO QCD corrections to WWbb production at hadron colliders*, *Phys. Rev. Lett.* **106** (2011) 052001, [1012.3975].

[248] G. Bevilacqua, M. Czakon, A. van Hameren, C. G. Papadopoulos and M. Worek, *Complete off-shell effects in top quark pair hadroproduction with leptonic decay at next-to-leading order*, *JHEP* **02** (2011) 083, [1012.4230].

[249] A. Denner, S. Dittmaier, S. Kallweit and S. Pozzorini, *NLO QCD corrections to off-shell top-antitop production with leptonic decays at hadron colliders*, *JHEP* **10** (2012) 110, [1207.5018].

[250] G. Heinrich, A. Maier, R. Nisius, J. Schlenk and J. Winter, *NLO QCD corrections to $W^+W^-b\bar{b}$ production with leptonic decays in the light of top quark mass and asymmetry measurements*, *JHEP* **06** (2014) 158, [1312.6659].

[251] R. Frederix, *Top Quark Induced Backgrounds to Higgs Production in the $WW^{(*)} \to ll\nu\nu$ Decay Channel at Next-to-Leading-Order in QCD*, *Phys. Rev. Lett.* **112** (2014) 082002, [1311.4893].

[252] F. Cascioli, S. Kallweit, P. Maierhoefer and S. Pozzorini, *A unified NLO description of top-pair and associated Wt production*, *Eur. Phys. J.* **C74** (2014) 2783, [1312.0546].

[253] K. Melnikov and O. I. Yakovlev, *Top near threshold: All alpha-S corrections are trivial*, *Phys. Lett.* **B324** (1994) 217–223, [hep-ph/9302311].

[254] V. S. Fadin, V. A. Khoze and A. D. Martin, *Interference radiative phenomena in the production of heavy unstable particles*, *Phys. Rev.* **D49** (1994) 2247–2256.

[255] W. Beenakker, F. A. Berends and A. P. Chapovsky, *One loop QCD interconnection effects in pair production of top quarks*, *Phys. Lett.* **B454** (1999) 129–136, [hep-ph/9902304].

[256] W. Bernreuther, A. Brandenburg, Z. G. Si and P. Uwer, *Top quark pair production and decay at hadron colliders*, *Nucl. Phys.* **B690** (2004) 81–137, [hep-ph/0403035].

[257] A. Czarnecki, M. Jezabek and J. H. Kuhn, *Lepton Spectra From Decays of Polarized Top Quarks*, *Nucl. Phys.* **B351** (1991) 70–80.

[258] A. Brandenburg, Z. G. Si and P. Uwer, *QCD corrected spin analyzing power of jets in decays of polarized top quarks*, *Phys. Lett.* **B539** (2002) 235–241, [hep-ph/0205023].

[259] K. Melnikov and M. Schulze, *NLO QCD corrections to top quark pair production and decay at hadron colliders*, *JHEP* **08** (2009) 049, [0907.3090].

[260] ATLAS collaboration and CMS collaboration, LHCTopWG Summary Plots, https://twiki.cern.ch/twiki/bin/view/LHCPhysics/LHCTopWGSummaryPlots.

[261] M. L. Mangano and J. Rojo, *Cross Section Ratios between different CM energies at the LHC: opportunities for precision measurements and BSM sensitivity*, *JHEP* **08** (2012) 010, [1206.3557].

[262] M. Czakon, M. L. Mangano, A. Mitov and J. Rojo, *Constraints on the gluon PDF from top quark pair production at hadron colliders*, *JHEP* **07** (2013) 167, [1303.7215].

[263] R. D. Ball et al., *Parton distributions with LHC data*, *Nucl. Phys.* **B867** (2013) 244–289, [1207.1303].

[264] L. A. Harland-Lang, A. D. Martin, P. Motylinski and R. S. Thorne, *Parton distributions in the LHC era: MMHT 2014 PDFs*, *Eur. Phys. J.* **C75** (2015) 204, [1412.3989].

[265] S. Alekhin et al., *HERAFitter*, *Eur. Phys. J.* **C75** (2015) 304, [1410.4412].

[266] D. d'Enterria and P. Z. Skands, eds., *Proceedings, High-Precision α_s Measurements from LHC to FCC-ee*, (Geneva), CERN, CERN, 2015.

[267] E. Boos, O. Brandt, D. Denisov, S. Denisov and P. Grannis, *The top quark (20 years after its discovery)*, *Phys. Usp.* **58** (2015) 1133–1158, [1509.03325].

[268] ATLAS collaboration, *Measurement of the inclusive cross-section of single top-quark t-channel production in pp collisions at $\sqrt{s}$ = 13 TeV*, .

[269] CMS collaboration, *Measurement of the inclusive cross section of single top-quark production in the t-channel at 13 TeV*, .

[270] ATLAS collaboration, G. Aad et al., *Comprehensive measurements of t-channel single top-quark production cross sections at $\sqrt{s} = 7$ TeV with the ATLAS detector*, *Phys. Rev.* **D90** (2014) 112006, [1406.7844].

[271] CMS collaboration, V. Khachatryan et al., *Measurement of the t-channel single-top-quark production cross section and of the $|V_{tb}|$ CKM matrix element in pp collisions at $\sqrt{s}$= 8 TeV*, *JHEP* **06** (2014) 090, [1403.7366].

[272] J. M. Campbell, R. Frederix, F. Maltoni and F. Tramontano, *Next-to-Leading-Order Predictions for t-Channel Single-Top Production at Hadron Colliders*, *Phys. Rev. Lett.* **102** (2009) 182003, [0903.0005].

[273] J. M. Campbell, R. K. Ellis and F. Tramontano, *Single top production and decay at next-to-leading order*, *Phys. Rev.* **D70** (2004) 094012, [hep-ph/0408158].

[274] Q.-H. Cao and C. P. Yuan, *Single top quark production and decay at next-to-leading order in hadron collision*, *Phys. Rev.* **D71** (2005) 054022, [hep-ph/0408180].

[275] Q.-H. Cao, R. Schwienhorst, J. A. Benitez, R. Brock and C. P. Yuan, *Next-to-leading order corrections to single top quark production and decay at the Tevatron: 2. t^- channel process*, *Phys. Rev.* **D72** (2005) 094027, [hep-ph/0504230].

[276] P. Falgari, P. Mellor and A. Signer, *Production-decay interferences at NLO in QCD for t-channel single-top production*, *Phys. Rev.* **D82** (2010) 054028, [1007.0893].

[277] P. Falgari, F. Giannuzzi, P. Mellor and A. Signer, *Off-shell effects for t-channel and s-channel single-top production at NLO in QCD*, *Phys. Rev.* **D83** (2011) 094013, [1102.5267].

[278] A. S. Papanastasiou, R. Frederix, S. Frixione, V. Hirschi and F. Maltoni, *Single-top t-channel production with off-shell and non-resonant effects*, *Phys. Lett.* **B726** (2013) 223–227, [1305.7088].

[279] G. Bordes and B. van Eijk, *Calculating QCD corrections to single top production in hadronic interactions*, *Nucl. Phys.* **B435** (1995) 23–58.

[280] T. Stelzer, Z. Sullivan and S. Willenbrock, *Single top quark production via W - gluon fusion at next-to-leading order*, *Phys. Rev.* **D56** (1997) 5919–5927, [hep-ph/9705398].

[281] T. Stelzer, Z. Sullivan and S. Willenbrock, *Single top quark production at hadron colliders*, *Phys. Rev.* **D58** (1998) 094021, [hep-ph/9807340].

[282] B. W. Harris, E. Laenen, L. Phaf, Z. Sullivan and S. Weinzierl, *The Fully differential single top quark cross-section in next to leading order QCD*, *Phys. Rev.* **D66** (2002) 054024, [hep-ph/0207055].

[283] Z. Sullivan, *Understanding single-top-quark production and jets at hadron colliders*, *Phys. Rev.* **D70** (2004) 114012, [hep-ph/0408049].

[284] Z. Sullivan, *Angular correlations in single-top-quark and Wjj production at next-to-leading order*, *Phys. Rev.* **D72** (2005) 094034, [hep-ph/0510224].

[285] M. Brucherseifer, F. Caola and K. Melnikov, *On the NNLO QCD corrections to single-top production at the LHC*, *Phys. Lett.* **B736** (2014) 58–63, [1404.7116].

[286] J. M. Campbell, R. Frederix, F. Maltoni and F. Tramontano, *NLO predictions for t-channel production of single top and fourth generation quarks at hadron colliders*, *JHEP* **10** (2009) 042, [0907.3933].

[287] M. A. G. Aivazis, J. C. Collins, F. I. Olness and W.-K. Tung, *Leptoproduction of heavy quarks. 2. A Unified QCD formulation of charged and neutral current processes from fixed target to collider energies*, *Phys. Rev.* **D50** (1994) 3102–3118, [hep-ph/9312319].

[288] N. Kidonakis, *Single top production at the Tevatron: Threshold resummation and finite-order soft gluon corrections*, *Phys. Rev.* **D74** (2006) 114012, [hep-ph/0609287].

[289] N. Kidonakis, *Higher-order soft gluon corrections in single top quark production at the LHC*, *Phys. Rev.* **D75** (2007) 071501, [hep-ph/0701080].

[290] N. Kidonakis, *Next-to-next-to-leading-order collinear and soft gluon corrections for t-channel single top quark production*, *Phys. Rev.* **D83** (2011) 091503, [1103.2792].

[291] M. Beccaria, G. Macorini, F. M. Renard and C. Verzegnassi, *Single top production in the t-channel at LHC: A Realistic test of electroweak models*, *Phys. Rev.* **D74** (2006) 013008, [hep-ph/0605108].

[292] M. Beccaria, C. M. Carloni Calame, G. Macorini, E. Mirabella, F. Piccinini, F. M. Renard et al., *A Complete one-loop calculation of electroweak supersymmetric effects in t-channel single top production at CERN LHC*, *Phys. Rev.* **D77** (2008) 113018, [0802.1994].

[293] ATLAS collaboration, G. Aad et al., *Evidence for single top-quark production in the s-channel in proton-proton collisions at $\sqrt{s}$ =8 TeV with the ATLAS detector using the Matrix Element Method*, *Phys. Lett.* **B756** (2016) 228–246, [1511.05980].

[294] CDF collaboration, T. A. Aaltonen et al., *Updated Measurement of the Single Top Quark Production Cross Section and Vtb in the Missing Transverse Energy Plus Jets Topology in $p\bar{p}$ Collisions at $\sqrt{s} = 1.96$ TeV*, *Phys. Rev.* **D93** (2016) 032011, [1410.4909].

[295] CDF, D0 collaboration, T. E. W. Group, *Combination of CDF and D0 Measurements of the Single Top Production Cross Section*, 0908.2171.

[296] D0 collaboration, V. M. Abazov et al., *Evidence for s-channel single top quark production in $p\bar{p}$ collisions at $\sqrt{s}$ = 1.96 TeV*, *Phys. Lett.* **B726** (2013) 656–664, [1307.0731].

[297] CDF, D0 collaboration, T. A. Aaltonen et al., *Tevatron Combination of Single-Top-Quark Cross Sections and Determination of the Magnitude of the Cabibbo-Kobayashi-Maskawa Matrix Element $\mathbf{V_{tb}}$*, *Phys. Rev. Lett.* **115** (2015) 152003, [1503.05027].

[298] CMS collaboration, S. Chatrchyan et al., *Measurement of the single-top-quark t-channel cross section in pp collisions at $\sqrt{s} = 7$ TeV*, *JHEP* **12** (2012) 035, [1209.4533].

[299] ATLAS collaboration, *Measurement of the Inclusive and Fiducial Cross-Section of Single Top-Quark t-Channel Events in pp Collisions at $\sqrt{s}$ = 8 TeV*, .

[300] ATLAS, CMS collaboration, *Combination of single top-quark cross-sections measurements in the t-channel at sqrt[s]=8 TeV with the ATLAS and CMS experiments*, .

[301] J. A. Aguilar-Saavedra, *Single top quark production at LHC with anomalous Wtb couplings*, *Nucl. Phys.* **B804** (2008) 160–192, [0803.3810].

[302] J. Gao, C. S. Li, L. L. Yang and H. Zhang, *Search for anomalous top quark production at the early LHC*, *Phys. Rev. Lett.* **107** (2011) 092002, [1104.4945].

[303] T. M. P. Tait and C. P. Yuan, *Single top quark production as a window to physics beyond the standard model*, *Phys. Rev.* **D63** (2000) 014018, [hep-ph/0007298].

[304] W. Buchmuller and D. Wyler, *Effective Lagrangian Analysis of New Interactions and Flavor Conservation*, *Nucl. Phys.* **B268** (1986) 621–653.

[305] G. L. Kane, G. A. Ladinsky and C. P. Yuan, *Using the Top Quark for Testing Standard Model Polarization and CP Predictions*, *Phys. Rev.* **D45** (1992) 124–141.

[306] J. A. Aguilar-Saavedra and G. C. Branco, *Probing top flavor changing neutral scalar couplings at the CERN LHC*, *Phys. Lett.* **B495** (2000) 347–356, [hep-ph/0004190].

[307] CDF collaboration, T. Aaltonen et al., *Search for the Flavor Changing Neutral Current Decay $t \to Zq$ in $p\bar{p}$ Collisions at $\sqrt{s} = 1.96$ TeV*, *Phys. Rev. Lett.* **101** (2008) 192002, [0805.2109].

[308] D0 collaboration, V. M. Abazov et al., *Search for flavor changing neutral currents in decays of top quarks*, *Phys. Lett.* **B701** (2011) 313–320, [1103.4574].

[309] ATLAS collaboration, G. Aad et al., *A search for flavour changing neutral currents in top-quark decays in pp collision data collected with the ATLAS detector at $\sqrt{s} = 7$ TeV*, *JHEP* **09** (2012) 139, [1206.0257].

[310] CMS collaboration, S. Chatrchyan et al., *Search for Flavor-Changing Neutral Currents in Top-Quark Decays $t \to Zq$ in pp Collisions at $\sqrt{s} = 8$ TeV*, *Phys. Rev. Lett.* **112** (2014) 171802, [1312.4194].

[311] ATLAS collaboration, G. Aad et al., *Search for flavour-changing neutral current top-quark decays to qZ in pp collision data collected with the ATLAS detector at $\sqrt{s} = 8$ Â TeV*, *Eur. Phys. J.* **C76** (2016) 12, [1508.05796].

[312] ATLAS collaboration, G. Aad et al., *Search for top quark decays $t \to qH$ with $H \to \gamma\gamma$ using the ATLAS detector*, *JHEP* **06** (2014) 008, [1403.6293].

[313] CMS collaboration, *Search for top quark decays t rightarrow qH with H rightarrow gammagamma in pp collisions at sqrts = 8 TeV*, .

[314] CMS collaboration, *Search for top quark decays via Higgs-boson-mediated flavor changing neutral currents in pp collisions at $\sqrt{s} = 8$ TeV*, .

[315] CMS collaboration, *Search for anomalous single top quark production in association with a photon*, .

[316] CMS collaboration, *Search for Flavour Changing Neutral Currents in single top events*, .

[317] CMS collaboration, *Search for anomalous Wtb couplings and top FCNC in t-channel single-top-quark events*, .

[318] D0 collaboration, V. M. Abazov et al., *Search for anomalous Wtb couplings in single top quark production in $p\bar{p}$ collisions at $\sqrt{s} = 1.96$ TeV*, *Phys. Lett.* **B708** (2012) 21–26, [1110.4592].

[319] D0 collaboration, V. M. Abazov et al., *Combination of searches for anomalous top quark couplings with 5.4 fb^{-1} of $p\bar{p}$ collisions*, *Phys. Lett.* **B713** (2012) 165–171, [1204.2332].

[320] CDF collaboration, T. Aaltonen et al., *Search for top-quark production via flavor-changing neutral currents in W+1 jet events at CDF*, *Phys. Rev. Lett.* **102** (2009) 151801, [0812.3400].

[321] D0 collaboration, V. M. Abazov et al., *Search for flavor changing neutral currents via quark-gluon couplings in single top quark production using 2.3 fb^{-1} of $p\bar{p}$ collisions*, *Phys. Lett.* **B693** (2010) 81–87, [1006.3575].

[322] ATLAS collaboration, *Search for single top-quark production via FCNC in strong interaction in $\sqrt{s} = 8$ TeV ATLAS data*, .

[323] ATLAS collaboration, G. Aad et al., *Search for single top-quark production via flavour-changing neutral currents at 8 TeV with the ATLAS detector*, *Eur. Phys. J.* **C76** (2016) 55, [1509.00294].

[324] ATLAS collaboration, G. Aad et al., *Search for anomalous couplings in the Wtb vertex from the measurement of double differential angular decay rates of single top quarks produced in the t-channel with the ATLAS detector*, *JHEP* **04** (2016) 023, [1510.03764].

[325] J. Andrea, B. Fuks and F. Maltoni, *Monotops at the LHC*, *Phys. Rev.* **D84** (2011) 074025, [1106.6199].

[326] J.-L. Agram, J. Andrea, M. Buttignol, E. Conte and B. Fuks, *Monotop phenomenology at the Large Hadron Collider*, *Phys. Rev.* **D89** (2014) 014028, [1311.6478].

[327] CDF collaboration, T. Aaltonen et al., *Search for a dark matter candidate produced in association with a single top quark in $p\bar{p}$ collisions at $\sqrt{s} = 1.96$ TeV*, *Phys. Rev. Lett.* **108** (2012) 201802, [1202.5653].

[328] CMS collaboration, V. Khachatryan et al., *Search for Monotop Signatures in Proton-Proton Collisions at $\sqrt{s} = 8$ TeV*, *Phys. Rev. Lett.* **114** (2015) 101801, [1410.1149].

[329] ATLAS collaboration, G. Aad et al., *Search for invisible particles produced in association with single-top-quarks in proton-proton collisions at $\sqrt{s} = 8$ TeV with the ATLAS detector*, *Eur. Phys. J.* **C75** (2015) 79, [1410.5404].

[330] ATLAS collaboration, G. Aad et al., *Evidence for the associated production of a W boson and a top quark in ATLAS at $\sqrt{s} = 7$ TeV*, *Phys. Lett.* **B716** (2012) 142–159, [1205.5764].

[331] CMS collaboration, S. Chatrchyan et al., *Evidence for associated production of a single top quark and W boson in pp collisions at $\sqrt{s} = 7$ TeV*, *Phys. Rev. Lett.* **110** (2013) 022003, [1209.3489].

[332] CMS collaboration, S. Chatrchyan et al., *Observation of the associated production of a single top quark and a W boson in pp collisions at $\sqrt{s}$ =8 TeV*, *Phys. Rev. Lett.* **112** (2014) 231802, [1401.2942].

[333] ATLAS collaboration, G. Aad et al., *Measurement of the production cross-section of a single top quark in association with a W boson at 8 TeV with the ATLAS experiment*, *JHEP* **01** (2016) 064, [1510.03752].

[334] ATLAS collaboration, *Combination of cross-section measurements for associated production of a single top-quark and a W boson at $\sqrt{s}$ = 8 TeV with the ATLAS and CMS experiments*, .

[335] M. C. Smith and S. Willenbrock, *QCD and Yukawa corrections to single top quark production via $q\bar{q} \to t\bar{b}$*, *Phys. Rev.* **D54** (1996) 6696–6702, [hep-ph/9604223].

[336] Q.-H. Cao, R. Schwienhorst and C. P. Yuan, *Next-to-leading order corrections to single top quark production and decay at Tevatron. 1. s^- channel process*, *Phys. Rev.* **D71** (2005) 054023, [hep-ph/0409040].

[337] R. Pittau, *Final state QCD corrections to off-shell single top production in hadron collisions*, *Phys. Lett.* **B386** (1996) 397–402, [hep-ph/9603265].

[338] J. van der Heide, E. Laenen, L. Phaf and S. Weinzierl, *Helicity amplitudes for single top production*, *Phys. Rev.* **D62** (2000) 074025, [hep-ph/0003318].

[339] D. Bardin, S. Bondarenko, L. Kalinovskaya, V. Kolesnikov and W. von Schlippe, *Electroweak Radiative Corrections to Single-top Production*, *Eur. Phys. J.* **C71** (2011) 1533, [1008.1859].

[340] S. G. Bondarenko and A. A. Sapronov, *NLO EW and QCD proton-proton cross section calculations with mcsanc-v1.01*, *Comput. Phys. Commun.* **184** (2013) 2343–2350, [1301.3687].

[341] S. Mrenna and C. P. Yuan, *Effects of QCD resummation on W+ h and t anti-b production at the Tevatron*, *Phys. Lett.* **B416** (1998) 200–207, [hep-ph/9703224].

[342] N. Kidonakis, *NNLL resummation for s-channel single top quark production*, *Phys. Rev.* **D81** (2010) 054028, [1001.5034].

[343] J. Alwall, R. Frederix, J. M. Gerard, A. Giammanco, M. Herquet, S. Kalinin et al., *Is $V_{(tb)} \simeq 1$?*, *Eur. Phys. J.* **C49** (2007) 791–801, [hep-ph/0607115].

[344] CDF, D0 collaboration, T. A. Aaltonen et al., *Observation of s-channel production of single top quarks at the Tevatron*, *Phys. Rev. Lett.* **112** (2014) 231803, [1402.5126].

[345] CDF collaboration, T. A. Aaltonen et al., *Evidence for s-channel Single-Top-Quark Production in Events with one Charged Lepton and two Jets at CDF*, *Phys. Rev. Lett.* **112** (2014) 231804, [1402.0484].

[346] CDF collaboration, T. A. Aaltonen et al., *Search for s-Channel Single-Top-Quark Production in Events with Missing Energy Plus Jets in $p\bar{p}$ Collisions at $\sqrt{s}$ =1.96 TeV*, *Phys. Rev. Lett.* **112** (2014) 231805, [1402.3756].

[347] ATLAS collaboration, *Search for s-Channel Single Top-Quark Production in pp Collisions at $\sqrt{s}$ = 7 TeV*, .

[348] CMS collaboration, *Measurement of the single top s-channel cross section at 8 TeV.*, .

[349] CDF collaboration, T. A. Aaltonen et al., *Search for Resonances Decaying to Top and Bottom Quarks with the CDF Experiment*, *Phys. Rev. Lett.* **115** (2015) 061801, [1504.01536].

[350] D0 collaboration, V. M. Abazov et al., *Search for $W' \to tb$ resonances with left- and right-handed couplings to fermions*, *Phys. Lett.* **B699** (2011) 145–150, [1101.0806].

[351] CMS collaboration, S. Chatrchyan et al., *Search for W' $\to$ tb decays in the lepton + jets final state in pp collisions at $\sqrt{s}$ = 8 TeV*, *JHEP* **05** (2014) 108, [1402.2176].

[352] ATLAS collaboration, G. Aad et al., *Search for $W' \to t\bar{b}$ in the lepton plus jets final state in proton-proton collisions at a centre-of-mass energy of $\sqrt{s}$ = 8 TeV with the ATLAS detector*, *Phys. Lett.* **B743** (2015) 235–255, [1410.4103].

[353] ATLAS collaboration, G. Aad et al., *Search for $W' \to tb \to qqbb$ decays in pp collisions at $\sqrt{s}$ $\hat{A}$ =$\hat{A}$ 8$\hat{A}$ TeV with the ATLAS detector*, *Eur. Phys. J.* **C75** (2015) 165, [1408.0886].

[354] CMS collaboration, V. Khachatryan et al., *Search for $W' \to tb$ in proton-proton collisions at $\sqrt{s}$ = 8 TeV*, *JHEP* **02** (2016) 122, [1509.06051].

[355] D0 collaboration, V. M. Abazov et al., *Search for charged Higgs bosons decaying to top and bottom quarks in $p\bar{p}$ collisions*, *Phys. Rev. Lett.* **102** (2009) 191802, [0807.0859].

[356] ATLAS collaboration, *Measurement of the cross-section for associated production of a top quark and a W boson at $\sqrt{s}$ = 8 TeV with the ATLAS detector*, .

[357] S. Frixione, E. Laenen, P. Motylinski, B. R. Webber and C. D. White, *Single-top hadroproduction in association with a W boson*, *JHEP* **07** (2008) 029, [0805.3067].

[358] T. M. P. Tait, *The tW^- mode of single top production*, *Phys. Rev.* **D61** (1999) 034001, [hep-ph/9909352].

[359] S. Zhu, *Next-to-leading order QCD corrections to bg -> tW- at CERN large hadron collider*, *Phys. Lett.* **B524** (2002) 283–288, [hep-ph/0109269].

[360] A. S. Belyaev, E. E. Boos and L. V. Dudko, *Single top quark at future hadron colliders: Complete signal and background study*, *Phys. Rev.* **D59** (1999) 075001, [hep-ph/9806332].

[361] A. Belyaev and E. Boos, *Single top quark tW + X production at the CERN LHC: A Closer look*, *Phys. Rev.* **D63** (2001) 034012, [hep-ph/0003260].

[362] J. M. Campbell and F. Tramontano, *Next-to-leading order corrections to Wt production and decay*, *Nucl. Phys.* **B726** (2005) 109–130, [hep-ph/0506289].

[363] N. Kidonakis, *Two-loop soft anomalous dimensions for single top quark associated production with a W- or H-*, *Phys. Rev.* **D82** (2010) 054018, [1005.4451].

[364] M. Beccaria, G. Macorini, F. M. Renard and C. Verzegnassi, *Associated tW production at lhc: A Complete calculation of electroweak supersymmetric effects at one loop*, *Phys. Rev.* **D73** (2006) 093001, [hep-ph/0601175].

[365] M. Beccaria, C. M. Carloni Calame, G. Macorini, G. Montagna, F. Piccinini, F. M. Renard et al., *A Complete one-loop description of associated tW production at LHC and a search for possible genuine supersymmetric effects*, *Eur. Phys. J.* **C53** (2008) 257–265, [0705.3101].

[366] ATLAS collaboration, G. Aad et al., *Search for single b^*-quark production with the ATLAS detector at $\sqrt{s} = 7$ TeV*, *Phys. Lett.* **B721** (2013) 171–189, [1301.1583].

[367] CMS collaboration, V. Khachatryan et al., *Search for the production of an excited bottom quark decaying to tW in proton-proton collisions at $\sqrt{s} = 8$ TeV*, *JHEP* **01** (2016) 166, [1509.08141].

[368] ATLAS collaboration, G. Aad et al., *Search for the production of single vector-like and excited quarks in the Wt final state in pp collisions at $\sqrt{s} = 8$ TeV with the ATLAS detector*, *JHEP* **02** (2016) 110, [1510.02664].

[369] CDF collaboration, T. A. Aaltonen et al., *Measurement of the leptonic asymmetry in $t\bar{t}$ events produced in $p\bar{p}$ collisions at $\sqrt{s} = 1.96$ TeV*, *Phys. Rev.* **D88** (2013) 072003, [1308.1120].

[370] CDF collaboration, T. A. Aaltonen et al., *Measurement of the inclusive leptonic asymmetry in top-quark pairs that decay to two charged leptons at CDF*, *Phys. Rev. Lett.* **113** (2014) 042001, [1404.3698].

[371] D0 collaboration, V. M. Abazov et al., *Measurement of Leptonic Asymmetries and Top Quark Polarization in $t\bar{t}$ Production*, *Phys. Rev.* **D87** (2013) 011103, [1207.0364].

[372] D0 collaboration, V. M. Abazov et al., *Measurement of the asymmetry in angular distributions of leptons produced in dilepton $t\bar{t}$ final states in $p\bar{p}$ collisions at $\sqrt{s}$=1.96 TeV*, *Phys. Rev.* **D88** (2013) 112002, [1308.6690].

[373] D0 collaboration, V. M. Abazov et al., *Measurement of the forward-backward asymmetry in the distribution of leptons in $t\bar{t}$ events in the lepton+jets channel*, *Phys. Rev.* **D90** (2014) 072001, [1403.1294].

[374] CMS collaboration, S. Chatrchyan et al., *Measurements of the $t\bar{t}$ charge asymmetry using the dilepton decay channel in pp collisions at $\sqrt{s} = 7$ TeV*, *JHEP* **04** (2014) 191, [1402.3803].

[375] ATLAS collaboration, G. Aad et al., *Measurement of the charge asymmetry in dileptonic decays of top quark pairs in pp collisions at $\sqrt{s} = 7$ TeV using the ATLAS detector*, *JHEP* **05** (2015) 061, [1501.07383].

[376] J. M. Campbell and R. K. Ellis, *Top-quark processes at NLO in production and decay*, *J. Phys.* **G42** (2015) 015005, [1204.1513].

[377] W. Bernreuther and Z.-G. Si, *Top quark and leptonic charge asymmetries for the Tevatron and LHC*, *Phys. Rev.* **D86** (2012) 034026, [1205.6580].

[378] A. Falkowski, M. L. Mangano, A. Martin, G. Perez and J. Winter, *Data driving the top quark forward–backward asymmetry with a lepton-based handle*, *Phys. Rev.* **D87** (2013) 034039, [1212.4003].

[379] J. A. Aguilar-Saavedra, D. Amidei, A. Juste and M. Perez-Victoria, *Asymmetries in top quark pair production at hadron colliders*, *Rev. Mod. Phys.* **87** (2015) 421–455, [1406.1798].

[380] J. H. Kuhn and G. Rodrigo, *Charge asymmetry in hadroproduction of heavy quarks*, *Phys. Rev. Lett.* **81** (1998) 49–52, [hep-ph/9802268].

[381] J. H. Kuhn and G. Rodrigo, *Charge asymmetry of heavy quarks at hadron colliders*, *Phys. Rev.* **D59** (1999) 054017, [hep-ph/9807420].

[382] J. H. Kuhn and G. Rodrigo, *Charge asymmetries of top quarks at hadron colliders revisited*, *JHEP* **01** (2012) 063, [1109.6830].

[383] L. G. Almeida, G. F. Sterman and W. Vogelsang, *Threshold Resummation for the Top Quark Charge Asymmetry*, *Phys. Rev.* **D78** (2008) 014008, [0805.1885].

[384] W. Hollik and D. Pagani, *The electroweak contribution to the top quark forward-backward asymmetry at the Tevatron*, *Phys. Rev.* **D84** (2011) 093003, [1107.2606].

[385] M. Czakon, P. Fiedler and A. Mitov, *Resolving the Tevatron Top Quark Forward-Backward Asymmetry Puzzle: Fully Differential Next-to-Next-to-Leading-Order Calculation*, *Phys. Rev. Lett.* **115** (2015) 052001, [1411.3007].

[386] CDF collaboration, T. Aaltonen et al., *Forward-Backward Asymmetry in Top Quark Production in $p\bar{p}$ Collisions at sqrts = 1.96 TeV*, *Phys. Rev. Lett.* **101** (2008) 202001, [0806.2472].

[387] CDF collaboration, T. Aaltonen et al., *Evidence for a Mass Dependent Forward-Backward Asymmetry in Top Quark Pair Production*, *Phys. Rev.* **D83** (2011) 112003, [1101.0034].

[388] CDF collaboration, T. Aaltonen et al., *Measurement of the top quark forward-backward production asymmetry and its dependence on event kinematic properties*, *Phys. Rev.* **D87** (2013) 092002, [1211.1003].

[389] CDF collaboration, T. A. Aaltonen et al., *Measurement of the forward-backward asymmetry of top-quark and antiquark pairs using the full CDF Run II data set*, *Phys. Rev.* **D93** (2016) 112005, [1602.09015].

[390] D0 collaboration, V. M. Abazov et al., *First measurement of the forward-backward charge asymmetry in top quark pair production*, *Phys. Rev. Lett.* **100** (2008) 142002, [0712.0851].

[391] D0 collaboration, V. M. Abazov et al., *Forward-backward asymmetry in top quark-antiquark production*, *Phys. Rev.* **D84** (2011) 112005, [1107.4995].

[392] D0 collaboration, V. M. Abazov et al., *Measurement of the forward-backward asymmetry in top quark-antiquark production in ppbar collisions using the lepton+jets channel*, *Phys. Rev.* **D90** (2014) 072011, [1405.0421].

[393] D0 collaboration, V. M. Abazov et al., *Simultaneous measurement of forward-backward asymmetry and top polarization in dilepton final states from $t\bar{t}$ production at the Tevatron*, *Phys. Rev.* **D92** (2015) 052007, [1507.05666].

[394] E. L. Berger, Q.-H. Cao, C.-R. Chen, C. S. Li and H. Zhang, *Top Quark Forward-Backward Asymmetry and Same-Sign Top Quark Pairs*, *Phys. Rev. Lett.* **106** (2011) 201801, [1101.5625].

[395] J. F. Kamenik, J. Shu and J. Zupan, *Review of New Physics Effects in t-tbar Production*, *Eur. Phys. J.* **C72** (2012) 2102, [1107.5257].

[396] S. J. Brodsky, G. P. Lepage and P. B. Mackenzie, *On the Elimination of Scale Ambiguities in Perturbative Quantum Chromodynamics*, *Phys. Rev.* **D28** (1983) 228.

[397] S. J. Brodsky and X.-G. Wu, *Eliminating the Renormalization Scale Ambiguity for Top-Pair Production Using the Principle of Maximum Conformality*, *Phys. Rev. Lett.* **109** (2012) 042002, [1203.5312].

[398] S. J. Brodsky and X.-G. Wu, *Application of the Principle of Maximum Conformality to the Top-Quark Forward-Backward Asymmetry at the Tevatron*, *Phys. Rev.* **D85** (2012) 114040, [1205.1232].

[399] N. Kidonakis, *The top quark rapidity distribution and forward-backward asymmetry*, *Phys. Rev.* **D84** (2011) 011504, [1105.5167].

[400] N. Kidonakis, *The top quark forward-backward asymmetry at approximate N^3LO*, *Phys. Rev.* **D91** (2015) 071502, [1501.01581].

[401] V. Ahrens, A. Ferroglia, M. Neubert, B. D. Pecjak and L. L. Yang, *The top-pair forward-backward asymmetry beyond NLO*, *Phys. Rev.* **D84** (2011) 074004, [1106.6051].

[402] A. V. Manohar and M. Trott, *Electroweak Sudakov Corrections and the Top Quark Forward-Backward Asymmetry*, *Phys. Lett.* **B711** (2012) 313–316, [1201.3926].

[403] K. Hagiwara, J. Kanzaki and Y. Takaesu, *On the W+4 jets background to the top quark asymmetry at the Tevatron*, *Nucl. Phys. Proc. Suppl.* **234** (2013) 93–96, [1205.5173].

[404] A. Mitov and G. Sterman, *Final state interactions in single- and multi-particle inclusive cross sections for hadronic collisions*, *Phys. Rev.* **D86** (2012) 114038, [1209.5798].

[405] P. Skands, B. Webber and J. Winter, *QCD Coherence and the Top Quark Asymmetry*, *JHEP* **07** (2012) 151, [1205.1466].

[406] M. Czakon, P. Fiedler, D. Heymes and A. Mitov, *NNLO QCD predictions for fully-differential top-quark pair production at the Tevatron*, *JHEP* **05** (2016) 034, [1601.05375].

[407] CMS collaboration, S. Chatrchyan et al., *Inclusive and differential measurements of the $t\bar{t}$ charge asymmetry in proton-proton collisions at $\sqrt{s} = 7$ TeV*, *Phys. Lett.* **B717** (2012) 129–150, [1207.0065].

[408] ATLAS collaboration, G. Aad et al., *Measurement of the top quark pair production charge asymmetry in proton-proton collisions at $\sqrt{s} = 7$ TeV using the ATLAS detector*, *JHEP* **02** (2014) 107, [1311.6724].

[409] CMS collaboration, V. Khachatryan et al., *Inclusive and differential measurements of the $t\bar{t}$ charge asymmetry in pp collisions at $\sqrt{s} = 8$ TeV*, *Phys. Lett.* **B757** (2016) 154–179, [1507.03119].

[410] CMS collaboration, V. Khachatryan et al., *Measurement of the charge asymmetry in top quark pair production in pp collisions at $\sqrt{(s)} = 8$ TeV using a template method*, *Phys. Rev.* **D93** (2016) 034014, [1508.03862].

[411] CMS collaboration, V. Khachatryan et al., *Measurements of $t\bar{t}$ charge asymmetry using dilepton final states in pp collisions at $\sqrt{s} = 8$ TeV*, *Phys. Lett.* **B760** (2016) 365–386, [1603.06221].

[412] ATLAS collaboration, G. Aad et al., *Measurement of the charge asymmetry in top-quark pair production in the lepton-plus-jets final state in pp collision data at $\sqrt{s} = 8$ TeV with the ATLAS detector*, *Eur. Phys. J.* **C76** (2016) 87, [1509.02358].

[413] ATLAS collaboration, G. Aad et al., *Measurements of the charge asymmetry in top-quark pair production in the dilepton final state at $\sqrt{s} = 8$ TeV with the ATLAS detector*, *Phys. Rev.* **D94** (2016) 032006, [1604.05538].

[414] J. A. Aguilar-Saavedra and A. Juste, *Collider-independent t tbar forward-backward asymmetries*, *Phys. Rev. Lett.* **109** (2012) 211804, [1205.1898].

[415] J. A. Aguilar-Saavedra, W. Bernreuther and Z. G. Si, *Collider-independent top quark forward-backward asymmetries: standard model predictions*, *Phys. Rev.* **D86** (2012) 115020, [1209.6352].

[416] CMS collaboration, S. Chatrchyan et al., *Measurements of $t\bar{t}$ spin correlations and top-quark polarization using dilepton final states in pp collisions at $\sqrt{s} = 7$ TeV*, *Phys. Rev. Lett.* **112** (2014) 182001, [1311.3924].

[417] CMS collaboration, V. Khachatryan et al., *Measurement of spin correlations in $t\bar{t}$ production using the matrix element method in the muon+jets final state in pp collisions at $\sqrt{s} = 8$ TeV*, *Phys. Lett.* **B758** (2016) 321–346, [1511.06170].

[418] CMS collaboration, V. Khachatryan et al., *Measurements of t t-bar spin correlations and top quark polarization using dilepton final states in pp collisions at sqrt(s) = 8 TeV*, *Phys. Rev.* **D93** (2016) 052007, [1601.01107].

[419] ATLAS collaboration, G. Aad et al., *Observation of spin correlation in $t\bar{t}$ events from pp collisions at sqrt(s) = 7 TeV using the ATLAS detector*, *Phys. Rev. Lett.* **108** (2012) 212001, [1203.4081].

[420] ATLAS collaboration, G. Aad et al., *Measurements of spin correlation in top-antitop quark events from proton-proton collisions at $\sqrt{s} = 7$ TeV using the ATLAS detector*, *Phys. Rev.* **D90** (2014) 112016, [1407.4314].

[421] ATLAS collaboration, G. Aad et al., *Measurement of Spin Correlation in Top-Antitop Quark Events and Search for Top Squark Pair Production in pp Collisions at $\sqrt{s} = 8$ TeV Using the ATLAS Detector*, *Phys. Rev. Lett.* **114** (2015) 142001, [1412.4742].

[422] W. Bernreuther and Z.-G. Si, *Distributions and correlations for top quark pair production and decay at the Tevatron and LHC.*, *Nucl. Phys.* **B837** (2010) 90–121, [1003.3926].

[423] W. Bernreuther and Z.-G. Si, *Top quark spin correlations and polarization at the LHC: standard model predictions and effects of anomalous top chromo moments*, *Phys. Lett.* **B725** (2013) 115–122, [1305.2066].

[424] D0 collaboration, V. M. Abazov et al., *Evidence for spin correlation in $t\bar{t}$ production*, *Phys. Rev. Lett.* **108** (2012) 032004, [1110.4194].

[425] D0 collaboration, V. M. Abazov et al., *Measurement of Spin Correlation between Top and Antitop Quarks Produced in $p\bar{p}$ Collisions at $\sqrt{s} = 1.96$ TeV*, *Phys. Lett.* **B757** (2016) 199–206, [1512.08818].

[426] F. Spano, *Unfolding in particle physics: a window on solving inverse problems*, *EPJ Web Conf.* **55** (2013) 03002.

[427] M. Czakon, D. Heymes and A. Mitov, *High-precision differential predictions for top-quark pairs at the LHC*, *Phys. Rev. Lett.* **116** (2016) 082003, [1511.00549].

[428] M. Czakon, D. Heymes and A. Mitov, *Dynamical scales for multi-TeV top-pair production at the LHC*, 1606.03350.

[429] M. Czakon, D. Heymes and A. Mitov, *Bump-hunting in LHC ttbar events*, 1608.00765.

[430] S. Alioli, P. Nason, C. Oleari and E. Re, *A general framework for implementing NLO calculations in shower Monte Carlo programs: the POWHEG BOX*, *JHEP* **06** (2010) 043, [1002.2581].

[431] J. Alwall, R. Frederix, S. Frixione, V. Hirschi, F. Maltoni, O. Mattelaer et al., *The automated computation of tree-level and next-to-leading order differential cross sections, and their matching to parton shower simulations*, *JHEP* **07** (2014) 079, [1405.0301].

[432] T. Gleisberg, S. Hoeche, F. Krauss, M. Schonherr, S. Schumann, F. Siegert et al., *Event generation with SHERPA 1.1*, *JHEP* **02** (2009) 007, [0811.4622].

[433] G. Bevilacqua, M. Czakon, M. V. Garzelli, A. van Hameren, A. Kardos, C. G. Papadopoulos et al., *HELAC-NLO*, *Comput. Phys. Commun.* **184** (2013) 986–997, [1110.1499].

[434] G. Corcella, I. G. Knowles, G. Marchesini, S. Moretti, K. Odagiri, P. Richardson et al., *HERWIG 6: An Event generator for hadron emission reactions with interfering gluons (including supersymmetric processes)*, *JHEP* **01** (2001) 010, [hep-ph/0011363].

[435] J. Bellm et al., *Herwig 7.0/Herwig++ 3.0 release note*, *Eur. Phys. J.* **C76** (2016) 196, [1512.01178].

[436] T. Sjostrand, S. Mrenna and P. Z. Skands, *A Brief Introduction to PYTHIA 8.1*, *Comput. Phys. Commun.* **178** (2008) 852–867, [0710.3820].

[437] A. Ferroglia, B. D. Pecjak and L. L. Yang, *Top-quark pair production at high invariant mass: an NNLO soft plus virtual approximation*, *JHEP* **09** (2013) 032, [1306.1537].

[438] A. Ferroglia, B. D. Pecjak, D. J. Scott and L. L. Yang, *QCD resummations for boosted top production*, *PoS* **TOP2015** (2016) 052, [1512.02535].

[439] M. Guzzi, K. Lipka and S.-O. Moch, *Top-quark pair production at hadron colliders: differential cross section and phenomenological applications with DiffTop*, *JHEP* **01** (2015) 082, [1406.0386].

[440] N. Kidonakis, *NNNLO soft-gluon corrections for the top-quark p_T and rapidity distributions*, *Phys. Rev.* **D91** (2015) 031501, [1411.2633].

[441] J. H. Kuhn, A. Scharf and P. Uwer, *Weak Interactions in Top-Quark Pair Production at Hadron Colliders: An Update*, *Phys. Rev.* **D91** (2015) 014020, [1305.5773].

[442] J. M. Campbell, D. Wackeroth and J. Zhou, *Electroweak Corrections at the LHC with MCFM*, *PoS* **DIS2015** (2015) 130, [1508.06247].

[443] D. Pagani, I. Tsinikos and M. Zaro, *The impact of the photon PDF and electroweak corrections on $t\bar{t}$ distributions*, *Eur. Phys. J.* **C76** (2016) 479, [1606.01915].

[444] M. Cacciari and N. Houdeau, *Meaningful characterisation of perturbative theoretical uncertainties*, *JHEP* **09** (2011) 039, [1105.5152].

[445] E. Bagnaschi, M. Cacciari, A. Guffanti and L. Jenniches, *An extensive survey of the estimation of uncertainties from missing higher orders in perturbative calculations*, *JHEP* **02** (2015) 133, [1409.5036].

[446] A. David and G. Passarino, *How well can we guess theoretical uncertainties?*, *Phys. Lett.* **B726** (2013) 266–272, [1307.1843].

[447] P. M. Stevenson, *Optimized Perturbation Theory*, *Phys. Rev.* **D23** (1981) 2916.

[448] P. M. Stevenson and H. D. Politzer, *OPTIMIZED PERTURBATION THEORY APPLIED TO FACTORIZATION SCHEME DEPENDENCE*, *Nucl. Phys.* **B277** (1986) 758–763.

[449] C. J. Maxwell and A. Mirjalili, *Complete renormalization group improvement: Avoiding factorization and renormalization scale dependence in QCD predictions*, *Nucl. Phys.* **B577** (2000) 209–220, [hep-ph/0002204].

[450] S. J. Brodsky and L. Di Giustino, *Setting the Renormalization Scale in QCD: The Principle of Maximum Conformality*, *Phys. Rev.* **D86** (2012) 085026, [1107.0338].

[451] S. J. Brodsky and X.-G. Wu, *Scale Setting Using the Extended Renormalization Group and the Principle of Maximum Conformality: the QCD Coupling Constant at Four Loops*, *Phys. Rev.* **D85** (2012) 034038, [1111.6175].

[452] M. Mojaza, S. J. Brodsky and X.-G. Wu, *Systematic All-Orders Method to Eliminate Renormalization-Scale and Scheme Ambiguities in Perturbative QCD*, *Phys. Rev. Lett.* **110** (2013) 192001, [1212.0049].

[453] S. J. Brodsky, M. Mojaza and X.-G. Wu, *Systematic Scale-Setting to All Orders: The Principle of Maximum Conformality and Commensurate Scale Relations*, *Phys. Rev.* **D89** (2014) 014027, [1304.4631].

[454] H.-H. Ma, X.-G. Wu, Y. Ma, S. J. Brodsky and M. Mojaza, *Setting the renormalization scale in perturbative QCD: Comparisons of the principle of maximum conformality with the sequential extended Brodsky-Lepage-Mackenzie approach*, *Phys. Rev.* **D91** (2015) 094028, [1504.01260].

[455] D0 collaboration, B. Abbott et al., *Direct measurement of the top quark mass at D0*, *Phys. Rev.* **D58** (1998) 052001, [hep-ex/9801025].

[456] CDF collaboration, T. Affolder et al., *Measurement of the top quark p_T distribution*, *Phys. Rev. Lett.* **87** (2001) 102001.

[457] CDF collaboration, T. Aaltonen et al., *First Measurement of the t anti-t Differential Cross Section d sigma/dM(t anti-t) in p anti-p Collisions at s**(1/2)=1.96-TeV*, *Phys. Rev. Lett.* **102** (2009) 222003, [0903.2850].

[458] D0 collaboration, V. M. Abazov et al., *Dependence of the $t\bar{t}$ production cross section on the transverse momentum of the top quark*, *Phys. Lett.* **B693** (2010) 515–521, [1001.1900].

[459] D0 collaboration, V. M. Abazov et al., *Measurement of differential $t\bar{t}$ production cross sections in $p\bar{p}$ collisions*, *Phys. Rev.* **D90** (2014) 092006, [1401.5785].

[460] CMS collaboration, V. Khachatryan et al., *Measurement of the differential cross section for top quark pair production in pp collisions at $\sqrt{s} = 8$ TeV*, *Eur. Phys. J.* **C75** (2015) 542, [1505.04480].

[461] ATLAS collaboration, G. Aad et al., *Measurements of top-quark pair differential cross-sections in the lepton+jets channel in pp collisions at $\sqrt{s} = 8$ TeV using the ATLAS detector*, 1511.04716.

[462] CMS collaboration, *Measurement of the differential cross section for $\mathrm{t\bar{t}}$ production in the dilepton final state at $\sqrt{s} = 13$ TeV*, .

[463] ATLAS collaboration, G. Aad et al., *Measurement of the differential cross-section of highly boosted top quarks as a function of their transverse momentum in $\sqrt{s} = 8$ TeV proton-proton collisions using the ATLAS detector*, *Phys. Rev.* **D93** (2016) 032009, [1510.03818].

[464] CMS collaboration, V. Khachatryan et al., *Measurement of the integrated and differential t-tbar production cross sections for high-pt top quarks in pp collisions at $\sqrt{s}$ = 8 TeV*, *Submitted to: Phys. Rev. D.* (2016) , [1605.00116].

[465] CMS collaboration, *Measurement of double differential cross sections for top quark pair production in pp collisions at sqrt[s] = 8 TeV*, .

[466] CMS collaboration, *Single top t-channel differential cross section at 8 TeV*, .

[467] CMS collaboration, *Measurement of the differential cross section for t-channel single-top-quark production at $\sqrt{s} = 13$ TeV*, .

[468] CMS collaboration, S. Chatrchyan et al., *Measurement of differential top-quark pair production cross sections in pp colisions at $\sqrt{s} = 7$ TeV*, *Eur. Phys. J.* **C73** (2013) 2339, [1211.2220].

[469] ATLAS collaboration, G. Aad et al., *Measurements of normalized differential cross sections for $t\bar{t}$ production in pp collisions at $\sqrt{s} = 7$ TeV using the ATLAS detector*, *Phys. Rev.* **D90** (2014) 072004, [1407.0371].

[470] ATLAS collaboration, G. Aad et al., *Differential top-antitop cross-section measurements as a function of observables constructed from final-state particles using pp collisions at $\sqrt{s} = 7$ TeV in the ATLAS detector*, *JHEP* **06** (2015) 100, [1502.05923].

[471] CMS collaboration, *First measurement of the differential cross section for ttbar production in the dilepton final state at sqrts = 13 TeV*, .

[472] ATLAS collaboration, M. Aaboud et al., *Measurement of top quark pair differential cross-sections in the dilepton channel in pp collisions at $\sqrt{s} = 7$ and 8 TeV with ATLAS*, 1607.07281.

[473] ATLAS collaboration, *Measurements of top-quark pair differential cross-sections in the lepton+jets channel in pp collisions at $\sqrt{s} = 13$ TeV using the ATLAS detector*, .

[474] CMS collaboration, *Measurement of the inclusive and differential tt production cross sections in lepton + jets final states at 13 TeV*, .

[475] G. Choudalakis, *On hypothesis testing, trials factor, hypertests and the BumpHunter*, in *Proceedings, PHYSTAT 2011 Workshop on Statistical Issues Related to Discovery Claims in Search Experiments and Unfolding, CERN,Geneva, Switzerland 17-20 January 2011*, 2011. 1101.0390.

[476] ATLAS collaboration, *Search for resonances decaying to photon pairs in 3.2 fb^{-1} of pp collisions at $\sqrt{s} = 13$ TeV with the ATLAS detector*, .

[477] CMS collaboration, *Search for new physics in high mass diphoton events in proton-proton collisions at 13TeV*, .

[478] ATLAS collaboration, M. Aaboud et al., *Search for resonances in diphoton events at $\sqrt{s}$=13 TeV with the ATLAS detector*, *JHEP* **09** (2016) 001, [1606.03833].

[479] CMS collaboration, V. Khachatryan et al., *Search for Resonant Production of High-Mass Photon Pairs in Proton-Proton Collisions at $\sqrt{s}$ =8 and 13 TeV*, *Phys. Rev. Lett.* **117** (2016) 051802, [1606.04093].

[480] ATLAS collaboration, *Search for scalar diphoton resonances with 15.4 fb^{-1} of data collected at $\sqrt{s}$=13 TeV in 2015 and 2016 with the ATLAS detector*, .

[481] CMS collaboration, V. Khachatryan et al., *Search for high-mass diphoton resonances in proton-proton collisions at 13 TeV and combination with 8 TeV search*, 1609.02507.

[482] M. L. Mangano, P. Nason and G. Ridolfi, *Heavy quark correlations in hadron collisions at next-to-leading order*, *Nucl. Phys.* **B373** (1992) 295–345.

[483] J. C. Collins, D. E. Soper and G. F. Sterman, *Factorization of Hard Processes in QCD*, *Adv. Ser. Direct. High Energy Phys.* **5** (1989) 1–91, [hep-ph/0409313].

[484] W. A. Bardeen, A. J. Buras, D. W. Duke and T. Muta, *Deep Inelastic Scattering Beyond the Leading Order in Asymptotically Free Gauge Theories*, *Phys. Rev.* **D18** (1978) 3998.

[485] G. Altarelli, R. K. Ellis and G. Martinelli, *Leptoproduction and Drell-Yan Processes Beyond the Leading Approximation in Chromodynamics*, *Nucl. Phys.* **B143** (1978) 521.

[486] T. van Ritbergen, J. A. M. Vermaseren and S. A. Larin, *The Four loop beta function in quantum chromodynamics*, *Phys. Lett.* **B400** (1997) 379–384, [hep-ph/9701390].

[487] M. Czakon, *The Four-loop QCD beta-function and anomalous dimensions*, *Nucl. Phys.* **B710** (2005) 485–498, [hep-ph/0411261].

[488] S. Moch, J. A. M. Vermaseren and A. Vogt, *The Three loop splitting functions in QCD: The Nonsinglet case*, *Nucl. Phys.* **B688** (2004) 101–134, [hep-ph/0403192].

[489] A. Vogt, S. Moch and J. A. M. Vermaseren, *The Three-loop splitting functions in QCD: The Singlet case*, *Nucl. Phys.* **B691** (2004) 129–181, [hep-ph/0404111].

[490] J. Pumplin, D. Stump, R. Brock, D. Casey, J. Huston, J. Kalk et al., *Uncertainties of predictions from parton distribution functions. 2. The Hessian method*, *Phys. Rev.* **D65** (2001) 014013, [hep-ph/0101032].

[491] P. M. Nadolsky and Z. Sullivan, *PDF uncertainties in WH production at Tevatron*, *eConf* **C010630** (2001) P510, [hep-ph/0110378].

[492] M. Cacciari, S. Frixione, M. L. Mangano, P. Nason and G. Ridolfi, *Updated predictions for the total production cross sections of top and of heavier quark pairs at the Tevatron and at the LHC*, *JHEP* **09** (2008) 127, [0804.2800].

[493] NNPDF collaboration, R. D. Ball, V. Bertone, F. Cerutti, L. Del Debbio, S. Forte, A. Guffanti et al., *Unbiased global determination of parton distributions and their uncertainties at NNLO and at LO*, *Nucl. Phys.* **B855** (2012) 153–221, [1107.2652].

[494] R. D. Ball et al., *Parton Distribution Benchmarking with LHC Data*, *JHEP* **04** (2013) 125, [1211.5142].

[495] A. D. Martin, A. J. T. M. Mathijssen, W. J. Stirling, R. S. Thorne, B. J. A. Watt and G. Watt, *Extended Parameterisations for MSTW PDFs and their effect on Lepton Charge Asymmetry from W Decays*, *Eur. Phys. J.* **C73** (2013) 2318, [1211.1215].

[496] ZEUS, H1 collaboration, F. D. Aaron et al., *Combined Measurement and QCD Analysis of the Inclusive e+- p Scattering Cross Sections at HERA*, *JHEP* **01** (2010) 109, [0911.0884].

[497] ZEUS, H1 collaboration, A. M. Cooper-Sarkar, *PDF Fits at HERA*, *PoS* **EPS-HEP2011** (2011) 320, [1112.2107].

[498] ZEUS, H1 collaboration, H. Abramowicz et al., *Combination of measurements of inclusive deep inelastic $e^{\pm}p$ scattering cross sections and QCD analysis of HERA data*, *Eur. Phys. J.* **C75** (2015) 580, [1506.06042].

[499] J. Gao, M. Guzzi, J. Huston, H.-L. Lai, Z. Li, P. Nadolsky et al., *CT10 next-to-next-to-leading order global analysis of QCD*, *Phys. Rev.* **D89** (2014) 033009, [1302.6246].

[500] S. Dulat, T.-J. Hou, J. Gao, M. Guzzi, J. Huston, P. Nadolsky et al., *New parton distribution functions from a global analysis of quantum chromodynamics*, *Phys. Rev.* **D93** (2016) 033006, [1506.07443].

[501] S. Alekhin, J. Blumlein and S. Moch, *Parton Distribution Functions and Benchmark Cross Sections at NNLO*, *Phys. Rev.* **D86** (2012) 054009, [1202.2281].

[502] M. R. Whalley, D. Bourilkov and R. C. Group, *The Les Houches accord PDFs (LHAPDF) and LHAGLUE*, in *HERA and the LHC: A Workshop on the implications of HERA for LHC physics. Proceedings, Part B*, 2005. hep-ph/0508110.

[503] D. Bourilkov, R. C. Group and M. R. Whalley, *LHAPDF: PDF use from the Tevatron to the LHC*, in *TeV4LHC Workshop - 4th meeting Batavia, Illinois, October 20-22, 2005*, 2006. hep-ph/0605240.

[504] A. Buckley, J. Ferrando, S. Lloyd, K. Nordstroem, B. Page, M. Ruefenacht et al., *LHAPDF6: parton density access in the LHC precision era*, *Eur. Phys. J.* **C75** (2015) 132, [1412.7420].

[505] S. Alekhin et al., *The PDF4LHC Working Group Interim Report*, 1101.0536.

[506] G. Watt, *Parton distribution function dependence of benchmark Standard Model total cross sections at the 7 TeV LHC*, *JHEP* **09** (2011) 069, [1106.5788].

[507] A. D. Martin, W. J. Stirling, R. S. Thorne and G. Watt, *Uncertainties on alpha(S) in global PDF analyses and implications for predicted hadronic cross sections*, *Eur. Phys. J.* **C64** (2009) 653–680, [0905.3531].

[508] G. 't Hooft and M. J. G. Veltman, *Regularization and Renormalization of Gauge Fields*, *Nucl. Phys.* **B44** (1972) 189–213.

[509] W. Siegel, *Supersymmetric Dimensional Regularization via Dimensional Reduction*, *Phys. Lett.* **B84** (1979) 193–196.

[510] Z. Bern and D. A. Kosower, *The Computation of loop amplitudes in gauge theories*, *Nucl. Phys.* **B379** (1992) 451–561.

[511] Z. Bern, A. De Freitas, L. J. Dixon and H. L. Wong, *Supersymmetric regularization, two loop QCD amplitudes and coupling shifts*, *Phys. Rev.* **D66** (2002) 085002, [hep-ph/0202271].

[512] J. C. Collins, *Renormalization*, vol. 26 of *Cambridge Monographs on Mathematical Physics*. Cambridge University Press, Cambridge, 1986.

[513] W. Bernreuther and W. Wetzel, *Decoupling of Heavy Quarks in the Minimal Subtraction Scheme*, *Nucl. Phys.* **B197** (1982) 228–236.

[514] K. G. Chetyrkin, J. H. Kuhn and C. Sturm, *QCD decoupling at four loops*, *Nucl. Phys.* **B744** (2006) 121–135, [hep-ph/0512060].

[515] M. Beneke, P. Falgari and C. Schwinn, *Soft radiation in heavy-particle pair production: All-order colour structure and two-loop anomalous dimension*, *Nucl. Phys.* **B828** (2010) 69–101, [0907.1443].

[516] W. Beenakker, T. Janssen, S. Lepoeter, M. Kraemer, A. Kulesza, E. Laenen et al., *Towards NNLL resummation: hard matching coefficients for squark and gluino hadroproduction*, *JHEP* **10** (2013) 120, [1304.6354].

[517] M. Cacciari, L. Del Debbio, J. R. Espinosa, A. D. Polosa and M. Testa, *A note on the fate of the Landau-Yang theorem in non-Abelian gauge theories*, *Phys. Lett.* **B753** (2016) 476–481, [1509.07853].

[518] V. A. Smirnov, *Evaluating Feynman integrals*, *Springer Tracts Mod. Phys.* **211** (2004) 1–244.

[519] V. A. Smirnov, *Feynman integral calculus*. 2006.

[520] V. A. Smirnov, *Analytic tools for Feynman integrals*, *Springer Tracts Mod. Phys.* **250** (2012) 1–296.

[521] K. G. Chetyrkin and F. V. Tkachov, *Integration by Parts: The Algorithm to Calculate beta Functions in 4 Loops*, *Nucl. Phys.* **B192** (1981) 159–204.

[522] F. V. Tkachov, *A Theorem on Analytical Calculability of Four Loop Renormalization Group Functions*, *Phys. Lett.* **B100** (1981) 65–68.

[523] S. Laporta, *High precision calculation of multiloop Feynman integrals by difference equations*, *Int. J. Mod. Phys.* **A15** (2000) 5087–5159, [hep-ph/0102033].

[524] C. Anastasiou and A. Lazopoulos, *Automatic integral reduction for higher order perturbative calculations*, *JHEP* **07** (2004) 046, [hep-ph/0404258].

[525] A. V. Smirnov, *Algorithm FIRE – Feynman Integral REduction*, *JHEP* **10** (2008) 107, [0807.3243].

[526] A. von Manteuffel and C. Studerus, *Reduze 2 - Distributed Feynman Integral Reduction*, 1201.4330.

[527] R. E. Cutkosky, *Singularities and discontinuities of Feynman amplitudes*, *J. Math. Phys.* **1** (1960) 429–433.

[528] C. Anastasiou and K. Melnikov, *Higgs boson production at hadron colliders in NNLO QCD*, *Nucl. Phys.* **B646** (2002) 220–256, [hep-ph/0207004].

[529] A. V. Kotikov, *Differential equations method: New technique for massive Feynman diagrams calculation*, *Phys. Lett.* **B254** (1991) 158–164.

[530] A. V. Kotikov, *Differential equations method: The Calculation of vertex type Feynman diagrams*, *Phys. Lett.* **B259** (1991) 314–322.

[531] A. V. Kotikov, *Differential equation method: The Calculation of N point Feynman diagrams*, *Phys. Lett.* **B267** (1991) 123–127.

[532] A. V. Kotikov, *New method of massive N point Feynman diagrams calculation*, *Mod. Phys. Lett.* **A6** (1991) 3133–3141.

[533] A. V. Kotikov, *New method of massive Feynman diagrams calculation*, *Mod. Phys. Lett.* **A6** (1991) 677–692.

[534] A. V. Kotikov, *New method of massive Feynman diagrams calculation. Vertex type functions*, *Int. J. Mod. Phys.* **A7** (1992) 1977–1992.

[535] E. Remiddi, *Differential equations for Feynman graph amplitudes*, *Nuovo Cim.* **A110** (1997) 1435–1452, [hep-th/9711188].

[536] V. A. Smirnov, *Applied asymptotic expansions in momenta and masses*, *Springer Tracts Mod. Phys.* **177** (2002) 1–262.

[537] V. A. Smirnov, *Analytical result for dimensionally regularized massless on shell double box*, *Phys. Lett.* **B460** (1999) 397–404, [hep-ph/9905323].

[538] J. B. Tausk, *Nonplanar massless two loop Feynman diagrams with four on-shell legs*, *Phys. Lett.* **B469** (1999) 225–234, [hep-ph/9909506].

[539] J. A. M. Vermaseren, *Harmonic sums, Mellin transforms and integrals*, *Int. J. Mod. Phys.* **A14** (1999) 2037–2076, [hep-ph/9806280].

[540] S. Moch and P. Uwer, *XSummer: Transcendental functions and symbolic summation in form*, *Comput. Phys. Commun.* **174** (2006) 759–770, [math-ph/0508008].

[541] MB Tools, http://mbtools.hepforge.org.

[542] M. Czakon, *Automatized analytic continuation of Mellin-Barnes integrals*, *Comput. Phys. Commun.* **175** (2006) 559–571, [hep-ph/0511200].

[543] S. Dittmaier, *A General approach to photon radiation off fermions*, *Nucl. Phys.* **B565** (2000) 69–122, [hep-ph/9904440].

[544] T. O. Eynck, E. Laenen, L. Phaf and S. Weinzierl, *Comparison of phase space slicing and dipole subtraction methods for gamma* —> anti-Q*, *Eur. Phys. J.* **C23** (2002) 259–266, [hep-ph/0109246].

[545] A. Bassetto, M. Ciafaloni and G. Marchesini, *Jet Structure and Infrared Sensitive Quantities in Perturbative QCD*, *Phys. Rept.* **100** (1983) 201–272.

[546] Y. L. Dokshitzer, V. A. Khoze, A. H. Mueller and S. I. Troian, *Basics of perturbative QCD*. 1991.

[547] S. Catani and M. Grazzini, *Infrared factorization of tree level QCD amplitudes at the next-to-next-to-leading order and beyond*, *Nucl. Phys.* **B570** (2000) 287–325, [hep-ph/9908523].

[548] S. Catani and M. H. Seymour, *A General algorithm for calculating jet cross-sections in NLO QCD*, *Nucl. Phys.* **B485** (1997) 291–419, [hep-ph/9605323].

[549] S. Catani, S. Dittmaier, M. H. Seymour and Z. Trocsanyi, *The Dipole formalism for next-to-leading order QCD calculations with massive partons*, *Nucl. Phys.* **B627** (2002) 189–265, [hep-ph/0201036].

[550] S. Frixione, Z. Kunszt and A. Signer, *Three jet cross-sections to next-to-leading order*, *Nucl. Phys.* **B467** (1996) 399–442, [hep-ph/9512328].

[551] Z. Nagy and D. E. Soper, *Parton showers with quantum interference*, *JHEP* **09** (2007) 114, [0706.0017].

[552] G. Bevilacqua, M. Czakon, M. Kubocz and M. Worek, *Complete Nagy-Soper subtraction for next-to-leading order calculations in QCD*, *JHEP* **10** (2013) 204, [1308.5605].

[553] R. Frederix, S. Frixione, F. Maltoni and T. Stelzer, *Automation of next-to-leading order computations in QCD: The FKS subtraction*, *JHEP* **10** (2009) 003, [0908.4272].

[554] K. Hagiwara, Y. Sumino and H. Yokoya, *Bound-state Effects on Top Quark Production at Hadron Colliders*, *Phys. Lett.* **B666** (2008) 71–76, [0804.1014].

[555] R. D. Ball and R. K. Ellis, *Heavy quark production at high-energy*, *JHEP* **05** (2001) 053, [hep-ph/0101199].

[556] G. F. Sterman, *Summation of Large Corrections to Short Distance Hadronic Cross-Sections*, *Nucl. Phys.* **B281** (1987) 310–364.

[557] S. Catani and L. Trentadue, *Resummation of the QCD Perturbative Series for Hard Processes*, *Nucl. Phys.* **B327** (1989) 323–352.

[558] M. Czakon and P. Fiedler, *The soft function for color octet production at threshold*, *Nucl. Phys.* **B879** (2014) 236–255, [1311.2541].

[559] M. Beneke, P. Falgari and C. Schwinn, *Threshold resummation for pair production of coloured heavy (s)particles at hadron colliders*, *Nucl. Phys.* **B842** (2011) 414–474, [1007.5414].

[560] T. Becher and M. Neubert, *Infrared singularities of scattering amplitudes in perturbative QCD*, *Phys. Rev. Lett.* **102** (2009) 162001, [0901.0722].

[561] T. Becher and M. Neubert, *On the Structure of Infrared Singularities of Gauge-Theory Amplitudes*, *JHEP* **06** (2009) 081, [0903.1126].

[562] T. Becher and M. Neubert, *Infrared singularities of QCD amplitudes with massive partons*, *Phys. Rev.* **D79** (2009) 125004, [0904.1021].

[563] S. M. Aybat, L. J. Dixon and G. F. Sterman, *The Two-loop soft anomalous dimension matrix and resummation at next-to-next-to leading pole*, *Phys. Rev.* **D74** (2006) 074004, [hep-ph/0607309].

[564] A. Ferroglia, M. Neubert, B. D. Pecjak and L. L. Yang, *Two-loop divergences of massive scattering amplitudes in non-abelian gauge theories*, *JHEP* **11** (2009) 062, [0908.3676].

[565] A. Mitov, G. F. Sterman and I. Sung, *The Massive Soft Anomalous Dimension Matrix at Two Loops*, *Phys. Rev.* **D79** (2009) 094015, [0903.3241].

[566] A. V. Belitsky, *Two loop renormalization of Wilson loop for Drell-Yan production*, *Phys. Lett.* **B442** (1998) 307–314, [hep-ph/9808389].

[567] A. Idilbi, C. Kim and T. Mehen, *Factorization and resummation for single color-octet scalar production at the LHC*, *Phys. Rev.* **D79** (2009) 114016, [0903.3668].

[568] G. Somogyi, *Angular integrals in d dimensions*, *J. Math. Phys.* **52** (2011) 083501, [1101.3557].

[569] T. Huber and D. Maitre, *HypExp: A Mathematica package for expanding hypergeometric functions around integer-valued parameters*, *Comput. Phys. Commun.* **175** (2006) 122–144, [hep-ph/0507094].

[570] I. Bierenbaum, M. Czakon and A. Mitov, *The singular behavior of one-loop massive QCD amplitudes with one external soft gluon*, *Nucl. Phys.* **B856** (2012) 228–246, [1107.4384].

[571] J. G. Korner, Z. Merebashvili and M. Rogal, *Laurent series expansion of massive scalar one-loop integrals to $O(epsilson^2)$*, *Phys. Rev.* **D71** (2005) 054028, [hep-ph/0412088].

[572] C. Anastasiou and S. M. Aybat, *The One-loop gluon amplitude for heavy-quark production at NNLO*, *Phys. Rev.* **D78** (2008) 114006, [0809.1355].

[573] J. G. Korner, Z. Merebashvili and M. Rogal, *NNLO $O(\alpha_s^4)$ results for heavy quark pair production in quark-antiquark collisions: The One-loop squared contributions*, *Phys. Rev.* **D77** (2008) 094011, [0802.0106].

[574] B. Kniehl, Z. Merebashvili, J. G. Korner and M. Rogal, *Heavy quark pair production in gluon fusion at next-to-next-to-leading $O(\alpha_s^{4)}$ order: One-loop squared contributions*, *Phys. Rev.* **D78** (2008) 094013, [0809.3980].

[575] R. Bonciani, A. Ferroglia, T. Gehrmann, D. Maitre and C. Studerus, *Two-Loop Fermionic Corrections to Heavy-Quark Pair Production: The Quark-Antiquark Channel*, *JHEP* **07** (2008) 129, [0806.2301].

[576] R. Bonciani, A. Ferroglia, T. Gehrmann and C. Studerus, *Two-Loop Planar Corrections to Heavy-Quark Pair Production in the Quark-Antiquark Channel*, *JHEP* **08** (2009) 067, [0906.3671].

[577] R. Bonciani, A. Ferroglia, T. Gehrmann, A. von Manteuffel and C. Studerus, *Two-Loop Leading Color Corrections to Heavy-Quark Pair Production in the Gluon Fusion Channel*, *JHEP* **01** (2011) 102, [1011.6661].

[578] U. Langenfeld, S. Moch and P. Uwer, *Measuring the running top-quark mass*, *Phys. Rev.* **D80** (2009) 054009, [0906.5273].

[579] J. Kodaira and L. Trentadue, *Summing Soft Emission in QCD*, *Phys. Lett.* **B112** (1982) 66.

[580] S. Catani, E. D'Emilio and L. Trentadue, *The Gluon Form-factor to Higher Orders: Gluon Gluon Annihilation at Small Q^- transverse*, *Phys. Lett.* **B211** (1988) 335–342.

[581] R. Bonciani, *Thesis (in italian)*, July, 1997, University of Florence.

[582] D. A. Kosower, *Antenna factorization of gauge theory amplitudes*, *Phys. Rev.* **D57** (1998) 5410–5416, [hep-ph/9710213].

[583] D. A. Kosower, *Antenna factorization in strongly ordered limits*, *Phys. Rev.* **D71** (2005) 045016, [hep-ph/0311272].

[584] A. Gehrmann-De Ridder, T. Gehrmann and E. W. N. Glover, *Antenna subtraction at NNLO*, *JHEP* **09** (2005) 056, [hep-ph/0505111].

[585] F. Maltoni, K. Paul, T. Stelzer and S. Willenbrock, *Color flow decomposition of QCD amplitudes*, *Phys. Rev.* **D67** (2003) 014026, [hep-ph/0209271].

[586] C. G. Papadopoulos and M. Worek, *Multi-parton cross sections at hadron colliders*, *Eur. Phys. J.* **C50** (2007) 843–856, [hep-ph/0512150].

[587] A. Gehrmann-De Ridder, T. Gehrmann and G. Heinrich, *Four particle phase space integrals in massless QCD*, *Nucl. Phys.* **B682** (2004) 265–288, [hep-ph/0311276].

[588] A. Gehrmann-De Ridder, T. Gehrmann, E. W. N. Glover and G. Heinrich, *Infrared structure of e+ e- —> 3 jets at NNLO*, *JHEP* **11** (2007) 058, [0710.0346].

[589] J. Currie, *Colourful antenna subtraction for gluon scattering*, *PoS* **RADCOR2013** (2013) 001, [1311.6113].

[590] G. Somogyi and Z. Trocsanyi, *A Subtraction scheme for computing QCD jet cross sections at NNLO: Regularization of real-virtual emission*, *JHEP* **01** (2007) 052, [hep-ph/0609043].

[591] G. Somogyi, Z. Trocsanyi and V. Del Duca, *Matching of singly- and doubly-unresolved limits of tree-level QCD squared matrix elements*, *JHEP* **06** (2005) 024, [hep-ph/0502226].

[592] G. Somogyi and Z. Trocsanyi, *A New subtraction scheme for computing QCD jet cross sections at next-to-leading order accuracy*, hep-ph/0609041.

[593] G. Somogyi, Z. Trocsanyi and V. Del Duca, *A Subtraction scheme for computing QCD jet cross sections at NNLO: Regularization of doubly-real emissions*, *JHEP* **01** (2007) 070, [hep-ph/0609042].

[594] G. Somogyi and Z. Trocsanyi, *A Subtraction scheme for computing QCD jet cross sections at NNLO: Integrating the subtraction terms. I.*, *JHEP* **08** (2008) 042, [0807.0509].

[595] U. Aglietti, V. Del Duca, C. Duhr, G. Somogyi and Z. Trocsanyi, *Analytic integration of real-virtual counterterms in NNLO jet cross sections. I.*, *JHEP* **09** (2008) 107, [0807.0514].

[596] G. Somogyi, *Subtraction with hadronic initial states at NLO: An NNLO-compatible scheme*, *JHEP* **05** (2009) 016, [0903.1218].

[597] P. Bolzoni, S.-O. Moch, G. Somogyi and Z. Trocsanyi, *Analytic integration of real-virtual counterterms in NNLO jet cross sections. II.*, *JHEP* **08** (2009) 079, [0905.4390].

[598] P. Bolzoni, G. Somogyi and Z. Trocsanyi, *A subtraction scheme for computing QCD jet cross sections at NNLO: integrating the iterated singly-unresolved subtraction terms*, *JHEP* **01** (2011) 059, [1011.1909].

[599] V. Del Duca, G. Somogyi and Z. Trocsanyi, *Integration of collinear-type doubly unresolved counterterms in NNLO jet cross sections*, *JHEP* **06** (2013) 079, [1301.3504].

[600] G. Somogyi, *A subtraction scheme for computing QCD jet cross sections at NNLO: integrating the doubly unresolved subtraction terms*, *JHEP* **04** (2013) 010, [1301.3919].

[601] V. Del Duca, C. Duhr, G. Somogyi, F. Tramontano and Z. Trocsanyi, *Higgs boson decay into b-quarks at NNLO accuracy*, *JHEP* **04** (2015) 036, [1501.07226].

[602] J. Gaunt, M. Stahlhofen, F. J. Tackmann and J. R. Walsh, *N-jettiness Subtractions for NNLO QCD Calculations*, *JHEP* **09** (2015) 058, [1505.04794].

[603] S. M. Freedman, *Subleading Corrections To Thrust Using Effective Field Theory*, 1303.1558.

[604] S. M. Freedman and R. Goerke, *Renormalization of Subleading Dijet Operators in Soft-Collinear Effective Theory*, *Phys. Rev.* **D90** (2014) 114010, [1408.6240].

[605] S. Catani and M. Grazzini, *An NNLO subtraction formalism in hadron collisions and its application to Higgs boson production at the LHC*, *Phys. Rev. Lett.* **98** (2007) 222002, [hep-ph/0703012].

[606] M. Grazzini, *NNLO predictions for the Higgs boson signal in the H —> WW —> lnu lnu and H —> ZZ —> 4l decay channels*, *JHEP* **02** (2008) 043, [0801.3232].

[607] G. Bozzi, S. Catani, D. de Florian and M. Grazzini, *Transverse-momentum resummation and the spectrum of the Higgs boson at the LHC*, *Nucl. Phys.* **B737** (2006) 73–120, [hep-ph/0508068].

[608] S. Catani, L. Cieri, D. de Florian, G. Ferrera and M. Grazzini, *Universality of transverse-momentum resummation and hard factors at the NNLO*, *Nucl. Phys.* **B881** (2014) 414–443, [1311.1654].

[609] M. Grazzini, S. Kallweit, D. Rathlev and A. Torre, *$Z\gamma$ production at hadron colliders in NNLO QCD*, *Phys. Lett.* **B731** (2014) 204–207, [1309.7000].

[610] M. Grazzini, S. Kallweit and D. Rathlev, *$W\gamma$ and $Z\gamma$ production at the LHC in NNLO QCD*, *JHEP* **07** (2015) 085, [1504.01330].

[611] F. Cascioli, T. Gehrmann, M. Grazzini, S. Kallweit, P. Maierhoefer, A. von Manteuffel et al., *ZZ production at hadron colliders in NNLO QCD*, *Phys. Lett.* **B735** (2014) 311–313, [1405.2219].

[612] T. Gehrmann, M. Grazzini, S. Kallweit, P. Maierhoefer, A. von Manteuffel, S. Pozzorini et al., *W^+W^- Production at Hadron Colliders in Next to Next to Leading Order QCD*, *Phys. Rev. Lett.* **113** (2014) 212001, [1408.5243].

[613] H. X. Zhu, C. S. Li, H. T. Li, D. Y. Shao and L. L. Yang, *Transverse-momentum resummation for top-quark pairs at hadron colliders*, *Phys. Rev. Lett.* **110** (2013) 082001, [1208.5774].

[614] H. T. Li, C. S. Li, D. Y. Shao, L. L. Yang and H. X. Zhu, *Top quark pair production at small transverse momentum in hadronic collisions*, *Phys. Rev.* **D88** (2013) 074004, [1307.2464].

[615] S. Catani, M. Grazzini and A. Torre, *Transverse-momentum resummation for heavy-quark hadroproduction*, *Nucl. Phys.* **B890** (2014) 518–538, [1408.4564].

[616] I. W. Stewart, F. J. Tackmann and W. J. Waalewijn, *N-Jettiness: An Inclusive Event Shape to Veto Jets*, *Phys. Rev. Lett.* **105** (2010) 092002, [1004.2489].

[617] R. Boughezal, X. Liu and F. Petriello, *N-jettiness soft function at next-to-next-to-leading order*, *Phys. Rev.* **D91** (2015) 094035, [1504.02540].

[618] I. W. Stewart, F. J. Tackmann and W. J. Waalewijn, *The Beam Thrust Cross Section for Drell-Yan at NNLL Order*, *Phys. Rev. Lett.* **106** (2011) 032001, [1005.4060].

[619] J. R. Gaunt, M. Stahlhofen and F. J. Tackmann, *The Quark Beam Function at Two Loops*, *JHEP* **04** (2014) 113, [1401.5478].

[620] J. Gaunt, M. Stahlhofen and F. J. Tackmann, *The Gluon Beam Function at Two Loops*, *JHEP* **08** (2014) 020, [1405.1044].

[621] T. Becher and M. Neubert, *Toward a NNLO calculation of the anti-B —> X(s) gamma decay rate with a cut on photon energy. II. Two-loop result for the jet function*, *Phys. Lett.* **B637** (2006) 251–259, [hep-ph/0603140].

[622] T. Becher and G. Bell, *The gluon jet function at two-loop order*, *Phys. Lett.* **B695** (2011) 252–258, [1008.1936].

[623] R. Boughezal, C. Focke, W. Giele, X. Liu and F. Petriello, *Higgs boson production in association with a jet at NNLO using jettiness subtraction*, *Phys. Lett.* **B748** (2015) 5–8, [1505.03893].

[624] R. Boughezal, C. Focke, X. Liu and F. Petriello, *W-boson production in association with a jet at next-to-next-to-leading order in perturbative QCD*, *Phys. Rev. Lett.* **115** (2015) 062002, [1504.02131].

[625] R. Boughezal, J. M. Campbell, R. K. Ellis, C. Focke, W. T. Giele, X. Liu et al., *Z-boson production in association with a jet at next-to-next-to-leading order in perturbative QCD*, *Phys. Rev. Lett.* **116** (2016) 152001, [1512.01291].

[626] M. Brucherseifer, F. Caola and K. Melnikov, *On the $O(\alpha_s^2)$ corrections to $b \to X_u e \bar{\nu}$ inclusive decays*, *Phys. Lett.* **B721** (2013) 107–110, [1302.0444].

[627] R. Boughezal, F. Caola, K. Melnikov, F. Petriello and M. Schulze, *Higgs boson production in association with a jet at next-to-next-to-leading order*, *Phys. Rev. Lett.* **115** (2015) 082003, [1504.07922].

[628] R. Boughezal, F. Caola, K. Melnikov, F. Petriello and M. Schulze, *Higgs boson production in association with a jet at next-to-next-to-leading order in perturbative QCD*, *JHEP* **06** (2013) 072, [1302.6216].

[629] F. Caola, A. Czarnecki, Y. Liang, K. Melnikov and R. Szafron, *Muon decay spin asymmetry*, *Phys. Rev.* **D90** (2014) 053004, [1403.3386].

[630] R. Boughezal, K. Melnikov and F. Petriello, *A subtraction scheme for NNLO computations*, *Phys. Rev.* **D85** (2012) 034025, [1111.7041].

[631] T. Binoth and G. Heinrich, *An automatized algorithm to compute infrared divergent multiloop integrals*, *Nucl. Phys.* **B585** (2000) 741–759, [hep-ph/0004013].

[632] M. Czakon and D. Heymes, *Four-dimensional formulation of the sector-improved residue subtraction scheme*, *Nucl. Phys.* **B890** (2014) 152–227, [1408.2500].

[633] M. Luscher, *A Portable high quality random number generator for lattice field theory simulations*, *Comput. Phys. Commun.* **79** (1994) 100–110, [hep-lat/9309020].

[634] F. James, *RANLUX: A FORTRAN implementation of the high quality pseudorandom number generator of Luscher*, *Comput. Phys. Commun.* **79** (1994) 111–114.

[635] A. van Hameren, *PARNI for importance sampling and density estimation*, *Acta Phys. Polon.* **B40** (2009) 259–272, [0710.2448].

[636] Z. Bern, L. J. Dixon, D. C. Dunbar and D. A. Kosower, *One loop n point gauge theory amplitudes, unitarity and collinear limits*, *Nucl. Phys.* **B425** (1994) 217–260, [hep-ph/9403226].

[637] Z. Bern, V. Del Duca and C. R. Schmidt, *The Infrared behavior of one loop gluon amplitudes at next-to-next-to-leading order*, *Phys. Lett.* **B445** (1998) 168–177, [hep-ph/9810409].

[638] D. A. Kosower, *All order collinear behavior in gauge theories*, *Nucl. Phys.* **B552** (1999) 319–336, [hep-ph/9901201].

[639] D. A. Kosower and P. Uwer, *One loop splitting amplitudes in gauge theory*, *Nucl. Phys.* **B563** (1999) 477–505, [hep-ph/9903515].

[640] Z. Bern, V. Del Duca, W. B. Kilgore and C. R. Schmidt, *The infrared behavior of one loop QCD amplitudes at next-to-next-to leading order*, *Phys. Rev.* **D60** (1999) 116001, [hep-ph/9903516].

[641] S. Catani and M. Grazzini, *The soft gluon current at one loop order*, *Nucl. Phys.* **B591** (2000) 435–454, [hep-ph/0007142].

[642] S. Weinzierl, *Does one need the $O(epsilon)$- and $O(epsilon^2)$-terms of one-loop amplitudes in an NNLO calculation ?*, *Phys. Rev.* **D84** (2011) 074007, [1107.5131].

[643] G. Passarino and M. J. G. Veltman, *One Loop Corrections for e+ e- Annihilation Into mu+ mu- in the Weinberg Model*, *Nucl. Phys.* **B160** (1979) 151–207.

[644] M. Czakon, A. Mitov and S. Moch, *Heavy-quark production in massless quark scattering at two loops in QCD*, *Phys. Lett.* **B651** (2007) 147–159, [0705.1975].

[645] M. Czakon, A. Mitov and S. Moch, *Heavy-quark production in gluon fusion at two loops in QCD*, *Nucl. Phys.* **B798** (2008) 210–250, [0707.4139].

[646] M. Czakon, *Tops from Light Quarks: Full Mass Dependence at Two-Loops in QCD*, *Phys. Lett.* **B664** (2008) 307–314, [0803.1400].

[647] J. Carter and G. Heinrich, *SecDec: A general program for sector decomposition*, *Comput. Phys. Commun.* **182** (2011) 1566–1581, [1011.5493].

[648] S. Borowka, J. Carter and G. Heinrich, *Numerical Evaluation of Multi-Loop Integrals for Arbitrary Kinematics with SecDec 2.0*, *Comput. Phys. Commun.* **184** (2013) 396–408, [1204.4152].

[649] S. Borowka and G. Heinrich, *Massive non-planar two-loop four-point integrals with SecDec 2.1*, *Comput. Phys. Commun.* **184** (2013) 2552–2561, [1303.1157].

[650] S. Borowka, G. Heinrich, S. P. Jones, M. Kerner, J. Schlenk and T. Zirke, *SecDec-3.0: numerical evaluation of multi-scale integrals beyond one loop*, *Comput. Phys. Commun.* **196** (2015) 470–491, [1502.06595].

[651] A. V. Smirnov and M. N. Tentyukov, *Feynman Integral Evaluation by a Sector decomposiTion Approach (FIESTA)*, *Comput. Phys. Commun.* **180** (2009) 735–746, [0807.4129].

[652] A. V. Smirnov, V. A. Smirnov and M. Tentyukov, *FIESTA 2: Parallelizeable multiloop numerical calculations*, *Comput. Phys. Commun.* **182** (2011) 790–803, [0912.0158].

[653] A. V. Smirnov, *FIESTA 3: cluster-parallelizable multiloop numerical calculations in physical regions*, *Comput. Phys. Commun.* **185** (2014) 2090–2100, [1312.3186].

[654] H. Ferguson and D. Bailey, *Numerical results on relations between fundamental constants using a new algorithm*, *Math. Comp.* **53** (1989) 649–656.

[655] P. Brown, G. Byrne and A. Hindmarsh, *VODE, A Variable-Coefficient ODE Solver*, *SIAM J. Sci. Stat. Comput.* **10** (1989) 1038–1051.

[656] A. von Manteuffel and C. Studerus, *Massive planar and non-planar double box integrals for light Nf contributions to gg->tt*, *JHEP* **10** (2013) 037, [1306.3504].

[657] R. Bonciani, A. Ferroglia, T. Gehrmann, A. von Manteuffel and C. Studerus, *Light-quark two-loop corrections to heavy-quark pair production in the gluon fusion channel*, *JHEP* **12** (2013) 038, [1309.4450].

[658] LHC Higgs Cross Section Working Group collaboration, S. Dittmaier et al., *Handbook of LHC Higgs Cross Sections: 1. Inclusive Observables*, 1101.0593.

[659] CMS collaboration, *Measurement of the top quark pair production cross section using $e\mu$ events in proton-proton collisions at $\sqrt{s} = 13$ TeV with the CMS detector*, .

[660] CDF collaboration, T. Aaltonen et al., *Measurement of the Differential Cross Section $d\sigma/d(\cos\theta t)$ for Top-Quark Pair Production in $p - \bar{p}$ Collisions at $\sqrt{s} = 1.96$ TeV*, *Phys. Rev. Lett.* **111** (2013) 182002, [1306.2357].

[661] K. Melnikov, A. Scharf and M. Schulze, *Top quark pair production in association with a jet: QCD corrections and jet radiation in top quark decays*, *Phys. Rev.* **D85** (2012) 054002, [1111.4991].

[662] S. Hoeche, J. Huang, G. Luisoni, M. Schoenherr and J. Winter, *Zero and one jet combined next-to-leading order analysis of the top quark forward-backward asymmetry*, *Phys. Rev.* **D88** (2013) 014040, [1306.2703].

[663] D0 collaboration, Supplemental information to Phys. Rev. D **90**, no. 7, 072011 (2014), http://www-d0.fnal.gov/Run2Physics/WWW/results/final/TOP/T14D/.

[664] S.-Q. Wang, X.-G. Wu, Z.-G. Si and S. J. Brodsky, *Predictions for the Top-Quark Forward-Backward Asymmetry at High Invariant Pair Mass Using the Principle of Maximum Conformality*, *Phys. Rev.* **D93** (2016) 014004, [1508.03739].

[665] B. Gripaios, A. Papaefstathiou and B. Webber, *Probing the Colour Structure of the Top Quark Forward-Backward Asymmetry*, *JHEP* **11** (2013) 105, [1309.0810].

[666] S. Mrenna and C. P. Yuan, *Effects of QCD resummation on distributions of top - anti-top quark pairs produced at the Tevatron*, *Phys. Rev.* **D55** (1997) 120–129, [hep-ph/9606363].

[667] CDF collaboration, Supplemental information to Phys. Rev. Lett. **111**, no. 18, 182002 (2013), http://www-cdf.fnal.gov/physics/new/top/2013/TopAngularXS/.

[668] M. Czakon, N. P. Hartland, A. Mitov, E. R. Nocera and J. Rojo, *Pinning down the large-x gluon with NNLO top-quark pair differential distributions*, 1611.08609.

[669] D. J. Broadhurst, N. Gray and K. Schilcher, *Gauge invariant on-shell Z(2) in QED, QCD and the effective field theory of a static quark*, *Z. Phys.* **C52** (1991) 111–122.

[670] O. V. Tarasov, A. A. Vladimirov and A. Yu. Zharkov, *The Gell-Mann-Low Function of QCD in the Three Loop Approximation*, *Phys. Lett.* **B93** (1980) 429–432.

[671] S. A. Larin and J. A. M. Vermaseren, *The Three loop QCD Beta function and anomalous dimensions*, *Phys. Lett.* **B303** (1993) 334–336, [hep-ph/9302208].

[672] G. P. Korchemsky and A. V. Radyushkin, *Renormalization of the Wilson Loops Beyond the Leading Order*, *Nucl. Phys.* **B283** (1987) 342–364.

[673] N. Kidonakis, *Two-loop soft anomalous dimensions and NNLL resummation for heavy quark production*, *Phys. Rev. Lett.* **102** (2009) 232003, [0903.2561].

[674] M. Czakon, DiaGen and IdSolver.

[675] R. H. Lewis, Fermat, http://home.bway.net/lewis/.

[676] J. A. M. Vermaseren, *New features of FORM*, math-ph/0010025.

[677] T. Hahn and M. Perez-Victoria, *Automatized one loop calculations in four-dimensions and D-dimensions*, *Comput. Phys. Commun.* **118** (1999) 153–165, [hep-ph/9807565].

[678] Gmm++ library, http://download.gna.org/getfem/html/homepage/gmm/index.html.

[679] D. Maitre, *HPL, a mathematica implementation of the harmonic polylogarithms*, *Comput. Phys. Commun.* **174** (2006) 222–240, [hep-ph/0507152].

[680] Bailey, Hida, Jeyabalan, Li and Thompson, Quad-double and arbitrary precision computing packages for C++/Fortran, http://crd-legacy.lbl.gov/~dhbailey/mpdist/.

Acknowledgements

First and foremost, I would like to thank Prof. Dr. Michał Czakon for his patient guidance and continuous support throughout my scientific education. In particular, I am grateful for giving me the opportunity to join his research group and, in the course of my PhD studies, contribute to a number of involved, state-of-the-art theory calculations in a wide field of elementary particle physics. Apart from allowing me to expand my professional knowledge, these projects offered me the chance to develop a broad spectrum of technical skills and gain experience in the work with advanced numerical methods and tools, which will certainly be of great value for my future career.

Moreover, I acknowledge the fruitful collaboration with Dr. Alexander Mitov, especially appreciating his invitation for a research visit at the Cavendish laboratory at the University of Cambridge. I would also like to extend my thanks to the other collaborators that accompanied me during my PhD period, namely Prof. Dr. Mikołaj Misiak and Prof. Dr. Matthias Steinhauser as well as Dr. Peter Bärnreuther, Dr. David Heymes and Dr. Tobias Huber. In addition, I wish to thank all current and former PhD students of the Institute for Theoretical Particle Physics and Cosmology of the RWTH Aachen university for interesting discussions and a productive environment.

I am furthermore very grateful to my whole family and friends for their enduring moral support and for providing me with welcome diversions from my "physics" life. Finally, my particular thanks go to my girlfriend Kathrin for her loving encouragements and patience during this time-intensive endeavor.